Electrooxidation of Small Organic Molecules Studied by Simultaneous *in situ* ATR-FTIRS and on-line Differential Electrochemical Mass Spectrometry

Dissertation

zur Erlangung des akademischen Grades

Doktor der Naturwissenschaften

(Dr. rer. nat.)

eingereicht an der

Fakultät für Naturwissenschaften

der Universität Ulm

von

Martin Heinen

geboren am 09.04.1979 in Düsseldorf

Ulm, im Februar 2010

Die vorliegende Arbeit wurde in der Zeit von Juni 2004 bis Februar 2010 an der Universität Ulm angeferigt.

Wissenschaftlicher Betreuer: Prof. Dr. R.J. Behm

Amtierender Dekan: Prof. Dr. A. Groß

Erstgutachter: Prof. Dr. Rolf Jürgen Behm
Zweitgutachter: Prof. Dr. Werner Tillmetz
Drittgutachter: Prof. Dr. Marc Koper

Tag der Promotion: 23.11.2010

Selected Publications

In this thesis, work contained in the following papers is included.

I. **M. Heinen,** Z. Jusys, R.J. Behm, Title: "Reaction pathways analysis and reaction intermediate detection via simultaneous DEMS and ATR-FTIRS" Handbook of Fuel Cells, Vol. 5, H. A. Gasteiger, W. Vielstich and H. Yokogawa (Eds.), John Wiley & Sons, Chichester, **2008**

II. **M. Heinen**, Y.-X. Chen, Z. Jusys, R.J. Behm, Title: "In situ ATR-FTIRS coupled with on-line DEMS under controlled mass transport conditions - A novel tool for electrocatalytic reaction studies", Electrochim. Acta 52, 5634-5643, **2007**

III. **M. Heinen**, Y.-X. Chen, Z. Jusys, R.J. Behm, Title: "CO adsorption kinetics and adlayer build-up studied by combined ATR-FTIR spectroscopy and on-line DEMS under continuous flow conditions", Electrochim. Acta 53, 1279-1289, **2007**

IV. **M. Heinen**, Y.-X. Chen, Z. Jusys, R.J. Behm, Title: "Room temperature CO_{ad} desorption/exchange kinetics on pt electrodes – A combined in situ IR and mass spectrometry study", Chem. Phys. Chem 8, 2484-2489, **2007**

V. Y.-X. Chen, **M. Heinen**, Z. Jusys, R.J. Behm, Title: "Kinetics and Mechanism of the Electrooxidation of Formic Acid - Spectroelectrochemical Studies in a Flow Cell", Angew. Chemie Int. Ed. 45, 981-985**, 2006**

VI. Y.-X. Chen, **M. Heinen**, Z. Jusys, R.J. Behm, Title: "Bridge-Bonded Formate: Active Intermediate or Spectator Species in Formic Acid Oxidation on a Pt Film Electrode?", Langmuir 22, 10399-10408, **2006**

VII. Y.-X. Chen, **M. Heinen**, Z. Jusys, R.J. Behm, Title: "Kinetic Isotope Effects in complex reaction networks: Formic acid electro-oxidation", Chem. Phys. Chem 8, 380-385, **2007**

My contribution to the papers:

I. I planned and made all measurements, evaluated the data and participated in the discussion and in writing the paper

II. I developed, together with Z. Jusys, the experimental set-up, planned and made all measurements, evaluated the data and participated in the discussion and wrote the draft of the paper

III. I planned and made all measurements, evaluated the data and participated in the discussion and wrote the draft of the paper

IV. I planned and made all measurements, evaluated the data and participated in the discussion and participated in writing the paper

V. I made all measurements, evaluated the data and participated in the discussion of the paper

VI. I made all measurements, evaluated the data and participated in the discussion of the paper

VII. I made all measurements, evaluated the data and participated in the discussion of the paper

TABLE OF CONTENTS

1 INTRODUCTION 9
1.1 Background 10
1.1.1 Energy - What comes after the Oil? 10
1.1.2 Principle of Fuels Cells 11
1.1.3 Electrode reactions and Fuels 13
1.2 Introduction to electrocatalysis 15
1.2.1 Electrocatalytic reactions – complex reaction networks 15
1.2.2 Experimental limitations 17
1.3 Development within the present work 18
1.4 Outline of the present work 20

2 SPECTRO-ELECTROCHEMICAL TECHNIQUES 23
2.1 Differential Electrochemical Mass Spectrometry 24
2.2 In situ IR spectroscopy 27

3 EXPERIMENTAL 31
3.1 General set-up 32
3.2 Experimental protocols 35
3.3 Calibration and performance of the experimental set-up 39
3.4 Simultaneous measurements of several m/z ratios 43
3.5 Specific evaluation of the DEMS data 45
3.5.1 CO_{ad} coverage determination 45
3.5.2 $^{13}CO_{ad}$ exchange rate determination 46
3.5.3 Number of electrons in adsorbate stripping experiments 47
3.6 Product detection during ethanol oxidation 47
3.7 Conversion of CO_L intensity into CO_{ad} coverage 51
3.8 Integration procedure for adsorbed acetyl species 56
3.9 Chemicals 59

4 CO ADSORPTION / OXIDATION / EXCHANGE 61
4.1 In situ ATR-FTIRS coupled with on-line DEMS under controlled mass transport conditions- A Novel Tool for Electrocatalytic Reaction Studies 63
4.1.1 Introduction 65
4.1.2 Results 65
4.1.2.1 Electrooxidation of preadsorbed CO monolayer at constant potential 65
4.1.2.2 Reaction of preformed PtO with CO under open-circuit conditions 72
4.1.2.3 Potentiodynamic CO bulk oxidation 75

4.1.3 Summary 80
4.2 CO Adsorption Kinetics and Adlayer Build-up studied by Combined ATR-FTIR Spectroscopy and on-line DEMS under Continuous Flow Conditions 83
4.2.1 Introduction 85
4.2.2 Results 87
4.2.2.1 Consumption of CO upon adsorption/oxidation and CO_{ad} coverage evolution: on-line mass spectrometry (DEMS) 87
4.2.2.2 CO adlayer build-up: time-resolved *in situ* ATR-FTIRS 94
4.2.2.3 CO_{ad} coverage dependence of the IR band intensities/frequencies determined from combined ATR-FTIRS/DEMS measurements 97
4.2.3 Summary 102
4.3 Room Temperature CO_{ad} Desorption/Exchange Kinetics on Pt Electrodes – A Combined in-situ IR and Mass Spectrometry Study 105
4.3.1 Introduction 107
4.3.2 Results 108
4.3.3 Summary 115

5 ADSORPTION / OXIDATION OF FORMIC ACID 117
5.1 Kinetics and Mechanism of Formic Acid Electrooxidation – Spectro-electrochemical Studies in a Novel Flow Cell Configuration 119
5.1.1 Introduction 121
5.1.2 Results 122
5.1.3 Summary 129
5.2 Bridge-bonded Formate - Active Intermediate or Spectator Species in Formic Acid Oxidation on a Pt Film Electrode? 131
5.2.1 Introduction 133
5.2.2 Results 134
5.2.2.1 Concentration effects in formic acid oxidation – Potentiodynamic measurements 134
5.2.2.2 Potential and concentration effects on formic acid oxidation – transient potentiostatic measurement 140
5.2.2.3 The effect of adsorbed acetate on formic acid oxidation 145
5.2.2.4 Kinetic isotope effects on formic acid oxidation 148
5.2.3 Discussion 150
5.2.4 Summary 156
5.3 Kinetic Isotope Effects in Complex Reaction Networks - An in-situ IR Study on Formic Acid Electrooxidation on Pt under controlled Mass Transport Conditions 159
5.3.1 Introduction 161
5.3.2 Results 161
5.3.3 Summary 169

6 ADSORPTION / OXIDATION OF ETHANOL 171
6.1 Adsorption/oxidation of ethanol (CH_3CH_2OH) 175
6.1.1 Introduction 176
6.1.2 Results 178
6.1.2.1 Ethanol Adsorbate detection and assignment 178
6.1.2.2 Potentiostatic adsorption/oxidation of ethanol 184
6.1.2.3 Potentiostatic ethanol adsorbate stripping 189
6.1.2.4 Potentiodynamic ethanol adsorbate stripping experiments 198
6.1.3 Summary 201
6.2 Adsorption/oxidation of $^{12}CH_3{}^{13}CH_2OH$ 203
6.2.1 Introduction 204
6.2.2 Results 204
6.2.2.1 Potentiodynamic adsorption/oxidation of $^{12}CH_3{}^{13}CH_2OH$ 204
6.2.2.2 Potentiostatic adsorption/oxidation of $^{12}CH_3{}^{13}CH_2OH$ 209
6.2.2.3 $^{12}CH_3{}^{13}CH_2OH$ adsorbate stripping experiments 216
6.2.2.4 Discussion 221
6.2.3 Summary 223
6.3 Adsorption/oxidation of CH_3CD_2OH - Kinetic Isotope effects 225
6.3.1 Introduction 226
6.3.2 Results 227
6.3.2.1 Potentiostatic adsorption/oxidation of CH_3CD_2OH 227
6.3.2.2 Comparison of the reaction kinetics (CH_3CH_2OH vs. CH_3CD_2OH) 230
6.3.2.3 Potentiostatic CH_3CD_2OH adsorbate stripping 236
6.3.2.4 Adsorption behavior and formation of adsorbed acetyl species 240
6.3.3 Summary 244
6.4 Mechanism for the electrooxidation of ethanol 245

7 ADSORPTION / OXIDATION OF BI-FUNCTIONAL C2 MOLECULES 249
7.1 Introduction 252
7.2 Results 253
7.2.1 Adsorbate detection 253
7.2.2 Ethylene glycol 257
7.2.2.1 Potentiodynamic oxidation of ethylene glycol 258
7.2.2.2 Potentiostatic electrolyte exchange experiments 261
7.2.2.3 Potentiodynamic adsorbate stripping experiments 265
7.2.3 Glycol aldehyde 269
7.2.3.1 Potentiodynamic oxidation of glycol aldehyde 270
7.2.3.2 Potentiostatic electrolyte exchange experiments 273
7.2.3.3 Potentiodynamic adsorbate stripping experiments 275
7.2.3.4 Summary 277
7.2.4 Glycolic Acid 279
7.2.4.1 Potentiodynamic oxidation of glycolic acid 280
7.2.4.2 Potentiostatic electrolyte exchange experiments 282

7.2.4.3 Potentiodynamic adsorbate stripping experiments 285
7.2.4.4 Summary 287
7.2.5 Glyoxal 289
7.2.5.1 Potentiodynamic oxidation of glyoxal 290
7.2.5.2 Potentiostatic electrolyte exchange experiments 292
7.2.5.3 Potentiodynamic adsorbate stripping experiments 295
7.2.5.4 Summary 297
7.2.6 Glyoxylic acid 299
7.2.6.1 Potentiodynamic oxidation of glyoxylic acid 300
7.2.6.2 Potentiostatic electrolyte exchange experiments 302
7.2.6.3 Potentiodynamic adsorbate stripping experiments 305
7.2.6.4 Summary 307
7.2.7 Oxalic acid 309
7.2.7.1 Potentiodynamic oxidation of oxalic acid 310
7.2.7.2 Potentiostatic electrolyte exchange experiments 312
7.2.7.3 Potentiodynamic adsorbate stripping experiments 314
7.2.7.4 Summary 316
7.3 Comparison of CO_{ad} formation rates 317
7.4 Summary 321

8 SUMMARY / ZUSAMMENFASSUNG 323
8.1 English version 324
8.2 Deutsche Fassung 329

9 Outlook 335

References 339
Abbreviations and Acronyms 369
Lebenslauf 371
Veröffentlichungsliste 373
Danksagung 379
Erklärung 381

1 INTRODUCTION

1.1 Background

1.1.1 Energy - What comes after the Oil?

In the International Energy Outlook (IEO2008) projection, the total world consumption of the marketed energy is projected to increase by 50 percent from 2005 to 2030 {OIL09}. Today's world energy supply is distributed between various energy sources: Liquid fuels, mainly oil (~36%), coal (~25%), gas (~23%), renewables (~9%), nuclear power (~7%){OIL09}. The fact that fossil fuels are dominating (~84%) is challenging the society in two ways, i) the fossil energy sources are finite and ii) the CO_2 emission from these fuels contributes significant to the global warming, via the greenhouse effect {OIL09B}. Consequently, there is a strong demand to substitute fossil fuels by other energy sources, which are non polluting and sustainable, like hydroelectric facilities, wind, solar, geothermal, municipal solid waste and biomass, which are summarized as the so-called "Renewables". These sources have the potential to decrease the consumption of coal and gas, which are mainly used for power generation and contribute to about 70% of the world electricity generation. In order to reduce the dependence on oil, which is used to about 80% for transportation, ways need to be found to use renewable energy sources also for mobile applications. One possibility is the use of electric vehicles that are powered by electricity stored in a battery. Batteries are used in several applications today and the technology is well established. However, they are heavy and their range is up to now limited to about 200 kilometers before they have to be recharged, which is time consuming. One often mentioned possible solution using electricity for transportation is the hydrogen society "dream scenario" {CRAB04}, where hydrogen produced from renewable sources is used as energy carrier in fuel cell systems, with zero or near zero emissions. The biggest challenge for this scenario is i) the production of hydrogen in a sustainable way, ii) the build-up of a novel infrastructure for the distribution of the hydrogen to the consumers, and iii) reliable and cheaper fuel cell systems with improved life time and efficiency.

Following a very general scheme for any kind of "catalysis", the transition from the "fossil energy source age" to the "Hydrogen dream scenario" is believed to take time due to the high "activation barrier". In a possible "transition state", which is more or less environmentally

friendly, fuels such as biofuels (ethanol, methanol), natural gas or hydrogen produced from, e.g., fossil fuels {RAME06}, can have some advantage by being less cost intensive, helping to establish reliable and cheaper fuel cell systems with improved life time and efficiency. “Catalysts” for a faster transition to the “hydrogen dream scenario” are i) high oil prices, by making alternatives to the conventional combustion engine more competitive, ii) regulations by governments steering the development in the industry in a sustainable direction, and iii) global warming requires significant reduction of the CO_2 emissions. These “catalysts” in turn result in an enhanced research in the field of fuel cells.

1.1.2 Principle of Fuels Cells

A fuel cell has close similarities to a battery, but in contrast to batteries the fuel cell does not have to be recharged but operates as long as the fuel is supplied. Whereas in batteries the electrodes are changed during charging/discharging, the fuel cell electrodes remain unchanged and only catalyze the conversion of the fuel directly into electrical energy. Therefore, batteries are energy storage systems and fuel cells are energy converters.

The principle of the fuel cell was discovered by German scientist Christian Friedrich Schönbein in 1838 and published in one of the scientific magazines of the time. Based on his work a forerunner of modern fuel cells was proposed and put into operation by Sir William Grove already in 1839, over 150 years ago. The idea was based on the fact that a Faradaic current can split water into hydrogen and oxygen. Sir W. Grove tried reversing the reaction generating electricity and water by combining hydrogen and oxygen, the basic principle of a fuel cell. Grove proved that his fuel cells worked, but as he had no entrepreneurial inclinations, and due to the development of the electrical generator by Werner von Siemens, the invention slumbered for more than 120 years. The first commercial use of fuel cells proceeded only within the Gemini project in 1961.

As mentioned before, finite fossil energy sources and global warming strongly catalyzed the further development of fuel cell systems and, a schematic sketch of a polymer electrolyte fuel cell (PEM-FC) is shown in Fig. 1.

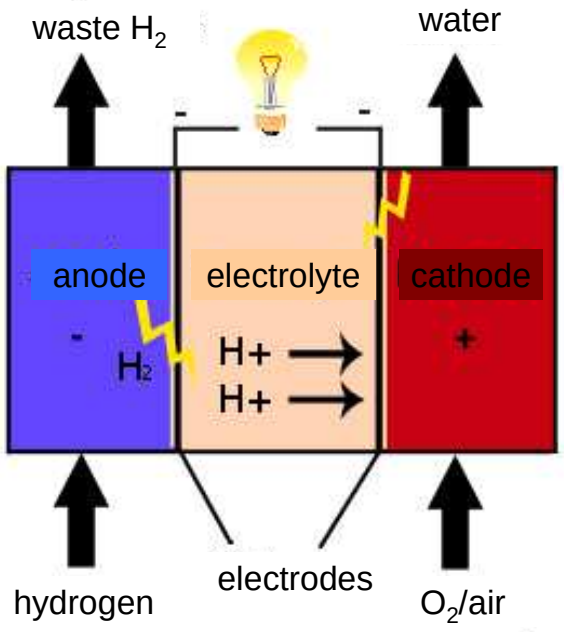

Fig. 1: Schematic drawing of a PEM-FC, for explanations see text. (Figure taken from {WBZU09B})

This type of fuel cell is presented since it has the biggest potential for automotive and mobile applications. Other types of fuel cells mainly differ in the electrolyte and operating conditions {WBZU09}. On the anode side, hydrogen flows in and a catalyst, most often carbon supported platinum (Pt/C), facilitates the dissociation of the hydrogen gas into hydrogen ions and electrons on the electrode surface (see below). The membrane, i.e. the electrolyte, in the middle of the cell has two functions, i) to separate the hydrogen gas and oxygen gas flow and ii) to allow that the hydrogen ions can pass through the membrane, reaching the cathode side. At the Pt/C cathode the hydrogen ions react with oxygen and electrons, producing water. The electrons flow from the anode to the cathode side via an electrical circuit with an electronic load. The cell reaction and the reactions at the anode and the cathode are displayed below:

Cell reaction: $H_2 + ½\ O_2 \rightarrow H_2O$

Anode: $H_2 \rightarrow 2\ H_{ad}$

$2H_{ad} \rightarrow 2H^+ + 2e^-$

Cathode: $O_2 \rightarrow 2O_{ad}$

$2O_{ad} + 4\ e^- + 4\ H^+ \rightarrow 2\ H_2O$

However, even in the most simply case of a H_2/O_2 fuel cell reaction, water is not the only product formed at the cathode. In model studies on the electrocatalytic oxygen reduction reaction (ORR) it could be shown that under certain conditions hydrogen peroxide is formed as a reactive intermediate {DAMJ67}{COLM07C}{SCHN07}, causing severe corrosion of the carbon support of the Pt/C catalyst and degradation of the membrane {LACO03}{MITT06}. This in turn results in a performance loss and reduced long term stability. These findings clearly underline the necessity to perform model studies on fuel cell relevant electrocatalytic reactions to gain a better understanding of the fuel cell performance.

1.1.3 Electrode reactions and Fuels

Since the polymer electrolyte separates the anode and the cathode and the electrical load is connected via and external load the anodic oxidation and the cathodic reduction can take place separately, so called “half-cell reactions”, enabling a direct conversion of chemical into electrical energy. As oxidizing agent at the cathode either oxygen from air, in acid electrolytes, or clean O_2, in alkaline media to avoid the formation of carbonates in the electrolyte, is used. The simplest fuel that can be oxidized at the cathode is clean hydrogen, which can be easily applied in stationary fuel cell systems. However, due to its poor energy to volume ratio hydrogen has either to be compressed at very high pressures (up to 700 bar) or cooled to down to temperatures below -270 °C to achieve a suitable range in automotive applications. Nowadays the compression of hydrogen is state of the art, although it is energy extensive and reduces the overall efficiency of the fuel cell system. Furthermore, new infrastructure of fuel stations must be developed for the distribution of the hydrogen fuel. Other possible fuels, such as methanol or ethanol have a much higher energy density and in addition, both fuels can be distributed via the already existing infrastructure for liquid fuels, circumventing main drawbacks in the “hydrogen dream scenario” (see also 1.1). The aforementioned fuels can either be transformed on-board to hydrogen via preferential oxidation (e.g. indirect alcohol fuel cell IAFC) {GEIS01} or directly electrooxidized at the anode (direct alcohol fuel cell DAFC). In the IAFC case the complexity of the whole system, i.e., hydrogen generation and removal of CO residues formed during the hydrogen production, is largely increased especially when the dynamic requirements of an automobile are taken into account. In the DAFC case, the electrocatalysis of the alcohol oxidation is crucial since the overall efficiency and the power output depend strongly on the completeness of the conversion to CO_2 and the kinetics of the alcohol electrooxidation. With the present state-of-

the-art electrocatalysts, DAFC`s are far from being used in mobile applications, but are already commercially available as power supply for portable and stationary applications.

To illustrated the electrocatalysis relevant for the aforementioned fuel cell systems the I/U curves for the half-cell reactions at the anode and the cathode of a H_2/air-PEM-FC and a DAFC, respectively, are shown in Fig. 2.

The voltage difference between the anode and the cathode is equivalent to the cell potential (in the absence of ohmic losses), which according to thermodynamic data is equivalent to 1.23 V. The dashed lines represent the “ideal” curves for the hydrogen oxidation reaction (HOR) and the oxygen reduction reaction (ORR), where ideal means that no kinetic losses occur. For the HOR on a Pt/C catalyst only negligible kinetics restrains are observed and nearly the “ideal” behavior is found. The overpotential (difference between “ideal” and measured voltage) for the ORR is about 300 to 400 mV, resulting in an overall cell voltage of about 800 to 900 mV under operating conditions. The overpotential in oxygen reduction is mainly attributed to the formation of PtOH and PtO at high electrode potentials, which is inactive for the ORR. For further details on the ORR, the reader is referred to a recent review {NORS04A}. The cell voltage is further strongly reduced when CO contaminated H_2 or alcohols are used as a fuel, due to an increased over-potential at the anode, which in turn significantly lowers the efficiency of the fuel cell. The over-potential is mainly attributed to

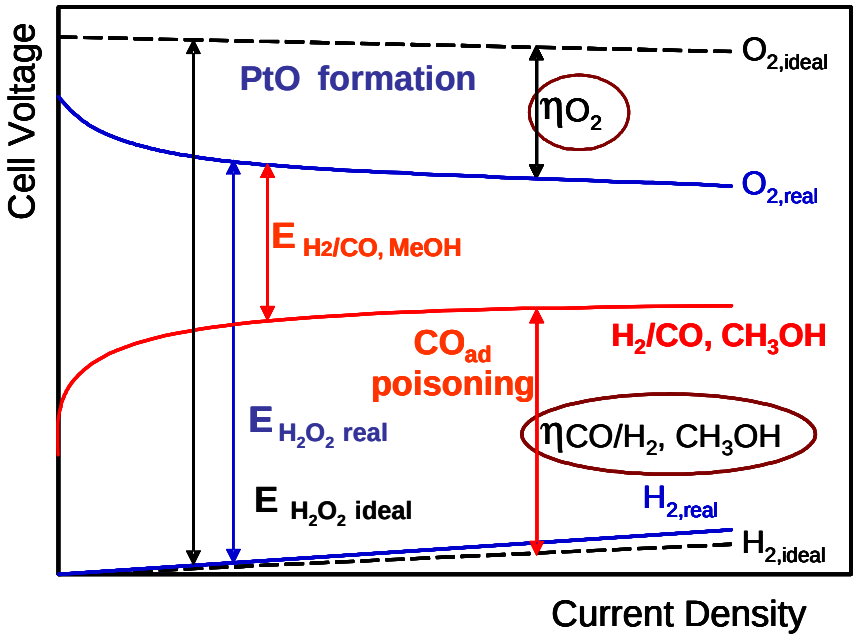

Fig. 2: Schematic U/I curve for a PEM-FC fed with different fuels. For details see text.

adsorption of CO on the Pt catalyst either from the gas phase or formed as an intermediate during the alcohol oxidation, blocking active site for the hydrogen and/or alcohol oxidation.

In the above paragraph, the general understanding of the drawbacks in an effective fuel cell operation and the electrode processes occurring at the cathode and the anode were presented. However, many questions regarding the detailed mechanistic and kinetic understanding of the surface processes in electrocatalytic reactions remained unsolved. These are in the main focus of the present work. Prior to the discussion of the intrinsic processes, in section 1.2 general aspects important for the understanding of electrocatalytic reactions, as well as experimental techniques and limitations for kinetic and mechanistic studies are presented.

1.2 Introduction to electrocatalysis

1.2.1 Electrocatalytic reactions – complex reaction networks

Catalytic and electrocatalytic reactions generally involve several elementary reaction steps, which can occur sequentially and/or in parallel. This often results in a reaction network. The rates of the individual elementary surface reactions and surface processes will depend sensitively on the nature and coverage of the adsorbed species, in addition to the respective reaction barriers and preexponential factors, and these in turn will be controlled by all participating reactions in the network. The adsorbed species may act as reactants, reaction intermediates, as inert, surface blocking spectator species, or even as catalyst poisons. Examples for such reaction networks are, e.g., the oxidation of the C_1 molecules methanol, formaldehyde and formic acid (see, e.g., the formal reaction scheme by Bagotzky {BAGO77}). The contributing partial reactions were discussed in detail recently {HOUS06}{JUSY08}. But also simpler reactions such as the O_2 reduction reaction with its two different pathways, the four-electron pathway leading to H_2O and the two-electron pathway leading to H_2O_2 {WROB64}, belong to this category.

In all of these cases, the microscopic understanding of the reaction process as well as a proper description of the reaction kinetics require a detailed knowledge of the nature and coverage of the adsorbed species present on the surface under reaction conditions. Furthermore, the contributions of the different partial reactions (partial reaction rates) need to be known, which are not accessible from the overall reaction rate measured by the Faradaic current. In electrocatalytic reactions, these two requirements can be met, e.g., by *in situ* spectroscopic measure-

ments performed in parallel to the electrochemical measurement. Examples of methods sensitive to adsorbed species include vibrational spectroscopy such as infrared spectroscopy {BEDE92}{IWAS97}{SUN98A}{OSAW02}{RODE03}, Raman spectroscopy {ZOU99B} {TIAN00B}{LUO01A}{LIU07}{REN08} or non-linear techniques (sum frequency generation - SFG) {TADJ96A}{DEDE00}{CHOU03}{LU05}, or electrochemical quartz crystal microbalance measurements {WILD94}{VISS97}{JUSY99}{UCHI02}{JERK04} {SANT04A}{STAL06}. In addition, the coverage of adsorbates can also be derived from measurement using radioactive molecules {CORR88A}{KOLI98}. Volatile reaction products can be detected on-line by mass spectroscopy (differential electrochemical mass spectrometry – DEMS {BRUC71}{WOLT82}{WOLT84}{IWAS90}{TORR03} {BALT04}) by spectroscopic techniques (IR detection in transmission mode {GAO04A}{HUAN02}{LIN97}{SANI02}) or, in the case of electroactive species, by electrochemical measurements using a second electrode for detection, as it is done in rotating ring disk measurements {FRUM59}{TARA83}{ADZI98}{MARK02} or in dual electrode flow cell measurements {GERI65}{COMP88}{JUSY04A}{WAKA05}. In addition, chromatographic techniques can be applied for off-line analysis of the reaction products {HITM96}{DAIL98}{TORR03}{BATI04A} or further details about the various techniques and their applications to electrocatalytic reaction studies the reader is referred to several reviews on this topic {IWAS94B}{IWAS97}{SUN98A}{NART03A}{RODE03}, {TORR03}{BALT04} a short description of the techniques applied in the present thesis, namely *in situ* IR spectroscopy and on-line DEMS, will be given in Chapter 2.

Furthermore, another aspect has to be considered when investigating complex reaction networks. It is well known from heterogeneous Catalysis that the product distribution in a catalyzed reaction approaches the equilibrium distribution with decreasing space velocity or increasing contact time, i.e., with increasing amount of catalyst and/or decreasing reactant flow rate {THOM97}. Similar principles apply also for electrocatalytic reactions, and recent studies on massive electrodes and on catalyst thin-film electrodes have indeed demonstrated considerable effects of catalyst loading and electrolyte flow rate on the product distribution in methanol oxidation {WANG01D}{JUSY03D}, ethanol oxidation {WANG04B}, or ethylene glycol oxidation {WANG06Q}, with an increasing amount of more completely oxidized/reduced reaction products for higher catalyst loadings or lower flow rates. This was explained by the so-called ‘desorption – re-adsorption – further reaction’ mechanism {JUSY03D}, {SCHN07}, {SEID08}. According to this mechanism, incompletely oxidized (re-

duced) reaction products such as formaldehyde or formic acid in methanol oxidation or hydrogen peroxide in O_2 reduction can re-adsorb after desorption into the electrolyte and undergo further reaction. In this mechanism, the probability for re-adsorption and further reaction, and hence for the formation of higher oxidation products, depends sensitively on the transport characteristics of the reactive species in the vicinity of the electrode {SEID08}. Very recently, transport effects were shown to play an important role also for oxygen reduction, leading to rather high H_2O_2 product yields under conditions of high space velocities {CHEN04H}·{SCHN07}·{SEID08}. These observations clearly underline the need to perform electrocatalytic measurements under well-defined transport conditions, in particular at controlled, enforced electrolyte flow.

1.2.2 Experimental limitations

As described above measurements of electrocatalytic reactions should in general be performed under well-defined transport conditions, and these conditions need to be identical if the results of measurements using different spectroscopic techniques shall be compared. This has consequences in particular for *in situ* IR experiments, which are mostly performed in a thin-layer geometry, with a thin electrolyte layer between electrode and an IR transparent window (typical thickness < 10 µm) {BEDE92}{IWAS97}{SUN98A} (see also Chapter 2.3). In this case, enforced electrolyte flow is essentially impossible and transport of reactants and products is possible only by diffusion. Hence, these species are essentially trapped in the thin electrolyte layer between working electrode and window. The accumulation of reaction intermediates and reaction products as well as the depletion of reactants in the thin electrolyte film can lead to considerable modifications in the reaction characteristics compared to electrochemical measurements performed in a different geometry {IWAS97}.

In recent years, various attempts have been made to overcome these limitations and to perform *in situ* IR measurements under defined flow conditions in an external reflection configuration {NICH88}{ROTH91}{LU05}{STAM05A}{ZHOU05F}{KUZU08} as well as in an internal reflection configuration {CHEN04F}·{HEIN04}·{MORS08} (see also Chapter 2.2). Other approaches involve the use of SFG techniques {LU05}.

A further significant advance in the mechanistic understanding of the reaction mechanism and the evaluation of complex reaction kinetics would be possible, if the *in situ* IR spectroscopy measurements could be combined with simultaneous on-line DEMS, under controlled

electrolyte transport conditions. This would not only provide time-correlated information on the nature and concentration of adsorbed reaction intermediates/side products (FTIRRAS) and volatile reaction educts/intermediates/products (DEMS), obtained under exactly identical reaction conditions, but also allow an absolute coverage determination by exploiting the quantitative nature of the DEMS measurements. Due to the high sensitivity of the DEMS measurements, and since they are not affected by pseudo-capacitive effects or substrate oxidation/reduction, the coverage determination by DEMS is very precise. Thus, combined DEMS-IR experiments would in many cases allow an exact determination of the intensity-coverage relation of the adsorbed species, which is important for a quantitative evaluation of IR measurements as basis for the mechanistic and kinetic interpretation. Due to specific requirements and restrictions for the respective methods and for the electrochemical cell design (see 2.2), this challenging task had not been solved up to now.

In response to these considerations a spectro-electrochemical set-up was developed in the present thesis, which allows for the first time to perform *in situ* IR spectroscopy (adsorbed species), on-line DEMS measurements (volatile reaction intermediates/products) and electrochemical measurements at the same time in a flow cell, under well-defined transport conditions {HEIN07}{FUHR08}. Measurements performed with this set-up contain the full information on adsorbed species as well as volatile reaction intermediates and (by)-products at each time, which is required for an understanding of complex reactions networks.

1.3 Development within the present work

This work aims at the mechanistic and kinetic understanding of the electrocatalysis of low-temperature Fuel Cell reactions, which as described above, has to a large extent been facilitated by the development and application of hyphenated techniques, which allow the simultaneous sensing of the electrochemical properties in parallel to the acquisition of other parameters by an additional, coupled physico-chemical probing method. During my diploma thesis, *in situ* ATR-FTIR spectroscopy was successfully coupled with an electrochemical flow cell, which in this reflection configuration allowed for the first time i) transient, time-resolved spectro-electrochemical measurements upon sudden exchange of the electrolyte under potential control, (ii) spectro-electrochemical adsorption/stripping measurements of non-volatile species, under well-defined mass transport conditions {HEIN04}{CHEN04F}. With this set-up, systematic measurements on the adsorption/oxidation of ethanol, acetaldehyde and

acetic acid were performed and the results were presented in my diploma thesis. The *in situ* ATR-FTIRS measurements were then extended during the PhD work to other fuel cell relevant molecules, such as methanol, formaldehyde, formic acid (in cooperation with Y.X. Chen and Z. Jusys) as well as ethylene glycol and its oxidative intermediates glycol aldehyde, glycolic acid, glyoxal, glyoxylic acid and oxalic acid.

The experimental set-up for *in situ* ATR-FTIR spectroscopy was then further improved and coupled with on-line DEMS, which delivers, in addition to the nature and concentration of adsorbed reaction intermediates/side products (FTIRRAS), quantitative data on the formation/consumption of volatile reaction educts/intermediates/products (DEMS), obtained under exactly identical reaction conditions (see previous section). The first experiments with this combined ATR-FTRS/DEMS set-up were focused on the adsorption/oxidation/exchange of CO, which was detected as adsorbate in the oxidation of the small organic molecules mentioned above. From these simultaneous ATR-FTIRS/DEMS measurements, amongst other, a direct, non-linear correlation between the CO_{ad} intensity and the CO_{ad} coverage was obtained. Furthermore, potential dependent structural changes in the CO_{ad} layer could be followed and explained. Both results are crucial for a quantitative analysis of the role of adsorbed CO in the course of small organic molecule oxidation.

This set-up was then used to study the adsorption/oxidation of

i) methanol and formaldehyde, which was mainly done by Y.X. Chen

ii) ethanol (own work), presented and discussed in Chapter 6

iii) ethylene glycol and its oxidative intermediates, presented and discussed in a diploma thesis Johannes Schnaidt)

iv) glycerol and its oxidative intermediates (Zulassungsarbeit Dorothee Denot)

v) glucose (diploma thesis Stefanie Eisele)

1.4 Outline of the present work

The reactions presented and discussed within this work are the CO adsorption/oxidation/desorption kinetics and the oxidation of formic acid, ethanol as well as ethylene glycol and its oxidative intermediates, namely glycol aldehyde, glycolic acid, glyoxal, glyoxylic acid and oxalic acid (see also above).

Before the results of the measurements are presented, I will provide an overview about the spectroscopic techniques applied in this thesis, namely on-line DEMS and in situ IR spectroscopy (Chapter 2). A description of the function, the possible experimental procedures and the performance of the novel combined ATR-FTIRS/DEMS set-up, which was entirely built during this thesis, is given in Chapter 3. In addition, experimental details are presented and discussed in this chapter.

Chapter 4 deals with the adsorption/oxidation/exchange of CO, which can be regarded as the "drosophila" in Surface Science in general and in electrocatalysis in particular. The first subsection demonstrates the successful build-up of the combined ATR-FTIRS/DEMS set-up, using CO bulk oxidation and CO_{ad} stripping as example (section 4.1, {HEIN07}). One of the simplest processes in an electrocatalytic reaction is the molecular adsorption of reactants, and the adsorption of CO on a Pt film electrode will be used as an example for the manifold information available from such combined measurements (section 4.2, {HEIN06B}). Somewhat more complicated, but highly relevant for electrocatalytic reactions, is the simultaneous adsorption and desorption of adsorbates in an adsorption-desorption equilibrium. This is illustrated in section 4.3, using the exchange of adsorbed isotope labeled ^{13}CO on a similar electrode by ^{12}CO as example (see section 4.3, {HEIN06}. In all cases, the well-defined transport conditions in the electro-chemical cell and the ability to rapidly exchange the electrolyte, e.g., by switching from CO-free to CO-containing electrolyte or from ^{13}CO to ^{12}CO containing electrolyte, is exploited.

The description and discussion of *in situ* ATR-FTIRS results on Formic acid oxidation are given in Chapter 5. Subsection 5.1 focuses on the quantification of the indirect pathway, in which formic is oxidized to CO_2 via adsorbed CO {CHEN04F}, whereas in section 5.2 the role of adsorbed formate in the course of formic acid oxidation is discussed {CHEN06K}. This section contains concentration dependent measurements, potentiostatic adsorption transients comparing the reaction characteristic of HCOOH and DCOOH and a comparison of

the formate intensity during formic acid oxidation in the presence of acetic acid. By comparing the rate for CO formation resulting from formic acid and deuterated formic acid, conclusions on the rate limiting step for the CO_{ad} formation will be derived in section 5.3 {CHEN07B}.

In Chapter 6, combined ATR-FTIRS/DEMS results on the electrooxidation of ethanol are presented and discussed. In section 6.1, I will present adsorption transients and adsorbate stripping experiments using unlabeled ethanol (CH_3CH_2OH), focusing on the detection and the assignment of the ethanol related adsorbates. In section 6.2 and 6.3 similar measurements will be presented for the adsorption/oxidation of carbon labeled ($^{12}CH_3{}^{13}CH_2OH$) and deuterated (CH_3CD_2OH) ethanol, respectively. Isotope labeling has three main advantages: i) the wavenumber of the adsorbed species is sensitive to isotope labeling and the change of the wavenumber reveals information on the nature of the adsorbate, ii) carbon labeled ethanol allows to distinguish which carbon atom is converted to CO_{ad} and oxidized to CO_2, and iii) kinetic isotope effects (KIE) contain information on the rate limiting step. The results presented and discussed in this Chapter are summarized in a detailed mechanism for the electrocatalytic oxidation of ethanol on a Pt electrode in acidic solution (section 6.4).

In Chapter 7, I will present and discuss the *in situ* ATR-FTIRS results on the adsorption and oxidation of ethylene glycol and its oxidative intermediates glycol aldehyde (GA), glycolic acid (GS), glyoxal (GOA), glyoxylic acid (GOS) and oxalic acid (OS). For each molecule, first the adsorbates detected in potentiostatic electrolyte exchange experiments will be assigned and the temporal development of the CO_{ad} formation is discussed. Subsequent adsorbate stripping experiments reveal further mechanistic details. Finally, the influence of the functional group on the rate for the C-C bond splitting is discussed.

In chapter 8, I will summarize the entire work in English and German language.

2 SPECTRO-ELECTROCHEMICAL TECHNIQUES

In this Chapter, I will discuss the general principle of the spectro-electrochemical techniques used in this work. Details concerning the instrumentation of the combined ATR-FTIRS/DEMS set-up developed in the framework of this thesis are presented and discussed in Chapter 3.

2.1 Differential Electrochemical Mass Spectrometry

The combination of electrochemical measurements and on-line mass spectrometry for product/educt analysis is a powerful tool to study electrochemical processes such as the oxidation of small organic molecules on various electrodes, e.g., polycrystalline Pt {WOLT84}{IWAS86}{WASM90}{JUSY01D}, carbon supported catalysts {JUSY08} or single crystal electrode {HART91}{BALT93}{SCHM94}. The possibility of coupling mass spectrometric product detection with an electrochemical cell was first suggested by Bruckenstein and Gadde {BRUC71}. In the first experimental set-up, a porous Pt electrode was used, which was on the one side in contact with the electrolyte while the other side was connected to the high vacuum chamber and the mass spectrometer (MS). Volatile reaction products formed at the Pt working electrode could pass through the electrode and be analyzed via the mass spectrometer. In the experimental set-up, called electrochemical mass spectrometry (EMS), however, the time delay between the product formation and the mass spectrometric detection was about 10 to 20 seconds {BRUC71}. Wolter et al. improved the EMS system by employing a porous Teflon membrane and a differentially pumped mass spectrometric chamber using two turbo-molecular pumps {WOLT84}. The time for transfer of the volatile reaction products to the mass spectrometric detection was about 1 second and the authors called the set-up “on-line Differential Mass Spectrometry (DEMS)”. Details of i) the interface between electrolyte and vacuum, ii) the vacuum system and iii) of cell types and working electrodes of the DEMS set-up are given in the following:

i) The interface between electrolyte and vacuum

The most crucial part of the DEMS set-up is the interface between the liquid electrolyte and the vacuum system, which on the one hand has to prevent liquid water from penetrating into the MS chamber, but on the other hand should allow reaction products to pass through. Therefore the interface normally consists of a porous Teflon membrane that due to its hydrophobicity is a barrier for the electrolyte but due to its porosity allows volatile species to

permeate into to MS chamber. The critical pore radius r, to avoid liquid water to be dragged into the MS chamber, depends on the surface tension of water and the contact angle between water and the Teflon membrane and was calculated to be r < 0.8 µm {WOLT84}. Typical membranes applied for DEMS measurements have pore radii of about 0.02 to 0.09 µm, thicknesses between 50 and 150 µm and a porosity of about 50% {SCHM00}. For mechanical stability, the Teflon membrane is supported by a highly porous stainless steel or a glass frit.

ii) The vacuum system

The vacuum system of a typical DEMS set-up is schematically illustrated in Fig. 3. It consists of two chambers that are both evacuated by turbo-molecular pumps, respectively. The electrochemical cell is connected via a porous Teflon membrane (see above) and an open-close valve (V) to the inlet chamber (IC) of the vacuum system. Depending on the pumping rate of the installed turbo-molecular pump and the area, thickness and porosity of the Teflon membrane, the pressure in the first chamber is about 10^{-3} to 10^{-4} mbar under operating conditions. Most of the gases (mostly water molecules) entering the vacuum system is efficiently pumped in this chamber. Since the pressure in the IC is too high for operating a mass spectrometer (MS) a second chamber (AC), in which the gases can be analyzed, is connected to the IC via small aperture (A). Depending on the area of the aperture and the pumping rate of the second TMP, the pressure in the AC is about 10^{-6}, which is sufficiently

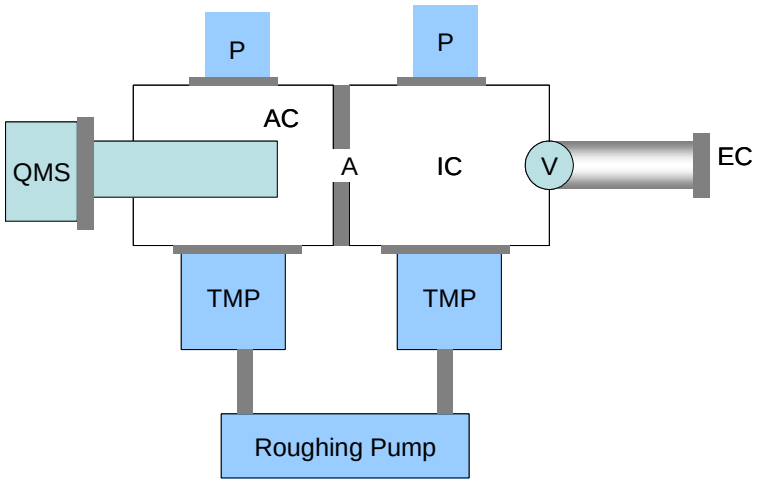

Fig. 3: Schematic representation of the vacuum system of a standard DEMS-setup. EC = electrochemical cell, V = open close valve, P = vacuum gauge, TMP = turbo molecular pump, QMS = quadrupole mass spectrometer, IC = inlet chamber, AC = analyzing chamber, A = Aperture

low to analyze the gases penetrating through the A from the IC via a mass spectrometer. Quadrupole mass spectrometers are usually used due to their simple instrumentation, high time resolution and the possibility to measure several masses in one experiment. They consist of an electron beam ionization, which converts the molecules into ions that are then separated by the quadrupole analyzer according to their mass to charge ratio (m/z) and detected by an ion collector, either a Faraday cup or a Channeltron. The ion source of the MS should be positioned close to the aperture to ensure that the highest numbers of molecules possible are ionized. For further details about the vacuum system see also refs. {TORR03}{BALT04}.

iii) Cell types and working electrodes

To achieve a small time delay between the electrochemical product formation and the mass spectrometric detection as well as to optimize the collection efficiency, i.e., the ratio of the molecules reaching the inlet chamber and the number of molecules formed at the electrode, several cell designs can be used.

For measurements with porous electrodes, a porous catalyst is sputtered or painted as a metallic lacquer onto the Teflon membrane, which is supported by a porous stainless steel frit, embedded into a stainless steel part that connects to the inlet chamber. The membrane is pressed onto the stainless steel parts by a Teflon part so that only volatile molecules can pass though the membrane into the vacuum system. An electrochemical glass cell is positioned on top of the inlet part and pressed against the Teflon part via tightening rings (for details and a schematic drawing see also {WOLT84}{TORR03}). If the volume of the glass cell is small, this set-up stands shows a very high collection efficiency, which depending on the measurement time can reach values up to 100%. A drawback, however, is that the mass transport to the electrode surface is controlled solely by diffusion. To work under defined mass transport conditions, experimental DEMS set-ups are described in the literature using rotating devices, as for example by Wasmus et al. {WASM90}. In their set-up, the electrode system can be rotated, which results in mass transport conditions identical to the well described rotating disc electrode set-up {WASM90}. But since the product molecules are flushed away from the catalysts surface, the collection efficiency decreases significantly. The first cell design allowing on-line DEMS measurements under well defined mass transport condition at high collection efficiency was introduced by Jusys et al., employing a dual thin-layer compartment flow cell {JUSY99}. This is schematically shown in Fig. 4.

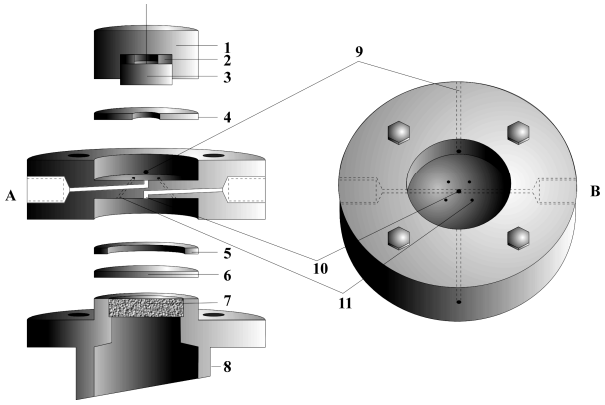

Fig. 4: Thin-layer dual flow-cell for on-line DEMS measurements. (1) Kel-F support, (2) Kalrez gasket, (3) glassy carbon support, (4,5) Teflon gaskets, (6) porous Teflon membrane, (7) stainless steel frit, (8) stainless steel connection to MS, (9) capillaries, (10) inlet-outlet capillaries, (11) connection between first and second compartment. (Figure taken from {JUSY99})

Molecules formed in a first compartment by an electrochemical reaction are flushed into a second compartment, where the electrolyte flows along a porous Teflon membrane, similar to the above mentioned designs, allowing volatile molecules to pass through the membrane into the vacuum system. In this set-up, the inlet system to the vacuum and the working electrode are separated, which in addition to the well defined mass transport conditions and the high collection efficiency, enables the use of massive electrodes, necessary, e.g., for electrochemical measurements on single crystals, or the combination of on-line DEMS with *in situ* ATR-FTIR spectroscopy (see also following section), where the working electrode needs to be deposited onto an IR transparent prism. This versatile dual thin-layer flow-cell was modified within the framework of this thesis and will be described in more detail in Chapter 3. For further information about the development of the DEMS technique, the reader is referred to review articles about this technique {BALT04}.

2.2 In situ IR spectroscopy

For the detection of adsorbed intermediates and the adlayer structure of a catalyst during the reaction, in situ Infrared (IR) spectroscopy is a very suitable technique. In principle, it can identify molecules with dipolar groups through their characteristic IR absorption frequency in the IR spectra '{NICHOLS1992A}{IWAS97}{RYCZ01}. In the case of adsorbed species, the IR spectra also contain information about properties such as the bonding configuration, the coordination of substrate atoms and the local chemical environment including vicinal molecules of the same or different species {RODE03}. The main experimental problem for

applying in situ IR spectroscopy to electrochemical systems is the strong absorption of the IR radiation in/by the electrolyte. To minimize this problem, two in principle different reflection configurations for the *in situ* IR spectroscopy have been developed, namely the external and the internal reflection configuration {RODE03}, which are schematically shown in Fig. 5.

External reflection configuration:

In the external reflection configuration, which was first applied by Bewick et al. for electrochemical measurements {BEWI82}, the IR beam is reflected on the metal/electrolyte interface from the solution side. Therefore, the incident and the reflected IR beam have to cross an IR transparent window and the solution layer between the window and the surface. To minimize the absorption from the solvent, measurements in this reflection configuration have to be performed in a thin-layer cell, where the thickness of the electrolyte layer between the electrode surface and the IR transparent window is limited to a few micrometers.

Internal reflection configuration – attenuated total reflection configuration

In the case of an internal reflection configuration, an IR transparent prism, with a high refraction index is used. The actual substrate/catalyst is deposited as a thin film on the reflecting side of the prism. The IR beam passes through the prism from the back side and is totally reflected at the prism/metal interface. An evanescent wave passes through the metal and interacts with the species, which are adsorbed on the metal surface or close to the surface.

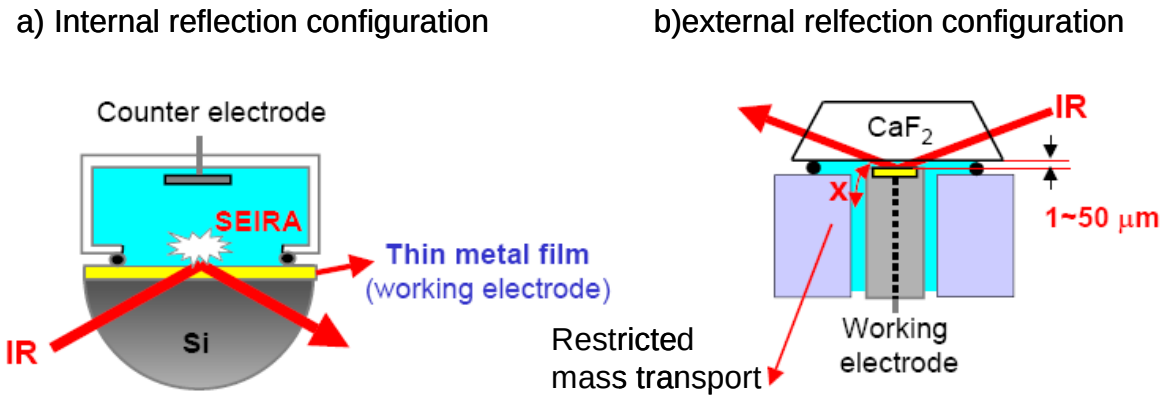

Fig. 5: Schematic drawing of a) internal and b) external reflection configuration. For details see text.

External vs. Internal reflection configuration

Both reflection configurations described above have their advantages and limitations compared to each other, which will be discussed in the following. Since in the external reflection configuration the IR beam penetrates through the electrolyte layer, adsorbates as well as species in the electrolyte can be detected, which is of advantage if the generation or the consumption of bulk species is of interest. On the other hand, it is cumbersome to distinguish between the bulk species and adsorbates {IWAS97}'{SUN99}. Furthermore, the thickness of the electrolyte layer between the electrode and the IR window is limited to about 10 μm in order to keep spectral contributions from the electrolyte at a tolerable level. Under these conditions, mass transport in the thin-layer gap is practically inhibited, which may result in strongly misleading conclusions on the reaction process due to the depletion of reactants as well as accumulation and possibly re-adsorption of by-products{IWAS97}. Furthermore, the electrochemical response in such measurements suffers from Ohmic losses induced by the resistance of the thin electrolyte layer. Therefore, dynamic electrochemical measurements are hardly possible. Consequently, the IR measurements in a thin-layer configuration are unsuitable for kinetic measurements {RODE03}. These are better performed in the internal reflection configuration, where the mass transport is not impeded and Ohmic loss effects are largely reduced. An additional advantage of the latter configuration is the enhancement of IR absorption on the rough metal films used as working, which according to a publication by Osawa results in a 10 to 50 times higher sensitivity {OSAW97A}'{OSAW02}. This technique is also known as “surface enhanced Infrared Absorption spectroscopy” (SEIRAS) and stands out due to the much higher surface sensitivity compared to usual IR spectroscopy. The consequences for electrochemical measurement are twofold: on the one hand, the detection limit is strongly reduced and on the other hand the acquisition time for the IR spectra can be significantly shortened (less averaging necessary), which makes the SEIRAS the technique of choice for time-resolved monitoring of reaction processes at surfaces and interfaces {OSAW97A}'{OSAW02}. Unfortunately, the thin metal films required for the internal reflection configuration are often unstable and with a few exceptions {WAND04}, their surfaces are ill-defined from a crystallographic point of view. Therefore, most IR studies dealing with structural aspects of the electrode/solution interface are performed on bulk single crystals in a thin-layer configuration {RODE03}.

3 EXPERIMENTAL

The experimental set-up for *in situ* ATR-FTIRS measurements used in the present work was put into operation during the time period of my diploma thesis and is described there as well as in a publication in "Angewandte Chemie" in detail {CHEN04F}·{HEIN06}. This set-up was further extended within my PhD thesis to allow us, for the first time, simultaneous on-line product/educt analysis in addition to the *in situ* ATR-FTIRS measurements during the same experiment. Therefore, in this Chapter only the more advanced combined ATR-FTIRS/DEMS set-up will be described.

3.1 General set-up

The experimental set-up, combines the advantages of two powerful spectroscopic techniques, namely the *in situ* FTIR spectroscopy and online-DEMS (see also Chapter 1 and 2) with electrochemical measurements and allows us, beside the acquisition of the Faradaic current, to gain information on the adsorbed species (FTIRS) and on the volatile reaction products (DEMS) formed during the reaction under well-defined flow conditions.

Set-up:

A schematic description of the combined ATR-FTIRS/DEMS set-up (see also {HEIN06B}·{HEIN07}·{HEIN08}) is given in Fig. 6. The central part, which is interfacing electrochemistry with two spectroscopies, is an electrochemical dual thin-layer flow cell, which is located in an IR spectrometer chamber. The electrolytes are supplied from two glass bottles connected to the cell inlet via a first triple port (TP1). One supply bottle is directly connected to TP1 via a glass connection; the other one is connected to TP1 via a Teflon capillary. The third port connects to the main counter electrode (Pt gauze). The outlet of the cell is equally connected to a second triple port (TP2), which leads to the reference electrode (reversible hydrogen electrode (RHE)), an additional counter electrode (Pt wire) and the electrolyte outlet or to a syringe pump. In the first case, the electrolyte flow is driven by the hydrostatic pressure in the electrolyte supply bottles (~ 50 µl s^{-1}); in the latter case it is controlled by the syringe pump. For details of the counter electrode assembly see refs. {JUSY99}{BALT04}. The working electrode is mounted on the first compartment of the flow cell (details see below); the second compartment connects via a porous Teflon membrane, which is supported on a stainless steel frit, and a metal bellow to the differentially pumped mass spectrometer chamber.

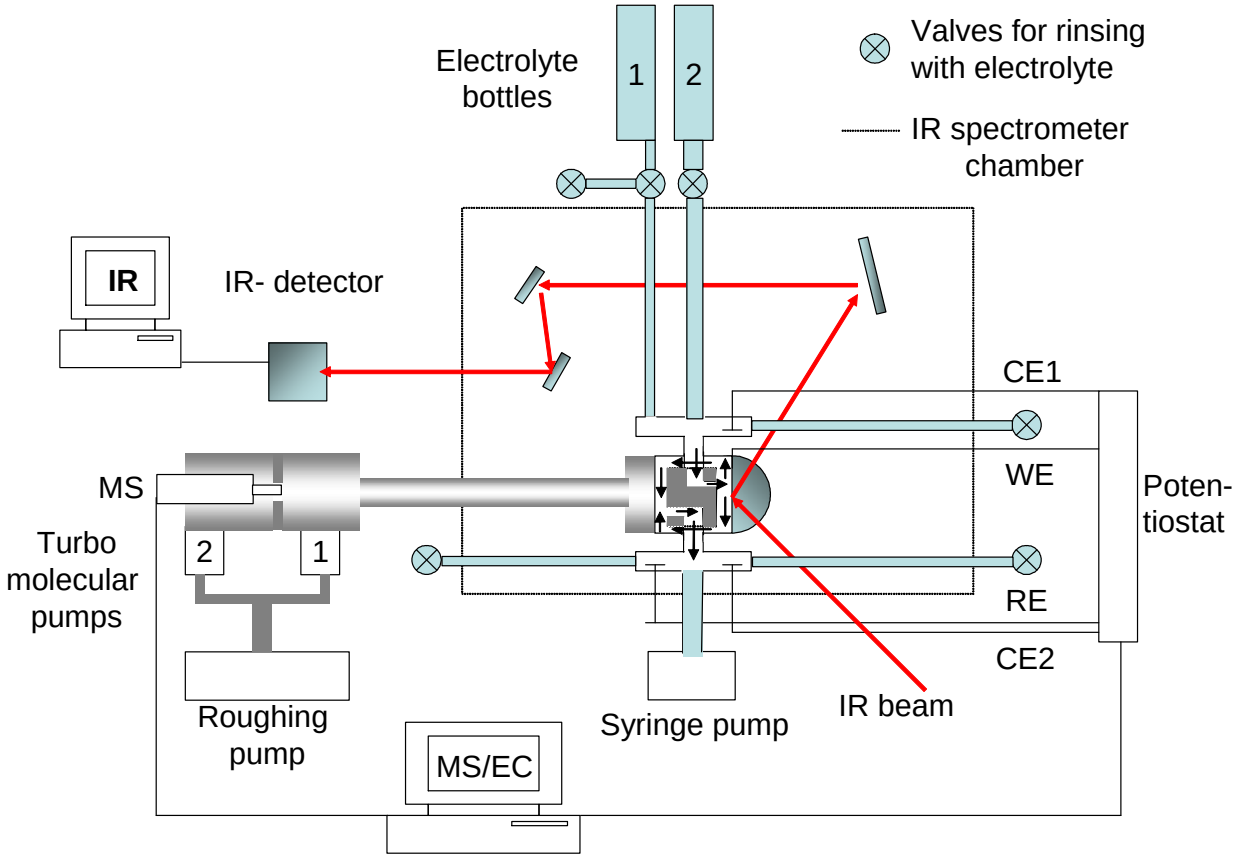

Fig. 6: Schematic description of the combined ATR-FTIRS/DEMS set-up. FC: Flow cell, CE: counter electrode, WE: working electrode, RE: reference electrode; other components see figure. (Figure taken from ref. Hein08)

ATR-FTIRS instrumentation:

For the IR measurements, a BioRad FTS 6000 spectrometer was used, which was equipped with liquid nitrogen cooled MCT detector. The IR spectrometer chamber was continuously flushed with nitrogen, and homemade reflection accessories (incident angle of 70°) were used. The acquisition time for an IR spectrum can be varied between about 10 ms spectrum^{-1} up to several minutes spectrum^{-1}, depending on the time scale of the experiment and the desired spectral resolution (32 cm^{-1} to 0.01 cm^{-1}). The IR intensities are plotted as absorbance, i.e., log (R_0/R), where R_0 and R describe the reflectances at the reference potential and sample potential, respectively. This data processing results in spectra with peaks pointing up for increased absorption ($R < R_0$) and peaks pointing down for a decrease in absorption ($R > R_0$) compared to the reference spectrum.

MS Instrumentation:

The mass spectrometric analysis was performed in a differentially pumped ultrahigh vacuum system. The two stages are pumped by two wide-range turbo-molecular pumps (Pfeiffer TMU 071P, 60 l s^{-1} (first stage) and TPU 180H, 180 l s^{-1} (second stage)), connected to a common roughing pump (Pfeiffer DUO 10, 10 m^3 h^{-1}). Under operating conditions, the pressure in the first stage is about 1×10^{-3} mbar, in the second stage a pressure of about 5×10^{-5} mbar is reached. A quadrupole mass spectrometer (Pfeiffer Vacuum, QMS 420) is mounted in the second stage such that the crossbeam ion source is positioned at the interconnection between the first and the second stage of the MS chamber. The mass spectrometer is controlled by a computerized data acquisition system, which allows following several mass signals in a single experiment. Further details about the instrumentation of the DEMS set-up and the vacuum system are given in ref. {HEIN07}, further general technical information can be found in refs. {TORR03}{BALT04'.

Cell design:

The dual thin-layer spectro-electrochemical flow-cell is built around a circular Kel-F cell body, which contains borings for the electrolyte inlet and outlet as well as six capillaries connecting between the first and second compartment (see Fig. 7). A hemi cylindrical Si prism (20 mm × 25 mm) with the working electrode deposited on its flat side was pressed via a circular tightening gasket (about 100 µm thick) and a Cu foil current collector against the Kel-F cell body, forming the first compartment. The exposed geometric area of the Pt-film is about 1 cm^2, resulting in a volume of the first compartment of about 10 µl. The second compartment was formed by pressing a porous Teflon membrane (Scimat®, 60 µm thick, 50% porosity, 0.2 µm pore diameter) via a tightening ring (Kalrez) to the cell body. The porous Teflon membrane itself is supported by a stainless steel frit.

Electrode preparation:

A thin Pt film (thickness 50 nm), electrolessly deposited on the flat site of a hemi-cylindrical Si-prism (OEC GmbH, 10 mm x 20 mm x 25 mm) was used as working electrode, following deposition procedures described in detail elsewhere {MIKI02}'{MIKI04}. Briefly, the prism was first polished using diamond paste, with grain size of 1 µm down to 0.25 µm, and ultrasonicated afterwards several times in MilliQ water, acetone and again MilliQ water to

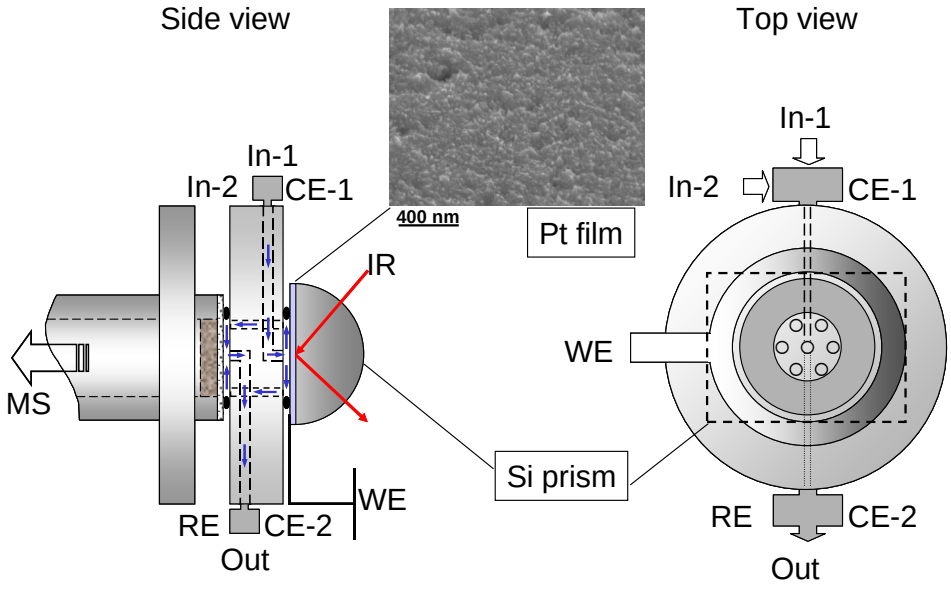

Fig. 7: Schematic diagram of the thin-layer flow-cell for simultaneous on-line DEMS and *in situ* ATR-FTIRS measurements and a SEM image (center) of the Pt thin-film deposited on the Si prism. In-1 and In-2: two inlet ports for electrolyte; CE-1 and CE-2: ports for the connecting two counter electrodes; WE and RE: ports for connecting to the working and reference electrodes; Out: electrolyte outlet port. (Figure taken from ref. Hein06B)

remove the residues from polishing. Next, the clean prism was dried in a N_2 stream and then dipped with the flat side into a solution of 1 mmol $PdCl_2$ in 0.5% HF for about 2 minutes, in order to create Pd nucleation sites required for the growth of the Pt thin film. The Si prism was again rinsed with MilliQ water, dried and heated to 60°C, before 1 ml of a Pt deposition solution (880 µl water, 1ml of a commercial Pt solution (lectroless PT 100 B, Ethone GmbH), 80 µl of 25% NH_3 in water and 20 µl of a commercial reducing agent (lectroless PT 100 Reducer, Ethone GmbH)) was dripped on the flat site of the prism. The prism was carefully rinsed with water after a homogenous Pt film was grown (typical time for Pt film formation under these conditions: 2 min). The Ohmic resistance of the resulting Pt film varies between 20 to 30 Ohm/cm and the roughness factor of these film electrodes is around 5, as determined from the hydrogen adsorption and desorption charge and from the CO_{ad} stripping charge.

3.2 Experimental protocols

In this section, the experimental protocols for the different type of experiments that can be performed with the combined ATR-FTIRS/DEMS set-up are presented. Furthermore, this section describes the advantages/disadvantages/limitations of the respective type of experiments.

Potentiodynamic measurements:

The potentiodynamic measurements presented in this thesis all follow the same experimental protocol (except of adsorbate stripping experiments, see below). First, the working electrode is precleaned by potential cycling between 0.06 and 1.3 V_{RHE} in base electrolyte, i.e. Ar purged 0.5 M H_2SO_4. The potential scan is then stopped at 0.06 V and the electrolyte is exchanged by changing from pure 0.5 M H_2SO_4 to a different solution, usually 0.5 M H_2SO_4, containing a defined concentration of CO or an organic molecule. After about 30, seconds the potential was cycled several times between 0.06 and 1.3 V. These potentiodynamic measurements give a qualitative overview about the surface processes and reaction products correlated with the adsorption/oxidation of the respective molecule. However, strongly adsorbed species like CO_{ad}, formed, e.g., in the negative-going scan might hinder the formation/detection of other adsorbates. Furthermore, the quantitative analysis of potentiodynamic data is complicated due to the convolution of potential and time effects.

Potentiostatic measurements – Adsorption transients

The convolution of potential and time effects is avoided in potentiostatic measurements, performed at constant potential, which are therefore more suitable to follow the kinetics of surface processes. In principle, adsorption transients can be performed in two different ways, which are described below.

a) Electrolyte exchange experiments:

Electrolyte exchange transients are standard experiment to follow the kinetics of the adlayer development and product formation at a constant potential. Prior to the electrolyte exchange experiment, the working electrode is cleaned by potential cycling between 0.06 and 1.3 V_{RHE} in base electrolyte, i.e., Ar purged 0.5 M H_2SO_4. The potential scan is stopped at the corresponding adsorption potential and the electrolyte is exchanged by switching from pure 0.5 M H_2SO_4 to a different solution, usually 0.5 M H_2SO_4, containing the molecule under study. After a certain adsorption time the electrolyte is changed back to base electrolyte (see also adsorbate stripping experiments below). One main advantage of electrolyte exchange experiments is that the measurements are performed on a precleaned Pt electrode and allow monitoring the temporal evolution of the adlayer under well defined mass transport to/from the electrode.

As mentioned before, the IR spectra are plotted as $A = R/R_{0,}$ where R_0 and R are the reflectance of a reference spectrum and of the sample spectrum, respectively, to remove all background contributions from the spectra. Ideally, the reference spectrum is acquired i) on a "clean" Pt surface, which means that depending on the electrode potential only water, hydrogen and/or (bi-)sulfate are adsorbed, and ii) at same potential, where the adsorption of the organic molecule is followed, to avoid potential induced changes in the adsorbate layer, which may complicate the interpretation of the IR spectra (details see potential step experiments). Both requirements are fulfilled in electrolyte exchange experiments and the reference spectrum can be acquired just before the electrolyte exchange is triggered. Therefore, this type of experiment is most appropriate for *in situ* IR spectroscopy. It is important to note that following the kinetics of the adlayer development by electrolyte exchange experiments using organic molecules is only possible in a flow cell configuration, where the organic molecules can be introduced to the cell under defined concentration conditions.

For the mass spectrometric product analysis, however, electrolyte exchange experiments can be unsuitable to follow the reaction kinetics. For example, when changing from Ar saturated 0.5 M H_2SO_4 to CO saturated 0.5 M H_2SO_4, the background pressure of CO in the MS chamber increases, resulting in an increase of the m/z = 28 (CO^+) signal by about two orders of magnitude. This makes it essentially impossible to determine the CO adsorption kinetics by following the consumption of CO in the electrolyte, due to adsorption of CO on the Pt surface (see also Chapter 4.2). The background increase in the m/z = 28 signal is much larger compared to the loss of CO due to adsorption. Therefore, DEMS experiments in which educt and the product contribute to the m/z current of interest, are better performed as potential step experiments (see below).

b) Potential-step experiments:

Potential step experiments were used in this work if the electrolyte exchange time is too slow to follow the fast kinetics of the adlayer build-up/transformation, i.e., the adlayer rearrangement is much faster than the time for complete electrolyte exchange, or if electrolyte exchange experiments are unsuitable for on-line product analysis (see above). In this type of experiment, the electrode potential is stepwise changed in a solution which already contains the molecule, whose adsorption/oxidation behavior shall be investigated. (Note: the experiment is only started after a stable background of the m/z currents has been established).

The potential is usually stepped first to 1.3 V for about 10 s to oxidize adsorbates formed previously on the Pt electrode, then the potential is stepped back to 0.06 V for 1 s to reduce the Pt-oxide layer formed at 1.3 V. Subsequently the potential is set to the so-called "adsorption potential" at which the adlayer development is followed by IR spectroscopy and product analysis is performed via on-line DEMS. Since the electrolyte remains the same during the experiment there is no strong background increase, as described for the electrolyte exchange experiments (see above), which would disturb the product analysis via DEMS. The main drawbacks of this type of experiment are that i) the initial Faradaic current response is dominated by capacitive contributions, ii) reaction products formed (only) at 1.3 V can be adsorbed and/or decompose at 0.06 V, iii) the choice of a proper IR reference spectrum can be complicated; taking a spectrum on a clean Pt surface at 1.3 or 0.06 V as reference results in a potential induced increase/decrease of sulfate/water bands in the IR spectra recorded at the corresponding adsorption potential. These bands might overlap with adsorbates formed from the adsorption/oxidation small organic molecule. The use of flow-cell strongly reduces the negative effect described in point ii) due to continuous removal of the reaction products from the electrode surface.

c) Adsorbate stripping experiments:

To gain further qualitative and quantitative information on the adsorbates formed during adsorption/oxidation of the reactants, "adsorbate stripping experiments" can be performed. Subsequent to an adsorption transient at constant potential, the electrolyte is changed from a solution containing the reactant to Ar saturated base electrolyte to remove the reactant from the cell and to follow the adlayer development and product formation in the absence of the reactant (potentiostatic adsorbate stripping). Furthermore, after a careful rinsing of the cell for about 5 minutes, a potential scan is started to either first negative (reductive stripping) or first positive (oxidative stripping) direction, in order to reduce or oxidize stable adsorbates formed during the adsorption/oxidation of the reactant (potentiodynamic adsorbate stripping). The most prominent example of potentiodynamic adsorbate stripping experiments is the so-called "CO_{ad} stripping", performed after the adsorption of CO from the gas phase (dissolved CO). The Faradaic charge obtained in the positive-going scan can be converted to the number of adsorbed CO molecules and as described in the next section, CO_{ad} stripping experiments upon CO adsorption are therefore suitable to calibrate the DEMS set-up. It is important to note that adsorption/stripping experiments using organic molecules is only possible using a flow cell,

where the organic molecules can be removed from the cell effectively and fast, maintaining constant electrode potential.

3.3 Calibration and performance of the experimental set-up

In this section, the experimental performance, in particular the time resolution of the combined ATR-FTIRS/DEMS set-up will be discussed.

First of all, for a quantitative data analysis, the DEMS set-up has to be calibrated, since the mass spectrometric current depends on parameters such as the electrolyte flow rate, the porosity of the Teflon membrane, the fraction of molecules reaching the analyzer and the ionization probability of the molecule {WOLT84}{BALT99}{JUSY99}{BALT04}. In a calibration experiment, the absolute number of molecules formed at the working electrode is derived from the Faradaic current in a well understood electrochemical reaction and the corresponding mass spectrometric current is measured. The calibration constant K^*, which is defined as

$K^* = n\, Q_{MS} / Q_F$ or $K^* = n\, I_{MS} / I_F$

where Q_{Ms} (I_{Ms}) describes the mass spectrometric charge (current), n the number of electrons consumed/released per molecule formation, and Q_F (I_F) the Faradaic charge (current) {WOLT84}. This way, the calibration constant for CO_2 can be derived from CO_{ad} stripping (see also section 3.2) or from CO bulk oxidation experiments {WOLT84}. For other analytes, other reactions have to be used, or the calibration constant can be determined from a solution with known concentration. Typically, K^* values for CO_2 are in the range of $1 - 3\times10^{-5}$ for the present set-up and the experimental conditions.

The finite electrolyte flow rate results in a delay between the Faradaic current response and the MS signal, due to the time required to transfer the reaction products from the working electrode to the membrane positioned in the second compartment. This time delay can be easily determined in a potential step experiment (see also section 3.2), as shown in Fig. 8. Here the potential was stepped from 0.06 V to 1.0 V in CO containing electrolyte. The Faradaic current increases at t = 0 s due to capacitive contributions and oxidation of CO to CO_2, and reaches a constant value after about 2 s, reflecting continuous oxidation of CO to CO_2. The mass spectrometric current response for the m/z = 44 signal increases at t = 0.5 s, i.e., 0.5 s after the potential step and the time delay strongly depends on the electrolyte flow

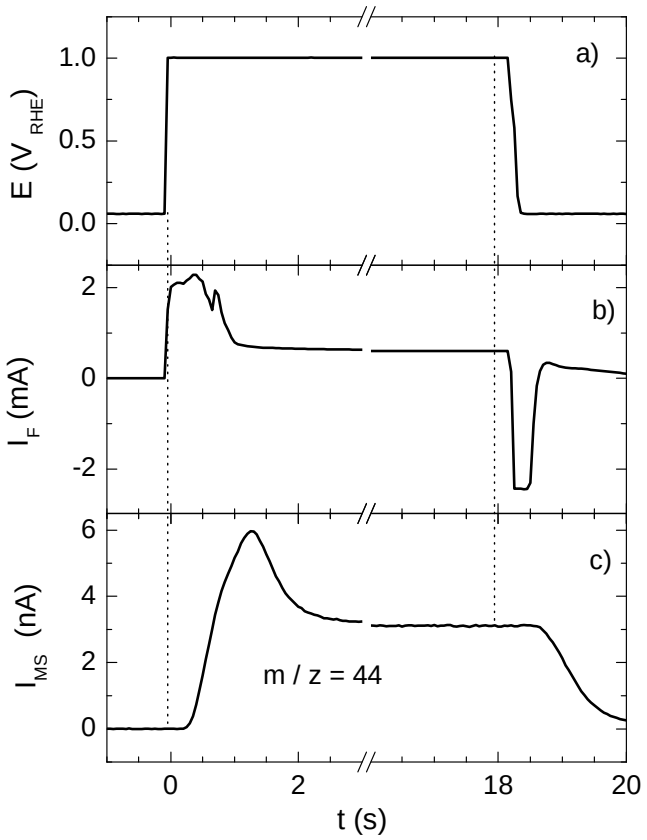

Fig. 8: Calibration of the delay time between Faradaic current and mass spectrometric product detection using potentiostatic CO bulk oxidation as example. The potential was stepped from 0.06 to 1.0 V (t = 0 s) and back to 0.06 V (t = 18 s), electrolyte: CO saturated 0.5 M H_2SO_4; electrolyte flow rate: 50 µl/s. (Figure taken from ref. Hein08)

rate. CO_2 formation reaches a constant value after about 3 s. The longer time required for reaching steady-state conditions is due to the finite tine required for reaching a homogeneous distribution of CO_2 in the electrolyte. The higher the electrolyte flow rate, the smaller the corresponding time delay. On the other hand, a higher electrolyte flow rate decreases the collection efficiency via the porous membrane due to a shorter residence time at the membrane inlet. This in turn results in a smaller sensitivity of the mass spectrometric detection. Therefore, the flow rate must be optimized to obtain both a reasonably fast time response and a high enough sensitivity {BALT04}. For a proper correlation between the Faradaic current and the mass spectrometric current response, this time delay needs to be corrected for. It should be noted that the same experiment could also be used to determine the K^* value for CO_2, comparing the Faradaic current and the m/z = 44 signal under steady-state conditions.

The time required for a complete exchange of the electrolyte exchange can be determined by IR spectroscopy, monitoring the disappearance of a weakly adsorbed species upon changing from an electrolyte containing this species to, e.g., base electrolyte. An example is given in Fig. 9, which shows the temporal development of the integrated intensity of adsorbed acetate (1410 cm^{-1}) {CORR88A}{RODE94B}{SHAO05} upon electrolyte change (see also section 3.2) from 0.5 M H_2SO_4 to 0.1 M acetic acid containing electrolyte at t = 0 seconds and back to 0.5 M H_2SO_4 at t = 73 s. After 2 - 3 s (t = 75 to 76 s), the integral band intensity of adsorbed acetate has decreased to less than 5% of the intensity measured when acetic acid was present in the electrolyte, and after about 4-5 s the peak attributed to adsorbed acetic acid was no longer detectable. Hence, the time required for a complete electrolyte exchange is about 4-5 seconds at a flow rate of 50 µl/s.

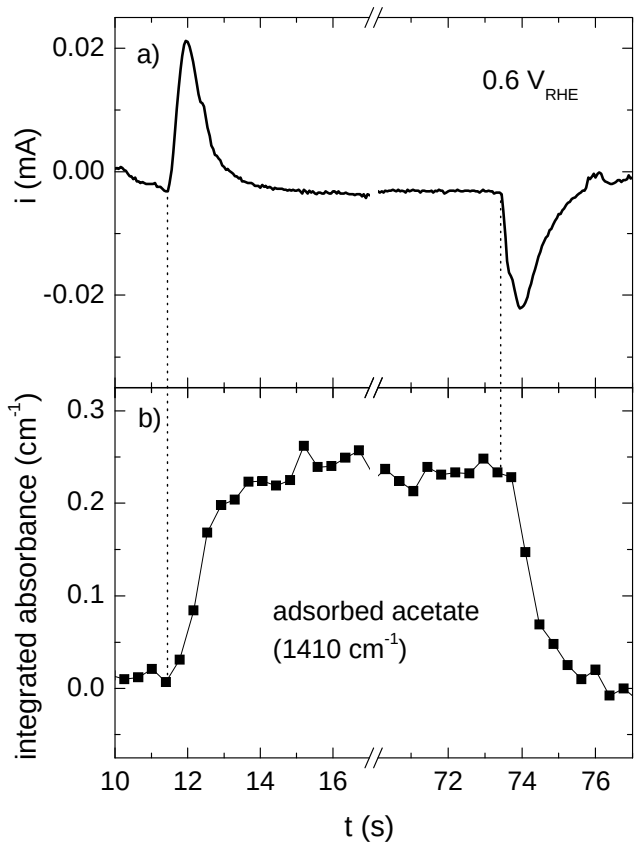

Fig. 9: Calibration of the time required for electrolyte exchange, using the potentiostatic adsorption of acetic acid on a Pt thin film electrode at constant potential as detected by ATR-FTIR as example. The electrolyte was exchanged from 0.5 M H_2SO_4 to 0.1 M acetic acid containing 0.5 M H_2SO_4 (t = 11 s) and back to 0.5 M H_2SO_4 (t = 73 s), electrolyte flow rate: 50 µl/s. (Figure taken from ref. Hein08)

Due to the resistance of the electrolyte in the thin-layer cell, Ohmic drop effects occur if too high Faradaic currents (above ≈ 5 mA) are collected. When potential step experiments are performed, this results in a delay between the time when the potential step is triggered and the time when the potential is applied at the electrode surface This delay can also be determined by means of IR spectroscopy. For this purpose, the potential was stepped from 0.06 to 0.6 V in 0.5 M H_2SO_4 solution, and the potential and Faradaic current responses were recorded with 100 points s^{-1}, as shown in Fig. 10a) and b), respectively. Simultaneously, IR spectra were acquired with a time resolution of 28 ms per spectrum. The resulting integral band intensity of adsorbed (bi-)sulfate is plotted in Fig. 10c). The intensity increases during the first 6 spectra, before reaching a steady-state value. Accordingly, it takes about 168 ms until the potential of the electrode surface has reached the applied value of 0.6 V. (The supply of (bi-)sulfate anions can be assumed to be infinitely fast on this time scale.) This finding agrees well with the measured potential at the working electrode during the potential step experiment, which shows a response time of about 150 ms.

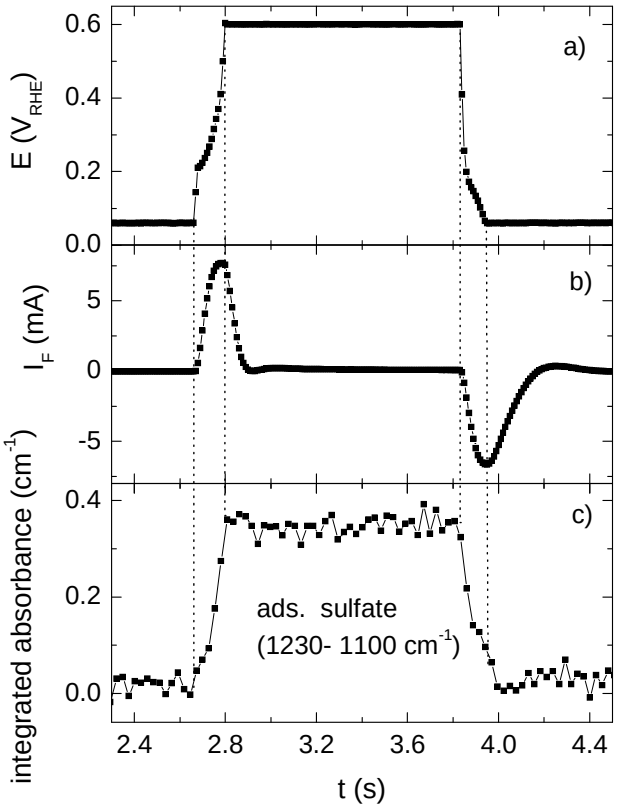

Fig. 10: Time required for the potential response due to the electrolyte resistance in the thin-layer flow cell, which is detected via the adsorption of (bi-)sulfate on a Pt thin film electrode upon a potential step. The potential was stepped from 0.06 to 0.6 V at t = 2.65 s and back to 0.06 V at 3.85 s. a) Measured potential response (at the working electrode), b) Faradaic current response, c) integrated intensity of adsorbed sulfate/bisulfate (1100 – 1240 cm^{-1}). Electrolyte: 0.5 M H_2SO_4, electrolyte flow rate 50 µl/s. (Figure taken from ref. Hein08)

3.4 Simultaneous measurements of several m/z ratios

The QMS 420 mass spectrometer used for the DEMS measurements in this work has the possibility to acquire several m/z currents "simultaneously". Here "simultaneously" means that the selected m/z ratios belong to the same "cycle" in the MS software (Quadstar), as schematically shown in Fig. 11. A selected m/z signal is measured for the so called "dwell time", which can be adjusted via the MS software, before the next m/z ratio is recorded. Since the change between the two m/z currents is not instantaneous the dwell-time was set to 50 ms, which is a sufficient time to establish a stable value for the new m/z signal. All m/z ratios belonging to a "cycle", preselected in the MS software, are then measured in a row.

The possibility of measuring several m/z currents simultaneously becomes important when studying electrochemical reactions via on-line DEMS in which several reaction products/educts are formed/consumed. However, the acquisition rate (data points per second per m/z current) as well as the signal to noise ration is decreased when several m/z ratios are acquired simultaneously and it has to be approved that the measured values are identical to the values if each m/z ratio is recorded separately. According to these prerequisites the dwell time was set to 50 ms.

Fig. 12 shows a potential step experiment in CO saturated 0.5 M H_2SO_4 in which the potential was stepped from 0.06 V to 1.0 V, following the different m/z currents of the reaction product CO_2 (details see figure caption). The m/z ratios plotted in the figure on the right hand side are measured in 4 separate potential step experiments, whereas the data in the figure on the left

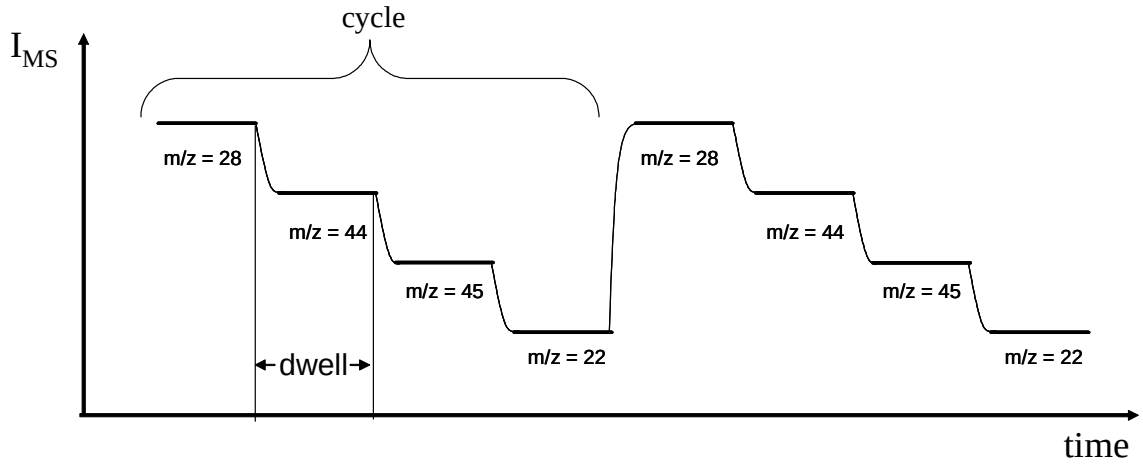

Fig. 11: Schematic drawing of the procedure when measuring several m/z ratios „simultaneously"

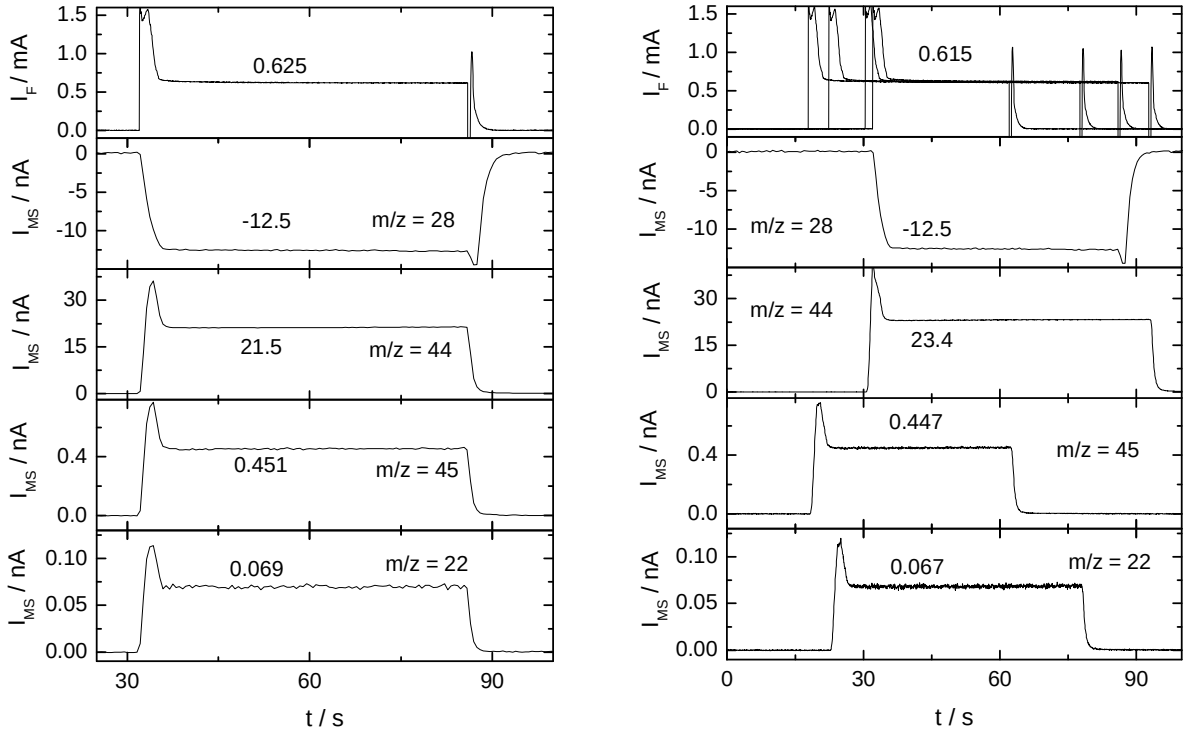

Fig. 12: Faradaic current response (a) and the m/z currents for different m/z currents (see figure) recorded during a Potential step experiment from 0.06 V to 1.0 V and back to 0.06 V in CO saturated 0.5 M H_2SO_4. The time when the potential steps were triggered is visible by the fast increase/decrease of the Faradaic current. Left panel: All m/z current were acquired simultaneously, right panel: the m/z currents were acquired in 4 different potential step experiments.

hand side were acquired simultaneously. In both cases the absolute values as well as the ratios of the m/z currents are practically identical, indicating that the acquisition of several m/z currents simultaneously does not influence the results of the measurements. Furthermore, when the same potential step is performed 4 times, small deviations in the flow rate will result in a change of the mass transport dependent oxidation of CO to CO_2 and consequently also the measured values of the m/z currents will change, clearly favoring the simultaneous acquisition of the m/z currents. However, the signal to noise ratio especially for the m/z = 22 current as well as the data acquisition rate has decreased from 20 points per second to 5 points per seconds per m/z current (50 ms x 4 m/z currents = 200 ms for one cycle) if the signals are acquired simultaneously.

3.5 Specific evaluation of the DEMS data

3.5.1 CO_{ad} coverage determination

In Chapter 4.2, the CO_{ad} coverage is determined from the mass spectrometric currents for m/z = 29 (^{13}CO consumption) and m/z = 45 ($^{13}CO_2$ production), as described in the following.

In order to calculate the instantaneous CO_{ad} surface coverage from the difference in the mass spectrometric currents, a quantitative calibration constant K* is used (see also section 3.3), which is defined as:

$K^* = 2 \times I_{MS} / I_F$

where I_F is the Faradaic current, measured in these measurements at 1 V (continuous, mass transport limited CO adsorption and oxidation). The factor 2 reflects the number of exchanged electrons per CO molecule that is oxidized to CO_2. I_{MS} is the difference between the mass spectrometric current (m/z = 29) at the background level (defined as 0) and that right after the potential step from 1.0 to 0.06 V (maximum adsorption rate). Please note that the m/z = 29 signal during the mass transport limited CO oxidation to CO_2 at 1.0 V contains contributions from the $^{13}CO^+$ fragment of the CO_2 produced under these conditions. Therefore the m/z signal at 0.06 V (no CO_2 formation) was used to calculate the K^* value, instead of the m/z = 29 signal at 1.0 V. The background level for the CO partial pressure corresponds to the maximum of the m/z = 29 signal with 5% CO/Ar purged electrolyte. It is obtained, when flowing CO-containing electrolyte over a CO_{ad} saturated surface at non-oxidative potentials, where no decrease of this signal is observed due to further CO adsorption or subsequent oxidation to CO_2. The calibration constant K* can then be used to convert the mass spectro-metric charge directly into a Faradaic charge, which is proportional to the number of consumed CO molecules. The same equation is also valid for calculating the calibration constant for CO_2, the I_{MS} in this case is the m/z = 45 current. This way, the CO_2^+ signal can also be converted into a Faradaic current, and thus be correlated to the amount of consumed CO molecules.

For adsorption potentials $E_{ad} < 0.5$ V, where no significant CO_2 production was measured (maximum 5 % of a CO monolayer formed within the first about 5 s at 0.5 V), the CO_{ad} surface coverage at any time can be calculated by integrating the mass spectrometric charge from t = 0 to the corresponding adsorption time, divided by the total charge {JUSY01A}. The latter corresponds to the saturation coverage at the adsorption potential, which is calculated by

integration of the area above the mass spectrometric current from t = 0 to t = 200 s. For calculation of the instantaneous CO_{ad} surface coverage at 0.6 V, where CO_{ad} oxidation to CO_2 is significant, we assume that the total consumption of CO (ΔCO_{total}), which is directly measured by DEMS (m/z = 29), can be expressed as:

$$\Delta CO_{tot} = \Delta CO_{ads} + \Delta CO_{ox}$$

where ΔCO_{ads} is the amount of adsorbed CO, and ΔCO_{ox} is the amount of CO oxidized to CO_2 (m/z = 45). Consequently, the instantaneous CO_{ad} coverage at 0.6 V is calculated using the difference $\Delta CO_{tot} - \Delta CO_{ox} = \Delta CO_{ads}$, following the same integration protocol for the resulting curve as described above.

3.5.2 $^{13}CO_{ad}$ exchange rate determination

In Chapter 4.3, the $^{13}CO_{ad}$ exchange rate is determined upon electrolyte exchange experiments by following the ^{13}CO partial pressure in the electrolyte with time. For the experiments, the sample was first presaturated by ^{13}CO at 0.1 V, then the electrolyte was exchanged against CO-free electrolyte (10 min), and subsequently it was switched to ^{12}CO-containing electrolyte. This experimental protocol was applied (instead of changing directly from ^{13}CO containing electrolyte to ^{12}CO containing electrolyte) to reduce the ^{13}CO content in the electrolyte sufficiently that ^{13}CO desorption can be measured (DEMS) and ^{13}CO re-adsorption is excluded. This will cause a slight decrease of the CO_{ad} coverage when changing to CO-free electrolyte, and a corresponding increase in the total CO_{ad} coverage when changing to ^{12}CO containing electrolyte. The $^{13}CO_{ad}$ coverage obtained in the absence of ^{13}CO in the electrolyte defines the total amount of exchangeable $^{13}CO_{ad}$. In the following, this will be referred to as $\theta_{CO,rel} = 1$. The difference between ^{13}CO background pressure and the ^{13}CO pressure at a given time t, where both are given by their respective mass spectrometric currents, corresponds to the instantaneous desorption rate at each moment. The ^{13}CO background pressure was determined in ^{12}CO containing solution after the exchange process was essentially completed. The total integrated area $\Delta p_{CO} \cdot dt$ of the ^{13}CO signal above the background level is equivalent to the amount of exchanged $^{13}CO_{ad}$, The amount of $^{13}CO_{ad}$ left on the surface after the exchange process was determined by subsequent CO_{ad} stripping experiments; this amount plus the exchanged $^{13}CO_{ad}$ are identical to the coverage of the saturated CO adlayer ($\theta_{CO,rel} = 1$). The relative $^{13}CO_{ad}$ coverage $\theta_{CO,rel}$ at a given time t is calculated as $1-\int c\, \Delta p_{CO} \cdot dt$, integrating from t = 0 to t. The constant c is defined such that at the end of the exchange measurement

the integrated area is equivalent to the total exchanged $^{13}CO_{ad}$ coverage as calculated from the subsequent stripping experiment.

3.5.3 Number of electrons in adsorbate stripping experiments

In Chapter 6, potentiodynamic adsorbate stripping experiments were performed subsequently to the adsorption/oxidation of the organic molecules. From these measurements the number of exchanged electrons n per CO_2 molecules is calculated, using the calibration constant K^* (see above):

$n = Q_{MS} / (Q_F \times K^*)$

In this equation, Q_{MS} is equivalent to the mass spectrometric charge measured in the potential region of interest in the first positive-going scan, and Q_F is the corresponding Faradaic charge in the same potential region. For a CO_{ad} stripping experiment, in which CO_{ad} was preformed from gas phase CO adsorption n is equivalent to 2 (see also section 3.5.1). Larger or smaller numbers of n, obtained in adsorbate stripping experiments subsequent to the adsorption of small organic molecules, indicate the presence of other adsorbed species beside CO_{ad} that can be oxidized to CO_2. Thus the value of n contains indirect information on the adlayer composition.

3.6 Product detection during ethanol oxidation

The main reaction products of ethanol oxidation are acetaldehyde, acetic acid and CO_2, besides small amounts of methane and ethane desorbing in the H_{upd}-region (see section 6.1.1). For a product analysis of the ethanol oxidation reaction via DEMS, several main aspects have to be considered: i) a high volatility of the reaction products is required, enabling the molecules to permeate through the porous Teflon membrane and pass into the MS chamber, ii) if an electron beam ionization is used, fragmentation of the molecules occurs, and iii) several products or their fragments can contributed to the same m/z ratio.

To test whether the products acetaldehyde and acetic acid can be detected with the present on-line DEMS set-up, electrolyte exchange experiments were performed, changing from 0.5 M H_2SO_4 to solutions containing 0.01 M of acetaldehyde and acetic acid, respectively. For comparison the m/z ratios for the corresponding molecules are taken from the literature {SDBS}. These experiments were performed at open circuit potential on a blank Si prism to

exclude any contribution from an electrochemical reaction on the m/z currents. The results for the electrolyte exchange to 0.01 M acetaldehyde containing solution are plotted in Fig. 13, measuring the signals of m/z = 15 (CH_3^+), 29 (CHO^+), 43 (CH_2CHO^+) and 44 (CH_3CHO^+) simultaneously. When the electrolyte exchange was initiated at t = 1057 s, all m/z signals strongly increase, reaching a nearly constant value after about 30 s. Hence, acetaldehyde can permeate through the membrane and be detected via the mass spectrometer, in agreement with previous DEMS reports {IWAS94}·{WANG06I}. When changing back to 0.5 M H_2SO_4 solution at t = 1970 s, the m/z signals decay to the background level within 30 s, at about t = 2000 s. This experiment also allows determining the relative intensity of the mass spectrometric signals for the different fragments of acetaldehyde in the present DEMS set-up. This was done by dividing the mass spectrometric currents of all m/z ratios through the mass spectrometric current of the m/z = 29 signal, resulting in a relative intensity of 1: 0.62: 0.36: 0.29 for m/z = 29, 44, 43 and 15, respectively.

Similar electrolyte exchange experiments as presented in Fig. 13 were also performed with acetic acid containing solutions. Essentially now increase in the characteristic m/z signals for acetic acid (m/z = 60, 45, 43 and 15) was found, indicating that acetic acid can not permeate through the Teflon membrane. Consequently, the formation of acetic acid upon ethanol oxidation can not be detected with the present DEMS set-up.

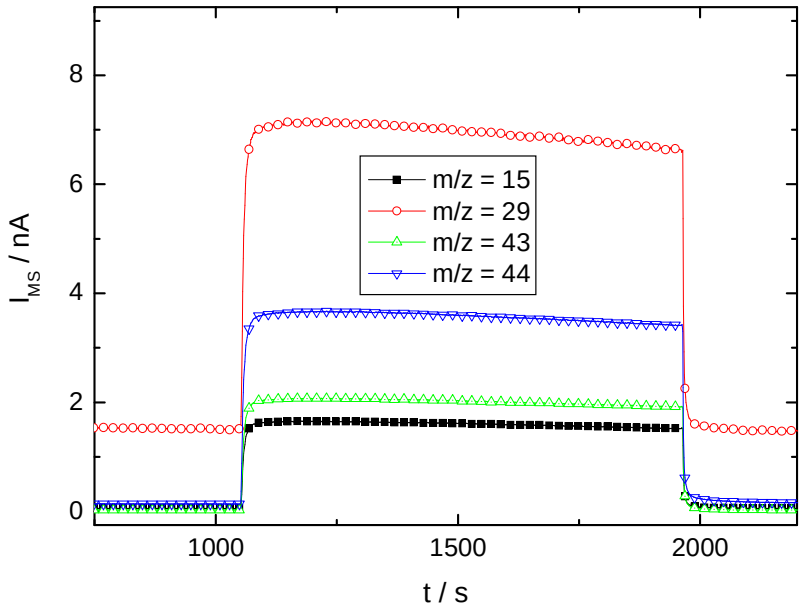

Fig. 13: Mass spectrometric current response for m/z 15 (CH_3^+), m/z = 29 CHO^+, m/z = 43 CH_3CO^+ and m/z = 44 (CH_3CHO^+) upon electrolyte exchange from 0.5 M H_2SO_4 to 0.01 M acetaldehyde containing solution on a blank Si prism at open circuit potential.

It should be noted that when changing to ethanol containing electrolyte, amongst other the signals for m/z = 44, 31, 29, 27 and 15 increase strongly, due to ethanol permeation into the mass spectrometer chamber. This hinders or even impedes an ethanol product analysis during electrolyte exchange experiments under oxidative potentials, since the small amounts of acetaldehyde and CO_2 are hardly detectable in the large background increase. Ethanol product analysis can therefore only be performed by potentiodynamic or potential step experiments in ethanol containing solutions, after a constant background level for the aforementioned m/z currents has been established (see also section 3.2).

The analysis of the ethanol oxidation products is further complicated due to the fact that CO_2 and acetaldehyde, both contribute to the same m/z = 44 signal. In order to selectively follow the CO_2 formation in the EOR, deuterated ethanol CD_3CH_2OH can be used, measuring solely CO_2 formation on m/z = 44 and acetaldehyde formation on m/z = 47 {SCHM96A}{FUJI99A}. In publications by Wang et al. {WANG04B}{WANG04O} the double ionized CO_2 signal on m/z = 22 (CO_2^{++}) was measured to discriminate CO_2 formation upon ethanol oxidation from acetaldehyde formation. In the present study, due to the possibility to record several m/z currents simultaneously, a different approach is introduced to determine the CO_2 formation, which is explained in the following.

The Faradaic current (a) and the m/z = 44 (b), 29 (c), 15 (d) responses are plotted during the potentiodynamic oxidation of CH_3CH_2OH on the Pt film electrode in Fig. 14, left panel. For potentials between 0.4 and 1.3 V, an oxidative current is measured, which is accompanied by an increase of all m/z signals (details of the potentiodynamic ethanol oxidation will be discussed in section 6.2.2.1). The m/z = 44 signal includes contributions from acetaldehyde (CH_3CHO^+) and $^{12}CO_2$, respectively, whereas the m/z = 29 signal results solely from acetaldehyde formation (CHO^+). The m/z current for $^{12}CO_2$ ($I(CO_2)$) can be calculated making use of the relative intensity of the acetaldehyde fragments (see above):

$$I(CO_2) = I^*(m/z = 44) = I(m/z = 44) - I(m/z = 29) \times 0.62$$

The resulting CO_2 related current is shown in Fig. 14b, right panel. To test whether this conversion is reliable the $I^*(m/z = 15)$ signal is plotted in Fig. 14c, right panel. $I^*(m/z = 15)$ was calculated via:

$$I^*(m/z = 15) = I(m/z = 15) - I(m/z = 29) \times 0.29$$

where the factor 0.29 is the relative intensity of the m/z =15 fragment of acetaldehyde (see Fig. 13). This calculation should results in an unstructured background signal if the procedure

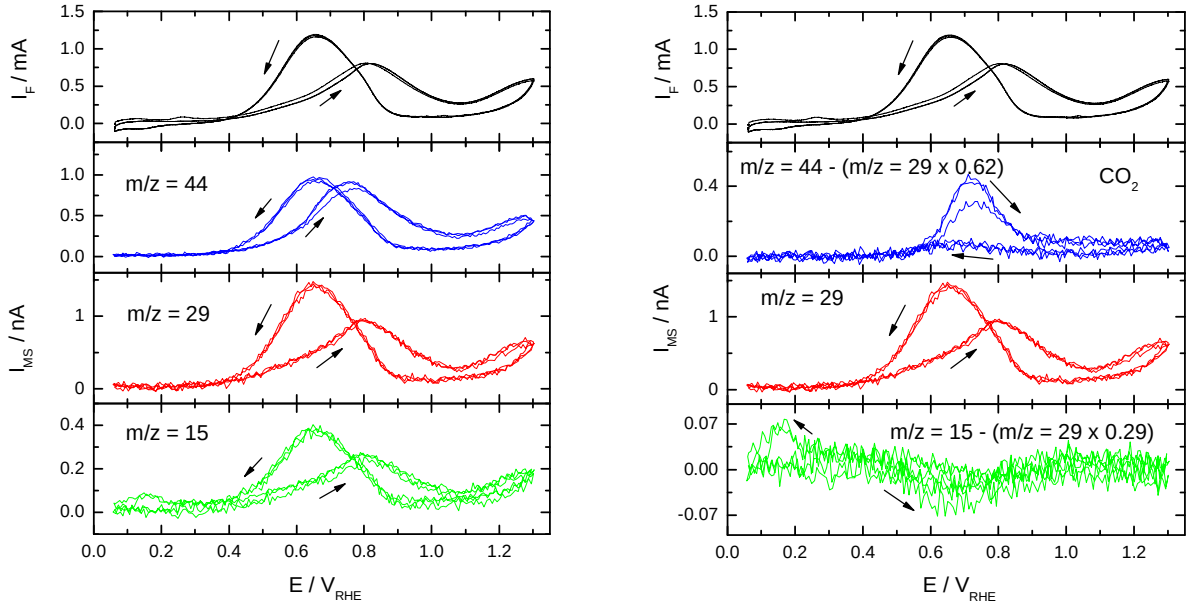

Fig. 14: Left panel: Simultaneously recorded m/z currents for m/z = 15, 29, 44 during the potentiodynamic oxidation of 0.044 M CH_3CH_2OH containing 0.5 M H_2SO_4. Sweep rate 10 mV/s, right panel: same experiment but instead of the m/z = 44 and m/z = 15 currents, I(CO_2) and I^*(m/z = 15) are shown (see text).

is correct and no other molecules contribute to the m/z = 15 current. The resulting I^*(m/z = 15) current is basically flat. The small increase at low potentials is related to desorption of CH_4 and the decrease of the m/z signal between 0.5 and 0.8 V is attributed to the consumption of ethanol, lowering the m/z = 15 background signal. The results confirm that with a precise determination of the relative intensities of fragments the contributions of several reaction products to the same m/z current can be de-convoluted in these DEMS measurements.

The potentiodynamic oxidation of ethanol is discussed in more detail in section 6.2.2.1, using carbon labeled ethanol ($CH_3{}^{13}CH_2OH$). However, it needs to be mentioned that the relative intensity of the $^{12}CH_3{}^{13}CHO$ fragments deviate significantly from the calibration experiment described above, where $^{12}CH_3{}^{12}CHO$ was used. The relative intensities of the $^{12}CH_3{}^{13}CHO$ fragments are about 1:0.79:0.52:0.4 for m/z = 29, 45, 44, and 15, respectively. These values were determined from potential step experiments to 0.6 V in 0.044 M $^{12}CH_3{}^{13}CH_2OH$, assuming that only $^{12}CH_3{}^{13}CHO$ is formed at this potential upon oxidation of ethanol. These values will be used to convert the m/z = 45 and 44 currents into I($^{13}CO_2$) and I($^{12}CO_2$), i.e. the currents for $^{13}CO_2$ and $^{12}CO_2$ formation, respectively. This approach for the calibration of the relative intensity of the $^{12}CH_3{}^{13}CH_2OH$ fragments was confirmed to be relatively precise (± 5%), performing a similar potential step experiment to 0.6 V in CH_3CH_2OH containing solution. In the latter experiment, a mean value of 0.64 was determined for the relative

intensity of the m/z = 44 signal. This is only slightly higher compared to the calibration experiment using acetaldehyde, in which a relative intensity of 0.62 was found for the m/z = 44 signal. The slightly higher value in the former experiment results from the formation of small amounts of CO_2 upon ethanol oxidation, contributing to the m/z =44 signal.

3.7 Conversion of CO_L intensity into CO_{ad} coverage

To calculate the CO_{ad} formation rate upon adsorption/oxidation of small organic molecules, a precise correlation between the CO_{ad} intensity and the CO_{ad} coverage is required, which so far has been a major drawback for quantitative evaluation of IR spectroscopic data in electrochemical measurements. In the present work, two different approaches were used, which will be described in the following:

i) Variation of adsorption time (Chapter 5):

In this approach, different CO_{ad} coverages were produced by varying the time for dissociative adsorption of HCOOH from 0.01 M HCOOH + 0.5 M H_2SO_4 solution in electrolyte exchange experiments (see section 3.2). The CO_{ad} coverages were determined from subsequent adsorbate stripping experiments (see section 3.2), assuming that CO_{ad} is the only stable adsorbate resulting from formic acid adsorption. A plot of the integrated CO_L and CO_M band intensities (IR measurements) and the CO_{ad} coverage (adsorbate stripping experiments) versus formic acid adsorption time is shown in Fig. 15. From this plot the following IR intensity – CO_{ad} coverage relations can be determined: At small relative CO_{ad} coverages ($\theta_{CO}/\theta_{COsat} < 0.33$) we find $\theta_{CO}/\theta_{COsat} = k_{COm} \times I_{COm}$ with k_{COm} equal to 2.26, while at larger CO_{ad} coverages ($\theta_{CO}/\theta_{COsat} > 0.33$) we obtain $\theta_{CO}/\theta_{COsat} = k_{COl} \times I_{COl} + 0.24$, with k_{COl} equal to 0.54, respectively. In addition, in the low coverage regime between $0.12 \times \theta_{COsat}$ and $0.24 \times \theta_{COsat}$, one may also use the CO_L related intensity via the relation $\theta_{CO}/\theta_{COsat} = k_{COl} \times I_{COl} + 0.12$, with $k_{COL} = 1.26$ {CHEN04F}.

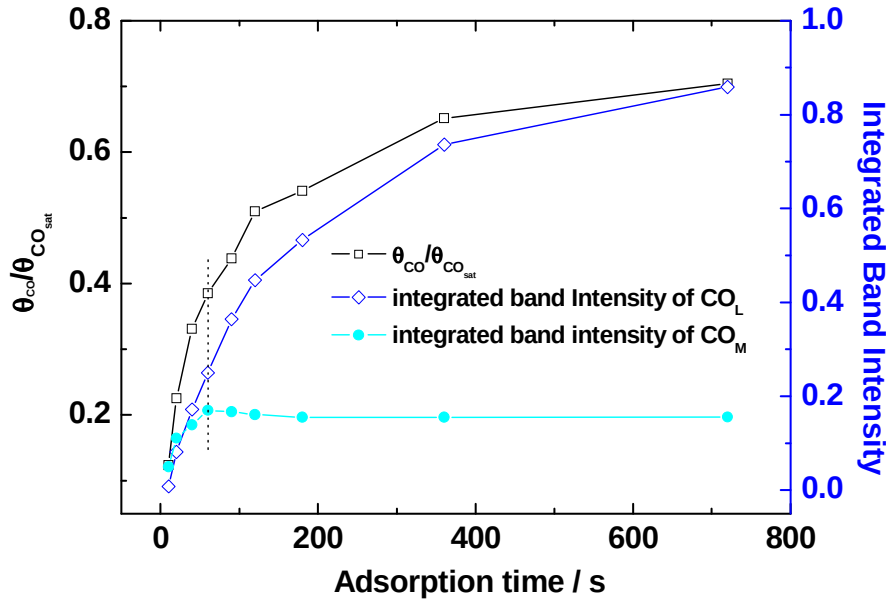

Fig. 15: Surface coverage and band intensity of CO_{ad} during dissociative adsorption of formic acid at 0.4 V. Electrolyte: 0.01 M HCOOH + 0.5 M H_2SO_4. (Figure taken from CHEN04F).

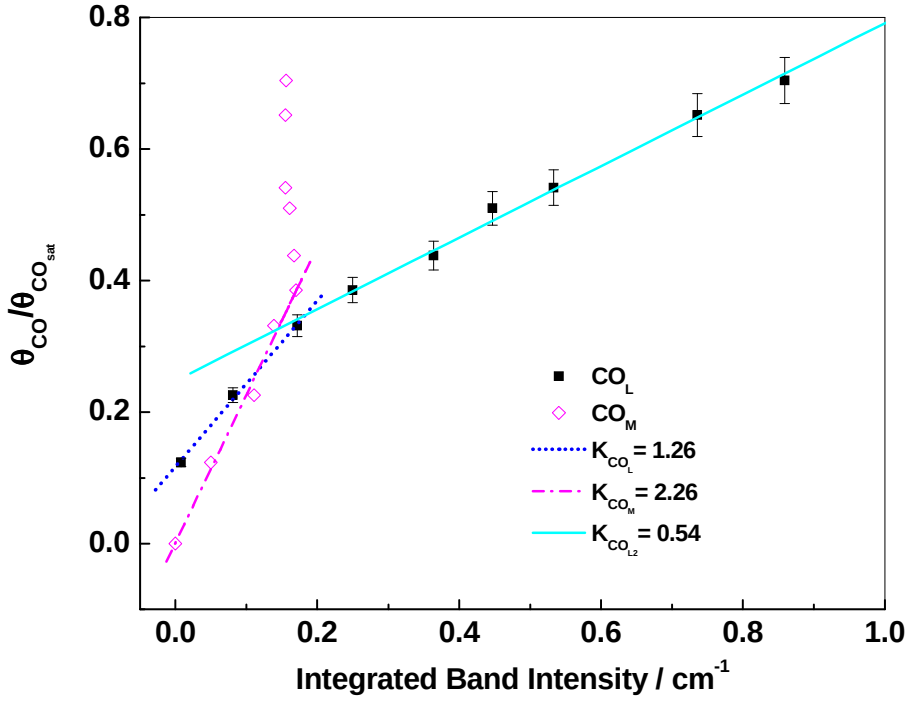

Fig. 16: CO_L and CO_M band intensities as a function of the CO_{ad} coverage, data from Fig. 15. (Figure taken from {Chen04F}.

ii) Combined DEMS/ATR-FTIRS approach (Chapter 6 and 7):

With the combined DEMS/ATR-FTIRS set-up, a calibration curve of the CO_{ad} intensity versus CO_{ad} coverage can be directly obtained from the CO adsorption transients. This is done by plotting the CO_L and/or the CO_M intensity (IR data) versus the CO_{ad} coverage (DEMS), as described in Chapter 4.2. A plot of the CO_{ad} coverage versus the CO_L intensity at 0.4 V, taken from Fig. 32, is shown in Fig. 17. In agreement with the first approach, different slopes are observed for the relation between CO_{ad} coverage and the CO_L intensity, depending on the CO_{ad} coverage, with higher slopes at low (0 – 0.05) and high (0.5 to 0.6) CO_L intensities (explanations for this behavior are given in Chapter 4.2). In the range between rel. CO_{ad} coverage of about 8% and 70%, the θ_{CO} – $I(CO_L)$ relation can be reasonably well fitted by a polynom of third order:

$$rel.\ \theta(CO) = 0.10504 + 1.63582 \times I(CO_L) - 2.59555 \times I(CO_L)^2 + 3.28731 \times I(CO_L)^3$$

At rel. θ(CO) < 8%, the CO_L intensity is essentially zero since CO adsorbs only in a multiply bonded configuration (see Chapter 4.2). Therefore, this coverage regime was ignored in the above fit. However, here it is important to note that the above equation is only valid for the specific Pt film electrode used in this calibration experiment. To convert the integral band intensity of CO_L measured on a different Pt film electrodes to the rel. CO_{ad} coverage, the difference in the absolute IR sensitivity of different Pt films has to be accounted for: on different Pt film electrodes, the same number of adsorbed CO molecules results in different integral CO_L band intensity of. Therefore, an enhancement factor N^* has to be introduced in the above equation:

$$rel.\theta(CO) = 0.10504 + 1.63582 \times [I(CO_L) \times N^*] - 2.59555 \times [I(CO_L) \times N^*]^2 + 3.28731 \times [I(CO_L) \times N^*]^3$$

To determine N^*, on each Pt film electrode a calibration experiment was performed, i.e., CO adsorption from a CO saturated 0.5 M H_2SO_4 solution at 0.06 V. From this experiment the integrated absorbance of CO_L on a CO_{ad} saturated surface at 0.06 V is obtained as a reference value for the IR sensitivity of the respective Pt film electrode. N^* is the ratio of the integrated CO_L absorbance at 0.06 V on the Pt film electrode used for the measurements of the calibration curve and that of the Pt film under study. For the Pt film electrode used for the calibration curve this value was equal to 0.58 cm^{-1}.

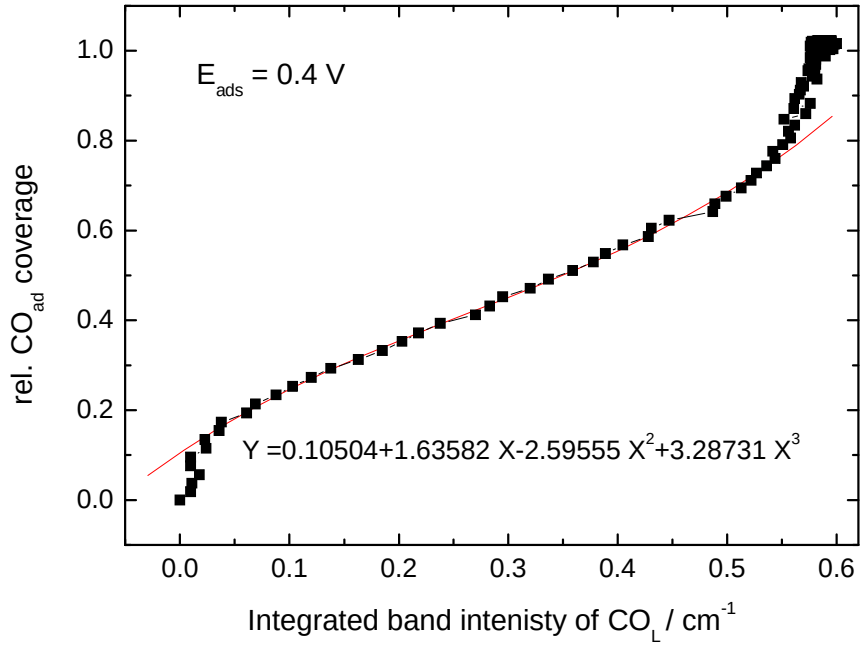

Fig. 17: Integral band intensity of adsorbed CO versus rel. CO_{ad} coverage (Filled squares) and fit of the data with a third order polynom (equation see figure)

The test the validity of this equation, it was applied to determine the rel. CO_{ad} coverage from the integrated CO_L intensity upon adsorption of formic acid (Fig. 16). On the Pt film used for the adsorption/stripping of formic acid, the integrated CO_L band intensity of a CO_{ad} monolayer at 0.06 V resulting from CO gas phase adsorption, was equal to 0.85 cm^{-1}. For this film electrode, N^* corresponds to a value of $0.58cm^{-1}/0.85cm^{-1}$ = 0.725. The rel. CO_{ad} coverage, as calculated from the integral band intensity of CO_L upon adsorption of formic acid via the polynom as well as the rel. CO_{ad} coverage determined from adsorbate stripping experiments (calibration approach i)) are shown in Fig. 18. Both curves are essentially identical for rel. CO_{ad} coverage below 0.7, supporting the above calibration. At higher rel. CO_{ad} coverage the polynomal fit is now longer valid (see above), and results in increasing deviations. The reason for the conversion of the integral band intensity of CO_L into the CO_{ad} coverage was to derive the CO_{ad} formation rate upon adsorption/oxidation of small organic molecules, where the rel. CO_{ad} coverage usually increases from 0 to about 60% (see Chapter 6 and 7). This is essentially the valid coverage regime for the polynomal fit in approach ii).

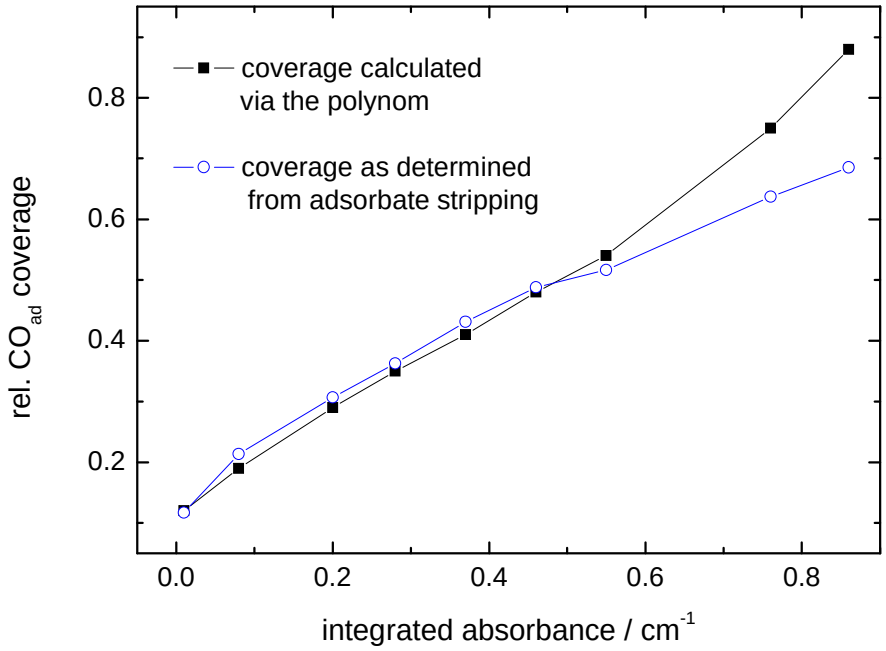

Fig. 18: Correlation between the integrated absorbance of CO_L and the CO_{ad} coverage for the adsorption of formic acid at 0.4 V. Filled squares: rel. CO_{ad} coverage as determined via the polynomial fit ($N^* = 0.725$); open circles: rel. CO_{ad} coverage as determined from the adsorbate stripping experiment (see Fig. 16).

However, it needs to be mentioned that approach ii) contains the assumption that the CO adlayer structure, i.e. the ratio between CO_L and CO_M, is identical for the adsorption of gas phase CO and the formation of the CO adlayer upon adsorption/oxidation of small organic molecules. For the adsorption of ethanol it will be shown that the deviations are rather small for low overall adsorbate coverages (see section 6.1.2.4).

As shown in section 4.2, the relation between the integrated CO_L intensity and the CO_{ad} coverage is strongly potential dependent. Therefore, the polynom presented above, is only valid for an adsorption potential of 0.4 V. Based on the CO_{ad} coverage versus integrated CO_L band intensity plots presented in section 4.2, similar polynomal fits can be provided for adsorption potentials of 0.06, 0.1, 0.2, 0.3, 0.5 and 0.6 V. These polynoms have the general form:

$$rel.\theta(CO) = a + b \times [I(CO_L) \times N^*] + c \times [I(CO_L) \times N^*]^2 + d \times [I(CO_L) \times N^*]^3$$

The respective coefficients (a,b,c and d) for different adsorption potentials (0.06, 0.1, 0.2, 0.3, 0.4, 0.5 and 0.6 V) are given in the following table:

	0.06 V	0.1 V	0.2 V	0.3 V	0.4 V	0.5 V	0.6 V
a	0.04833	0.04239	0.08751	0.16147	0.10504	0.16379	0.17859
b / cm	1.41167	1.27937	1.68271	1.28993	1.63582	1.65840	2.50440
b / cm^2	-1.33436	-0.96793	-2.80190	-1.10612	-2.59555	-2.58023	-5.03299
b / cm^3	2.76633	2.00748	3.69974	1.47752	3.28731	3.23565	5.79866

Table 1: Respective coefficients (a,b,c and d) of the third order polynom to convert the integrated CO_L band intensity into the CO_{ad} coverage at different adsorption potentials (0.06, 0.1, 0.2, 0.3, 0.4, 0.5 and 0.6 V). Note: the rel. CO_{ad} coverages obtained via the equations are only valid if the resulting CO_{ad} coverage is i) larger than the value for the respective coefficient a and ii) below about 0.7.

3.8 Integration procedure for adsorbed acetyl species

Upon ethanol adsorption on the Pt film electrode at 0.4 V, adsorbed acetyl species are detected by *in situ* ATR-FTIR spectroscopy via an absorption band centered at 1635 cm^{-1} (Fig. 19 lower spectrum; see also section 6.1.2.1). However, also the adsorption of gas phase CO results spectral features in this wavenumber region (Fig. 19 upper spectrum; see also section 4.2).

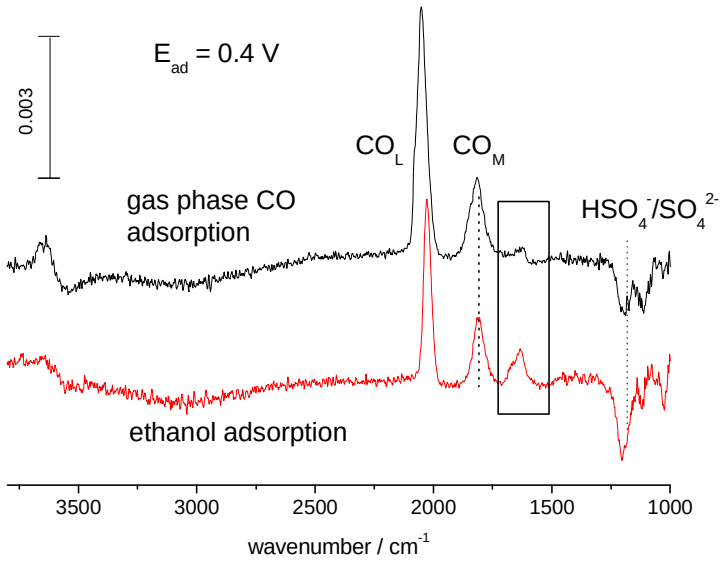

Fig. 19: Selected ATR-FTIR spectra at 0.4 V with comparable CO_L intensity upon adsorption of gas phase CO (upper spectrum; electrolyte: 0.5 M H_2SO_4 purged with 5% CO/Ar mixture) and upon ethanol adsorption (lower spectrum; electrolyte: 0.044 M ethanol containing 0.5 M H_2SO_4).

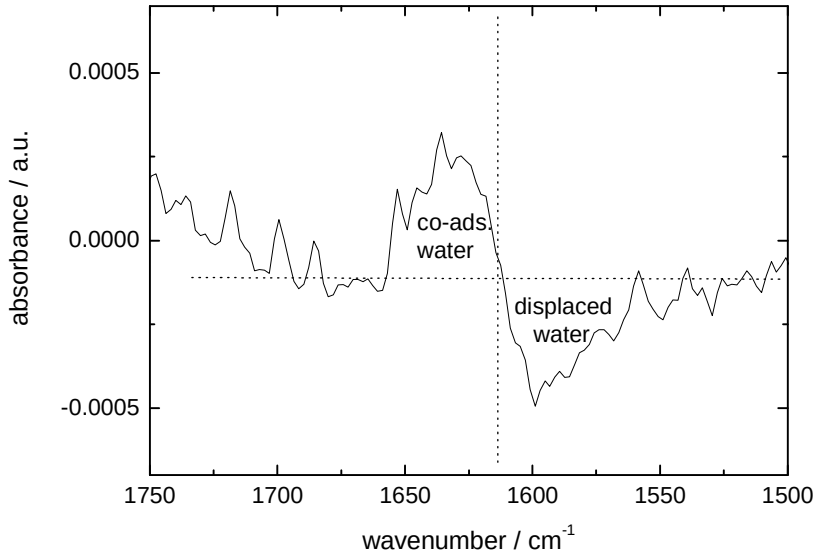

Fig. 20: Selected ATR-FTIR spectrum at 0.4 V upon gas phase CO adsorption. Electrolyte: 0.5 M H_2SO_4 purged with 5% CO/Ar mixture

For clarity, the spectral region between 1750 and 1500 cm^{-1} upon gas phase CO adsorption at 0.4 V is enlarged in Fig. 20, which shows a positive IR absorption band centered at 1635 cm^{-1} due to water co-adsorbed with CO {MIKI02}. Furthermore, a negative IR absorption band is visible at about 1600 cm^{-1}, which is assigned to interfacial water displaced from the Pt surface by more strongly adsorbing CO_{ad}.

The intensities of both bands, i.e. displaced water and water co-adsorbed with CO_{ad}, strongly depend on the CO_{ad} coverage (see section 4.2) and contribute to the integral band intensity of adsorbed acetyl species detected upon ethanol adsorption at 1635 cm^{-1}. For a quantitative analysis of the temporal evolution of the adsorbed acetyl species upon ethanol adsorption, the contributions of both water bands have to be removed. For this purpose it was exploited that the area of water co-adsorbed with CO and the area of water displaced by CO_{ad} have an opposite sign, i.e., the integral band intensity of water co-adsorbed with CO is positive, whereas the integral band intensity of displaced water is negative. By finding a proper integration range, both areas should cancel, resulting in an effective value of zero. This approach was tested for gas phase CO adsorption at 0.4 V, and the integral band intensity in the spectral region between 1710 and 1580 cm^{-1}, as well as 1710 and 1500 cm^{-1} are plotted versus the rel. CO_{ad} coverage in Fig. 21a, and b, respectively. When integrating from 1710 to 1580 cm^{-1} (Fig. 21a), the integral absorbance continuously increases with increasing rel. CO_{ad} coverage. In this spectral regime the water co-adsorbed with CO_{ad} dominates and the displaced water contributes only partly. Consequently, with increasing CO_{ad} coverage and

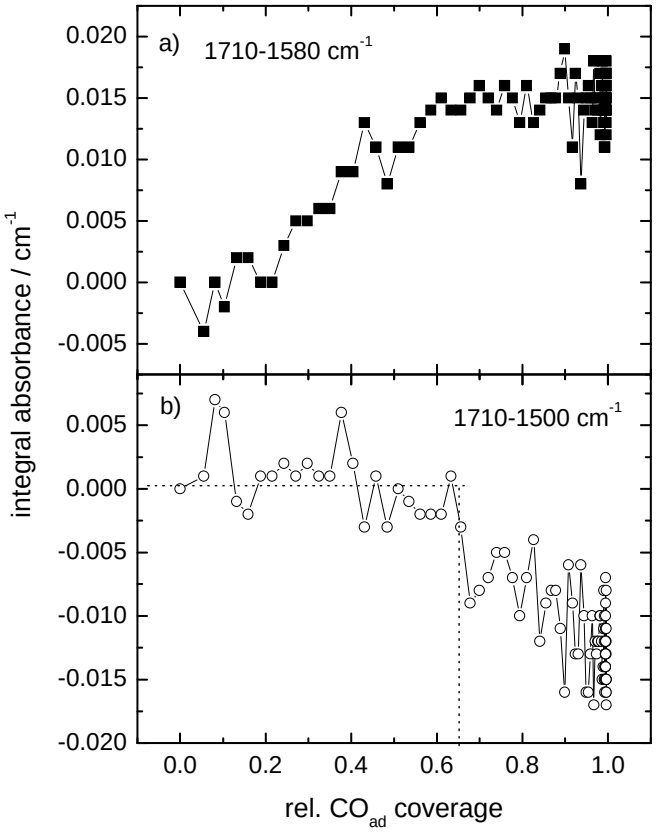

Fig. 21: Integral absorbance within the spectral region as indicated in the figure upon gas phase CO adsorption at 0.4 V. Electrolyte: 0.5 M H_2SO_4 purged with 5% CO/Ar.

thus increasing amount of water co-adsorbed with CO {MIKI02} the integral absorbance between 1710 and 1580 cm^{-1} increases. When the integration was done between 1710 and 1500 cm^{-1} (Fig. 21b), the integral absorbance is essentially zero for rel. CO_{ad} coverage below 0.65, having a scatter of about 0.005 cm^{-1}. At higher rel. CO_{ad} coverages contributions of multiply bonded CO_{ad} (1920 cm^{-1} to ~ 1710 cm^{-1}) result in a lift up of the base line for the integration, and the integrated absorbance decreases. However, the rel. CO_{ad} coverage upon ethanol adsorption does not exceed values of 0.6 and hence it can be assumed that the contributions of water co-adsorbed with CO and displaced water can on the integral band intensity of adsorbed acetyl species can be ignored, if an integration range of 1710 to 1500 $cm^{-1}$is used. However, the extension of the integration range from 1710 to 1580 cm^{-1} to 1710 to 1500 cm^{-1} results in an increased sensitivity to changes in the IR baseline. The temporal development of the integral band intensity of adsorbed acetyl species upon ethanol adsorption, integrating from 1710 to 1500 cm^{-1}, are presented and discussed in section 6.1.2.2.

3.9 Chemicals

0.5 M H_2SO_4 was used as base electrolyte, which was prepared from Millipore Milli Q water (18.2 MΩ/cm) and suprapure sulfuric acid (Merck). The base electrolyte was purged by high purity Ar (MTI Gase, 6.0), or saturated with CO (^{12}CO: Messer-Griesheim, N 4.7, ^{13}CO: Chemotrade Leipzig, 99.9%). Solutions with lower CO concentrations, as used in Chapter 4.1, were prepared by saturating the electrolyte with mixtures of 10% ^{12}CO in Ar, or 1% ^{12}CO and rest Ar (10% CO/Ar and 1% CO/Ar). For the CO adsorption transients presented in Chapter 4.2, 0.5 M H_2SO_4 was saturated with a mixture of 5% ^{13}CO in Ar, prepared from pure ^{13}CO (Chemotrade Leipzig, 99.9%) and Ar via a mass flow controller (MKS, model 147). Solutions containing small organic molecules (Chapter 5,6 and 7), were prepared from the base electrolyte (0.5 M H_2SO_4) and the respective chemicals, as listed in table 2.

Chemical	**Purity**	**Company**
acetic acid (CH_3COOH)	suprapure 100%	Merck
acetaldehde (CH_3CHO)	for synthesis ≥ 99%	Merck
formic acid (HCOOH)	for analysis ≥ 97%	Merck
formic acid (DCOOH)	97 atom % D	Merck
ethanol (CH_3CH_2OH)	gradient ≥ 99.9%	Merck
ethanol ($CH_3{}^{13}CH_2OH$)	99 atom % C	Sigma Aldrich
ethanol (CH_3CD_2OH)	98 atom % D	Sigma Aldrich
ethylene glycol ($HOCH_2$-CH_2OH)	pro analysis 99.5%	Merck
glycol aldehyde ($HOCH_2$-CHO)	dimer, >98%	Fluka
glyoxal (OHC-CHO)	40% solution in water	Merck
glycolic acid (HOOC-CH_2OH)	pro analysis 99.5%	Merck
glyoxylic acid HOOC-CHO)	for synthesis 97%	Merck
oxalic acid (HOOC-COOH)	dihydrate pro analysis	Merck

Table 2: Chemicals used for preparation of electrolytes containing small organic moleclues

4 CO ADSORPTION / OXIDATION / EXCHANGE

In this Chapter, combined ATR-FTIRS/DEMS results on the electrochemical adsorption/oxidation/exchange of CO are presented. As mentioned before, CO can be regarded as the drosophila of surface science, and it is especially relevant for fuel cell applications since it is the main surface poison for Pt based catalysts in polymer electrolyte fuel cells. Furthermore, adsorbed CO is a reaction intermediate resulting from the adsorption/oxidation of small organic molecules: Consequently, the understanding of its potential dependent reaction kinetics and the related CO_{ad} structure is crucial for the interpretation of the reaction pathways of the small organic molecules, which is the main part of my thesis. The results presented and discussed in this Chapter were published in three papers. In the first one we introduced the combined ATR-FTIRS/DEMS set-up as a novel tool for electrocatalytic reaction studies and the oxidation of CO was taken as an example (section 4.1, ref. {HEIN07}). The second publication concerns the CO adsorption kinetics and adlayer build-up, which on the hand shows the manifold information of such simultaneous ATR-FTIRS/DEMS measurements and on the other provides an unique CO_{ad} coverage/intensity profile as a function of the electrode potential {HEIN06B}. This is especially important for the quantitative evaluation of the CO_{ad} formation rates resulting from the adsorption/oxidation of the small organic molecules, as presented in Chapter 6 and 7. Finally, the room temperature CO_{ad} desorption/exchange kinetics will be presented and discussed in section 4.3 {HEIN06}. This work shows that CO_{ad} desorption is possible from a Pt electrode at 0.06 V at room temperature.

4.1 In situ ATR-FTIRS coupled with on-line DEMS under controlled mass transport conditions- A Novel Tool for Electrocatalytic Reaction Studies

M. Heinen, Y.X. Chen[1], Z. Jusys, and R.J. Behm[*]

Institute of Surface Chemistry and Catalysis, Ulm University, D-89069 Ulm, Germany

[1] Pres. address: National Laboratory for Physical Sciences at the Microscale, Department of Chemical Physics, University of Science and Technology of China, Hefei, China

Published in: Electrochimica Acta 52, 5634-5643, **2007**

ABSTRACT

We present a novel combination of *in-situ* attenuated total reflection-infrared spectroscopy (ATR-FTIRS) and on-line differential electrochemical mass spectrometry (DEMS) *via* a dual thin-layer electrochemical flow-cell, which allows i) simultaneous detection of stable adsorbed species and adsorbed reactive intermediates and side products by ATR-FTIR spectroscopy, ii) quantitative determination of volatile reaction products and by-products by DEMS, and iii) determination of the overall reaction kinetics by measuring the Faradaic current under controlled mass transport of reactants and reaction products to and from the electrode. The wealth of information and the insight into reaction mechanism and kinetics accessible from these complementing techniques are demonstrated taking the oxidation of CO on a Pt thin film electrode as example, including the electrooxidation of a preadsorbed CO monolayer at constant potential (0.6 V), the open-circuit reduction of preformed PtO by chemical reaction with CO, and potentiodynamic continuous CO bulk electrooxidation.

4.1.1 Introduction

As already mentioned in Chapter 1.2 and Chapter 1.3, coupling adsorbate detection by means of *in situ* ATR-FTIR spectroscopy, with on-line product analysis via on-line DEMS, in a single experiment, under well defined mass transport conditions, forms a powerful tool for studying electrocatalytic reaction networks. This tool was developed and applied for the first time in our group and this section is meant to demonstrate the potential of this new hyphenated technique for electrocatalytic measurements using the oxidation of CO as an example.

First, the oxidation of preadsorbed CO_{ad} at constant potential is followed. The combined ATR-IR and DEMS CO_{ad} oxidation transients allow the determination of the intensity and frequency of the CO_{ad} related IR signals under oxidation conditions (0.6 V) as a function of the CO_{ad} coverage, where the latter is determined by the simultaneous quantification of the CO_2 formation by DEMS. Comparison of the intensity-coverage and frequency-coverage relation determined this way with theoretical predictions gains information on the distribution of the remaining CO_{ad} species on the surface during the reaction process. Second, the CO_2 formation and the build-up of a CO adlayer during chemical reduction of a preformed oxide layer on the Pt electrode, by reaction with CO, under open circuit conditions, are followed. In this case, the time-correlation between the two techniques allows evaluating the correlation between CO adsorption and CO_{ad} oxidation and an exact determination of the onset of CO_{ad} formation, i.e., of the build-up of the CO adlayer. Finally, in the third example, CO bulk oxidation under defined flow conditions is used for the evaluation of the Stark shift of the CO_{ad} related IR signals under conditions, where CO_2 formation is negligible. This way we want to test whether under these adsorption/oxidation conditions deviations from the Stark shift can be observed. The latter was derived from IR and sum frequency generation measurements in a thin-layer configuration with reduced reactant transport, in CO_{ad} stripping and in CO bulk oxidation experiments {LU05}'{STAM05A}.

4.1.2 Results

4.1.2.1 Electrooxidation of preadsorbed CO monolayer at constant potential

"CO_{ad} stripping" experiments are usually performed in a potentiodynamic way (see section 3.2). However, to avoid effects related to the varying potential in potentiodynamic

measurements, electrooxidation (stripping) of the CO adlayer was performed in potentiostatic reaction transients, stepping the electrode potential from the adsorption potential to the reaction potential (see section 3.2). CO was preadsorbed at 0.06 V for about 5 min from CO-saturated electrolyte. Subsequently, the electrolyte supply was switched to pure supporting electrolyte to remove CO residues from the electrolyte, keeping the potential fixed (0.06 V). Then, the potential was stepped to 0.6 V, while following the reaction by simultaneous acquisition of chronoamperometric Faradaic and mass spectrometric currents and FTIR spectra. The corresponding Faradaic current (a) and mass spectrometric m/z = 44 ion current (b) transients as well as the time-dependent CO_{ad} (c) and (bi)sulfate (d) integral band intensity profiles are displayed in Fig. 22.

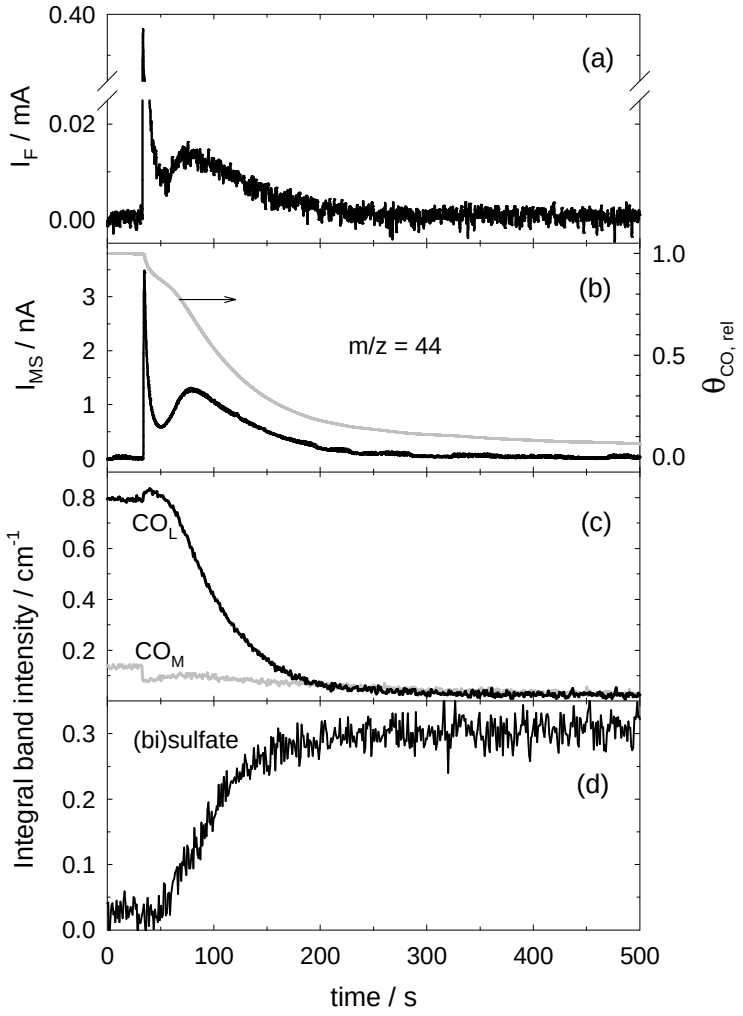

Fig. 22: Simultaneously measured chronoamperometric transients recorded upon potential-step (from 0.06 to 0.6 V) oxidation of a saturated CO adlayer (CO adsorption for 5 min at 0.06 V) on a Pt thin-film electrode in CO-free 0.5 M H_2SO_4 solution (electrolyte flow rate *ca.* 50 µl s^{-1}). a) Faradaic and b) mass spectrometric currents (m/z=44), c, d) time-dependent IR band intensity profiles for CO_L and CO_M (c), and (bi)sulfate (d).

The Faradaic current transient (Fig. 22 a) shows a characteristic initial current spike, followed by an exponential decay. Subsequently, the signal turns into a broad peak centered at *ca*. 40 s after the potential-step, and finally the current decays to nearly zero. At this point, the CO adlayer is nearly completely oxidized. The chronoamperometric transient reproduces the typical response for potential-step oxidation of a preadsorbed CO adlayer at 0.6 V on Pt electrodes, including polycrystalline{GILM63}{MCCA76}{SANT87}, single crystal {SANT87}{SANT91A}{AKEM00}{KORZ01}{LEBE02}{LEBE02B}' ' and nanoparticle ' '{FRIE00}{MAIL04A}{AREN05B}{WANG05N}{ANDR06} Pt electrodes. The shape of these transients is generally explained by nucleation and growth kinetics, the tailing is attributed to CO_{ad} surface diffusion to reactive sites {LEBE02B}. The initial current spike, upon stepping the electrode potential, is most commonly interpreted as purely pseudo-capacitive charging. Therefore, possible losses of CO_{ad} in this peak due to CO_{ad} oxidation are often ignored in the kinetic analysis due to the unknown contribution of CO_{ad} oxidation therein {SANT91A}{PETU98}{MAIL04A}{AREN05B}{ANDR06}.The time delay-corrected m/z = 44 ion current (black line) and the corresponding CO_{ad} coverage values (grey line), calculated mass spectrometric m/z = 44 current, are plotted in Fig. 22 b). Also for the ion current a distinct initial spike appears which subsequently decays within the first few seconds. It occurs in parallel to the Faradaic current spike, suggesting an instantaneous onset of the CO_{ad} oxidation. With increasing time, the mass spectrometric m/z=44 current largely follows the Faradaic current signal. The CO_{ad} coverage (Fig. 22 b, grey line) decreases by about 10% within the initial spike, followed by a further decay in coverage during the main peak.

Information on the dynamic changes in the CO adlayer are obtained from time resolved ATR-FTIRS measurements carried out simultaneously. Selected IR spectra recorded during the first 4 min of the reaction are presented in Fig. 23. (Note that the spectra for the initial 10 s are presented with an increment of 1 s to better resolve the fast adlayer dynamics). Two positive bands located in the region from 2100 to 2000 cm^{-1} and 1900 to 1700 cm^{-1} (depending on the CO_{ad} coverage) correspond to linear and multiply bonded CO_{ad}, denoted as CO_L and CO_M, respectively. Two small positive features at *ca*. 3650 and 1630 cm^{-1} are assigned to water co-adsorbed with CO, two negative bands in the region from 3600 to 3300 cm^{-1} and at *ca*. 1600 cm^{-1} are related to stretching and bending modes of water displaced by CO_{ad} at the solid|liquid interface {MIKI02}. Another pair of positive peaks, developing at frequencies below 1300 cm^{-1}, is assigned to adsorbed (bi-)sulfate species {IWAS94B}{LACH02}{FUTA05}. The

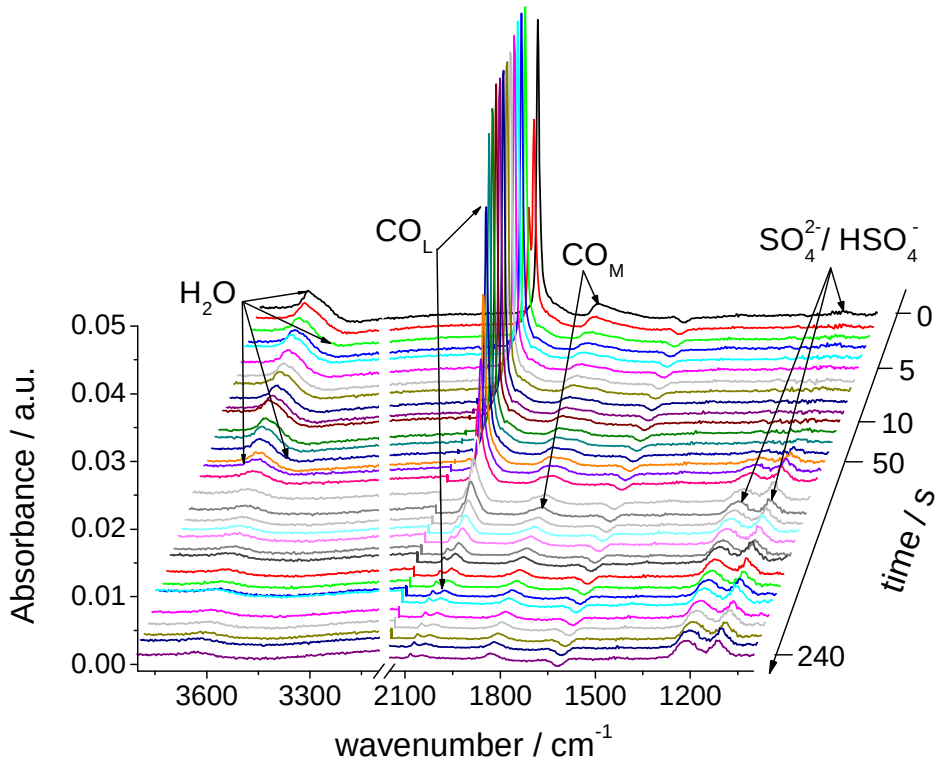

Fig. 23: Selected time-resolved ATR-FTIRS spectra recorded upon potential-step (from 0.06 to 0.6 V) oxidation of a saturated CO adlayer on a Pt thin-film electrode, corresponding to the spectro-electrochemical transients shown in Fig. 22. Each spectrum contains one interferogram with an integration time of 1 s. The spectrum at t = 0 s corresponds to a saturated CO adlayer at 0.06 V, before stepping the potential. For band assignments see text (reference potential: 0.06 V).

positive direction of the IR absorption bands results from re-adsorption of (bi-)sulfate on the surface upon oxidative CO_{ad} removal at 0.6 V {GAMB93}.

The CO_L band intensity first increases slightly with decreasing CO_{ad} coverage, most likely due to a re-polarization of the adlayer. At very high CO_{ad} surface coverage de-polarization of the CO_{ad} molecules results in a decrease of the CO absorption coefficient. This in turn causes the decrease of the CO_{ad} related intensity with increasing CO_{ad} coverage (see also Fig. 32a). The splitting of the CO_L band in the first spectrum directly after the potential step is an experimental artifact, which results from the fact that this spectrum was collected during the potential step and contains contributions from 0.06 V and from 0.6 V. At longer times and decreasing CO_{ad} coverage (Fig. 22b, grey line), the CO_L band intensity decreases continuously, accompanied by a red-shift of the CO band (see Fig. 23 and Fig. 24 c). The CO_M band intensity decreases initially upon the potential-step, but then slightly increases again (Fig. 22 c, grey line). At the same time, the band becomes narrower (Fig. 23), due to the removal of both higher (ν >1880 cm^{-1}) and lower frequency (ν <1800 cm^{-1}) components, and the

frequency of the band center changes from 1865 to 1825 cm^{-1}. The increase of the CO_L and decrease of the CO_M integral band intensity upon the potential step was explained by a potential-induced site conversion in the CO adlayer, from CO_M to CO_L, when stepping the potential from 0.06 to 0.6 V {SUN06}. Based on the present data, the change in site population may also be induced or affected by the concomitant decrease of the CO_{ad} coverage, which during the first second after the potential step amounts to *ca*. 5% of the adlayer coverage. The continuing slight increase in CO_M band intensity with time, up to 50 s after the potential step, can result from decreasing interactions between CO_{ad} oscillators with decreasing CO_{ad} coverage, which in turn leads to a reduced intensity transfer from the lower to the higher frequency component {VILL94}.

The temporal evolution of the positive feature at *ca*. 3650 cm^{-1}, which decreases with time spent at 0.6 V and follows the development of the CO_L band intensity, supports the previous assignment of this peak to water co-adsorbed with CO_{ad} {MIKI02}. Furthermore, the spectra signal i) an increase in (displaced) water adsorption and ii) adsorption of (bi-)sulfate species upon the potential-step. The former is indicated by the slight decrease of the negative IR band in the region at *ca*. 3550 cm^{-1}, which is related to this species, the latter is evidenced by the appearance of a pair of bands located at frequencies below 1300 cm^{-1} {IWAS94B}{LACH02}{FUTA05} (Fig. 23). The time delay between the onset of CO_{ad} oxidation and of (bi-)sulfate adsorption, which starts *ca*. 20 s after the potential step, can be understood from the space requirement for (bi-)sulfate adsorption, which is adsorbed in a tetrahedral configuration {NART94}{LACH02}{FUTA05}, requiring the removal of more than one neighboring CO_{ad} species for adsorption of a (bi)sulfate species. It should be noted that (bi-)sulfate adsorption mainly occurs during the main peak in the Faradaic current transient (Fig. 22a), indicating that this current transient peak involves the current (charge) of (bi)sulfate adsorption and therefore cannot be quantitatively converted into a CO_{ad} oxidation current. Accordingly, the Faradaic charge commonly used for estimating the CO_{ad} coverage will also include the (bi-)sulfate adsorption charge and therefore overestimate the CO_{ad} coverage. This is avoided by using the mass spectrometric m/z = 44 charge, which is not sensitive to these effects, if the K^* value is calculated from potentiostatic CO oxidation (see Fig. 8).

As mentioned in the introduction, a quantitative interpretation of the IR spectroscopy data is of special interest, in particular the correlation between the (integrated) peak intensity or the peak frequency and the CO_{ad} coverage. Using the CO_{ad} coverage determined from the mass

spectrometric data, we obtain the band intensity – CO_{ad} coverage relation for the CO_L and CO_M species and the band frequency - CO_{ad} coverage relation for the CO_L species displayed in Fig. 24. Potential-induced Stark effects are absent in these measurements (except for the initial moment of the potential step), and therefore the data plotted in Fig. 24 provide an absolute calibration of the IR spectral features *vs*. the CO_{ad} coverage during continuing oxidation at constant potential, which has not been available so far.

The integral CO_L band intensity (Fig. 24a) increases slightly after the potential step, concomitant with a decrease in CO_{ad} coverage by *ca*. 10%. Subsequently, it decays monotonically with further decreasing coverage. Relating the CO intensities to the CO_{ad} coverage, at a

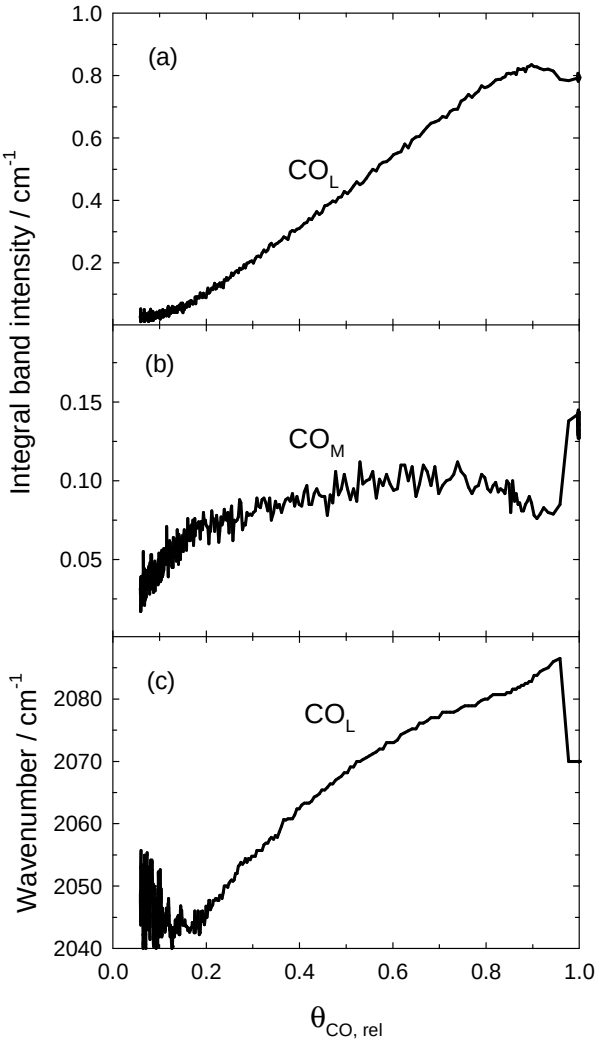

Fig. 24: CO_{ad} coverage (relative CO_{ad} coverage) dependence of the integrated intensities of the CO_L (a) and CO_M (b) bands and of the peak frequency of the CO_L band (c) upon potential-step (from 0.06 to 0.6 V) oxidation of a saturated CO adlayer on a Pt thin-film electrode in CO-free 0.5 M H_2SO_4 solution (spectro-electrochemical data: Fig. 22 and Fig. 23).

constant potential of 0.6 V and starting from the highest coverage, the CO_L band intensity first increases slightly with decreasing CO_{ad} coverage from 0.95 to 0.85 $\theta_{CO,sat}$ ($\theta_{CO,sat}$: CO_{ad} saturation coverage), and then decreases in an approximately linear fashion, in agreement with a report by Chang et al. {CHAN90C}. However, at a coverage below about 0.2 $\theta_{CO,sat}$, the slope of the coverage-intensity plot is significantly smaller than at higher coverages. The CO_M intensity (Fig. 24b) first steeply decreases from 1 to 0.95 $\theta_{CO,sat}$, increases slightly for coverages from 0.95 to 0.7 and subsequently decreases from 0.7 to 0.15 $\theta_{CO,sat}$. At coverage below 0.15 $\theta_{CO,sat}$, it decreases linearly with coverage.

Assuming that at low coverage CO_{ad}-CO_{ad} interaction are negligible and that the cross sections for CO_L and CO_M signals are about equal, this means that at low CO_{ad} coverages CO_L and CO_M adsorption are about equally favorable, as indicated by the comparable integrated band intensities of CO_L and CO_M, as well as the similar increase of both with CO_{ad} coverage.At higher coverages ($\theta_{CO} > 0.15\ \theta_{CO,sat}$), the CO_L intensity increases essentially linearly with coverage, while the CO_M intensity remains about constant. These observations can be explained in two different ways (or a combination of both): In the first case, preferential adsorption of CO in a linearly bonded configuration prevails at coverages higher than 0.15 $\theta_{CO,sat}$. In the other model, the change in the intensity increase of the CO_{ad} related signals is due to an increasing intensity transfer from CO_M to CO_L {SEVE95}, resulting in a strong increase of the CO_L intensity, whereas the CO_M intensity remains more or less constant, although the total amount of multiply bonded CO_{ad} increases. Based on the present data, we cannot rule out either of the two possibilities, but the very precise intensity-coverage correlation (and the frequency-coverage relation, see below) obtained by these measurements provides an ideal basis for a theoretical modeling of these effects. In the high-coverage regime, the deviation of the CO_L intensity from a linear behavior most likely results from static and dynamic CO_{ad}-CO_{ad} interactions {SCHW89}, {SEVE95}.

The present data also give additional information on the origin of the initial fast decay of the CO_M intensity, upon stepping the potential to 0.6 V (see the abrupt CO_M intensity decrease upon the potential step; Fig. 22c, grey line), which could result either from a fast potential-induced site conversion or from an initial preferential oxidation of CO_M species. Considering that for stepping the potential from 0.06 to 0.4 V, in the absence of CO_{ad} oxidation, a similar CO_M intensity loss is observed, we attribute this effect to a potential induced site conversion rather than to preferential CO_M oxidation. Preferential oxidation of CO_M, in the limit of low

coverages, would also be in contrast to the observation that the ratio of CO_L and CO_M intensities at low coverage is about one. The weak increase in CO_M intensity at higher coverages (see Fig. 22c or Fig. 24b) is attributed to decreasing CO_M to CO_L intensity transfer at lower coverage due to decreasing CO_{ad}-CO_{ad} interactions (see above).

The resulting variation of the CO_L band frequency *vs*. the CO_{ad} coverage is shown in Fig. 24c. The CO_L band frequency increases by *ca*. 16 cm^{-1}, upon stepping the potential from 0.06 to 0.6 V, corresponds to a Stark shift of about 29 cm^{-1} V^{-1}. This value agrees perfectly with both theoretical estimates {KORZ86} and the experimentally determined Stark shift determined from potentiodynamic measurements {WASI01B}{LU05}{STAM05A}{FROM06}. After this mainly potential-induced perturbation (initial electrooxidation also causes a loss of *ca*. 5% of the CO adlayer), the further decrease of the CO_L band frequency at CO_{ad} coverages below 0.95 $\theta_{CO,sat}$ is solely related to the variation of the interactions between adsorbed CO molecules, caused by the decreasing CO_{ad} coverage.

In contrast to the CO_L intensity, the CO_L frequency does not exhibit a linear relation with the CO_{ad} coverage. Instead, it decays continuously, but with changing slope with decreasing CO_{ad} coverage. The continuous variation of the CO_L frequency with the CO_{ad} coverage excludes the possibility of CO_{ad} islands with fixed local CO_{ad} density. A further interpretation has to await future modeling studies.

4.1.2.2 Reaction of preformed PtO with CO under open-circuit conditions

In this section, the focus is on the correlation between Pt-oxide reduction and build-up of the CO adlayer during interaction of the Pt-oxide layer with CO-saturated electrolyte. For these measurements, PtO was first formed at 1.2 V for ca. 1 min in CO-free supporting electrolyte, followed by disabling the potential control of the working electrode and switching the electrolyte supply to CO-saturated solution (after *ca*. 8 sec.). A chronopotentiometric open-circuit potential (OCP) transient (t = 0 corresponds to open-circuiting), recorded during reaction of the preformed PtO with CO, is shown in Fig. 25a.

Already in CO free electrolyte the potential slightly drifts from 1.20 to about 1.15 V (t = 0 to t = 8s), approaching the open circuit potential of about 1.0 V of a Pt electrode in 0.5 M H_2SO_4. Upon admission of the CO-saturated supporting electrolyte to the electrode, the OCP decreases steeply, decaying to *ca*. 0.55 V under steady-state conditions. This decay is clearly related to oxide reduction by reaction with CO, since in open-circuit experiments in 0.5 M

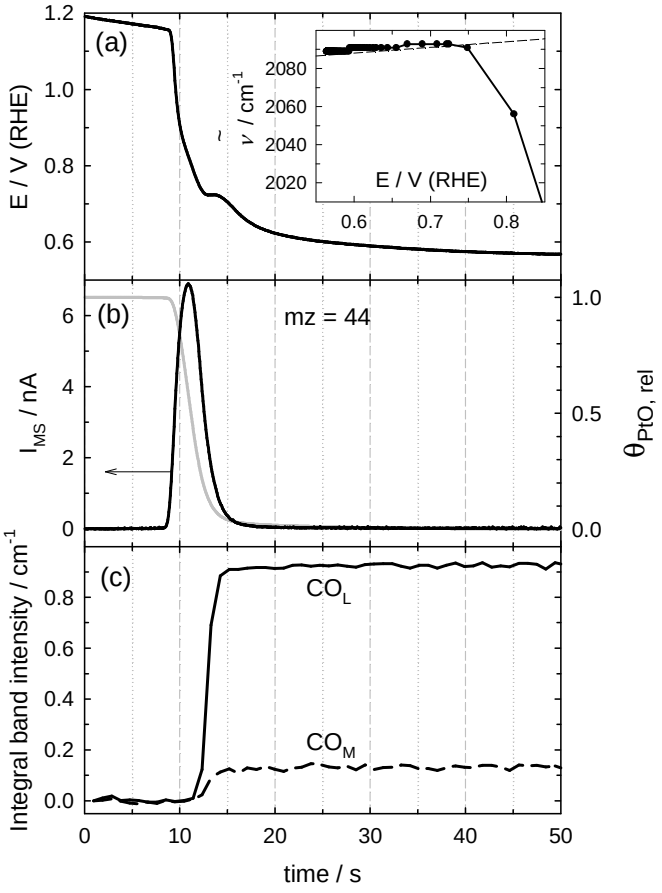

Fig. 25: Simultaneously recorded chronopotentiometric (a) and mass spectrometric ion current (m/z=44) (b) transients and time-dependent IR band intensity profiles for CO_L and CO_M (c) measured upon interaction of a preformed PtO layer (preformed at 1.2 V for 1 min) with CO-saturated solution (admission stars at *ca*. 8 s) under open-circuit conditions (t = 0 s corresponds to open-circuiting, reference potential: 1.2 V). Inset in c): CO_L frequency as a function of the open circuit potential (dashed line indicates a 30 cm^{-1} V^{-1} Stark tuning slope).

H_2SO_4 purged with Ar, only a rather small decrease of the OCP to about 1.0 V was found within a comparable time interval {JUSY01}. The general shape of the chronopotentiometric OCP transient, including the step at ~0.7 V, largely resembles that reported in previous studies {WATA75A}{PODL05}, when considering the different conditions for PtO formation and the CO transport conditions in the above studies. The time delay-corrected CO_2 formation transient shows a clear m/z = 44 ion current peak (Fig. 25b, black line), which starts with the steep decrease in the open-circuit potential (Fig. 25a).

The maximum CO_2 formation rate is reached at an OCP of *ca*. 0.8 V. Subsequently, the CO_2 formation rate decreases again, reaching the background level *ca*. 10 s after the admission of CO-saturated solution to the electrode surface. The highest rate of CO_2 formation achieved under open-circuit conditions (Fig. 25b) corresponds to the rate of continuous CO oxidation at $E \geq 0.85$ V in potentiodynamic experiments (see Fig. 26b in section 4.1.2.3), suggesting that

in both cases the mass transport limited CO oxidation rate is attained. Although the behavior of the OCP transient had been tentatively assigned to the reduction of the preformed PtO by chemical reaction with CO under open-circuit conditions {WATA75A}{PODL05}, the present DEMS data provide direct proof of the CO oxidation reaction under these conditions on a Pt electrode. For comparison, open-circuit reduction of electrochemically preformed PtO by CO and CO_2 formation were recently detected on a Ru-modified polycrystalline Pt electrode by *in situ* IR spectroscopy in a thin-layer configuration {CHRI04}).

Upon partial consumption of the PtO, the electrode surface is no more homogeneous and consists of PtO and Pt. In this situation, the CO molecules approaching the surface can adsorb on Pt sites and react with neighboring residual PtO species (Langmuir-Hinshelwood mechanism), emptying new free sites for CO adsorption. Upon increasing reduction of the PtO, the highest reaction rate is attained at a PtO coverage of about 0.5 of the maximum coverage, as expected from the above mentioned Langmuir-Hinshelwood mechanism. With further consumption of PtO, the increasing lack of oxygen donor species results in a rapid decrease of the CO oxidation rate (Fig. 25b, black line).

Quantifying the amount of CO_2 formed upon open-circuit interaction of preformed PtO with CO, by comparison with the amount formed upon CO_{ad} stripping, yields a value of about 1.6 $\theta_{CO,sat}$. Assuming that the saturated CO_{ad} coverage for polycrystalline Pt electrode is 0.8 ML {WEAV92}, this leads to an oxygen coverage of *ca*. 1.28 ML. This result is of comparable magnitude as the value of ~1 PtO monolayer derived for PtO formation under present conditions from the formation and reduction charge {ANGE73}{BIRS93}{JERK04} {PODL05}. Steps in the open-circuit potential development had been attributed to surface segregation of subsurface oxygen {WATA75A}; in the present case subsurface oxygen appears to be unlikely. The relative PtO coverage $\theta_{PtO}/\theta_{PtO,max}$ at any time can be evaluated as the difference of the initial coverage ($\theta_{PtO,max}$) and the CO consumption determined from the ion current charge for CO_2 formation accumulated up to that time. The resulting PtO coverage transient ($\theta_{PtO}/\theta_{PtO,max}$) is included as a grey line in Fig. 25b (scale is given on the right-hand axis).

The build-up of the CO adlayer during this reaction, which provides information also on the surface diffusion and reaction behavior of the preformed oxide and the CO_{ad} species, was followed simultaneously by IR. In principle two different cases are possible during the reaction of CO_{ad} with the oxygen species: i) CO_{ad} and the O_{ad} species coexist on the Pt surface or ii) CO_{ad} formation is only detected after a complete removal of the oxygen species. A plot of the

CO_L and CO_M intensities with time is given in Fig. 25c. These data show that the appearance of the CO_L and CO_M features is delayed compared to the CO_2 formation (Fig. 25b). The CO_{ad} related IR bands start to appear only when passing the maximum rate of CO_2 formation, at a Pt oxide coverage of about 0.5 $\theta_{PtO,sat}$, followed by a fast increase to the maximum intensity. This is reached when the CO oxidation rate (PtO coverage) becomes negligible. The IR data clearly show that both CO_{ad} and oxygen species coexist on the surface.

Despite of the constant values of the integral band intensities for CO_{ad} (Fig. 25c) and the absence of further CO_2 formation (Fig. 25b), the open-circuit potential still slowly decreases with time (Fig. 25a). This slight variation is accompanied by a slight decrease in the CO_L related IR band frequency (see inset, Fig. 25a). During the reaction, the frequency of the linearly adsorbed CO_L is mainly influenced by two effects, namely the Stark shift, which results in a frequency decrease with decreasing (open-circuit) potential, and the varying CO_{ad} coverage, which leads to an increase in CO_{ad} frequency with increasing CO_{ad} coverage {KORZ86}. Therefore, the increasing frequency for potentials higher than 0.75 V is mainly attributed to a CO_{ad} coverage increase, whereas the decreasing frequency in the later stages of the reaction, for potentials less than 0.75 V, is most likely attributed to the Stark shift, which over-compensates effects from a possible small increase of the CO_{ad} coverage.

The combined data lead to the following conclusions on the reaction of PtO with CO under open circuit conditions: *i*) Initially the reaction (CO oxidation) is slow due to the limited availability of CO adsorption sites (possibly at defects of the PtO monolayer) at high oxide coverages; *ii*) with time, the availability of these sites and therefore also the reaction rate increase, and the highest reaction rate is achieved at about 0.5 $\theta_{PtO,max}$; *iii*) upon further consumption of PtO the reaction rate decreases steadily, due to the increasing lack of reactive oxygen species. At the same time, the CO adlayer begins to build up and reaches its maximum coverage at the end of the reaction.

4.1.2.3 Potentiodynamic CO bulk oxidation

Compared with potentiodynamic CO_{ad} stripping, CO bulk oxidation extends the range of essentially constant CO_{ad} coverage to more positive potential due to the continuous compensation of oxidation induced losses in the CO_{ad} coverage by CO adsorption from the bulk, until at higher potential the oxidation rate becomes too high and the reaction rate increases rapidly. The absolute shift of the onset potential for CO oxidation and the steepness

of the increase in the reaction current and the CO_2 formation rate depend sensitively on the CO transport to the electrode. Previous IR measurements in a thin-layer external reflection FTIRRAS configuration were significantly affected by the slow CO diffusion in that set-up {BATI04B}, and also measurements with a freely accessible working electrode, e.g., IR measurements in an internal reflection ATR-FTIRS cell {SUN99A}, or measurements using second harmonic generation (SHG) {AKEM00}{POZN03}{POZN04}, sum frequency (SFG) generation {CHOU03B}{LU05}, or combined SHG and reflectance spectroscopy {FROM05}{FROM06}, suffered from the same limitations. For all of these cases, rather small values for the CO bulk oxidation current suggest that these measurements resemble more the oxidation of preadsorbed CO in the presence of *some* CO in the vicinity of the electrode rather than that of bulk CO oxidation with enforced and controlled continuous CO delivery to the electrode surface. Similar limitations apply also to the thin-layer flow-cell set-up for *in situ* IR microscopy measurements {ZHOU05F}.

The combined IR-DEMS flow-cell measurements not only allow, for the first time, to perform *in situ* IR measurements under enforced and controlled transport conditions, but also to record simultaneously the CO_2 formation rate and thus determine the onset of CO oxidation. As mentioned in the introduction, this allows a precise determination of the range of constant CO_{ad} coverage in the positive-going potential scan, assuming that the surface is CO_{ad} saturated during the preceding negative-going scan and that potential induced desorption of CO_{ad} is negligible. In the range of constant CO_{ad} surface coverage determined that way via on-line DEMS possible potential-induced effects on the frequency of the CO_{ad} related signals other than the Stark effect can be mapped out. This is a main advantage of the combined ATR-FTITS/DEMS approach, compared to purely IR based data, in which the range of constant CO_{ad} coverage is unknown. Therefore, in the latter case the interpretation of the IR spectroscopic data is complicated due to a possible convolution of CO_{ad} coverage, CO adlayer structure and potential-induced effects.

Fig. 26 presents the results of the simultaneous ATR-FTIRS/DEMS measurements for continuous (bulk) CO potentiodynamic oxidation on a Pt film electrode in CO-saturated 0.5 M H_2SO_4 solution during repetitive potential cycling (electrolyte flow 50 µl s^{-1}, scan rate 10 mV s^{-1}). At potentials below 0.7 V, the H_{upd} adsorption/desorption features typical for a polycrystalline Pt electrode are fully suppressed, due to the presence of a saturated CO adlayer (Fig. 26a, c). In the positive-going potential scan, the Faradaic current increases steeply at 0.92 V, and passes through a sharp anodic current peak at *ca*. 0.94 V.

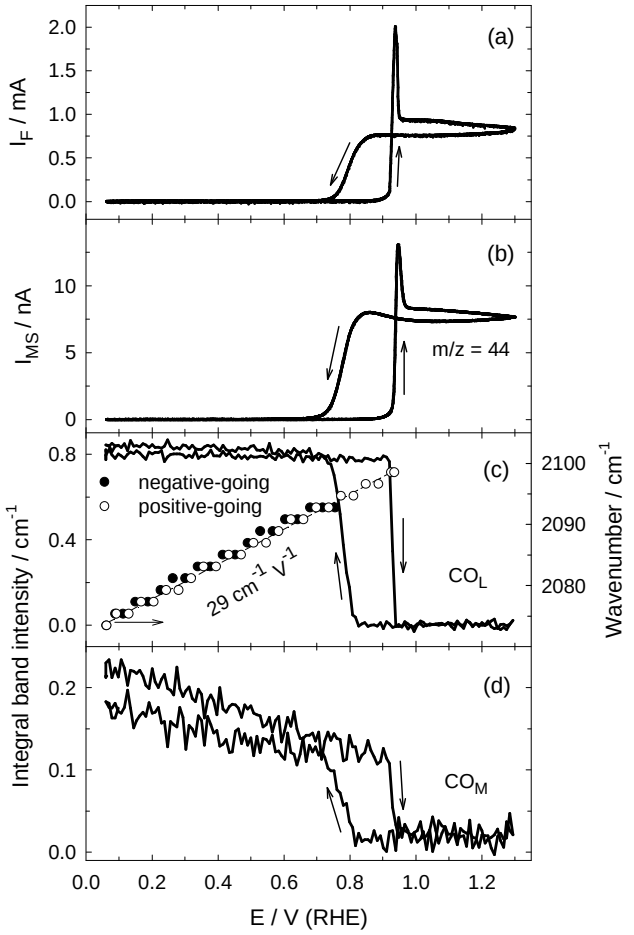

Fig. 26: Simultaneously measured cyclic voltammograms of the Faradaic (a) and mass spectrometric ion (m/z = 44) (b) currents, and of the potential-dependent IR band intensities and frequencies for the CO_L (c) and of the intensities for the CO_M (d) signal on a Pt thin-film electrode during potential scanning (10 mV s^{-1}) in CO-saturated 0.5 M H_2SO_4 solution under well-defined mass transport conditions (electrolyte flow rate *ca.* 50 µl s^{-1}, reference potential: 0.06 V).

After that peak, the Faradaic current returns to the mass transport affected current for continuous CO oxidation. The onset of the anodic current in the positive-going scan relates to the "ignition" of the oxidation of the saturated CO adlayer, which was formed during cycling at lower (non-oxidative) potentials. When the potential scan is reversed at 1.3 V, the current remains at the mass transport limited value during the negative-going sweep down to 0.85 V. At that point the current drops rather quickly due to the decreasing formation of oxy-species, and reaches zero at potentials below 0.7 V (Fig. 26a). Overall, the CV features for continuous oxidation of CO on the Pt thin film in the thin-layer flow-cell largely resemble those for bulk CO electrooxidation on polycrystalline and single crystal Pt rotating disk measurements {BREI60}{STON67} {KITA95B}{MARK99C} and in wall-jet disk electrode measurements {BERG98A} {STAL06}, indicating reasonably well-established mass transport in all cases. The observed hysteresis of the anodic CO oxidation current increase/decrease in the positive-

and negative-going scans is due to a kinetically induced shift of the PtO formation/reduction potential, which has been equally observed for the oxidation and reduction of PtO {ANGE73}. It should be noted that in the first positive-going scan (not shown), after CO adsorption at 0.06 V, a distinct pre-peak is observed the potential region from 0.5 to 0.9 V, which is not present in subsequent scans. Similar effects have been reported in previous studies ,{KITA95B}{WIEC95A}{MARK99}{BATI04B}.

The simultaneously measured m/z=44 ion current signal (CO_2 formation, Fig. 26b) follows the Faradaic current (Fig. 26a) response on the electrode potential, revealing that both Faradaic and mass spectrometric currents originate solely from electrooxidation of CO. Both the Faradaic and the mass spectrometric currents display a clear mass transport limitation in the potential region of PtO formation; the magnitude of this current is about 10 – 20 times higher than that reported for "bulk CO oxidation" without enforced convection {LU05}. The mass transport limited current for continuous CO (bulk) oxidation, which is of similar magnitude as the maximum rate in the open-circuit CO oxidation by reaction with PtO (section 4.1.2.3), appears in the potential region, where the Pt surface is covered by an oxide film. In this potential region the potentiodynamic CO oxidation is limited by the CO transport to the surface, indicating that the formation of the oxygen species on the Pt surface is faster compared to the mass transport limited adsorption of CO. Therefore, we assume this current to result from Pt oxidation and subsequent chemical reaction of CO with the electrochemically generated PtO (see before) {STON67}{BERG98A}{STAL06}. This equally results in an overall two-electron process, as a sum of the electrochemical PtO formation (two electrons) and non-electrochemical reaction between CO and electrochemically generated PtO {STAL06}. Considering that the CO oxidation rate in the positive-going and in the negative-going scan are slightly different (see Fig. 26a and b), the CO bulk oxidation rate in the oxide formation range can not solely depend on the mass transport, but is also affected by the stability of the oxide species, which increases with increasing upper potential limit.

In situ FTIR spectra were acquired in parallel to the Faradaic (Fig. 26a) and mass spectrometric (Fig. 26b) current signal. The integrated intensities of the bands attributed to linearly (CO_L) and multiply bound (CO_M) CO_{ad} are plotted in Fig. 26c and d, respectively. At non-oxidative potentials, the CO_L band intensity is about constant in the positive- and negative-going potential sweep (Fig. 26c, solid line), whereas the CO_M band intensity decreases with increasing potential (Fig. 26d). Since CO_{ad} oxidation in the potential region

from 0.06 to 0.8 V is negligible (Fig. 26b), the decrease of the CO_M band intensity by *ca*. 40% upon potential increase can not be explained by a preferential oxidation of CO_M to CO_2 (see section 4.1.2.1). Instead, it was attributed to potential-induced changes of the adlayer structure (potential-induced site conversion from CO_M to CO_L) {LEBE02C}{LU05}. The absence of a corresponding increase in the CO_L intensity, opposite to the decrease of the CO_M intensity, is not surprising, since at these high coverages the CO_L intensity does hardly vary with the CO_{ad} coverage (see Fig. 24a) and as it will be shown in section 4.2, the cross section of adsorbed CO decreases with the electrode potential (see Fig. 32a). On the other hand, slightly lower saturation coverages were reported for CO adsorption on different Pt surfaces for potentials positive of 0.35 V, but still in the non-oxidative regime {CUES06}. Similar potential-induced variations in the steady-state CO_{ad} coverage can also not be excluded for the present case, but the dependence of the CO_{ad} related intensities on the CO_{ad} coverage as a function of the electrode potential will be discussed in detail in section 4.2.

At potentials from 0.9 V to 0.95 V in the positive-going scan, the integral band intensities for both CO_L (Fig. 26c, solid line) and CO_M (Fig. 26d) decrease steeply down to the background level, which is reached at 0.95 V, and maintained from 1.3 to 0.85 V in the negative-going scan. The decrease of the CO_{ad} related IR intensities is accompanied by CO oxidation (Fig. 26a, b). Due to the fast production of active oxygen-donor species and their equally fast reaction with CO_{ad}, the steady-state CO_{ad} coverage at these high potentials is negligible, and consequently, no CO_{ad} related IR signals are detected. This agrees perfectly with the largely mass-transport limited CO_{ad} oxidation rate, which means that CO is essentially consumed upon adsorption. At *ca*. 0.8 V in the negative-going scan, both the CO_L and CO_M bands re-appear, and their intensities increase steeply with further decreasing potential. At the same time, the CO_2 formation rate decreases sharply, i.e., the CO_2 formation drops with the onset of CO_{ad} accumulation, indicative of a crossover from mass transport limitation to kinetic limitation, e.g., due to decreasing oxy-species formation or a potential-induced change in the activation barrier for the combination of CO_{ad} and adsorbed oxygen species.

Finally, a linear potential-dependent frequency shift dv/dE (~29 cm^{-1} V^{-1}) of the CO_L band frequency is observed over the entire range of constant CO_{ad} coverage in both the positive- and negative-going scan (Fig. 26c), up to about 0.9 and 0.8 V, respectively, as expected for a situation dominated by the potential-induced Stark effect {KORZ86}{MARK02A}{LU05}. An anomalous Stark-tuning slope, as reported by V. Stamenkovic *et al*. {STAM05A} (IRAS in external reflection configuration) and G.Q. Lu (sum frequency generation) *et al*. {LU05}

between 0.6 and 0.8 V, is not observed in the present study. As mentioned before, in solely IR based studies the range of constant CO_{ad} coverage is unknown. Furthermore, the range of constant CO_{ad} coverage strongly depends on the CO mass transport to the surface. For example: in a CO stripping experiment (CO free electrolyte; CO mass transport to the surface is zero) the range of constant CO_{ad} coverage is limited to potentials below 0.55 V (not accounting for the so-called pre-peak) whereas, the range of constant CO_{ad} coverage upon CO oxidation in CO containing electrolyte is increased to about 0.9 V (see Fig. 26). Due to the pure mass transport in the work by Stamenkovic et al. and Lu et al., which is evidenced by the small mass transport limited currents, compared to the enforced high mass transport in the our work, the range of constant CO_{ad} coverage in the former two studies will shift to lower potentials. Therefore, a convolution of the Stark effect and a change in the CO_{ad} surface coverage results in the observation of an "anomalous" Stark effect, opposite to our work, where the CO_{ad} coverage is essentially constant. The observation, that in our study the frequency shift follows the expected Stark-tuning slope, also confirms the initial assumption, that increased CO_{ad} desorption at higher potentials does not significantly affect the steady-state CO_{ad} coverage in the potential range up to the onset of CO_{ad} oxidation. Contributions from CO oxidation were excluded based on the DEMS measurements.

4.1.3 Summary

The potential of the novel ATR-FTIRS/DEMS set-up for mechanistic and kinetic studies of electrocatalytic reactions was demonstrated taking CO oxidation on a Pt film as an example and new insight into the CO oxidation were gained.

Spectro-electrochemical data simultaneously acquired during CO_{ad} monolayer oxidation at constant potential, after stepping the electrode potential from 0.06 to 0.6 V in CO-free 0.5 M H_2SO_4 solution, allow distinguishing between CO_{ad} oxidation, pseudo-capacitive contributions and contributions from (bi-)sulfate re-adsorption on CO-free sites, and provide information on the dynamics of the adlayer. The high sensitivity of the mass spectrometric CO_2 detection allows a precise determination of the CO_{ad} coverage at each time of the transients (in the absence of CO_{ad} desorption), which is the basis for an equally precise determination of the relations between the intensity of the CO_{ad} related IR signals and the CO_{ad} coverage (*intensity-coverage correlation*) and between the frequency of these signals and the CO_{ad} coverage (*frequency-coverage correlation*). Comparison with theoretical models should allow conclusions on the distribution of the CO_{ad} on the surface during the reaction.

For chemical CO oxidation under open circuit conditions, by reaction of CO with a preformed PtO adlayer, the combined IR-DEMS data show that *i)* the rapid change in the open circuit potential is indeed due to CO_2 formation, that *ii)* the CO_2 formation rate is initially slow, increases with PtO removal and passes through a maximum at about 0.5 ML PtO coverage, where the CO_2 formation rate is presumably CO transport limited, and that *iii)* the build-up of a CO adlayer starts only after much of the PtO has been reductively removed, at an oxide coverage of about 0.5 $\theta_{PtO,sat}$. Obviously, CO_{ad} surface diffusion and reaction are sufficiently fast to prevent the build-up of a CO adlayer in the earlier stages of the reaction, at oxide coverages >0.5 $\theta_{PtO,sat}$ and potentials >0.8 V.

During CO bulk oxidation under enforced mass transport conditions, simultaneous on-line mass spectrometry and *in situ* IR spectroscopy measurements allow to precisely define the onset of CO_{ad} oxidation and hence the potential range of essentially constant CO_{ad} coverage, due to continuous replacement of oxidized CO by adsorption from the electrolyte. Over this entire potential range, from 0.06 to 0.9 V in the positive-going scan, the frequency of linearly adsorbed CO shows a Stark-tuning slope of 29 cm^{-1} V^{-1}, in good agreement with theoretical predictions. Within this potential range we find no deviations from a linear Stark shift. In the PtO region the absence of any detectable CO_{ad} bands suggests a negligible CO_{ad} steady-state coverage under these conditions, pointing to a fast, mass transport limited CO oxidation.

In total, these results convincingly demonstrate the potential of the novel spectro-electro-chemical multi-technique set-up, operating under enforced and controlled mass-transport conditions, for mechanistic and kinetic studies of electrocatalytic reactions.

4.2 CO Adsorption Kinetics and Adlayer Build-up studied by Combined ATR-FTIR Spectroscopy and on-line DEMS under Continuous Flow Conditions

M. Heinen, Y.X. Chen[1], Z. Jusys, and R.J. Behm[*]

Institute of Surface Chemistry and Catalysis, Ulm University, D-89069 Ulm, Germany

[1] Pres. address: National Laboratory for Physical Sciences at the Microscale, Department of Chemical Physics, University of Science and Technology of China, Hefei, China

Published in: Electrochimica Acta 53, 1279-1289, **2007**

ABSTRACT

Using a novel combined spectro-electrochemical DEMS/ATR-FTIRS technique, the CO adsorption kinetics on a Pt film electrode were studied, performing transient CO adsorption experiments at different constant potentials (0.06 to 0.6 V). CO adsorption and CO_{ad} coverage were determined continuously from the CO consumption measured by on-line differential electrochemical mass spectrometry (DEMS). Simultaneously measured FTIR spectra, recorded *in-situ* in an attenuated total reflection (ATR) configuration, allow a direct correlation of the IR band intensity and frequency with CO_{ad} surface coverage at different constant potentials. The data show that i) the CO adsorption kinetics are independent of the adsorption potential up to 0.5 V, ii) a significant potential dependence of the ratio between CO_L and CO_M for the same coverage, that iii) in the regime of very high CO_{ad} coverages there is no proportional relation between CO_{ad} coverage and $CO_{L,M}$ intensity, and iv) a distinct tendency for CO_{ad} island formation at $E_{ads} < 0.2$ V and > 0.4 V, most likely due to coadsorption of H-upd at the lower potentials and (bi)sulfate at higher potentials. Finally, at 0.6 V, CO_{ad} oxidation follows a Langmuir-Hinshelwood mechanism with the highest CO_2 formation rate at a relative CO_{ad} coverage of ~0.4.

4.2.1 Introduction

The kinetics and dynamics of adsorption processes as the initial step for subsequent surface reactions have been investigated extensively over the last decades, and the molecular adsorption of CO on metal surfaces was one of the model systems {CAMP90}. In contrast to gas phase adsorption studies, the dynamics and kinetics of CO adsorption have rarely been investigated quantitatively in an electrochemical environment {KAZA72}CZER78}{JUSY01A}, although CO adsorption is highly relevant for various applications, e.g., for the CO induced poisoning of metal electrodes or metal catalysts in low temperature fuel cells when operated with CO contaminated H_2-rich feed gases. One reason for the lack of quantitative studies are experimental problems: Measurements of the adsorption rate require controlled mass transport conditions to avoid artifacts arising from insufficient mass transport. In the latter case, the resulting kinetics are strongly affected or even controlled by diffusion in the electrolyte. Furthermore, they require an exact determination of the amount of adsorbed species. Purely electrochemical measurements are in most cases not sufficient, since the Faradaic current measured during adsorption is influenced by hydrogen and/or anion displacement, depending on the adsorption potential. Therefore, other, spectroscopic methods have to be applied to follow the evolution of the adsorbate coverage during the adsorption process, preferentially continuously during the experiment. Examples for CO adsorption measurements include the use of labeled ^{14}CO, which allows to quantify the amount (coverage) of adsorbed CO by measuring the emitted radiation as a function of time {CZER78}, or, more recently, the use of on-line differential electrochemical mass spectrometry (DEMS), measuring the CO partial pressure in CO containing electrolyte during adsorption {JUSY01A}. The authors of the former study concluded on first order adsorption kinetics, independent of the potential, although mass transport effects are likely to significantly affect the measured “adsorption kinetics” in the set-up used {CZER78}. In the latter study, DEMS was used to follow the CO uptake on carbon supported Pt catalysts in the presence of H_2 by measuring the CO partial pressure during adsorption {JUSY01A}, which can be converted into the adsorption rate and into the CO_{ad} coverage.

In this section, I present and discuss the results of a combined electrochemical and *in situ* spectroscopic study on the adsorption of CO on a Pt film, which was performed in the combined ATR-FTIRS/DEMS set-up. CO adsorption transients were measured at different potentials under continuous electrolyte flow, warranting a well-defined mass transport to the

electrode. Because of the simultaneous acquisition of the DEMS and IR data, these measurements allow an unambiguous correlation between CO_{ad} coverage and vibrational characteristics such as the intensity and frequency of the C-O stretch vibration during adsorption, at different adsorption potentials (Note: in the previous section 4.1 the CO_{ad} coverage/intensity profile was obtained for the oxidative removal of the adlayer). This provides information on the structure of the developing adlayer, which has not been accessible so far. Most of the numerous IR studies on the vibrational properties of CO adlayers on Pt (see reviews by Iwasita et al. {IWAS97} and Sun et al. {SUN98A}), were carried out in an external reflection configuration, where the thin electrolyte layer (<10 μm thickness) between metal electrodes and the optical window almost completely inhibits mass transport in this layer. In this configuration, reactant transport is solely possible by diffusion, which renders quantitative measurements of dynamic processes involving reactant transport essentially impossible. In those studies, the CO_{ad} coverage was mostly varied by oxidation during a potential scan, leading to a convolution of potential and CO_{ad} coverage effects. Only in few cases, the adsorbate coverage was adjusted by time-controlled adsorption from dilute, CO containing solutions or by oxidation of part of the CO adlayer prior to a subsequent potential scan {CHAN90C}'{CHAN91G}'{LEBE02C}. From such measurements, Stark shifts of 30 cm^{-1} V^{-1} were determined within the potential region of constant CO_{ad} coverage at saturation {KORZ86}{CHAN90C}{CHAN91G}{LU05}{STAM05A}{FROM06}, which increased to about 41-43 cm^{-1} V^{-1} with decreasing CO_{ad} coverage {CHAN90C}'{CHAN91G}. Deviations from this Stark shift were reported recently by Chen et al. for CO_{ad} coverages <0.3 ML and at potentials in the H_{upd} region. They were attributed to potential induced CO_{ad} island formation, mediated by H-upd co-adsorption {CHEN07A}. Studying the coverage-dependent intensity or frequency shifts at constant potential was more complicated, since the CO_{ad} coverage had to be calculated from subsequent CO stripping measurements {CHEN04F}'{LOPE05A}'{LOPE06} or from the decrease of the hydrogen-upd charge {LEBE02C}. Both types of measurements can not be performed continuously during CO adsorption, making it impossible to continuously follow the build-up of the CO adlayer.

A linear correlation between CO_{ad} coverage and the intensity of linearly adsorbed CO (CO_L), which was reported in {LEUN88A}{CHAN90C}, was used to estimate the CO_{ad} coverage in many IR studies. However, electronic effects, modifying the polarizability of the CO_{ad} bond {PERS81}, and dynamic coupling between CO dipoles {PERS85A}'{SEVE95}, are expected to cause deviations from a linear relation between CO_L intensity and CO_{ad} coverage.

Additional deviations can be introduced by a varying, coverage dependent ratio of linearly adsorbed CO to CO adsorbed on multiply coordinated sites. The experimental problems connected with an exact CO_{ad} coverage determination during the IR measurements are overcome in the combined ATR-FTIRS/DEMS set-up, where CO_{ad} coverage quantification by on-line DEMS and *in situ* IR characterization of the developing CO adlayer occur simultaneously.

In the following, the development of the CO_{ad} coverage versus time at different adsorption potentials from the mass spectrometric data will be determined, using the evolution of the ^{13}CO partial pressure in the electrolyte during adsorption of a 5% ^{13}CO/Ar mixture on a Pt thin film electrode. For this experiment, ^{13}CO was used instead of ^{12}CO, since the background signal for m/z = 29 is significantly lower compared to that of the m/z =28 signal, which is dominated by N_2 from the air, and consequently the signal-to-noise ratio is much better when following the CO consumption on m/z = 29. In the second part, the simultaneously measured FTIR spectra and the evolution of the spectral features as function of adsorption time are presented and discussed. Finally, the CO_{ad} related IR intensities are correlated with the CO_{ad} coverage, calculated from on-line DEMS at different adsorption potentials, which allows us to determine the shift of the vibrational frequency of linear adsorbed CO (CO_L) with CO_{ad} coverage at constant potential, i.e., without contributions from the Stark effect. Consequences for the evolution of the adlayer structure at different potentials will be discussed.

4.2.2 Results

4.2.2.1 Consumption of CO upon adsorption/oxidation and CO_{ad} coverage evolution: on-line mass spectrometry (DEMS)

The Faradaic current responses during potential step experiments from 1.0 to 0.06 V for one second (t = 0 s) and then (t = 1 s) to the constant adsorption potential are presented in Fig. 27a (adsorption potentials: 0.06, 0.1, 0.2, 0.3, 0.4, 0.5 and 0.6 V, for clarity only 0.1, 0.2, 0.4 and 0.6 V are shown, electrolyte: 0.5 M H_2SO_4 saturated with 5% ^{13}CO/Ar). The potential steps result in a complex Faradaic current response, which is initially (about 2-3 s) dominated by PtO reduction, H-upd adsorption and capacitive contributions (depending on the final adsorption potential). With further adsorption time, the Faradaic response resembles results obtained in previous potential step measurements in CO containing 0.5 M H_2SO_4 solution {BATI04B}: For adsorption at 0.06 V (not shown) and 0.1 V, the Faradaic current is positive and about

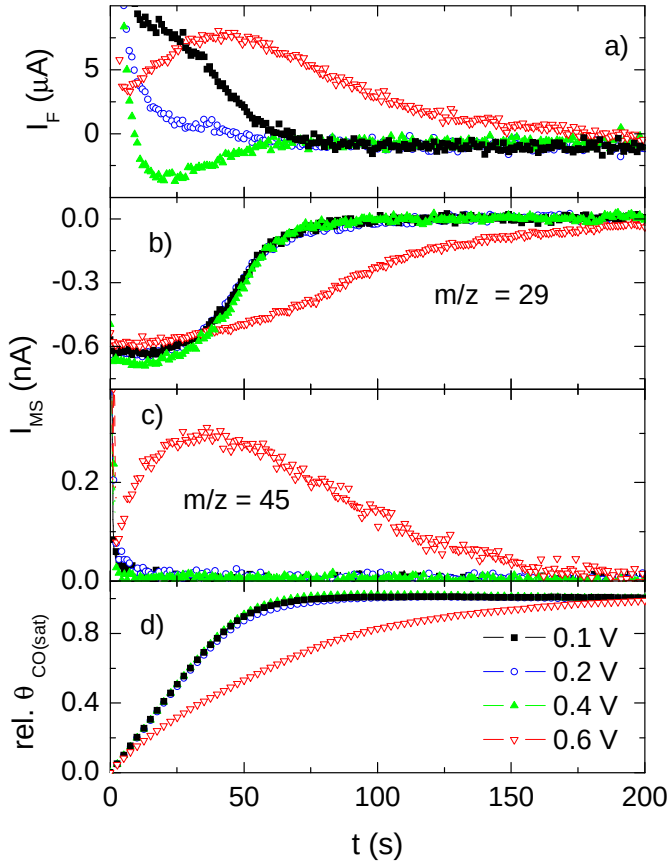

Fig. 27: CO adsorption transients recorded on a Pt thin film electrode in 0.5 M H_2SO_4 saturated with 5% ^{13}CO/Ar. The potential was stepped to the respective adsorption potential (t = 1 s) after the Pt electrode was held at 1.0 V for 30 s and then at 0.06 V for 1 s (t = 0 s – t = 1 s) (adsorption potentials 0.1, 0.2, 0.4, and 0.6 V). a) Faradaic current response; b, c) mass spectrometric currents for m/z = 29 and 45, respectively; d) calculated evolution of the relative CO_{ad} coverage $\theta_{CO.rel}$ with time.

constant for ~25 s, before steadily decaying to zero in the following ~70 s. The positive current response results from H_{upd} displacement by the more strongly adsorbing CO. When stepping the potential to 0.3, 0.4, or 0.5 V (only 0.4 V is shown), a negative current response is observed, due to displacement of adsorbed (bi-)sulfate {BERG98A}{BERG98A} {LACH02}{FUTA05}. For adsorption at 0.2 V, where the H_{upd} coverage is already significantly lower than at more cathodic potentials, both H_{upd} displacement (positive current) and (bi-)sulfate displacement (negative current) occur, resulting in total in a small positive current. At 0.6 V, the Faradaic current is influenced by (bi-)sulfate displacement and CO_{ad} oxidation, resulting in a Faradaic current increase for about 40 s after the potential step to 0.6 V, and a slow decrease to nearly zero at t = 200 s. Due to these different contributions, it would be hardly possible to quantitatively determine the CO_{ad} coverage as function of time and to derive the CO adsorption kinetics from the Faradaic current alone at different potentials.

The build-up of the CO_{ad} adlayer with adsorption time was directly followed by monitoring the mass spectrometric current for m/z = 29 (Fig. 27b). CO adsorption/oxidation results in a decrease of the CO partial pressure (or concentration) in the electrolyte from the background level (determination of the background level see section 3.5.1). Stepping the potential from 1.0 V to 0.06 V and then to the respective adsorption potential, the measured mass spectrometric current remains about constant for all adsorption potentials for ca. 30 s, before it starts to increase. For $E_{ads} \leq 0.5$ V, the background level for m/z = 29 is reached in about 100 s, where the Pt surface is saturated with CO_{ad}. No significant potential dependence in the mass spectrometric signals are observed, the small differences in the initial 25 s do not exceed the experimental accuracy of about ±5%. For adsorption at 0.6 V, the situation is completely different. Even after 200 s, the background level is not fully reached and the increase of the m/z = 29 signal is much slower compared to the lower adsorption potentials. This can be explained by competing oxidation of CO_{ad} to CO_2, which results in an additional consumption of CO. This can be seen also from the mass spectrometric response for the m/z = 45 signal, indicative of CO_2 formation at this potential, while CO_2 formation is essentially inhibited for lower adsorption potentials, except for the first few seconds (for discussion see below).

Fig. 27c shows the evolution of the m/z = 45 current with CO adsorption time for all applied potentials, which was followed to test for a possible loss of CO by CO_{ad} oxidation. The initially positive value of the CO_2 signal, which is observed for all adsorption potentials, is mostly caused by the finite time to remove the CO_2 from the electrolyte, after the mass transport limited CO_2 formation at 1.0 V, down to the background level at 0.06 V. An additional small contribution from reaction between remaining oxy-species and CO will be discussed below. For adsorption at 0.6 V, the CO_2 formation rate increases with adsorption time for 40 s, and then drops slowly to nearly zero at 200 s, mirroring the Faradaic current response in Fig. 27a. Furthermore, a noticeable difference between the Faradaic and the mass spectrometric current response in the slope of the initial increase indicates that at 0.6 V the Faradaic current involves contributions from (bi-)sulfate displacement. These contributions are highest in the initial stage, where the CO adsorption rate is highest.

The inset in Fig. 27c shows an enlarged presentation of the first two seconds after the potential step from 1 to 0.06 V, which is followed (at t = 1 s) by the potential step to the respective adsorption potential. The black line shows the mass spectrometric current decreasing from the mass transport limited CO_2 formation at 1.0 V (t = 0) to the background level at 0.06 and 0.1 V. When stepping the potential from 0.06 to 0.2, 0.3, 0.4, 0.5 and 0.6 V,

respectively, an increasing amount of CO_2 is detected. It is well known that CO oxidation at constant potential starts at E_{ad} > 0.5 V on polycrystalline Pt {CZER78}, whereas in CO_{ad} stripping experiments the onset of CO_2 formation can be detected at potentials down to about 0.3 V and below, depending on the adsorption potential {GAST95A}{JUSY01A}. The present data, however, demonstrate that CO oxidation on Pt is possible at potentials as low as 0.2 V, if preformed oxygen (OH_{ad} or Pt oxides) is present on the surface. These species were formed before, during the potential excursion to 1.0 V, and were not fully reduced after 1 s at 0.06 V. CO_{ad} oxidation to CO_2 on Pt for potentials down to 0.2 V has not been reported so far. Furthermore, since CO_2 formation is inhibited upon CO adsorption at 0.06 and 0.1 V, we propose that at these low potentials (and the low coverage of these oxy-species) the activation barrier for the reaction between these oxy-species and CO_{ad} to CO_2 is too high for measurable CO_2 formation. Apparently, the activation barrier decreases with increasing potential and already at 0.2 V the surface reaction between adsorbed oxy-species and CO_{ad} assumes a measurable rate. It is interesting to note that on Pt_3Sn/C catalysts, where the formation of adsorbed oxy-species from water is much more facile, CO_2 formation also starts at about 0.2 V {GAST95B}{SCHM99G}. Although the barrier for reaction of co-adsorbed CO_{ad} and oxy-species on bimetallic Pt_3Sn/C catalysts may differ significantly from that on Pt, due to the stronger interaction of Sn with oxygen, it is tempting to tentatively consider this agreement in the onset potential for CO_{ad} oxidation on Pt and on Pt_3Sn as support for the bi-functional mechanism postulated for these bimetallic catalysts {WATA75A}.

Integration of the area between the background level of the m/z=29 intensity and the actual signal at the different adsorption potentials leads to the respective CO_{ad} saturation coverages (see also section 3.5.1). The values are summarized in table 3.

	Stripping		Adsorption transients						
E_{ads} / V	0.06	0.4	0.06	0.1	0.2	0.3	0.4	0.5	0.6
Q / mC	1.22	1.20	1.25	1.29	1.28	1.31	1.32	1.21	1.15

Table 3: CO_{ad} stripping charges measured from CO_{ad} stripping experiments (left two columns, adsorption potentials 0.06 and 0.4 V) and calculated from the m/z = 29 current measured during the CO adsorption transients (right columns, different potentials as indicated in the table)

For adsorption at 0.6 V, corrections for CO_2 formation as derived from Fig. 27c were included, whereas at potentials ≤ 0.5 V the total amount of CO_2 formed during CO adsorption, was less than 2% of a CO saturated monolayer, which was ignored for the CO_{ad} coverage

calculation (for details see section 3.5.1). The saturation coverage is essentially identical for adsorption potentials up to 0.4 V, but starts to decrease at more positive potentials, in good agreement with the data reported by Czerwinski et al. {CZER78}, and Cuesta and coworkers {LOPE05A}{CUES06}{LOPE06}. Furthermore, comparing the values derived from the adsorption transients with those from subsequent CO_{ad} stripping, slightly higher CO_{ad} coverages are consistently observed in the former case (difference about 7%), confirming results of previous reports {VILL94}{LOPE05A}{HEIN06}. The difference between the two coverage values is attributed to the presence of CO in the electrolyte in the transient measurements, resulting in a higher steady-state CO_{ad} coverage, while during the CO_{ad} stripping experiments the electrolyte is free of CO and partial desorption occurs after removal of CO from the electrolyte. Correspondingly, Villegas et al. estimated from STM measurements that the CO_{ad} saturation coverage on Pt(111) is about 0.75 monolayers (ML) with CO in the electrolyte, decreasing to about 0.68 ML without CO in the electrolyte {VILL94}.

The evolution of the CO_{ad} coverage with time is plotted in Fig. 27d for the different adsorption potentials. For adsorption at $E \leq 0.5$ V, the adsorption traces are practically identical (the small deviations occurring after about 40 s are within the experimental accuracy of ± 5 %). From the data in Fig. 27b and Fig. 27d, we can calculate the effective sticking coefficient $s(\theta)$ as a function of coverage (Fig. 28), which is defined as the ratio of the rate for CO adsorption at a given coverage to the rate of incoming CO molecules. It is important to note that the sticking coefficient calculated this way represents an effective value. It describes the probability that a CO molecule impinging on the film will be adsorbed. In contrast to an ultrahigh vacuum (UHV) experiment, where the sticking probability is defined as the probability to adsorb within a single hit, CO molecules arriving in the diffusion layer at the Pt film may hit the film surface many times before they finally adsorb or leave the diffusion layer. Since we also do not know the absolute rate of CO molecules arriving at the film surface, we calculate the relative effective sticking coefficients $s^*_{rel}(\theta)$, dividing the effective sticking coefficient by the initial effective sticking coefficient obtained at the same adsorption potential (see Fig. 28). Technically, this was done by dividing the actual CO adsorption rate at time t, which is proportional to the difference between the m/z = 29 current at time t and the m/z = 29 current at saturation (t=200 s), by the maximum CO adsorption rate determined in

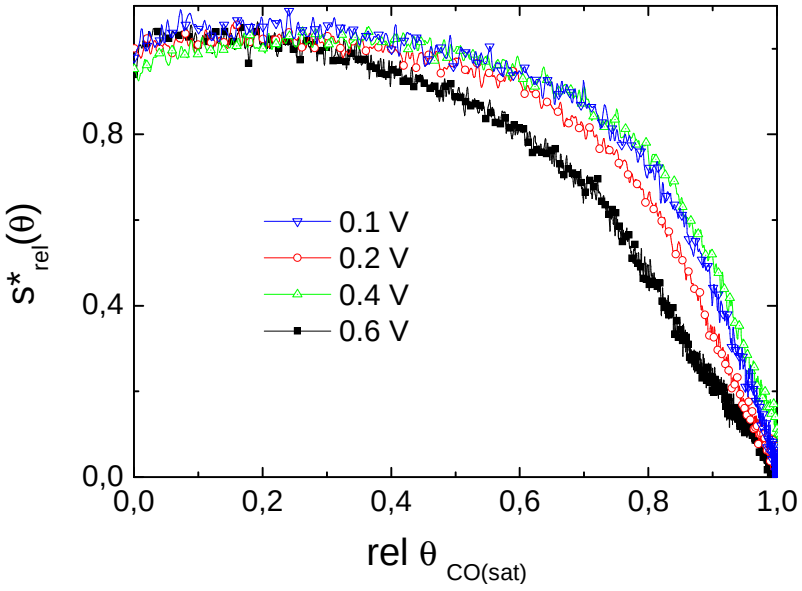

Fig. 28: Plot of the relative effective sticking coefficient $s^*_{rel}(\theta_{CO})$ (see text) as a function of the relative CO_{ad} coverage $\theta_{CO,rel}$ for different adsorption potentials (data from Fig. 27, adsorption potentials see figure).

the same way at t = 1s. Because of the independence of the coverage-exposure curves from the adsorption potential (until reaching oxidative potentials at 0.6 V), also the $s^*_{rel}(\theta)$ vs. $\theta_{CO,rel}$ curves are independent of the adsorption potential in this potential range. Starting at a value of $s^*_{rel}(\theta) = 1$, the relative sticking coefficient remains constant up to a relative CO_{ad} coverage $\theta_{CO,rel} \approx 0.4$, before it continuously decreases to 0 at higher CO_{ad} coverages. As discussed previously for CO adsorption on supported Pt/C catalysts at one fixed potential {JUSY01A}, the coverage dependence of the relative effective sticking coefficient is far from the linear dependence expected for first-order Langmuir adsorption kinetics. Instead, it rather resembles the precursor-type adsorption kinetics described by Kisliuk {KISL57}{KISL58}, where the possibility of repeated adsorption attempts from a precursor site results in higher values of the relative sticking coefficient at medium coverage values than expected from the first-order Langmuir adsorption kinetics. For the electrochemical adsorption experiment, however, the microscopic picture has to be modified. The repeated adsorption attempts are not performed by a CO molecule adsorbed on a precursor site, e.g., on top of an occupied CO adsorption site, but by CO molecules within the diffusion layer or even within the porous Pt film, which will hit the surface many times and thus try to adsorb many times before leaving the diffusion layer. Therefore, although closely resembling the adsorption characteristics for a precursor adsorption mechanism, the present data are not sufficient to support this mechanism, which in fact has been observed for gas phase CO adsorption on Pt(111)

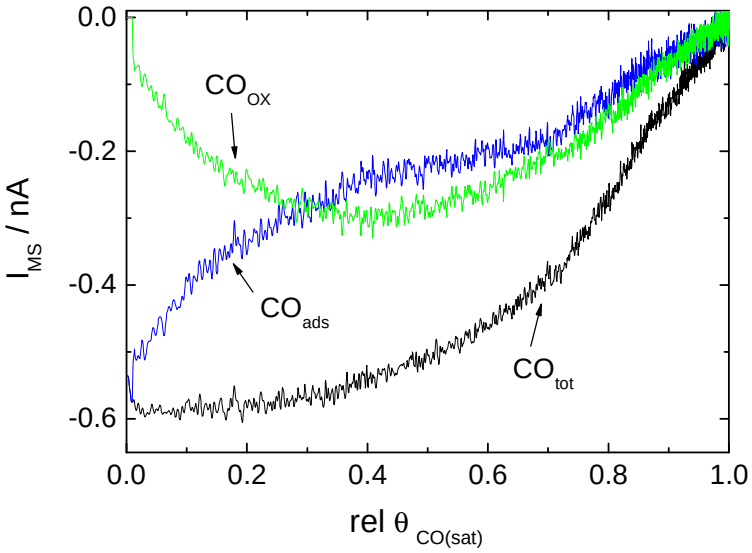

Fig. 29: Total CO consumption (CO partial pressure, CO_{tot}) versus the calculated CO_{ad} coverage for adsorption at 0.6 V, and contributions from CO oxidation (CO_2 formation, CO_{ox}), and CO adsorption (CO consumption – CO_2 formation CO_{ads}).

{ERTL77}. Instead, the electrochemical flow cell data presented here can be explained also by the multiple collision process at the solid/liquid interface. On the other hand, it is important to note that a precursor-type adsorption process, though not supported, is also not excluded by these results. For clarifying this question, quantitative modeling of the adsorption process in the diffusion layer is required and in progress.

For CO adsorption at 0.6 V, the increase of the CO_{ad} coverage up to t = 5 s is identical to that at the lower adsorption potentials, but for longer adsorption times the increase is slower due to competing oxidation of CO_{ad} to CO_2 (see Fig. 27c). As mentioned above, these two contributions (CO consumption due to CO adsorption and due to CO_{ad} oxidation to CO_2) can be separated by measuring the (total) CO consumption (m/z = 29) and the CO_2 formation rates (m/z = 45). Fig. 29 shows the total CO consumption, as well as the partial contributions by CO oxidation to CO_2 (determined from the m/z = 45 current, which was converted to a m/z=29 signal, details see section 3.5.1) and by CO adsorption (see section 3.5.1) as a function of CO_{ad} coverage. Formally, these data are compatible with the generally accepted Langmuir-Hinshelwood mechanism for CO_{ad} oxidation on a Pt-electrode at 0.6 V, with a maximum rate of CO_2 formation at a CO_{ad} coverage of $\theta_{CO,rel} \approx 0.4$. Assuming that the coverage of the oxy-species necessary to oxidize CO_{ad} to CO_2 is highest on the initial, CO_{ad}-free Pt surface, the increase of the CO_{ad} oxidation rate with CO_{ad} coverage at 0.6 V can be either explained by i) the increasing probability of neighboring pairs of CO_{ad} and adsorbed

oxy species or ii) by a decreasing reaction barrier for the combination of CO_{ad} and adsorbed oxygen species due to a decrease in the CO adsorption energy at higher CO_{ad} coverages {MARK02}. According to point ii) the CO_{ad} oxidation rate a low CO_{ad} coverage should be small, since these CO_{ad} molecules have the highest adsorption energy, which in turn results in a higher activation barrier for the combination of adsorbed oxygen species and CO_{ad}. This statement is further supported by results of the CO oxidation transients at 0.6 V, as presented in Fig. 22, which show that the last ~7% of the CO adlayer take very long to be oxidized. Finally, the data suggest that at 0.6 V the Pt surface is poisoned under the present conditions due to the slow combination of CO_{ad} and oxy-species, rather than due to a slow oxy-species formation rate. The latter effect only becomes dominant when the surface coverage of CO_{ad} is rather high.

4.2.2.2 CO adlayer build-up: time-resolved *in situ* ATR-FTIRS

To follow also the structural development of the CO adlayer during the adsorption process, *in situ* FTIR spectra were recorded simultaneously upon CO adsorption/oxidation. Fig. 30 displays representative sets of IR spectra measured simultaneously with the measurements shown in Fig. 27, upon adsorption in 5% ^{13}CO/Ar saturated 0.5 M H_2SO_4 solution at 0.1 and 0.4 V, respectively. Two positive bands in the region from 1700 to 1850 cm^{-1} and from 1950 to 2050 cm^{-1} are attributed to linearly and multiply-bonded $^{13}CO_{ad}$ (denoted as CO_L and CO_M). The peak frequencies of both the CO_L and CO_M bands shift to higher frequencies with increasing CO_{ad} coverage (see also Fig. 32), reflecting the weakening of the Pt-CO bond due to repulsive interactions between adjacent CO_{ad} {BLYH64} as well as increasing dipole- dipole coupling {HOLL85}. The CO_L band peak frequency of the saturated CO_{ad} adlayer shifts from 2025 cm^{-1} at 0.1 V via 2034 cm^{-1} at 0.4 V to 2039 cm^{-1} at 0.6 V (spectra not shown here) due to the Stark effect, in good agreement with previous observations on polycrystalline and single crystal Pt electrodes at similar potentials {KUNI84}{KORZ86}{IWAS97} {WASI01B}. The shape of the CO_M band at saturation coverage (last spectrum in Fig. 30) is rather symmetric at 0.4 V (center at 1830 cm^{-1}), while at 0.1 V (center at 1845 cm^{-1}) the band exhibits a rather asymmetric shape with a much higher intensity at higher frequencies. The asymmetric shape of the CO_M band and its variation with potential are tentatively explained by a potential dependent occupation of different adsorption sites on the polycrystalline Pt film electrode.

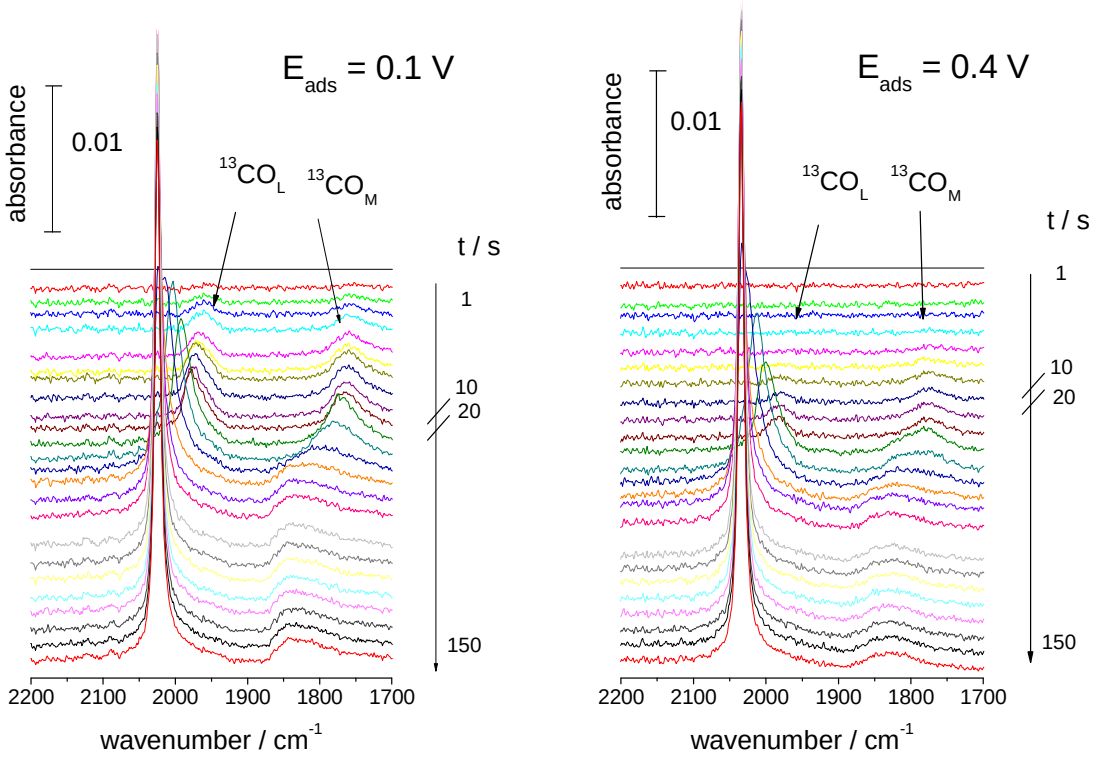

Fig. 30: Sets of *in situ* ATR-FTIR spectra recorded during potential step experiments (see Fig. 27) in 0.5 M H_2SO_4 saturated with 5% ^{13}CO/Ar at a) 0.1 V and b) 0.4 V adsorption potential, respectively. The reference spectra were taken at the same potential in CO-free 0.5 M H_2SO_4 solution (resolution 2 cm^{-1}, acquisition time 1s).

For comparison, Lebedeva et al. {LEBE02C} reported bands at 1871 and 1886 cm^{-1} at 0.1 and at 0.4 V, respectively, on a Pt(322) single crystal at saturation coverage, which they attributed to bridge-bonded CO_{ad} on (100) steps and (111) terraces. The former feature dominates the spectra due an intensity transfer from the lower frequency band to the higher frequency band due to dipole-dipole coupling {LEBE02C}. On Pt(443) and Pt(332), the frequency of the CO_M related IR-band (1817 to 1828 cm^{-1}) is shifted to significantly lower values compared to Pt(322), but also related to adsorption on (111) terraces {LEBE02C}.

In addition to the potential induced change in peak shape, also the peak height of the CO_M band varies with potential. It is about 1.5 times higher for adsorption at 0.1 V (0.0015) than at 0.4 V (0.001) (last spectrum of Fig. 30). The higher CO_M intensity at lower potentials, which agrees well with results by Kim et al. {KIM93}{KIM94} and Lebedeva et al. {LEBE02C}, is explained by the general tendency of CO to adsorb in high-coordination adsorption sites at more negative electrode potentials {CHAN90A}{IWAS97}. This trend is clearly visible in Fig. 31a and b, which show the integrated intensities of the CO_L and CO_M bands as a function of the adsorption time.

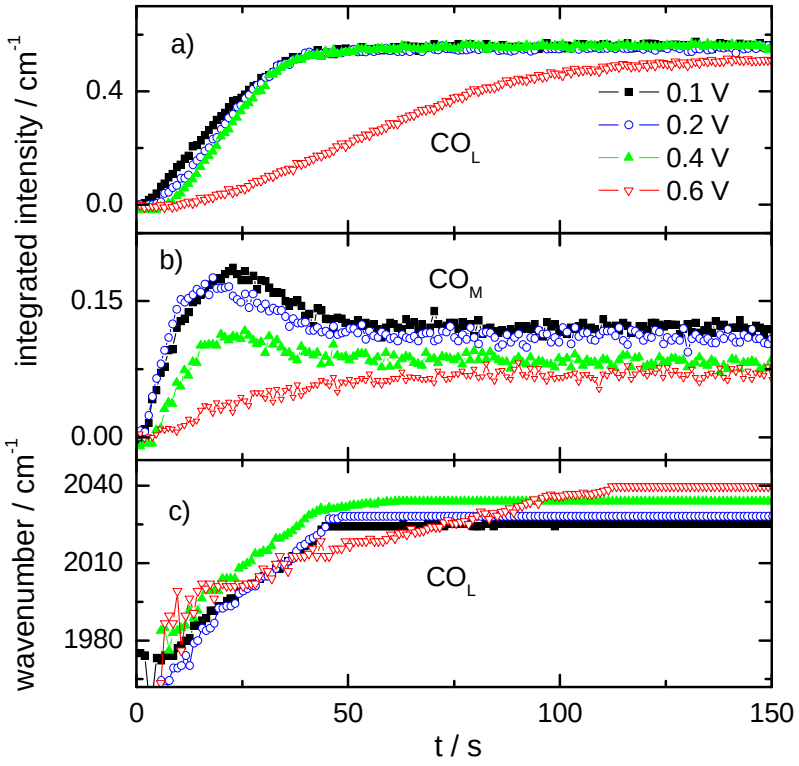

Fig. 31: Integrated a) CO_L and b) CO_M band intensities and c) CO_L and d) CO_M frequencies plotted versus adsorption time at different constant adsorption potentials (0.1, 0.2, 0.4 and 0.6 V).

The integrated band intensity of CO_L (Fig. 31a) increases first rather slowly and then, after a delay of 5-10 s, much more steeply, independent of the adsorption potential. It reaches constant values after about 50 seconds for adsorption at 0.1, 0.2 and 0.4 V. For adsorption at 0.6 V, the increase of the CO_L intensity is considerably slower, due to the competing oxidation of CO_{ad} to CO_2, and saturation is reached only after about 150 s. Whereas the CO_L intensities at saturation (t = 150 s) are practically identical for all potentials, except for the slightly lower intensity for adsorption at 0.6 V, the onset of the increase in CO_L intensity is shifted to longer adsorption times with increasing potential. In contrast to the delayed onset of the CO_L intensity increase during adsorption (Fig. 31a), the intensity of the CO_M band first increases rapidly, passes through a maximum after about 25 s and then decreases again (Fig. 31b). This maximum in CO_M intensity is more pronounced at potentials below 0.3 V, and completely disappears for adsorption at 0.6 V. The final CO_M intensity, at saturation after 150 s, depends on the adsorption potential, with increasing potentials resulting in lower CO_M intensities. These results can be interpreted as follows: At medium and higher CO_{ad} coverages, additional CO adsorption occurs preferentially on on-top sites, in a linear configuration (CO_L), independent of the adsorption potential. At low coverages, adsorption on multiply bound adsorp-

tion sites (CO_M) is more favorable. The transition from preferential CO_M to preferential CO_L adsorption depends on the adsorption potential, at lower potentials, this transition occurs at higher coverages than at higher potentials. Furthermore, at lower potentials (0.06 – 0.3 V) the CO_M passes through a maximum and decreases again at higher coverages, which may be related to re-conversion of CO_M to CO_L with increasing CO_{ad} coverage at these potentials. However, the possibility of intensity transfer from the lower frequency component (CO_M) to the higher frequency component (CO_L) has also to be considered {CHAN90C}{VILL94}{LEBE02C}. In Fig. 31c, the development of the CO_L band wavenumber is plotted versus the CO adsorption time. For all potentials, the frequency of the linearly adsorbed CO_L species increases continuously with adsorption time and reaches a saturation level. Since the spectral transients for CO adsorption, recorded at constant electrode potential, are free from potential induced modifications due to the Stark effect, the increase of the peak frequency with adsorption time purely reflects the increasing repulsive interactions within the CO adlayer and the increasing dipole-dipole coupling with increasing CO_{ad} coverage. Interestingly, the frequency vs. time curves are not parallel, as would be expected from a simple Stark shift and similar adsorption rates (see DEMS data above), but cross each other. Only at saturation, the frequencies increase about linearly with potential, from about 2025 cm^{-1} (0.1 V) over 2028 (0.2 V) and 2033 (0.4 V) to 2039 cm^{-1} (0.6 V), in good agreement with the well-known Stark shift of 30 cm^{-1}/V for saturated CO adlayers on Pt electrodes {KORZ86}{CHAN90C}{LU05}{STAM05A}{WASI01A}. This phenomenon will be discussed in more detail below, together with Fig. 32.

4.2.2.3 CO_{ad} coverage dependence of the IR band intensities/frequencies determined from combined ATR-FTIRS/DEMS measurements

So far, the IR data described in the previous section were discussed describing the trends of the intensity and frequency of the CO_{ad} related IR bands with increasing CO adsorption. For a more quantitative analysis of the IR data, the CO_{ad} related peak intensities and frequencies are plotted as a function of the CO_{ad} coverage (Fig. 32), which was derived from the simultaneously measured DEMS data presented in section 4.2.2.1. In general, the intensity of linearly bonded CO_{ad} increases slowly at low coverages (< 0.2), increases more strongly and linearly at intermediate CO_{ad} coverages ($0.2 < \theta_{CO,rel} < 0.8$), and finally reaches a saturation value at high CO_{ad} coverages ($\theta_{CO,rel} > 0.8$). These observations contrast reports of a linear intensity-

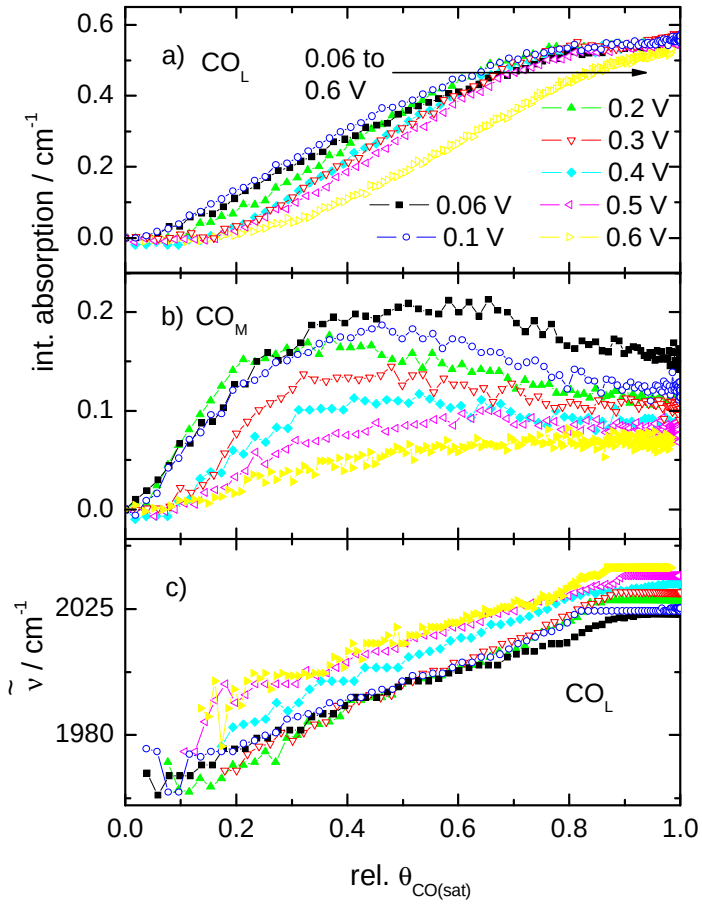

Fig. 32: Integrated a) CO_L and b) CO_M band intensities and c) CO_L frequencies plotted versus the relative CO_{ad} coverage $\theta_{CO,rel}$ at different constant adsorption potentials (0.06, 0.1, 0.2, 0.3, 0.4, 0.5 and 0.6 V).

coverage relation {CHAN90C}, but are in full agreement with the data in section 4.1.2.1, showing a similar CO_L intensity vs. CO_{ad} coverage profile for CO_{ad} monolayer oxidation at 0.6 V {HEIN06A} and with results obtained under UHV conditions {SCHW89}. (Note that in section 4.1.2.1, the saturation coverage was determined in the absence of CO in the electrolyte, whereas in the present case the saturation coverage is measured under steady-state conditions, in a 5% ^{13}CO/Ar saturated electrolyte.) For higher adsorption potentials, the changes in the CO_{ad} coverage versus CO_L-intensity profile are as follows: i) the CO_L band appears only at increasingly higher CO_{ad} coverage (see before), ii) the slope of the CO_L intensity versus CO_{ad} coverage in the linear regime is higher, and iii) deviations from a linear CO_L intensity – CO_{ad} coverage dependence at high CO_{ad} coverages become increasingly pronounced. Reasons for these trends will be discussed below, after presenting the data for the CO_M species.

The intensity of multiply bonded CO_M also increases with CO_{ad} coverage (Fig. 32 b) up to a relative CO_{ad} coverage of 40 - 60 %, depending on the potential. Further CO uptake leads to a slow decay of the CO_M intensity. This decrease is more strongly pronounced for low adsorption potentials (0.06 to 0.3 V), is hardly visible for adsorption at 0.4 V, and for adsorption at 0.5 and 0.6 V, the CO_M related intensity increases continuously from the CO_{ad} free to the CO_{ad} saturated surface. At saturation coverage, the CO_M intensity decreases with increasing potential, while at low CO_{ad} coverages the increase of the CO_M related intensity is slower at higher potentials.

The results of the integrated IR band intensities vs. CO_{ad} coverage plots provide direct experimental proof that i) the polarizability of the C=O bond decreases with increasing potential, as evidenced by the lower CO_{ad} related intensities at higher potentials and identical CO_{ad} coverage, that ii) multiply bonded CO_M is relatively preferred at low potentials and at lower coverages, whereas site conversion from CO_M to CO_L and/or preferential adsorption of CO in on-top configuration occurs at higher potentials and coverages. These results agree with findings in previous studies, showing a decrease of the CO_L intensity for increasing potential (at fixed CO_{ad} coverage) '{KUNI84}{CHAN90C}{WASI01B}{LEBE02C}.

Details on the adsorption configuration at low CO_{ad} coverages, in particular on the distribution of CO_M and CO_L species, can be extracted from the IR spectra recorded at $\theta_{CO,rel} \approx 0.13$, which are shown in Fig. 33.

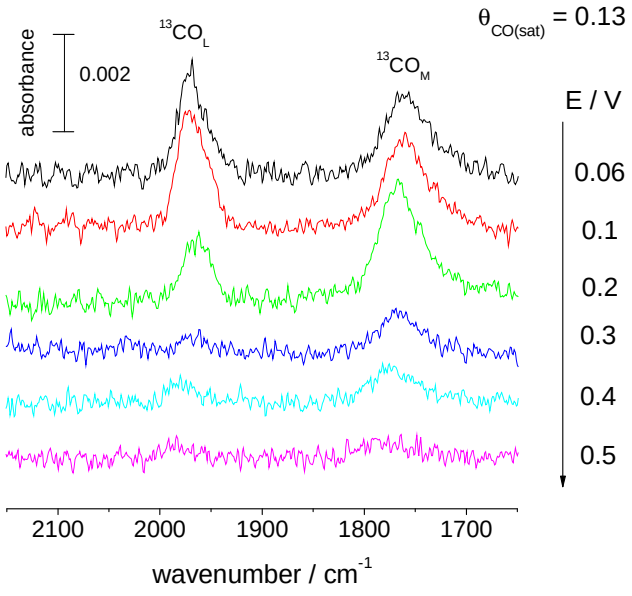

Fig. 33: *In situ* ATR-FTIR spectra recorded at $\theta_{CO,rel} = 0.13$ (6 s after the potential step to the respective adsorption potential, see Fig. 27) at different adsorption potentials as indicated in the figure.

Whereas for adsorption at 0.06 and 0.1 V the intensity of linearly adsorbed CO_L is larger than that of multiply bonded CO_M, the latter signal is clearly dominating at 0.2 and 0.3 V. The preferential adsorption in a multiply bonded configuration at 0.2 and 0.3 V, and at low CO_{ad} coverage, is opposite to the increased CO_M intensity at lowerpo tential obtained at saturation coverage (see above). This implies that under these conditions another contribution overcompensates the still existing tendency for preferential adsorption of CO in a multiple configuration at lower potentials (see below). Further details on the CO adlayer structure become apparent when plotting the vibrational frequency of linearly adsorbed CO versus the relative CO_{ad} coverage (Fig. 32c). In general, the frequency increases with CO_{ad} coverage for all adsorption potentials. The value of the saturation frequency shifts from 2023 at 0.06 V to 2025 cm^{-1} at 0.1 V and increases linearly with 30 cm^{-1} V^{-1} to 2039 cm^{-1} at 0.6 V, in agreement with the Stark shift reported previously {KORZ86}{WASI01B}{LU05}{STAM05A}. At lower CO_{ad} coverages, however, the frequency shift with adsorption potential deviates from the 30 cm^{-1} V^{-1} shift expected from the Stark effect. These findings imply that in addition to the CO_{ad} coverage and the adsorption potential, other effects also have an influence on the frequency. To further illustrate these effects, the frequency of linearly adsorbed CO is plotted at selected constant CO_{ad} coverages versus the adsorption potential (Fig. 34).

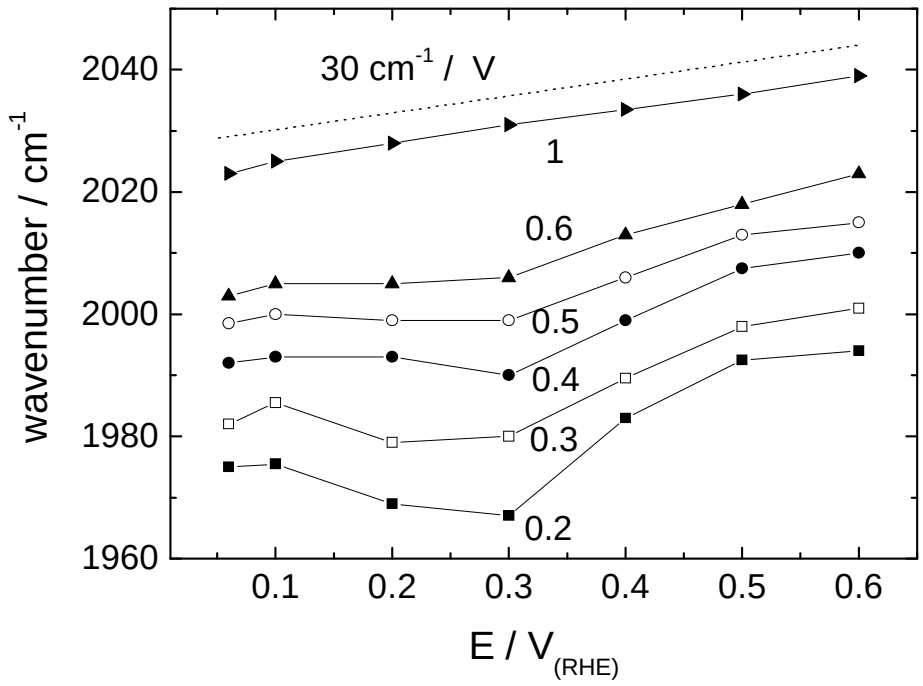

Fig. 34: Frequency of linearly adsorbed CO_L as a function of the adsorption potential at selected relative CO_{ad} coverages, as indicated in the figure.

The slope of 30 cm^{-1} V^{-1} shift expected from the Stark effect is included as dashed line for comparison. It is practically identical with the experimental trend for saturation coverage. For decreasing CO_{ad} coverage, however, an increasingly pronounced frequency minimum develops at a potential of about 0.3 V. This trend is in good agreement with earlier results reported by Weaver and coworkers {CHAN90C}{PARK01C} and closely resembles recentobservations by Chen et al. {CHEN07A}, who detected a reversible blue-shift of the CO_L frequency with decreasing potential, which is opposite to the Stark shift, when following the frequency of linearly adsorbed CO during potential a sweep between 0.35 and 0.06 V at different relative CO_{ad} coverages below 0.6 (0.43 monolayers) in CO-free 0.5 M H_2SO_4 solution. This blue shift of the frequency was explained by CO_{ad} island formation (with higher local CO_{ad} coverage), induced by co-adsorption of H-upd at low CO_{ad} coverage and low potentials {CHEN07A}. Furthermore, assuming that the CO molecules are randomly distributed on the Pt surface at a potential around 0.3 V, where both the hydrogen-upd and (bi-)sulfate coverages are low and the distribution of the CO_{ad} molecules is dominated by the repulsive interactions between these species, the strong increase in the CO_L frequency from 1967 to 1992 cm^{-1} from 0.3 to 0.5 V (125 cm^{-1} V^{-1}) at a relative CO_{ad} coverage of 0.2 suggests, that a similar CO_{ad} island formation also occurs when going to higher potential, most likely caused by co-adsorption of (bi-)sulfate. Compression of CO_{ad} molecules into islands by co-adsorption of sulfate was proposed recently also by Lu et al. {LU05} and Stamenkovic et al. {STAM05A}. This proposal was based on IR spectroscopy and sum-frequency generation measurements, following the frequency shift of the CO_L band with potential during CO_{ad} stripping.

The local compression of the CO adlayer can also affect the CO_{ad} site occupation, due to the decreasing tendency for CO_M adsorption at higher coverages. Correspondingly, we expect the highest fraction of CO_M intensity (lowest CO_L/CO_M intensity ratio) in the potential range between 0.2 and 0.4 V, where the adlayer is assumed to be homogeneously distributed, while at higher and lower potentials island formation sets in. These effects in CO_L/CO_M population are clearly visible at low coverages ($\theta_{CO,rel}$ = 0.13, see Fig. 33), while at saturation coverage the CO_L:CO_M intensity ratio continuously increases with potential.

The combined DEMS and IR data have shown that the adlayer build-up is strongly affected by the potential, specifically by the potential dependent co-adsorption of H-upd and/or (bi-) sulfate. The formation of CO_{ad} islands in turn requires sufficient CO_{ad} mobility on the (partly) H-upd or (bi-)sulfate covered Pt surface.

4.2.3 Summary

On-line DEMS and *in situ* ATR-FTIRS data measured simultaneously during CO adsorption have provided new insights into the CO adsorption kinetics and the build-up and structural configuration of the CO adlayer on Pt at different adsorption potentials (0.06 – 0.6 V). The measurements were performed under continuous electrolyte flow, ensuring controlled reactant transport, in a novel combined ATR-FTIRS/DEMS set-up. From the consumption of CO detected by on-line DEMS, the development of the instantaneous CO_{ad} coverage was derived for adsorption potentials ≤ 0.5V, revealing identical adsorption kinetics. At 0.6 V, the build-up of the CO adlayer is delayed due to CO_{ad} oxidation. The contributions from the two processes to the overall CO consumption measured by DEMS, CO adsorption and CO oxidation to CO_2, could be separated by subtracting the CO_{ad} coverage-dependent CO_2 formation rate measured by DEMS, which allowed determining the actual CO adsorption rate at 0.6 V as well. The increasing CO_2 formation rate with increasing CO_{ad} coverage up to a relative CO_{ad} coverage of about $\theta_{CO,rel} = 0.4$ supports the general assumption that CO_{ad} oxidation follows a Langmuir-Hinshelwood mechanism. Furthermore, it suggests that either CO diffusion to the oxy-species or a higher activation barrier for the reaction of CO_{ad} with oxy-species at low CO_{ad} coverage rather than oxy-species formation is the rate limiting step for initial CO_{ad} oxidation at coverages $\theta_{CO,rel} < 0.4$.

The ATR-FTIRS spectra, recorded simultaneously with the DEMS data, have shown that the intensity of linearly (CO_L) and multiply bonded (CO_M) CO_{ad}, at a constant CO_{ad} coverage, depends strongly on the potential. The intensity of both CO_L and CO_M decreases with increasing potential, which was attributed to a decrease in polarizability of the CO_{ad} species at higher potentials. This again is related to the increasing frequency and hence stronger C=O bond at higher potentials (Stark shift). The intensity of CO_L is linearly correlated with the CO_{ad} coverage in the coverage regime $0.2 < \theta_{CO,rel} < 0.8$. At higher coverages, depolarization effects caused by (static) adsorbate-adsorbate interactions and dynamic dipole-dipole coupling between neighboring CO_{ad} molecules lead to deviations from the linear relation. At low coverages, preferential adsorption in a multiply bonded configuration also causes deviations from the linear relation.

At low potentials and low coverages, the CO_M adsorption configuration for CO is preferred. With increasing coverage, the intensity of linearly adsorbed CO_L increases much stronger than the intensity for multiply adsorbed CO, which was attributed to preferential adsorption of

CO in a linear configuration (at higher CO_{ad} coverage) and intensity transfer from the lower (CO_M) to the higher (CO_L) frequency component due to dynamic coupling. At low and medium CO_{ad} coverages ($\theta_{CO,rel} < 0.6$), a minimum of the vibrational frequency of linearly adsorbed CO was found for potentials around 0.3 V. This led to the conclusion that the increase in frequency for going to lower potentials, opposite to the Stark effect, and the even more pronounced up-shift in frequency than expected from the Stark effect for going to higher potentials, is due to CO_{ad} island formation with higher local CO_{ad} coverage. Most likely, this potential induced island formation results from co-adsorption of H-upd or (bi)sulfate at E < 0.25 V and E > 0.4 V, respectively. The local adlayer compression affects also the CO_{ad} site occupation, with the lowest CO_L/CO_M intensity ratio in the potential range between 0.2 and 0.4 V at CO_{ad} coverages $\theta_{CO,rel} \leq 0.2$.

4.3 Room Temperature CO_{ad} Desorption/Exchange Kinetics on Pt Electrodes – A Combined in-situ IR and Mass Spectrometry Study

Martin Heinen, Yan-Xia Chen[1], Zenonas Jusys, and Rolf Jürgen Behm*

Institute of Surface Chemistry and Catalysis, Ulm University, D-89069 Ulm, Germany

[1] pres. address: National Laboratory for Physical Sciences at the Microscale, Department of Chemical Physics, University of Science and Technology of China, Hefei, China

Published in: Chem. Phys. Chem 8, 2484-2489, **2007**

ABSTRACT

The room temperature desorption and exchange of CO in a saturated CO adlayer on a Pt electrode, at potentials far below the onset of oxidation, was investigated by isotope labeling experiments, using a novel spectro-electrochemical setup, which allows the simultaneous detection of adsorbed species by in-situ IR spectroscopy and of volatile (side) products and reactants by on-line mass spectrometry under controlled electrolyte flow conditions. Time-resolved IR spectra show a rapid, statistical exchange of preadsorbed $^{13}CO_{ad}$ by $^{12}CO_{ad}$ in ^{12}CO containing electrolyte; mass spectrometric data reveal first-order exchange kinetics, with the rate increasing with CO partial pressure. The increasing CO_{ad} desorption rate in equilibrium with a CO containing electrolyte is explained by a combination of an increasing CO_{ad} coverage upon increasing the CO pressure, and a decrease of the CO adsorption energy with coverage, due to repulsive CO_{ad}-CO_{ad} interactions.

4.3.1 Introduction

The question of whether CO_{ad} desorption from Pt metal electrodes is possible at room temperature in an electrochemical environment or whether CO_{ad} removal under these conditions can be achieved only by oxidation has attracted considerable interest during recent years {HERR00}{WASZ01}{BEHM05}{MCGO06}, both from a basic science point of view, for the molecular scale understanding of CO adsorption in an electrochemical environment, and from practical reasons: This question plays an important role in fuel cell technology, since the strategies for the development of CO tolerant anode catalysts for low temperature polymer electrolyte fuel cells (PEFCs) may be very different depending on whether improved desorption (reduced CO_{ad} adsorption energy) or oxidation (enhanced OH_{ad} formation or CO_{ad} + OH_{ad} reaction) is strived for as main pathway for CO_{ad} removal.

So far, the general and commonly accepted understanding was that CO_{ad} desorption from Pt electrodes does not occur at temperatures below 60°C at cathodic potentials below the onset of CO_{ad} oxidation (see ’{HERR00}{BEHM05}). In most studies, CO_{ad} desorption was determined by oxidation of the adsorbed CO, from the decay of the CO_{ad} coverage at elevated temperatures {HERR00}{BEHM05}. This procedure, however, is limited in accuracy and hence leaves small desorption induced losses in adsorbate coverage undetected. A different approach was followed in isotope exchange experiments, where the CO_{ad} displacement by isotope labeled CO was detected by mass spectrometry during subsequent CO_{ad} stripping {IWAS88}, by *in situ* monitoring of the adsorption process using radioactive tracer techniques {WASZ01}{MCGO06}, or by *in situ* IR detection in an external reflection configuration {CHAN90C}{KIM94B}{SEVE95}. These experiments, which were performed without enforced mass transport, led to diverging results; detailed kinetic data and a mechanistic understanding of the underlying processes are still lacking {MCGO06}.

In this Chapter, the exchange and desorption of CO_{ad} and, in particular, its kinetics in equilibrium with CO containing electrolyte, are investigated, using isotope labeling techniques (^{13}CO) and the combined ATR-FTIRS/DEMS set-up, which allows the simultaneous identification and quantitative determination of adsorbed species, volatile reaction products/educts and overall reaction rates under well-defined reaction conditions and under enforce electrolyte transport {HEIN06}{HEIN06A}.

First time-resolved sequences of IR spectra are presented, which clearly show that $^{13}CO_{ad}$ is rapidly exchanged by $^{12}CO_{ad}$ when gas phase ^{12}CO is present in the electrolyte and that the time for complete exchange depends on the concentration of the ^{12}CO. For a quantitative evaluation of the exchange rate and the resulting $^{13}CO/^{12}CO$ fractional coverages on-line (DEMS) was employed, following the desorption of ^{13}CO during exposure of a ^{13}CO presaturated Pt film electrode to ^{12}CO in a continuous flow of ^{12}CO containing electrolyte. Changes in the CO adlayer composition were simultaneously followed by *in situ* IR spectroscopy under identical conditions, which provides additional mechanistic information on the CO_{ad} exchange process.

Comparable strategies, following the desorption of ^{13}CO from carbon supported Pt and PtRu catalysts by mass spectrometry {DAVI04}{DAVI05}{DAVI08} or by monitoring the changes in the adlayer on Pt(111) by IR spectroscopy {ANDE05B}, were applied in previous studies on CO exchange at the gas|solid interface, but have not been possible under electrochemical conditions with well-defined mass transport to/from the electrode, where the latter is crucial to avoid re-adsorption of exchanged CO.

4.3.2 Results

After saturation of the Pt film electrode with $^{13}CO_{ad}$ at 0.1 V, the IR spectra exhibit the characteristic features of $^{13}CO_{ad}$ covered Pt, with a distinct band at 2022 cm^{-1} (linear CO_{ad} – CO_L) and a broad feature centered at 1836 cm^{-1} (multiply bound CO_{ad} – CO_M), as illustrated in the first spectrum (t = 0) in Fig. 35 (see also Fig. 30). Exposing this electrode to ^{12}CO saturated 0.5 M H_2SO_4 solution after an intermitting rinsing period with CO free electrolyte (see preceding section) results in a rapid change in the vibrational spectra, with the CO_{ad} related bands broadening and shifting to higher wavenumbers (Fig. 35). After about 600 s, the shift is largely completed (CO_L: 2072 cm^{-1}, CO_M: 1880 cm^{-1}). Further exposure to ^{12}CO-saturated electrolyte results only in marginal changes in band shape and position. The time required for complete exchange increases with decreasing CO concentration in the electrolyte; in 10% ^{12}CO/Ar saturated solution, complete exchange takes more than 20 min and for 1% CO/Ar, this requires more than 30 min. Also the combined intensity of the $^{12}CO_L$ and $^{13}CO_L$ bands (Fig. 36a) and the wavenumbers (Fig. 36b) at the end of the exchange process, under close to steady-state conditions, depend on the CO concentration (1% CO/Ar: 2070 cm^{-1}, 10% CO/Ar: 2071.5 cm^{-1}, 100% CO: 2072 cm^{-1}). After returning to CO free electrolyte (see vertical lines in Fig. 36), they change back to values representative for a slightly lower CO_{ad}

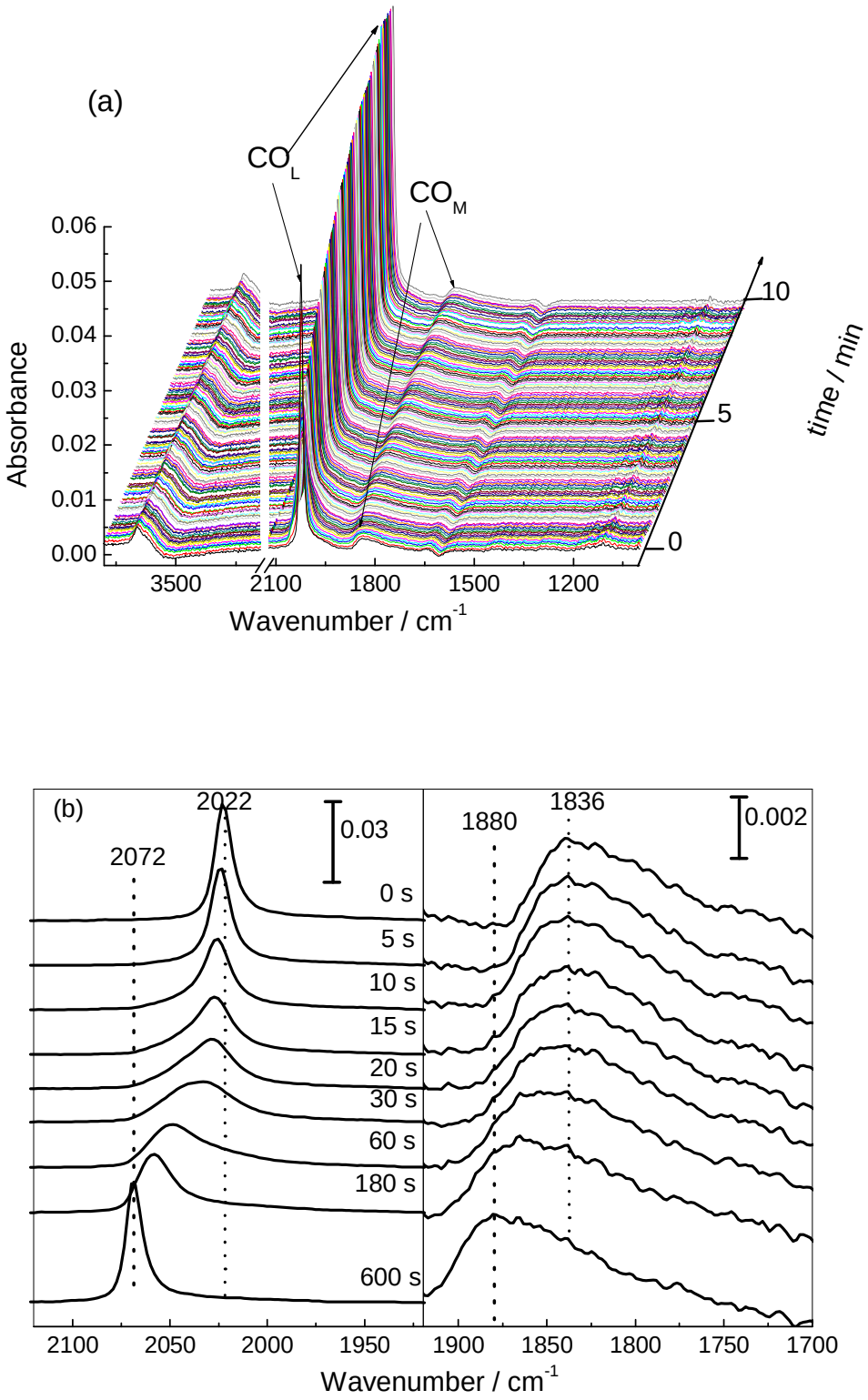

Fig. 35: Sequence of *in situ* ATR-IR spectra (a) and details of the spectral regions typical for the CO_L and CO_M vibration (b), recorded upon exposing a $^{13}CO_{ad}$ presaturated Pt thin-film electrode to ^{12}CO saturated solution (potential 100 mV, electrolyte flow rate ~50 $\mu l \cdot s^{-1}$).

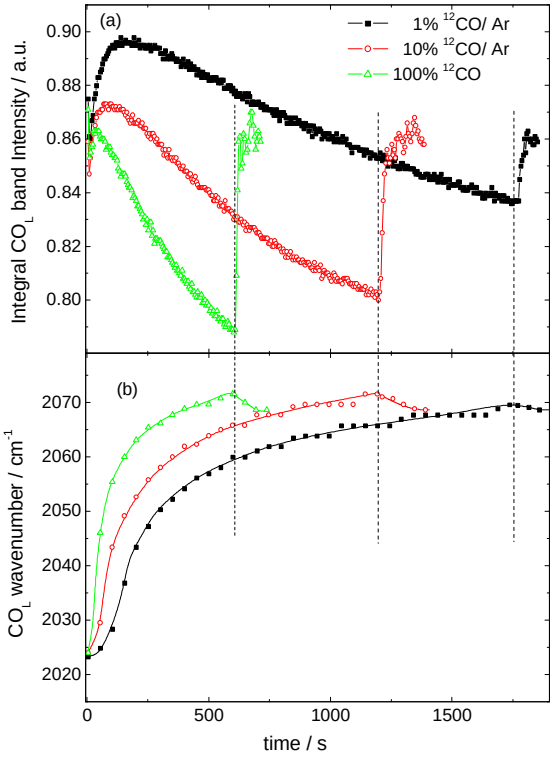

Fig. 36: Temporal evolution of the combined integrated $^{13}CO_L$ and $^{12}CO_L$ intensities (a) and wavenumbers (b) of the CO_L peak upon exposing a $^{13}CO_{ad}$ presaturated Pt thin-film electrode in CO free 0.5 M H_2SO_4 to ^{12}CO saturated solution at 100 mV, and changing back to CO free base electrolyte (see vertical lines).

coverage, which is identical for all three experiments. Similar $^{13}CO_{ad}/^{12}CO_{ad}$ isotope exchange measurements performed at 0.06 V and 0.35 V result in data largely identical to those obtained at 0.1 V, with the only difference that the peak positions are slightly shifted due to the Stark effect.

The IR spectroscopic features observed during the exchange of $^{13}CO_{ad}$ by $^{12}CO_{ad}$, with a continuous shift of the CO_L and CO_M bands (Fig. 35), differ from the intuitive expectation of a decay of the ^{13}CO related bands and a simultaneous appearance of a second set of bands characteristic for $^{12}CO_{ad}$, which would then grow on the expense of the $^{13}CO_{ad}$ related bands. In contrast, the transition from the ^{13}CO to the ^{12}CO adlayer proceeds via a broadening of the CO_L band to higher wavenumbers without distinct spectral contributions relevant to ^{13}CO or ^{12}CO vibrational frequencies. The broad CO_M band is shifted accordingly during the isotope exchange process (Fig. 35b). Furthermore, the combined intensity of the CO_L bands ($^{12}CO_{ad}$ and $^{13}CO_{ad}$) does not remain constant or change steadily, as would be expected in a simple model with identical or slightly different absorption cross-sections for ^{13}CO and ^{12}CO. Instead, it passes through a maximum (see Fig. 36a) when varying the coverage of the respective species, while, except for a small increase at t = 0, the total CO_{ad} coverage remains

constant. Both of these trends can be explained by effects related to vibrational coupling between the different CO_{ad} isotopomers, which had been discussed in detail in previous experimental and theoretical studies for isotopically mixed CO adlayers on different metal surfaces and electrodes {PERS81}{PERS85A}{KIM94B}{SEVE95}.

The above data clearly confirm that under electrochemical conditions, at potentials in the H-upd region and at room temperature, CO exchanges rapidly (compared to the extremely low CO_{ad} oxidation rate on a Pt electrode at this potential) upon exposure of the $^{13}CO_{ad}$ covered Pt electrode to ^{12}CO containing solution. These findings agree with previous observations by Iwasita and Vogel {IWAS88} and McGovern et al. {MCGO06}. They agree well also with results for CO_{ad} exchange at the solid-gas interface, on Pt(111) {ANDE05B} and on supported Pt and PtRu catalysts {DAVI04}. Based on the continuous shift in CO_L band frequency, CO_{ad} exchange occurs statistically and does not result in separated phases of the two different CO_{ad} species, i.e., it does not proceed via a nucleation and growth process.

For a quantitative evaluation of the exchange rate and the resulting $^{13}CO/^{12}CO$ fractional coverages, we used the simultaneously measured DEMS data, following the ^{13}CO partial pressure in the electrolyte with time during the exchange process (Fig. 37). Integration of the ^{13}CO signal then yields the displaced $^{13}CO_{ad}$ coverage (= adsorbed $^{12}CO_{ad}$ coverage) at any given time (for details of the calculations see section3.5.2). Plotting the fractional coverage of $^{13}CO_{ad}$ as a function of the exchange time reveals first order exchange kinetics, with a rate constant decreasing with decreasing ^{12}CO concentration in the electrolyte (Fig. 38a). The slope of the logarithmic plots in Fig. 38b reflects the desorption rates for the three different CO concentrations, yielding values of k_{des}(1% CO in Ar) = 0.0014 s^{-1}, k_{des}(10% CO in Ar) = 0.003 s^{-1}, k_{des}(100% CO) = 0.0073 s^{-1}. The increasing rate for CO_{ad} desorption and CO_{ad} exchange with CO concentration in the electrolyte is explained by a combination of two effects, i) by an increase of the total CO_{ad} coverage with increasing CO concentration in the presence of CO in the electrolyte (IR data), and ii) a pronounced decrease of the CO adsorption energy with CO_{ad} coverage at high coverages close to saturation {HEIN06} {LOPE05A}{LOPE06}. This explanation is based on the plausible assumption that i) exchange is possible only by adsorption on an adsorption site that was previously vacated by a desorbing CO_{ad} molecule, and that ii) the exchange rate is governed by the desorption rate of CO_{ad} at the given temperature and coverage, and not stimulated by energy transfer from an adsorbing CO molecule.

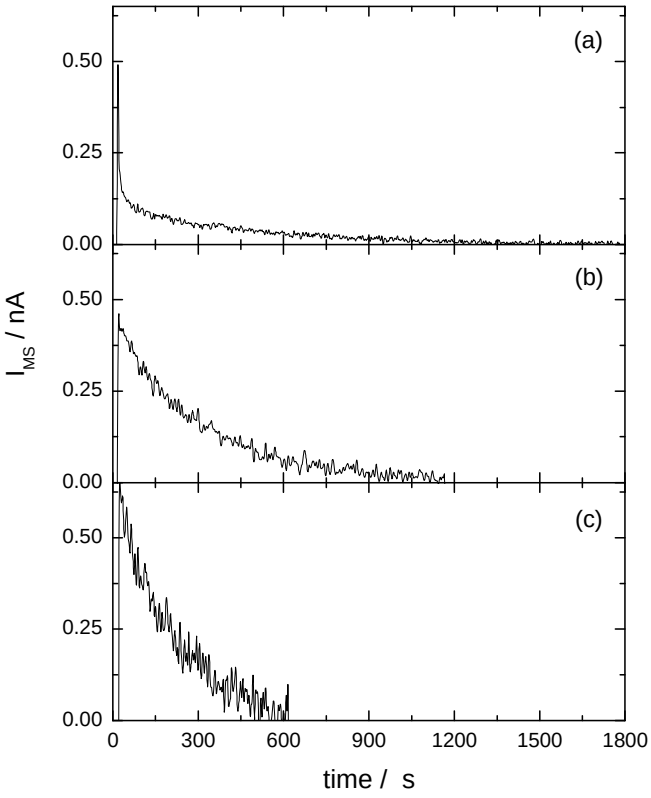

Fig. 37: Temporal evolution of the m/z = 29 currents (desorbing ^{13}CO) during ^{13}CO exchange at 0.1 V by electrolytes containing different concentrations of ^{12}CO. (a) 1% CO/Ar, b) 10% CO/Ar and c) CO saturated 0.5 M H_2SO_4 solution.

A pronounced decrease of the COad adsorption energy at high CO_{ad} coverages close to saturation was indeed reported for CO adsorption on various noble metal surfaces {CAMP90}, including Pt(111) {ERTL77}, and was explained by strongly repulsive CO_{ad}-CO_{ad} interactions. For Pt(111), the CO adsorption energy (under UHV conditions) decreases from 140 kJ mol^{-1} at low coverages to 60 kJ mol^{-1} at saturation, with most of the decrease occurring at high coverages close to saturation {ERTL77}. In the presence of CO in the gas phase (or dissolved in the electrolyte), the coverage increases slightly, which is indicated also by the vibrational frequency, and the activation energy for desorption decreases accordingly. This results in a measurable increase of the desorption rate. If the CO_{ad} is removed from the gas phase, the CO_{ad} coverage decreases to a value where the COad desorption rate becomes negligible, due to the increasing CO adsorption energy, and the CO adlayer is stable again (see also) {DAVI04}{DAVI05}.

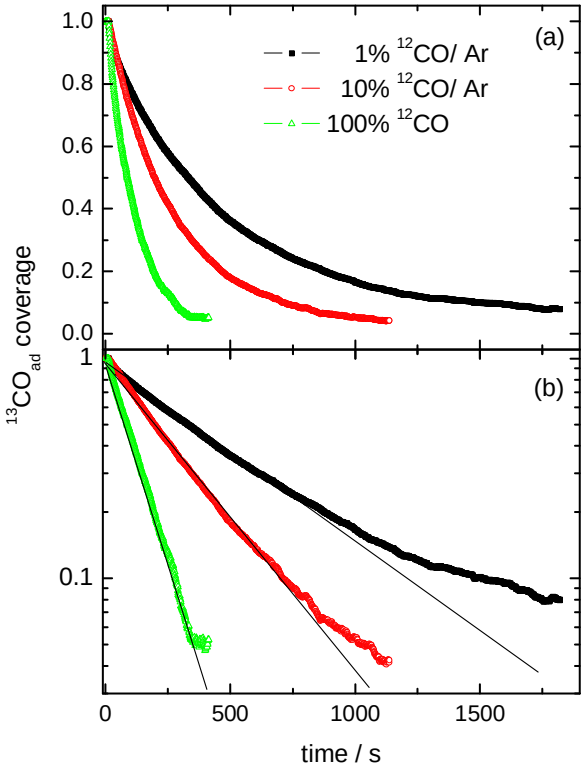

Fig. 38: Temporal evolution of the relative $^{13}CO_{ad}$ coverage (at constant total CO_{ad} coverage) upon exposing a $^{13}CO_{ad}$ presaturated Pt thin-film electrode to ^{12}CO saturated solution at 100 mV in electrolytes with different CO concentrations (see figure) as calculated from the ^{13}CO partial pressure (see text).

The desorption rate for CO can be described by first order Langmuir desorption kinetics with a coverage dependent activation barrier for desorption E^*_{des} (θ(CO)):

$$r_{des} = \frac{N_0 \times \theta(CO)}{dt} = (N_0 \times \theta(CO) \times \nu) \times \exp\left(\frac{-E^*_{des}(\theta(CO))}{R \times T}\right)$$

Since CO adsorption is not activated, the activation energy for CO desorption is almost identical to the CO adsorption energy. If CO_{ad} desorbs randomly with similar desorption probabilities for $^{12}CO_{ad}$ and $^{13}CO_{ad}$ species, the total CO_{ad} coverage θ(CO) remains constant during exchange, and the exchange rate r_{ex} is controlled by the desorption rate, then the exchange rate is proportional to the ^{13}CO relative coverage θ(^{13}CO) (at constant total CO_{ad} coverage) and we obtain the relation:

$$r_{ex} = \frac{N_0 \times \theta(^{13}CO)}{dt} = (N_0 \times \theta(^{13}CO) \times \nu) \times \exp\left(\frac{-E^*_{des}(\theta(CO))}{R \times T}\right)$$

This assumes, that after each desorption process subsequent adsorption of a CO molecule is fast, and that the CO gas phase (or the CO dissolved in the electrolyte) consists purely of ^{12}CO, i.e., the desorbing ^{13}CO is immediately removed. Integrating this over time, we obtain:

$$\ln\theta(^{13}CO) = k_{des} \times t + \ln\theta_0(^{13}CO),$$

which perfectly explains the first-order exchange kinetics observed experimentally. The increasing rate with higher ^{12}CO concentration is caused by the pronounced decrease in the activation energy for CO desorption $E^*_{des}(\theta(CO))$ with the (total) CO_{ad} coverage $\theta(CO)$. The pronounced decay of the CO adsorption energy explains also the observed red-shift of the CO_L signal upon removal of the CO from the electrolyte. With decreasing coverage, the repulsive CO_{ad}-CO_{ad} interactions become weaker, and the increasing back donation to the $2\pi^*$ orbital of the CO molecules results in a weakening of the C-O bond {BLYH64}

Finally, using the coverage information from the DEMS data, the wavenumbers of the CO_L band during CO isotope exchange in Fig. 36 can be re-plotted vs. the $^{13}CO_{ad}$ coverage in the CO adlayer at a constant total CO_{ad} coverage (Fig. 39). In this plot, effects from the different adsorption rates for different ^{12}CO partial pressures are canceled.

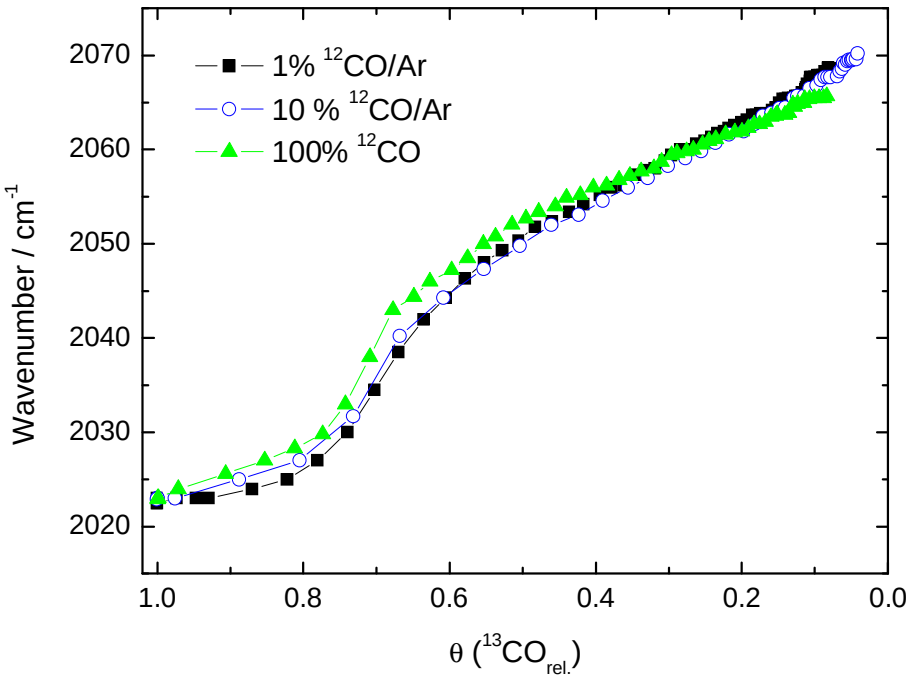

Fig. 39: Shift of the frequency of linearly adsorbed CO during the exchange process as function of the $^{13}CO_{ad}$ coverage (at constant total CO_{ad} coverage) in electrolytes with different ^{12}CO concentrations (see figure).

The sigmoidal shape of these curves agrees well with data reported for adsorption of $^{12}CO/^{13}CO$ isotope mixtures {CHAN90C}{VILL94}{KIM94B}, and with the results of model calculation {PERS81}{PERS85A}{SEVE95}. The observed correlation between CO_L wavenumber and $^{13}CO_{ad}$ coverage at constant potential and constant total CO_{ad} coverage can be explained by vibrational coupling between the CO_{ad} molecules {PERS81}{PERS85A}{CHAN90C}{KIM94B}{SEVE95}. In total, these data demonstrate that the presence of gas phase CO in the electrolyte establishes an adsorption/desorption equilibrium already at room temperature. Similar results of a rapid CO_{ad} exchange on Pt and PtRu fuel cell catalysts upon interaction with a CO containing atmosphere were reported previously by Davies et al., who followed the CO exchange in gas phase experiments, in the absence of an electrolyte {DAVI04}{DAVI05}. In these experiments, however, possible effects of the electrolyte and the potential could not be accounted for. Very recently, this author could confirm the result of a complete exchange of preadsorbed ^{13}CO by ^{12}CO in the gas phase, also for an operating fuel cell with reaction temperatures between 25 and 150°C, measuring the desorbing ^{13}CO at the fuel cell exhaust {DAVI08}. This group equally observed first-order exchange kinetics and complete exchange within 10 min at 25°C. In such measurements, however, care has to be taken to avoid artifacts caused by the significant time required for the gas to pass through the cell and by the varying composition of the gas phase in the cell along the flow field (integral reactor {THOM97}), which complicates a quantitative evaluation.

4.3.3 Summary

Using the combined ATR-FTIRS/DEMS set-up for the simultaneous *in situ* IR spectroscopic and on-line mass spectrometric detection of adsorbed species under controlled mass transport conditions, it was found that adsorbed CO on a Pt electrode exchanges rapidly already at room temperature, when being in contact with CO containing electrolyte, at potentials far below the onset of electrochemical CO_{ad} oxidation. This is attributed to a decrease in the desorption barrier, caused by a combination of two effects, a slight increase in CO_{ad} coverage upon interaction with the CO gas phase and a pronounced decay of the CO adsorption energy with coverage, due to repulsive CO_{ad}-CO_{ad} interactions. Exchange is controlled by thermal desorption of CO_{ad} and proceeds via statistical replacement of individual CO_{ad} molecules rather than via formation of isotopomer islands.

5 ADSORPTION / OXIDATION OF FORMIC ACID

This Chapter deals with the electrochemical oxidation of formic acid and the results presented here are taken from three publications. The data presented in this Chapter where measured using *in situ* ATR-FTIR spectroscopy in a thin-layer flow cell without mass spectrometric product detection. Since CO_2 is the only reaction product in formic acid oxidation and the Faradaic current can be correlated to the CO_2 formation, mass spectrometric product detection was not required. However, IR spectroscopy was employed simultaneously with the electrochemical measurements to gain additional information on adsorbed species in the course of formic acid oxidation to CO_2.

The presentation of the results will start with a paper, published in Angewandte Chemie, evaluating the contributions of the different reaction pathways to the overall reaction current of formic acid oxidation. Based on the finding that the two pathways discussed in the literature are only minority pathways a third reaction pathway was postulated (section 5.1) {CHEN04F}. This lead to an intense discussion between our group and the group of Prof. Osawa about the role of adsorbed formate species in the course of formic acid oxidation, which were proposed to be the reactive intermediate in the direct oxidation of formic acid to CO_2 {MIKI02}{CHEN03}. However, the results discussed in section 5.2, indicate that adsorbed formate species are rather spectator species than active intermediates in the rate limiting step of formic acid oxidation {CHEN06K}. To get further insight into the rate limiting step of CO_{ad} formation, resulting from formic acid adsorption/oxidation, measurements with deuterated formic acid were performed. Based on a difference in the kinetic isotope effect (KIE) for the CO_{ad} formation (KIE = 3) and for the overall reaction to CO_2 (KIE = 1.9) conclusions on the transition state for CO_{ad} formation are derived (section 5.3) {CHEN07Z}.

5.1 Kinetics and Mechanism of Formic Acid Electrooxidation – Spectro-electrochemical Studies in a Novel Flow Cell Configuration

Yan Xia Chen[1], Martin Heinen, Zenonas Jusys, and Rolf Jürgen Behm*

Institute of Surface Chemistry and Catalysis, Ulm University, D-89069 Ulm, Germany

[1] Pres. address: National Laboratory for Physical Sciences at the Microscale, Department of Chemical Physics, University of Science and Technology of China, Hefei, China

Published in: Angewandte Chemie Int. Ed. 45, 981-985**, 2006**

Table of Contents:

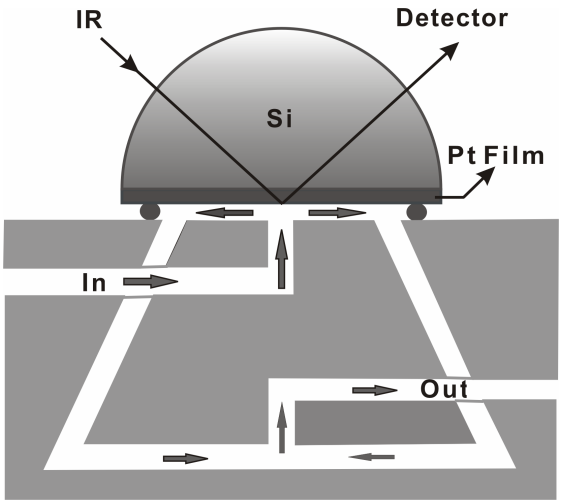

A novel spectro-electrochemical flow-cell with well-defined mass transport, allowing time-resolved electrochemical and in-situ FTIR spectroscopy measurements under continuous electrolyte flow and, e.g., upon electrolyte exchange, is developed. Its potential for mechanistic and kinetic studies is demonstrated for the electrooxidation of formic acid, where quantitative kinetic measurements of the IR intensities reveal the existence of a third reaction pathway, in addition to those suggested previously, which is dominant under present reaction conditions.

5.1.1 Introduction

The oxidation of formic acid on Pt group metal electrodes is of ongoing interest, both as model reaction for the mechanistic understanding of the electrooxidation of small organic molecules and because of its technical relevance for fuel cell applications {BREI67A}{CAPO73B}{CAPO73}{PARS88}{BEDE92}{JARV98}{SUN98A}{HAMN99} {HERR03}{WASZ03}. It was generally accepted that this reaction proceeds via the so-called 'dual path' mechanism {BREI67A}{CAPO73B}{CAPO73}{CAPO73C}{WATA73}. The *indirect pathway* proceeds via the initial dehydration of formic acid, most likely of an adsorbed molecular $HCOOH_{ad}$ precursor, to form adsorbed CO, which is then, in a second step, oxidized to CO_2. In the *direct pathway*, formic acid is supposed to be 'directly' oxidized to CO_2, via one or several weakly adsorbed reaction intermediates, without the formation of CO_{ad} {CAPO73B}{CAPO73}{PARS88}{BEDE92}{JARV98}{SUN98A}{HAMN99}. Support for the indirect reaction pathway was mainly gained from the IR spectroscopic observation of CO_{ad} under reaction conditions {BEDE83}{KUNI87}{JARV98}{VIEL03}. The postulation of a second pathway was initially based on the observation that HCOOH oxidation is possible at potentials well below the onset of CO_{ad} oxidation {CAPO73B}{CAPO73}{PARS88}. First definitive evidence for the second pathway came from differential electrochemical mass spectrometric (DEMS) experiments involving isotope labeling {WOLT85}. In contrast to the *indirect pathway*, the *direct pathway* does, at least formally, not require addition of oxygen from OH_{ad} or O_{ad}, and therefore can occur already at potentials below the onset of OH_{ad} formation (>0.4 V on Pt) {CAPO73}{WOLT85}{MARK99A}{ANDE02A}. For the *direct pathway*, adsorbed -COH or CHO {WILH87}, –COOH {CAPO73}{SUN88}{LAMY91}, or formate (HCOO) {KUTS63}{GOME97}{SAMJ05}{SAMJ05A} species have been suggested as reactive intermediates, mainly based on electrochemical *in situ* IR measurements. Here it is important to note that the IR studies, except for the studies from Osawa's group, had been performed in an external reflection configuration, where trapping of (side-)products or depletion of reactants in the thin electrolyte layer between working electrode and optical window can cause artifacts and hence result in misleading conclusions {IWAS97}.

Based on the *in situ* infrared spectroscopy data presented in this Chapter, the contribution of both, the direct and the indirect pathway, to the overall reaction current measured for the electrooxidation of formic acid will be determined. The indirect pathways is quantified via

time-resolved measurements of the build-up and oxidative removal of the CO adlayer in potential-step and electrolyte-exchange experiments, showing that at potentials between 0.4 and 0.7 V the *indirect pathway* represents a minority pathway and contributes by less than 0.1% at $E \leq 0.6$ V at room temperature. Based on a comparison between the intensity of adsorbed formate and the overall Faradaic currents in electrolyte exchange experiment using different concentrations of formic acid, it is concluded that the formate species visible in IR can not be the reactive intermediate for the dominant reaction pathway {CHEN04F}. This leads to the proposal of a new scheme for the mechanism of formic acid oxidation on Pt, which involves three different pathways, i) the *indirect pathway*, via CO_{ad} formation (formic acid dehydration) and oxidation, ii) a *formate pathway*, involving the formation and subsequent oxidation of formate to CO_2, and iii) a *direct pathway*, which has been tentatively attributed to direct dehydrogenation of an adsorbed molecular $HCOOH_{ad}$ precursor {CHEN04F}.

5.1.2 Results

The interaction of formic acid with Pt electrodes at potentials below oxide formation leads to the build-up of an adsorbate layer, where the chemical nature/composition depends critically on the electrode potential {WOLT85}. The accumulation of the adsorbed species was followed in potentiostatic, transient experiments under continuous electrolyte flow, changing from pure base electrolyte (0.5 M H_2SO_4) to formic acid containing electrolyte (0.5 M H_2SO_4 + 0.1 M HCOOH, t = 0 – 4.5 min) and, after reaching steady-state conditions (4.5 min), back again to pure base electrolyte (adsorption/oxidation potential 0.4 V, 0.5 V, 0.6 V). The nature of the adsorbed species is evident from the sequence of IR spectra in Fig. 40, which were taken during these transient experiments at a constant potential of 0.5 V. Characteristic features of these spectra are three positive bands, one with a peak frequency of ca. 1322 cm^{-1}, which was attributed to bridge-bonded adsorbed formate ($HCOO_{ad}$) {COLU92}{MIKI02}, and two peaks centered at ca. 2010 and 1790 cm^{-1}, which are related to linearly-bonded (CO_L) and multiply-bonded (CO_M) adsorbed CO (CO_{ad}). In addition, the spectra exhibit a broad negative band in the region from 1000 to 1250 cm^{-1}, which corresponds to displaced (bi)sulfate {IWAS97}. The presence of significant amounts of other adsorbates can be excluded based on the IR data. Spectra taken at 0.4 and 0.6 V exhibit similar characteristics as the above ones.

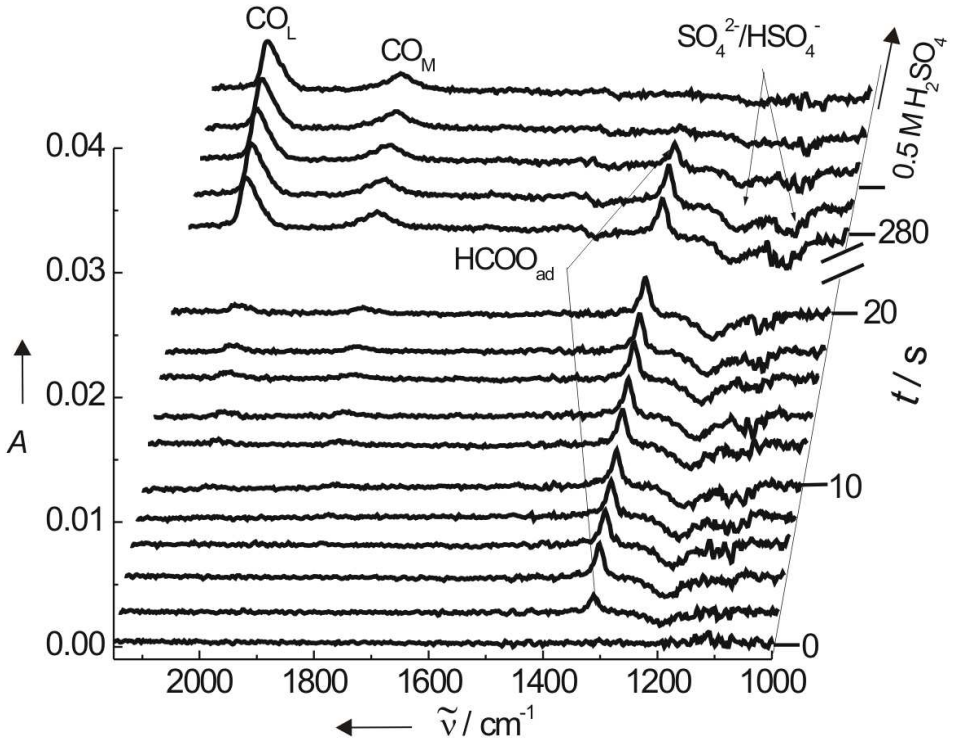

Fig. 40: Selected IR spectra recorded during adsorption/oxidation of formic acid on a Pt thin film electrode at 0.5 V. Electrolyte exchange at t = 0 s from 0.5 M H_2SO_4 to 0.1 M HCOOH + 0.5 M H_2SO_4 and back after ca. 4.5 min. Electrolyte flow rate: 50 µl/s, cell volume: 10-20 µl.

More quantitative information on the build-up of the adsorbate layer and on the relation between adsorbate coverage and the Faradaic reaction current is derived from the current densities in the chronoamperometric transients (Fig. 41a) and from the integrated intensities of the IR signals as a function of time at the different adsorption potentials (Fig. 41b-d). The current densities increase steeply when switching from the supporting electrolyte to HCOOH containing solution (t=0), reaching a maximum after ca. 3 s, and then decrease slowly with time under a continuous flow of HCOOH containing electrolyte. When changing back to pure supporting electrolyte after ca. 4.5 min, they instantaneously drop to zero.

In contrast to the steep increase of the current densities the intensities of the CO_L (Fig. 41b) and CO_M (Fig. 41c) related signals develop slowly upon changing to 0.1M HCOOH containing solution over the entire adsorption time (4.5 min). Both the final CO_{ad} coverage and the initial rate for CO_{ad} formation are highest for adsorption at 0.4 V, lower at 0.5 V and very low at 0.6 V. When the electrolyte is switched back to HCOOH free solution, the intensities of the CO_{ad} signals (Fig. 41b) decrease only slowly, as expected from the slow

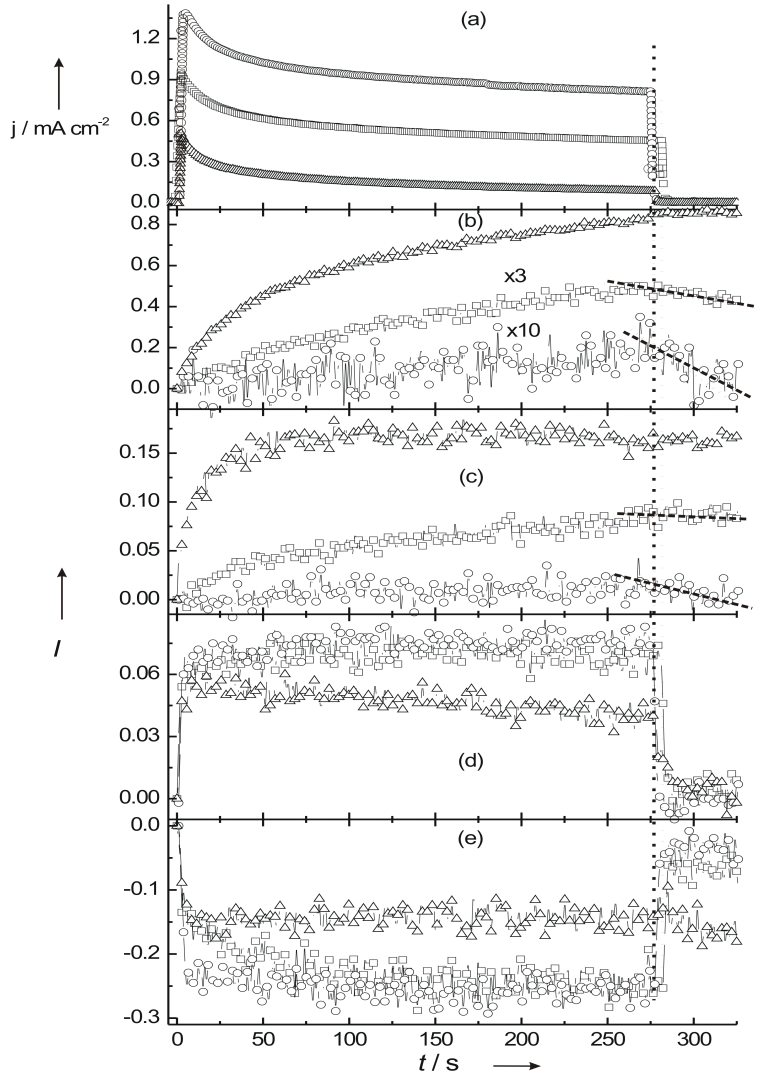

Fig. 41: Chronoamperometric transients (a) and evolution of the IR peak intensities related to adsorbed (b) CO_L and (c) CO_M species, to (d) adsorbed formate and (e) (bi)sulfate during the interaction of formic acid with the Pt thin film electrode at 0.4 (triangles), 0.5 (squares) and 0.6 V (circles) (experimental conditions see Fig. 40).

kinetics of CO_{ad} electrooxidation at potentials of 0.6 V and below. The $HCOO_{ad}$ related intensities (Fig. 41d) show an abrupt increase when switching to HCOOH containing solution, reaching an approximately constant value ca. 3 s after the electrolyte exchange. For adsorption at 0.4 V, a slight subsequent decay of the formate band intensity with time is found, probably due to formate replacement by CO_{ad}. Formate adsorption/formation is accompanied by a decrease in the (bi)sulfate band intensity (Fig. 41e), which approximately mirrors the temporal evolution of the formate intensity (Fig. 41d), implying that sulfate/bisulfate is displaced by more strongly adsorbed formate species. Similar to the current density, the formate intensity drops instantaneously to zero when changing back to pure supporting electrolyte, accompanied by a similarly fast increase in the (bi-)sulfate intensity.

Only at 0.4 V, the (bi-)sulfate intensity remains virtually constant, despite of the abrupt decay in the formate intensity. This is tentatively explained by a combination of two effects. It is expected that formate is randomly distributed in the CO adlayer and that at the high CO_{ad} coverage a relaxation of the CO adlayer is energetically more feasible than adsorption of the large and weakly adsorbed sulfate anions.

The above results clearly show that formic acid oxidation is accompanied by the formation of adsorbed formate, in agreement with findings in a previous study {MIKI02}, and that under present reaction conditions the build-up of these formate species is much faster than the formation of CO_{ad}. Hence, the rate for formic acid dehydrogenation/$HCOO_{ad}$ formation (in this term also contributions from adsorption of formate anions from the electrolyte are included) is much higher than that for formic acid dehydration (CO_{ad} formation) under present reaction conditions.

The reaction rates for formic acid dehydration to CO_{ad} and subsequent CO_{ad} oxidation can be determined quantitatively from the IR data using the relation between the IR intensities of the CO_M species at low CO_{ad} coverages and the CO_L related intensity in the medium CO_{ad} coverage regime, which were determined in calibration measurements (see section 3.7). The CO_{ad} oxidation rate under steady-state conditions is determined from the initial slope of the CO_{ad} intensity-time curve, right after changing back from 0.1 M HCOOH containing solution to HCOOH free electrolyte (Fig. 41b), assuming that the CO_L to CO_M population ratios do not vary significantly between 0.4 and 0.6 V {CHAN90B}. For clarity, the intensities of the CO_L species at 0.5 V (squares) are magnified by a factor of three and at 0.6 V (circles) by a factor of ten. Using a CO_{ad} saturation coverage of 0.7 monolayers (ML), turnover frequencies (TOFs) of 6.4×10^{-5} and 3.3×10^{-4} molecules $site^{-1}$ s^{-1} for CO_{ad} oxidation to CO_2 at 0.5 and 0.6 V, respectively, can be determined under present steady-state reaction conditions. At 0.4 V, the rate for CO_{ad} oxidation is below the detection limit (table 4). The increase of the CO_{ad} oxidation rate with potential agrees with the common explanation of an enhanced OH_{ad} formation at higher potentials ('electrochemical activation') and the results for the CO_{ad} adsorption/oxidation, as presented in Chapter 4.2. In the same way the initial rates for CO_{ad} formation (HCOOH dehydration) on the initial, CO_{ad} and $HCOO_{ad}$ free Pt surface can be calculated from the initial slopes of the CO_{ad} intensity profiles, after switching from base electrolyte to HCOOH containing solution. This yields values of 2.0×10^{-2}, 1.8×10^{-3} and 3.2×10^{-4} molecules $site^{-1}$ s^{-1} for the turnover frequencies at 0.4, 0.5 and 0.6 V, respectively (see table 4).

Reaction	**TOF /** molecules s^{-1} $site^{-1}$		
	0.4 V	0.5 V	0.6 V
HCOOH dehydration (to CO_{ad}) at θ_{CO}=0	2.0×10^{-2}	1.8×10^{-3}	3.2×10^{-4}
CO_{ad} oxidation (steady state)	~0	6.4×10^{-5}	3.3×10^{-4}
Total HCOOH oxidation to CO_2 (steady state, 4.5 min)	0.3	1.4	2.5

Table 4: Turnover frequencies (TOF) for i) formic acid dehydration to COad on a clean Pt surface (in the limit of very small CO_{ad} and OH_{ad} coverages), and for ii) CO_{ad} oxidation to CO_2 and iii) total oxidation of formic acid to CO_2 under steady state conditions, determined after 4.5 min under continuous flow of 0.1 M HCOOH + 0.5 M H_2SO_4 at different reaction potentials.

In the later stages of the adsorption process, the increase in CO_{ad} coverage represents the difference of CO_{ad} formation (formic acid dehydration) and CO_{ad} oxidation, under steady-state conditions the two rates are equal. At 0.6 V, the rates for CO_{ad} oxidation (on a partly CO_{ad} covered Pt surface) and formic acid dehydration (on a bare Pt surface) are of comparable magnitude, which explains the rather low steady-state CO_{ad} coverage detected at this potential. At 0.4 V, the CO_{ad} oxidation rate is negligible, resulting in the observed pronounced accumulation of CO_{ad} with time up to saturation. The absolute values of the initial dehydration rates as well as the fact that at 0.4 V the initial rate for formic acid dehydration is about (more than) one order of magnitude higher than at 0.5 V (0.6 V) agree well with results derived by Sun et al. from electrochemical transients {SUN98A}.

The relative contribution of the indirect reaction pathway to the total rate of formic acid oxidation to CO_2 under present steady-state conditions can be calculated from the ratio of the rate for CO_{ad} oxidation determined above and the Faradaic current under these conditions, using the values obtained from the chronoamperometric transients (Fig. 41a) after 4.5 min of formic acid oxidation (table 4). Comparing the TOFs of 0.28, 1.4 and 2.5 molecules·$site^{-1}$·s^{-1} for formic acid oxidation to CO_2 in total at potentials of 0.4, 0.5 and 0.6 V, respectively, and the above turnover frequencies for CO_{ad} oxidation at these potentials, it is concluded that the indirect pathway, via dehydration of a $HCOOH_{ad}$ precursor to CO_{ad} and its further oxidation

to CO_2, contributes less than 0.1% (<0.01%) to the total rate for formic acid oxidation at 0.5 V (0.6 V), respectively.

Interestingly, the ratio of the formate band intensities at the end of the HCOOH oxidation period at different potentials (Fig. 41d) differs significantly from that of the Faradaic currents (Fig. 41a): 90% (0.5 V) and 50% (0.4 V) of the formate intensity at 0.6 V result in Faradaic currents of 55% (0.5 V) and ~10% (0.4 V) of the value at 0.6 V, respectively. Since the dehydration pathway does not contribute significantly under these conditions, this observation requires either a potential dependent variation (electrochemically activation) of both adsorbed formate formation and its oxidation to CO_2, or the existence of another, third reaction pathway. For more information on this point, similar transient oxidation measurements as in Fig. 41 at the same potential (0.6 V) were performed, using two different formic acid concentrations. Representative results are shown in Fig. 42.

Comparing the Faradaic currents for the oxidation of 0.7 mM and 70 mM HCOOH solution at 0.6 V current densities of 0.045 mA·cm^{-2} and 0.85 mA·cm^{-2} after 100 s are measured, i.e., roughly a factor of twenty between the two electrolytes. The IR spectra acquired at t = 100 s, in contrast, show that the respective formate intensities differ only by about a factor of five.

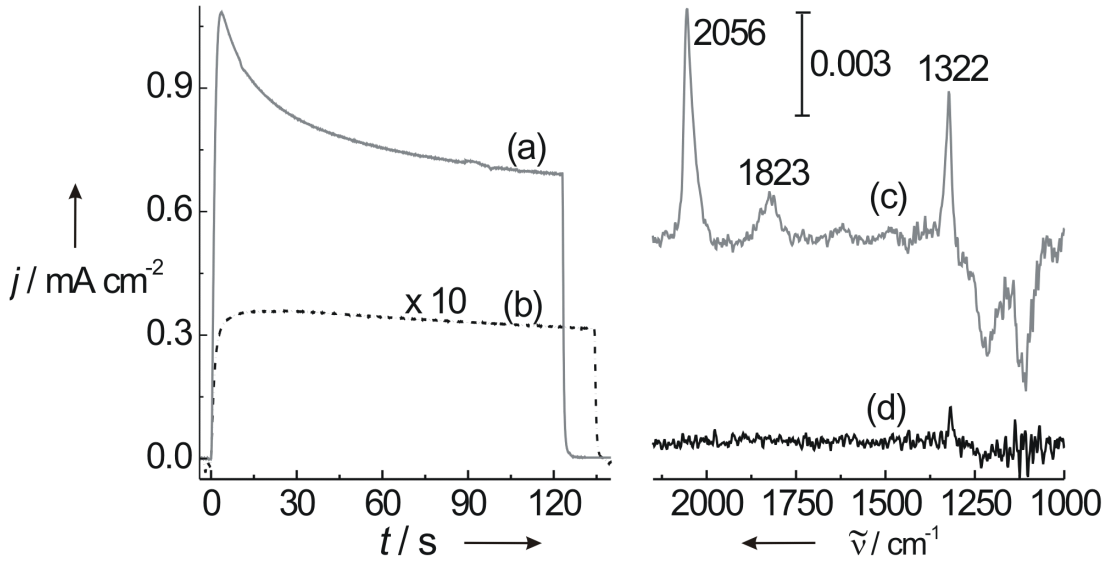

Fig. 42: Chronoamperometric transients (a , b) and IR spectra of adsorbed formate (c , d) on a Pt thin film electrode at 0.6 V in solution containing 70 mM (a, c) and 0.7 mM HCOOH (b, d). The spectra were acquired 100 s after changing to formic acid containing solution.

Hence, even at similar reaction potential the total steady-state rates for HCOOH oxidation are not at all proportional to the respective formate coverages. (This statement and the role of adsorbed formate in the course of formic acid oxidation are further discussed in section 5.2 where, amongst others, measurements with a systematic variation of the formic acid concentration over two orders of magnitude are presented and discussed). Considering the negligible contribution of the indirect pathway under these conditions and assuming that the rate for formate decomposition is linearly related to the formate coverage, this clearly indicates that there must be a third reaction pathway. Its contribution to the total reaction rate cannot be calculated precisely from these data, but an upper limit for its contribution can be estimated. Assuming that for 0.7 mM HCOOH solution the Faradaic current results completely from the formate pathway, the five times higher formate band intensity in 70 mM HCOOH solution could at most result in a five times higher current density. The experimentally observed increase by a factor of twenty is only possible, if the reaction pathway via the adsorbed formate species, which is detected by IR and which dominates the formate IR signal (‘formate pathway’), contributes less than 25% to the total anodic current. Hence, although the IR spectra do not give any indication of another adsorbed species, this third pathway is dominant for room temperature oxidation of 0.1 M formic acid solution. This can either be explained by an additional, so far unresolved adsorbed reaction intermediate, whose surface concentration/coverage is very low (short lifetime under reaction conditions), or by a direct reaction of weakly adsorbed $HCOOH_{ad}$ species. (The theoretical possibility of a flat lying formate species with a very low IR cross-section is ruled out considering the necessity of a reasonable substrate-adsorbate bond for a stable reaction intermediate.) Here the latter explanation is favored and a triple path mechanism is proposed, which starts with a weakly adsorbed $HCOOH_{ad}$ precursor, that can subsequently either be directly oxidized to CO_2 (direct pathway), or undergo dehydration to CO_{ad} (‘indirect pathway’), or is dehydrogenated to stable bridge-bonded adsorbed formates (formate pathway), as it is schematically depicted in Fig. 43. The stable, adsorbed intermediates resulting in the last two pathways can then, in a third step, be oxidized to CO_2. In this scheme, adsorbed formates are indeed reaction intermediates, but, different from recent concepts {SAMJ05A}, not in the dominant reaction pathway.

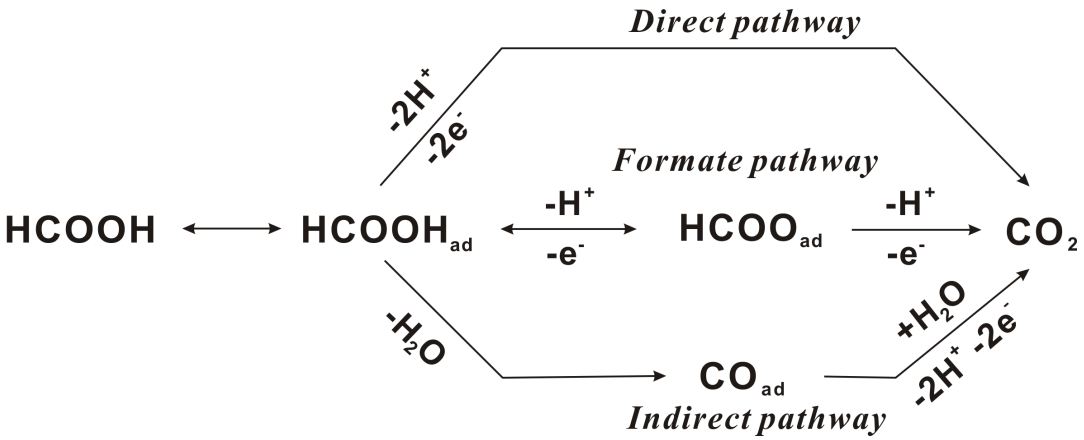

Fig. 43: Tentative reaction scheme for formic acid oxidation on Pt derived from the present data, which includes three different reaction pathways, the 'indirect' pathway, the 'formate pathway' and the 'direct' pathway. The formate pathway relates to the formate species detected by IR (see text).

5.1.3 Summary

Based on quantitative spectro-electrochemical kinetic studies of the electrooxidation of formic acid on a Pt film electrode in acidic solution at constant potentials between 0.4 and 0.6 V and under well-defined mass transport conditions, the contributions of the indirect pathway as well as of the formate pathway have been quantified. Furthermore, a clear proof has been provided that under current reaction conditions both of them represent minority pathways. Therefore, a new mechanistic scheme for the electrooxidation of formic acid has been introduced, in which the direct oxidation of weakly adsorbed $HCOOH_{ad}$ species to CO_2 is proposed for the dominant reaction pathway.

5.2 Bridge-bonded Formate - Active Intermediate or Spectator Species in Formic Acid Oxidation on a Pt Film Electrode?

Y.-X. Chen[1], M. Heinen, Z. Jusys, and R.J. Behm[*]

Institute of Surface Chemistry and Catalysis, Ulm University, D-89069 Ulm, Germany

[1] Pres. address: National Laboratory for Physical Sciences at the Microscale, Department of Chemical Physics, University of Science and Technology of China, Hefei, China

Published in: Langmuir 22, 10399-10408, **2006**

ABSTRACT

We present and discuss the results of an in-situ IR study on the mechanism and kinetics of formic acid oxidation on a Pt film/Si electrode, performed in an attenuated total reflection (ATR) flow cell configuration under controlled mass transport conditions, which specifically aimed at elucidating the role of the adsorbed bridge-bonded formates in this reaction. Potentiodynamic measurements show a complex interplay between formation and desorption/oxidation of COad and formate species, and the total Faradaic current. The notably faster increase of the Faradaic current compared to the coverage of bridge-bonded formate in transient measurements at constant potential, but with different formic acid concentrations reveals that adsorbed formate decomposition is not rate-limiting in the dominant reaction pathway. If being reactive intermediate at all, the contribution of formate adsorption/decomposition to the reaction current decreases with increasing formic acid concentration, accounting for at most 15% for 0.2 M DCOOH at 0.7 VRHE. The rapid build-up/removal of the formate adlayer and its similarity with acetate or (bi-)sulfate adsorption/desorption indicate that the formate adlayer coverage is dominated by a fast dynamic adsorption-desorption equilibrium with the electrolyte, and that formate desorption is much faster than its decomposition. The results corroborate the proposal of a triple pathway reaction mechanism including an indirect pathway, a formate pathway and a dominant direct pathway, as presented previously (Y.X. Chen et al., Angew. Chem. Int. Ed. 45 (2006) 981), in which adsorbed formates act as site-blocking spectator in the dominant pathway rather than as active intermediate.

5.2.1 Introduction

The triple pathway for the electrooxidation of formic acid, as introduced in the above section, is in contrast to a proposal in recent *in situ* IR studies {SAMJ05}, which claimed that bridge-bonded adsorbed formates represent the reaction intermediate in the dominant reaction pathway, via formate formation and subsequent decomposition to CO_2. The proposal was mainly based on the close similarity between the potential dependent formate band intensity and cyclic voltammograms, the fast displacement of labeled adsorbed formates by unlabeled formates during electrolyte exchange from $H^{12}COOH$ to $H^{13}COOH$ containing solution, and the ability to reasonably well model the oscillatory formic acid oxidation behavior with a rate law including second order kinetics for formate decomposition {SAMJ05A}.

The results discussed in section 5.2, aim at resolving this discrepancy and provide further data elucidating the role of these bridge-bonded adsorbed formate species in formic acid electrooxidation on Pt. In the previous chapter, for the oxidation of 0.7 mM and 70 mM formic acid containing solutions, it was shown that the intensity of adsorbed formate and the Faradaic current are not proportional to each other. In the following, the relation between formate coverage (IR band intensity) and Faradaic current will be evaluated systematically by electrochemical *in situ* IR spectroscopic measurements in a thin-layer flow cell over a wide range of formate coverages. This was achieved i) by varying the formic acid concentration over more than two orders of magnitude and by competing adsorption of acetate.

In section 5.2.2.1, results of potentiodynamic measurements for a qualitative overview are shown and the combined electrochemical and IR data are related to existing electrochemical data {OKAM04}. Section 5.2.2.2 presents electrolyte exchange transients at constant potential and different concentration (1 – 500 mM) for quantitative evaluation of the relation between the intensity of adsorbed formate and the overall Faradaic current. Next, the influence of the competing adsorption of acetate was investigated on formic acid oxidation during reaction in $HCOOH/CH_3COOH$ mixtures. Adsorbed acetate is known to be inert under these conditions and can be considered to purely act as a rate inhibiting spectator species. Furthermore, the potential dependent behavior of formate and acetate species is compared (section 5.2.2.3). In addition, kinetic isotope effects were investigated by comparing formic acid oxidation in 0.1 M HCOOH and DCOOH under otherwise identical reaction conditions (section 5.2.2.4). The implications of these results on the mechanism of formic acid oxidation

on Pt, with special attention on the role of adsorbed formates in that reaction are discussed (section 5.2.3)

5.2.2 Results

5.2.2.1 Concentration effects in formic acid oxidation – Potentiodynamic measurements

The influence of the DCOOH concentration on the DCOOH oxidation current on Pt is illustrated in the set of CVs (2nd cycle) in Fig. 44, which were recorded in DCOOH solutions of different concentrations (2, 5, 10, 25, 50 and 200 mM, scan rate 10 mV s^{-1}). The general shape of the CVs resembles that of HCOOH oxidation CVs on similar Pt film electrodes published earlier {CHEN06F} and presented in section 5.1 {CHEN04F}, with a characteristic oxidation prewave at 0.4 – 0.7 V, a distinct oxidation peak at 0.87 V, and formic acid oxidation on the oxidized Pt substrate at E > 1.1 V. Similar features appear in the reverse, negative-going scan, but with a pronounced hysteresis. With decreasing DCOOH concentration, the general shape of the CVs is maintained, with the following systematic changes: i) the current generally decreases and the maximum of the main peak in the positive-going scan decreases and shifts to more cathodic potentials, reaching 0.71 V at 2 mM solution (0.78 V at 10 mM solution); ii) at lowest concentrations, this peak develops a multiplett structure with additional shoulders at ~0.6 and ~0.8 V and H desorption becomes more pronounced. iii) In the negative-going scan, the onset of the reaction shifts to more cathodic potentials with decreasing concentration, from 0.95 to 0.85 V and a similar shift occurs also for the main maximum, and iv) the lower potential shoulder at 0.5 V develops into a distinct peak, leading to a plateau-like shape at 25 mM and a dominant low potential peak at lower concentrations. These trends largely resemble those published before by Okamoto et al. for HCOOH oxidation at comparable concentrations {OKAM04}. The difference between CVs recorded in DCOOH and in HCOOH solution is illustrated for 50 mM solution in Fig. 44, bottom. The main differences are: (i) the higher current in HCOOH containing electrolyte than in DCOOH containing solution (ca. 2-3 times for 50 mM solution). (ii) At E > 1.1 V the current difference between HCOOH and DCOOH containing solution is even more pronounced, amounting to a factor of 6 for 50 mM solutions. These differences reflect the kinetic isotope effect, which will be discussed further in section 5.2.2.4.

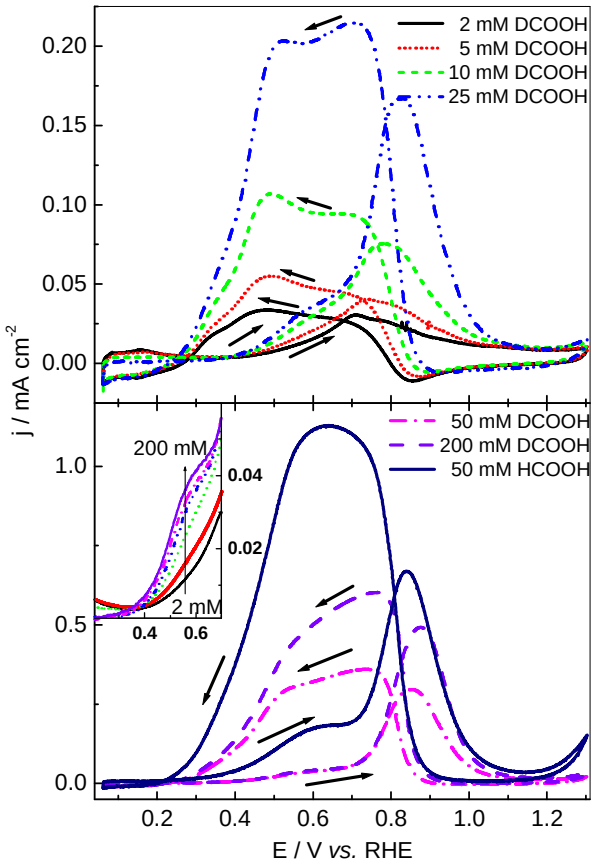

Fig. 44: Cyclic voltammograms of a Pt thin film electrode in DCOOH + 0.5 M H_2SO_4 solutions with different DCOOH concentrations from 2 to 200 mM (concentrations see figure, scan rate 10 mV s^{-1}). For comparison, the CV for 50 mM HCOOH + 0.5 M H_2SO_4 solution is also included. Inset: I-U curves in the region from 0.2 to 0.7 V for the different concentrations.

Simultaneously with measuring the CVs on the Pt thin film electrode, *in situ* ATR-FTIR spectra were recorded in increments of 50 mV (Fig. 45). Except for small differences in band frequency and intensity as well as in the potential for the appearance/disappearance of the characteristic bands, the sets of spectra recorded with different DCOOH concentrations are very similar to each other. Therefore, only two representative sets taken in solutions with DCOOH concentrations of 2 and 200 mM, respectively, are shown here (Fig. 45a,b). In these series the changes are referenced to a background spectrum at 1.2 V (in the negative-going scan), where DCOOH related adsorbates are absent. The peak assignment and also the their appearance follows recent descriptions {MIKI02}{CHEN03}{CHEN04F}. Two positive bands with peaks at ca. 2060 and 1820 cm^{-1} are attributed to linearly bonded CO_{ad} (CO_L) and multifold-bonded CO_{ad} (CO_M), where the latter includes contributions from CO_{ad} on bridge and multifold sites, respectively (Fig. 45). A rather narrow, weak signal centered at ca. 1298 cm^{-1} is assigned to adsorbed formate ($DCOO_{ad}$) in a bridged-bonded configuration, bound via

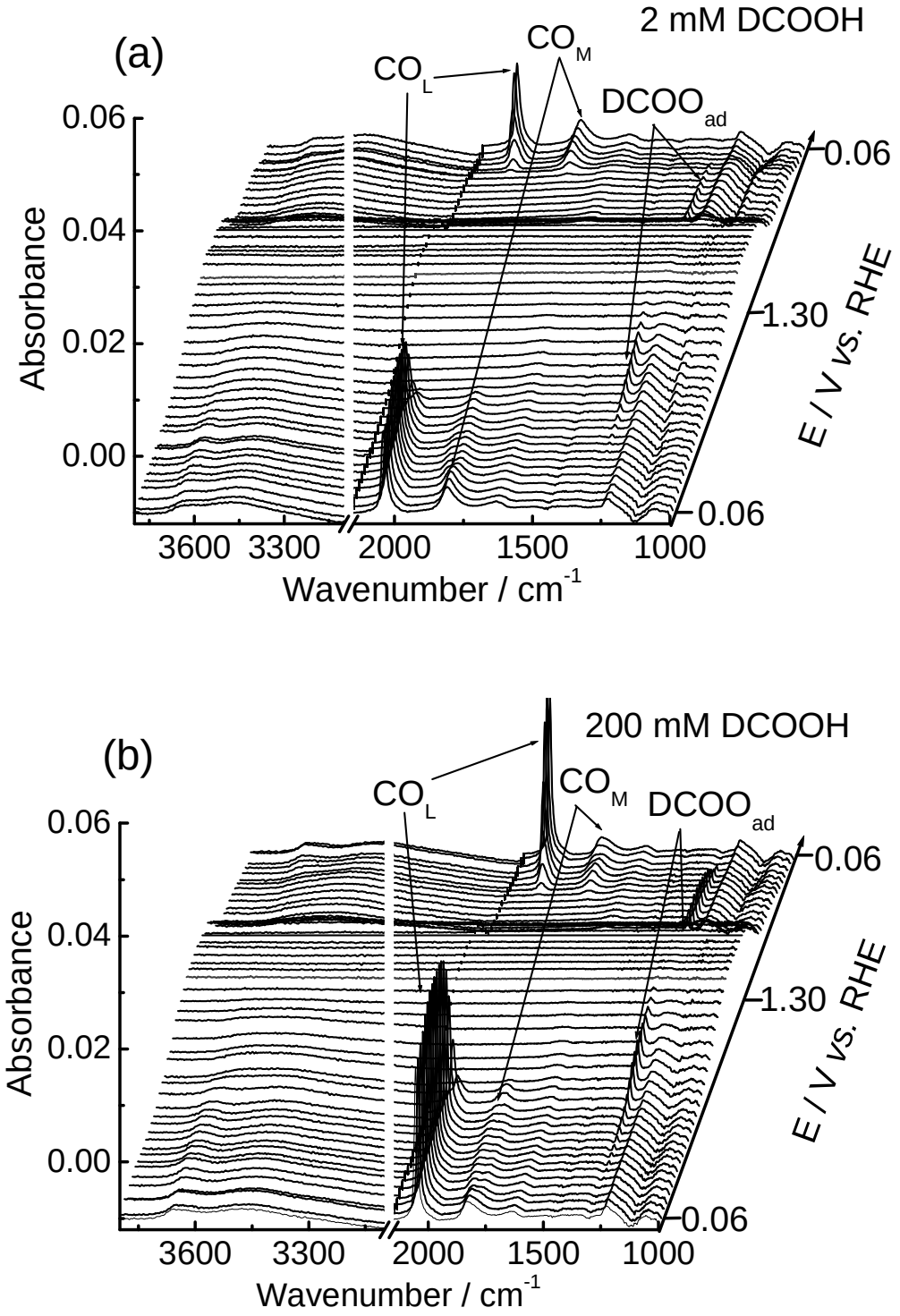

Fig. 45: Representative sets of ATR-FTIR spectra of the interface during DCOOH oxidation on a Pt thin film electrode in 0.5 M H_2SO_4 solution with (a) 2 mM and (b) 200 M DCOOH. The potential was scanned from 0.05 to 1.3 V and then back to 0.05 V; the corresponding CVs are shown in Fig. 44. The background spectrum was taken at 1.2 V in the backward scan.

two oxygen atoms to the Pt surface. Other weak bipolar bands around 1620 cm^{-1} and those above 3000 cm^{-1} arise from the deformation and stretching vibration from adsorbed water, respectively {MIKI02}. The potential dependent band characteristics of these peaks result from both the change in electrode potential as well as water displacement by adsorbed CO and formate. Bands below 1280 cm^{-1} are assigned to sulfate/bisulfate {NART94} (see Fig. 45). No other bands besides those mentioned above have been observed in these measurements.The band intensity-potential profiles of the adsorbed CO_{ad} and formate species obtained at different DCOOH concentrations are plotted in Fig. 46. The profiles for 200 mM DCOOH solution largely resemble those published for 100 mM HCOOH at room temperature recently {MIKI02}{CHEN06F}. The change in DCOOH concentration leads to the following systematic changes (with decreasing DCOOH concentration):

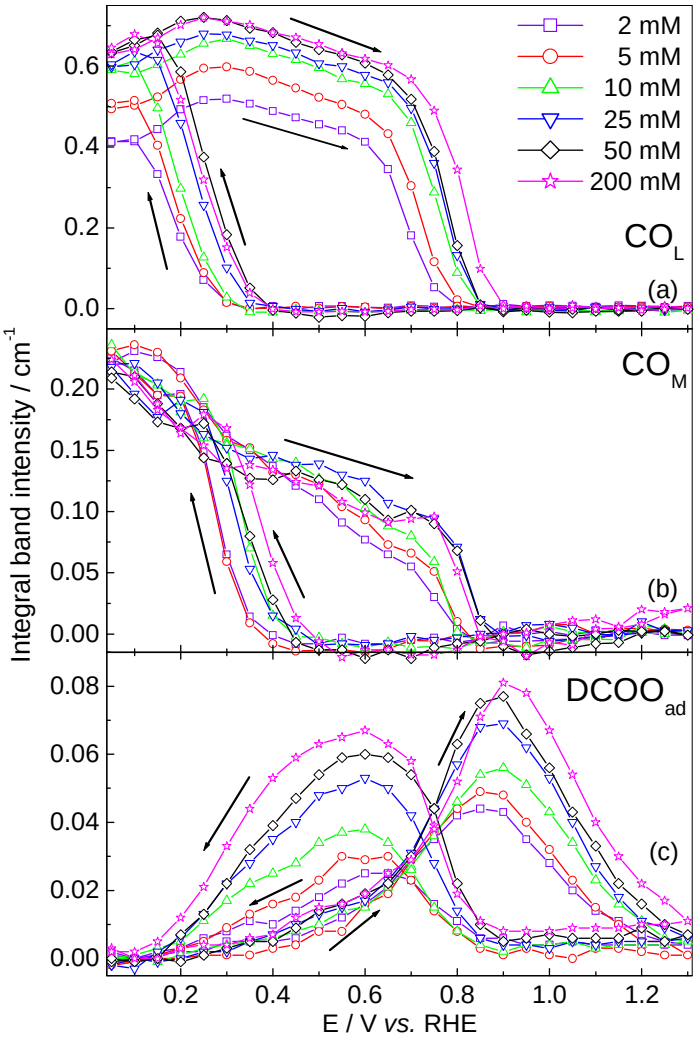

Fig. 46: Dependence of the integral intensity of the CO_L (a), CO_M (b) and formate (c) band on the electrode potential. The experimental conditions are the same as in Fig. 44 and 45.

i) The intensity of the CO_L species decreases steadily in the potential range between the cathodic potential limit and the onset of the steep intensity decay at ~0.7 V.

ii) The onset for this decay shifts to lower potentials, from ~0.7 V in 200 mM to 0.6 V in 2 mM DCOOH solution. A similar shift occurs for the complete disappearance of the CO_L signal.

iii) For the CO_M intensity, the concentration effects are less pronounced in the positive-going scan, with a slight loss of intensity in the range up to 0.5 V. At potentials anodic of this value, the differences become more pronounced and the clear distinction between a smoothly decaying part below 0.75 V and a steeply decaying part at above 0.75 V (200 mM solution) disappears with decreasing concentration, resulting in an almost continuous decay of the CO_M intensity over the entire potential range for the lowest concentration. Together with these changes, the potential for complete disappearance of the CO_M intensity shifts to lower values, from 0.9 (200 mM) to 0.85 V (2 mM solution).

iv) The formate intensity does not change much in the lower potential range (0.35 – 0.65 V) and in the steeply ascending part of the main peak. The peak itself shifts to lower potentials, from 0.9 V in 200 mM to ~0.85 V in 2 mM solution, and decreases in intensity. Also the subsequent intensity decay shifts to lower potentials, with the potential for complete formate removal shifting from 1.3 (200 mM solution) to 1.2 V (2 mM solution).

v) In the negative-going scan, the onset for formate adsorption shifts slightly to lower potentials, by about 50 mV for going from 200 to 2 mM solution, and a similar shift is observed for the onset of CO_M and CO_L formation. Similar to the behavior in the positive-going scan, the intensity in the formate peak decreases significantly, by about 50%, when changing to the most dilute solution. A significant decay is obtained also in the CO_L intensity in the potential range from 0.4 to 0.05 V.

vi) In dilute solutions (≤ 10 mM), the Faradaic current increase between 0.7 and 0.5 V in the negative-going scan is accompanied by an initial increase and subsequent decrease in the adsorbed formate intensity, while CO_{ad} accumulation has not yet started. In the potential range between 0.6 and 0.5 V, an increasing Faradaic current is measured, accompanied by a decreasing formate intensity/coverage. At higher concentrations, the Faradaic current decreases in this potential range (0.7 - 0.5 V), together with an initial increase (from 0.75 to 0.6 V) and subsequent decrease in the adsorbed formate intensity (coverage).

The data presented so far allow a number of qualitative conclusions on the kinetics of the underlying processes CO_{ad} formation (formic acid dehydration), CO_{ad} oxidation, formate adsorption/formation, formate desorption, formate decomposition to CO_2 and direct formic acid oxidation (formic acid dehydrogenation):

The increase of the anodic current in the potential range between 0.5 and 0.9 V in both positive-going and negative-going scan with increasing concentration is primarily caused by the increase in the *direct* (non-formate) *pathway*. This is evidenced by the much stronger increase in Faradaic current than in adsorbed formate intensity/coverage.

The low currents in the potential range below 0.5 V are attributed to a combination of a low CO_{ad} oxidation rate and an increased $HCOOH_{ad}$ dehydration (CO_{ad} formation) rate. The rather high CO_{ad} coverages results in a surface poisoning.

The shift of the Faradaic current peak and of the decay in CO_{ad}/formate intensity to more anodic potentials in concentrated solutions indicates that Pt oxidation is inhibited by the presence of a CO or formate adlayer.

The combination of an increasing Faradaic current and a decreasing formate intensity (coverage) with decreasing potential in the negative-going scan, which is observed for dilute solutions and at potentials from 0.6 to 0.5 V, can be explained by two different effects: Either the contribution of the indirect pathway (via CO_{ad}) increases, and/or the contribution of the direct pathway increases. The first case would indicate that CO_{ad} oxidation is faster than CO_{ad} formation, as evidenced by the absence of CO_{ad} species under these conditions. The latter case, which could arise from a potential induced desorption of formate, would mean that adsorbed formates act as reaction blocking species for the direct pathway. The same conclusion can be drawn from the decay in Faradaic current at higher concentrations (≥ 25 mM), together with increasing formate intensity (coverage) in the potential range 0.7 – 0.6 V. This will be discussed further in sections 5.2.2.2 and 5.2.2.3.

Adsorbed sulfate only appears at low DCOOH concentration and CO_{ad} coverage, and its band intensity-potential profile is rather similar to that of formate (and acetate, see section 5.2.2.3), suggesting that they all result from anion adsorption.

5.2.2.2 Potential and concentration effects on formic acid oxidation – transient potentiostatic measurement

More quantitative information on the reaction kinetics can be obtained from transient experiments at constant potential, where time and potential effects are not convoluted. As already mentioned in the experimental part (see section 3.2) for the IR spectroscopic analysis of the adlayer development these measurements should be performed as electrolyte exchange experiments, which are only possible in a flow cell configuration with defined electrolyte transport to/from the electrode {HEIN04}. Selected spectra recorded at different potentials (0.1 – 0.7 V) 3 s after the electrolyte exchange from 0.5 M H_2SO_4 to 0.5 M H_2SO_4 + 0.1 M DCOOH solution, are shown in Fig. 47. After this time, the formate band intensity has reached its maximum value or steady-state values (see Fig. 48).

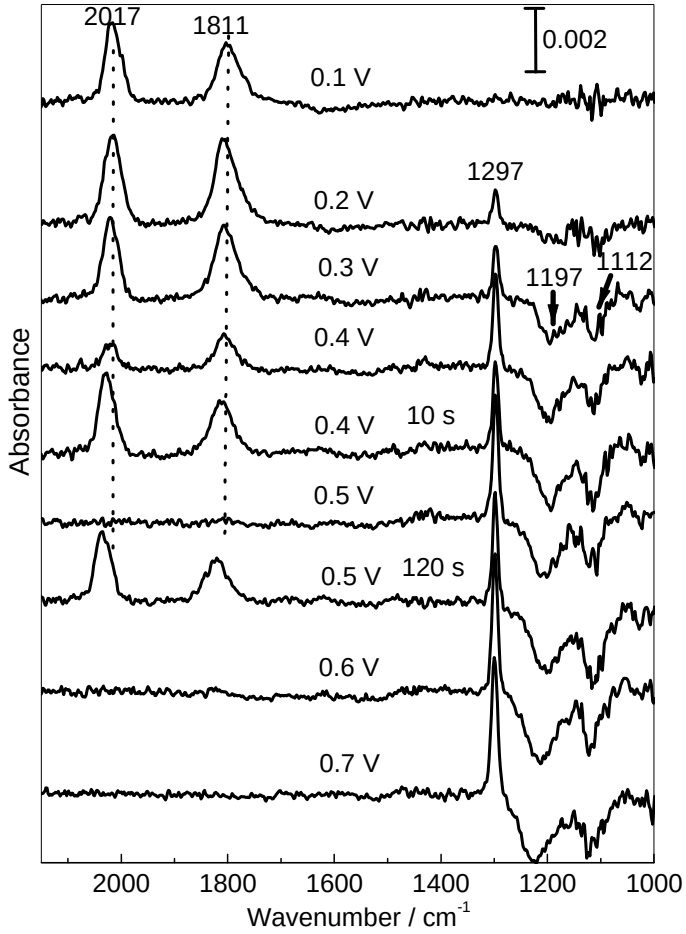

Fig. 47: ATR-FTIR spectra recorded on the Pt film electrode at different potentials (from 0.2 to 0.7 V in increments of 100 mV) and 3 s (unless specified other in the figure) after solution exchange from 0.5 M H_2SO_4 to 0.5 M H_2SO_4 + 0.1 M DCOOH

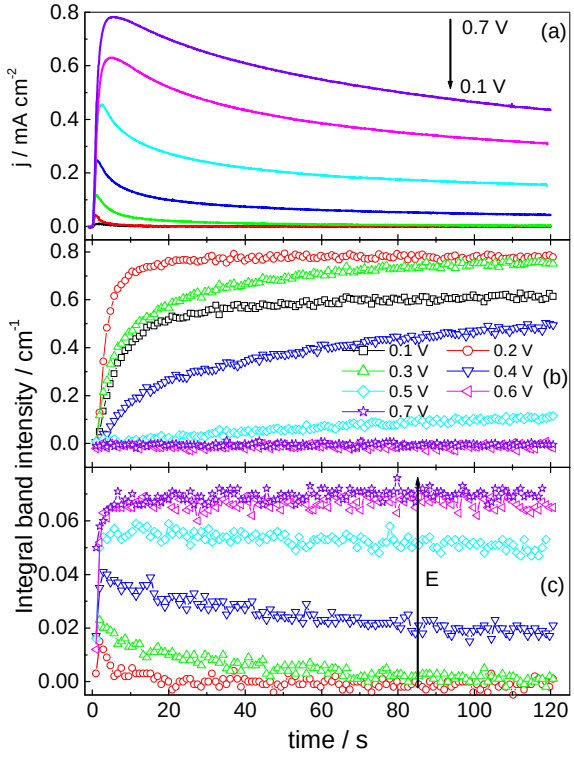

Fig. 48: (a) Chronoamperometric and CO_L (b) as well as adsorbed formate (c) band intensity transients recorded on a Pt film electrode at different electrode potentials upon solution exchange from 0.5 M H_2SO_4 to 0.5 M H_2SO_4 + 100 mM DCOOH.

For additional information, also a few spectra taken at later times after the electrolyte exchange are included, where significant amounts of CO_{ad} have accumulated. The corresponding chronoamperometric transients as well as intensity-time profiles for CO_L and adsorbed formate species are displayed in Fig. 48a, b and c. Similar transients and adsorbed formate intensity-time profiles recorded upon electrolyte exchange at constant potential (0.7 V), but for different DCOOH concentrations (2 – 200 mM) are presented in Fig. 49 a and b, respectively. At 0.7 V, the steady-state CO_{ad} coverages are negligible due to slow formic acid dehydration (CO_{ad} formation) {CHEN04F} and fast CO_{ad} oxidation. Therefore the CO_{ad} intensity-time profiles are not included. The current transients clearly show increasing Faradaic currents with increasing potential (in 100 mM solution, Fig. 48) and with increasing DCOOH concentrations (at a constant potential of 0.7 V, Fig. 49). Furthermore, the current transients all exhibit the same general shape, with a rapid initial increase, a maximum after 2 - 10 s, and a subsequent decay, which at $E \geq 0.5$ V is approximately exponential. The initial current maximum is hardly obvious at low formic acid concentrations and becomes more pronounced at higher concentrations (≥ 50 mM). The rapid initial increase is related to the fast increase in formic acid concentration at the electrode (ca. 3 s for reaching 95% of the final

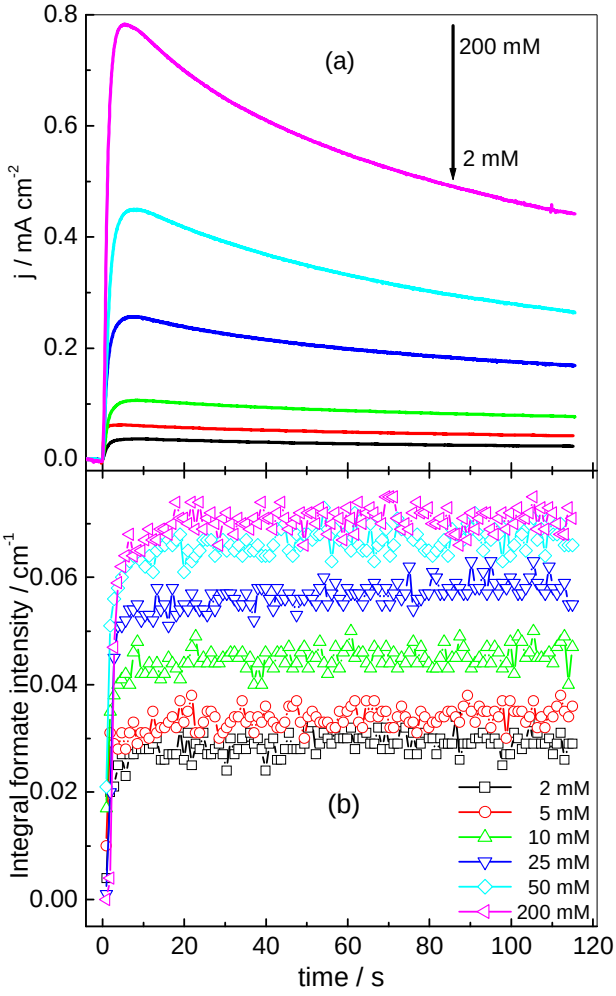

Fig. 49: (a) Chronoamperometric transients and (b) adsorbed formate band intensity transients upon solution exchange from 0.5 M H_2SO_4 to 0.5 M H_2SO_4 + DCOOH with different DCOOH concentrations (2, 5, 10, 25, 50 and 200 mM) at 0.7 V.

concentration), while the subsequent decay is due to deactivation, e.g., by accumulation of CO_{ad} and $DCOO_{ad}$. Since the measurements were performed at constant potential, contributions from double-layer charging to the current maximum can be excluded, in contrast to potential step experiments.

The adsorbed formate intensity-time profiles equally show a rapid increase and a clear maximum 3 - 5 s after the electrolyte exchange for lower potentials (0.1 – 0.5 V), followed by a slow decay of the intensity. At higher potentials (>0.5 V), the formate intensity directly approaches its steady-state value. This is reached within about 5 - 10 s, depending on the concentration. The anodic current starts to decrease, when the formate intensity reaches about 80% of its maximum value. During the transients, the frequency of the adsorbed formates shows no resolvable changes at a given potential, despite of the significant change in intensity

(with time or with concentration). The CO_L intensity-time profiles show negligible intensity at 0.7 V, and increasingly higher steady-state intensities at lower potentials. The lower the potential, down to 0.2 V, the more quickly the final steady-state value is reached. At the same potential, the CO_{ad} frequencies increase with coverage {IWAS97}.

These data clearly demonstrate, that i) at lower potentials, in the range 0.2 – 0.5 V, a (dilute) formate adlayer is quickly built up, either by adsorption of formate anions from the solution or by decomposition of a $HCOOH_{ad}$ precursor to $HCOO_{ad}$ on the surface, and that ii) at longer adsorption times, equivalent to higher CO_{ad} coverages, the weakly adsorbed formate species are increasingly displaced by strongly bound CO_{ad} molecules. The decreasing value of the initial formate intensity maximum at lower potentials (below 0.5 V), is explained by potential related changes in the adsorption-desorption equilibrium of formates at these rather low potentials. Furthermore, rapid CO_{ad} formation at these potentials may also affect formate adsorption.

The rate for CO_{ad} formation ($HCOOH_{ad}$ dehydration) rate on a CO_{ad} free surface at a given potential, which is indicated by the initial increase $(dI/dt)_{t=0}$ of the CO_L intensity at that potential, decreases with increasing potential, from 0.2 to 0.7 V.

At higher potentials, in particular for 0.6 and 0.7 V, the current transients show a pronounced decay after passing through the maximum, losing, e.g., about 50% of the maximum value for 0.7 V in 100 mM solution. In contrast, the adsorbed formate intensity decays very little (0.5 V) or not at all (0.6 and 0.7 V, Fig. 48 and Fig. 49). This observation excludes a linear correlation between adsorbed formate intensity/coverage and Faradaic current at a given potential. In fact, at none of these potentials above 0.4 V, the decay in the Faradaic current with time can be correlated linearly with the temporal evolution of the adsorbed formate intensity. Considering, that under these conditions CO_{ad} oxidation contributes only very little to the total Faradaic current {CHEN04F}{CHEN06F}, these data clearly confirm our previous statement that the formate pathway, via formation and decomposition of the adsorbed formate visible in the IR spectra, can not represent the dominant pathway for formic acid oxidation on a Pt electrode under these conditions. This will be discussed in more detail in section 5.2.3.

Inspection of the concentration dependence of the Faradaic current and the formate band intensities (Fig. 49) furthermore shows that at 0.7 V, there is little difference between the temporal evolution of the adsorbed formate intensity and the Faradaic current at the lowest

concentrations, while they become increasingly different for higher concentrations. For all concentrations investigated, the adsorbed formate intensity quickly reaches its steady-state value, while the Faradaic current passes through an increasingly pronounced initial maximum at concentrations >10 mM. For instance, at 200 mM, the current decays by ca. 40% within 2 min (Fig. 49a). Hence, also these data exhibit a pronounced non-linear relation between Faradaic current and adsorbed formate intensity at constant potential.

Plots of the current values at the maximum of the Faradaic current, 3 - 10 s after the electrolyte exchange, and after 120 s (steady-state conditions), against the steady-state $DCOO_{ad}$ coverage at these points are presented in Fig. 50. Here it is assumed that the formate coverage is proportional to the formate intensity (see above). This plot shows a pronounced non-linear variation of the Faradaic current with $DCOO_{ad}$ coverage, increasing from about 0.018 mA/cm^2 at the lowest concentration (1 mM) to 0.9 mA/cm^2 for the initial current maximum and from 0.01 to 0.49 mA/cm^2 under steady-state conditions. The implications of this non-linear relation on the reaction mechanism will be discussed in section 5.2.3

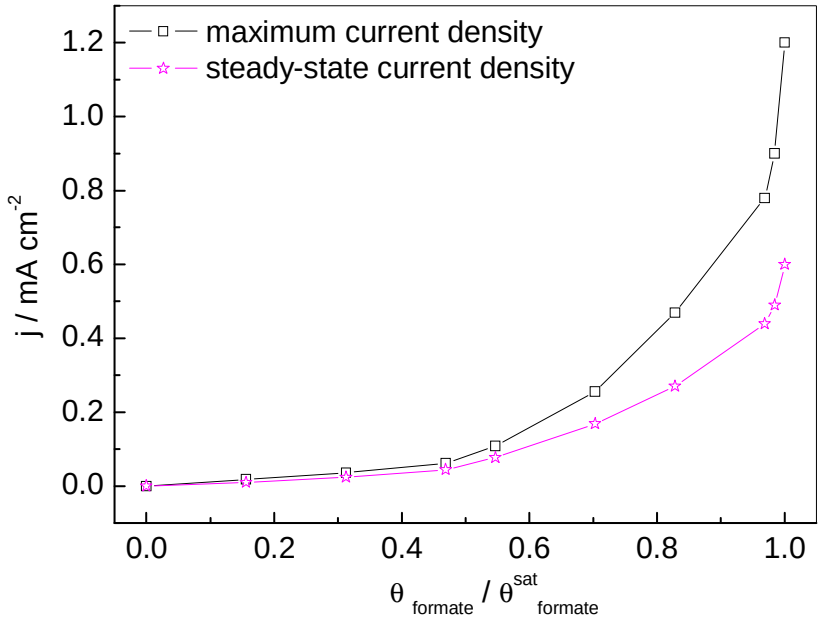

Fig. 50: Variation of the anodic current 3 to 10 s (initial current maximum, □) and 120 s (steady-state conditions, ✯) after electrolyte exchange with $DCOO_{ad}$ coverage (data from Fig. 49).

5.2.2.3 The effect of adsorbed acetate on formic acid oxidation

It is well known that adsorbed acetate cannot be decomposed or electrochemically oxidized to CO2 at room temperature and only acts as spectator species, which blocks surface sites {CORR88A}{IWAS96A}{HEIN04}. Furthermore, it is, similar to adsorbed formate species, adsorbed via two oxygen atoms to the surface {CORR88A}. Therefore, in order to obtain further information on the role of adsorbed formate species, the acetate adsorption/desorption behavior is compared to that of formate adsorption/decomposition/ desorption, performing similar measurements as those described above in solutions containing both HCOOH and CH_3COOH. Representative chronoamperometric transients, recorded at 0.7 V upon changing from supporting electrolyte to solutions with 0.07 M HCOOH + x M CH_3COOH solutions (CH_3COOH concentration x is 0, 0.01, 0.1 and 1 M, respectively), are shown in Fig. 51a; IR spectra, recorded 5 s after the solution exchange are presented in Fig. 51b.

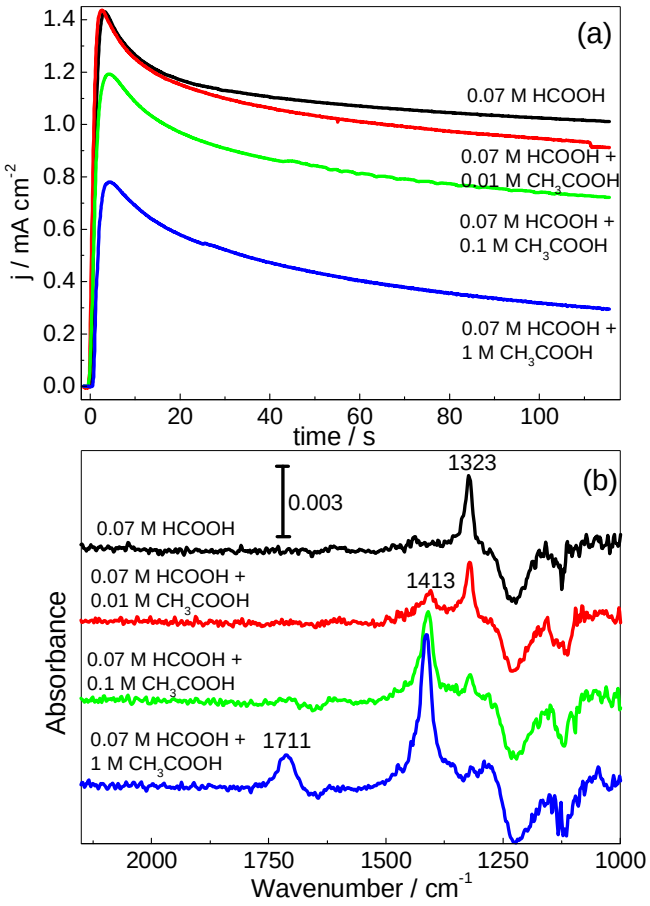

Fig. 51: (a) Chronoamperometric transients and (b) ATR-FTIR spectra recorded ˜5 s after electrolyte exchange (see Fig. 48) on a Pt film electrode at 0.7 V in 70 mM HCOOH + 0.5 M H_2SO_4 solution containing different concentrations of acetic acid (0, 0.01,0.1 and 1 M).

In acetic acid containing solutions, in addition to the features described before, a band with a peak frequency of ca. 1711 cm^{-1} is detected, which, however, only appears at very high acetic acid concentrations (1 M). Since it also does not change its peak frequency with electrode potential, this band is assigned to the C=O stretch mode in acetic acid molecules in the solution close to the interface {CORR88}'{SHAO05}{HEIN10}. Another band with a peak centered at 1410 cm^{-1}, which changes its frequency with potential from 1406 at 0.1 V to about 1413 cm^{-1} at 0.85 V {HEIN10}, is assigned to the symmetric carboxylate stretch mode of bridge-bonded adsorbed acetate (CH_3COO_{ad}). With increasing acetic acid concentration, the acetate band intensity increases, while that of formate decreases. Correspondingly, the anodic current densities decreases, although the formic acid concentration is kept constant (Fig. 51), indicating that competing adsorption of acetate increasingly blocks active surface sites for formic acid oxidation. The bands from both acetate and formate appear immediately after switching to the HCOOH/CH_3COOH containing solutions, and their intensities reach steady-state values within 3-10 s after electrolyte change, similar to our previous observations of the formate band in section 5.2.2.2. Again, the relation between the decay of the anodic current and of the adsorbed formate intensity is far from being linear. Increasing the CH_3COOH concentrations from 0.01 via 0.1 to 1.0 M, at a constant HCOOH concentration of 0.07 M, decreases the anodic current to 90, 75 or 50% (5 s after electrolyte switch) of its value in CH_3COOH free solution and at an identical/constant electrode potential of 0.7 V. In contrast, the formate band intensity decreases to 67, 33 or 20%, of that value, respectively. For a fixed HCOOH/CH_3COOH concentration ratio, the Faradaic current decays with time, while the band intensities for both formate and acetate do not change with time after their initial appearance. Again, formate coverage and formic acid oxidation rate are not linearly correlated. Furthermore, combined cyclic voltammetry (scan rate 10 mV s^{-1}, Fig. 52) and *in situ* IR measurements (intensity-potential profiles, see Fig. 53) were carried out with similar HCOOH/CH_3COOH mixtures as used for the potentiostatic measurements presented above. The CVs show no significant effects of the additional acetic acid except for the pronounced decay in Faradaic current and charge, which is attributed to the blocking of surface sites by adsorbed acetate. In the intensity-potential profiles, a rather similar potential dependence of formate and acetate is found, indicating that the formation and removal of adsorbed formate is dominated by similar effects as that of adsorbed acetate, i.e. mainly by electrostatic forces and the CO_{ad} coverage. In that case, formate decomposition to CO_2, which was postulated to be

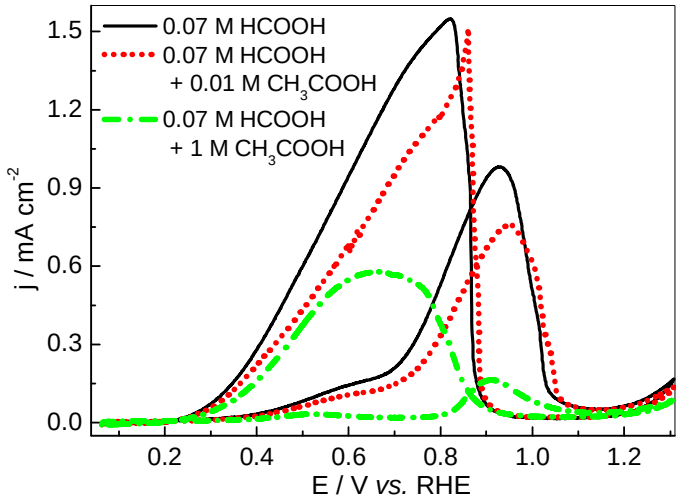

Fig. 52: Cyclic voltammograms of formic acid oxidation at Pt thin film electrode in 70 mM HCOOH + 0.5 M H_2SO_4 with (a) 0, (b) 0.01 and (c) 1 M acetic acid (scan rate: 10 mV s^{-1}).

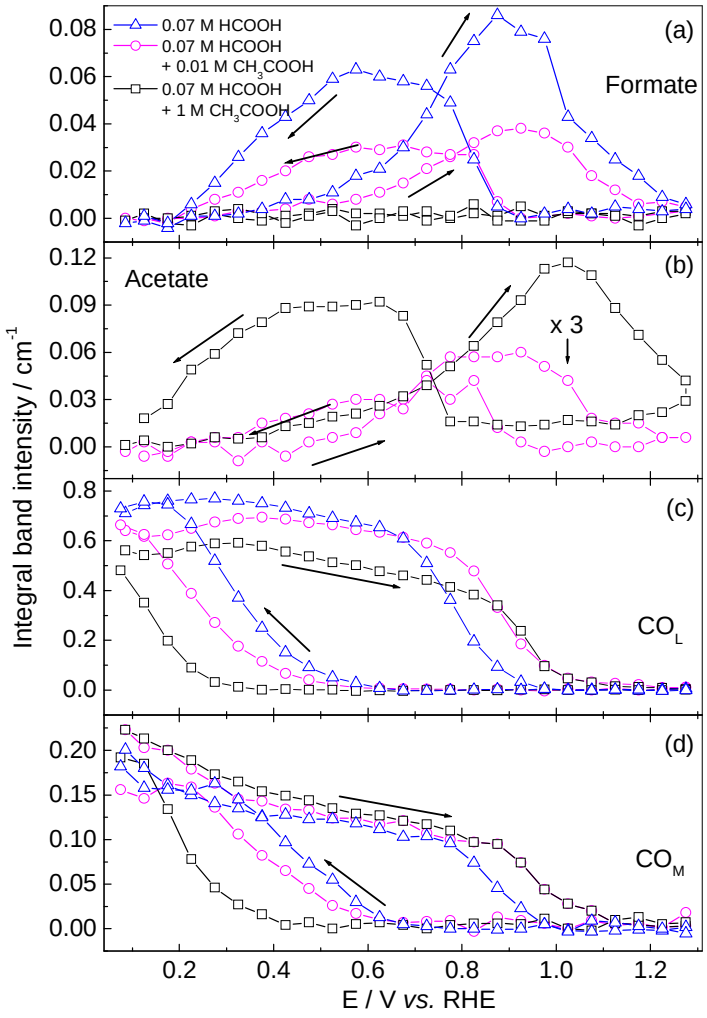

Fig. 53: Dependence of the band intensity of (a) adsorbed formate, (b) adsorbed acetate, (c) CO_L and (d) CO_M on the electrode potential. Experimental conditions as in Fig. 52.

the rate limiting step in the formate pathway by Samjeske et al {SAMJ05}{SAMJ05A}, must be slower than the potential controlled formate adsorption/desorption. In addition, the presence of adsorbed acetate reduces the CO_L intensity at potentials below 0.75 V in the positive-going scan. In the negative-going scan, the onset of CO_{ad} formation is shifted to more cathodic potentials with increasing acetate concentration. These trends, which are opposite to those induced by increasing formic acid concentration (see Fig. 48 and previous section), indicate that adsorbed acetate blocks surface sites for formic acid adsorption and its subsequent dehydration to CO_{ad}. It also hinders CO_{ad} oxidation in the positive-going scan, as evidenced by a positive shift for the decrease of the CO_{ad} signal. Most probably, this occurs by inhibiting OH_{ad} formation.

In total, these potentiodynamic measurements in HCOOH/CH_3COOH mixtures revealed a similar shape of the potential-dependent formate and acetate band intensity profiles as well as a strongly non-linear relationship between formate band intensity and Faradaic current. Furthermore, adsorption and desorption/decomposition of adsorbed formates is fast and occurs on a similar time-scale as observed for other anions such as acetate and (bi-)sulfate. The implications of these findings on the formic acid oxidation mechanism will be discussed in more detail in section 5.2.3.

5.2.2.4 Kinetic isotope effects on formic acid oxidation

Formic acid oxidation is known to exhibit a pronounced kinetic isotope effect for the oxidation of DCOOH compared to the oxidation of HCOOH {TRIP91}, indicating that H-C bond breaking is among the rate determining steps. Assuming that adsorption and desorption of formate species are not affected by C-H bond breaking, while formate oxidation to CO_2 is expected to be influenced by this step (see reaction scheme in Fig. 43), the steady-state formate coverage (in the absence of other adsorbates) contains information on relative rate of formate decomposition to CO_2 compared to formate desorption. Identical formate coverages for HCOOH and DCOOH solution can be expected, if this is mainly determined by the adsorption/desorption equilibrium (formate decomposition to CO_2 is slow relative to formate adsorption/desorption), and different steady-state coverages, if formate decomposition is of comparable (or faster) rate as formate adsorption/desorption. Therefore, potentiostatic electrolyte exchange experiments were performed with HCOOH and DCOOH, respectively, under otherwise identical conditions, following the evolution of the Faradaic current (Fig. 54a) and of the adsorbate layer upon changing from supporting electrolyte to 0.1 M HCOOH

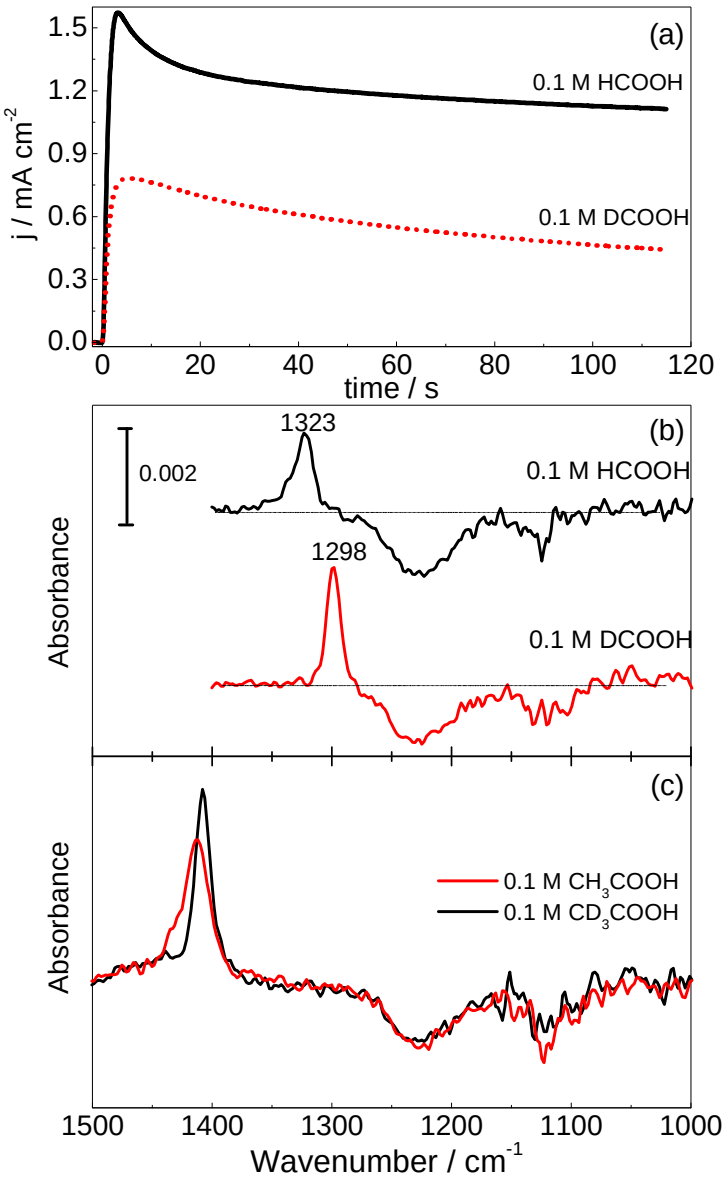

Fig. 54: a) Chronoamperometric transients and IR spectra (b, c) recorded on a Pt film electrode 0.7 V in 0.5 M H_2SO_4 solution containing 0.1 M HCOOH or DCOOH (a, b) or 0.1 M CH_3COOH or 0.1 M CD_3COOH (c), respectively.

or DCOOH containing solution, respectively. (Note: Since this section focuses on the relation between formate coverage and Faradaic current, the influence of the deuteration on the CO_{ad} formation kinetics will only be discussed in section 5.3.) In a first set of measurements, the reaction was investigated at 0.7 V, where CO_{ad} coverages are negligible. The anodic current density from DCOOH is ca. half of that for HCOOH, in good agreement with observations in section 5.2.2.1. Representative ATR-FTIR spectra, taken 5 s after the solution exchange to formic acid containing electrolytes, are shown in Fig. 54b. In both spectra the steady-state coverages of the adsorbed formate species are reached. Dominant feature is the peak at 1298

cm^{-1} related to bridge-bonded $DCOO_{ad}$ (1322 cm^{-1} for $HCOO_{ad}$). The integrated band intensity of the formate band is nearly the same for $DCOO_{ad}$ and $HCOO_{ad}$, though the peak height of $DCOO_{ad}$ is somewhat higher than that of $HCOO_{ad}$. A similar behavior, a narrower and higher peak of the deuterated species than of the unlabeled species at identical integrated band intensities, was observed also for adsorbed acetate (Fig. 54c), where it is certain that the coverage of CD_3COO_{ad} is the same as that of normal acetate under these conditions {CORR88}'{IWAS96A}. Therefore, the formate coverages resulting from DCOOH and HCOOH are likely to be identical, despite of the rather significant differences in the Faradaic currents after 5 s in the two solutions. Since the CO_{ad} coverage at 0.7 V is negligible, this observation clearly proves that the formate coverage is governed by the formate adsorption/desorption equilibrium (adsorption from $HCOO^-$ or by deprotonation of $HCOOH_{ad}$). The formate intensity/coverage is basically not affected by adsorbed formate decomposition to CO_2, supporting the previous conclusions that the latter process is slow compared to formate adsorption/desorption (see preceding section).

5.2.3 Discussion

In the following, the implications of the results presented in the preceding sections on the mechanistic understanding of formic acid oxidation on Pt will be discussed, focusing on the role of the adsorbed, bridge-bonded formate species identified recently in this reaction {KUTS63}{CHEN04F}{SAMJ05}{SAMJ05A}{CHEN06F}. It should be emphasized that in this discussion it is explicitly referred to the formate species identified by its IR signal at 1320 cm^{-1}, which was considered as reaction intermediate in the formate pathway {SAMJ05}. Other, possibly existing stable formate intermediates such as flat-lying formates, which based on recent density functional calculations {HART05A}{HART06}{NEUR08} are unlikely to exist as stable species, but can not be ruled out from the data, would be considered as separate species and not as reaction intermediate in the *formate pathway* discussed here.

As mentioned in the introduction, formic acid oxidation has been traditionally described by the 'dual pathway mechanism' {BREI67A}, which includes the *indirect pathway*, proceeding via formation and oxidation of CO_{ad}, and a *direct pathway*, which leads directly to CO_2. Details and possible reaction intermediates of the *direct pathway*, including adsorbed -COH or CHO {WILH87}, or –COOH {CAPO73}, have been under debate {SUN88}{LAMY91} (see Introduction). More recently, based on highly surface sensitive electrochemical *in situ* IR studies by surface-enhanced IR absorption spectroscopy (SEIRAS) in an ATR configuration

similar as used here, adsorbed bridge-bonded formate ($HCOO_{ad}$) had been identified and proposed as reaction intermediate {GOME97}{SAMJ05}{SAMJ05A}. This proposal was mainly based on i) the close similarity between the IR intensity profiles of the adsorbed formate species and the Faradaic current in cyclovoltammetric measurements, ii) on the fast exchange of $H^{12}COO_{ad}$ against $H^{13}COO_{ad}$ and reverse upon electrolyte exchange, and iii) on the ability to reasonably well model the observed current oscillations by second order kinetics for formate decomposition.

In the proposed 'triple pathway' mechanism (see section 5.1 and Fig. 43), which closely resembles the 'dual pathway' mechanism, adsorbed formate species are an intermediate in one reaction pathways. But in contrast to Samjeske et al. this pathway does not represent the dominant majority reaction pathway under standard reaction conditions {CHEN04F}. Since the contribution of the *indirect pathway* is negligible under these reaction conditions {CHEN04F}{SAMJ05A}{CHEN06F}, we proposed a third pathway (*direct pathway*), which does not involve the bridge-bonded adsorbed formate species detected by IR as reaction intermediate and which contributes most of the current under these reaction conditions. Consequently, the *formate pathway* in this new mechanistic proposal is equivalent to the *direct pathway* in the recent interpretation of the 'dual path' mechanism by Osawa and coworkers {MIKI02}{SAMJ05}{SAMJ05A}. The main difference between these two mechanistic models relates to the role of the adsorbed, bridge-bonded formate species. In the proposal by Osawa and coworkers, this represents the reaction intermediate in the dominant reaction pathway, and formate decomposition is the rate determining step. In the 'triple pathway' mechanism, formate can be considered more as a spectator species, which under most reaction conditions contributes little to the total Faradaic current and acts more as a reaction inhibiting species.

Most simply, these two mechanisms can be distinguished by the correlation between adsorbed formate coverage and Faradaic current. In the simplest case, e.g., for formate decomposition to CO_2 via direct transfer of a proton to a nearby water molecule, one could assume a linear relation between adsorbed formate coverage and reaction rate under identical reaction conditions, in particular at identical reaction potential.

$$r = -\frac{\partial \theta_f}{\partial t} = k\theta_f \qquad (1)$$

where k is the rate constant for formate decomposition and θ_f denotes the adsorbed formate

coverage (first-order kinetics). Samjeské et al. recently proposed a rate equation for this process, which assumes decomposition to $CO_{2,ad}$ and H_{ad} and therefore requires a neighboring empty site for formate decomposition {SAMJ05}{SAMJ05A}:

$$r = -\frac{\partial\theta_f}{\partial t} = k\theta_f\left(1 - 2\theta_f - \theta_{CO}\right) \qquad (2)$$

The third factor describes the number of empty sites, which is identical to the total number of sites minus the sites occupied by adsorbed formates and by adsorbed CO (θ_{CO}). According to the authors the formate species are counted double in that model to account for bridge bonding.

First, the simple first-order rate law given in (1) will be used, and then the implications of the second-order rate law described in (2) on the interpretation of the present data are discussed. It is clear already from the correlation between Faradaic current and adsorbed formate coverage in Fig. 50, which was obtained for different DCOOH concentrations between 1 and 500 mM that the Faradaic current/formate coverage diagram has an increasing slope. It is important to note that for the above mentioned ratio the relevant parameter is the formate coverage and not the formic acid concentration. This means, the measured Faradaic current can be used directly, without correction for transport limited contributions. The latter would have been necessary when evaluating the correlation between formic acid concentration and Faradaic current.

Considering that the contribution of the indirect pathway is negligible (See section 5.1), the contribution of the formate pathway can be determined from the data in Fig. 50, assuming a first-order formate decomposition and a linear relation between formate related IR intensity and formate coverage (see section 5.2.2.2). For this estimate, it is further assumed that at the lowest DCOOH concentrations and hence lowest $DCOO_{ad}$ coverages and at 0.7 V the contribution of the *direct pathway* is negligible and basically all of the Faradaic current is provided by the *formate pathway*. In that case, the increase in Faradaic current provided by the *formate pathway* at higher formate coverages can be calculated from the increase in formate intensity/coverage (note: here a linear correlation between formate intensity and formate coverage is used, following the assumption made in the publication by Samjeske et al. {SAMJ05}). Going from 1 mM to 200 mM solution, this increases by a factor of 6.3, while the increase of the Faradaic current is around a factor of 50 for the maximum current and 48 for the current after 120 s. Consequently, only 15% of the additional current in 200 mM

solution can come from formate decomposition, while 85% must come from the other pathways. Considering again the negligible contribution from the 'indirect' CO_{ad} pathway, this additional current (85%) is attributed to the *direct pathway* described above in Fig. 43. It should be noted that this estimate, which is based on the assumption of negligible contributions from the *indirect pathway* and from the *direct pathway* at 0.7 V at the lowest concentration, provides only a lower limit for the contribution of the *direct pathway* in 0.2 M solution. Lower contributions of the *formate pathway* to the Faradaic current in 2 mM solution, which are easily possible, will lead to a higher contribution of the *direct pathway* in 0.2 M solution.

Now the consequences of the second-order mechanism proposed by Samjeské et al. are considered. In that model, the Faradaic current should increase less fast with increasing formate coverage, because of the decreasing number of neighbored empty sites aside the respective adsorbed formate species, which is described by the factor $(1-2\theta_f-\theta_{CO})$. Although at the reaction conditions of the experiment presented in Fig. 50 the CO_{ad} coverage is negligible, this factor decreases with increasing formate coverage, leading to lower Faradaic currents at similar formate coverage than obtained for first-order kinetics (see also Fig. 5 in ref. {SAMJ05A}). This is in clear contrast to the experimental data, which show a faster than linear increase of the Faradaic current with θ_f, as it would be expected from first-order kinetics. The much faster increase of the Faradaic current with formate coverage than expected from both models for formate decomposition is therefore clear proof that this reaction can not represent the dominant reaction pathway, and that a third reaction path is necessary, which was introduced as *direct pathway* in Fig. 43.

Similar conclusions can also be drawn from the non-linear correlation between formate coverage and Faradaic current during the deactivation phase in the reaction transients in Fig. 48 and Fig. 49, and from the results of the acetate co-adsorption experiments in section 5.2.2.3. In the latter case a strong decrease of the formate coverage upon addition of acetic acid is observed, while the Faradaic current decreased much less, which is equally not compatible with a dominant *formate pathway*.

In total, the combined electrochemical and *in situ* IR spectroscopic kinetic measurements provide clear proof that the *formate pathway*, via formation and decomposition of the IR visible adsorbed formate species, can not be the dominant reaction pathway, and hence necessitates the inclusion of a third reaction pathway as dominant pathway, the *direct pathway* described in Fig. 43.

This result leaves three questions to be answered: i) which processes are responsible for the rapid build-up and disappearance of the formate adlayer in transient measurements, ii) what is the nature of the *direct* (non-formate) *pathway* in Fig. 43, and iii) are adsorbed formates (here: the IR visible bridge-bonded species) reactive at all under these reaction conditions or do they purely act as inert, site blocking spectator species?

To i) Considering the very fast build-up and removal of the formate layer in potential step transients, which is below the time resolution of the experiments, and the close similarity with adsorption/desorption of other anions such as acetate and (bi-)sulfate, we postulate that the formate adlayer exists in a dynamic adsorption-desorption equilibrium with formate anions/formic acid molecules in the bulk electrolyte (see Fig. 41). As demonstrated in different experiments in the preceding sections, e.g., by the similar formate coverages for HCOOH and DCOOH oxidation, adsorption and desorption of formate are very fast compared to other reactions affecting the formate adlayer coverage, in particular the oxidative formate decomposition to CO_2 (section 5.2.2.4). From the equilibrium constant of HCOOH ($K_{eq} = 2\times10^{-4}$ M^{-1} l), the bulk concentration of $HCOO^-$ anions in solution with 0.5 M H_2SO_4 + 0.1 M HCOOH is around 2×10^{-5} M. Due to positive charging of the electrode, the concentration will even be higher in the range of the double-layer. Therefore, the concentration of formate anions in front of the electrode surface is sufficient to account for the adsorption rate. An adsorption-desorption equilibrium with formate anions agrees well also with the similar time-scale observed for adsorption and desorption of other anions such as (bi-)sulfate and acetate (see section 5.2.2.3), and the similar potential dependence of the adsorption characteristics of these three species.

To ii) For the mechanism of the direct pathway in Fig. 43, we tentatively proposed that it may proceed via a weakly adsorbed, molecular $HCOOH_{ad}$ type precursor, which due to its weak adsorption is present only in small steady-state concentrations {CHEN04F}. For the reaction itself one may speculate, that interaction of the Pt surface with formic acid or formate results either in stable formate adsorption or in direct decomposition to CO_2, depending on the orientation of the molecule when approach the electrode surface. As shown in recent density functional calculation on the electrooxidation of methanol {HART05A} and formic acid {HART06} on Pt, interaction of the two oxygen atoms with the Pt results in a stable formate species. Approaching the surface with the carbon-bound H atom of the formic acid molecule, C-H bond breaking, with the transfer of this H atom to the Pt substrate, and simultaneous H transfer of the oxygen bound H atom to the oxygen atom of a nearby water molecule, leads to

direct formation of CO_2. In that case, one would expect an increasing reaction rate for the direct pathway with increasing formic acid concentration and decreasing coverage of reaction inhibiting species such as adsorbed acetate, CO_{ad} and, for this pathway, also adsorbed formate. Indications for a rate-inhibiting role of adsorbed formate species had been discussed in the preceding sections. At present, there are no indications for a reaction intermediate in the *direct pathway*. The reaction may equally well proceed directly, without involving a reaction intermediate, via an activated transition state. But also the possibility of a short-living intermediate, which would be present in very low coverages, can not be excluded. This question can hardly be solved experimentally, and more detailed calculations have to be awaited (see last paragraph of this section).

In response to iii), there is clear experimental evidence that adsorbed formates are present on the surface during formic acid oxidation under steady-state conditions at potentials between 0.4 and 1.0 V {CHEN04F}{MIKI02}{SAMJ05}{SAMJ05A}. In adsorption transients on the clean Pt surface, it appears already at 0.2 V, and is subsequently replaced by more strongly adsorbing CO_{ad}. Results obtained under ultrahigh vacuum (UHV) conditions clearly demonstrate that adsorbed formate species can be thermally decomposed to CO_2 at temperatures around room temperature {COLU92}{COLU93A}. In an electrochemical environment, a similar experiment, testing the stability of a formate adlayer in the absence of formic acid in the electrolyte, is not possible because of the very fast equilibration of the formate adlayer with the electrolyte, via adsorption/desorption of formate. In the presence of formic acid in the electrolyte, on the other hand, it is experimentally very hard to detect a considerably slower decomposition of the formate species to CO_2, which might possibly occur, in parallel to the rapid adsorption-desorption equilibrium. However, Samjeske et al. {SAMJ05} tried to derive the rate for formate decomposition to CO_2 from the fast decay of the $H^{13}COO_{ad}$ band intensity upon an isotope exchange experiment, changing from $H^{13}COOH$ to $H^{12}COOH$ containing solution. From our point of view the decrease in the $H^{13}COO_{ad}$ band intensity represents mainly the rate for adsorbed formate adsorption/desorption and thus the finite time required removing $H^{13}COOH$ from the electrochemical cell, rather than that for the much slower formate oxidation (see sections 5.2.2.2 and 5.2.2.3). In that case, the Faradaic current measured during the exchange mostly results from the reaction in the direct pathway rather than from adsorbed formate oxidation. Also the qualitative correlation between formate coverage and Faradaic current cannot really be accepted as hard proof for the existence of the formate pathway, considering the significant differences between the two features and the

varying other parameters (potential, CO_{ad} coverage etc.). Finally, kinetic isotope effects are also not helpful for distinguishing between direct formic acid oxidation (*direct pathway*) and adsorbed formate decomposition to CO_2 (*formate pathway*), since in both cases C-H bond breaking is likely to be among the rate limiting steps.

Hence, although decomposition of adsorbed formates to CO_2 appears plausible, is supported also by the UHV data cited before and can clearly not be excluded by the present data, unambiguous, direct proof for this is still lacking. Because of the very fast adsorption/desorption of adsorbed formates in dynamic equilibrium with the bulk electrolyte, the direct proof or exclusion of adsorbed formates as reaction intermediate, via time-resolved -measurements, will require a much better time resolution than achieved in the present experiments.

5.2.4 Summary

It was shown for a number of different reaction situations, including formic acid oxidation at different concentrations or formic acid oxidation in the presence of acetate, that at identical potential the Faradaic current increases much faster with increasing formic acid concentration or decreasing acetate concentration than the coverage of bridge-bonded adsorbed formate species. This is neither compatible with a first-order kinetics for formate decomposition (linear relation between formate coverage and Faradaic current) nor with the second-order rate law proposed by Samjeské et al. {SAMJ05A} (slower increase of the Faradaic current with increasing formate coverage than in first order kinetics). This demonstrates that adsorbed formate can not be considered as reaction intermediate in the dominant reaction pathway at medium and higher HCOOH concentrations above 50 mM. Furthermore, it requires the addition of a third dominant pathway (contribution ≥ 85% at 0.7 V, 0.2 M DCOOH, room temperature), which does neither proceed via the bridge-bonded adsorbed formate (*formate pathway*) nor via adsorbed CO (*indirect pathway*), but by direct reaction to CO_2 (*direct pathway*), we had suggested earlier in the ‘triple pathway’ mechanism. Accordingly, adsorbed formates mainly act as reaction blocking spectator species, similar to adsorbed acetate. The very fast adsorption/desorption of formate in electrolyte exchange or potential step experiments, below the time resolution of the experiments, and its similar characteristics compared to acetate or (bi-)sulfate adsorption, indicate that adsorbed formate species are in a fast dynamic adsorption-desorption equilibrium with formate (or formic acid molecules) in the electrolyte. Isotope experiments verify that C-H (C-D) bond breaking is among the rate

determining steps for formic acid oxidation and that under present reaction conditions formate adsorption/desorption is much faster than formate decomposition to CO_2. Finally, the participation of these adsorbed formate species in a minority pathway can not be excluded by the existing data and appears likely, although hard, direct evidence for this pathway is lacking.

Furthermore, in a very recent theoretical study by Neurock et al. {NEUR08} it was indeed stated that the activation of C-H bond of adsorbed formate species is prohibitive and that the computational results indicate that adsorbed formate species are formed on the Pt surface at high potentials but act as spectators. According to the theoretical study, the dominant pathway for CO_2 formation proceeds via the initial activation of the C-H bond. The subsequent activation of the O-H bond of the formed hydroxyl carbonyl is very low {NEUR08}. These statements are in complete agreement with the triple pathway introduced in section 5.1 and the experimental findings in section 5.2, and contradict the proposal by Samjeske et al. {SAMJ05}{SAMJ05A}.

5.3 Kinetic Isotope Effects in Complex Reaction Networks - An in-situ IR Study on Formic Acid Electrooxidation on Pt under controlled Mass Transport Conditions

Y.-X. Chen[1], M. Heinen, Z. Jusys, and R.J. Behm[*]

Institute of Surface Chemistry and Catalysis, Ulm University, D-89069 Ulm, Germany

[1] Pres. address: National Laboratory for Physical Sciences at the Microscale, Department of Chemical Physics, University of Science and Technology of China, Hefei, China

Published in: Chem. Phys. Chem 8, 380-385, **2007**

ABSTRACT

The determination of kinetic isotope effects (KIEs) for different reaction pathways and reaction steps in a complex reaction network, where KIEs may affect the overall reaction in various different ways including dominant and minority pathways or the build-up of a reaction inhibiting adlayer, is demonstrated for formic acid electrooxidation on a Pt film electrode, by quantitative electrochemical *in-situ* IR spectroscopic measurements under controlled mass transport conditions. The ability to separate effects resulting from different contributions, which is not possible using purely electrochemical kinetic measurements, allows conclusions on the nature of the rate limiting steps and their transition state in the individual reaction pathways: The potential-independent value of ~1.9 for the KIE for formic acid dehydration (CO_{ad} formation) in the indirect pathway, and of ~3 for the CO_{ad} coverage normalized KIE in formic acid oxidation to CO_2 (direct pathway) indicate that i) C-H bond breaking is rate limiting in both reaction steps, that ii) the transition states for these reactions are different, and that iii) the configurations of the transition states involve rather strong bonds to the transferred D/H species, either in the initial or in the final state, for the direct pathway and, even more pronounced, for formic acid dehydration (CO_{ad} formation).

5.3.1 Introduction

In contrast to the extensive discussions about the role of adsorbed formate (see section 5.1 and 5.2), there seems to be general agreement, that under most reaction conditions, the *indirect pathway* of formic acid oxidation, i.e. the formation of adsorbed CO and its subsequent oxidation to CO_2, contributes very little to the total reaction process, usually on about one percent or less {CHEN04F}{SAMJ05}{SAMJ05A}{CHEN06F}. Accordingly, CO_{ad} mainly acts as an irreversibly adsorbed catalyst poison rather than as a reaction intermediate. Despite these numerous proposals on the reaction mechanism, however, details on the molecular scale mechanism and on the nature of the transitions states in the different pathways are largely unknown. These are the topics of the present section, which aims at deriving mechanistic information by determining pathway-specific kinetic isotope effects. This objective was approached by simultaneous electrochemical and quantitative *in situ* IR spectroscopic flow-cell experiments, where the build-up of the CO adlayer and the evolution of the Faradaic current was followed upon interaction of a clean, CO_{ad}-free Pt film electrode with deuterated (DCOOH) or unlabelled (HCOOH) formic acid solution at different adsorption potentials under controlled flow conditions.

Previous mechanistic investigations of KIEs in C1 molecule oxidation reactions relied, with few exceptions {JUSY94}{KORT01}, on electrochemical measurements, mostly cyclic voltammetry, comparing the total Faradaic currents during the potential scan {WIEC77}{VANE80}{TRIP91}{HOLZ94}. In those cases, the differences in adlayer composition and coverages during the reaction and possible contributions from different reaction pathways for the different isotopomers render an accurate evaluation of reaction specific KIE factors impossible.

5.3.2 Results

Fig. 55 shows Faradaic current density transients recorded upon changing from pure base electrolyte to 0.02 M formic acid containing solution, at different constant potentials from 0.1 to 0.5 V (a): HCOOH, b): DCOOH). These transients resemble previous data presented in section 5.1 and 5.2, with a steep initial increase and, after passing through a sharp maximum, an initially fast and then increasingly slower decay. Steady-state conditions are reached after 300 s only at lower potentials, while for $E \geq 0.4$ V slow changes in the reaction occur also at

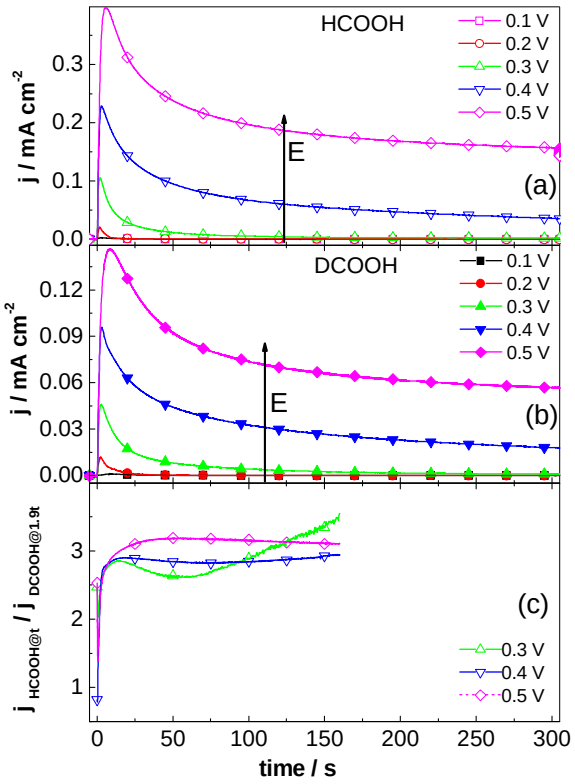

Fig. 55: Current density transients recorded at different constant potentials on a Pt film electrode after changing from pure 0.5 M H_2SO_4 base electrolyte to 0.02 M HCOOH (a) and DCOOH (b) containing solution at different constant potentials (0.1 0.5 V) as indicated in the figure. c) Temporal evolution of the measured effective kinetic isotope effects at different electrode potentials as derived from the Faradaic current density for HCOOH and the time-normalized current density for DCOOH oxidation (time scale for DCOOH oxidation was divided by 1.9) at different potentials (see figure).

later times (see also below). Furthermore, the transients reveal a clear increase in the current densities with electrode potentials for both HCOOH and DCOOH oxidation. At the same potential, current densities from HCOOH are higher than those from DCOOH.

Fig. 56 shows sequences of IR spectra recorded upon the electrolyte exchange (Figs. 47 a, c: HCOOH; Figs. 47 b, d: DCOOH), at 0.1 (Fig. 56a, b) and 0.4 V (Fig. 56c, d). The spectra, which closely resemble similar data in section 5.1 and 5.2, clearly illustrate the formation of adsorbed CO species, on on-top (linear) CO_L (2000 - 2065 cm^{-1}) and on bridge or multifold sites (CO_M, 1790 - 1880 cm^{-1}). The spectra show a clear increase in band intensity and peak frequency of the $CO_{L,M}$ band with time, reflecting an increasing CO_{ad} coverage. At potentials higher than 0.2 V and at relatively low CO_{ad} coverages, a characteristic peak at ~1320 cm^{-1} {MIKI02}{CHEN03} (1295 cm^{-1} for $DCOO_{ad}$ {SAMJ05A}) is observed, which is related to adsorbed, bridge-bonded formates (see also sections 5.1. and 5.2).

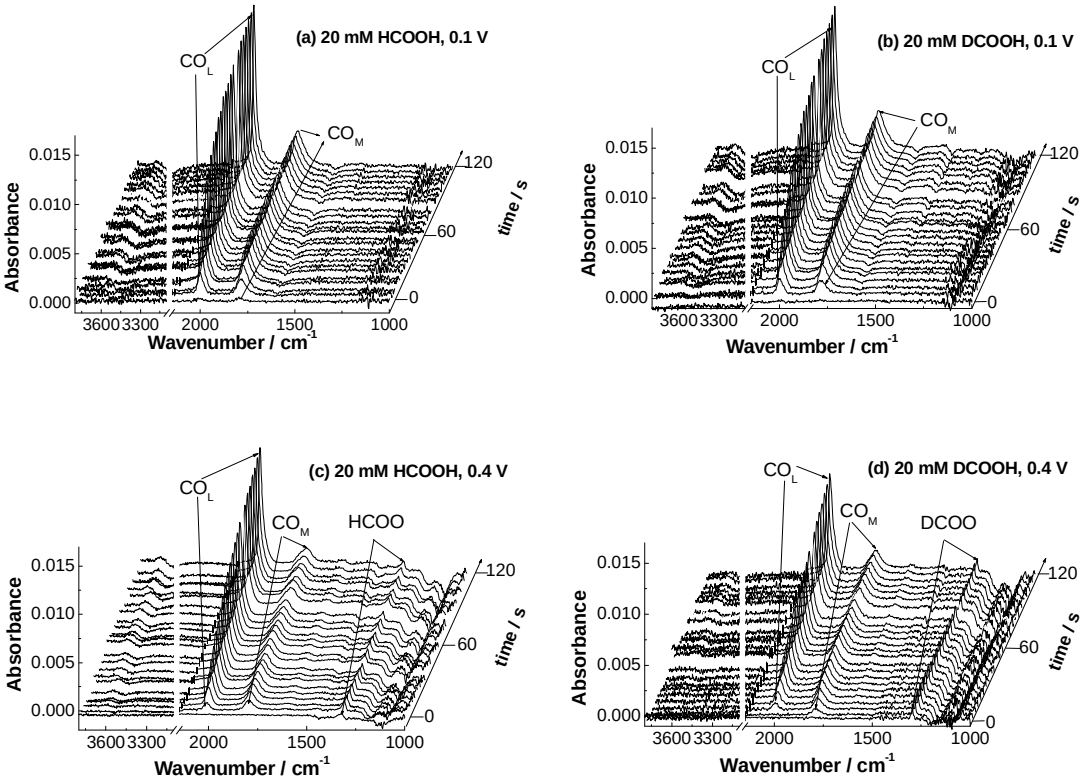

Fig. 56: Sequences of *in situ* IR spectra recorded on a Pt film electrode after changing from pure 0.5 M H_2SO_4 base electrolyte to 0.5 M H_2SO_4 + 0.02 M HCOOH or DCOOH at constant potential ((a, c) HCOOH, (b, d) DCOOH, (a, b) 0.1 V, (c, d,) 0.4 V).

Intensity-time profiles (Fig. 57a: CO_L, Fig. 57c: CO_M), evaluated from the integrated IR intensities of the CO_L and CO_M species during formic acid adsorption/oxidation at different adsorption potentials between 0.1 and 0.5 V as a function of time, show that the build-up of the CO adlayer is rapid in the potential range 0.1 – 0.4 V and significantly slower at 0.5 V. The highest rates for CO_{ad} formation are measured at 0.2 V. Furthermore, the CO_{ad} band intensity/time profiles reveal slower reaction kinetics for CO_{ad} formation during DCOOH adsorption: (--○--) than during HCOOH adsorption (--■--).The potential dependence in the CO_{ad} formation can be described by a steady increase of the formic acid decomposition rate to CO_{ad} with decreasing potential, plus an additional second process, most likely due to increasing surface blocking by adsorbed H-upd atoms, which leads to a reduction in CO_{ad} formation at very cathodic potentials. This interpretation is supported also by the lower CO_{ad} saturation coverage at 0.1 V, which, in agreement with previous observations on Pt film electrodes and on carbon supported catalysts, is only about ⅔ of that at higher potentials (0.2 – 0.4 V) {CHEN04F}{JUSY08}. Possibilities for the physical origin for the decrease of the CO_{ad}

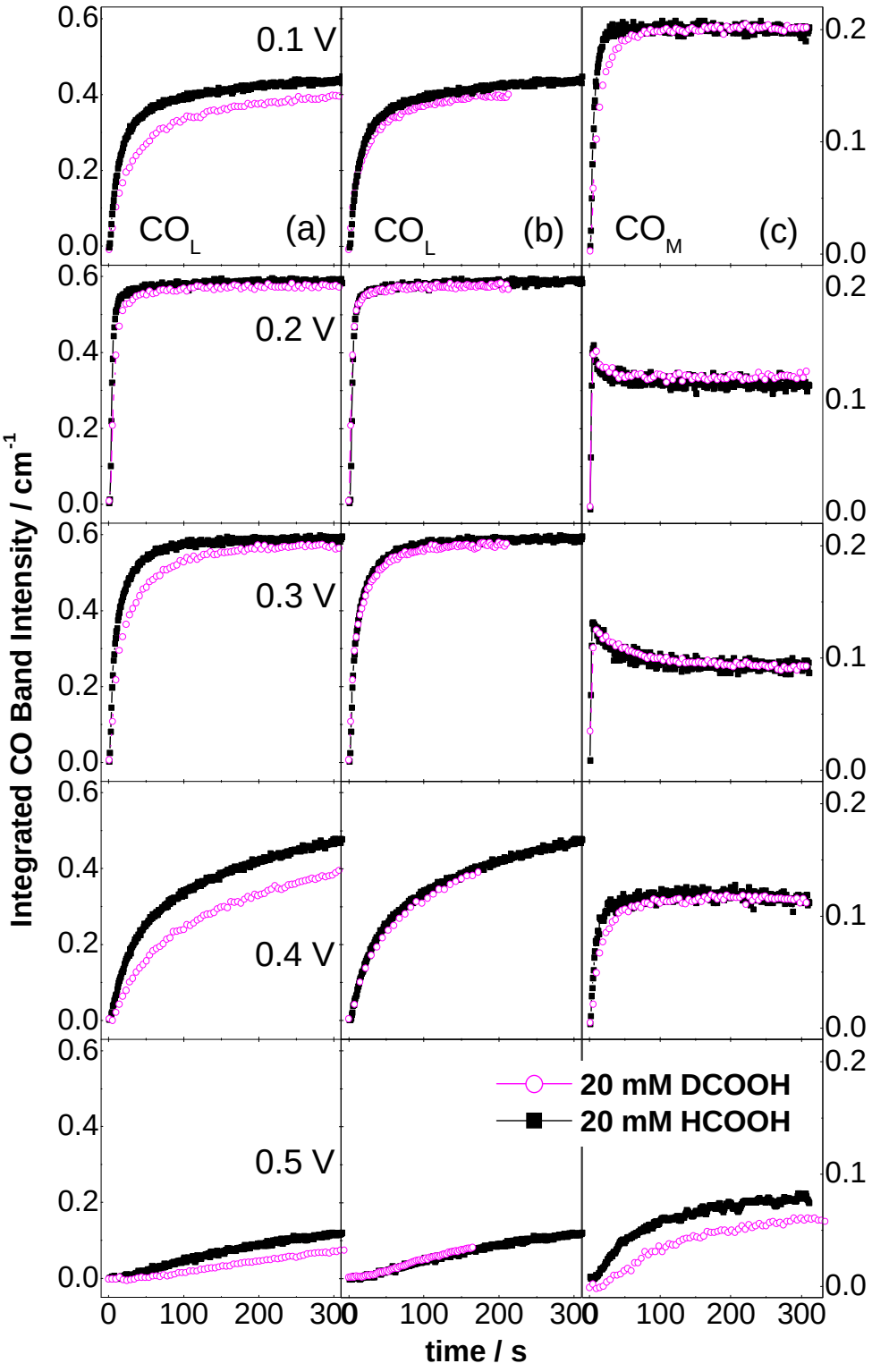

Fig. 57: Integrated CO_L (left column) and CO_M (right column) band intensities on a Pt film electrode as a function of time after changing from 0.5 M H_2SO_4 to 0.5 M H_2SO_4 + 0.02 M HCOOH, --■--) or DCOOH (--○--)) at different constant potentials (0.1 - 0.5 V) as indicated in the figure. Central column: HCOOH and DCOOH based intensities as in the left columns, but with the time scale for DCOOH adsorption divided by 1.9.

formation rate with potential might be i) potential dependent changes in the concentrations or orientation of the likely precursors, of HCOOH molecules and $HCOO^-$ anions, near the interface, or ii) effects related to the polarity of the transition state for CO_{ad} formation.

The difference in the CO_{ad} formation kinetics from HCOOH and DCOOH can be eliminated by plotting the CO_{ad} intensities on a normalized time scale, where the time scale for the deuterated reactant was divided by 1.9 (Fig. 57b) to account for the slower build-up of COad from the deuterated formic acid. The normalized intensity-time profiles are practically identical at all potentials, except at 0.5 V, where differences develop after ca. 500 s adsorption and result in a lower steady-state CO_{ad} coverage for DCOOH than for HCOOH (Fig. 58), which is explained by the onset of CO_{ad} oxidation, as will be discussed in detail later. The observation of a constant factor of 1.9 between the rates for CO_{ad} formation from HCOOH and DCOOH adsorption at potentials between 0.1 and 0.5 V provides clear proof that C-H bond breaking is indeed rate-limiting for CO_{ad} formation by formic acid decomposition. In agreement with the IR spectroscopic data presented in sections 5.1 and 5.2 and recent results of highly surface sensitive IR studies {SAMJ05}{SAMJ05A}, no indication for a precursor for CO_{ad} formation that is bound to the Pt surface via its carbon end is found. This means, either there is no stable adsorbed precursor for CO_{ad} formation other than weakly adsorbed $HCOOH_{ad}$ species, or CO_{ad} is formed by decomposition of $HCOO_{ad}$. The latter appears, however, unlikely, in view of recent theoretical results {HART06}{NEUR08} and considering the opposite potential dependence of the two processes, with enhanced CO_{ad} formation at lower potentials and increased formate adsorption at higher potentials. Finally, if there were an additional electrochemical reaction step occurring on a comparable time scale with C-H bond breaking, this would result in a potential dependence of the measured kinetic isotope effect for CO_{ad} formation. The KIE of 1.9 measured for CO_{ad} formation is significantly smaller than the value of about 7 calculated for gas phase C-H bond breaking at room temperature {MELA80}. The difference in KIEs is explained by the different transition states in both situations: For the gas phase reaction, the KIE was calculated assuming that the transition state is close to complete dissociation, which leaves the difference in zero point energies of the initial states as difference in activation barrier for the two isotopomers. For the electrocatalytic reaction, C-H bond breaking is expected to go along with Pt-H (and presumably Pt-C) bond formation, which leaves a substantial difference in zero point energies in the transition state and thus reduces the difference in the activation energy for this process between the two different isotopomers and consequently also the measured KIE.

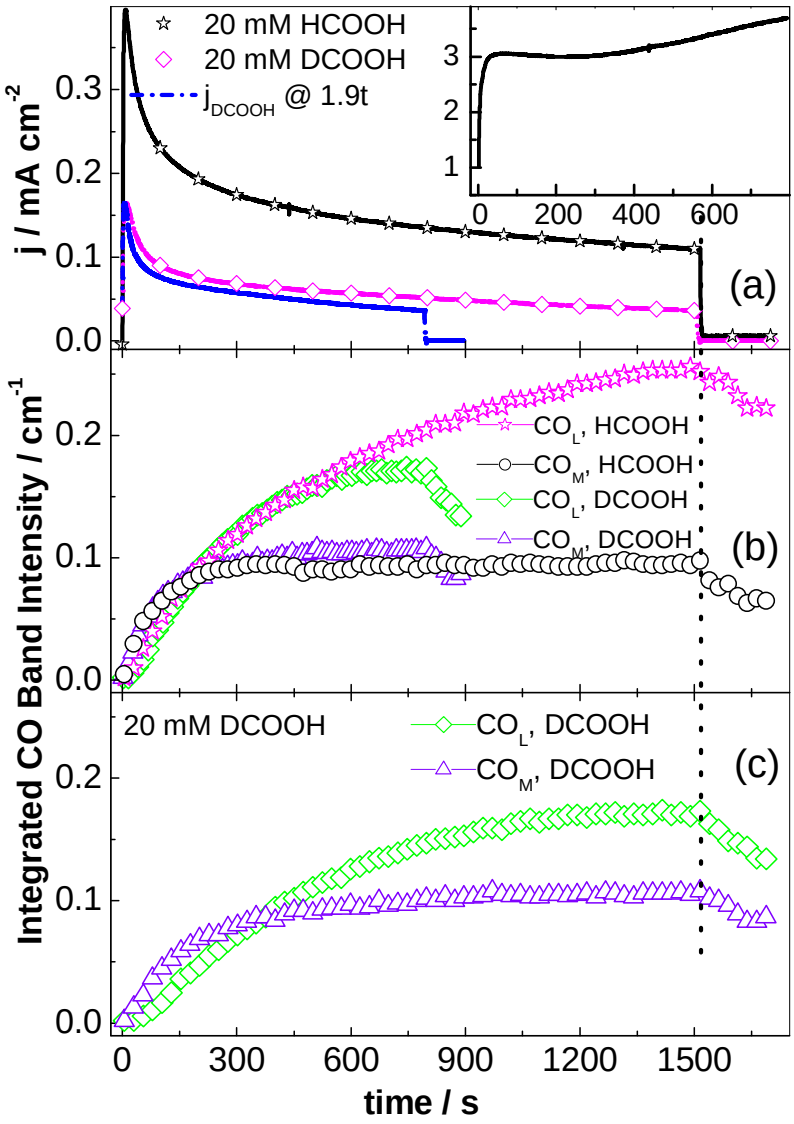

Fig. 58: Faradaic current density (a) and integrated band intensity of $CO_{L,M}$ as a function of time during long-term adsorption of 0.5 M H_2SO_4 + 0.02 M HCOOH (b) or DCOOH (c) on a Pt film electrode at 0.5 V and upon switching back to 0.5 M H_2SO_4 after 25 min, while holding the electrode at 0.5 V. a) --☆--: 20 mM HCOOH solution, --◊--: 20 mM DCOOH solution, -·-·: 20 mM DCOOH solution, but with normalized time scale (divided by 1.9); b) --☆-- and --○--: CO_L and CO_M from 20 mM HCOOH solution, --◊-- and --Δ--: CO_L and CO_M from 20 mM DCOOH solution with normalized time scale (divided by 1.9); c) --◊-- and --Δ--: CO_L and CO_M from 20 mM DCOOH solution. Inset in a): Kinetic isotope effect at 0.5 V as a function of time as derived from the Faradaic current from HCOOH and DCOOH (time-normalized).

At 0.5 V and higher CO_{ad} coverage, an increasing deviation between the CO_{ad} build-up from HCOOH and DCOOH is found at longer adsorption times. Even when correcting for the KIE by using the normalized time scale for DCOOH adsorption, assuming that the KIE for C-H bond breaking and thus the ratio between CO_{ad} formation in unlabeled and deuterated formic acid is the same as at more cathodic potentials, an increasing difference in the measured CO_{ad} formation rates is observed after 500 s (Fig. 58). This is attributed to CO_{ad} oxidation, which at this potential and at higher CO_{ad} coverages reaches rates comparable in magnitude to those for CO_{ad} formation. Since the rate constant for CO_{ad} oxidation is independent of the hydrogen isotope in the original formic acid molecule, at $E \geq 0.5$ V the effective build-up of the CO adlayer from DCOOH should be more strongly affected by simultaneous CO_{ad} oxidation than that from HCOOH because of its lower CO_{ad} formation rate, in good agreement with observations.

The CO_{ad} oxidation rate at steady-state conditions under the present reaction conditions can be derived from the initial decay of the CO_L intensity after changing back to pure supporting electrolyte. Using the IR intensity – CO_{ad} coverage calibration given in section 3.7, this leads to rates of 2.8×10^{-4} molecules site^{-1} s^{-1} (HCOOH) and 2.2×10^{-4} molecules site^{-1} s^{-1} (DCOOH) at steady-state CO_{ad} coverages and a potential of 0.5 V. The difference between the two rates results from the different steady-state CO_{ad} coverages for the two reactants. When comparing with the steady-state formic acid oxidation current (total Faradaic current in Fig. 58a), the CO_{ad} oxidation rate is less than 0.1% of the total formic acid oxidation rate (0.29 molecules site^{-1} s^{-1} (HCOOH) and 0.08 molecules site^{-1} s^{-1} (DCOOH)) under these reaction conditions, confirming the previous statement that under most reaction conditions the *indirect pathway*, via CO_{ad} formation / CO_{ad} oxidation is a minority pathway for formic acid oxidation.

Finally, a normalized KIE for formic acid oxidation is introduced, which describes the KIE in the Faradaic current measured under similar reaction conditions, i.e., at the same potential and at similar adlayer composition and coverage. In the present case, this describes the KIE for the direct oxidation of formic acid to CO_2, which has been shown to be the by far dominant reaction pathway under these conditions (indirect pathway contributes at most by 0.1%) on the bare Pt surface. Its determination requires the additional knowledge of the CO_{ad} coverage during the reaction process, which, in these measurements, can be provided by the IR data. Faradaic currents for similar adlayer composition are obtained by using the normalized time scale for DCOOH oxidation, i.e., by dividing the time scale for DCOOH oxidation by 1.9 in this case. The resulting time-normalized Faradaic currents for DCOOH oxidation are then

used to determine the normalized KIEs at different potentials, by relating them to the HCOOH oxidation current at the same potential. Fig. 55c shows the resulting evolution of the normalized KIEs at potentials between 0.3 and 0.5 V. At potentials <0.3 V, this evaluation is not possible because of the too low currents and even at 0.3 V it becomes problematic at longer reaction times.

For all three potentials, the normalized KIE quickly increases right after switching to formic acid containing solution and reaches practically constant values around three after 10 – 15 s. Hence, also the normalized KIE, measured for formic acid oxidation at comparable CO ad-layer coverages, is higher than 1, indicating that C-H bond breaking is part of the rate limiting step in the direct oxidation of formic acid to CO_2. The initially lower values, obtained within the first 10 s, are attributed to contributions from H-upd and anion displacement in the initial phase after the electrolyte exchange. The practically constant value of the normalized KIE with time, which is equivalent to an increasing CO_{ad} coverage, reveals that the KIE is independent of the CO_{ad} coverage, as long as this is identical for both isotopomers.

In total, also for the dominant direct pathway for formic acid oxidation, C-H bond breaking is rate limiting, but in this case the rate limiting step exhibits a KIE (about 3), which is significantly higher than that for CO_{ad} formation (1.9). Following the above arguments, this points to a transition state with a less stable C-H bond than that for CO_{ad} formation, where isotope effects are less pronounced than in the initial state. In this case, the difference in the activation barriers is larger than for a reaction involving a transitions state with a more strongly bound H atom, which is the case for formic acid dehydration to CO_{ad}.

At potentials $E \geq 0.5$ V and longer adsorption times, where CO_{ad} oxidation becomes significant under present reaction conditions, the situation becomes more complex. Under these conditions, the measured KIE results from both the KIE in the dominant *direct pathway* and the difference in CO_{ad} coverage for both isotopomers, which remains even on a time normalized scale. Here it is again assumed that HCOOH oxidation occurs only on CO_{ad}-free surface sites, which results in the most simple case, in a linear decay of the formic acid oxidation rate with CO_{ad} coverage. Therefore, even after normalization of the adsorption time scale, the measured KIE does not reflect the KIE in the dominant reaction pathway, but represents a convolution of the KIE in the *direct pathway* as majority reaction pathway under these conditions (see section 5.2) and the different CO_{ad} coverages. Because of the lower steady-state CO_{ad} coverage during DCOOH adsorption/oxidation, the measured DCOOH oxidation rate

should be higher than expected for the (higher) CO_{ad} coverage obtained otherwise (in the absence of CO_{ad} oxidation), and therefore the measured, effective KIE obtained under steady-state conditions should be lower than the actual KIE in the rate-limiting step of the dominant pathway under these conditions. The experimental data show, however, an increase of the normalized KIE at longer reaction times. As measured in a number of similar experiments, the increase of the normalized KIE always starts when the CO_{ad} coverages, resulting from the two reactants, on a normalized time scale, begin to deviate. Hence, it is clearly related to the build-up of the CO adlayer.

Finally, it is expected that at even higher potentials ($E \geq 0.75$ V), where the steady-state CO_{ad} coverages are very low {CHEN06F}, surface poisoning should play no significant role, and the measured effective KIE should again be identical to the normalized KIE in the rate limiting step of the dominant reaction pathway.

5.3.3 Summary

Investigating the interaction of formic acid with a Pt film electrode by combined electrochemical and *in situ* IR measurements under controlled transport conditions, it was demonstrated that i) the formation of CO_{ad} during interaction of formic acid with Pt, which is formally described as dehydration of HCOOH, exhibits a potential independent KIE for C-H bond breaking ($k_{C\text{-}H}/k_{C\text{-}D} = 1.9$) in the potential range 0.1 – 0.5 V, and that ii) the KIE in the dominant direct pathway (direct oxidation to CO_2) is significantly higher than that for CO_{ad} formation, reaching values of around 3. These values indicate that in both pathways C-H bond breaking is rate-limiting and that the transition state in the latter pathway exhibits a weaker C-H (or Pt-H) bond than that for CO_{ad} formation. Finally, at more anodic potentials (here 0.5 V), the onset of the competing CO_{ad} oxidation, which is not affected by a KIE related to the HCOOH/DCOOH reactants, results in a change in reaction characteristics and thus in the formic acid oxidation rate, by creating CO adlayers with different steady-state coverages for the two isotopomers, so that the measured effective KIE can no longer be assigned to a single reaction step and its related KIE. The data demonstrate the potential of *in situ* spectro-electrochemical measurements for identifying and quantifying reaction pathway specific KIEs in a complex reaction network as basis for conclusions on the nature of the rate limiting steps and transition states in the individual reaction pathways.

6 ADSORPTION / OXIDATION OF ETHANOL

The measurements on the electrooxidation of ethanol continue the work started during my diploma thesis, in which I studied the adsorption/oxidation of ethanol, acetaldehyde and acetic acid by potentiodynamic and potentiostatic measurements, making use of *in situ* ATR-FTIR spectroscopy under well defined flow conditions {HEIN04}. The new data presented in this thesis will confirm and extend the conclusions drawn in the diploma thesis, by employing the combined ATR-FTIRS/DEMS set-up in combination with the use of isotopically labeled ethanol. Especially for a complex reaction network such as ethanol electrooxidation, the simultaneous detection of adsorbates via IR spectroscopy and the quantification of volatile reaction products are very helpful for the understanding of the reaction kinetics and the reaction mechanism. The use of isotopically labeled ethanol has additional advantages: i) the isotope shift in the IR absorption band of adsorbed species, supports their assignment, ii) carbon labeling of ethanol allows to distinguish between the CO_{ad} formation from the alcohol and methyl group of ethanol and to determine their respective rates separately, and iii) deuterated ethanol shows a kinetic isotope effect in the CO_{ad} formation rate, which allows us to gain deeper insight into the rate limiting step for C-C bond breaking.

The present Chapter is divided into four sections. In section 6.1, I will present and discuss adsorption transients and adsorbate stripping experiments using unlabeled ethanol (CH_3CH_2OH). The IR absorption bands detected upon adsorption/oxidation of ethanol are assigned to specific adsorbed species, and the assignment is supported by selected *in situ* ATR-FTIR spectra for the adsorption of $^{12}CH_3{}^{13}CH_2OH$ and CH_3CD_2OH. From the temporal evolution of the CO adlayer, the CO_{ad} formation rate from ethanol decomposition on a clean Pt surface will be determined for the first time. Furthermore, adsorbed acetyl species are identified as precursor for CO_{ad} formation, and a quantitative relation between the intensity and the coverage of these species is established.

Potentiodynamic, potentiostatic and adsorbate stripping experiments employing carbon labeled ethanol ($^{12}CH_3{}^{13}CH_2OH$) are presented and discussed in section 6.2. The results show that both carbons atoms of ethanol can be converted to CO_{ad} and the potential dependent CO_{ad} formation rates are determined separately. A new mechanistic picture is provided, in which the rather fast CO_{ad} formation rate from the methyl group of ethanol already at 0.4 V, is tentatively explained by the formation of an activated $CH_{x,ad}$ radical and its subsequent reaction with water.

Adsorption transients and potential step experiments recorded upon adsorption/oxidation of CH_3CD_2OH are presented and discussed in section 6.3. The slower CO_{ad} formation rate upon adsorption/oxidation of CH_3CD_2OH, compared to CH_3CH_2OH, is attributed to a kinetic isotope effect in the formation of adsorbed acetyl.

Finally, the results presented and discussed in this Chapter are summarized in a detailed mechanism for the electrocatalytic oxidation of ethanol on a Pt electrode in acidic solution (section 6.4).

6.1 Adsorption/oxidation of ethanol (CH_3CH_2OH)

6.1.1 Introduction

The electrocatalytic oxidation of ethanol has been investigated intensively, since it is on the one hand an interesting model system for the adsorption/oxidation of small organic molecules and on the other hand due to the potential application of ethanol as a liquid fuel in Direct Alcohol Fuel Cell (DAFC) {WANG95}{SCHM96A}{SUN98A}{FUJI99A}{LAMY01A}{DESO02}. Compared to methanol, which is already applied as fuel in commercially available direct methanol fuel cells (DMFC), ethanol stands out due to its higher theoretical energy density and its biocompatibility. However, as already mentioned in section 1.1.3, the overall efficiency of a DAFC depends strongly on the completeness of the conversion of the alcohol to the final reaction product CO_2, which in the case of ethanol oxidation requires the splitting of a rather stable C-C bond. Therefore, the activity and selectivity for CO_2 formation of the state-of-the-art anode electrocatalysts for a direct ethanol fuel cell operating at temperatures, which are compatible with available proton conductive membranes, are still too low {NONA02}. In a recent high temperature/high pressure DEMS study on a Pt/C electrodes it was concluded complete oxidation of ethanol to CO_2 is possible for temperatures of about 140°C ethanol {SUN08}. One possible way for developing better electrocatalysts is to improve their performance by adding additional components to the active metal (binary/ternary catalysts){SHIB89B}{MANN06}{WANG06I}{COLM06D}{DOSA06}{JIAN07}{SIMO07}. Furthermore, a detailed mechanistic under-standing of the adsorption and electrooxidation of ethanol, identifying the rate limiting steps and possible active intermediates occurring in these processes, can support the research for more active and selective electrocatalysts.

The different reaction products of the electrocatalytic ethanol oxidation reaction (EOR) are acetaldehyde, acetic acid and CO_2. The formation of CO_2 was identified and quantified by DEMS {WILL85A}{BITT88}{IWAS94}{GOOT96}{DESO02}{IWAS02B}{WANG04B}{WANG04O}{WANG06I}{COLM06D}{SUN08}. Acetaldehyde and acetic were quantitatively analyzed via high pressure liquid chromatographic (HPLC) {HITM94}{TARN97}{VIGI04}{SIMO07}. The ratio of these products was found to depend on the temperature {WANG95}{ARIC98A}{WANG04B}{RAO07}{ROUS06}{SUN08}, ethanol concentration {WANG95}{LAMY02}{WANG04B} , the reaction potential and the nature of the active metal {FUJI99A}{IANN99}{DESO02}{MEND02}{CAMA05A}{WANG06I}.

IR spectroscopy, mainly in an external reflection configuration, was applied to detect the

reaction products, which are accumulated in the thin electrolyte layer, as well as the adsorbates formed during ethanol adsorption or during its electrooxidation {LEUN88}{HOLZ88}{BITT88}{IWAS89}{LEUN89}{GOOT96}{XIA97C}{IWAS94A} {IWAS94}{SHIN96A}{IWAS02B}{TORR03}{HEIN04}{VIGI04}{SHAO05}. The main reaction products detected by IR spectroscopy were CO_2, with a characteristic signal at 2341 cm^{-1}, and acetic acid with signals at 1712 and 1282 cm^{-1} {TORR03}. Unfortunately, the bands related to acetaldehyde appear in the wavenumber region of acetic acid, which hinders the interpretation of the IR spectra and especially the quantification of the product ratio (acetaldehyde formation: acetic acid formation). The main adsorbate detected by IR spectroscopy is CO_{ad}, adsorbed on on-top, bridge and hollow sites {LEUN88}{HOLZ88}{BITT88}{IWAS89}{LEUN89}{GOOT96}{XIA97C}{IWAS94A} {IWAS94}{SHIN96A}{IWAS02B}{TORR03}{HEIN04}{VIGI04}{SHAO05}. Besides CO_{ad}, adsorbed acetate was detected at potentials positive of 0.6 V with a signal at 1408 cm^{-1} {CORR88A}. Adsorbed acetyl species were proposed as reaction intermediates to form CO_{ad} and $CH_{x,ad}$ species by Iwasita et al. {IWAS94A} and by Hitmi et al. {HITM94}, although these species were not observed spectroscopically. In two recent publications {HEIN04}{SHAO05} highly surface sensitive ATR-FTIR spectroscopy was employed to study the adsorption/oxidation of ethanol on Pt thin film electrodes. In these measurements, an IR absorption band was found at 1635 cm^{-1} during the continuous, potentiodynamic ethanol and acetaldehyde oxidation, which was assigned either to adsorbed acetaldehyde or an adsorbed acetyl species. In potentiostatic adsorption transients the intensity of this band was highest at 0.4 V {HEIN04}, and the identification of the weak band as adsorbed acetaldehyde/acetyl species was so far based only on its frequency, which is typical for a carbonyl bond. However, several open questions concerning the band detected at 1635 cm^{-1} remain:

i) Is the band detected at 1635 cm^{-1} really correlated to a species resulting from the adsorption/oxidation of ethanol? Adsorbed water appears in the same spectral region (1630 cm^{-1}) and the band at 1635 cm^{-1} might also be explained by a change in the water structure due to adsorption/oxidation of ethanol.

ii) What is the structure of the adsorbate, responsible for the absorption band at 1635 cm^{-1}? So far, adsorbed acetyl species or adsorbed acetaldehyde have been discussed in the literature.

iii) What is the role these species in the course of the ethanol oxidation reaction? Adsorbed acetyl species have long been proposed to be the reactive intermediate for CO_{ad} formation, however, no direct experimental prove was provided.

In the present section, these question will be addressed, based on potentiostatic electrolyte exchange experiments from 0.5 M H_2SO_4 to 0.044 M CH_3CH_2OH containing solution and back to 0.5 M H_2SO_4, at 0.2, 0.4 and 0.6 V. Selected *in situ* ATR-FTIR spectra recorded in the initial stages of ethanol adsorption, i.e., 3-4 s after the first electrolyte exchange, are presented in section 6.1.2.1. To support the assignment of the IR absorption band detected at 1635 cm^{-1} to adsorbed acetyl species, similar *in situ* ATR-FTIR spectra recorded upon adsorption of $^{12}CH_3{}^{13}CH_2OH$ and CH_3CD_2OH are also shown.

Due to the experimental limitations of the *in situ* spectroscopic techniques (see section 1.2.2), it has been hardly possible to follow the temporal evolution of the adsorbed species, upon continuous adsorption/oxidation of ethanol. With the present set-up, however, these limitations were resolved, and the kinetics of the developing adlayer are determined quantitatively in section 6.1.2.2. From the initial increase in the CO_L band intensity with time, the CO_{ad} formation rate upon adsorption/oxidation of ethanol on the clean Pt electrode will be determined. Based on a potentiostatic adsorbate stripping experiments at 0.4 V (section 6.1.2.3), adsorbed acetyl species are identified as precursor for CO_{ad} formation and a quantitative relation between the intensity and the coverage of these species is established. Finally, potentiodynamic adsorbate stripping experiments are presented and discussed in section 6.1.2.4, and a summary is provided in section 6.1.3.

6.1.2 Results

6.1.2.1 Ethanol Adsorbate detection and assignment

This section focuses on the detection and assignment of the adsorbates resulting from the adsorption/oxidation of ethanol. As explained in the experimental part (section 3.2), for this purpose electrolyte exchange experiments are the most appropriate method. ATR-FTIR spectra acquired about 4 s after an electrolyte exchange from 0.5 M H_2SO_4 to 0.044 M ethanol (CH_3CH_2OH) containing electrolyte at 0.2, 0.4 and 0.6 V are presented in Fig. 59. The time of 4 s was chosen, since at this time the CO_{ad} coverage is still small and the spectra are not dominated by the IR bands of adsorbed CO. Furthermore, in the initial stages of the ethanol adsorption other adsorbates with a low coverage and/or with a low IR absorption coefficient and/or which are displaced upon continuous ethanol adsorption by the formation of more strongly adsorbing CO, are more clearly visible.

IR absorption bands of linear and multiply bound CO_{ad} are visible at about 2070-2010 cm^{-1} and 1900-1800 cm^{-1}, respectively, for all adsorption potentials. The wavenumber of the bands increases with increasing CO_{ad} coverage and potential (see also section 4.2). A more detailed discussion of the potential dependent kinetics of the CO_{ad} formation will be given in section 6.1.2.2. Adsorbed CO is known to act as strongly adsorbing poison for Pt based catalysts; on the other hand, CO_{ad} is a reactive intermediate to form CO_2, which is the final product in the complete oxidation of ethanol {IWAS89}{LEUN89}{SHIN96A}{GOOT96}{TORR03}{VIGI04}. Fig. 59 also shows absorption bands at 1410 cm^{-1}. In agreement with literature this band is attributed to adsorbed acetate, which is bonded to the surface via the two oxygen atoms {CORR88A}{SHAO05}. A small shoulder at about 1355 cm^{-1} is assigned to the CH_3 deformation of adsorbed acetate {CORR88A}{SHAO05}. Adsorbed acetate is only visible during ethanol adsorption at 0.6, but not at 0.4 and 0.2 V. This is explained by the fact that for acetic acid/acetate formation during ethanol oxidation adsorbed OH species are necessary. The onset of OH_{ad} formation on a Pt electrode was reported to occur at potentials above 0.5 V {CLIM06}. Consequently, the oxidation of ethanol to acetic acid, which can be detected by highly surface sensitive ATR-FTIR spectroscopy via the formation of adsorbed acetate, can only be followed at potentials above 0.5 V. Adsorbed acetate are spectator species in the course of ethanol oxidation and are in a fast ad-sorption/desorption equilibrium with acetic acid {CORR88A}{HEIN04} (see also section 5.2).

An additional feature in Fig. 59 is an absorption band at 1635 cm^{-1}, which is found for ethanol adsorption at 0.4 and 0.6 V, but is hardly visible at 0.2 V. For adsorption at 0.4 V, the band has its absorption maximum at 1635 cm^{-1} with a small shoulder at higher wavenumbers. This shoulder is more pronounced at 0.6 V, resulting in two overlapping peaks centered at 1635 and 1650 cm^{-1}, respectively. A similar absorption band was already observed in potentiodynamic {HEIN04}{SHAO05} and potentiostatic {HEIN04} measurements on the ethanol and acetaldehyde oxidation/adsorption on Pt film electrodes. Based on the finding that the band resulting from acetaldehyde and ethanol adsorption are identical, the band at 1635 cm^{-1} was assigned to an adsorbed acetaldehyde/acetyl species. The different possible structures proposed in both studies are shown in Fig. 60:

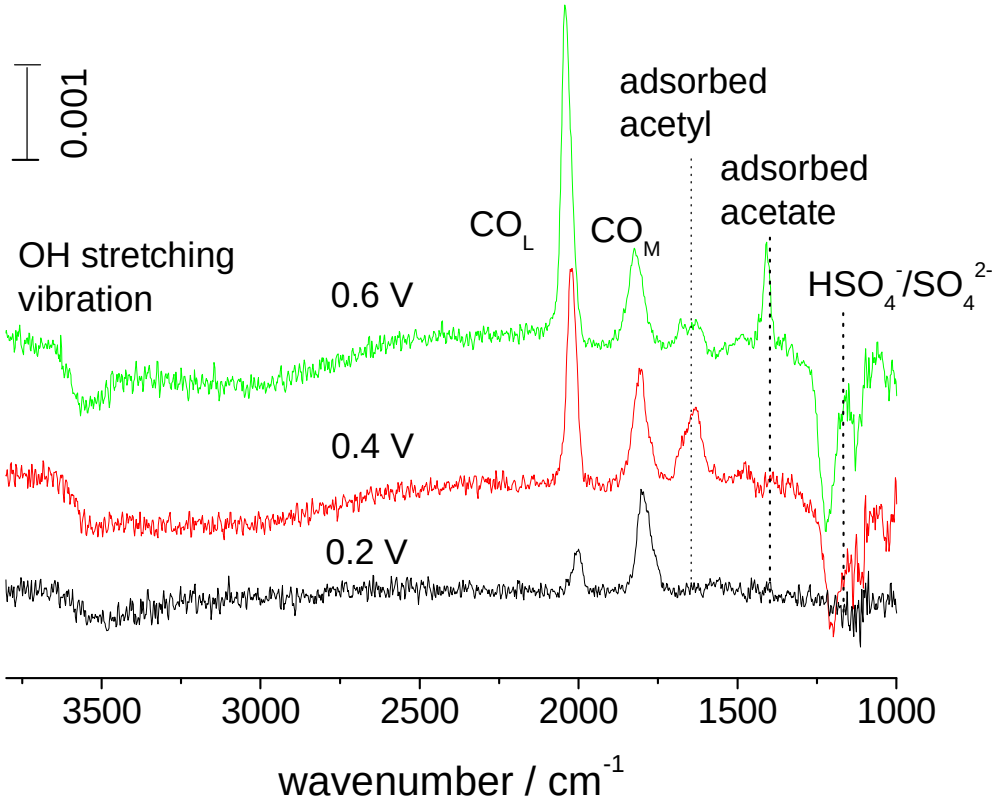

Fig. 59: ATR-FTIR spectra recorded 4 s after the electrolyte exchange from 0.5 M H_2SO_4 to 0.044 M ethanol containing solution at different constant adsorption potentials (see figure). Reference spectrum was recorded at the respective adsorption potential just before the electrolyte exchange.

The species is either adsorbed directly via the α-carbon atom (A) or via the oxygen atom (B) to the Pt surface. According to the IR selection rules, an adsorption configuration with a flat lying C=O bond (C) can be excluded, since a change in the dipole moment perpendicular to the electrode surface is a prerequisite to detect the vibration by means of IR spectroscopy. However, it needs to be mentioned that interfacial water and water co-adsorbed with CO also result in absorption bands at about 1630 cm^{-1}, with CO_{ad} coverage dependent intensity profiles (see spectra presented in sections 4.1 and 4.2).

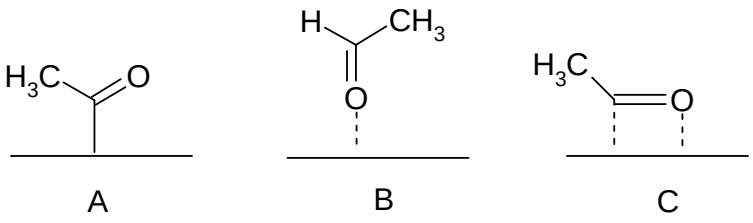

Fig. 60: Possible adsorption configuration of the species assigned to the IR band detected at 1635 cm^{-1}.

To further clarify the assignment of this band and to exclude water to be the origin of the band at 1635 cm^{-1}, we performed potentiostatic measurements using isotopically labeled ethanol ($^{12}CH_3{}^{13}CH_2OH$ and CH_3CD_2OH). Fig. 61 shows the ATR-FTIR spectra acquired about 4 s after an electrolyte exchange from 0.5 M H_2SO_4 to 0.044 M ethanol containing solutions at 0.2, 0.4, and 0.6 V on the Pt thin film electrode, using CH_3CH_2OH (open circles), $CH_3{}^{13}CH_2OH$ (open triangles) and CH_3CD_2OH (filled squares), respectively. Again, the spectra acquired 4 s after the electrolyte exchange are chosen, since at this time the IR spectra are not yet dominated by the growing CO_{ad} bands and thus weakly adsorbed species and species with a low steady-state coverage and/or low absorption coefficient are more clearly resolved.

Compared to the IR spectra measured upon adsorption/oxidation of unlabeled ethanol, the corresponding spectra of $^{12}CH_3{}^{13}CH_2OH$ show in principle the same potential dependent characteristic bands, namely linearly (2040 - 1990 cm^{-1}) and multiply bonded (1850 – 1750 cm^{-1}) CO_{ad} at 0.2, 0.4 and 0.6 V, adsorbed acetate (1384 cm^{-1}, at 0.6 V) and adsorbed acetyl species (1605 cm^{-1}, at 0.4 and 0.6 V). However, due to the isotope labeling, the wavenumbers of the bands are characteristically red-shifted compared to unlabeled ethanol. For instance, the band of adsorbed acetate shifts from 1410 cm^{-1} (CH_3COO_{ad}) to about 1384 cm^{-1} ($CH_3{}^{13}COO_{ad}$), in agreement with the isotope shift of around 25 cm^{-1} reported earlier {SHIN96A}{TORR03}{FARI07}. A slightly smaller red-shift of about 15 cm^{-1} is detected for the shoulder of adsorbed acetate, which is now centered at 1340 cm^{-1} and is tentatively assigned to the CH_3 deformation of adsorbed acetate {SHAO05}. However, so far it is not clear why the intensity of this band increases strongly upon carbon labeling, resulting in two well resolved peaks centered at 1384 and 1340 cm^{-1} at 0.6 V, whereas for the adsorption of unlabeled ethanol or acetic acid the intensity of the shoulder at 1355 cm^{-1} is very small compared to the band at 1410 cm^{-1}.

Most interestingly, a red-shift is also detected for the band at 1635 cm^{-1}, which shifts to about 1605 cm^{-1} when $^{12}CH_3{}^{13}CH_2OH$ is used. This unambiguously confirms that this band is related to the adsorption/oxidation of ethanol and clearly excludes that the band originates from adsorbed water. The CO_L band, especially at 0.6 V, is split in two overlapping peaks with maxima at about 2040 cm^{-1} and at about 1995 cm^{-1}, which can be attributed to $^{12}CO_L$ and $^{13}CO_L$, respectively. Consequently, these measurements allow distinguishing which carbon atom of the ethanol molecule is converted to CO_2 {IWAS94A}{TORR03}{FARI07}. The potential dependent kinetics of the $^{13}CO/^{12}CO$ formation will be discussed in section 6.2.

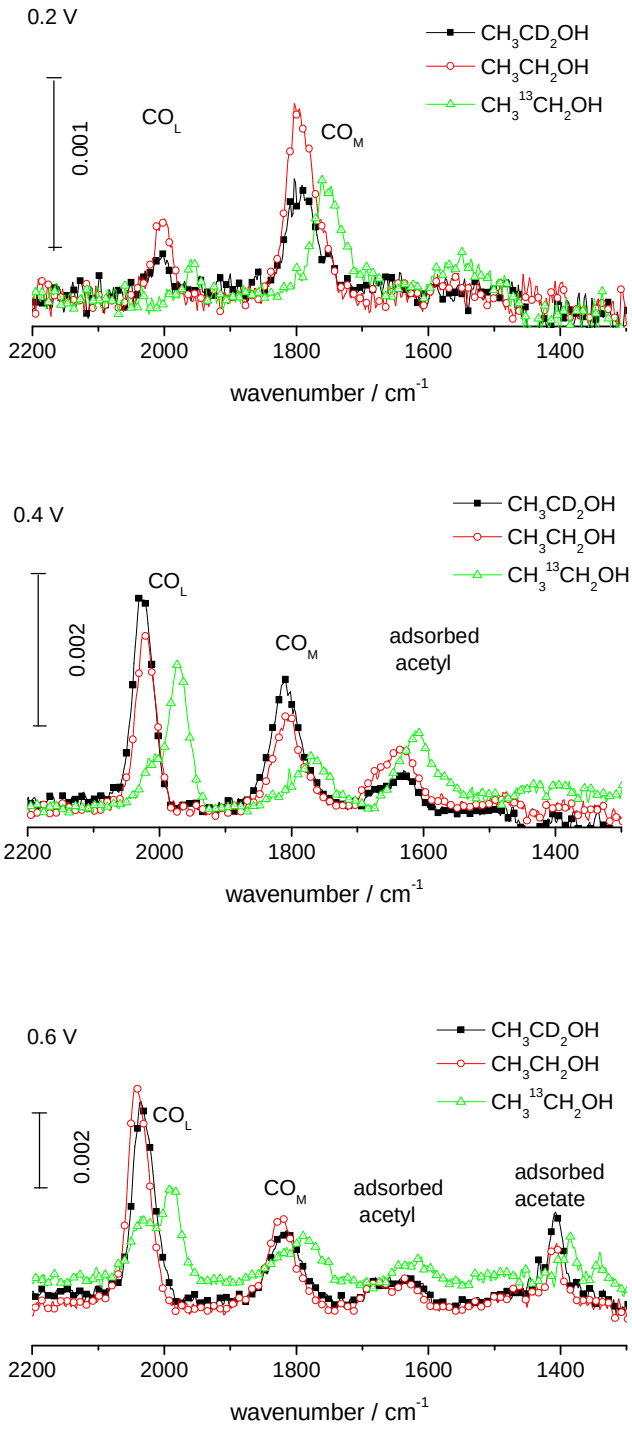

Fig. 61: ATR-FTIR spectra recorded 4 s after the electrolyte exchange from 0.5 M H_2SO_4 to 0.044 M CH_3CH_2OH, CH_3CD_2OH or $CH_3{}^{13}CH_2OH$ containing solution (see figure) at different constant adsorption potentials (see figure). Reference spectra were recorded at the respective adsorption potential in 0.5 M H_2SO_4 just before the electrolyte exchange.

For the adsorption/oxidation of CH_3CD_2OH, linearly (2070 – 2020 cm^{-1}) and multiply bonded (1900 – 1800 cm^{-1}) CO_{ad} are detected at 0.2, 0.4 and 0.6 V. Adsorbed acetate is visible at 1410 cm^{-1} (0.6 V), whereas adsorbed acetyl species are found at 1635 cm^{-1} (0.4 and 0.6 V). In contrast to the red-shift of the IR bands upon using carbon labeled ethanol, no band shifts were detected for the deuterated ethanol. This finding is self-evident for the CO_{ad} bands and adsorbed acetate, since for both adsorbates the deuterium atoms are removed. However, also the wavenumber of the band centered at 1635 cm $^{-1}$ does not change when CH_3CD_2OH is used, instead of CH_3CH_2OH. Comparing this finding with the proposed structures in Fig. 60, the absence of an isotope shift of this band agrees well with the structure of the adsorbed acetyl (Fig. 60 A) rather than with that of an adsorbed acetaldehyde, which still contains a C-D bond (Fig. 60 B). Hollenstein et al. calculated and measured the values for the C=O stretching vibration in gas phase CH_3CHO (1750 cm^{-1}) and CH_3CDO (1734 cm^{-1}). The reported frequencies as measured in the liquid phase were 1714 and 1702 cm^{-1} for CH_3CHO and CH_3CDO, respectively {HOLL71}. From these data, an isotope shift of 12 to 16 cm^{-1} can be deduced if the α-H atom of acetaldehyde is replaced by deuterium. Assuming a similar isotope shift of 12 to 16 cm^{-1} for adsorbed acetaldehyde (Fig. 60 B), this shift significantly exceeds the present spectral resolution of 4 cm^{-1}. Therefore, the absence of an isotope shift of the band detected at 1635 cm^{-1} upon adsorption of CH_3CH_2OH and CH_3CD_2OH, respectively, clearly excludes the adsorption configuration B in Fig. 60, as the origin for this band.

Based on the above discussion, the IR bands detected during the adsorption/oxidation of CH_3CH_2OH and their assignments are summarized in table 5:

Wavenumber / cm^{-1}	Assignment	**Potential / V_{RHE}**
2080 – 2020	Linearly adsorbed CO (CO_L)	0.1 – 0.7
1920 -1750	Multiply adsorbed CO (CO_M)	0.1 – 0.7
1410-1400	O-C-O stretching of adsorbed acetate	0.6 – 0.9
1355	CH_3 in plane bending of adsorbed acetate	0.6 – 0.9
1650-1635	C=O stretching of adsorbed acetyl (structure A in Fig. 60)	0.3 – 0.6

Table 5: Assignment of the bands detected in the IR spectra during adsorption/oxidation of CH_3CH_2OH

6.1.2.2 Potentiostatic adsorption/oxidation of ethanol

After the assignment of the IR bands to specific adsorption configurations in the previous section, I will now focus on the temporal evolution of the adsorbates. Series of *in situ* ATR-FTIR spectra recorded upon an electrolyte exchange from 0.5 M H_2SO_4 to 0.044 M ethanol containing solution (t = 30s) and back to 0.5 M H_2SO_4 (t = 300 s), at 0.2, 0.4 and 0.6 V, respectively, are presented in Fig. 62. At all potentials, linearly (2010 $\rightarrow$ 2055 cm^{-1}) and multiply (1803 $\rightarrow$ 1823 cm^{-1}) adsorbed CO_{ad} are developing on the surface, whereas adsorbed acetyl species (1635 cm^{-1}) are only detected at 0.4 and 0.6 V. An IR band attributed to adsorbed acetate (1410 cm^{-1}) appears in the spectra only at 0.6 V (see previous section).

The development of the integral band intensities of CO_L (Fig. 63b), adsorbed acetyl species (Fig. 63c) and adsorbed acetate (Fig. 63d) as well as the Faradaic currents (Fig. 63a) are plotted versus time in Fig. 63, for adsorption potentials of 0.2 V (filled squares), 0.4 V (open circles) and 0.6 V (filled triangles), respectively. For all adsorption potentials, the Faradaic currents increase steeply upon ethanol exposure, pass through a maximum and decrease with time. The initial maximum as well as the steady-state currents strongly increase with potential, in agreement with earlier reports {WANG04O}{WANG06I} (Note: the Faradaic current was multiplied with a factor of 3 and 10 for adsorption at 0.4 and 0.2 V, respectively). At 0.2 V, the Faradaic current already decreases to zero during ethanol exposure, whereas at 0.4 and 0.6 V, the Faradaic currents only decreases to zero, when the cell is rinsed with ethanol free solution at t = 300 s.

The temporal development of the integral band intensities of CO_L is plotted in Fig. 63b, for ethanol adsorption at 0.2 V (filled squares), 0.4 V (open circles) and 0.6 V (filled triangles), respectively. At 0.2 V, the integral band intensity of CO_L continuously increases upon ethanol exposure. At 0.4 and 0.6 V, the initial increase is much faster compared to 0.2 V, and the integral band intensity of CO_L reaches an essentially constant value with time. The highest final value for the integral band intensity of CO_L is reached at 0.4 V. At 0.6 V, the CO_L intensity decreases, when the cell is rinsed with ethanol free solution at t = 300 s, due to the ongoing oxidation of CO_{ad} to CO_2 without further CO_{ad} formation under the present conditions. The continuous oxidation of CO_{ad} to CO_2 also explains the significantly smaller steady-state CO_L intensity at 0.6 V compared to 0.4 V, where CO_{ad} oxidation is not possible (see section 4.2). The very slow CO_{ad} formation at 0.2 V is attributed to the presence of H_{upd}, which hinders the adsorption/oxidation of ethanol {WANG04O}{WANG06I}.

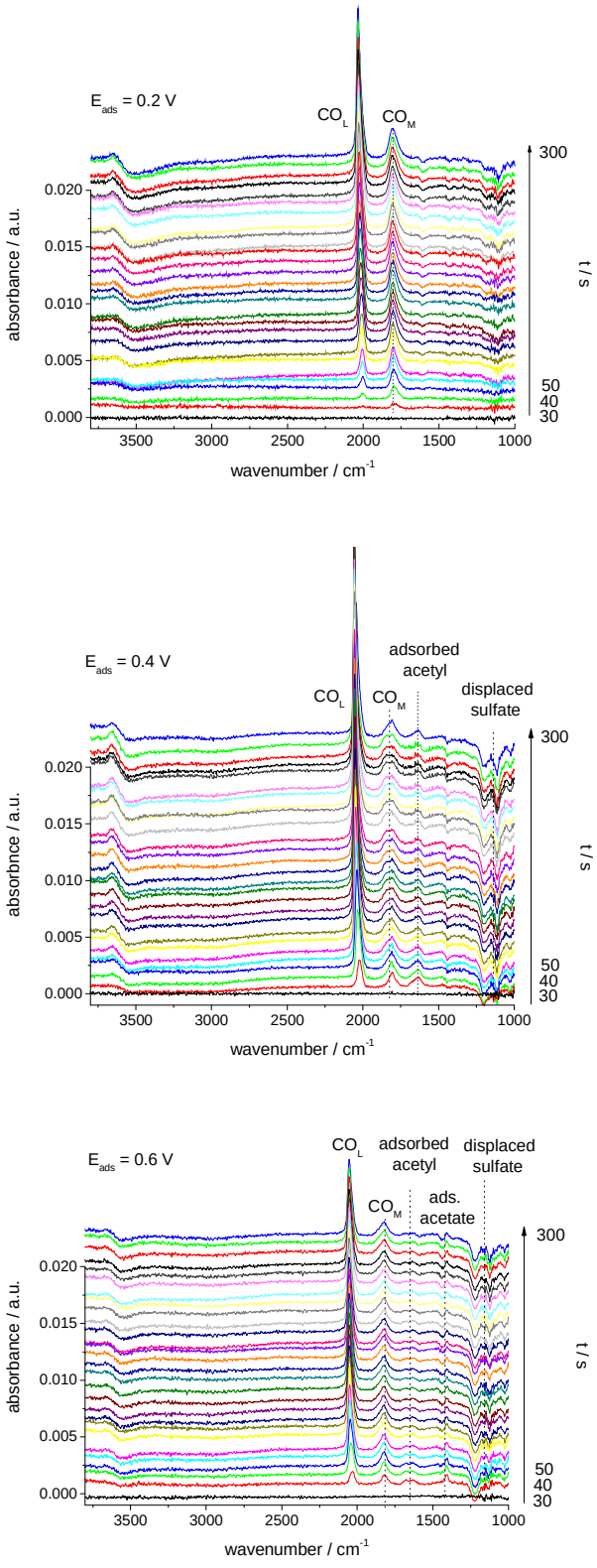

Fig. 62: Temporal evolution of the *in situ* ATR-FTIR spectra recorded during ethanol adsorption on a Pt thin film electrode upon electrolyte exchange from base electrolyte (0.5 M H_2SO_4) to 0.044 M ethanol containing 0.5 M H_2SO_4 (t = 30s) at different potentials, as indicated in the figure. The reference spectra were recorded at the respective adsorption potential in 0.5 M H_2SO_4 just before the electrolyte exchange. Time resolution 0.9 s per spectrum, each 10th spectrum is shown. Spectral resolution: 4 cm^{-1}.

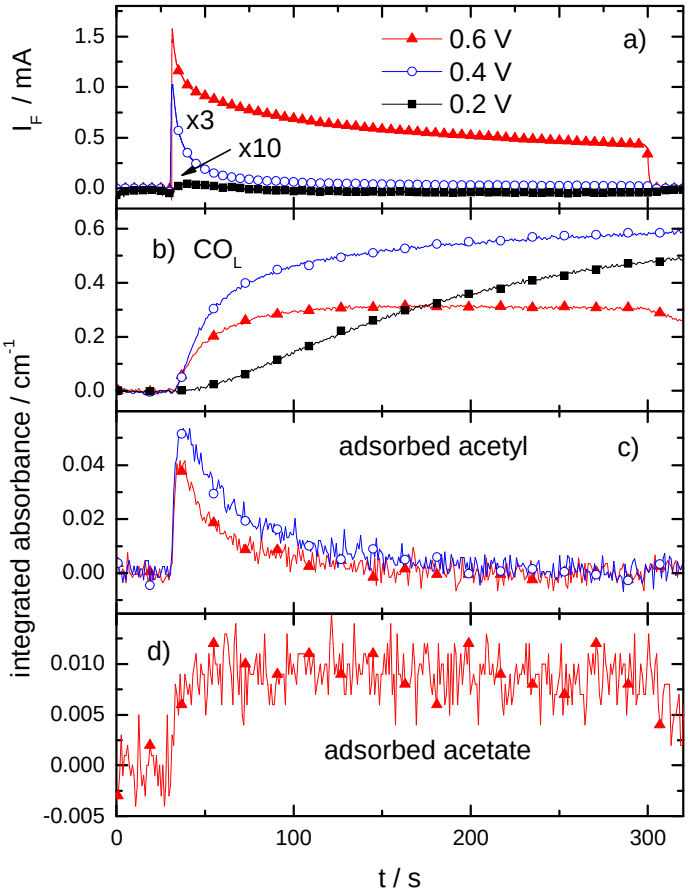

Fig. 63: Temporal evolution of Faradaic current (a), integrated band intensity of adsorbed CO_L (b), adsorbed acetyl detected (c) and adsorbed acetate (d), during an electrolyte exchange from 0.5 M H_2SO_4 to 0.044 M ethanol containing solution at t = 30 s, and back to 0.5 M H_2SO_4 at t = 300 s, at 0.2 V (filled squares), 0.4 V (open circles) and 0.6 V (filled triangles), respectively. Data taken from the *in situ* ATR-FTIR spectra presented in Fig. 62.

For a quantitative analysis of the CO_{ad} coverage development, the integral band intensity of CO_L can be converted into the CO_{ad} coverage via the relations described in section 3.7. The resulting plots of the CO_{ad} coverage versus time are shown in Fig. 64a. The shapes are essentially identical to the shape of the integral band intensity of CO_L described above, and are therefore not describe in detail. Based on this plot, the final CO_{ad} coverages at the end of the adsorption transient (t = 300s) are equal to about 32%, 41% and 34% of a Pt monolayer, for ethanol adsorption at 0.2, 0.4 and 0.6 V, respectively. To support the validity of the CO_{ad} coverage/time plots, these values can be compared to the CO_{ad} coverage as determined from subsequent adsorbate stripping experiments (see section 6.1.2.4). From the latter experiments, CO_{ad} coverages of 27 and 39 % of a saturated Pt ML were derived, after ethanol adsorption at 0.2 and 0.4 V, respectively. These values are in good agreement with those obtained via the conversion of the integral band intensity.

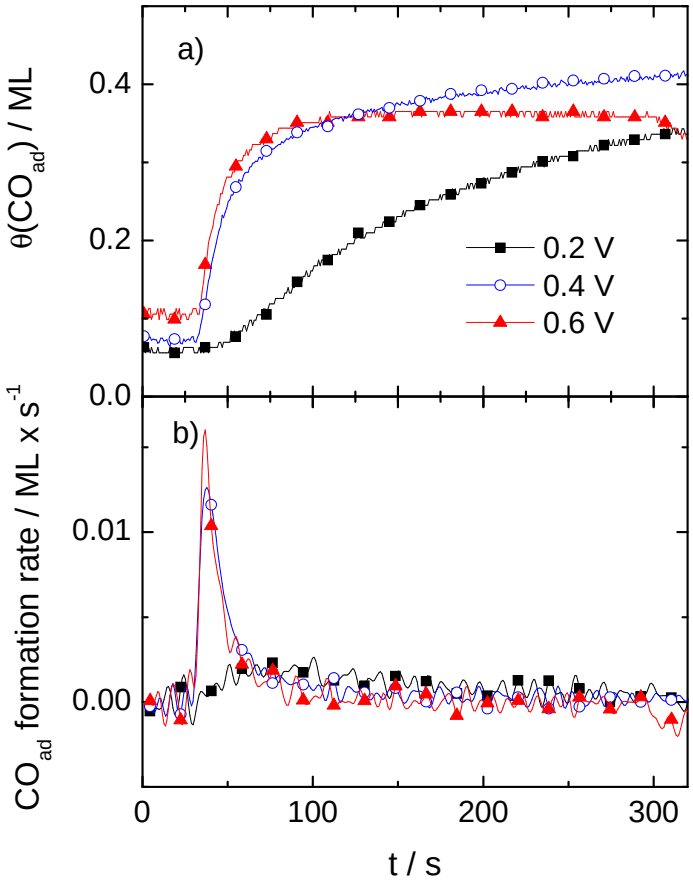

Fig. 64: a) Temporal evolution of CO_{ad} coverage, as determined from the integral band intensity of CO_L in Fig. 65 (details see text); b) derivative of the curves in a). Filled squares: ethanol adsorption for 300 s, open circles ethanol adsorption for 10 s (see also Fig. 65)

At 0.6 V, the continuous oxidation of CO_{ad} to CO_2 hinders a comparison with the adsorbate stripping results. However, it needs to be mentioned that the different polynoms used for this conversion are only valid for specific CO_{ad} coverage regimes (see section 3.7, table 1). At very low CO_{ad} coverages, CO adsorbs mainly in multiply bound configuration, and CO_L is not detectable for CO_{ad} coverages above a critical value, which is strongly potential dependent (see section 4.2.2.3). As a consequence, the CO_{ad} coverages determined via the polynoms at t = 0, are not zero. However, as soon as a CO_L band is detected in the spectra the coverage CO_{ad} coverage determination via the polynom is reliable.

The derivative of the CO_{ad} coverage versus time plot, which is equivalent to the CO_{ad} formation rate, is shown in Fig. 64b as a function of time. At 0.4 and 0.6 V, the CO_{ad} formation rate increases steeply directly after the electrolyte exchange to ethanol containing solution at t = 30 s, passes through a sharp maximum at about t = 38 s and decreases in the following. At 0.2 V, the initial CO_{ad} formation rate as well as the decrease with time is

significantly smaller. The highest values of the CO_{ad} formation rates are about 0.002, 0.013 and 0.015 molecules $\times$ site^{-1} $\times$ s^{-1}, for ethanol adsorption at 0.2, 0.4 and 0.6 V, respectively. To the best of my knowledge, this is the first time that values for the potential dependent CO_{ad} formation rate on a Pt surface for the adsorption/oxidation of ethanol were determined.

The temporal development of the integrated band intensity of adsorbed acetyl species upon ethanol adsorption is obtained by integrating each IR spectrum in Fig. 62, from 1710 to 1500 cm^{-1}. The resulting integral band intensities are plotted versus time in Fig. 63c, for ethanol adsorption at 0.4 V (open circles) and 0.6 V (filled triangles), respectively. At 0.2 V, adsorbed acetyl species can not be detected. As mentioned before also IR features attributed to displaced water (1600 cm^{-1}) and water co-adsorbed with CO (1635 cm^{-1}) appear in this spectral region. However, as described in detail in section 3.8, their contributions are completely removed when integrating from 1710 to 1500 cm^{-1}. The shapes of the intensity of adsorbed acetyl species versus time plots are essentially identical for ethanol adsorption at 0.4 and 0.6 V. They show a steep initial increase and decrease to values below the detection limit during ongoing ethanol adsorption. However, at 0.4 V the integral band intensity of adsorbed acetyl is higher compared to 0.6 V.

Adsorbed acetyl species are produced directly upon admission of ethanol to the clean electrode surface, at the onset of CO_{ad} formation, and the intensity of adsorbed acetyl reaches its maximum already few seconds after changing to ethanol containing solution, whereas the CO_L intensity increases continuously with adsorption/oxidation time (Fig. 65b). The latter observation is compatible with CO_{ad} formation via decomposition of adsorbed acetyl species during ethanol adsorption/oxidation, as it was proposed earlier by Iwasita et al. {IWAS94} and Hitmi et al. {HITM94}. However, since in both studies, adsorbed acetyl species could not be unambiguously identified, the experimental support of their proposal was insufficient for a clear mechanistic decision. Also the present finding that the intensity of adsorbed acetyl species increases very steeply upon ethanol adsorption, accompanied by the onset of CO_{ad} formation is not a definite proof for the decomposition of adsorbed acetyl to CO_{ad}. Also a continuous formation of CO_{ad}, resulting, e.g. directly from ethanol adsorption, could explain the finding of a continuous increase in the CO_{ad} coverage and a decrease in the intensity of adsorbed acetyl, due to displacement by more strongly adsorbed CO (see also formate displacement by CO_{ad} formation upon formic acid adsorption/oxidation as shown in Fig. 48).

Additional strong experimental support for the proposal that adsorbed acetyl species are the precursor for CO_{ad} formation will be given in the next section, based on a potentiostatic adsorbate stripping experiment.

The integral band intensity of adsorbed acetate versus time plot is shown in Fig. 63d, for ethanol adsorption at 0.6 V. At 0.2 and 0.4 V, adsorbed acetate can not be detected. Upon ethanol exposure at 0.6 V, the integral band intensity of adsorbed acetate increases steeply and then decreases slightly with ongoing ethanol adsorption/oxidation. Adsorbed acetate species are known to be in a fast adsorption/desorption equilibrium with acetic acid {CORR88A}{HEIN04}{BERN08}. Consequently, the integral band intensity of adsorbed acetate decreases, when the cell is rinsed with ethanol free solution at t = 300 s. The presence of adsorbed acetate indicates the oxidation of ethanol to acetic acid at 0.6 V, in agreement with earlier reports {HITM94}{IWAS94}{TORR03}.

6.1.2.3 Potentiostatic ethanol adsorbate stripping

As mentioned above, it was proposed earlier by Iwasita et al. {IWAS94A} and Hitmi et al. {HITM94} that adsorbed acetyl species act as precursor for C-C bond splitting and that they decompose to CO_{ad} and $CH_{x,ad}$. Their proposal was based on the observation of an increase in CO_L intensity after reductive ethanol adsorbate stripping experiments in the H_{upd} region, which was explained by an increase in CO_{ad} coverage due to a decomposition of some C2 adsorbates, most likely adsorbed acetyl/acetaldehyde species {IWAS94A}. However, adsorbed acetyl species could not be identified spectroscopically and in none of the above studies, a kinetic analysis of the adlayer development was provided to support this mechanistic proposal.

In the following, I will perform a quantitative, kinetic analysis of the decomposition of adsorbed acetyl species during an ethanol adsorption transient at 0.4 V. If adsorbed acetyl decomposes to CO_{ad} and $CH_{x,ad}$ and it is the only precursor for CO_{ad} formation, then it should be possible to determine the CO_{ad} formation rate upon ethanol adsorption, at any time, via the coverage of adsorbed acetyl species, assuming a linear correlation between acetyl coverage and CO_{ad} formation rate ($r(CO_{ad}) = k \times \theta(\text{acetyl})$). Two different electrolyte exchange experiments at a constant potential of 0.4 V will be presented and compared to each other: in the first experiment the electrolyte, is exchanged from 0.5 M H_2SO_4 to 0.5 M H_2SO_4 + 0.044 M ethanol containing solution at t = 30 s and back to 0.5 M H_2SO_4 at t = 300 s (‘continuous

ethanol adsorption'). The results of this experiment were already discussed in the previous section. The second experiment is identical to the first one, but the second electrolyte exchange, in which the ethanol containing solution was removed via rinsing the cell with ethanol free 0.5 M H_2SO_4, was done already at t = 40 s ('decomposition transient'). These experiments allow following the adsorbate development in the presence (first experiment) and in the absence (second experiment) of ethanol in the electrolyte. The potential of 0.4 V was chosen for the adsorption transient, since at higher potentials CO_{ad} oxidation to CO_2 sets in, whereas at lower potentials $CH_{x,ad}$ starts to desorb as methane (see also next section).

The temporal development of the Faradaic currents (Fig. 65a) as well as the integral band intensities of CO_L (Fig. 65b), adsorbed acetyl species (Fig. 65c) and adsorbed acetate resulting from CH_3CH_2OH adsorption at 0.4 V are plotted versus time in Fig. 65, for 10 s (open circles) and 300 s (filled squares) of ethanol exposure, respectively. In the initial 10 s after the electrolyte exchange to 0.044 M CH_3CH_2OH, the Faradaic currents are identical and both currents increase steeply, pass through a maximum and decay with further adsorption time. The Faradaic current reaches a value of 8 μA at t = 300 s when ethanol is continuously flowing through the cell (Fig. 65a, filled squares). It decreases to zero already at t = 44 s when changing from 0.044 M CH_3CH_2OH containing electrolyte back to ethanol free 0.5 M H_2SO_4 solution at t = 40 s (Fig. 65a, open circles).

The temporal development of the integral band intensities of CO_L is plotted in Fig. 65b, for 300 s of ethanol adsorption (filled squares) and 10 s of ethanol exposure, respectively. When ethanol is adsorbed for 300 s, the CO_L band intensity continuously increases and the CO_{ad} formation rate decreases with increasing CO_{ad} intensity. A final value for the integral band intensity of CO_L of about 0.6 cm^{-1} is reached at t = 300 s. In of the second experiments (changing back from ethanol containing electrolyte to 0.5 M H_2SO_4 at t = 40 s), the CO_L band intensity increases further also in ethanol free 0.5 M H_2SO_4. The final CO_L integral band intensity is about 0.4 cm^{-1} at t = 300 s, which is about 65% of that obtained during the continuous ethanol adsorption. When ethanol was adsorbed for only 10 s (Fig. 65c, open symbols), the intensity of adsorbed acetyl species also increases steeply, passes through a maximum at about t = 38 s and then decreases strongly when the ethanol containing solution is exchanged to 0.5 M H_2SO_4 (dashed vertical line in Fig. 65). The decrease in acetyl intensity is more pronounced compared to that during continuous ethanol adsorption. In both experiments, the intensity of adsorbed acetyl species is essentially zero at the end of the experiment, indicating that these species are completely decomposed under the present experimental conditions.

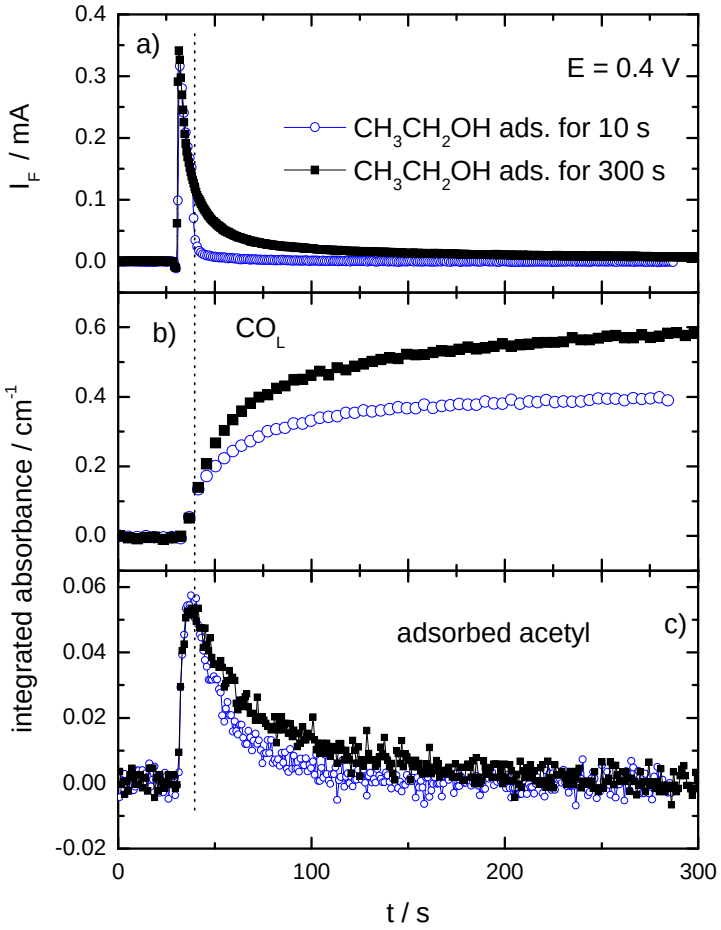

Fig. 65: Temporal evolution of a) Faradaic current, b) integrated band intensity of adsorbed CO_L and c) integrated band intensity of adsorbed acetyl detected (1635 cm^{-1}) during/after ethanol adsorption at 0.4 V for 10 s (open circles) and 300 s (filled squares), respectively. The dashed line indicates the time when the electrolyte was changed back from 0.044 M CH_3CH_2OH containing solution to 0.5 M H_2SO_4 after 10 s of ethanol adsorption.

The data clearly show that the intensity of CO_L increases also in the absence of ethanol in the electrolyte, which can only be explained by the decomposition of a strongly adsorbed intermediate that was formed during the adsorption of ethanol. After removal of the ethanol containing electrolyte at 0.4 V, it is still present on the Pt surface and its decomposition to CO_{ad} results in a further increase of the CO intensity. Adsorbed acetyl species, detected via an IR absorption band at 1635 cm^{-1} can still be seen in the IR spectra recorded after the electrolyte exchange at t = 40 s (Fig. 65c), open circles). Its integral band intensity decreases steeply and qualitatively correlates with the decreasing rate for CO_{ad} formation. This suggests strongly that adsorbed acetyl species are indeed a precursor for the formation of adsorbed CO.

The decrease of the integral band intensity of adsorbed acetyl and the increase in the CO_{ad} coverage upon the decomposition transient can be evaluated quantitatively to further support

the idea of adsorbed acetyl decomposition to $CO_{ad,}$ and to test whether adsorbed acetyl is the main or only precursor for CO_{ad} formation. When the cell is rinsed with ethanol free solution, at t = 40 the formation of adsorbed acetyl species is essentially zero, and the decomposition of one adsorbed acetyl results in the formation of CO_{ad}. Based on measurements with carbon labeled ethanol (section 6.2.2.2), it will be shown that at 0.4 V, also the carbon atom of the methyl group can be converted to CO_{ad} and that the coverage of CO_{ad} from the methyl group is about 80 % of the amount of CO_{ad} molecules formed from the carbon atom of alcohol group. The remaining 20% of the carbon atoms of the methyl group form $CH_{x,ad}$ species that can not be oxidized to CO_{ad} at 0.4 V (see section 6.2.2.3). Based on these findings, it is assumed that the decomposition of one adsorbed acetyl produces 1.8 CO_{ad} molecules.

$$-d\theta(Acetyl) = 1.8 \times d\theta(CO_{ad})$$

The CO_{ad} coverage increase in ethanol free solution, i.e., after the electrolyte exchange to 0.5 M H_2SO_4 at t = 40 s, is shown in Fig. 66 as filled squares. In this plot, the CO_{ad} coverage at t = 40 s, which is about 14% of a Pt monolayer, was defined as zero. The open circles in Fig. 66, correspond to the acetyl intensity (Fig. 65c), which was i) set to zero at t = 40 s (real value 0.045 cm^{-1}) and ii) multiplied with a scaling factor S of -2.6. This value was chosen so that the modified intensity of adsorbed acetyl and the CO_{ad} coverage curve meet at t = 280 s.

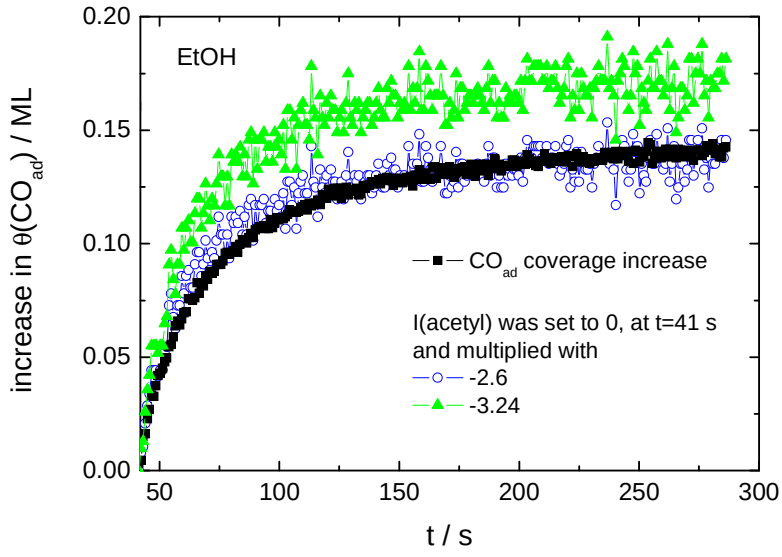

Fig. 66: Filled squares: CO_{ad} coverage increase in ethanol free solution taken from Fig. 65a. The CO_{ad} coverage was set to zero to 0, when the cell was rinsed with ethanol free solution at t = 40 s. The integral band intensity of adsorbed acetyl was set to zero at t = 40s and multiplied with a factor of -2.6 (open circles) or -3.24 (filled triangles), respectively. Explanations for the choice of the different values are given in the text.

After this scaling, the temporal evolutions of the integral band intensity of adsorbed acetyl and of the CO_{ad} coverage are essentially identical. Only from t = 75-150 s, the mirrored acetyl intensity is slightly higher, which indicates that besides the decomposition of adsorbed acetyl an additional source for CO_{ad} formation is present on the surface (see below). The good correlation between the decrease of the intensity of adsorbed acetyl with the CO_{ad} coverage increase in ethanol free solution provides a strong experimental support that adsorbed acetyl species are the dominating source for CO_{ad} formation. As evident from Fig. 66, the CO_{ad} coverage increase in ethanol free solution is about 14.5 %. Taking into account that in total one acetyl decomposes to about 1.8 CO_{ad} molecules and that all CO_{ad} molecules are formed by decomposition of adsorbed acetyl, this corresponds to a coverage of adsorbed acetyl of about 8% of a Pt monolayer. From this, a relation between the coverage of adsorbed acetyl and its integral band intensity can be established. The integral band intensity of adsorbed acetyl at t = 40 s was equivalent to 0.045 cm^{-1}, which according to the above discussion corresponds to a coverage of about 0.08 ML. Assuming a linear relation between the intensity of adsorbed acetyl and its coverage, the coverage of adsorbed acetyl at any time can now be obtained by multiplying its integral band intensity with a proportionality constant P, which is equivalent to 0.08 ML/0.045 cm^{-1} or 1.8 ML/cm^{-1}.

Based on the above discussion, the scaling factor S used in Fig. 66, should be equivalent to the number CO_{ad} molecules formed per acetyl molecule, i.e., 1.8, multiplied with the proportionality constant P, which was determined to be 1.8 ML/cm^{-1}. The resulting value of 3.24, however, is significantly larger than the value of 2.6, which was used as scaling factor in Fig. 66, and does not fit reasonably well the decrease in intensity of adsorbed acetyl to the CO_{ad} coverage increase (Fig. 66, filled triangles). In stead, the CO_{ad} coverage increase derived from the decomposition of adsorbed acetyl would be significantly too large. Assuming that at 0.4 V, one acetyl molecules decomposes to 1.8 CO_{ad} molecules (see section 6.2.2.3), this indicates that the proportionality constant P was overestimated.

A different way to obtain a value for P is to divide the best scaling factor, i.e., (-2.6), by the number of molecules formed per acetyl molecules (1.8), which gives a value for P of about 1.4 ML/cm^{-1}. Employing this value for P, the coverage of adsorbed acetyl at t =40 s corresponds to 0.045 $cm^{-1}\times$ 1.4 ML/cm^{-1}, which is equivalent to 6.3 % of a Pt ML. Taking into account that the decomposition of one acetyl results in the formation of 1.8 CO_{ad} molecules, the predicted CO_{ad} coverage increase is 11.3 % of a ML, which is slightly smaller compared to that of 14.5 % obtained from the increase in the CO_L band intensity.

In section 6.2.2.4, where I will discuss similar measurements with $^{12}CH_3{}^{13}CH_2OH$, it is postulated that upon decomposition of adsorbed acetyl species adsorbed CH_xO_{ad} species are formed, which can be further converted to CO_{ad}. For the present ethanol decomposition transient (Fig. 65), this finding implies that when the cell was rinsed at t=40 s with ethanol free solution, besides CO_{ad} and adsorbed acetyl these CH_xO_{ad} species are present on the Pt surface. Their further oxidation to CO_{ad} contributes to the overall CO_{ad} coverage increase of 0.145 ML. Taking this into account, it is reasonable that the CO_{ad} coverage increase as determined solely from the decomposition of adsorbed acetyl species (11.3% of a ML) is smaller compared to the measured CO_{ad} coverage increase (14.5% of a ML). Throughout the present work, a proportionality constant P of 1.4 ML/cm^{-1} will be used to convert the integrated band intensity of adsorbed acetyl species into the acetyl coverage. This enables to predict the CO_{ad} coverage increase in the absence of ethanol in the solution due to decomposition of adsorbed acetyl species in number of different experiments (see sections 6.2.2.3 and 6.3.2.3).

In the following, I will try to derive a kinetic model that gives a quantitative correlation between the CO_{ad} formation rate and the integral band intensity of adsorbed acetyl. In the simplest case, it is assumed that the decomposition of adsorbed acetyl species follows first order kinetics, and the decomposition of one adsorbed acetyl results in the instantaneous formation of 1.8 CO_{ad} molecules and 0.2 molecules of $CH_{x,ad}$ species (see section 6.2.2.3 for experimental support of this assumptions). In this model, the CO_{ad} formation rate ($r(CO_{ad})$, is equal to the coverage of adsorbed acetyl species ($\theta(A)$), multiplied with a reaction constant k:

$$r(CO_{ad}) = \frac{d[\theta(CO_{ad})]}{dt} = k \times \theta(A) \times 1.8$$

Based on the adsorption transients presented in Fig. 65, I will test whether the model describes the kinetics of acetyl decomposition in an appropriate way, by determining $\theta(CO_{ad})/dt$ in two ways: i) from the derivative of the CO_{ad} coverage versus time plot and ii) via the integral band intensity of adsorbed acetyl species, applying the above equation.

The resulting plots for the CO_{ad} formation rate versus time upon adsorption of ethanol for 10 s (a) and 300 s (b), as calculated via the intensity of adsorbed acetyl species is shown in Fig. 67, using a value of 0.1 s^{-1} for k (open circles). This value for k was chosen to fit the highest CO_{ad} formation rate calculated via the integral band intensity of adsorbed acetyl, to the highest CO_{ad} formation rate determined from the integral band intensity of CO_L. The latter is replotted

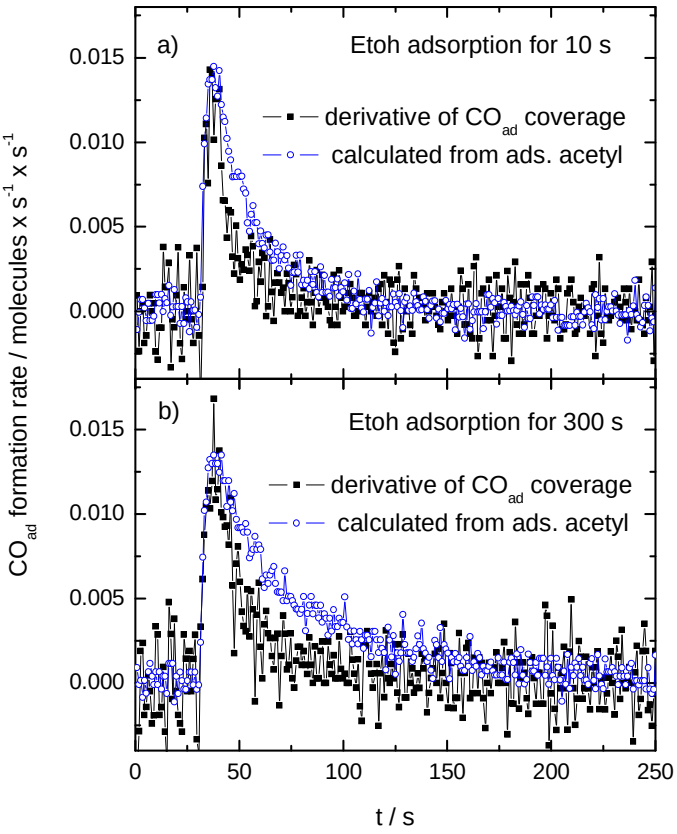

Fig. 67: Plot of $d\theta(CO_{ad})/dt$ versus time upon adsorption of ethanol for 10 s (a) and 300 s (b). Filled squares: $d\theta(CO_{ad})/dt$ determined via the derivative of the CO_{ad} coverage versus time plot (see Fig. 65); open circles: coverage of adsorbed acetyl taken from Fig. 65 multiplied with 0.1 s^{-1}.

in Fig. 67 as filled squares. I will start the discussion with the results from the experiment, in which ethanol was adsorbed for 10 s, followed by an additional electrolyte exchange to ethanol free solution at t = 40 s (Fig. 67 a). In this experiment, both curves, i.e., the $d\theta(CO_{ad})/dt$ curve calculated via the intensity of adsorbed acetyl species and the $d\theta(CO_{ad})/dt$ curve determined from the integral band intensity of CO_L have the same initial slope and pass through a maximum of 0.014 molecules $\times$ $site^{-1}$ $\times$ s^{-1} at about t = 38 s. At longer times (t = 50 – 100s), however, the CO_{ad} formation rate determined from the integral band intensity of CO_L decreases to a value of about zero at t = 120 s, whereas the CO_{ad} formation rate derived from the integral band intensity of adsorbed acetyl species decreases significantly slower. These trends are essentially identical for the experiment, in which ethanol was adsorbed for 300 s (Fig. 67 b), but here the deviations between both curves at longer times are more pronounced, compared to the first experiment (ethanol adsorption for 10 s, see (Fig. 67a).

These non-linear deviations, which are especially obvious in Fig. 67b, can not be removed by a simple adjustment of k, indicating that either the mechanistic proposal that adsorbed acetyl species decompose to CO_{ad} and $CH_{x,ad}$, or the applied kinetic model is oversimplified.

However, the finding that the deviations between the CO_{ad} formation rate determined from the CO_{ad} coverage versus time plot and via the integral band intensity of adsorbed acetyl are small, suggests that the mechanistic proposal is reasonable, but that there is one contribution missing, which becomes increasingly important with increasing time and increasing coverage of adsorbed species. This can be accounted for in the kinetic model by including the number of free sites N, available for the decomposition of adsorbed acetyl. In this model, the CO_{ad} formation rate from decomposition of adsorbed acetyl species is determined by the following equation:

$$\frac{d[\theta(CO_{ad})]}{dt} = k \times \theta(A) \times 1.8 \times (1 - \sum \theta(adsorbed\ species))^n$$

where n represents the reaction order with respect to the number of neighboring empty surface sites, required for the decomposition of adsorbed acetyl. Based on the present data, however, a precise determination of the number of free Pt sites, i.e., $1-\Sigma\theta$(adsorbed species), is hardly possible, due to following uncertainties: i) It is not precisely known how many sites are blocked by a single CO molecule or one adsorbed acetyl and how do these values change with coverage, and ii) the coverage of adsorbed species, which are not detected by IR spectroscopy, e.g., adsorbed $CH_{x,ad}$ is unknown. To apply the above equation in a simplified picture, it is assumed that i) one CO molecule as well as one adsorbed acetyl block two Pt sites, respectively, independent of the overall adsorbate coverage and that ii) no other adsorbates are present on the surface in significant amounts. With these assumptions, the number of free Pt sites (N) can be estimated via:

$$N = 1 - 2 \times \theta(CO_{ad}) - 2 \times \theta(adsorbed\ \ acetyl)$$

and the following relation between CO_{ad} formation rate and the coverage of adsorbed acetyl species is obtained:

$$\frac{d[\theta(CO_{ad})]}{dt} = k \times \theta(A) \times 1.8 \times (1 - 2 \times \theta(CO_{ad}) - 2 \times \theta(A))^n$$

This equation includes two parameters, i.e., the reaction constant k and the reaction order n. The resulting plots for $d\theta(CO_{ad})/dt$ versus time upon adsorption of ethanol for 10 s (a) and

300 s (b), as calculated via the above equation for first and second order in the number of free Pt sites, are displayed as open circles in the left and right panel of Fig. 68, respectively. The values for the rate constant k were chosen to fit the highest CO_{ad} formation rate calculated via the integral band intensity of adsorbed acetyl to the CO_{ad} formation rate determined from the integral band intensity of CO_L, which is included in Fig. 68 for comparison (filled squares). A rate constant k of 0.13 s^{-1} for the decomposition of adsorbed acetyl species is obtained for n = 1. The value for k increases up to about 0.22 s^{-1}, when using n = 2.

Applying the above kinetic model, in both experiments, ethanol adsorption for 10 and 300 s, respectively, the CO_{ad} formation rate determined via the integral band intensity of adsorbed acetyl matches quite well the CO_{ad} formation rate calculated via the derivative of the CO_{ad} coverage versus time plot, for both values of n. The finding that the CO_{ad} formation rate can be related with the integral band intensity of adsorbed acetyl provides strong experimental support for the decomposition of adsorbed acetyl species to CO_{ad} during ethanol adsorption at 0.4 V and quantitatively confirms the previous proposal that adsorbed acetyl species represent

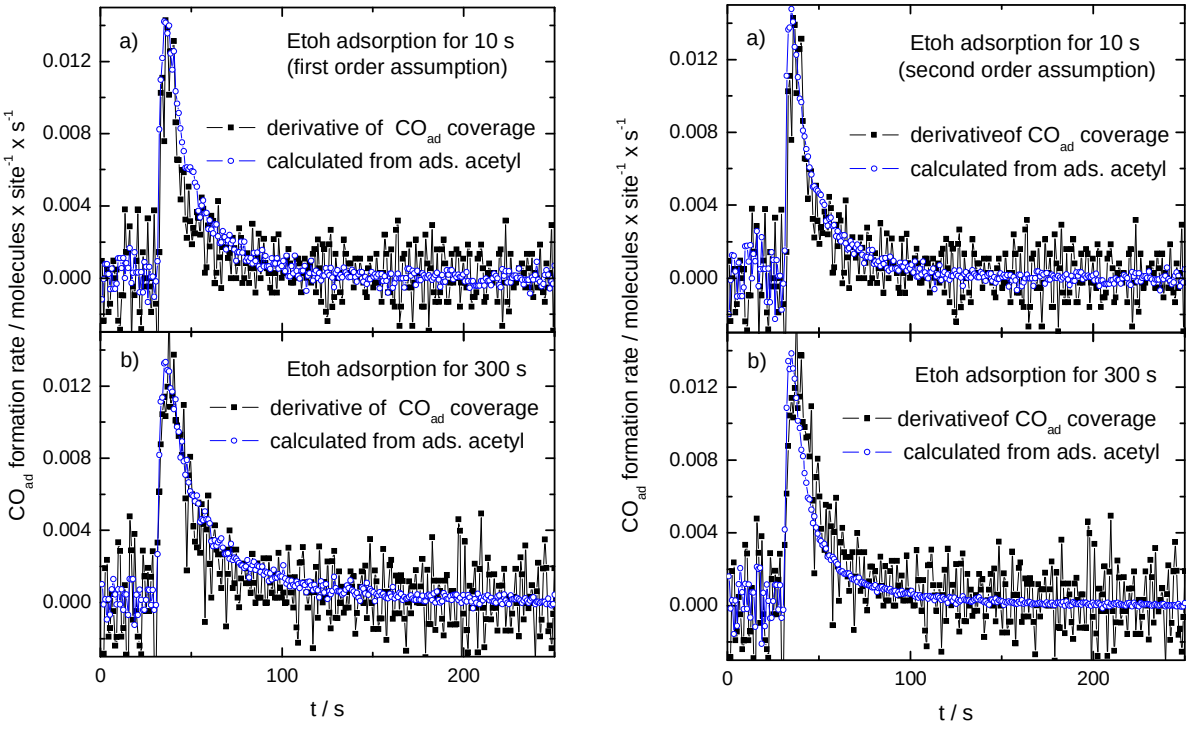

Fig. 68: Plot of the CO_{ad} formation rate versus time upon adsorption of ethanol for 10 s (a) and 300 s (b), using the assumption of first (left panel) and second (right panel) order in the number of free Pt sites. Filled squares: CO_{ad} formation rate determined via the derivative of the integral band intensity of CO_L (see Fig. 65); open circles: CO_{ad} formation rate calculated via the intensity of adsorbed acetyl taken from Fig. 65; k = 0.13 s^{-1} for the left panel and 0.22 s^{-1} for the right panel. (details see text).

the precursor for CO_{ad} formation {HITM94}{IWAS94}. Furthermore, it can now be concluded that the formation of CO_{ad} via decomposition of adsorbed acetyl species is the main pathway for the C-C bond splitting upon ethanol adsorption under the present experimental conditions. However, since both, first order or second order plots, fit reasonably well with the CO_{ad} formation rate, it is not possible to extract the number of free Pt sites required for the decomposition of adsorbed acetyl based on the present data. Thus, the rate constant for the decomposition of adsorbed acetyl can not be determined very precisely. Nevertheless, without any modification, the above kinetic equation allows to predict the CO_{ad} formation rate upon adsorption/oxidation of CH_3CD_2OH, from the integral band intensity of adsorbed acetyl species, as discussed in section 6.3.2.3.

6.1.2.4 Potentiodynamic ethanol adsorbate stripping experiments

After the ethanol adsorption transients at 0.2 and 0.4 V, which were presented in the preceding sections, the cell was rinsed for additional 5 min. with 0.5 M H_2SO_4. Subsequently, potentiodynamic adsorbate stripping experiments were performed to gain further information on the adlayer composition as well as a quantitative value for the CO_{ad} coverage, resulting on the Pt film electrode after ethanol adsorption. In Fig. 69, the CV (a) and the integrated absorbencies of linearly (b) and multiply (c) bonded CO_{ad} and the mass spectrometric current response for m/z = 44 are shown, during the potentiodynamic adsorbate stripping experiments following the adsorption of ethanol at for 300 s at 0.2 V (filled squares) and at 0.4 V (open circles) and for ethanol adsorption for 10 s at 0.4 V (filled triangles). Besides CO_L and CO_M, no other adsorbates were detected via *in situ* ATR-FTIR spectroscopy during the potentiodynamic adsorbate stripping experiments. Since CO_{ad} can be oxidized at 0.6 V, the CO_{ad} coverage already decreases during the rinsing procedure at that potential (see also Fig. 63b). Therefore, only the stripping experiments following the adsorption transients up to 0.4 V are presented. The potentiodynamic adsorbate stripping experiments were started in the positive-going direction after ethanol adsorption at 0.2 V, and first in the negative-going direction after ethanol adsorption at 0.4 V.

I will start the discussion with of the adsorbate stripping experiment, in which the potential was directly scanned positively to 1.3 V after ethanol adsorption at 0.2 V and rinsing the cell with ethanol-free solution (Fig. 69, filled squares). The Faradaic current increases at about 0.55 V and passes through a maximum at 0.7 V. At potentials positive of 0.8 V, OH_{ad}/Pt oxide formation sets in. In addition, as evidenced by small amounts of CO_2 formation (Fig. 69d),

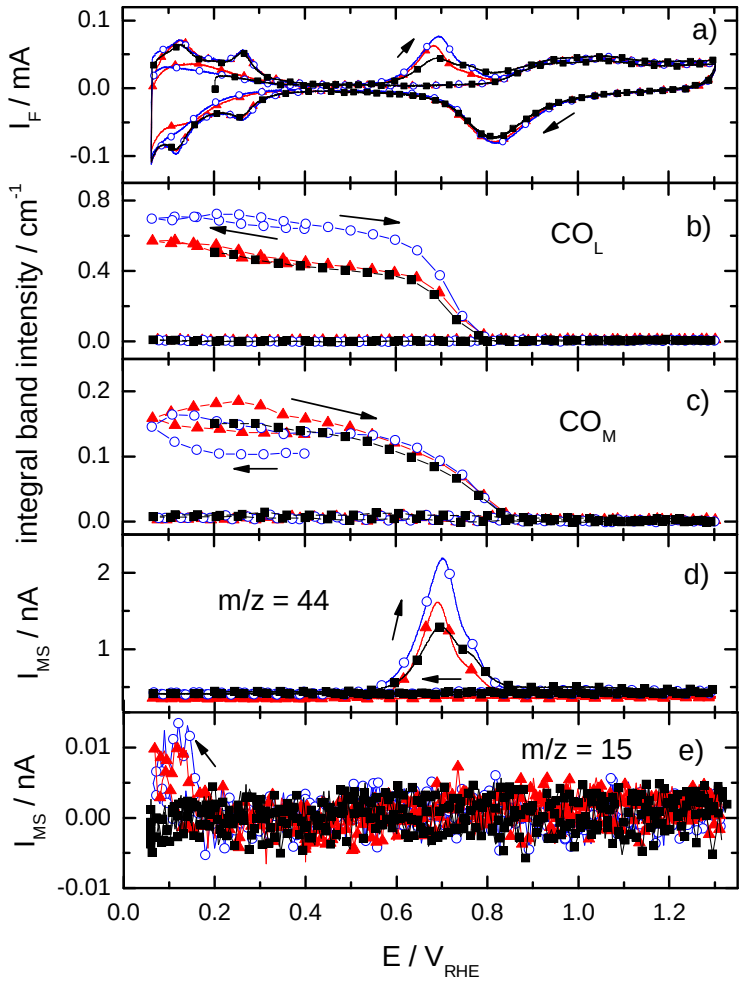

Fig. 69: Adsorbate stripping subsequent to the potentiostatic ethanol adsorption/oxidation at 0.2 V for 300 s (filled squares), at 0.4 V for 300 s (open circles) and at 0.4 V for 10 s (filled triangles): a) CV and the integrated absorbances of b) linear bonded CO and c) multiply bonded CO and d) the mass spectrometric current response for m/z = 44; scan rate = 10 mV/s; electrolyte 0.5 M H_2SO_4.

also residues from ethanol adsorption are oxidized in this potential range, most likely $CH_{x,ad}$ species {SCHM94}{WANG04O}. The first current peak is mainly attributed to the oxidation of CO_{ad} formed during ethanol adsorption at 0.2 V, as evidenced by the decreasing intensity of the CO_L and CO_M bands plotted in Fig. 69b and c, respectively, and the CO_2 formation detected by DEMS (Fig. 69d). However, the number of electrons released per CO_2 molecule formed in the Faradaic current peak at 0.7 V is 2.4 (for details concerning the calculation of n see section 3.5.3), indicating that also a small fraction of other ethanol decomposition products were present on the surface and oxidized to CO_2.

In the ethanol adsorbate stripping experiment performed after ethanol adsorption at 0.4 V, the potential was first cycled into the H_{upd} region (‘reductive stripping’), before the potential was scanned to 1.3 V (Fig. 69). When decreasing the electrode potential from 0.4 to 0.06 V, the

increase in the mass spectrometric current for m/z = 15 clearly indicates the formation/desorption of methane from the surface at potentials below 0.2 V, in agreement with previously reported data {IWAS94}{WANG06I}. The simultaneously recorded IR data show that during the first potential cycle to 0.06 V and back to 0.4 V, the CO_L and much more pronounced the CO_M band intensities increased, in agreement with earlier reports {IWAS89}{GOOT96}. Here it is important to compare the intensity of adsorbed CO at a constant potential, e.g., at 0.4 V before and after the potential excursion to the H_{upd}-region. Due to the potential-induced CO_{ad} island formation and potential-induced modifications of the polarisabiltity of the C=O bond, the integral band intensities of the CO_L and CO_M bands depends strongly on the potential, even at constant overall CO_{ad} coverage (see section 4.2). Iwasita et al. attributed the increase in the integral band intensity of CO_L after the potential excursion to 0.06 V to an increase in the CO_{ad} coverage, most likely due to the decomposition of absorbed acetyl species to CO_{ad} and $CH_{x,ad}$. However, based on the present *in situ* ATR-FTIR spectra, adsorbed acetyl species could not be detected on the Pt surface after ethanol adsorption at 0.4 V. Furthermore, the wavenumber of CO_L at 0.4 V was about 2051 cm^{-1} before the potential excursion to 0.06 V. In the subsequent positive-going scan at 0.4 V, the wavenumber is essentially constant (2050 cm^{-1}), similar to the findings by Iwasita el al. {IWAS94}. This is in contrast to an increase in the CO_{ad} coverage, which would result in an increase in the CO_L wavenumber (see Chapter 4.2). A more reasonable explanation for the slight increase in the CO_L and more pronounced increase in CO_M integral band intensity upon the potential excursion to 0.06 V is a structural re-arrangement of the CO adlayer, at essentially constant CO_{ad} coverage. Most likely, this is caused by the reductive desorption of $CH_{x,ad}$ at potentials below 0.2 V.

When the potential is increased further up to 1.3 V (Fig. 69), the same features as the directly positive-going adsorbate stripping experiment described above are observed. The Faradaic current increases at 0.6 V and passes through a maximum at 0.7 V. At potentials more positive than 0.8 V, the Pt film electrode is oxidized again. In contrast to the previously discussed direct oxidative stripping, no additional oxidative current is measured in the potential range between 1 and 1.3 V, and the Faradaic current follows the base CV for pure Pt. The Faradaic current peak centered at 0.7 V can again be attributed to the oxidation of CO_{ad} formed during the adsorption of ethanol at 0.4 V or during the subsequent cycling in the H_{upd} region, as evidenced by the decreasing intensities of the CO_L and CO_M bands and by the CO_2 formation. The numbers of electrons released per CO_2 molecules in the Faradaic current

peak centered at 0.7 V are 1.9 and 2.1 for ethanol adsorption for 300 and 10 s, respectively, indicating that only oxidation of CO_{ad} to CO_2 contributes to the Faradaic current.

Assuming that the CO_2 formation below 0.85 V originates only from CO_{ad} oxidation, the CO_{ad} coverage ($\theta_(CO_{ad})$ can be calculated from the mass spectrometric charge for m/z = 44. The results are summarized in table 6.

E_{ads}/V_{RHE} (ethanol exposure time)	0.2 (300 s)	0.4 (300 s)	0.4 (10 s)
$\theta(CO_{ad})$ in % of a Pt ML	27±3	39±4	29±3

Table 6: CO_{ad} coverage resulting from ethanol adsorption at constant potential, as calculated from the mass spectrometric m/z = 44 signal in the potential regime from 0.06 to 0.85 V (details see text).

The highest CO_{ad} coverage was obtained for ethanol adsorption for 300 s at 0.4 V. The presence of H_{upd} at 0.2 V resulted in a rather slow CO_{ad} formation rate at these potentials (see section 6.1.2.2). Hence, the CO_{ad} coverages formed from dissociative ethanol adsorption for an identical adsorption time of 300 s is smaller at 0.2 V than that of 0.4 V. The potential dependent CO_{ad} coverages as a function of the adsorption potential are discussed in more detail elsewhere {HEIN04}{WANG04O}. The CO_{ad} coverage is only slightly smaller if ethanol was adsorbed at 0.4 V for 10 s compared to ethanol adsorption for 300 s, although the exposure time was reduced by a factor of 30. This indicates that already after 10 s the Pt surface is covered largely with species that are irreversibly adsorbed under the present experimental conditions. According to the results of the *in situ* ATR-FTIR spectra presented in the preceding section, besides CO_{ad} these are mainly adsorbed acetyl species.

6.1.3 Summary

Employing the combined *in situ* ATR-FTIRS/DEMS flow cell set-up, new insights into the mechanism and kinetics of the ethanol electrooxidation were provided. Besides linearly and multiply bound CO_{ad}, adsorbed acetate and adsorbed acetyl species were identified via *in situ* ATR-FTIR spectroscopy. The assignment of the IR band detected at 1635 cm^{-1} to adsorbed acetyl species was supported by i) an isotope shift of about 35 cm^{-1} to lower wavenumber, when 13C labeled ethanol was used and ii) the absence of an isotope shift of this band for the adsorption of CH_3CD_2OH. In potentiostatic electrolyte exchange experiments presented in section 6.1.2.2, the temporal evolution of adsorbed species, namely, linearly and multiply bonded CO_{ad}, adsorbed acetate and adsorbed acetyl, upon ethanol adsorption could be

followed quantitatively for the first time. CO_{ad} formation rates of 0.002, 0.013 and 0.015 molecules $\times$ site^{-1} $\times$ s^{-1} were determined on the clean Pt surface for ethanol adsorption at 0.2, 0.4 and 0.6 V, respectively. Potentiostatic adsorbate decomposition transients provided strong experimental support for the proposal that adsorbed acetyl species are the precursor for CO_{ad} formation. Furthermore, based on the CO_{ad} coverage increase in the absence of ethanol in the solution, a quantitative relation between the integral band intensity of adsorbed acetyl and its coverage was established.

6.2 Adsorption/oxidation of $^{12}CH_3{}^{13}CH_2OH$

6.2.1 Introduction

In isotope labeling experiments using *in situ* IR spectroscopy, it was found that at potentials below 0.26 V adsorbed CO_{ad} species mainly originate from the alcohol group, whereas as higher potentials CO_{ad} is also formed from the methyl group {IWAS94} {SHIN96A}{FARI07}. Although it is generally accepted and well supported experimentally that the methyl group of ethanol can be converted to CO_{ad} already at potentials ≤ 0.4 V {IWAS94}{SCHM94}{SHIN96A}{TORR03}{FARI07} the underlying mechanism is not clear. A decomposition of adsorbed acetyl species to CO_{ad} and $CH_{x,ad}$ and subsequent oxidation of the $CH_{x,ad}$ species to CO_{ad} appears to be rather unlikely at potentials below 0.4 V. Under these conditions, adsorbed oxygen-containing species, which could facilitate the oxidation of the rather inactive $CH_{x,ad}$ species, are not present on the Pt surface. Furthermore, up to now essentially no data are available on the kinetics of the CO_{ad} formation rates from the methyl group and the alcohol group.

In the present section, I will present results on the adsorption/oxidation ethanol employing carbon labeled $^{12}CH_3{}^{13}CH_2OH$ and the combined ATR-FTIRS/DEMS flow-cell up. In the first subsection, the Faradaic current response upon potentiodynamic oxidation of $^{12}CH_3{}^{13}CH_2OH$ is analyzed, employing the full information available from combined ATR-FTIRS/DEMS measurements on adsorbed species and volatile reaction products. Based on potentiostatic adsorption transients, the CO_{ad} formation rates from the carbon atom of the methyl and the alcohol group of ethanol are determined separately (section 6.2.2.2). Adsorbate stripping experiments are presented in section 6.2.2.3, which allow to derive the coverage of $^{12}CO_{ad}$ and $^{13}CO_{ad}$, formed upon adsorption of $^{12}CH_3{}^{13}CH_2OH$ at different potentials. Finally, a detailed discussion of the results is given, which results in the proposal of a modified reaction scheme for the decomposition of adsorbed acetyl (section 6.2.2.4).

6.2.2 Results

6.2.2.1 Potentiodynamic adsorption/oxidation of $^{12}CH_3{}^{13}CH_2OH$

Selected *in situ* ATR-FTIR spectra recorded during the potentiodynamic oxidation of a solution containing 0.044 M of $^{12}CH_3{}^{13}CH_2OH$ are presented in Fig. 70 (first cycle). The reference spectrum was acquired in 0.5 M H_2SO_4 at 0.06 V. Linearly (CO_L) and multiply

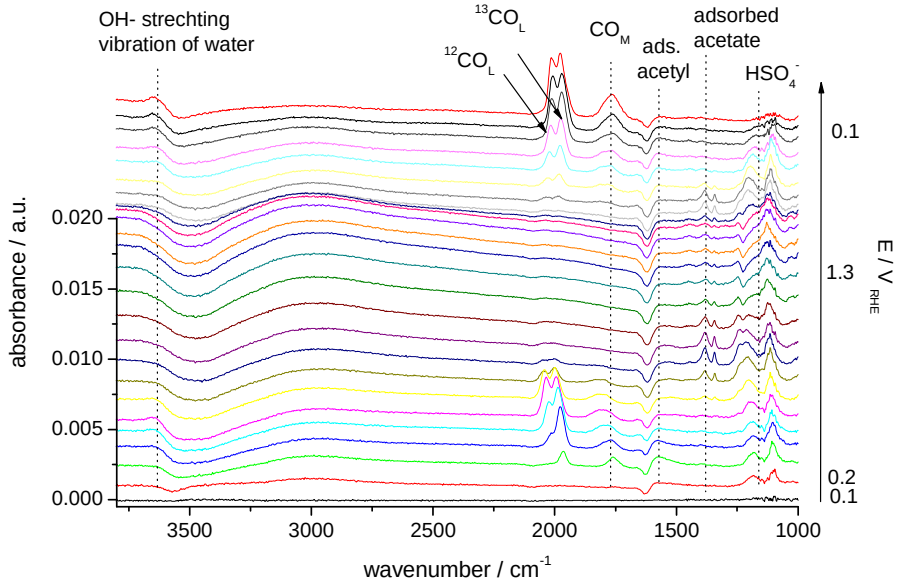

Fig. 70: Selected ATR-FTIR spectra recoded during the first cycle of the potentiodynamic oxidation of $^{12}CH_3{}^{13}CH_2OH$, sweep rate 10 mV/s. electrolyte 0.044 M $^{12}CH_2{}^{13}CH_2OH$ in 0.5 M H_2SO_4, flow rate 50 µl/s. Acquisition rate for the IR spectra: 4.9 s/spectrum, each second spectrum is shown.

(CO_M) bonded CO_{ad} are detected at about 2050 to 1976 cm^{-1} and 1855 and 1730 cm^{-1} {LEUN88}{WIEL96}{MIKI02}, respectively, for potentials between 0.3 and 0.8 V in the first positive-going scan and between 0.7 and 0.06 in the subsequent negative-going potential scan. Especially at higher potential, the CO_L band is clearly split into two bands centered at about 2044 and 1996 cm^{-1}, indicating the formation of $^{12}CO_L$ and $^{13}CO_L$, respectively. Due to dipole-dipole coupling and intensity transfer form the lower frequency to the higher frequency site {KORZ86}{CHAN90C}{SEVE95}, the $^{12}CO_L$ intensity is enhanced and the $^{13}CO_L$ intensity is reduced, which hinders a precise coverage determination of the respective CO_{ad} coverage during potentiodynamic ethanol bulk oxidation (see next sections).

A negative band at 3530 cm^{-1} is accompanied by a positive band at higher wavenumber (3640 cm^{-1}). These bands are assigned to the stretching mode of water, with the negative band being due to water replaced from the surface by CO and the positive band being due to water co-adsorbed with CO_{ad}. {ATAK96} {MIKI02}{FUTA05}. The corresponding band of the HOH-bending mode appears at 1620 cm^{-1}. A double-band caused by the adsorption of (bi-)sulfate appears at about 1210 and 1100 cm^{-1} {NART94}{IWAS97}{FUTA05}. Another double-band assigned to adsorbed acetate appears at potentials between 0.7 V and 1.1 V at ca. 1385 and 1340 cm^{-1}, respectively. A further positive band at about 1600 cm^{-1}, which is formed only in the first positive-going scan between 0.3 and 0.6 V, is attributed to adsorbed acetyl (see also section 6.1.2.1).

In Fig. 71, the extensive information available from combined ATR-FTIRS/DEMS measurements during the potentiodynamic oxidation of carbon labeled ethanol is summarized, showing the Faradaic current response (a), and the mass spectrometric currents for (b) $^{13}CO_2$ (I^*(m/z = 45), (c) $^{12}CO_2$ (I^*(m/z = 44), (d) m/z = 30 ($^{13}CHO^+$) and (e) the I^* (m/z = 15) signals (for details about the conversion of I (m/z = 45), I(m/z = 44) and I(m/z = 15) into the signals for $^{13}CO_2$ and $^{12}CO_2$ formation and the I^*(m/z = 15) current, respectively, see experimental, section 3.6). Furthermore, Fig. 71 contains the integral band intensities of (f) CO_L, i.e., the sum of $^{12}CO_L$ and $^{13}CO_L$, (g) CO_M and (h) adsorbed acetate extracted from the IR spectra shown in Fig. 70. A discrimination between the $^{12}CO_L$ and $^{13}CO_L$ band intensity is of little use due to the intensity transfer from the lower to the higher frequency vibration {KORZ86}{CHAN90C}{SEVE95}, resulting in a misleading interpretation of the intensities in terms of coverage (see also sections 6.2.2.2 and 6.2.2.3). Furthermore, this effect can also cause deviations between the sum of the integral band intensity of $^{12}CO_L$ and $^{13}CO_L$ and the overall CO_{ad} coverage.

Starting at 0.06 V in the first positive-going scan, a small Faradaic current is measured at about 0.25 V (open circles in Fig. 71). No CO_2 (Fig. 71b, c) or acetaldehyde (Fig. 71d) formation can be detected at this potential. However, the Faradaic current is accompanied by the onset of CO_{ad} formation as evidenced by the increase of the CO_M (Fig. 71g) and CO_L (Fig. 71f) band intensities. Therefore, the Faradaic current can partly be assigned to the dissociative adsorption of $^{12}CH_3{}^{13}CH_2OH$ to form $^{13}CO_{ad}$ (see Fig. 70, and also section 6.2.2.2), which in turn poisons the catalyst surface and explains the decrease in the Faradaic current between 0.25 and 0.4 V. The integral band intensity of CO_M increases slightly before that of CO_L, which is in agreement with the findings in section 4.2, where it was shown that at low overall CO_{ad} coverages and especially between 0.2 and 0.3 V, CO adsorbs preferentially in a multiply bonded configuration. At higher potentials, the Faradaic current increases again, resulting in a current peak at about 0.84 V, which contains a shoulder centered at about 0.7 V. The shoulder in the Faradaic current at 0.7 V is accompanied by a steep increase in $^{13}CO_2$ and $^{12}CO_2$ formation (for details about the conversion of I(m/z = 45) and I(m/z 44) signals into the $^{13}CO_2$ and $^{12}CO_2$ signals, respectively, see section 3.6) as well as a shoulder in the m/z =30 current increase, related to the formation of acetaldehyde. This in combination with the steep decrease in the intensity of linearly (Fig. 71f) and multiply bonded (Fig. 71g) CO_{ad} at 0.7 V indicates that the CO_2 formation at 0.7 V can be attributed to the oxidation of CO_{ad}, which was formed at lower potentials during the first positive-going potential scan (see Fig. 71f,g).

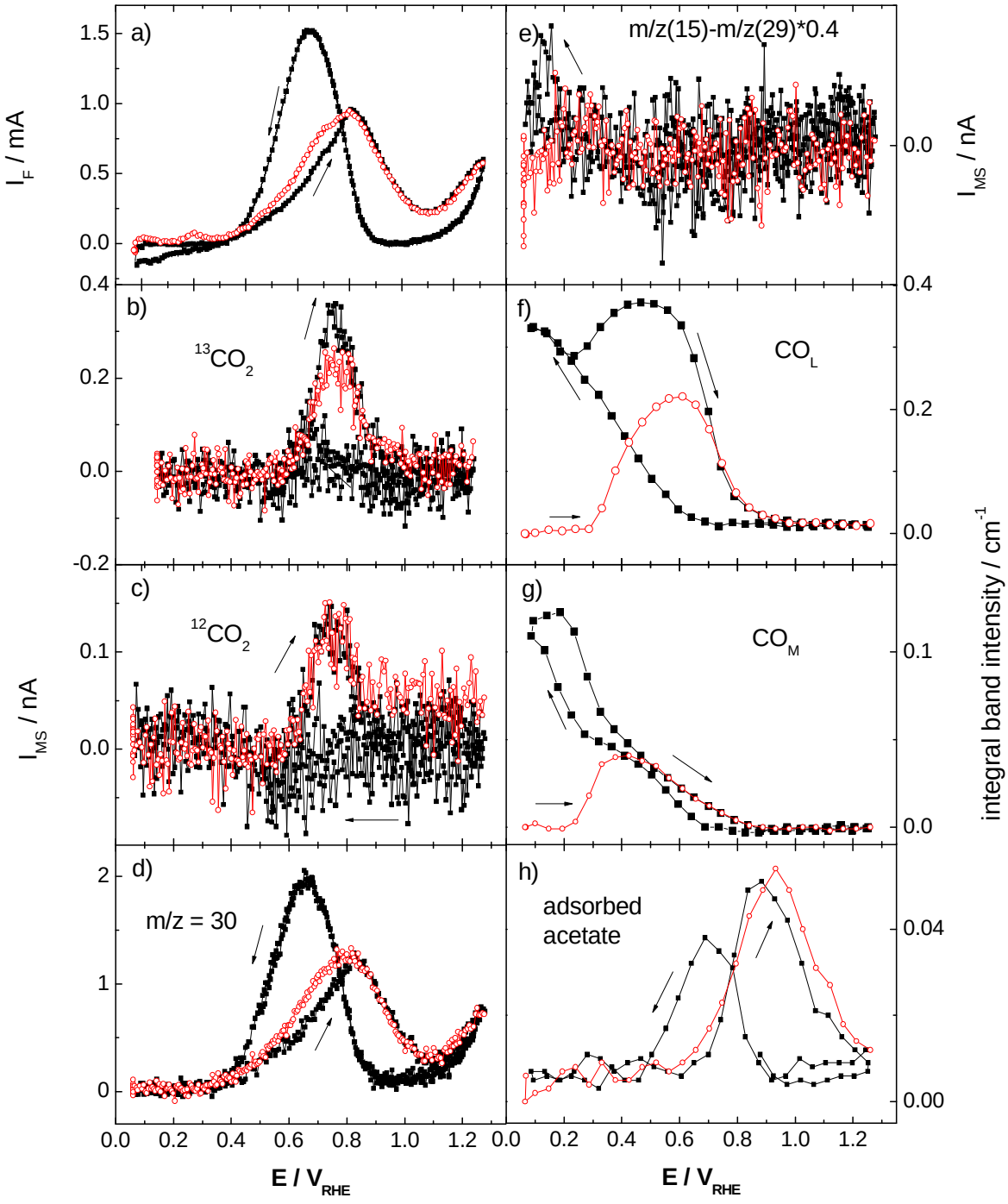

Fig. 71: Potentiodynamic ethanol bulk-oxidation; a) CV and mass spectrometric currents for b) $^{13}CO_2$ formation, c) $^{12}CO_2$ formation, d) m/z = 30, and e) the converted m/z 15 signal (the conversion was done following the procedure described in section 3.6) as well as the integrated absorbance of f) linearly bonded CO, i.e. the sum of $^{12}CO_L$ and $^{13}CO_L$ (see text) , g) multiply bonded CO and h) adsorbed acetate taken from the IR spectra in Fig. 70, v = 10 mV/s; electrolyte 0.044 M $^{12}CH_3{}^{13}CH_2OH$ in 0.5 M H_2SO_4. **Open circles:** first positive-going scan, **filled squares:** continuous cycling in ethanol containing solution.

The shoulder in the Faradaic current at 0.7 V can therefore be assigned to the continuous oxidation of ethanol to acetaldehyde and to the oxidation of CO_{ad}, which was preformed at lower potentials during the potential sweep in ethanol containing electrolyte.

At the main Faradaic current peak centered at 0.84 V, the $^{13}CO_2$ and $^{12}CO_2$ formation rates are already decreasing (Fig. 71b,c), whereas the m/z = 30 current mirrors the Faradaic current response, indicating that at this potentials the Faradaic current is mainly correlated with the formation of acetaldehyde. Furthermore, also acetic acid is formed at 0.84 V, as evidenced by the steep increase in the integral band intensity of adsorbed acetate starting at about 0.7 V and having a maximum at about 0.95 V (Fig. 71h). The main Faradaic current around 0.84 V is mainly caused by the oxidation of ethanol to incompletely oxidized side products, namely acetaldehyde and acetic acid, in agreement with previous reports {IWAS94}{WANG04B}.

Between 0.84 and about 1.0 V, the Faradaic current decreases, this is most likely attributed to the oxidation of Pt to catalytically less active PtO. The slow increase of the Faradaic current at E > 1.0 V must be related to the onset of ethanol oxidation on the oxide covered Pt surface, which is accompanied by an increase in the m/z = 30 current (Fig. 71d), indicating the formation of acetaldehyde {IWAS94}{WANG04B}. The contribution of CO_2 formation to the Faradaic current (Fig. 71b,c), and hence the rate for C-C bond splitting, has to be very small at these potentials {IWAS94}{WANG04B}. It is interesting to note that at potentials above 1.0 V, the CO_2 formation mainly originates from oxidation of the methyl group (Fig. 71c). This can be explained most simply by oxidation of $CH_{x,ad}$ species which were formed upon dissociative ethanol adsorption in the first positive-going scan{LAI09}, to CO_2 {IWAS94}{FARI07}.

The integral band intensities of adsorbed acetate (Fig. 71h) and adsorbed sulfate (data not shown) decrease from 0.95 to 1.3 V. This is the typical potential dependence of the integral band intensity of adsorbed anions, which are most likely displaced at very positive potentials by more strongly adsorbing oxygen containing species. Acetic acid formation can therefore not be followed via the IR intensity of adsorbed acetate, at potentials above 0.95.

In the negative-going scan, the ethanol oxidation first decreases and starts again at about 0.85 V, together with the reduction of Pt surface oxide. Subsequently, the Faradaic current passes through a peak centered at 0.65 V, and then decreases rapidly, reaching zero current at about 0.35 V. Also in this case, the Faradaic current peak can be assigned mainly to the oxidation of ethanol to acetaldehyde and acetic acid, as evidenced by the increase in m/z = 30 current Fig.

71d) and the increase in the integral band intensity of adsorbed acetate Fig. 71h). The CO_2 formation in the negative-going scan is much lower compared to the positive-going scan, while for the overall Faradaic current this is opposite. Hence, in the negative-going scan, ethanol oxidation proceeds to a much higher extent via formation of incomplete oxidation products, namely acetaldehyde and acetic acid, than in the positive-going scan {IWAS94}{WANG04B}. This can be understood when taking into account that the CO_2 formation in the positive-going scan is dominated by the oxidation of CO_{ad}, formed and accumulated at low potentials Fig. 71f) and g).

At potentials below 0.2 V, the I^*(m/z = 15) current increases. This is attributed to the reduction of $CH_{x,ad}$ species, which are formed upon C-C bond splitting, to methane {IWAS94}{WANG04B}{WANG06D}{WANG06I}{LAI09}.

In the second positive-going scan, the Faradaic current response exhibits systematic differences compared to the first positive-going scan: i) the current peak at 0.25 V is suppressed, ii) the onset of ethanol oxidation is shifted to higher potentials, and iii) the shoulder at 0.7 V current is smaller. These differences are attributed to the higher CO_{ad} coverage in the second positive-going scan which can be seen from the integrated intensity of CO_{ad} plotted in Fig. 71f) and g).

The detection of both $^{12}CO_2$ as well as $^{13}CO_2$, during potentiodynamic oxidation of ethanol clearly shows that both carbon atoms of ethanol can be oxidized to CO_2. The oxidation of the carbon atom at the alcohol group dominates slightly, in agreement with literature data {SHIN96A}{FARI07}{LAI09}. However, due to the convolution of potential and time effects, more quantitative information on the potential dependent kinetics of CO_{ad}/CO_2 formation can hardly be derived from the potentiodynamic measurements. Therefore, electrolyte exchange experiments at constant potentials were performed to derive further details of the potential dependence of CO_{ad}/CO_2 formation, which are presented in the next section.

6.2.2.2 Potentiostatic adsorption/oxidation of $^{12}CH_3{}^{13}CH_2OH$

The temporal evolution of IR spectra acquired during the $^{12}CH_3{}^{13}CH_2OH$ adsorption transients at different constant potentials is shown in Fig. 72. At 0.2 V, only $^{13}CO_L$ (1958 $\rightarrow$ 1990 cm^{-1}) and $^{13}CO_M$ (1747 $\rightarrow$ 1766 cm^{-1}) can be detected in the spectra, whereas at 0.4 V, besides $^{13}CO_{ad}$ (1968 $\rightarrow$ 1980 cm^{-1}) a band correlated to $^{12}CO_L$ (2024 $\rightarrow$ 2037 cm^{-1}) is found

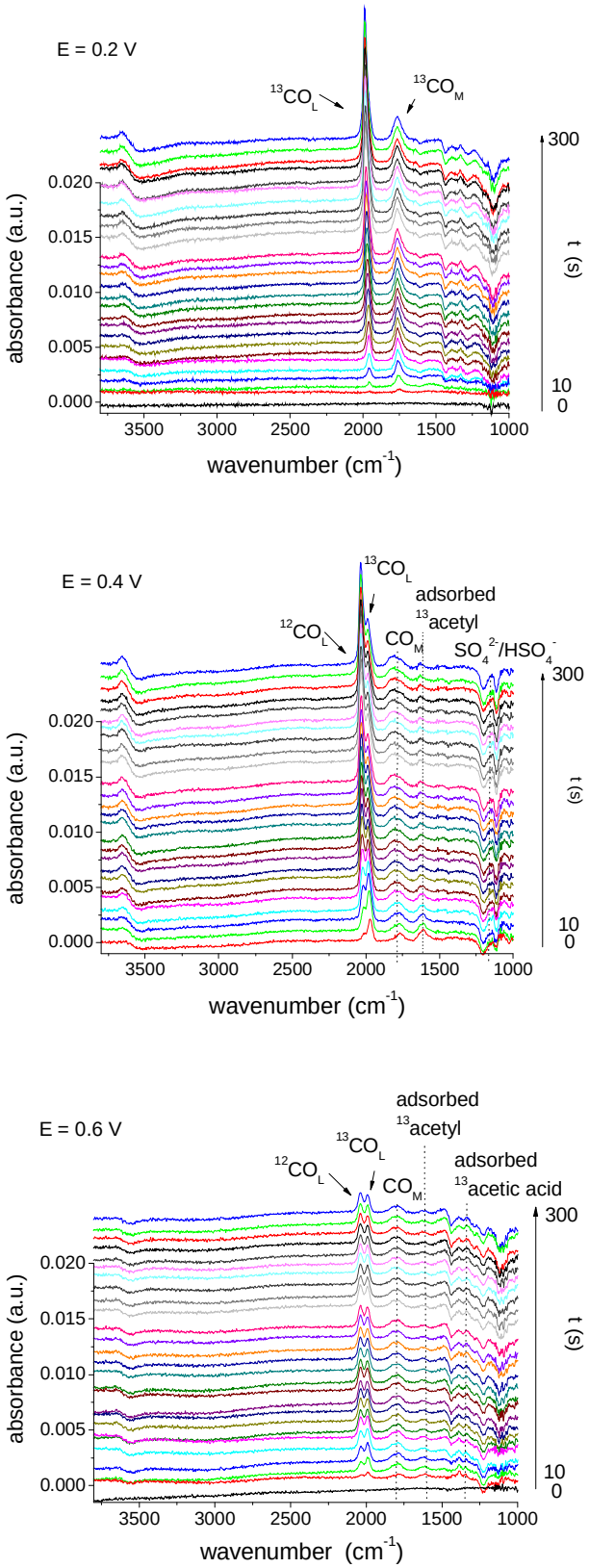

Fig. 72: Temporal evolution of ATR-FTIR spectra recorded during the adsorption of isotope labeled ethanol at 0.2, 0.4 and 0.6 V upon exchange from 0.5 M H_2SO_4 solution to electrolytes containing 0.044 M of $^{12}CH_3{}^{13}CH_2OH$. The reference spectra were collected at the corresponding adsorption potential in 0.5 M H_2SO_4 just before the electrolyte exchange. Time resolution: 0.9 s per spectrum, each 11th spectrum is shown.

as well. Compared to the intensity of the $^{13}CO_L$ band, the $^{12}CO_L$ intensity is small in the first 10 s, reaches about similar intensity as that of the $^{13}CO_L$ band after 50 s, and is even higher after 5 min. of ethanol adsorption. As mentioned before, dipole-dipole coupling between the CO_{ad} molecules hinders the quantification of the corresponding $^{12}CO_{ad}$ and $^{13}CO_{ad}$ coverages during adsorption, but the final, quasi steady-state coverages of both adsorbates can be easily derived from DEMS adsorbate stripping measurements (see next section). Furthermore, besides CO_{ad} an additional band can be detected at 1600 cm^{-1}, which was assigned to adsorbed acetyl species (see section 6.1.2.1). The band reaches its highest intensity several seconds after ethanol adsorption at this potential (0.4 V), and it decreases with ongoing ethanol oxidation. For adsorption at 0.6 V, IR absorption bands related to $^{13}CO_L$ (1984 $\rightarrow$ 1992 cm^{-1}), $^{12}CO_L$ (2028 $\rightarrow$ 2039 cm^{-1}), CO_M (1790 cm^{-1}), adsorbed acetyl (1610 cm^{-1}) and adsorbed acetate (1384 cm^{-1}) were detected (Note: due to the broad IR absorption band of CO_M a separation between $^{13}CO_M$ and $^{12}CO_M$ is hardly possible). Different from ethanol adsorption at 0.4 V, the intensity of the $^{12}CO_{ad}$ and $^{13}CO_{ad}$ bands are identical already about 20 s after starting ethanol adsorption. Finally, the intensity of both bands is significantly lower during adsorption at 0.6 V compared to 0.4 V and 0.2 V, due to the onset of CO_{ad} oxidation to CO_2. In agreement with previous studies, CO_{ad} is formed only from the alcohol group at 0.2 V, whereas at 0.4 and 0.6 V both $^{12}CO_{ad}$ and $^{13}CO_{ad}$ are detected {SHIN96A}{FARI07}{LAI09}.

From the initial increase in the CO_L band intensity, the CO_{ad} formation on a clean Pt surface can be determined as described in section 6.1.2.2. At 0.2 V, a value of 0.002 molecules $\times$ $site^{-1}$ $\times$ s^{-1} is calculated for the $^{13}CO_{ad}$ formation rate, which is identical to the value derived for the adsorption of unlabeled ethanol (section 6.1.2.2). Since no $^{12}CO_{ad}$ is detected, the $^{12}CO_{ad}$ formation rate at 0.2 V has to be very small.

For an analysis of the initial CO_{ad} formation process at 0.4 V, enlarged IR spectra recorded within the first 10 s upon ethanol adsorption are presented in Fig. 73. Directly after the electrolyte exchange to ethanol containing solution (t = 0.9 s), adsorbed acetyl species are detected on the Pt surface via the IR absorption band at 1600 cm^{-1}. The formation of CO_{ad}, which adsorbs preferentially in a multiply bonded configuration at low coverages (see section 4.2), sets in simultaneously.

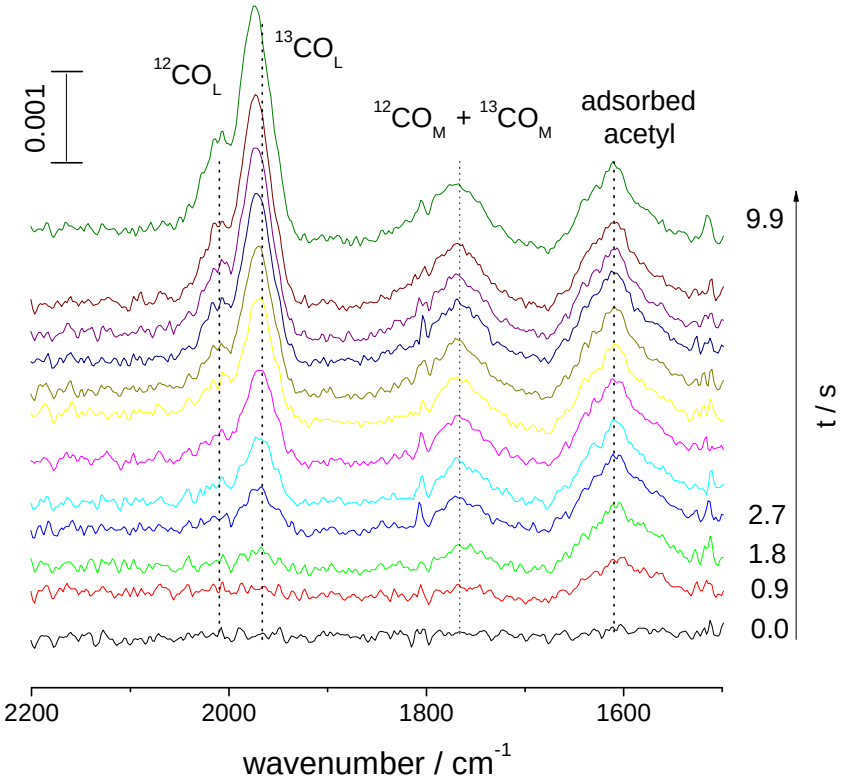

Fig. 73: ATR-FTIR spectra recorded during the adsorption of isotope labeled ethanol (0.044 M $^{12}CH_3{}^{13}CH_2OH$ in 0.5 M H_2SO_4) at 0.4 upon exchange from 0.5 M H_2SO_4 solution. The reference spectra were collected at the corresponding adsorption potential in 0.5 M H_2SO_4 just before the electrolyte exchange. Time resolution: 0.9 s per spectrum.

A t = 2.7 s, linearly bonded ^{13}CO appears in the spectra (1970 cm^{-1}). It is accompanied by a smaller band at higher wavenumber (2015 cm^{-1}), which is characteristic for $^{12}CO_L$. The respective CO_{ad} surface coverages can be derived from the integral band intensities of $^{12}CO_L$ and $^{13}CO_L$, assuming that the intensity transfer from the lower to the higher wavenumber is negligible at low overall CO_{ad} coverage. As shown before (section 6.1.2.2), the CO_{ad} formation rates can be derived from the initial increase in the CO_L band intensity increase (here: t = 4.5 to t = 25 s). To determine the $^{12}CO_{ad}$ and $^{13}CO_{ad}$ formation rates separately, the CO_L band was deconvoluted in to a $^{13}CO_L$ and a $^{12}CO_L$ band via two Gaussian fittings centered at 1990 and 2010 cm^{-1}, respectively. Values of 0.011 and 0.005 molecules × site ×s^{-1} are obtained for the $^{13}CO_{ad}$ and $^{12}CO_{ad}$ formation rates, respectively. This is in very good agreement with the overall CO_{ad} formation rate of 0.014 molecules × site ×s^{-1}, derived for the adsorption of unlabeled ethanol. In Fig. 74, the ratio of the $^{12}CO_{ad}/^{13}CO_{ad}$ coverage is plotted versus time, from t = 4.5 s up to t = 25 s. This time range was chosen since at shorter times, the intensity of the $^{12}CO_L$ band is hardly visible and at longer times, i.e., at higher CO_{ad}

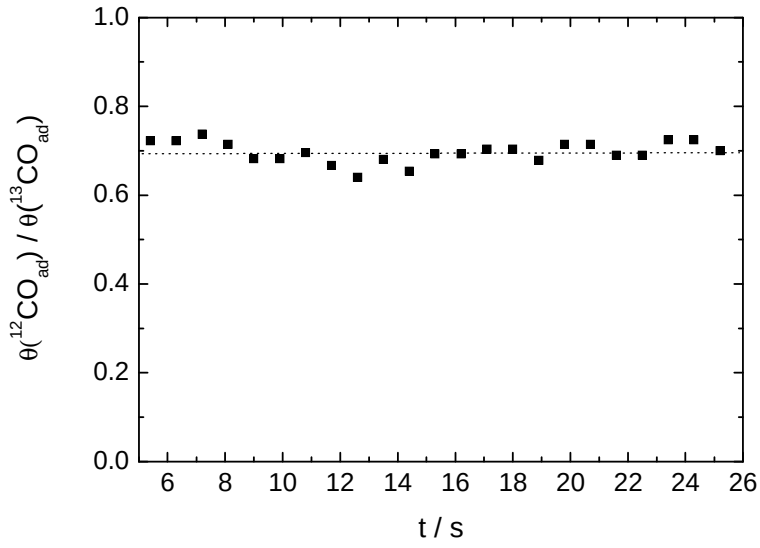

Fig. 74: Ratio of $^{12}CO_{ad}/^{13}CO_{ad}$ coverage upon ethanol adsorption at 0.4 V, as determined from the respective integral band intensity of $^{12}CO_L$ and $13CO_L$, plotted versus adsorption time (details see text).

coverages, intensity transfer from $^{13}CO_L$ to $^{12}CO_L$ {KORZ86}{CHAN90C} makes the determination of the CO_{ad} coverage, which is derived from the integral band intensity of CO_L, cumbersome. Based on the evaluation of the IR data, the ratio of $\theta(^{12}CO_{ad})/\theta(^{13}CO_{ad})$ is about 0.68, essentially independent of the adsorption time for t = 5 to t = 25 s. These values are slightly larger than would be expected from the more than two times faster formation rate of $^{13}CO_{ad}$ compared to the $^{12}CO_{ad}$ formation rate. An accurate way to determine the $^{12}CO_{ad}$ and $^{13}CO_{ad}$ coverage after ethanol adsorption is to perform adsorbate stripping experiments (see below and next section). At 0.6 V, about equal $^{12}CO_{ad}$ and $^{13}CO_{ad}$ coverages can be deduced from the similar integral band intensities of $^{12}CO_{ad}$ and $^{13}CO_{ad}$. CO_{ad} formation rates of about 0.0036 and 0.0034 molecules $\times$ site^{-1} $\times$ s^{-1} are determined on a clean Pt surface at 0.6 V for the $^{12}CO_{ad}$ and $^{13}CO_{ad}$ formation rates, respectively.

In total, at 0.2 V essentially only the carbon atom of the alcohol group can be converted to CO_{ad}, whereas at 0.6 V both carbon atoms of ethanol contribute to an about equal extent to the overall amount of CO_{ad}/CO_2 formation, in agreement with earlier reports {SHIN96A}{FARI07}. These finding can be qualitatively explained by the mechanistic model that adsorbed acetyl species decompose to CO_{ad} and $CH_{x,ad}$ species. At 0.2 V, the latter species desorbed as methane due to the presence of H_{upd}, whereas they are oxidized to CO_{ad} and subsequently to CO_2 at 0.6 V, which can be explained by the presence of OH_{ad} species under these conditions. However, the fast rate for the formation of CO_{ad} from the carbon atom of the methyl group already at 0.4 V is surprising. Based on the mechanistic proposal that

adsorbed acetyl decomposes to CO_{ad} and $CH_{x,ad}$, the oxidation of the later species to CO_{ad} is expected to be rather slow on a Pt electrode at 0.4 V, since the coverage of adsorbed oxygen species is essentially zero under these conditions {CLIM06}. To further investigate this interesting finding, additional measurements were performed at 0.4 V.

In the following, I will present three different types of experiment. In each experiment, ethanol was adsorbed at 0.4 V upon an electrolyte exchange from 0.5 M H_2SO_4 to 0.044 M $^{12}CH_3{}^{13}CH_2OH$ containing solution at t = 30 s. The electrolyte was changed back to 0.5 M H_2SO_4 either at t = 300 s (Fig. 75, filled squares) or already after 25 s of ethanol exposure (Fig. 75 open circles). In the third experiment, the electrolyte was also changed back to 0.5 M H_2SO_4 after 25 s of ethanol exposure, but in addition the potential was simultaneously stepped to 0.06 V. The resulting Faradaic currents, CO_L intensities and adsorbed acetyl related band intensities are plotted as a function of time in Fig. 75. As mentioned before, dipole-dipole coupling effects hinder a correct separation into individual ^{13}CO and ^{12}CO absorption bands at high CO_{ad} coverages. Therefore, in Fig. 75b the integral intensity of both $^{13}CO_L$ + $^{12}CO_L$ is plotted. The individual rates for $^{12}CO_{ad}$ and $^{13}CO_{ad}$ formation were deduced from the initial intensity increases, where effects of dipole-dipole coupling are expected to be small (see above).

I will first present the results of the two ethanol adsorption transients at 0.4 V, which only differ in the time of ethanol adsorption (Note: Similar experiments were already presented and discussed for the adsorption/oxidation of unlabeled ethanol (see section 6.1.2.3)) Upon exposure to ethanol at 0.4 V, the Faradaic currents increase steeply, pass through a sharp maximum and then decay. When ethanol is adsorbed for 300 s, the Faradaic current decreases to a very low value (~0.02 mA) after 5 min. It immediately decreases to zero upon changing to ethanol-free electrolyte either at t = 55 s (open circles) or 300 s (filled squares), respectively. In contrast to the Faradaic current transients, the development of the integrated band intensities of adsorbed CO and adsorbed acetyl species at 0.4 V is almost independent of the ethanol adsorption time. Also after electrolyte exchange after 25 s, the CO_L intensity continues to increase, in a similar way as observed for continuing ethanol exposure. Parallel to the increase in the integral band intensity of CO_L, the intensity of the adsorbed acetyl band decreases continuously. This intensity decay is rather similar to that during continuing ethanol exposure, with a slightly steeper decay. Accordingly, the final intensities of the CO_L band and the acetyl band are only slightly lower when ethanol was removed after 25 s compared to continuing ethanol exposure, in good agreement with similar experiments for the

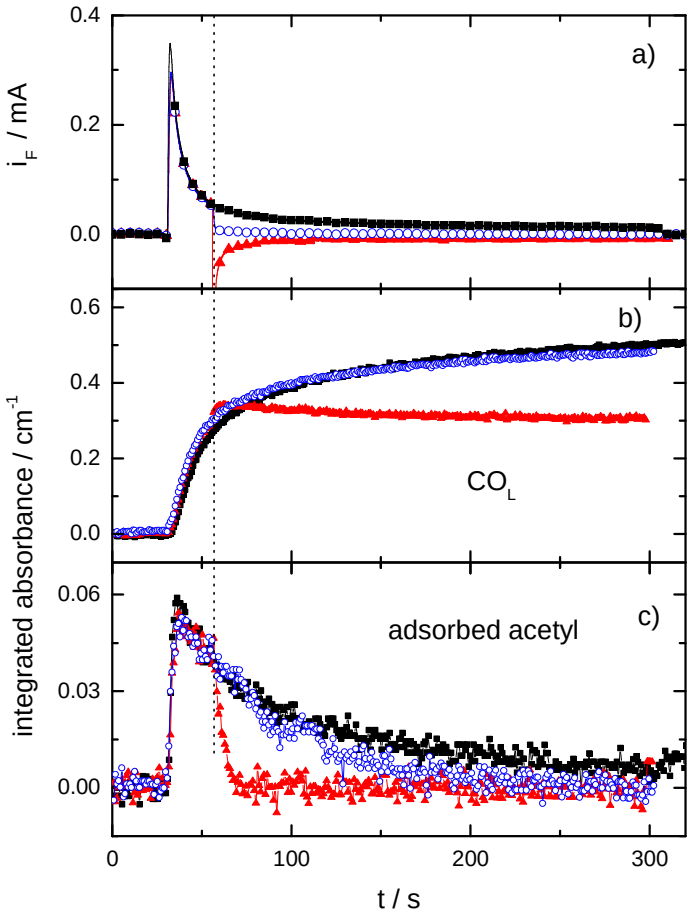

Fig. 75: Temporal development of a) Faradaic current, b) integrated band intensity of adsorbed CO ($^{12}CO_L$ + $^{13}CO_L$), and c) integrated band intensity of adsorbed acetyl detected (1600 cm^{-1}) during/after ethanol adsorption. **Filled squares:** Electrolyte exchange at 0.4 V from 0.5 M H_2SO_4 to 0.044 M $^{12}CH_3{}^{13}CH_2OH$ containing solution at t = 30 s and back to 0.5 M H_2SO_4 at t = 300 s. **Open circles:** Electrolyte exchange at 0.4 V from 0.5 M H_2SO_4 to 0.044 M $^{12}CH_3{}^{13}CH_2OH$ containing solution at t = 30 s and back at t = 55 s. **Filled triangles:** Electrolyte exchange at 0.4 V from 0.5 M H_2SO_4 to 0.044 M $^{12}CH_3{}^{13}CH_2OH$ containing solution at t = 30 s and back to 0.5 M H_2SO_4 at t = 55 s. Simultaneously with the 2nd electrolyte exchange, the potential was stepped from 0.4 V to 0.06 V.

adsorption/oxidation of unlabeled ethanol (see section 6.1.2.3). Adsorbate stripping experiments performed after the respective adsorption experiments reveal only slightly smaller overall CO_{ad} coverage after ethanol adsorption for 25 s and subsequent waiting for 5 min, compared to ethanol exposure for 300 s (see next section).

I will now present the results of the combined "electrolyte exchange/potential step" experiment, changing from 0.5 M H_2SO_4 to 0.044 M $^{12}CH_3{}^{13}CH_2OH$ containing 0.5 M H_2SO_4 solution at t = 30 s and back to 0.5 M H_2SO_4 at t = 55s at 0.4 V. Simultaneously with the second electrolyte exchange a potential step to 0.06 V was performed (Fig. 75, filled triangles). Upon changing to ethanol containing solution, the Faradaic current first increases

steeply and then decreases slightly with further adsorption. When the potential is stepped to 0.06 V (simultaneously with the second electrolyte exchange), a negative current spike is observed, due to capacitive charging and the reductive adsorption of hydrogen. In addition, the reduction of $CH_{x,ad}$ species to methane contributes to the negative current spike {WANG04O}. Similar to the adsorption transients presented above an increase in the integral band intensity of CO_L indicates the formation of CO_{ad} during adsorption/oxidation of ethanol at 0.4 V. When the potential is stepped to 0.06 V, the integral band intensity jumps up, which is explained by an increasing absorption coefficient of CO_{ad} at lower potentials, as discussed in section 4.2 for the adsorption of gas phase CO. After the potential step to 0.06 V, the integral band intensity of CO_L remains essentially constant, indicating that at 0.06 V no additional CO_{ad} is formed.

The integral band intensity of adsorbed acetyl increases steeply in ethanol containing solution and decreases slightly with adsorption time. After the potential step to 0.06 V, the intensity decreases much more pronounced and reaches a value of zero at t = 60 s. Fast decomposition of adsorbed acetyl to CO_{ad} at 0.06 V can be excluded, since the overall CO_{ad} coverage does not increase after the potential was stepped to 0.06 V (Fig. 75b, filled triangles). Therefore, the steep decrease in the intensity of adsorbed acetyl at 0.06 V, is attributed to desorption of adsorbed acetyl species, most likely caused by protonation and subsequent desorption as acetaldehyde and/or by adsorption of more strongly bond H_{upd}.

6.2.2.3 $^{12}CH_3{}^{13}CH_2OH$ adsorbate stripping experiments

After the adsorption transients presented in the previous section, the cell was rinsed for 5 min. with 0.5 M H_2SO_4 while the potential was kept constant. Then potentiodynamic ethanol adsorbate stripping experiments were performed, which are described in the following for ethanol adsorption at 0.2 and 0.4 V.

In Fig. 76, the Faradaic current response (a) and the mass spectrometric currents for m/z = 45 (b), m/z = 44 (c) and m/z = 15 (d) are plotted, which were recorded during the potentiodynamic adsorbate stripping performed after adsorption of $^{12}CH_3{}^{13}CH_2OH$ at 0.2 V for 5 min.. In the first negative-going potential scan and the subsequent positive-going scan, the Faradaic current response shows a suppressed H_{upd} region, due to the presence CO_{ad}, as evidenced by the integral band intensity of CO_L (Fig. 76b). The Faradaic current increases at about 0.55 V and passes through a maximum at 0.68 V. At potentials positive of 0.8 V, OH_{ad}/Pt oxide formation sets in and in addition, also residues from ethanol adsorption are

oxidized in this potential range. The first current peak is mainly attributed to the oxidation of CO_{ad} formed during ethanol adsorption at 0.2 V, as evidenced by the decrease of the integral band intensity of CO_L (Fig. 76b) and by the $^{13}CO_2$ and $^{12}CO_2$ formation detected by DEMS (Fig. 76c and d). For potentials between 0.5 and 0.85 V, the amount of $^{12}CO_2$ is about 5% of that of $^{13}CO_2$. Therefore, it can be concluded that upon adsorption of $^{12}CH_3{}^{13}CH_2OH$ at 0.2 V, $^{12}CO_{ad}$ only contributes to about 5% to the overall amount of CO_{ad}, whereas the large majority of 95% can be assigned to $^{13}CO_{ad}$. This is in agreement with the IR data presented in the preceding section, which showed that only $^{13}CO_{ad}$ and hardly any $^{12}CO_{ad}$ has developed during adsorption of ethanol at 0.2 V. In the adsorbate stripping experiment, small amounts of $^{12}CO_2$ are formed at potentials above 0.85 V. This is attributed to the oxidation of $^{12}CH_{x,ad}$ to $^{12}CO_2$ {IWAS94}{SCHM94}.

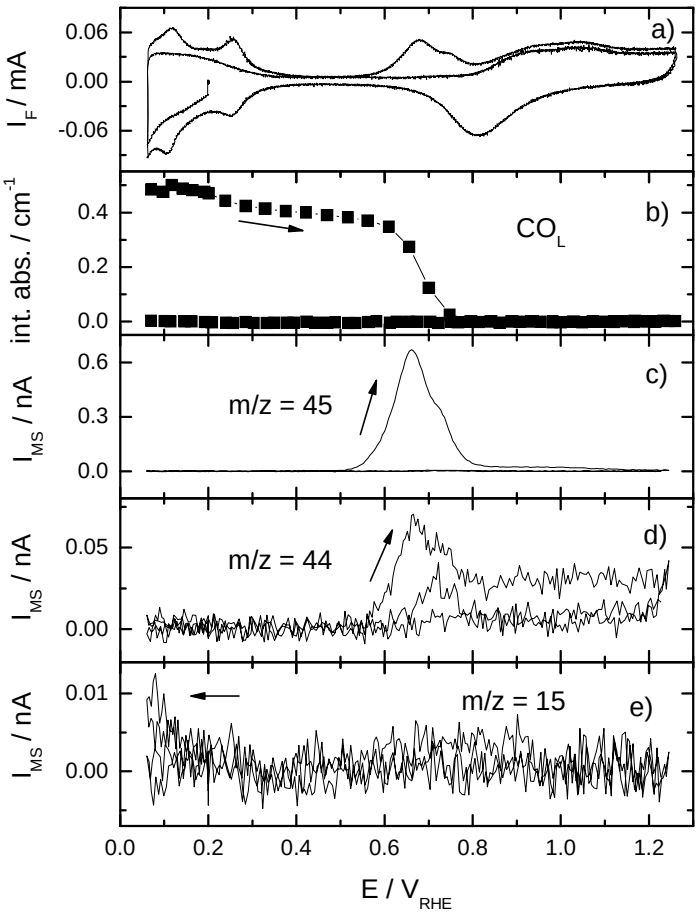

Fig. 76: Potentiodynamic adsorbate stripping experiment performed subsequent to the potentiostatic $^{12}CH_3{}^{13}CH_2OH$ adsorption/oxidation at 0.2 V: a) Faradaic current response, b) integral band intensity of CO_L, i.e., the sum of $^{12}CO_L$ and $^{13}CO_L$ bands and the mass spectrometric currents for c) m/z = 45, d) m/z = 44 and e) m/z = 15. Scan rate: 10 mV/s; electrolyte 0.5 M H_2SO_4.

The small increase in the m/z = 15 signal in the first negative-going scan (Fig. 76e) indicates the formation of methane, formed by reduction of $CH_{x,ad}$ species {IWAS94}{WANG04O}. The Faradaic current response (a), the integral band intensity of CO_L, i.e., the sum of $^{12}CO_L$ and $^{13}CO_L$ (b), and the mass spectrometric currents for m/z = 45 (c), m/z = 44 (d) and m/z = 15 (e) recorded during the potentiodynamic adsorbate stripping, performed after each of the three different $^{12}CH_3{}^{13}CH_2OH$ ethanol adsorption transients at 0.4 V (see previous section), are plotted in Fig. 77.

I will start the presentation with the adsorbate stripping experiments, which was performed after the adsorption of ethanol at 0.4 V for 300 s (Fig. 77, filled squares). In the directly positive-going scan, the Faradaic current increases at about 0.55 V, passes through a maximum at 0.68 V and decreases at more positive potentials. At potentials above 0.9 V, a small Faradaic

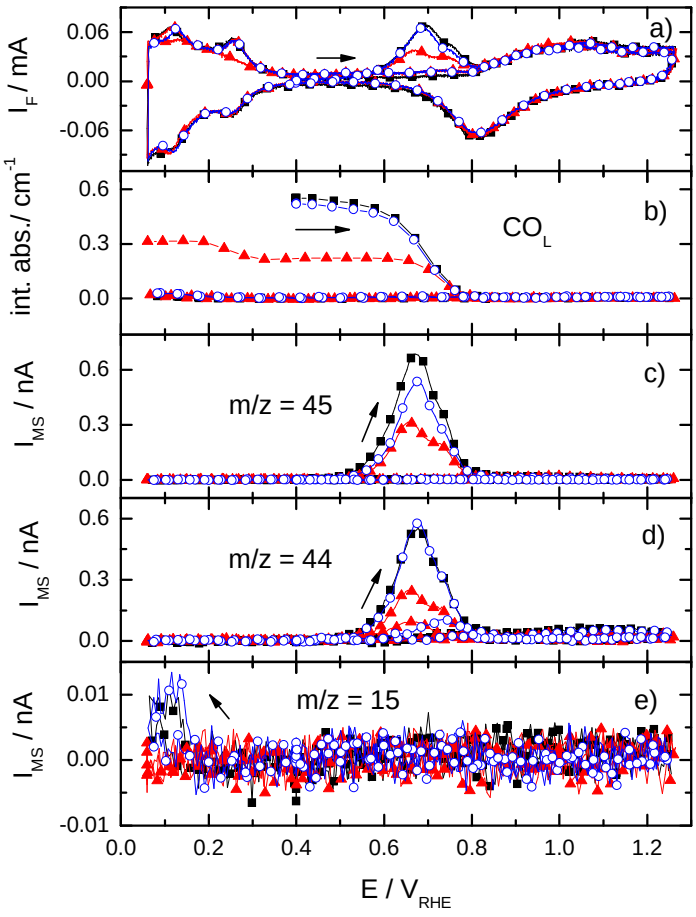

Fig. 77: Three potentiodynamic adsorbate stripping experiments in 0.5 M H_2SO_4, performed after potentiostatic $^{12}CH_3{}^{13}CH_2OH$ adsorption/oxidation at 0.4 V for i) 5 min (filled squares), ii) 25 s (open circles) and iii) 25 s with a simultaneous potential step to 0.06 V, respectively (see also Fig.75). a) Faradaic current response, b) integral band intensity of CO_L, i.e., the sum of $^{12}CO_L$ and $^{13}CO_L$ bands and the mass spectrometric currents for c) m/z = 45, d) m/z = 44 and e) m/z = 15. Scan rate: 10 mV/s; electrolyte 0.5 M H_2SO_4.

current is measured, in addition to the oxidation of Pt. The first current peak at 0.68 V, can be attributed to the oxidation of CO_{ad} formed during ethanol adsorption at 0.4 V, as evidenced by the steep decrease of the CO_L band (Fig. 77b) and the $^{13}CO_2$ and $^{12}CO_2$ formation detected by DEMS ((Fig. 77c and d). In the potential regime between 0.5 and 0.85 V, the amount of $^{12}CO_2$ and $^{13}CO_2$ are equivalent to 7.8 nC and 9.35 nC, which corresponds to 19% and 22.5% of an adlayer that is saturated with CO from the gas phase (41.4 nC), respectively. Correspondingly, the $^{12}CO_{ad}$ coverage formed upon $^{12}CH_3{}^{13}CH_2OH$ adsorption at 0.4 V for 300 s and subsequent waiting at 0.4 V for 5 min. in ethanol free solution, is 82% of the $^{13}CO_{ad}$ coverage. This is in reasonable agreement with earlier reports {IWAS94}{SCHM94}. Furthermore, this value is only slightly higher compared to the 68% (see Fig. 74), derived from the integral band intensity of $^{12}CO_L$ and $^{13}CO_L$ for the initial stages of the ethanol adsorption.

At potentials above 0.85 V, mainly $^{12}CO_2$ is formed (2.35 nC) and only little $^{13}CO_2$ formation (0.52 nC) can be detected V (Fig. 77, filled squares). This is attributed to the oxidation of $^{12}CH_{x,ad}$ to $^{12}CO_2$ {IWAS94}{SCHM94}. Furthermore, the total amount of $^{12}CO_2$ and $^{13}CO_2$ formed in the whole potential regime between 0.5 and 1.3 V are essentially identical. The small increase in the m/z = 15 signal in the negative-going scan (Fig. 76e), indicates that even after the first positive-going potential scan up to 1.3 V, some $CH_{x,ad}$ species remain on the surface, which can be desorbed as methane in the H_{upd} range {IWAS94}{WANG04O}.

The results of the second adsorbate stripping experiment, which was performed after the adsorption of ethanol at 0.4 V for 25 s, are shown in Fig. 77, as open circles. The general shape and features are essentially identical to the adsorbate stripping experiment after ethanol adsorption for 300 s and therefore not discussed in detail. In the potential regime between 0.5 and 0.85 V, the amounts of $^{12}CO_2$ and $^{13}CO_2$ are equivalent to 7.8 nC and 7.2 nC, which corresponds to 19% and 17.4% of an adlayer that is saturated with CO from the gas phase (41.4 nC), respectively. The finding that significantly more $^{12}CO_2$ than $^{13}CO_2$ is formed is surprising, although in an earlier publication by Schmiemann et al. a similar observation was reported {SCHM94}. However, based on the *in situ* ATR-FTIR spectra it can be related to an experimental artifact. Already before ethanol was introduced to the cell, small amounts of $^{12}CO_{ad}$ are detected on the surface via IR spectroscopy, most likely due to $^{12}CO_{ad}$ formation upon decomposition of very strongly adsorbed ethanol residues. The coverage of $^{12}CO_{ad,}$ which build-up already before the Pt electrode was exposed to ethanol, is equal to about 5% of a saturated CO adlayer. Therefore, its contribution to the $^{12}CO_2$ formation can be estimated to be about 2 nC. After this correction, the amount of $^{12}CO_2$ formed in the potential regime

between 0.5 and 0.85 V corresponds to 5.8 nC, which is about 80% of the amount of $^{13}CO_2$ formed in this potential regime.

Finally, the results of the potentiodynamic adsorbate stripping experiment, which was performed after ethanol adsorption at 0.4 V for 25 s followed by an immediate potential step to 0.06 V (see Fig. 75 filled triangles), are presented in Fig. 77, as filled triangles. The Faradaic current shows i) a slightly suppressed $H_{upd,}$ due to the presence of $CO_{ad,}$ and ii) a small peak at about 0.67 V, which can be assigned to the oxidation of CO_{ad} to CO_2. The amounts of $^{12}CO_2$ and $^{13}CO_2$ formed in the first positive-going scan between 0.5 and 0.85 V, correspond to 3.8 and 4.5 nC, which is equivalent to 9.2 and 10.8% of a saturated CO adlayer, respectively. However, also in this adsorption transient, a $^{12}CO_{ad}$ coverage of about 5% was formed already before the Pt electrode was exposed to ethanol containing solution at 0.4 V. After this correction, the $^{12}CO_{ad}$ coverage resulting from adsorption/oxidation of ethanol at 0.4 V is about 40% of that $^{13}CO_{ad}$.

An interesting finding is that the overall CO_{ad} coverage differs significantly, when ethanol is adsorbed for 25 s at 0.4 V, and this potential is held for additional 5 min. in ethanol free solution, or adsorbing ethanol also for 25 s, but followed by potential step to 0.06 V. In the first experiment, an overall CO_{ad} coverage of 27 % was determined, whereas for the latter experiment, this value is only 14%. In both ethanol adsorption transients (see previous section), the integral band intensity of adsorbed acetyl species at t = 55 s was equal to 0.05 cm^{-1}. This corresponds to a coverage of 7 % (0.05 cm^{-1} × 1.4 ML/cm^{-1}) of a Pt monolayer, using the relation between acetyl intensity and coverage, as derived in section 6.1.2.3. When the precursor for CO_{ad} formation, i.e., adsorbed acetyl species, are desorbed upon the potential step to 0.06 V, the CO_{ad} coverage did not change during the waiting time at 0.06 V. However, if the potential is kept at 0.4 V in ethanol free solution, the decomposition of 0.07 monolayers of adsorbed acetyl resulted in the formation of an additional CO_{ad} coverage, which is equivalent to 12.5 % of a Pt monolayer, taking into account that one adsorbed acetyl species decomposes to 1.8 CO_{ad} molecules (see above). This value is in very good agreement with the quantitative adsorbate stripping results, which revealed that the total CO_{ad} coverage is larger by about 13% of a Pt ML when ethanol was adsorbed for 25 s at 0.4 V and keeping the potential constant in ethanol free solution for additional 5 min.

6.2.2.4 Discussion

As mentioned in the introduction, it is generally accepted that for potentials ≥ 0.4 V both carbon atoms of ethanol can be converted to CO_{ad}. However, the mechanistic picture in which adsorbed acetyl species decompose to CO_{ad} and $CH_{x,ad}$ {HITM94}{IWAS94}{SHAO05} and the latter species are subsequently oxidized further to CO_{ad} is not convincing, especially for a potential of 0.4 V, which is below the onset of OH_{ad} formation on Pt electrodes {Clim06}. Furthermore, the very similar values for the ratio of the $^{12}CO_{ad}/^{13}CO_{ad}$ coverage in the initial stages of ethanol adsorption (68% based on the IR data in section 6.2.2.2) and that obtained after adsorption of ethanol for 5 min. and subsequent waiting at 0.4 V for additional 5 min. in ethanol free solution (82% based on the DEMS data in section 6.2.2.3), can hardly be explained based on the above described mechanism: If the conversion of the methyl group of ethanol to CO_{ad} is rather fast already at 0.4 V, which was indicated by the similar rates for $^{13}CO_{ad}$ (0.011 molecules × $site^{-1}$ × s^{-1}) and $^{12}CO_{ad}$ (0.005 molecules × $site^{-1}$ × s^{-1}) formation, it is expected that after ethanol adsorption at 0.4 V and waiting at this potential for 5 min. in ethanol free solution, the coverage of $^{12}CO_{ad}$ and $^{13}CO_{ad}$ should be identical. This, however, is in contrast to $^{12}CH_3{}^{13}CH_2OH$ adsorbate stripping experiments, where it was found that the $^{12}CO_{ad}$ coverage after ethanol adsorption for 5 min. is only about 82% of that of $^{13}CO_{ad}$. These findings indicate that either i) the CO_{ad} formation rate determined from the $^{12}CO_L$ is strongly overestimated, possibly due to intensity transfer from $^{13}CO_L$ to $^{12}CO_L$, and the CO_{ad} formation rate from the methyl group is in fact very small, or ii) the mechanistic proposal that adsorbed acetyl species decompose to CO_{ad} and $CH_{x,ad}$ {IWAS94}{HITM94}{SHAO05} is oversimplified.

This question can be answered via the combined "electrolyte exchange/potential step" experiment, presented in the section 6.2.2.2. According to the above mechanistic model {HITM94}{IWAS94}{SHAO05} adsorbed acetyl species decompose to CO_{ad} and $CH_{x,ad}$. If the oxidation of $^{12}CH_{x,ad}$ to $^{12}CO_{ad}$ is much slower compared to the direct formation of $^{13}CO_{ad}$, it is expected that $^{12}CH_{x,ad}$ accumulates on the Pt surface upon ethanol adsorption at 0.4 V. A potential step from 0.4 to 0.06 V, should result in a very fast removal of $^{12}CH_{x,ad}$, due to desorption as methane, whereas $^{13}CO_{ad}$ remains on the Pt surface. Hence, the precursor for $^{12}CO_{ad}$ formation is desorbed, the subsequent adsorbate stripping experiment should show that mainly $^{13}CO_{ad}$ has formed. In clear contrast, the results of the "electrolyte exchange/potential step" experiment demonstrated that the ratio of $^{12}CO_{ad}/^{13}CO_{ad}$ coverage is

only slightly decreased, indicating that the formation of $^{12}CO_{ad}$ is indeed quite fast already at 0.4 V. However, the question remains, why upon adsorption of ethanol at 0.4 V for 5 min. and subsequent waiting at this potential in ethanol free solution for additional 5 min., the ratio between $^{12}CO_{ad}$ and $^{13}CO_{ad}$ does not increase to 1 but remains at about 0.82. This is tentatively explained by a modified mechanistic picture for the decomposition of adsorbed acetyl species. In a first step, adsorbed acetyl changes its configuration and binds to surface via both carbon atoms, by loosing one hydrogen atom of the methyl group (See scheme below). This adsorption configuration can react in two different ways: it decomposes i) to CO_{ad} and adsorbed CH_xO_{ad} species in a concerted reaction with water from the electrolyte, or ii) to CO_{ad} and $CH_{x,ad}$ species either via the loss of an additional hydrogen or the addition of an electron or an hydrogen atom from the Pt surface. The CH_xO_{ad} species is rapidly converted to $^{12}CO_{ad}$, whereas $CH_{x,ad}$ species are assumed to be rather stable and can not be further converted to CO_{ad} at 0.4 V under the present experimental conditions. In this mechanistic model, the $^{12}CO_{ad}$ formation rate can be rather fast, even at potentials where adsorbed oxygen species are not available on the Pt surface, e.g., at 0.4 V. Furthermore, the final coverage of $^{12}CO_{ad}$ and $^{13}CO_{ad}$ will depend sensitively on the reaction of the CH_2CO_{ad} intermediate (see Fig. 78), which either decomposes to $^{13}CO_{ad}$ and $^{12}CH_2OH_{ads}$ or to $^{13}CO_{ad}$ and a rather

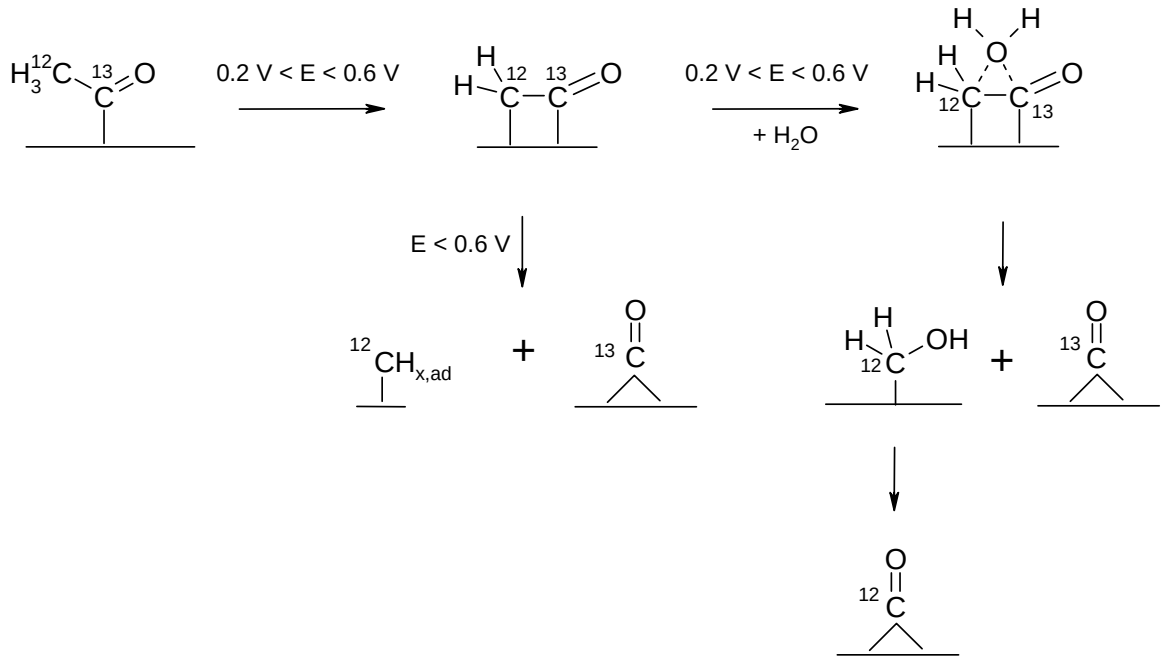

Fig. 78: Schematic picture for the decomposition of adsorbed acetyl and the formation of CO_{ad}.

inactive $^{12}CH_{x,ad}$ species. Taking into account, that at 0.2 V essentially only $^{13}CO_{ad}$ and hardly any $^{12}CO_{ad}$ is formed, this suggests that at this potential conversion of the CH_2CO_{ad} intermediate to $CH_{x,ad}$ species is preferred, e.g., by the addition of H_{upd}. At 0.4 V, where the H_{upd} coverage is already very small, the reaction of the CH_2CO_{ad} intermediate with bulk water becomes favorable, and about 80% of the carbon atoms of the methyl group of ethanol are converted to CO_{ad}. Finally, at 0.6 V, the methyl group can be converted completely to CO_{ad} and subsequently be oxidized to CO_2. Here it should be mention that at 0.6 V, the reaction pathway via decomposition of adsorbed acetyl contributes only to about 2-3 % to the overall ethanol oxidation reaction at room temperature.

6.2.3 Summary

Employing the *in situ* ATR-FTIRS/DEMS flow cell set-up in combination with carbon labeled ethanol ($^{12}CH_3{}^{13}CH_2OH$) new insights into the fundamental mechanism and the kinetics of the ethanol electrooxidation were obtained. In the potentiodynamic ethanol bulk oxidation, it was shown qualitatively that both carbon atoms of ethanol can form CO_{ad}, which can be further oxidized to CO_2. Based on potentiostatic electrolyte exchange experiments, for the first time the rates for the CO_{ad} formation from the methyl and the alcohol group could be determined separately, as a function of the adsorption potential. At 0.2 V, only $^{13}CO_{ad}$ formation was detected and the formation rate was equal to 0.002 molecules $\times$ site^{-1} $\times$ s^{-1}. At 0.4 V, CO_{ad} formation from both carbon atoms of ethanol is possible and values of 0.005 and 0.011 molecules $\times$ site^{-1} $\times$ s^{-1} were derived for the CO_{ad} formation rate from the methyl and the alcohol group of ethanol, respectively. At 0.6 V, both rates were similar, having values of 0.0036 and 0.0034 molecules $\times$ site^{-1} $\times$ s^{-1} for $^{13}CO_{ad}$ and $^{12}CO_{ad}$ formation. The surprisingly fast formation of CO_{ad} from the methyl group at a potential where adsorbed oxygen species are not present on the Pt surface, i.e., at 0.4 V, was further supported in quantitative potentiodynamic adsorbate stripping experiments and was tentatively explained by a modified mechanistic picture for the decomposition of adsorbed acetyl species. This includes a CH_2CO_{ad} intermediate, which either decomposes to $^{13}CO_{ad}$ and $^{12}CH_2OH_{ads}$ in a concerted reaction with water from the solution or to $^{13}CO_{ad}$ and a rather inactive $^{12}CH_{x,ad}$ species. In this mechanism the formation of CO_{ad} from the methyl group of ethanol is possible without the necessity of adsorbed oxygen species on the Pt surface.

6.3 Adsorption/oxidation of CH_3CD_2OH - Kinetic Isotope effects

6.3.1 Introduction

As already mentioned before (section 5.3), kinetic isotope effects (KIEs) have long been used to unravel mechanistic details in chemical and electrochemical reactions {WIEC77}{MELA80}{TRIP91}{HOLZ94}. The most challenging aspect, however, is to relate a KIE derived from the reaction kinetics to a specific rate limiting step, since in a complex reaction network different reaction pathways and reaction steps contribute to the overall reaction kinetics. It was demonstrated for the adsorption/oxidation of formic acid (section 5.3), how the KIE for a specific reaction pathway, i.e., dehydration of formic acid to CO_{ad}, can be determined quantitatively, based on electrochemical *in situ* ATR-FTIR spectroscopy measurements. The ethanol oxidation reaction is even a more complex reaction network, and the KIE in the CO_{ad} formation upon adsorption of deuterated ethanol was not determined in an electrochemical environment up to now.

Adsorbed acetyl species were identified above as the precursor for C-C bond splitting in the course of ethanol electrooxidation (see sections 6.1 and 6.2). Employing ethanol, which is deuterated only at the carbon atom of the alcohol group (CH_3CD_2OH), the expected KIE effects can be qualitatively predicted. For the formation of an adsorbed acetyl, both C-H bonds at the α-carbon have to be split, and a kinetic isotope effect in the formation rate of this species is expected, when CH_3CD_2OH is used. On the other hand, since the adsorbed acetyl species does not contain any C-D bond, its decomposition to CO_{ad} should show no kinetic isotope effect. Consequently, the relation between the CO_{ad} formation rate upon adsorption/oxidation of CH_3CD_2OH, and the intensity/coverage of the adsorbed acetyl species should follow the same equation, as it was derived for adsorption/oxidation of CH_3CH_2OH for an adsorption potential of 0.4 V, including the value for the rate constant k (see section 6.1.2.3).

In the present section, the KIE in the ethanol oxidation reaction will be investigated, based on *in situ* ATR-FTIRS measurements employing CH_3CD_2OH. I will start with the presentation of results that were recorded during potentiostatic electrolyte exchange experiments at 0.2, 0.4 and 0.6 V. The temporal evolution of the adsorbed species will be analyzed and the potential dependent CO_{ad} formation rates are determined quantitatively (section 6.3.2.1). A comparison of the CH_3CD_2OH and CH_3CH_2OH reaction kinetics is presented in section 6.3.2.2, focusing on the KIE in the formation of adsorbed acetyl and the CO adlayer build-up. Potentiostatic adsorbate stripping experiments are presented in section 6.3.2.3. An increase in the CO_{ad}

coverage in the absence of ethanol in the solution can be quantitatively related to the decomposition of adsorbed acetyl species, and thus support the mechanistic proposal that adsorbed acetyl species are the precursor for CO_{ad} formation. Finally, I will present and discuss results of a potential step experiment, focusing on the adsorption behavior and on the formation of adsorbed acetyl species (section 6.3.2.4). Two questions are tackled in this section: i) are adsorbed acetyl species in an adsorption-desorption equilibrium or are they irreversibly adsorbed, and ii) are adsorbed acetyl species a reactive intermediate for the formation of acetaldehyde or do they result from the formation and adsorption of acetaldehyde? The mechanistic and kinetic insights into the electrooxidation of ethanol are summarized in section 6.3.3.

6.3.2 Results

6.3.2.1 Potentiostatic adsorption/oxidation of CH_3CD_2OH

In Fig. 79, the development of the Faradaic currents (a) and the integral band intensities of CO_L (b), adsorbed acetyl species (c) and adsorbed acetate (d), recorded upon electrolyte exchange experiments from 0.5 M H_2SO_4 to 0.044 M CH_3CD_2OH containing solution at t = 30 s and back to 0.5 M H_2SO_4 at t = 300 s, are plotted versus time for adsorption potentials of 0.2 (filled squares), 0.4 (open circles) and 0.6 V (filled triangles), respectively.

At 0.2 V, only very small values for the Faradaic are measured during the electrolyte exchange experiment. This is attributed to the presence of H_{upd}, which strongly reduces the ethanol adsorption/oxidation rate under these conditions {WANG04B}. At 0.4 V and 0.6 V, the Faradaic current increases steeply, passes through a maximum and decreases upon ongoing ethanol adsorption/oxidation. It decreases immediately to zero, when the cell is rinsed with ethanol free solution at t = 300 s. Furthermore, the initial current increase as well as the steady-state currents strongly increase with potential from 0.2 to 0.6 V.

The development of the CO_L band intensities upon ethanol adsorption at 0.2 V (filled squares), 0.4 V (open circles) and 0.6 V (filled triangles), respectively, are plotted in Fig. 79b. Upon ethanol exposure at 0.2 V, the integral band intensity of CO_L increases slowly with a constant slope. At 0.4 and 0.6 V, the initial increase is much faster, compared to 0.2 V, and the integral band intensity of CO_L reaches an essentially constant value with time after about 150 s. The highest final value for the CO_L band intensity is reached at 0.4 V. The very slow

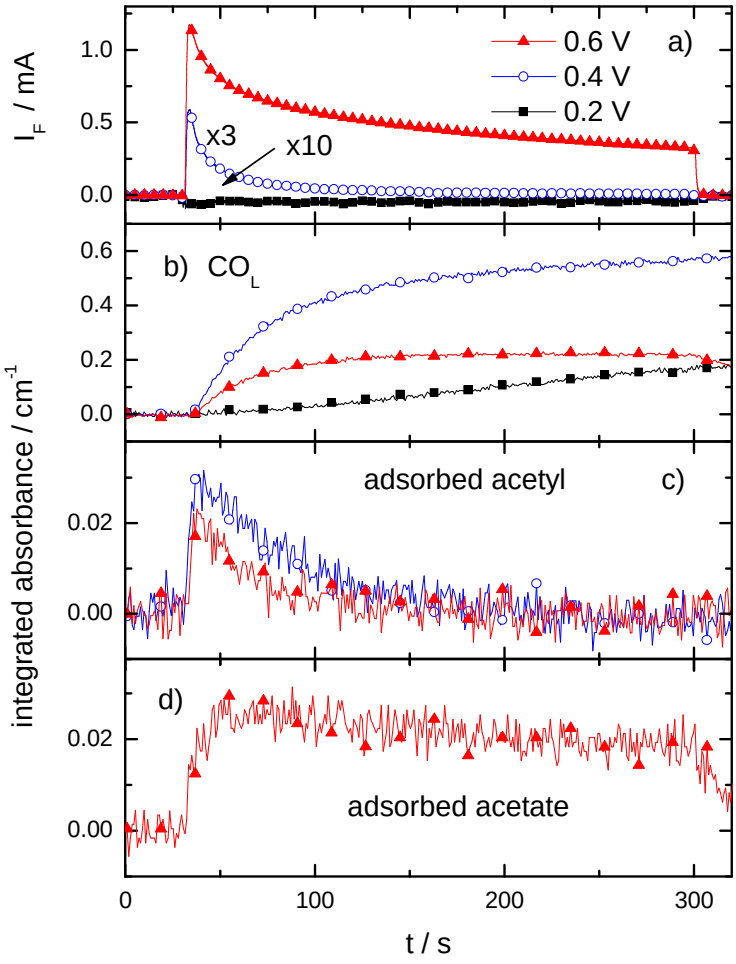

Fig. 79: Temporal evolution of the Faradaic currents (a) and the integral band intensities of CO_L (b), adsorbed acetyl species (c) and adsorbed acetate (d), recorded upon an electrolyte exchange experiments from 0.5 M H_2SO_4 to 0.044 M CH_3CD_2OH containing solution (t = 30 s) and back to 0.5 M H_2SO_4 (t = 300 s) at 0.2 (filled squares), 0.4 (open circles) and 0.6 V (filled triangles), respectively. The Faradaic current was multiplied with a factor of 10 and 3 for CH_3CD_2OH adsorption at 0.2 and 0.4 V, respectively. Electrolyte flow rate: 50 µl × s^{-1}.

CO_{ad} formation at 0.2 V is attributed to the presence of H_{upd}, which hinders the adsorption/oxidation of ethanol {WANG04O}{WANG06I}. The smaller steady-state CO_{ad} coverage at 0.6 V is attributed to the onset of CO_{ad} oxidation to CO_2 (DEMS data, not shown). Consequently, the CO_L intensity decreases upon rinsing with ethanol free solution at t = 300 s under these conditions, due to the ongoing oxidation of CO_{ad} to CO_2 without further CO_{ad} formation from ethanol adsorption/oxidation.

The development of the integral band intensity of adsorbed acetyl upon ethanol adsorption at 0.4 V (open circles) and 0.6 V (filled triangles), respectively, is plotted in Fig. 79c (Note: contributions of the water bands to the integral band intensity of adsorbed acetyl were removed; for details see section 3.8). At 0.2 V, adsorbed acetyl species can not be detected. The shape of the intensity of adsorbed acetyl versus time plots is identical for ethanol

adsorption at 0.4 and 0.6 V, with a steep initial increase and a subsequent decrease to values below the detection limit during ongoing ethanol adsorption. Furthermore, the integral band intensity of adsorbed acetyl is higher at 0.4 V, compared to 0.6 V, which qualitatively correlates with the steeper increase in the integral band intensity of CO_L at 0.4 V.

Finally, the integral band intensity of adsorbed acetate is plotted versus time in Fig. 79d, for ethanol adsorption at 0.6 V. At 0.2 and 0.4 V, adsorbed acetate can not be detected. Upon ethanol exposure at 0.6 V, the integral band intensity of adsorbed acetate increases steeply and then decreases slightly with ongoing ethanol adsorption/oxidation. The presence of adsorbed acetate indicates the oxidation of ethanol to acetic acid at 0.6 V, in agreement with earlier reports {IWAS94}{HITM94}{TORR03}. Since adsorbed acetate is in a fast adsorption/desorption equilibrium with acetic acid, its intensity decreases when the cell is rinsed with ethanol free solution at t = 300 s, due to desorption of adsorbed acetate as acetic acid {CORR88A}{HEIN04}.

For a quantitative analysis of the above data, the integral band intensity of CO_L can be converted into the CO_{ad} coverage via the relations described in section 3.7. The resulting plots of the CO_{ad} coverage versus time are shown in Fig. 80. The shapes of the curves are essentially identical to that of the integral band intensity of CO_L described above, and are therefore not described in detail. The final CO_{ad} coverage at the end of the adsorption

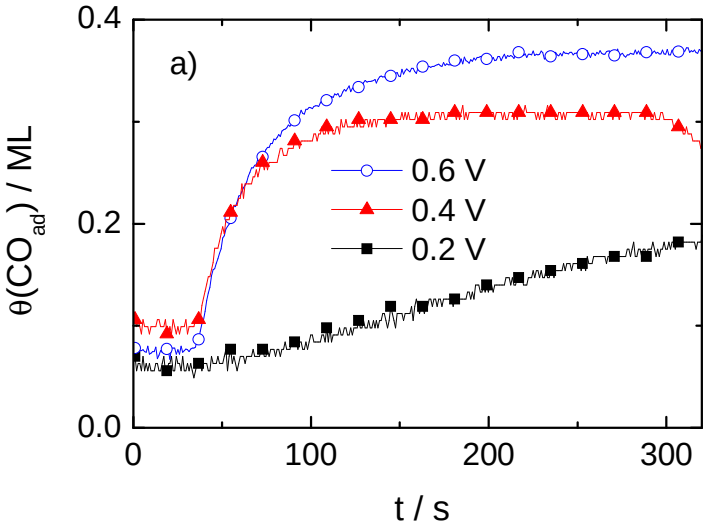

Fig. 80: Temporal evolution of the CO_{ad} coverage upon an electrolyte exchange from 0.5 M H_2SO_4 to 0.044 M CH_3CD_2OH at t = 30 s and back to ethanol free solution at t = 300 s, at 0.2 V (filled squares), 0.4 V (open circles) and 0.6 V (filled triangles), respectively.

transient (t = 300s) are equal to about 18%, 37% and 30% of a Pt monolayer, for ethanol adsorption at 0.2, 0.4 and 0.6 V, respectively. From the initial slope of the CO_{ad} coverage versus time plot, the CO_{ad} formation rates on a clean Pt surface can be determined and values of 5×10^{-4}, 0.008 and 0.007 molecules $\times$ site^{-1} $\times$ s^{-1} are derived for CH_3CD_2OH adsorption at 0.2, 0.4 and 0.6 V, respectively. These values will be compared to the CO_{ad} formation rates upon adsorption of CH_3CH_2OH in the next section.

6.3.2.2 Comparison of the reaction kinetics (CH_3CH_2OH vs. CH_3CD_2OH)

In this section, the influence of deuteration on the ethanol adsorption/oxidation kinetics will be analyzed, based on a comparison of adsorption transients employing CH_3CH_2OH and CH_3CD_2OH. The results of the transients were already presented before (CH_3CH_2OH in section 6.1.2.2 and CH_3CD_2OH in section 6.3.2.1) and are re-plotted in the present section, for convenience.

In Fig. 81, the Faradaic current response (a) and the integral band intensity of CO_L(b) and adsorbed acetyl species (c) recorded upon an electrolyte exchange to CH_3CH_2OH (filled squares) and CH_3CD_2OH (open circles), respectively, are shown for an adsorption potential of 0.4 V. When CH_3CD_2OH is used the shape of Faradaic current response is very similar to that of CH_3CH_2OH except of a 1.8 times higher maximum value in the initial spike and in the steady-state current at about t = 300 s. The differences in the Faradaic current between deuterated and undeuterated ethanol are in agreement with literature data and are explained by a kinetic isotope effect in the oxidation of ethanol to acetaldehyde, which requires the splitting of C-H or C-D bonds, respectively.

In Fig. 81c, the integral absorbance of adsorbed acetyl species, is shown for both above mentioned electrolyte exchange experiments, using CH_3CH_2OH (filled squares) and CH_3CD_2OH (open circles). The shapes of the integral band intensities of adsorbed acetyl species are very similar in both cases. However, the maximum value is about 1.7 times higher when unlabeled ethanol is adsorbed (0.051 cm^{-1}) compared to deuterated ethanol (0.03 cm^{-1}). This difference can be attributed to a KIE in the rate constant for the formation of acetaldehyde/adsorbed acetyl species, which requires the splitting of two either one/two C-H or two C-D bonds.

The development of the integrated band intensity of CO_L is plotted in Fig. 81b, for adsorption of CH_3CH_2OH (filled squares) and CH_3CD_2OH (open circles), respectively. The shape for the

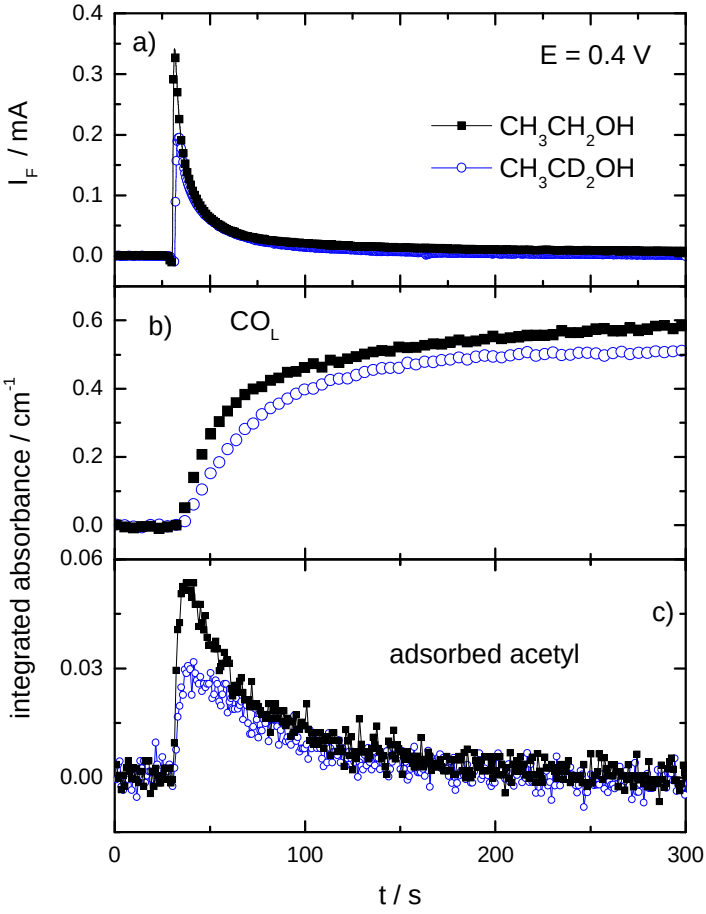

Fig. 81: Temporal evolution of a) Faradaic current, b) integrated band intensity of adsorbed CO_L (squares) and CO_M (circles) and c) integrated band intensity of adsorbed acetyl detected at 1635 cm^{-1} during adsorption of CH_3CH_2OH (filled symbols) and CH_3CD_2OH (open symbols) at 0.4 V.

CO_{ad} intensity development with time for the unlabeled and the deuterated ethanol is identical and was already discussed before. However, for the initial CO_{ad} formation rates values of 0.014 and 0.008 molecules $\times$ $site^{-1}$ $\times$ s^{-1} are obtained for adsorption of unlabeled and labeled ethanol, respectively, indicating that the CO_{ad} formation rate is about 1.7 times faster, when unlabeled ethanol is adsorbed. The above described data perfectly fit to the model, in which the decomposition of adsorbed acetyl species is the rate limiting step for the CO_{ad} formation. A KIE in the formation of adsorbed acetyl resulted in a 1.7 times smaller coverage of adsorbed acetyl in the initial stages of CH_3CD_2OH adsorption, compared to the adsorption/oxidation of CH_3CH_2OH. For the decomposition of adsorbed acetyl to CO_{ad}, no KIE is expected, since all C-D bonds were split already upon the formation of adsorbed acetyl. A 1.7 times smaller coverage of the precursor for CO_{ad} formation, i.e., adsorbed acetyl, correlates very well with a 1.7 times smaller initial CO_{ad} formation rate for the adsorption/oxidation of CH_3CD_2OH. In other words, the effective KIE obtained for the CO_{ad}

formation rate can be related to a KIE in the rate constant for the formation of acetaldehyde/adsorbed acetyl and not in the C-C bond splitting rate itself.

In Fig. 82, the Faradaic current response (a) and the integral band intensity of CO_L(b) and adsorbed acetyl species (c) recorded upon an electrolyte exchange to CH_3CH_2OH (filled squares) and CH_3CD_2OH (open circles), respectively, are shown for an adsorption potential of 0.2 V. For the adsorption/oxidation of CH_3CH_2OH a positive Faradaic current is measured in the first about 50 s after the electrolyte exchange to 0.044 M ethanol containing solution, indicating the oxidation of ethanol to acetaldehyde. For the adsorption/oxidation of CH_3CD_2OH, however, no oxidative Faradaic current can be detected at all, within the accuracy of the measurements. This difference is attributed to a KIE in the ethanol oxidation to acetaldehyde, which requires the splitting of one C-H bond and one O-H bond. Although the

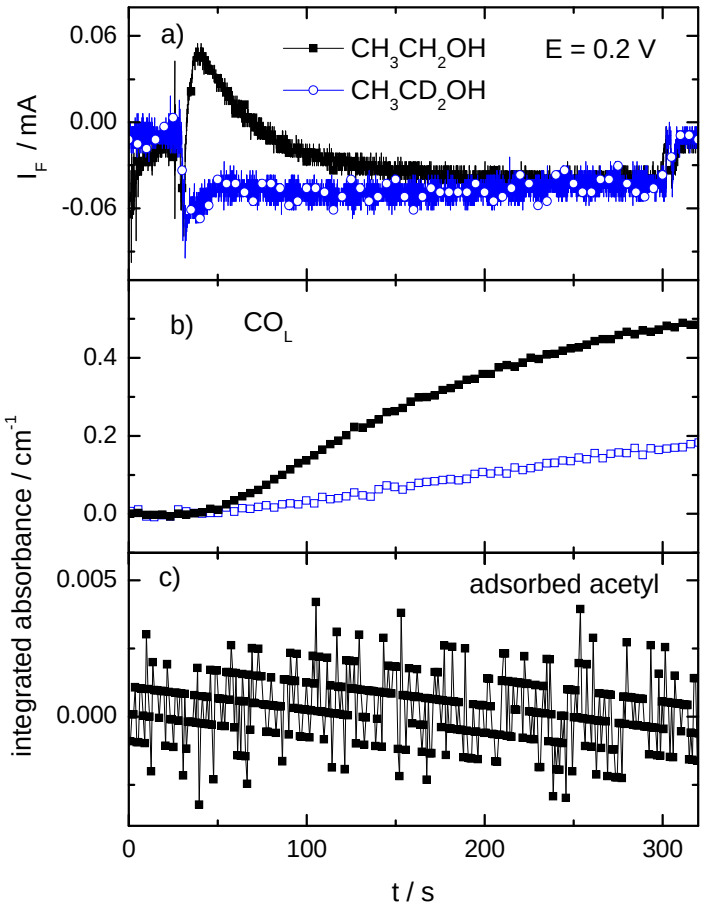

Fig. 82: Temporal evolution of a) Faradaic current, b) integrated band intensity of adsorbed CO_L (squares) and CO_M (circles) and c) integrated band intensity of adsorbed acetyl detected at 1635 cm^{-1} during adsorption of CH_3CH_2OH (filled symbols) and CH_3CD_2OH (open symbols) at 0.2 V.

KIE for the oxidation of ethanol at 0.2 V can not be determined precisely (between 5 ± 2), it is larger compared to 0.4 V, where the Faradaic currents only differed by a factor of about 2.

The coverage of adsorbed acetyl species at 0.2 V (Fig. 82c) is significantly smaller compared to ethanol adsorption at 0.4 V. It can not be detected for the adsorption of deuterated ethanol and within the experimental accuracy it is also hardly detectable for the adsorption of unlabeled ethanol. The strongly reduced intensity of adsorbed acetyl species at 0.2 V, compared to 0.4 V can be understood when taking into account i) the much smaller Faradaic current response for the adsorption/oxidation of both unlabeled and labeled ethanol at 0.2 V, compared to the Faradaic current at 0.4 V. This in turn results in a decreased formation rate of acetaldehyde, which is the precursor for the formation of adsorbed acetyl, and ii) the rate constant for C-C bond splitting is proposed to increases with decreasing electrode potential {FAN04B}. Both trends result in a strongly reduced steady-state intensity/coverage of adsorbed acetyl at 0.2 V, since its potential dependend formation rate is lower and the rate constant for its decomposition is higher at compared to 0.4 V.

The development of the integral band intensity of CO_L during the adsorption of CH_3CH_2OH (filled squares) and CH_3CD_2OH (open circles) is plotted in Fig. 82b. The CO_L intensity starts to increase continuously, after the electrolyte exchange at t = 30 s for the adsorption of both unlabeled and labeled ethanol. The initial CO_{ad} formation rates are 0.002 and 5×10^{-4} molecules $\times$ site^{-1} $\times$ s^{-1} for the adsorption of unlabeled and deuterated ethanol, respectively. Hence the CO_{ad} formation rate upon adsorption of CH_3CH_2OH is about 4 times faster compared to the adsorption of CH_3CD_2OH.

In good agreement with the proposal of adsorbed acetyl being the precursor for CO_{ad} formation and its decomposition being the rate liming step for C-C bond splitting, the larger KIE in the oxidation of ethanol and hence the formation of adsorbed acetyl species at 0.2 V, compared to 0.4 V, resulted in larger differences in the CO_{ad} formation rate at 0.2 V. Furthermore, the much smaller steady-state intensity of adsorbed acetyl species correlates well with a much smaller rate for CO_{ad} formation. Finally, it is important to emphasize that the coverage of the precursor for CO_{ad} formation, i.e., adsorbed acetyl species, is below the detection limit for ethanol adsorption at 0.2 V. This indicates that under these conditions the rate limiting step for the CO_{ad} formation is not the C-C bond breaking but rather the ethanol adsorption and subsequent oxidation to acetaldehyde and acetyl species.

The Faradaic current response (a), the integral band intensity of CO_L, CO_M (b) and adsorbed acetyl species during the electrolyte exchange experiment at 0.6 V are shown in Fig. 83. For the adsorption/oxidation of both CH_3CH_2OH and CH_3CD_2OH, the Faradaic currents increase steeply after the electrolyte exchange at t = 30 s, and subsequently decrease to constant positive values. At t = 300 s, when the electrolyte was changed back to ethanol free solution, the Faradaic currents immediately drop to zero. The initial current peak and the steady-state oxidative currents are about 1.2 times higher when unlabeled ethanol is used, although the CO_{ad} coverage at any time is higher in the latter experiment (see below). This finding indicates that also at 0.6 V, the oxidation of deuterated ethanol shows a KIE.

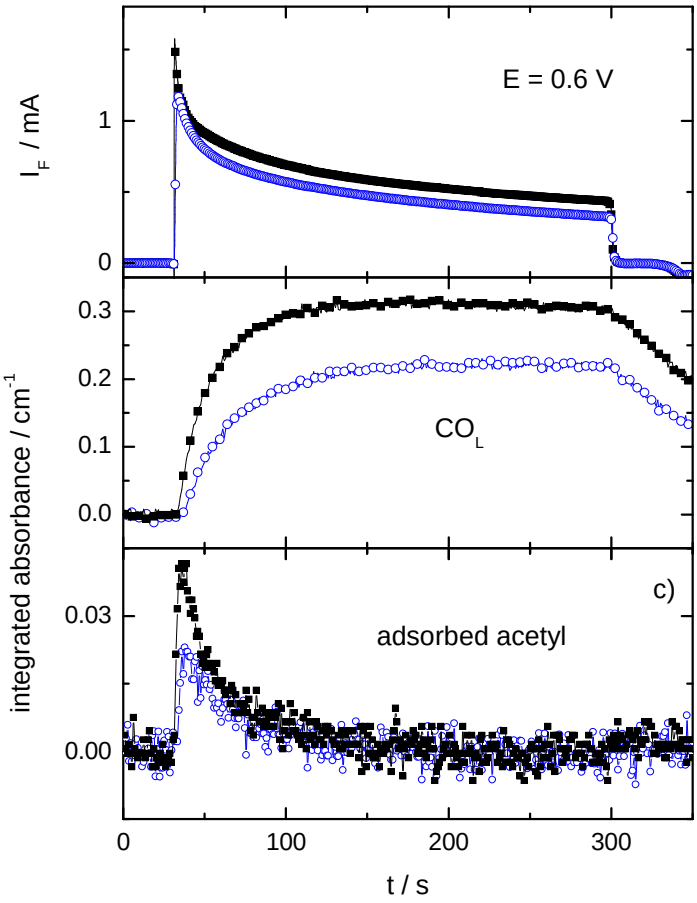

Fig. 83: Temporal evolution of a) Faradaic current, b) integrated band intensities of adsorbed CO_L (squares) and CO_M (circles) and c) integrated band intensity of adsorbed acetyl detected at 1635 cm^{-1} during an electrolyte exchange from 0.5 M H_2SO_4 to 0.044 M ethanol containing solutions at 0.6 V(filled squares: 0.044 M CH_3CH_2OH and open circles: 0.044 M CH_3CD_2OH).

CH_3CD_2OH (open circles). For both, unlabeled and deuterated ethanol, the shape of the integral band intensities follows the Faradaic current responses discussed above. They pass through an initial maximum and decrease to essentially zero at t = 150 s. The maximum value of the integrated intensity of adsorbed acetyl species is about 1.8 times larges when unlabeled ethanol is adsorbed, compared to the adsorption of deuterated ethanol. This can be explained by the KIE in the formation of adsorbed acetyl species, which requires the spitting of two C-D in the case of CH_3CD_2OH.

The development of CO_L intensities during the adsorption of CH_3CH_2OH (filled squares) and CH_3CD_2OH (open circles) is plotted in Fig. 83b. Upon exposure of the Pt electrode to ethanol containing solutions, the integral CO_L band intensity increases after the electrolyte exchange at t = 30 s and reaches a steady-value at about t = 100 s. The resulting steady-state CO_{ad} coverage is larger when CH_3CH_2OH is used, compared to the adsorption of CH_3CD_2OH. Upon the second electrolyte exchange to ethanol free base solution at t = 300 s, a decrease of the CO_L intensity is attributed to the oxidation of CO_{ad} to CO_2, without further CO_{ad} formation. From the initial increase in the CO_L band intensity, the CO_{ad} formation rates on a clean Pt surface can be determined (see section 6.1.2.2), whereas the CO_{ad} formation rates under close to steady-state conditions can be obtained from the decrease of the CO_L intensity upon rinsing (see section 6.1.2.2). For the initial CO_{ad} formation rate, values of 0.015 and 0.008 molecules $\times$ site^{-1} $\times$ s^{-1} are derived for the adsorption of CH_3CH_2OH and CH_3CD_2OH, respectively. From these values, an effective KIE of about 1.8 can be determined for the CO_{ad} formation on a clean Pt surface at 0.6 V. However, the CO_{ad} formation/oxidation rates under steady state conditions are very similar, having values of about 0.014 and 0.012 molecules $\times$ site^{-1} $\times$ s^{-1} for the adsorption of unlabeled and deuterated ethanol, respectively.

For the adsorption/oxidation of ethanol at 0.6 V, a KIE in the Faradaic current response was found, when using CH_3CD_2OH, which in turn resulted in a 1.8 times smaller coverage of adsorbed acetyl in the initial stages of ethanol adsorption. Furthermore, an identical value of 1.8 was also found for the KIE in the CO_{ad} formation rate on the clean Pt surface. This agrees quite well with the mechanistic picture, in which adsorbed acetyl species are the precursor for CO_{ad} formation and its subsequent decomposition is the rate limiting step for C-C bond splitting. A 1.8 times smaller initial acetyl coverage correlates quantitatively with a 1.8 times slower CO_{ad} formation rate for the adsorption of CH_3CD_2OH. Based on these data the measured KIE in the CO_{ad} formation can be assigned to a KIE in the formation of adsorbed acetyl species.

It needs to be mentioned that especially for the adsorption/oxidation of CH_3CH_2OH the maximum intensity of adsorbed acetyl species is significantly smaller at 0.6 V compared to the adsorption at 0.4 V, although its formation should be faster (higher Faradaic current) and the rate for C-C bond splitting was reported to decrease with increasing potential {FAN04B}. The slightly smaller intensity of adsorbed acetyl species at 0.6 V can be tentatively explained by the presence of activated oxygen species on the Pt surface, most likely OH-species, which can react with the adsorbed acetyl to form acetic acid {HITM94}{SHAO05}. Indeed, the formation of adsorbed acetate can be detected for potentials above 0.5 V via *in situ* ATR-FTIR spectroscopy (see section 6.1.2.1). Due to this second reaction pathway for adsorbed acetyl species, which becomes possible only for potentials above 0.55 V (onset of OH_{ad} formation {CLIM06}), the steady state coverage of adsorbed acetyl species is smaller for ethanol adsorption/oxidation at 0.6 V, compared to 0.4 V.

6.3.2.3 Potentiostatic CH_3CD_2OH adsorbate stripping

In this section, I will present results of two potentiostatic adsorbate stripping experiments to quantitatively confirm the mechanistic proposal that adsorbed acetyl species are the precursor for CO_{ad} formation. Similar to the measurements for the adsorption/oxidation of unlabeled ethanol (see section 6.1.2.3), two different CH_3CD_2OH electrolyte exchange experiments performed at 0.4 V will be presented. In both experiments, the electrolyte is first changed from 0.5 M H_2SO_4 to 0.044 M CH_3CD_2OH containing solution. Then, the electrolyte is changed back to 0.5 M H_2SO_4 after 300 s ('continuous ethanol adsorption') and 10 s ('decomposition transient') of ethanol exposure, respectively. The results of both CH_3CD_2OH adsorption transients are plotted in Fig. 84. Starting with the continuous CH_3CD_2OH adsorption/oxidation (Fig. 84, filled squares), the Faradaic current (Fig. 84a) increases right after the electrolyte exchange to 0.044 M CH_3CD_2OH at t = 30 s, reaches a maximum at t = 35 s and subsequently decreases to small values. According to the mass spectrometric response in similar potential step experiments, the positive current can be attributed to the formation of acetaldehyde. The initial Faradaic current response for the 'potentiostatic adsorbate stripping' experiment, i.e., CH_3CD_2OH adsorption/oxidation for 10 s (Fig. 84, open circles), is identical to the continuous ethanol adsorption, but it immediately drops to zero, when the cell is rinsed with ethanol free solution at t = 41 s (dashed line).

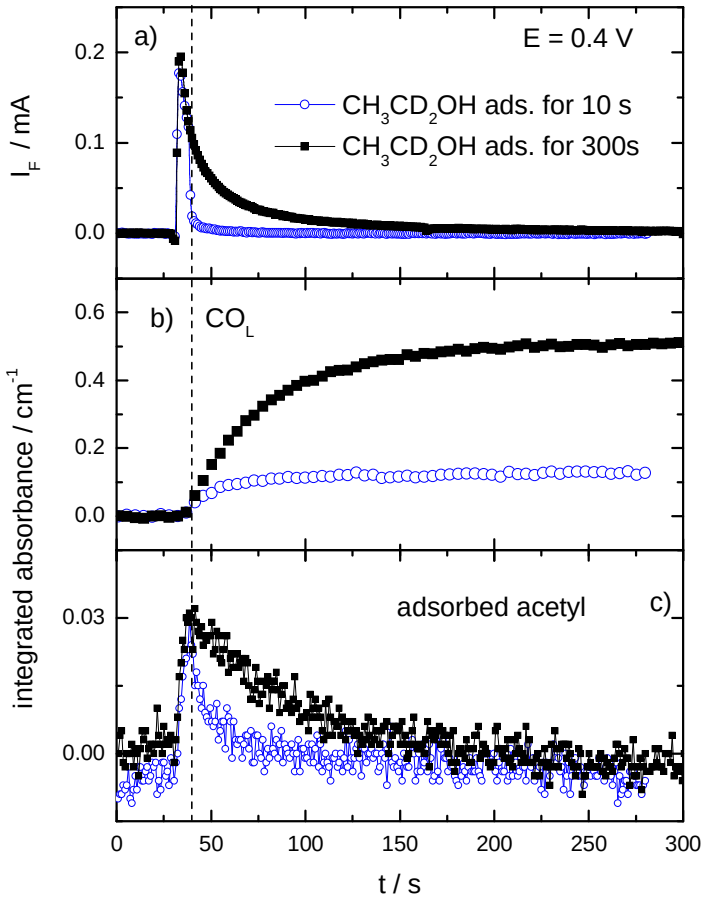

Fig. 84: Temporal evolution of a) Faradaic current, b) integrated band intensity of adsorbed CO_L and c) integrated band intensity of adsorbed acetyl detected (1635 cm^{-1}) during/after ethanol adsorption at 0.4 V for 10 s (open circles) and 300 s (filled squares), respectively. The dashed line indicates the time when the electrolyte was changed back from 0.044 M CH_3CD_2OH containing solution to 0.5 M H_2SO_4 after 10 s of ethanol adsorption.

The development of the integral band intensity of CO_L is shown in Fig. 84b, for 300 s (filled squares) and 10 s (open circles) of ethanol exposure, respectively. For the continuous ethanol adsorption the CO_L band intensity with time and reaches a constant value of about 0.57 cm^{-1} at t = 300s. When the electrode is exposed to ethanol for 10 s, the CO_L intensity also increases with time, but already saturates at t = 75 s. The final CO_L intensity in the latter experiment is only 0.14 cm-1, which is about 4 times lower compared to the continuous ethanol adsorption.

For a quantitative analysis of the CO_{ad} formation rate at 0.4 V, the CO_L band intensity can be converted into the CO_{ad} coverage via the relation described in section 3.7. The CO_{ad} coverage versus time plots resulting, upon ethanol adsorption for 300 s (filled squares) and 10 s (open circles), respectively, are shown in Fig. 85. From the initial increase of the CO_{ad} coverage, CO_{ad} formation rates of 0.008 molecules $\times$ $site^{-1}$ $\times$ s^{-1} are derived. Furthermore, in the absence

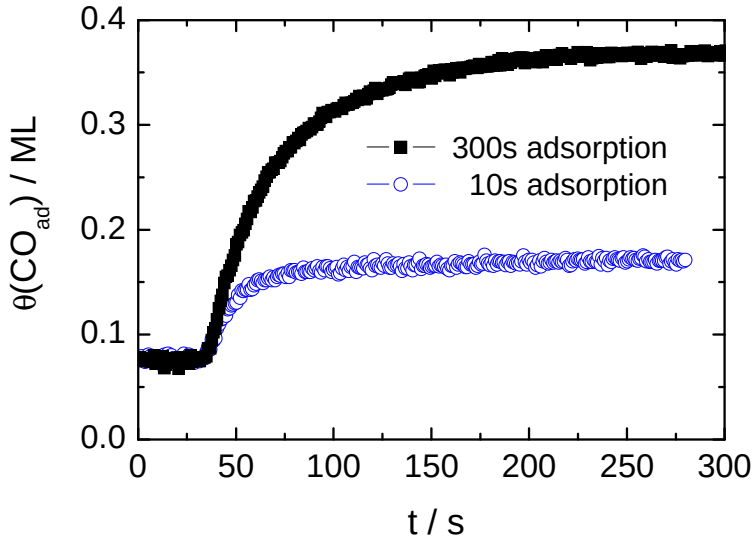

Fig. 85: Temporal evolution of the CO_{ad} coverage upon an electrolyte exchange experiment from 0.5 M H_2SO_4 to 0.044 M CH_3CD_2OH at t = 30 s (filled squares) and back to 0.5 M H_2SO_4 at t = 40 s (open circles).

of ethanol in the solution (Fig. 85, open circles, t = 41 – 280 s) the CO_{ad} coverage increases from about 11% to 17%, which is equivalent to 6% of a Pt ML. This increase can be quantitatively related to the decomposition of adsorbed acetyl species (see below).

The development of the integrated band intensities of adsorbed acetyl species is shown in Fig. 84c for 300 s of ethanol adsorption (filled squares). Upon exposure to ethanol at 0.4 V, the intensity of adsorbed acetyl species increases steeply, passes through a maximum and decreases slightly during ongoing ethanol adsorption. When ethanol was adsorbed only for 10 s (Fig. 84c, open symbols), the intensity of adsorbed acetyl species also increases steeply, passes through a maximum at t = 36 s and strongly decreases when the ethanol containing solution is exchanged to 0.5 M H_2SO_4 at t = 41 s (dashed line in Fig. 84), very similar to the findings for the adsorption/oxidation of unlabeled ethanol (see section 6.1.2.3). The decrease in adsorbed acetyl intensity is much more pronounced compared to continuous ethanol adsorption, reaching a value of essentially zero at t = 75 s. The integral band intensity of adsorbed acetyl is about 0.02 cm^{-1}, when the cell is rinsed with ethanol free solution at t = 41 s. Applying the relation between the integral band intensity of adsorbed acetyl and its coverage established in section 6.1.2.3, this corresponds to a coverage of adsorbed acetyl of 0.02 $cm^{-1} \times 1.4$ ML/cm^{-1}, which is equivalent to 2.8% of a ML. Assuming that in total one adsorbed acetyl decomposes to 1.8 CO_{ad} molecules (see section 6.2.2.3), in the absence of ethanol in the solution, the CO_{ad} coverage is expected to increase by about 5 % of a Pt ML, solely from the decomposition of adsorbed acetyl to CO_{ad}. This value is very close to the

increase of the CO_{ad} coverage of about 6%, which was determined from the increase in the integral band intensity of CO_L upon rinsing with ethanol free solution.

Based on potentiostatic adsorbate stripping experiments using CH_3CH_2OH (section 6.1.2.3), a quantitative description of the adsorbed acetyl decomposition kinetics by an appropriate rate law was derived (for details see section 6.1.2.3)

$$\frac{d[\theta(CO_{ad})]}{dt} = k \times \theta(A) \times 1.8 \times (1 - 2 \times \theta(CO_{ad}) - 2 \times \theta(A))^n$$

For the adsorption/oxidation of CH_3CD_2OH, a KIE in the formation of adsorbed acetyl species resulted in a decrease of its coverage (see previous section). Its subsequent decomposition, however, should show no KIE since all C-D bonds of CH_3CD_2OH were already split upon the formation of adsorbed acetyl. Therefore, the rate law derived for the decomposition of adsorbed acetyl species upon adsorption of CH_3CH_2OH should also be applicable to describe the decomposition kinetics of adsorbed acetyl formed upon adsorption/oxidation of CH_3CD_2OH, without any modifications of the reaction constant.

In Fig. 86, the derivatives of the CO_{ad} coverage versus time plots (Fig. 85) for CH_3CD_2OH adsorption for 10 (a) and 300 s (b), respectively, are shown as filled squares. The open circles correspond to the CO_{ad} formation rate, which was determined from the coverage of adsorbed acetyl species, employing the above rate equation and assuming first (left panel) and second order (right panel) in the number of free Pt sites (for details see section 6.1.2.3). For the decomposition kinetics of adsorbed acetyl species the rate constants, which were derived for the adsorption/oxidation of CH_3CH_2OH, were used. Especially for the assumption of first order in the number of free Pt sites (left panel in Fig. 86), the CO_{ad} formation rates determined via the integral band intensity of CO_L and via the coverage of adsorbed acetyl species, fit reasonably well. The finding that the rate equation for the decomposition of adsorbed acetyl, which was derived for the adsorption/oxidation of CH_3CH_2OH can be used without any modifications to determine the CO_{ad} formation rate upon adsorption/oxidation of CH_3CD_2OH, strongly supports the validity of the mechanistic model that adsorbed acetyl species are the precursor for the C-C bond splitting and that its decomposition is the rate limiting step for CO_{ad} formation. This model was used throughout Chapter 6 to explain the experimental findings.

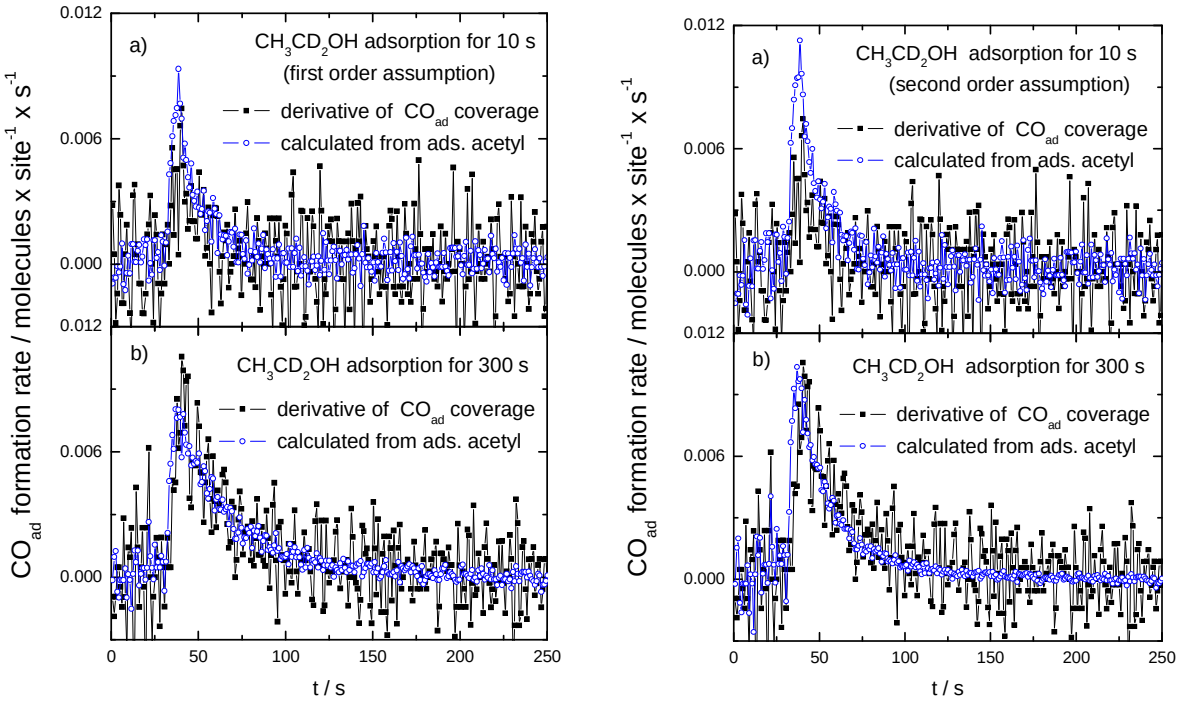

Fig. 86: Plot of the CO_{ad} formation rate versus time upon adsorption of CH_3CD_2OH for 10 s (a) and 300 s (b), using the assumption of first (left panel) and second (right panel) order in the number of free Pt sites. **Filled squares:** CO_{ad} formation rate determined via the derivative of the CO_{ad} coverage versus time plot in Fig. 85); **open circles**: CO_{ad} formation rate calculated via the intensity of adsorbed acetyl taken from Fig. 84; k = 0.13 s^{-1} for the left panel and 0.22 s^{-1} for the right panel (details see text).

However, it needs to be mentioned that based on the accuracy of the present data and the simplifying assumptions in the above rate equation for site occupation of adsorbed acetyl species and CO_{ad}, which were required to determine the number of free Pt sites (see section 6.1.2.3), it is hardly possible to decide whether the decomposition of adsorbed acetyl species follows first or second order kinetics in the number of free Pt sites.

6.3.2.4 Adsorption behavior and formation of adsorbed acetyl species

In this section, I will focus on the adsorption behavior and on the formation of adsorbed acetyl species. Two questions are addressed in this section: i) are adsorbed acetyl species in an adsorption-desorption equilibrium with acetaldehyde species or irreversibly adsorbed, and ii) are adsorbed acetyl species a reactive intermediate for the formation of acetaldehyde or do they result from the acetaldehyde formation? Two sequential pathways seem to be reasonable for the formation of adsorbed acetyl species and the reaction product acetaldehyde (see Fig 87):

Model 1:

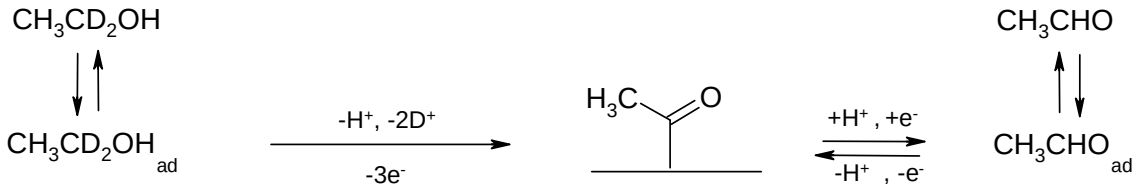

Model 2:

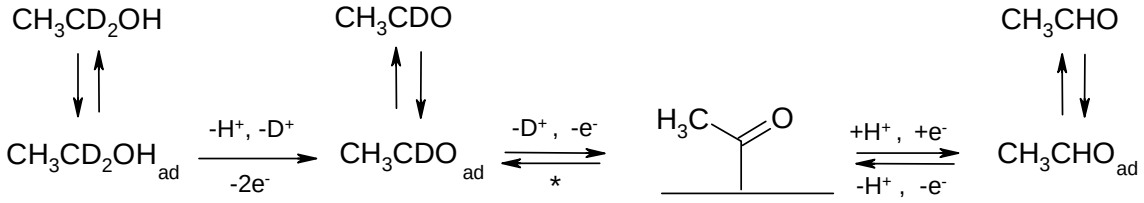

Fig. 87: Schematic drawing of two possible pathways for the formation of adsorbed acetyl species. For details see text (*Note: in 0.5 M H_2SO_4 this reaction pathway can be neglected due to the very low concentrations of D^+ compared to H^+).

In the first model, adsorbed acetyl species are directly formed by decomposition of adsorbed ethanol and they either decompose further to CO_{ad} and $CH_{x,ad}$ species (pathway not included in the figure) or they desorb reversibly as acetaldehyde. In the second model, ethanol is first oxidized to adsorbed acetaldehyde that either reversibly desorbs or is subsequently converted to adsorbed acetyl. Using CH_3CD_2OH as reactant, "model 1" should lead to acetaldehyde were both deuterium atoms have been removed (CH_3CHO), whereas according to "model 2" deuterated acetaldehyde (CH_3CDO) should be formed. If adsorbed acetyl species can desorb as acetaldehyde, also in "model 2" CH_3CHO should be formed to a certain extent, since the reaction of adsorbed acetyl with H atoms (from water) is much more likely than the reaction with D atoms (Note: the concentration of D-atoms in the solution is several orders of magnitude smaller compared to that of the H atoms). The question which reaction product is formed upon exposure of the Pt film electrode to CH_3CD_2OH and consequently which reaction pathway dominates can be answered by employing product analysis via on-line DEMS measurements (for details about the product analysis of ethanol oxidation reaction see experimental).

In Fig. 88, a potential step experiment in 0.5 M H_2SO_4 solution containing 0.044 M CH_3CD_2OH is shown, where the potential was first stepped from 0.06 to 1.3 V for 30 s to

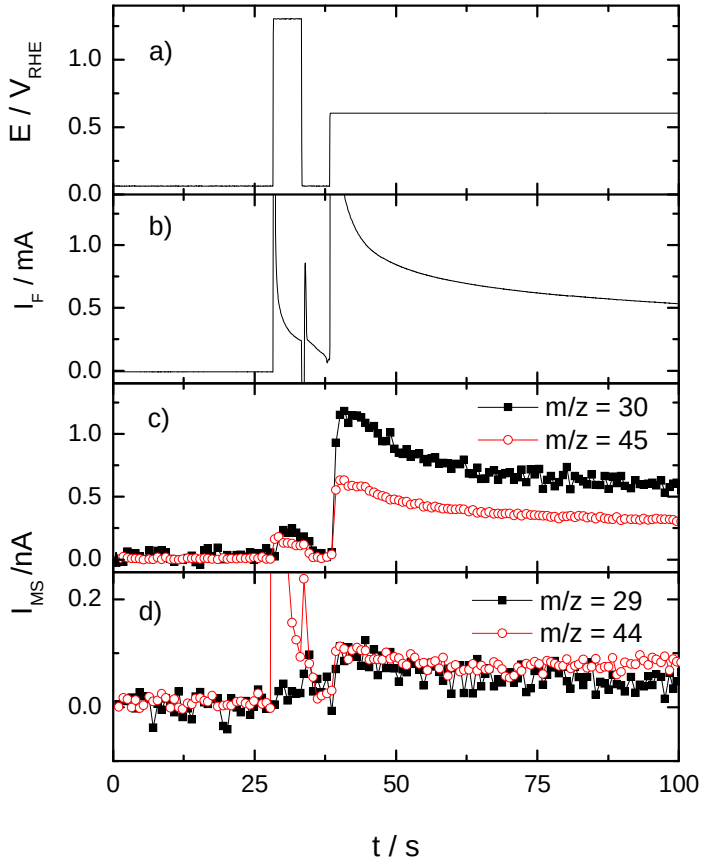

Fig. 88: a) Applied electrode potential, b) Faradaic current response, c) mass spectrometric currents for m/z = 30 (CDO^+) and m/z 45 (CH_3CDO^+), and d) mass spectrometric currents for m/z = 29 (CHO^+) and m/z 44 (CH_3CHO^+, CO_2^+) during a potential step experiment in 0.5 M H_2SO_4 containing 0.044 M CH_3CD_2OH.

remove adsorbates formed at 0.06 V. Subsequently, the potential was stepped for 5 s to 0.06 V to reduce the PtO film before the potential was set to 0.6 V (Fig. 88a). The Faradaic current (Fig. 88b) steeply increases when the potential was stepped to 1.3 V, due to ethanol adsorbate oxidation (current spike, CO_2 formation) and the continuous ethanol oxidation at this potential. A reductive Faradaic current spike is measured when the potential was stepped back to 0.06 V, attributed to the reduction of PtO as well as the formation of an H_{upd} layer. When the potential was increased to 0.6 V, again an oxidative current is recorded, reflecting the oxidation of adsorbed hydrogen and the continuous oxidation of ethanol. The response of the simultaneously measured mass spectrometric currents at m/z = 45 and 30, which are characteristic for the formation of deuterated acetaldehyde (CH_3CDO), and for the mass spectrometric currents for the m/z = 44 and 29 signals, correlated with the formation of unlabeled acetaldehyde (CH_3CHO), are plotted in Fig. 88c) and Fig. 88d), respectively. However, the formation of CO_2 also contributes to the m/z = 44 current, as discussed in the following (see also section 3.6). When the potential was stepped to 1.3 V at t = 30 s, the m/z =

44 signal steeply increased and subsequently decreased to the background value. Since there was no corresponding increase in m/z = 29 signal, the formation of unlabeled acetaldehyde can be excluded (see also section 3.6) and the m/z = 44 current is attributed to the formation of CO_2, most likely resulting from the oxidation of adsorbed CO formed from dissociative ethanol adsorption at 0.06 V. The small increase in both, the m/z = 45 and m/z = 30 signals, indicates the formation of deuterated acetaldehyde at 1.3 V. After the potential step to 0.06 V, the mass spectrometric currents for all m/z ratios decreased to the background level. When stepping from 0.06 V to 0.6 V, both the m/z = 45 and m/z = 30 currents steeply increased, followed by a slight decay before reaching a constant value. This clearly indicates the formation of CH_3CDO, as expected for model 2 described in Fig. 87. But also the m/z = 44 and m/z = 29 signals increased when the potential was stepped to 0.6 V. The resulting currents are, however, significantly smaller. From the ratio of the m/z = 30 current and m/z = 29 current, a product ratio of CH_3CDO : CH_3CHO of 15:1 is calculated at the current maximum as well as under close to steady-state conditions, indicating that almost 94% of the resulting acetaldehyde still contains a D-atom. This product ratio is very close to the value of 98% that can be expected from the degree of deuteration of the CH_3CD_2OH (98%) used in these experiments. Hence, essentially only CH_3CDO is formed. The m/z = 44 signal is higher than expected from the m/z = 29 signal (see section 3.6), which is attributed to CO_2 formation at 0.6 V. The CO_2 current efficiency is determined to be about 2%, in agreement with the literature {WANG04O}.

Based on the finding that mainly CH_3CDO and hardly any CH_3CHO is formed during the potential step to 0.6 V in 0.044 M CH_3CD_2OH containing electrolyte, it can be concluded that in a first reaction step ethanol is oxidized to acetaldehyde, which can subsequently be further oxidized to adsorbed acetyl species (model 2 in Fig. 87). Model 1, in which it was assumed that adsorbed acetyl species act as the precursor for acetaldehyde formation, disagrees with the experimental findings and can therefore be excluded as the main reaction pathway for acetaldehyde formation. Furthermore, the data indicate that adsorbed acetyl species are not in a fast adsorption-desorption equilibrium with acetaldehyde, but are instead irreversibly adsorbed for potentials above 0.4 V (Note: Desorption of adsorbed acetyl species was found to be rather fast at 0.06 V (see section 6.2.2.3)).

6.3.3 Summary

Based on combined *in situ* ATR-FTIRS/DEMS adsorption transients, a kinetic isotope effect was found in the CO_{ad} formation upon adsorption/oxidation of CH_3CD_2OH. This was quantitatively related to a kinetic isotope effect in the formation of adsorbed acetyl species, which requires C-D bond splitting. A rate equation, which was derived for the adsorption of CH_3CH_2OH, was employed successfully, without any modifications, to correlate the CO_{ad} formation rate upon adsorption/oxidation of CH_3CD_2OH to the coverage of adsorbed acetyl species. Finally, it was shown that essentially only CH_3CDO, and not CH_3CHO, is formed during oxidation of CH_3CD_2OH, which lead to the conclusion that adsorbed acetyl is not an active intermediate to form acetaldehyde, but rather formed upon re-adsorption of acetaldehyde.

6.4 Mechanism for the electrooxidation of ethanol

The mechanistic information on the adsorption/oxidation of ethanol derived from the combined ATR-FTIRS/DEMS measurements under well-defined flow conditions and the use of isotopically label ethanol can be summarized in the following reaction scheme.

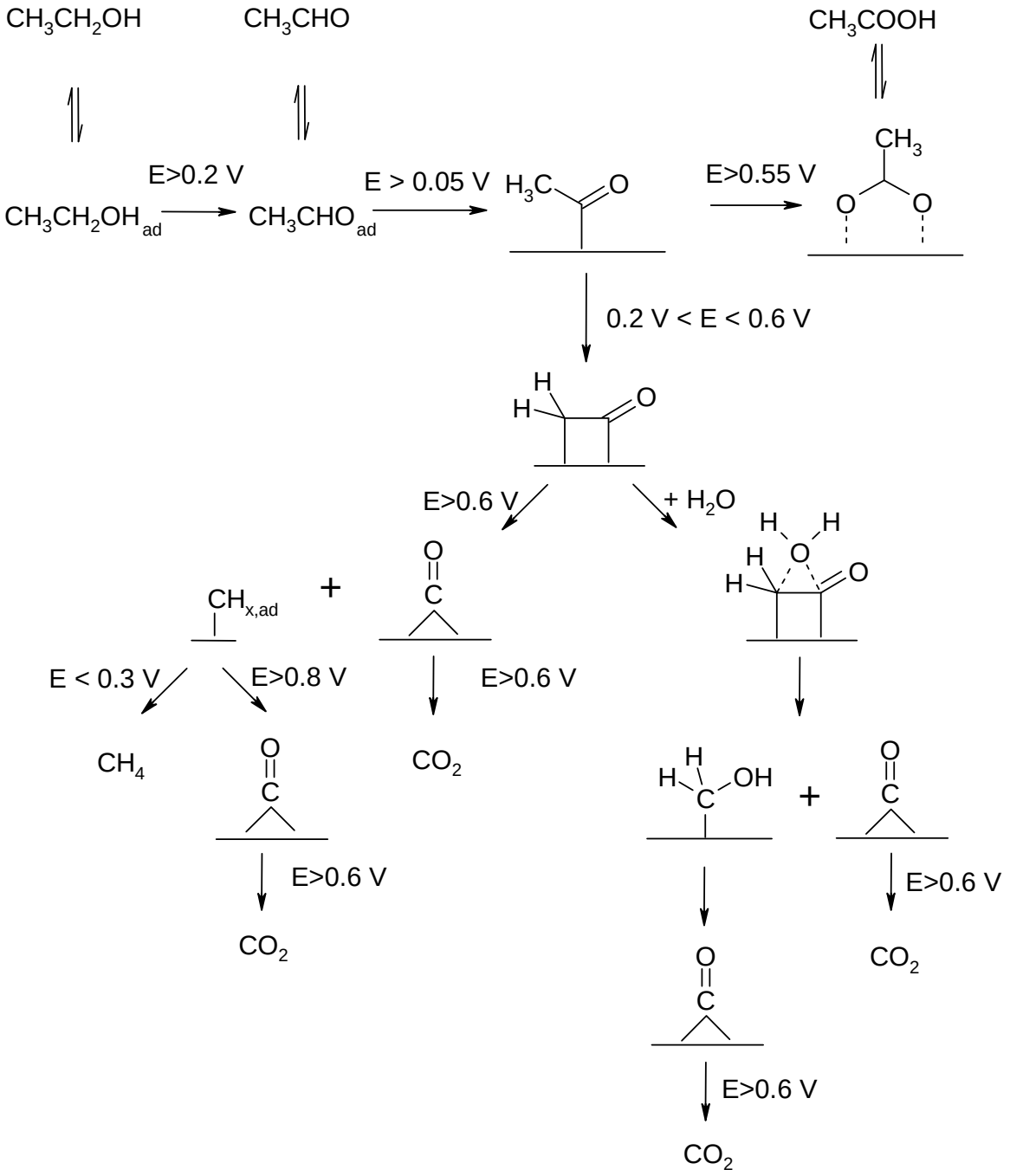

Fig. 89: Schematic drawing of ethanol oxidation reaction mechanism on a Pt film electrode.

The first step in the adsorption/oxidation of ethanol is the formation of acetaldehyde, which in turn results in the formation of adsorbed acetyl species (1635 cm^{-1}). These species were unambiguously identified in different experiments, and the assignment was further supported by an isotope shift of about 25 cm^{-1} when carbon labeled ethanol was adsorbed. Between 0.2 and 0.6 V, the decomposition of adsorbed acetyl species was proposed to proceed via the formation of a CH_2CO_{ad} species. Depending on the electrode potential, the latter species either reacts with water to form CO_{ad} and a CH_xO_{ad} species, which is rapidly converted further to CO_{ad}, or results in the formation of CO_{ad} and a rather stable $CH_{x,ad}$ species. The latter species either desorbs from the Pt surface as methane at low potentials or is oxidized to CO_2 at very positive potentials. Besides the decomposition of adsorbed acetyl, which includes C-C bond splitting via an adsorbed CH_2CO_{ad} intermediate, adsorbed acetyl can also be oxidized to acetic acid at potentials more positive than 0.55 V, where adsorbed oxygen species are present on the Pt surface. Desorption of adsorbed acetyl species as acetaldehyde is rather slow and essentially negligible for potentials ≥ 0.4 V, based on the finding that only deuterated acetaldehyde was detected via on-line DEMS upon potential step experiments to 0.6 V. At 0.06 V, however, acetyl desorption is much faster compared to its decomposition.

Besides the qualitative mechanistic picture for the ethanol electrooxidation, the *in situ* ATR-FTIRS data were also analyzed quantitatively. The CO_{ad} formation rates upon ethanol adsorption/oxidation at different constant potentials were determined, and employing $^{12}CH_3{}^{13}CH_2OH$, it was even possible to derive the $^{12}CO_{ad}$ and $^{13}CO_{ad}$ formation rates separately. The surprisingly fast formation of CO_{ad} from the methyl group already at 0.4 V resulted in a modification of the mechanistic picture for the decomposition of adsorbed acetyl species (see above). Furthermore, a relation between the intensity of adsorbed acetyl and its coverage was established. This allowed relating quantitatively the CO_{ad} coverage increase in the absence of ethanol in the solution, to decomposition of adsorbed acetyl species. Finally, a rate equation for the decomposition of adsorbed acetyl species was derived, which correlates the CO_{ad} formation rate to the coverage of adsorbed acetyl species. In complete agreement with the above mechanistic picture, a kinetic isotope effect (KIE) was found upon adsorption/oxidation of CH_3CD_2OH for the CO_{ad} formation rate, which was quantitatively related to a KIE in the formation rate of adsorbed acetyl species.

7 ADSORPTION / OXIDATION OF BI-FUNCTIONAL C2 MOLECULES

In this Chapter, measurements concerning the adsorption/oxidation behavior of ethylene glycol (EG) and its oxidative intermediates, namely glycol aldehyde (GA), glycolic acid (GS), glyoxal (GOA), glyoxylic acid (GOS) and oxalic acid (OS) are presented and discussed. As already mentioned in the introduction (section 1.3), these measurements were performed using the *in situ* ATR-FTIRS flow cell set-up, since at that time the combined ATR-FTIRS/DEMS set-up had not been developed. I will focus on the assignment of the adsorbed species detected via *in situ* ATR-FTIR spectroscopy upon adsorption/oxidation of the aforementioned organic molecules and discuss their impact on the electrooxidation of ethylene glycol. In the mean time, I supervised a diploma thesis by Johannes Schnaidt, in which the combined ATR-FTIRS/DEMS set-up was employed for studying the aforementioned C2 molecules. The insights from that work are incorporated in this Chapter.

The electrooxidation of ethylene glycol is a complex reaction network in which beside CO_2, five incompletely oxidized side products can be formed (see also 7.1). In such kind of consecutive reaction the formation and subsequent re-adsorption of the possible side products (glycol aldehyde, glycolic acid glyoxal, glyoxylic acid, oxalic acid) plays an important role and therefore a detailed understanding of the adsorption/oxidation behavior of the aforementioned C2 molecules is a key issue to investigate the mechanism of the EG oxidation reaction. Furthermore, these six C2 molecules are nice model systems to study the influence of the functional group on the C-C bond splitting rate, which can be easily followed by the CO_{ad} formation rate measured via *in situ* ATR-FTIRS.

After a short introduction to the EG oxidation reaction (section 7.1), the presentation of the results (section 7.2) will start with the assignment of the IR absorption bands detected during adsorption/oxidation of the six C2 molecules (section 7.2.1). Therefore, the IR spectra acquired on a clean Pt surface are compared at 0.1 and 0.6 V for the adsorption of all six C2 molecules. Subsequently, the presentation of the results of each molecule (section 7.2.x, where x = 2,.., 7, for EG, GA, GS, GOA, GOS and OS, respectively) is structured as follows: First the *in situ* ATR-FTIR spectra recorded during potentiodynamic oxidation are shown, and the absorption bands are assigned and their potential dependent appearance is discussed (section 7.2.x.1, where x = 2,.., 7, for EG, GA, GS, GOA, GOS and OS, respectively). Based on the adsorbates detected via IR spectroscopy the potentiodynamic oxidation of the respective C_2 molecule will be analyzed. In section 7.2.x.2, the kinetics of the adlayer development, followed in potentiostatic electrolyte exchange experiments, is presented and discussed. These measurements allow estimating the potential dependence of the C-C bond

splitting rate from the slope of the CO_{ad} intensity increase at different, constant potentials, as a function of the adsorption potential. Subsequently to the adsorption transients potentiodynamic adsorbate stripping experiments were performed, revealing additional information on the adlayer composition (section 7.2.x.3).

Finally the adsorption/oxidation behavior of the six C2 molecules is compared, and the strong influence of the functional group on the reactivity is discussed (section 7.3 and 7.4).

7.1 Introduction

The electrocatalytic oxidation of ethylene glycol (EG) was studied intensively in the last decades due to its potential application as fuel for direct alcohol fuel cells{KADI82} {KOKK82}{LEUN88}{CHRI89A}{ORTS90}{LEUN90A}{BELG91}{CHAN91F}{WIEL 96} {GOOT96}{LIMA03}{FAN04B}{WANG06Q}{WANG08F}. In addition to classical electrochemical methods IR spectroscopy {HAHN87}{LEUN88}{CHRI89A} {LEUN90A} {KADI90}{CHAN91F}{JIAN93}{GOOT96}{WIEL96}{LIMA03}{FAN04B}{DEMA07}', differential electrochemical mass spectrometry (DEMS){GOOT96} {WANG06Q} {WANG08F} and chromatographic methods {BELG91}{DEMA07} were used to analyze adsorbates, intermediates and products of the electrooxidation of EG. This way, partially oxidized C2 species (glycol aldehyde, glyoxal, glycolic acid, glyoxylic acid, oxalic acid) as well as C1 species (formaldehyde, formic acid) and CO_2 were detected. As main adsorbate, CO_{ad} could be identified {HAHN87}{LEUN88}{CHRI89A}, which is a poison at lower potentials and can be oxidized to CO_2 at higher potentials. Besides CO_{ad}, other absorption bands in the wavenumber region between 1730 and 1744 cm^{-1} and between 1240 and 1245 cm^{-1} were detected by Hahn et al. by employing EMIRS {HAHN87}. Similar absorption bands were detected by SPAIRS {LEUN88}{CHAN91F}{JIAN93} and by SNIFTIRS {CHRI89A} during the ethylene glycol adsorption/oxidation. These bands were assigned to the C= O stretching (1730 – 1740 cm^{-1}) and the C-O stretching (1240 – 1245 cm^{-1}) modes of glycol aldehyde and glycolic acid. Based on IR results, a parallel pathway mechanism was proposed, with the formation of the C2 species by oxidation of the OH-groups on the one hand and with the formation of CO_2 from CO_{ad} oxidation by splitting the C-C bond on the other hand {WIEL96}.

Studies on the electrooxidation of EG using IR spectroscopy were so far carried out only in an external configuration, in which i) the IR absorption bands from adsorbed species and bulk species can hardly be distinguished and ii) the mass transport is strongly inhibited (see also Chapters 1.2 and 1.3). These difficulties can be overcome by using the *in situ* ATR-FTIRS flow-cell set-up, developed and described here, which in addition to its highly surface sensitivity stands out due to the well defined mass transport required for kinetic studies (see also Chapters 1.2 and 1.3).

7.2 Results

7.2.1 Adsorbate detection

This section aims at assigning the IR absorption bands detected during the adsorption/oxidation of the six C2 molecules, namely ethylene glycol (EG), glycol aldehyde (GA), glycolic acid (GS), glyoxal (GOA), glyoxylic acid (GOS) and oxalic acid (OS). The assignment is based on a comparison of the spectral features observed during the adsorption/oxidation of the respective molecules.

Fig. 90 shows sets of IR spectra recorded during potentiostatic adsorption transients of ethylene glycol (EG), glycol aldehyde (GA), glycolic acid (GS), glyoxal (GOA), glyoxylic acid (GOS) and oxalic acid (OS) at 0.1 and 0.6 V. All spectra presented were acquired 3-4 seconds after the electrolyte exchange from 0.5 M H_2SO_4 to a solution containing 0.1 M of the respective organic compound, since under these conditions the CO_{ad} coverage is still small and less strongly adsorbed species with a low absorption coefficient and/or low coverage are more clearly visible. All adsorbed species detected in the whole potential regime that was investigated are present either at 0.1 or 0.6 V.

At 0.1 V, the IR spectra after adsorption of EG and GS are featureless, indicating that EG and GS can either not adsorb at this low potentials or the EG/GS adsorbate coverage is below the detection limit. On the other hand, adsorption of GA, GOA, GOS and OS, is possible and dissociative adsorption results in two bands at 2020 cm^{-1} and 1800 cm^{-1}, which are attributed to linearly and multiply bond CO_{ad}, respectively {LEUN88}{WIEL96}. The negative bands at 3450 and 1610 cm^{-1} are assigned to displaced water, and the positive band at 3650 cm^{-1} to water co-adsorbed to CO {MIKI02}. For the molecules containing an aldehyde function, such as GA, GOA, and GOS, an additional positive band is found at 1640, 1645 and 1710 cm^{1}, respectively, which is assigned to the respective adsorbed acetyl species, bond to the surface via the carbon atom of the aldehyde group. This assignment is based on i) the vibrational frequencies of these adsorbates, which are in the typical region of carbonyl bonds, and ii) the close similarity between the bands detected during the adsorption/oxidation of ethanol and acetaldehyde.

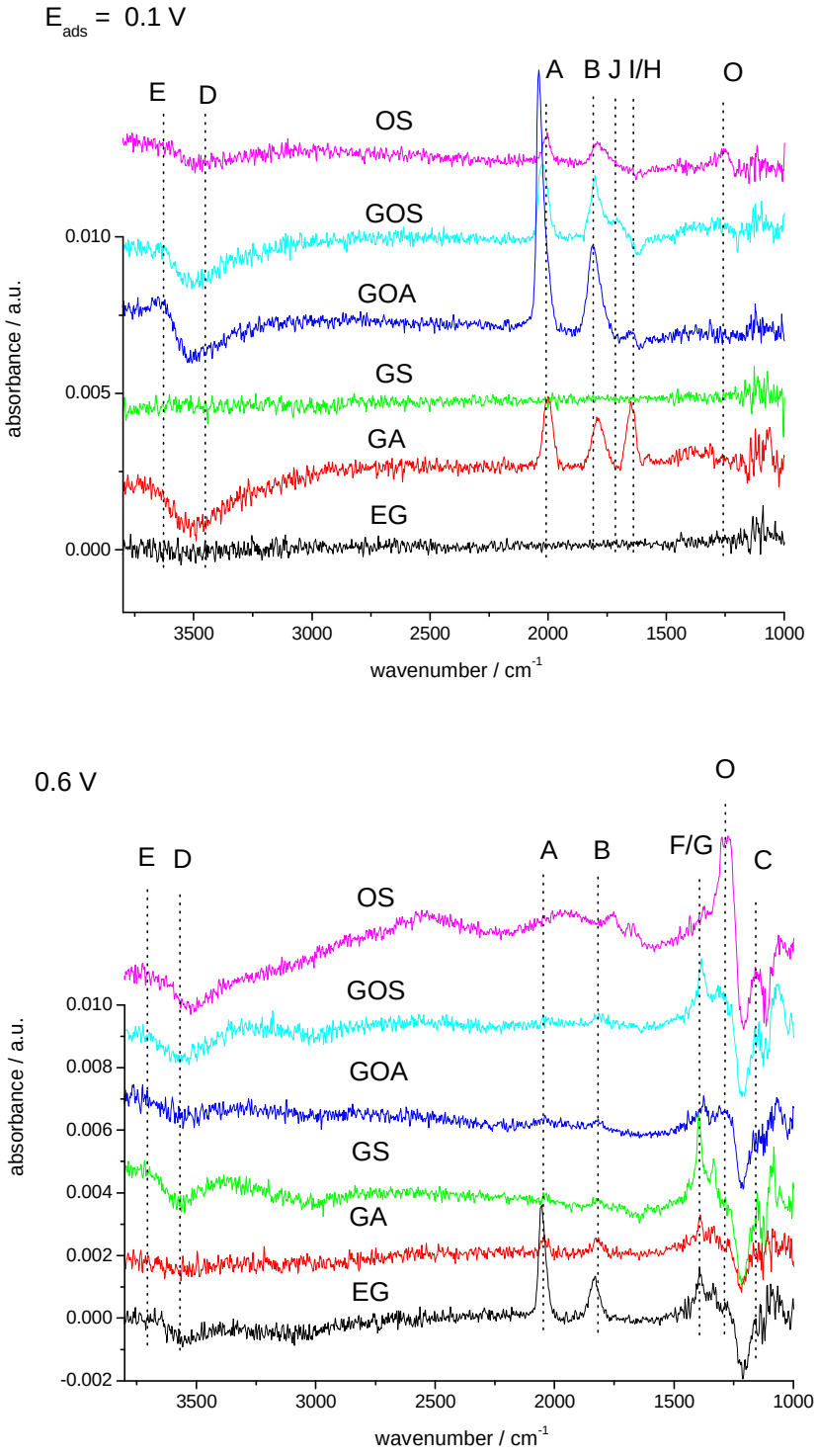

Fig. 90: Series of ATR-FTIR spectra recorded during electrolyte exchange experiments at 0.1 (top) and 0.6 V (bottom) from 0.5 M H_2SO_4 to solutions containing 0.1 M of ethylene glycol (EG), glycol aldehyde (GA), glycolic acid (GS), glyoxal (GOA), glyoxylic acid (GOS) and oxalic acid (OS), respectively. The selected spectra were acquired about 2-3 seconds after the electrolyte exchange was triggered and the reference spectra were recorded at 0.1 V in 0.5 M H_2SO_4, respectively. The detected IR bands are labeled with A,B,C,D,E,F,G,H,I,J and O (assignments see text, and table at the end of the section).

As already mentioned before, so far all IR spectroscopic studies investigated the adsorption of EG and its intermediates on Pt were performed in external reflection configuration, where adsorbate detection in this spectral region is cumbersome due the low surface sensitivity resulting in strong interference with signals from water and reaction products {IWAS97}. Therefore, the IR bands assigned to the adsorbed aldehydes have not been observed in the literature so far. No other IR spectral features are detected for the aforementioned three molecules at 0.1 V. Only for the adsorption of oxalic acid, an additional band is detected at 1280 cm^{-1}, which is attributed to the adsorbed oxalic acid bound to the surface via two oxygen atoms {HORA72}{BERN04}.

At 0.6 V, all spectra show IR features between 1400 and 1200 cm^{-1}, which is the typical wavenumber region for O-C-O vibration modes of adsorbed carboxylic acids {CORR88}{CHEN03}{SHAO05}. The IR spectrum acquired during the adsorption of GS shows a characteristic double peak at 1396 and 1333 cm^{-1}, which is attributed to adsorbed glycolate bound perpendicularly to the surface via two oxygen atoms. This characteristic feature is also found in the spectra recorded for the adsorption/oxidation of EG and GA, indicating that both molecules can be oxidized to GS at 0.6 V in agreement with previous reports {WIEL96}{DAIL98}. Also the adsorption of GOS results in a characteristic double peak, compared to GS adsorption, however, the peaks are slightly red-shifted and are now centered at 1384 and 1310 cm^{-1}. This band is attributed to adsorbed glyoxylate, which is again bound to the Pt surface via the two oxygen atoms of the carboxyl function. It is also found for the adsorption/oxidation of GOA, indicative for the oxidation of GOA to GOS at 0.6 V. The IR band assigned to adsorbed OS at 1285 cm^{-1} is slightly blue-shifted compared to its position at 0.1 V, due to the Stark shift. Two small bands centered at 1760 and 1680 cm^{-1}, respectively, are detected upon adsorption of OS, which can not be assigned so far.

In all spectra, a negative double peak is detected at about 1210 and 1100 cm^{-1}, which is caused by the displacement of adsorbed (bi-) sulfate present on the electrode surface at 0.6 V {NART94}{IWAS97}{FUTA05}. The IR absorption bands mentioned above are summarized in table 7:

Wavenumber / cm^{-1}	Functional group or chemical species	Short cut
2080 – 2020	CO_L	A
1920 -1750	CO_M	B
1235 – 1100	Adsorbed sulfate/bisulfate	C
3450/1620	Displaced water	D
3650	Water co-adsorbed with CO	E
1396/1333	Adsorbed glycolate	F
1385/1310	Adsorbed glyoxylate	G
1640	Adsorbed glycol aldehyde	H
1645	Adsorbed glyoxal	I
1710	Adsorbed glyoxylic acid	J
1265	adsorbed bioxalate	O
1750, 1680, 1370	not assigned	

Table 7: Summary of all detected IR bands during the adsorption/oxidation of EG, GA, GS, GOA, GOS and OS. The shortcuts in the table are used throughout Chapter 7 for the notation of the bands in the spectra. The potential dependence as well as the appearance of these bands during the adsorption/oxidation of the six C2 molecules will be discussed in the following sections.

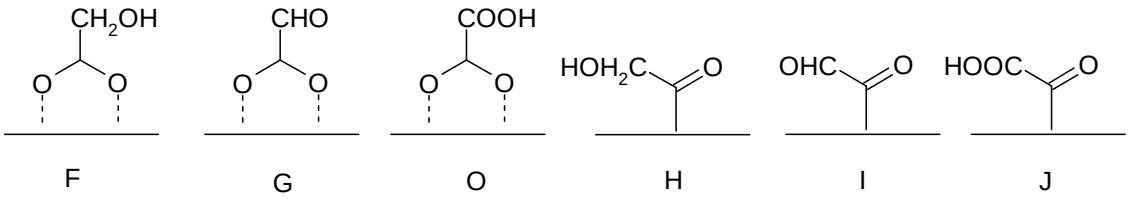

Fig. 91: Schematic drawing of adsorbates detected during adsorption of EG, GA, GS, GOA, GOS and OS.

7.2.2 Ethylene glycol

7.2.2.1 Potentiodynamic oxidation of ethylene glycol

The ATR-FTIR spectra shown in Fig. 92 were recorded during the potentiodynamic bulk-oxidation of 0.1 M ethylene glycol in 0.5 M H_2SO_4. The reference spectrum was measured in 0.5 M H_2SO_4 at 0.06 V. Between 0.1 and 0.8 V in the positive-going scan and 0.7 and 0.1 V in the negative-going scan, linearly (CO_L) and multiply (CO_M) bonded CO_{ad} {LEUN88}{WIEL96}{MIKI02} are detected. In the positive-going scan, the CO_L band center shifts from 2029 to 2071 cm^{-1} upon increasing the potential from 0.3 V to 0.6 V. At 3530 cm^{-1} a negative band appears, accompanied by a positive band at higher wavenumber (3640cm^{-1}). As already discussed, these bands are assigned to the stretching mode of water. The negative band is due to water replaced from the surface by CO and the positive band is due to water co-adsorbed with CO_{ad} {ATAK96}{MIKI02}{FUTA05}. The corresponding band of the HOH-bending mode appears at 1610 cm^{-1}. A double peak caused by the adsorption of (bi-)sulfate is detected at about 1210 and 1100 cm^{-1} {NART94}{IWAS97}{FUTA05}. Another double peak assigned to adsorbed glycolate appears at potentials between 0.8 and 1.0 V at ca. 1395 and 1333 cm^{-1}.

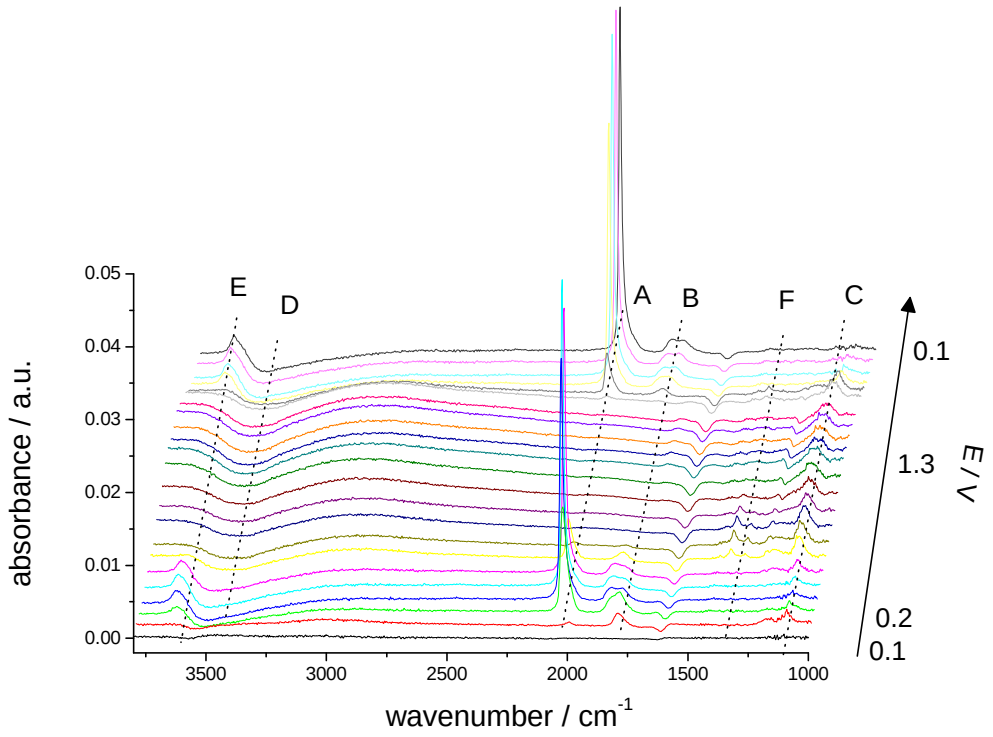

Fig. 92: IR-spectra acquired during potentiodynamic EG bulk-oxidation; v = 10 mV/s; temporal resolution 4.95 s/spectrum; electrolyte 0.1 M EG in 0.5 M H_2SO_4; reference spectrum at 0.06 V in 0.5 M H_2SO_4

The Faradaic current response (a) recorded during the potentiodynamic electrooxidation of ethylene glycol, as well as the integrated IR intensities of the adsorbates CO_L (b), CO_M (c) and adsorbed glycolate (d) are shown in Fig. 93, for the first positive-going scan (filled squares) and the subsequent potential cycle (open circles).

Starting at 0.06 V in the first positive-going scan, the Faradaic current starts to increase at about 0.2 V (peak I), which correlates with the onset of CO_{ad} formation. The oxidative current is therefore at least partly attributed to the oxidation of ethylene glycol to CO_{ad}, which involves C-C bond breaking. In the following ($0.2 < E < 0.35$ V), the Faradaic current decreases with increasing potential due to further dissociative adsorption of ethylene glycol, where the resulting CO_{ad} poisons the Pt surface. At potentials above 0.55 V, the Faradaic current increases very sharply and reaches a maximum at about 0.74 V (peak II). This sharp increase is explained by the oxidative removal of CO_{ad} to CO_2, as can be seen from the decrease in CO_{ad} intensities. Consequently, this Faradaic current peak contains contributions from CO_{ad}

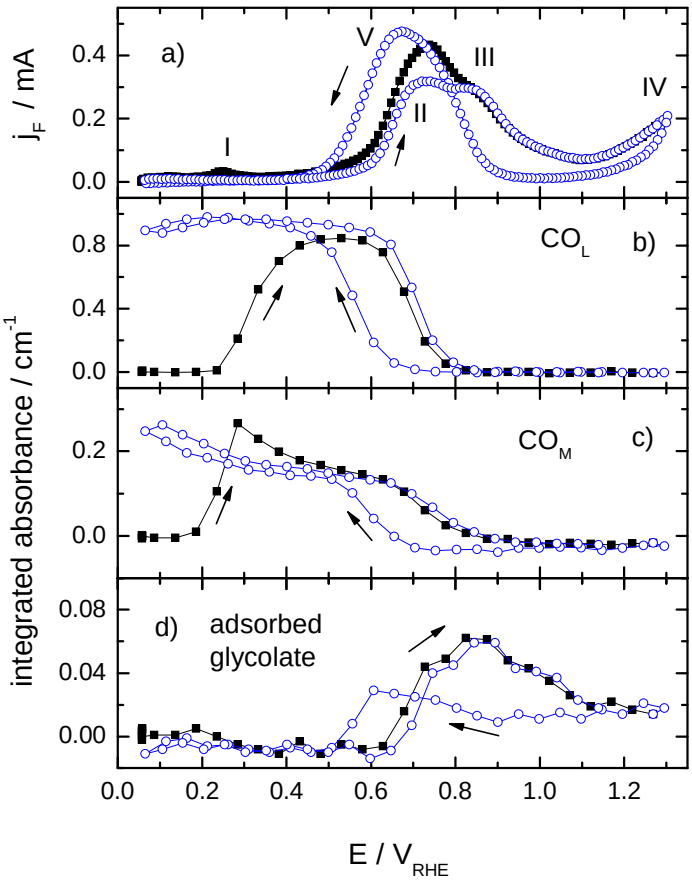

Fig. 93: Potentiodynamic EG bulk-oxidation; a) CV and integrated absorbance of b) linearly bonded CO, c) multiply bonded CO and d) adsorbed glycolate taken from the IR spectra in Fig. 92, v = 10 mV/s; electrolyte 0.1 M EG in 0.5 M H_2SO_4. Filled squares: first positive-going scan; open circles: continuous cycling.

oxidation. Furthermore, a reaction product of EG oxidation that can be detected after the oxidative removal of CO_{ad}, via the IR bands at band at 1396/1333 cm^{-1} assigned to adsorbed glycolate, is glycolic acid. The integral band intensity of adsorbed glycolate correlates well with the Faradaic current peak III. Qualitatively, this correlation is explained by a convolution of two effects: i) an increased glycolic acid formation rate at more positive potentials, most likely due to a higher coverage of oxygen species on the Pt film electrode and ii) ii) an increasing integral band intensity of adsorbed glycolate, at constant glycolic acid concentration, with increasing potential (see also section 7.2.4.2), where the adsorption/oxidation of glycolic acid is presented and discussed. At potentials above 0.84 V, the Faradaic current decreases, most likely due to the formation of Pt-oxide and increases again at potentials above 1.1 V (peak IV). The IR spectra in this potential region do not contain additional information adsorbed species or reaction products. In two recent on-line DEMS studies it was concluded that incomplete oxidation of EG prevails in this potential region, based on the finding that hardly any CO_2 is formed at potentials above 1.1 V.

In the negative-going scan, the Faradaic current is essentially zero between 1.1 and 0.9 V. When the reduction of Pt oxide sets in at about 0.85 V, the Faradaic current increases due to the onset of EG oxidation and reaches a maximum at 0.67 V (peak V). The sharp decrease of the Faradaic current for potentials below 0.67 V is attributed to a fast accumulation of CO_{ad} on the Pt surface, as evidenced by the increase in the integral band intensities of CO_L and CO_M species (Fig. 93b, c). As a reaction product of EG oxidation in the negative-going scan, glycolic acid can be detected via an increase of the integral band intensity of adsorbed glycolate (Fig. 93d). The Faradaic current in the negative-going scan is higher than in the positive-going scan. Based on the finding that the integrated absorbencies of CO_L and CO_M in the negative-going scan are significantly smaller compared to those in the positive-going scan (Fig. 93b, c), a possible reason for the larger Faradaic current in the negative-going scan is the lower coverage of surface blocking CO_{ad} species.

In the second positive-going scan, systematic changes in the Faradaic current response compared to the first positive-going scan are observed, namely i) current peak I is suppressed, ii) the onset of ethylene glycol is shifted to higher potentials, iii) the current peak II is smaller and iv) peak III is better resolved. The differences in the current peaks I – III are attributed to the higher CO_{ad} coverage at the onset of the second positive-going scan, as can be seen from the integral band intensities of CO_{ad} plotted in Fig. 93b and c.

7.2.2.2 Potentiostatic electrolyte exchange experiments

For more detailed information on the reaction kinetics and adlayer build-up, adsorption/oxidation transients at different, constant potentials were measured, which avoid the convolution of potential and time effects. The current transients recorded in electrolyte exchange experiments at 0.1, 0.2, 0.4 and 0.6 V are shown in Fig. 94a), together with the integral absorbances of b) CO_L, c) CO_M, d) adsorbed glycolate and e) adsorbed glycol aldehyde as taken from the corresponding ATR-FTIR spectra (not shown).

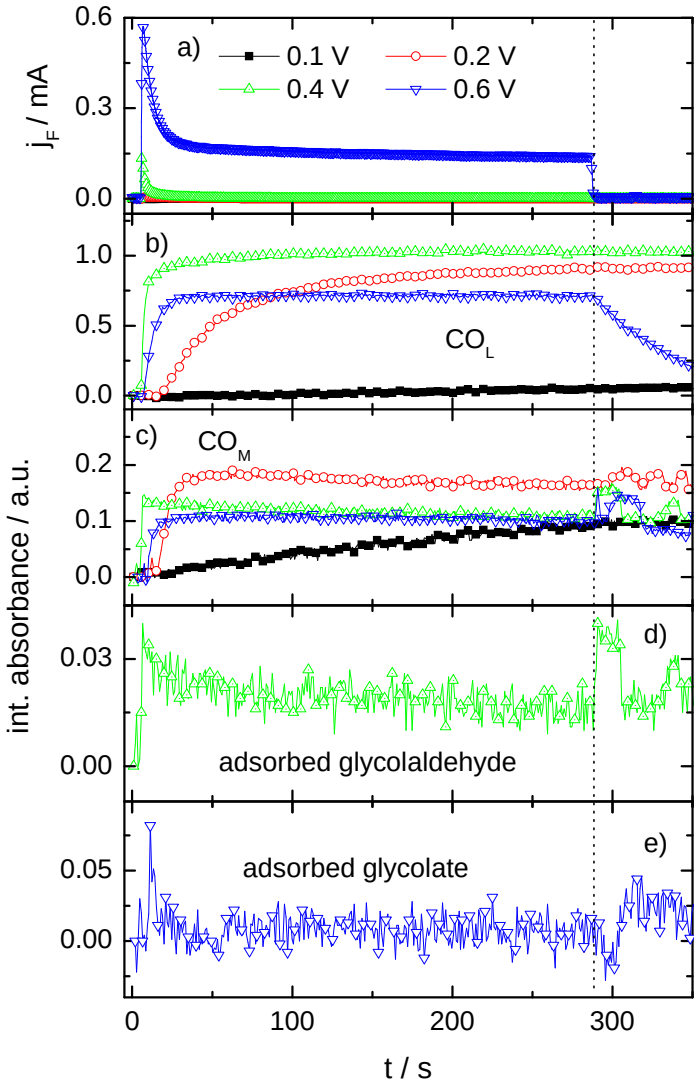

Fig. 94: Potentiostatic EG bulk-oxidation at different constant potential (see figure); a) Faradaic current density and integrated absorbance of: b) linearly bonded CO, c) multiply bonded CO, d) adsorbed glycolate and e) adsorbed glycol aldehyde; electrolyte 0.1 M EG in 0.5 M H_2SO_4. The dashed vertical line indicates the electrolyte exchange to EG free 0.5 M H_2SO_4.

At 0.1 V, a small cathodic current is visible, which could be explained by the onset of hydrogen evolution. The formation of CO_{ad} is slow, but the intensities of CO_L and CO_M increase continuously. Possible reasons for the low CO_{ad} formation rate are surface blocking by H_{upd} {WANG06Q} or slow adsorption kinetics of ethylene glycol at low potentials.

At higher potentials (≥ 0.2 V), anodic currents are measured. After the addition of EG, the Faradaic currents rise steeply and pass through a maximum, followed by a roughly exponential decay. This is attributed to surface blocking, primarily by CO_{ad}. The integral band intensity of CO_L is found to increase steeply in the first 10 seconds, after the electrolyte exchange to 0.1 M ethylene glycol containing solution at 0.4 and 0.6 V, and to approach a steady-state value with time. The maximum final value of the integrated CO_L absorption, i.e., at t = 280 s, is found at potentials between 0.3 V and 0.5 V (only 0.4 V is shown). At potentials ≤ 0.2 V, the CO_{ad} formation rate is too slow for saturating the surface, within the EG adsorption time of 5 min., whereas at 0.6 V, CO_{ad} is continuously oxidized to CO_2, resulting in a lower CO_{ad} coverage under steady-state conditions (see section 4.2). At 0.6 V, the decrease in the integrated band intensities of CO_M and more pronounced of CO_L show that the CO_{ad} coverage is further decreased during rinsing with sulfuric acid at t > 280 s (dashed vertical line in Fig. 94). This decrease is due to CO_{ad} oxidation without further CO_{ad} formation. (Note: the sudden increase/decrease in the CO_M band intensity after the electrolyte exchange to EG free 0.5 M H_2SO_4 is an experimental artifact, which is tentatively assigned to a slight deviation of the IR background upon the electrolyte exchange. A similar behavior of the CO_M band was not seen when the measurements were repeated using the combined ATR-FTIRS/DEMS set-up (see diploma thesis by Johannes Schnaidt {SCHN08}). The integral band intensity of adsorbed glycolate (Fig. 94e) upon EG adsorption/oxidation at 0.6 V steeply increases upon the electrolyte exchange to EG containing solution, passes through a maximum at t = 15 s and decreases to nearly zero during further adsorption of EG. Adsorbed glycolate can only be detected for EG adsorption/oxidation at 0.6 V, indicative of the formation of glycolic acid at this potential. At lower potentials, adsorbed glycolate can not be detected. Its formation relies on the presence oxygen species on the Pt surface, which are formed on the Pt electrode at potentials above 0.55 V.

Adsorbed glycol aldehyde, detected at 1640 cm^{-1} (Fig. 94d), is only visible at 0.4 V. The band intensity increases steeply upon the electrolyte exchange, reaching a steady-state value about 2-3 seconds after the electrolyte exchange It needs to be mentioned that also water co-adsorbed to CO contributes to the signal at 1640 cm^{-1} (see sections 4.2). Therefore, the

temporal development of the adsorbed glycol aldehyde can not be followed properly via the integral band intensity of the band at 1640 cm^{-1}. However, the IR spectra acquired 2-3 seconds after the electrolyte exchange clearly show an absorption band at 1640 cm^{-1}, which is attributed to adsorbed glycol aldehyde. The experimental finding that the intensity of adsorbed glycol aldehyde is highest at 0.4 V, similar to the potential dependence of adsorbed acetyl species during ethanol adsorption/oxidation (see section 6.1.2.1) can be tentatively explained when assuming a similar mechanism for the adsorption/oxidation of EG and ethanol (see section 6.4). At potentials below 0.4 V, the formation of adsorbed glycol aldehyde is significantly slower than its subsequent decomposition to CO_{ad}, resulting in a coverage below the detection limit of the present set-up, whereas at 0.6 V, the intensity of adsorbed glycol aldehyde is smaller compared to 0.4 V due to the onset of oxidation of adsorbed glycol aldehyde to glycolic acid (see also Fig. 94 d). (Note: As mentioned before, the sudden increase/decrease in the integral band intensity after the electrolyte exchange to EG free 0.5 M H_2SO_4 is an experimental artifact, which is tentatively assigned to a slight deviation of the IR background upon the electrolyte exchange. These changes were not seen when the measurements were repeated using the combined ATR-FTIRS/DEMS set-up (see diploma thesis by Johannes Schnaidt {SCHN08}).

In a publication of Fan et al., the potential dependent C-C bond splitting rate on a Pt (100) electrode was estimated from the time dependent CO_{ad} layer build up, by comparing the charges measured for the adsorbate oxidation as a function of the adsorption time {FAN04B}. These authors have found a volcano type curve with a maximum rate for dissociative adsorption at 0.3 and 0.4 V_{RHE}. From the present IR data, the potential dependent rate for C-C bond splitting rate, or more precisely the CO_{ad} formation rate on a clean Pt surface, can be determined very accurately from the increase in integral band intensity of CO_L ($dI(CO_L)/dt$) at different adsorption potentials. For this purpose, the integral intensity of CO_L has to be converted into the CO_{ad} coverage, which was done via a mathematical correlation derived in section 3.7. The CO_{ad} formation rate, in terms of molecules $\times$ $site^{-1}$ $\times$ s^{-1}, on a clean Pt surface is equivalent to the initial slope of the CO_{ad} coverage versus time plot. Using the IR intensities for evaluating the rates for the CO-adlayer build-up, is reliable for $E \leq 0.6$ V. At higher potentials, the build-up of the CO adlayer is strongly affected by the competing oxidation of CO_{ad} to CO_2. Already at 0.6 V, CO_{ad} oxidation to CO_2 is possible (see section 4.2). Its influence on the CO_{ad} build-up, however, can be neglected. In section 4.2, it was shown that the CO_{ad} oxidation rate at 0.6 V is very slow at small CO_{ad} coverages. It increases with

increasing CO_{ad} coverage up to $\theta(CO_{ad,rel}) = 0.4$, following a Langmuir Hinshelwood mechanism. In the case of EG adsorption at 0.6 V, the initial CO_{ad} coverage is zero and accordingly the CO_{ad} oxidation rate is expected to be very small and does not affect the CO_{ad} build-up. During continuous EG adsorption/oxidation at 0.6 V, the CO_{ad} formation and oxidation rates are equally fast, as evidenced by the constant integral band intensities of CO_L and CO_M. The CO_{ad} oxidation rate under steady-state conditions can now be estimated from the slope of the CO_{ad} coverage decrease ($d\theta(CO_{ad})/dt$) upon electrolyte exchange to EG free 0.5 M H_2SO_4 (dashed line in Fig. 94b; see also section 5.1.2), assuming that the CO_{ad} formation rate is zero in the absence of EG in the electrolyte. The determined value for $d\theta(CO_{ad})/dt$ upon rinsing with 0.5 M H_2SO_4 is -0.005 molecules $\times$ site^{-1} $\times$ s^{-1}, which is about 1/10 of the CO_{ad} formation rate resulting from EG adsorption at 0.6 V on a clean Pt surface ($d\theta(CO_{ad})/dt = 0.05$, see table 8). Furthermore, the CO_{ad} oxidation rate under steady-state conditions is much larger compared to the initial CO_{ad} oxidation rate upon EG adsorption/oxidation, where the overall CO_{ad} coverage is significantly smaller (Fig. 94b; see discussion above). The results of the CO_{ad} formation rates at different constant potentials are summarized in table 8.

E_{ads}/V_{RHE}	0.1	0.2	0.3	0.4	0.6
$\Delta\theta(CO_{ad})/\Delta t$ [ML/s]	$1\times 10^{-4}\pm 3\ 10^{-5}$	0.012±0.002	0.04±0.01	0.1±0.02	0.05±0.01

Table 8: CO_{ad} formation rate upon adsorption/oxidation of EG on a clean Pt electrode at different potentials. The rates are given in terms of monolayers/second (ML/s), which is equivalent to molecules $\times$ site^{-1} $\times$ s^{-1}.

The potential dependent CO_{ad} formation rate, has a maximum at about 0.4 V and decreases at higher potentials. Quantitatively, our IR data are in reasonable agreement with the publication by Fan et al., where the highest rate for C-C bond splitting at 0.3 V was reported to be about 0.005 molecules $\times$ site^{-1} $\times$ s^{-1} for a solution containing 2 mmol of EG. Based on the present IR data, which were performed in 100 mmol containing EG electrolyte, the highest rate at 0.4 V is equivalent to about 0.1 molecules $\times$ site^{-1} $\times$ s^{-1}, which is about 20 times larger compared to the value reported by Fan et al. for the low concentration of EG.

Also the general potential dependence of the CO_{ad} formation rate agrees with the data reported by Fan et al., although the curve calculated from our IR data is shifted to higher potentials. The slow adsorption/dissociation at low potentials is attributed to site blocking by

the H_{upd}, which hinders EG adsorption. The decrease in the measured rate for C-C bond splitting can be explained in two principally different ways: i) the rate constant for C-C bond splitting decreases with increasing potential or ii) a potential independent rate constant and a decrease in the steady-state coverage of the precursor for C-C bond splitting. The latter was shown to be the case for the adsorption/oxidation of ethanol, where the coverage of adsorbed acetyl species was smaller at 0.6 V compared to 0.4 V (see section 6.3.2.2). This was tentatively explained by the presence of OH_{ad} species on the Pt surface, facilitating the oxidation of adsorbed acetyl species to acetic acid. The smaller coverage of adsorbed acetyl in turn resulted in a smaller rate for CO_{ad} formation (see section 6.3.2.2). For the adsorption/oxidation of EG at 0.6 V, the coverage of adsorbed glycol aldehyde is below the detection limit and therefore smaller compared to 0.4 V, where it could be detected upon EG adsorption/oxidation. Therefore, the decreasing rate of C-C bond splitting with increasing potential measured upon EG adsorption/oxidation is tentatively attributed to a decrease of coverage of the precursor for C-C bond splitting, i.e., adsorbed glycol aldehyde, in close analogy to the mechanism that was proposed for the adsorption/oxidation of ethanol.

7.2.2.3 Potentiodynamic adsorbate stripping experiments

Following to the adsorption transients presented above, potentiodynamic adsorbate stripping experiments were performed to gain further information on the adlayer composition as well as a quantitative value for the CO_{ad} coverage, which was established on the Pt film electrode after EG adsorption for 5 minutes. In Fig. 95, the CV (a) and the integrated absorbencies of linearly (b) and multiply (c) bonded CO_{ad} are shown, recorded during the potentiodynamic adsorbate stripping following the adsorption of ethylene glycol at 0.1, 0.2 and 0.4 V. Since CO_{ad} can be oxidized at 0.5 V and higher potentials, the adsorbate coverage decreases during the rinsing procedure (see also Fig. 94b). Therefore, only the stripping experiments following the adsorption transients up to 0.4 V are presented (for clarity, the data for 0.06 and 0.3 V are also not shown, but the values for the CO_{ad} coverage are summarized in table 9). The general characteristics of all CV's are identical. In all the CV's, the H_{upd} is suppressed due to the presence of adsorbates, namely CO_L and CO_M, as evidenced by the IR absorption bands at 2050 cm^{-1} and 1850 cm^{-1}, respectively.

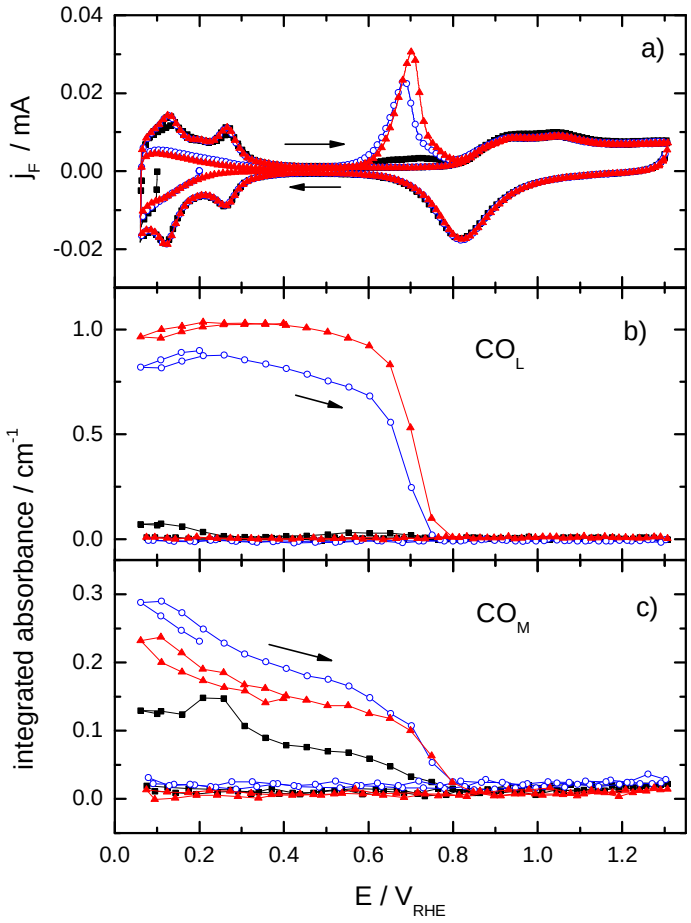

Fig. 95: Adsorbate stripping subsequent to the potentiostatic EG adsorption/oxidation at 0.1 (filled squares), 0.2 (open circles) and 0.4 V (filled triangles): a) CV and the integrated absorbances of b) linear bonded CO and c) multiply bonded CO.; v = 10 mV/s; electrolyte 0.5 M H_2SO_4.

In the positive-going potential scan, a Faradaic current peak appears at about 0.7 V, which is accompanied by a sharp decrease of the CO_{ad} related IR bands down to 0, clearly relating the Faradaic current to CO_{ad} electrooxidation. No further significant current peaks, in addition to the characteristic features of a clean Pt electrode, are found at higher potentials or in the subsequent negative and positive-going scans. Hence the oxidative removal of CO_{ad} at 0.7 V in the first positive-going scan leads to a clean Pt surface, which is confirmed by the IR spectroscopy data.

Assuming that only CO_{ad} oxidation to CO_2 contributes to the current, the CO_{ad} coverage θ_{CO} can be calculated from the charge of the peak at 0.7 V, which is referred to as the coverage $\theta_{CO,sat}$ gained via CO adsorption at 0.06 V. The results are summarized in table 9.

E_{ads}/V_{RHE}	0.06	0.1	0.2	0.3	0.4
Rel. $\theta(CO_{ad})$ / %	5	17	62	63	64

Table 9: Relative CO_{ad} coverage resulting from EG adsorption at constant potential, as calculated from the Faradaic current peak at 0.7 V (details see text).

The maximum coverage was obtained at 0.4 V (table 9), which agrees with the finding of Wang et al. on carbon supported Pt {WANG06Q}, although the coverage is slightly higher in the present study. The presence of H_{upd} at 0.06 and 0.1 V results in slow kinetics for CO_{ad} formation at these potentials (see section 7.2.2.2). Hence, the CO_{ad} coverages formed from dissociative adsorption at 0.06 and 0.1 V are smaller.

In the following, the potential dependent shapes of the CO_{ad} related intensities are discussed in more detail. The integrated absorption of the CO_L band decreases slightly in the negative-going potential scan, whereas the integrated absorption of the CO_M band increases. A similar behavior of the CO_L and CO_M intensities of was reported by Chen et al., when scanning the electrode potential from 0.4 to 0.06 V at a defined, constant CO_{ad} coverage of 0.3 and 0.43 ML {CHEN07A}. The change in intensity was attributed to a potential dependent, reversible change in the CO adlayer (see also Chapter 4.2). Since for the data discussed here, the changes in CO_L and CO_M intensity in the negative potential scan are also reversible, it is assumed that the overall CO_{ad} coverage does not change during the potential scan in the H_{upd} region. Therefore, one can conclude that no additional CO_{ad} is formed in the negative-going potential scan, which indicates that CO_{ad} is the only stable adsorbate formed during the adsorption of EG at potentials between 0.06 and 0.4 V.

The decrease of both the CO_L and the CO_M signals between 0.2 and 0.55 V in the positive-going scan is mainly attributed to a decrease of the polarisability of adsorbed CO_{ad} with increasing potential (see Chapter 4.2). The increase of the CO_M band between 0.2 and 0.3 V detected for the stripping experiment after the adsorption at 0.1 V as well as the finding that the CO_M intensity is smaller for 0.4 V than for 0.2 V, are explained by a preferential adsorption of CO in multiply bond configuration at potentials between 0.2 and 0.3 V and low total CO_{ad} coverages (see Chapter 4.2).

7.2.3 Glycol aldehyde

7.2.3.1 Potentiodynamic oxidation of glycol aldehyde

Similar to EG adsorption/oxidation, the potentiodynamic bulk-oxidation of a 0.1 M glycol aldehyde solution in 0.5 M H_2SO_4 was followed by *in situ* IR spectroscopy and the resulting ATR-FTIR spectra are shown in Fig. 96. The reference spectrum was acquired in 0.5 M H_2SO_4 at 0.06 V.

Linearly (CO_L) and multiply (CO_M) bonded CO_{ad} {LEUN88}{WIEL96}{MIKI02} are detected between 0.1 and 0.8 V in the positive-going scan and between 0.7 and 0.1 V in the negative-going scan. Beside CO_{ad}, adsorbed glycol aldehyde (H) and adsorbed glycolate (F) are the only adsorbates related to the adsorption/oxidation of glycol aldehyde. The potential dependent variation of the signal intensities is presented in Fig. 97, which includes the Faradaic current response (a) recorded during the potentiodynamic electrooxidation of glycol aldehyde, as well as the integrated IR intensity of the detected adsorbates CO_L (b), adsorbed glycolic acid (c) and adsorbed glycol aldehyde (d).

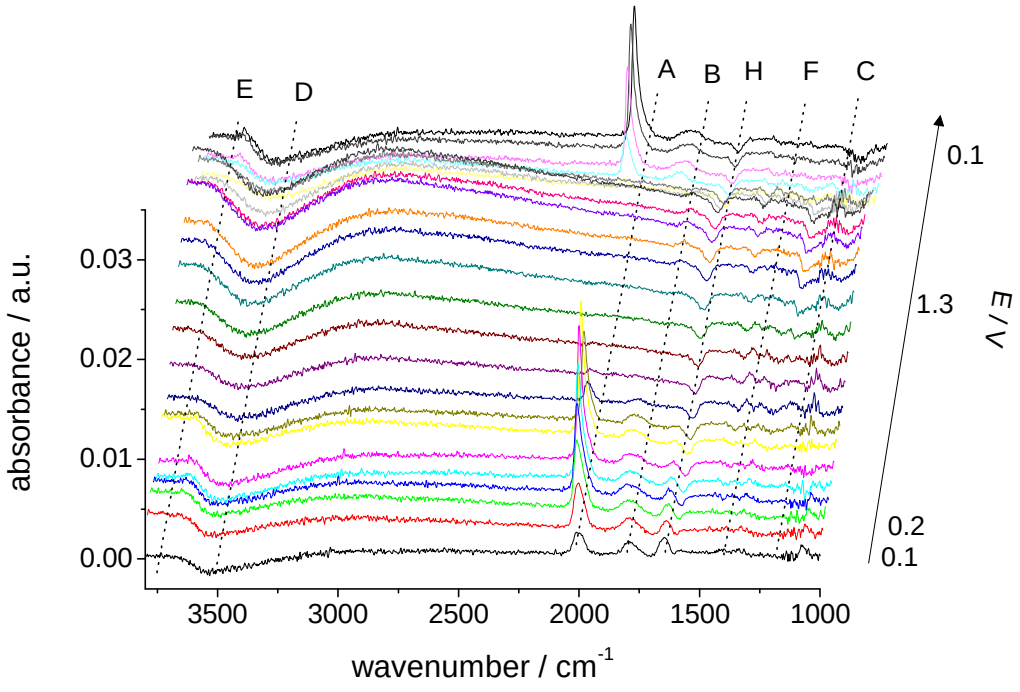

Fig. 96: IR-spectra acquired during potentiodynamic GA bulk-oxidation; v = 10 mV/s; temporal resolution 4.95 s/spectrum; electrolyte 0.1 M GA in 0.5 M H_2SO_4; reference spectrum at 0.06 V in 0.5 M H_2SO_4. A and B: linear and multiply adsorbed CO, C: adsorbed/displaced sulfate, E and D: co-adsorbed and displaced water, H: adsorbed glycol aldehyde, F: adsorbed glycolate (see also table 7).

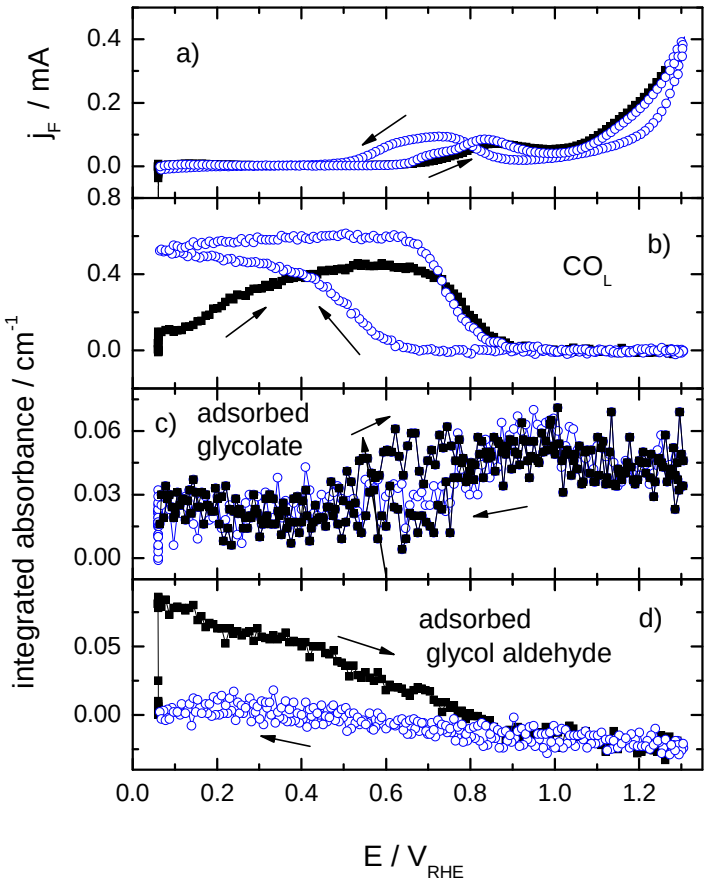

Fig. 97: Potentiodynamic GA bulk-oxidation; a) CV and integrated absorbance of b) linearly bonded CO, c) adsorbed glycolate and d) adsorbed glycol aldehyde taken from the IR spectra in Fig. 96, v = 10 mV/s; electrolyte 0.1 M GA in 0.5 M H_2SO_4. Filled squares: first positive-going scan; open circles: continuous cycling.

In the first positive-going scan, the first maximum of the Faradaic current peak is centered at about 0.82 V, with a small shoulder at about 0.7 V. As already discussed for the potentiodynamic oxidation of EG, the shoulder at 0.7 V is attributed to the oxidation of CO_{ad} to CO_2. This is further supported by the decrease of the CO_L signal, having the steepest decrease at 0.7 V. During the Faradaic current peak centered at 0.82 V, however, the CO_L intensity decreases to zero. Based on the IR data it is hardly possible to conclude whether CO_{ad} is not formed at this high potentials or whether it is formed and oxidized rapidly to CO_2. Both effects can be responsible for the low CO_{ad} coverage under these conditions. In a recent DEMS study it was reported that the Faradaic current at 0.82 V has no analogon in the CO_2 signal and the Faradaic current was attributed to the formation of incomplete oxidation products {WANG08F}. Furthermore, in the present study, the Faradaic current peak at 0.82 V correlates well with the increase in the integrated intensity of adsorbed glycolate, indicating the incomplete oxidation of glycol aldehyde to glycolic acid at this potential

{WIEL96}{DAIL98}. However, the formation of other C2 products, especially glyoxal, can not be excluded from the present data and is in fact very likely {HORA83B}{SHIB94M}.

At potential above 1.1 V, the Faradaic current increases again up to the positive potential limit of 1.3 V. Since at this high potential an oxidation of the Pt surface results in a change in the reflectivity {MIKI02}, the IR spectra do not deliver further insight into the processes responsible for the Faradaic current increase. Obviously the oxidation of glycol aldehyde on a PtO surface is possible. It was reported that at this high potentials incomplete oxidation of glycol aldehyde to glycolic acid and glyoxal prevails {HORA83B}{SHIB94M}. In the negative-going, scan a broad oxidation peak is found between 0.9 and 0.55 V, which coincides with the presence of the adsorbed glycolate (Fig. 97c). This is indicative for the oxidation of glycol aldehyde to glycolic acid in this potential regime. For potentials below 0.55 V, the current drops steeply to zero due to the formation of adsorbed CO (Fig. 97b). Finally, a reductive current is detected at 0.06 V, which according to recent DEMS results correlates with the formation of ethane and acetaldehyde {SCHN08}{WANG08F}. The Faradaic current in the second positive-going scan shows practically the same features as in the first positive-going scan and is therefore not discussed in detail.

The integral band intensities of CO_L and adsorbed glycol aldehyde, however, differ significantly between the first and the second positive-going scan. Already during the initial waiting time of 30 s at 0.06 prior to the potential scan (see also Chapter 3.3), the intensity of adsorbed glycol aldehyde as well as the intensity of CO_L increased. In the first positive-going scan, the CO_L integral band intensity continuously increases up to about 0.6 V, before decreasing to zero at potentials above 0.8 V, due to the onset of CO_{ad} oxidation to CO_2. In the negative-going scan, the integral band intensity of CO_L increases continuously for potentials below 0.6 V down to 0.06 V, resulting in a higher CO_L intensity at the onset of the subsequent positive-going scan compared to the CO_L integral band intensity in the first positive-going scan.

The band for adsorbed glycol aldehyde, in contrast, decreases continuously in the first positive-going scan, reaching a value of zero at about 0.8 V. In the subsequent negative-going scan, this band can not be detected, most likely due the higher CO_{ad} coverage formed in the negative-going scan (Fig. 97b). Further details on the time dependent adlayer development at constant potential are discussed in the next section.

7.2.3.2 Potentiostatic electrolyte exchange experiments

The Faradaic current response (a), the integral band intensity of CO_L (b) and CO_M (c) as well as the integral band intensity of adsorbed glycol aldehyde (d) and adsorbed glycolate (e) upon electrolyte exchange from 0.5 M H_2SO_4 to 0.1 M glycol aldehyde containing solution at 0.1, 0.2, 0.4 and 0.6 V are plotted in Fig. 98. At all potentials, GA adsorption results in an initial oxidative current peak. With increasing adsorption time, the Faradaic currents decay to very small values. The initial current spikes correlate with the onset of CO_{ad} formation and can therefore be attributed to the dissociative adsorption of glycol aldehyde to CO_{ad}.

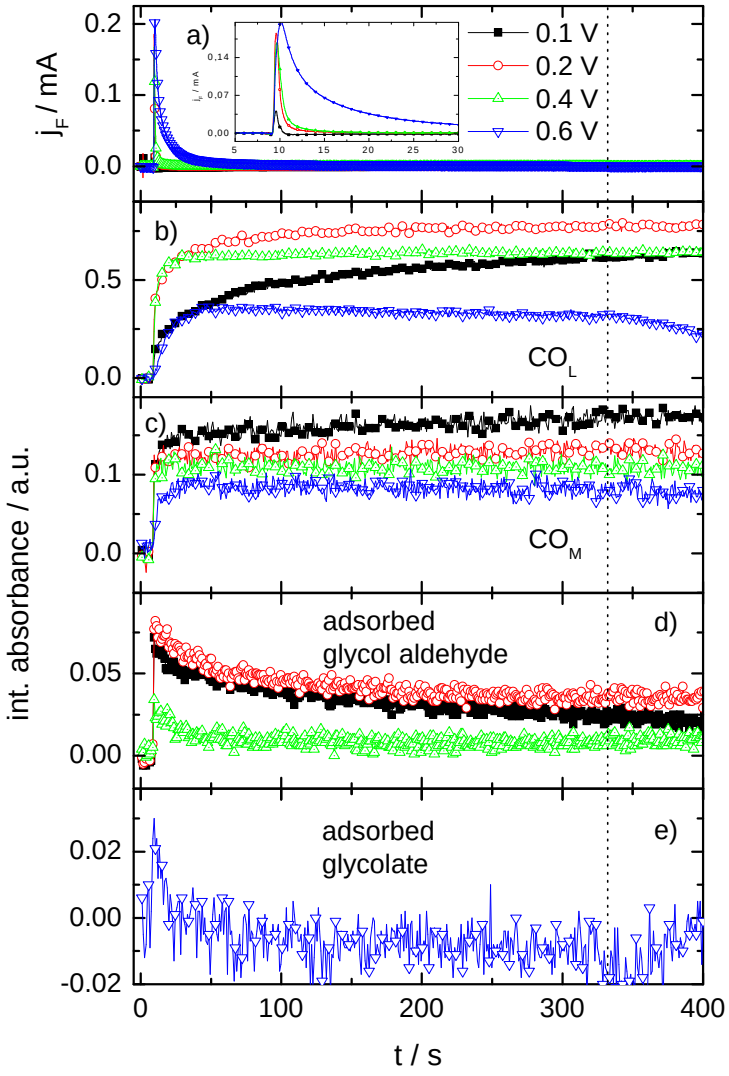

Fig. 98: Potentiostatic GA bulk-oxidation at different constant potential (see figure); a) Faradaic current density and integrated absorbance of: b) linearly bonded CO, c) multiply bonded CO, d) adsorbed glycol aldehyde and f) adsorbed glycolate; electrolyte 0.1 M GA in 0.5 M H_2SO_4; dashed vertical line at t = 330 s indicate the time when the cell was rinsed with 0.5 M H_2SO_4.

At 0.1 and 0.2 V, the Faradaic current also contains contributions from H_{upd} displacement by more strongly adsorbing CO. The fast increase in the CO_{ad} coverage at all potentials can also explain the subsequent fast decrease of the Faradaic current. At 0.1 V, a small reductive current is recorded. In a recent DEMS study the Faradaic current was attributed to the formation of acetaldehyde and ethane {WANG08F}. With increasing adsorption potential, the initial Faradaic current spike grows and the subsequent current decrease is slower.

For all adsorption potentials, the integral band intensities of CO_L and CO_M increase steeply after the electrolyte exchange to GA containing solution and the CO_L intensities saturate at t = 300 s (0.1 V), t = 100 s (0.2 V), t = 30 s (0.4 V) and t = 50 s at 0.6 V, respectively. At 0.6 V the CO_L intensity starts to decreases ($\Delta\theta(CO_{ad})/\Delta t$ = -0.001 molecules $\times$ site^{-1} $\times$ s^{-1}) when the cell was rinsed with GA free 0.5 M H_2SO_4 solution, due to oxidation of CO_{ad} without further formation of CO_{ad} from dissociative adsorption of GA (see also section 7.2.3.2). At all adsorption potentials, the CO_M intensities reach a constant value after about 20 s after the electrolyte exchange was triggered. As already discussed for the potentiostatic adsorption/oxidation of EG (see 7.2.2.2), the rate for CO_{ad} formation on a clean Pt surface at different adsorption potentials up to 0.6 V can be estimated from the slope of the initial increase of the CO_L band intensity. The resulting values are summarized in table 10. Please note that the error of the values in the table are rather large, due to very fast CO_{ad} formation rate and the fact that already after 2 to 3 s the CO_{ad} coverage versus time plot bends significantly. To calculate the CO_{ad} formation rate on the clean Pt electrode only the very initial values for the CO_L intensities, up to 3 s after the electrolyte exchange, were used.

Similar to EG adsorption, a high rate for CO_{ad} formation is measured at 0.4 V (EG: 0.1 ML/s). In contrast to EG adsorption, however, the highest value for the CO_{ad} formation rate upon adsorption/oxidation of GA is obtained at 0.2 V. Even at 0.1 V rather high rates for CO_{ad} formation are determined, suggesting that most likely the aldehyde functionality in GA is responsible for the fast adsorption at low potentials (0.06 to 0.2V) {WANG08F}.

E_{ads}/V_{RHE}	0.1	0.2	0.4	0.6
$\Delta\theta(CO_{ad})/\Delta t$ [ML/s]	0.04±0.015	0.14±0.1	0.10±0.04	0.02±0.005

Table 10: CO_{ad} formation rates upon adsorption/oxidation of GA on a clean Pt electrode at different potentials. The rates are given in terms of monolayers/second (ML/s), which is equivalent to molecules $\times$ site^{-1} $\times$ s^{-1}.

This suggestion is further supported by the strong IR band detected at 0.1 and 0.2 V, which is attributed to adsorbed glycol aldehyde (Fig. 98d). The intensity of this band increases steeply upon electrolyte exchange to GA containing solution. Since this band is detected prior to CO_L and CO_M formation, the IR spectra suggest that C-C bond splitting is not instantaneous and that the precursor for CO_{ad} formation, i.e., adsorbed glycol aldehyde, still contains an intact C-C bond. This proposal is further supported by the finding that the intensity of the aldehyde band decreases with time, accompanied by an increase of the CO_L and the CO_M bands. This behavior is tentatively explained by the decomposition of adsorbed glycol aldehyde to CO_{ad}. A similar intensity-adsorption time profile was already found for the adsorption of ethanol, where it could be shown that the adsorbed acetyl species are indeed the precursor for CO_{ad} formation in the course of ethanol oxidation (see section 6.1.2.3).

7.2.3.3 Potentiodynamic adsorbate stripping experiments

The CV (a) and the integrated absorbances of linearly (b) and multiply (c) bonded CO_{ad} recorded during the potentiodynamic adsorbate stripping resulting from adsorption of 0.1 M glycol aldehyde containing solution for 5 min. at 0.1, 0.2 and 0.4 are shown in Fig. 99. The general characteristics of the CV's are similar to those of ethylene glycol stripping, showing, i) a suppressed H_{upd} region due to the presence CO_L and CO_M and ii) a peak at about 0.68 V attributed to the oxidation of CO_{ad}. However, for the stripping subsequent to the adsorption of glycol aldehyde at 0.1 V, there is a positive current signal above that of the base CV of a clean Pt electrode, in the potential regime between 0.8 and 1.2 V, indicating the oxidation of other adsorbates besides CO_{ad}. Assuming that only CO_{ad} oxidation to CO_2 contributes to the Faradaic current peak at 0.7 V, the relative CO_{ad} coverage $\theta_{CO,rel.}$ can be calculated from the charge of the peak at 0.7 V, by integrating the Faradaic current over time in the potential regime from 0.4 V to 0.85 V. The charge is referred to the coverage $\theta_{CO,sat}$ gained via CO adsorption at 0.06 V. and the results are summarized in table 11.

The maximum adsorbate coverage was found at 0.1 V. It decreases with increasing adsorption potential, which agrees with the finding of Wang et al. on a carbon supported Pt catalyst electrode {WANG08F}. For the adsorbate stripping subsequent to GA adsorption at 0.2 V the integrated absorption of the CO_L band is constant during the negative-going potential scan, whereas the integrated absorption of the CO_M band grows. A similar reversible change in the CO_M intensity was reported by Chen et al., when scanning the electrode potential from 0.4 to 0.06 V at defined, constant CO_{ad} coverages of 0.3 and 0.43 ML. The change in intensity was

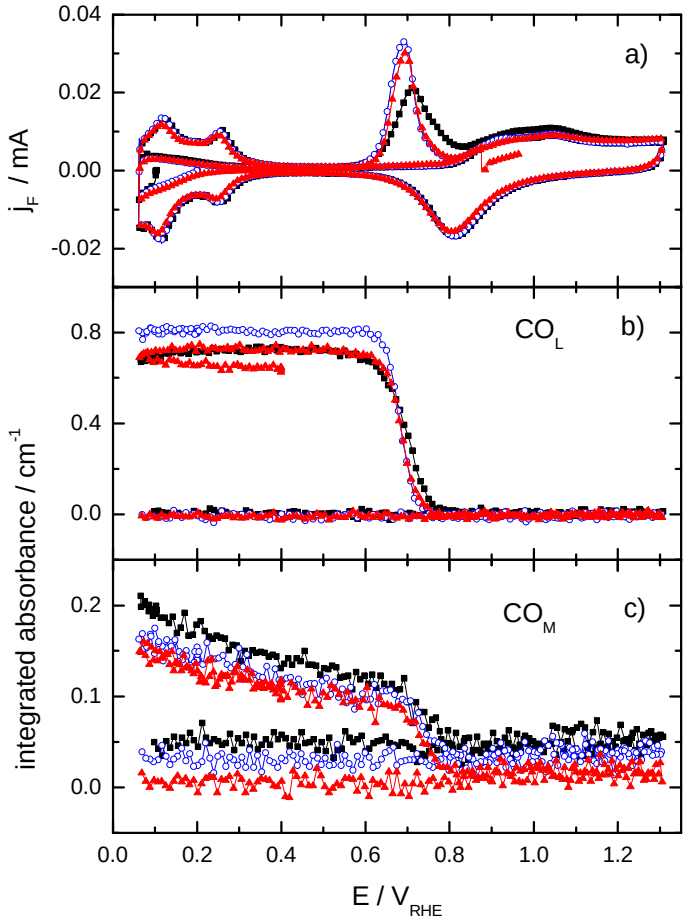

Fig. 99: Adsorbate stripping subsequent to the potentiostatic GA adsorption/oxidation at 0.1 (filled squares), 0.2 (open circles) and 0.4 V (filled triangles): a) CV and the integrated absorbances of b) linear bonded CO and c) multiply bonded CO.; v = 10 mV/s; electrolyte 0.5 M H_2SO_4.

E_{ads}/V_{RHE}	0.06	0.1	0.2	0.3	0.4
Rel. $\theta(CO_{ad})$ / %	53	80	79	79	72

Table 11: Relative CO_{ad} coverage resulting from GA adsorption at constant potential, as calculated from the Faradaic current peak at 0.7 V (details see text).

attributed to a potential dependent, reversible change in the CO adlayer structure {CHEN07A} (see also Chapter 4.2). Since for the data discussed here the changes in CO_M intensity in the negative potential scan are also reversible, it is assumed that the overall CO_{ad} coverage does not change during the potential scan in the H_{upd} region. Therefore, one can conclude that similar to the potentiodynamic stripping of ethylene glycol adsorbates (see section 7.2.2.3), no additional CO_{ad} is formed in the negative-going potential scan, which

supports that CO_{ad} is the only stable adsorbate formed during the decomposition of GA at 0.2 V. However, for the adsorbate stripping scan performed after GA adsorption at 0.4 V, both the CO_L as well as the CO_M bands increase in the first negative-going scan. In the subsequent positive-going scan at 0.4 V the CO_L band intensity is still larger compared to the intensity at 0.4 V prior to the potential excursion to the H_{upd} region. Since the changes in the CO_L intensity are irreversible, the higher CO_L intensities are attributed to an increased CO_{ad} coverage, resulting form decomposition of stable C2 adsorbates to CO_{ad} during the potential cycling in the H_{upd} region. These C2 adsorbates are tentatively assigned to adsorbed glycol aldehyde species which are detected at 0.4 V prior to the adsorbate stripping. After the potential excursion to the H_{upd} region, the band is no more visible in the IR spectra, indicating that this adsorbate is either reductively desorbed and/or decomposed to CO_{ad}. The former case was shown to be correct for the stripping of ethanol adsorbates applying simultaneous ATR-FTIRS/DEMS measurements (see section 6.2.2.3).

7.2.3.4 Summary

GA dissociative adsorption results in the fast build-up of a CO adlayer for adsorption potentials ≤ 0.6 V. In electrolyte exchange experiments it was shown that at low potential (0.06 to 0.2V), , adsorbed glycol aldehyde is detected on the surface prior to CO_{ad} formation, indicating that this species detected at 1640 cm^{-1} is the precursor for CO_{ad} formation. At high potentials the formation of GS was proven via the IR band detected at 1396 and 1333 cm^{-1}, which was assigned to adsorbed glycolate. The relatively high Faradaic currents and CO_{ad} formation rates determined from potentiodynamic and potentiostatic measurements show that GA is a rather reactive intermediate in the course of EG oxidation.

7.2.4 Glycolic Acid

7.2.4.1 Potentiodynamic oxidation of glycolic acid

The ATR-FTIR spectra acquired during the potentiodynamic bulk-oxidation of 0.1 M glycolic acid containing 0.5 M H_2SO_4 solution are shown in Fig. 100. The reference spectrum was measured in 0.5 M H_2SO_4 at 0.06 V. Besides linearly and multiply adsorbed CO at 2060 and 1800 cm^{-1}, respectively, adsorbed glycolate is the only adsorbate (1395 and 1335 cm^{-1}) detected by IR spectroscopy, during potentiodynamic oxidation of glycolic acid. The Faradaic current response (a) recorded during the potentiodynamic electrooxidation of glycolic acid, as well as the potential dependence of the integrated IR intensity of the detected adsorbates CO_L (b), CO_M (c) and adsorbed glycolate (d) are plotted in Fig. 101.

Only a very small Faradaic current peak, centered at 0.8 V, and an increasing current for potentials above 1.2 V are measured during the potentiodynamic oxidation of glycolic acid in the first positive-going scan. In the subsequent negative-going scan, the Pt-oxide reduction current, normally centered at 0.8 V, overlaps with a small positive current correlated to the oxidation of glycolic acid at potentials between 0.8 and 0.4 V. The nearly featureless Faradaic current response upon potentiodynamic oxidation of glycolic acid (Fig. 101a) already indicates that the rate for glycolic acid oxidation/decomposition on the Pt electrode is very slow.

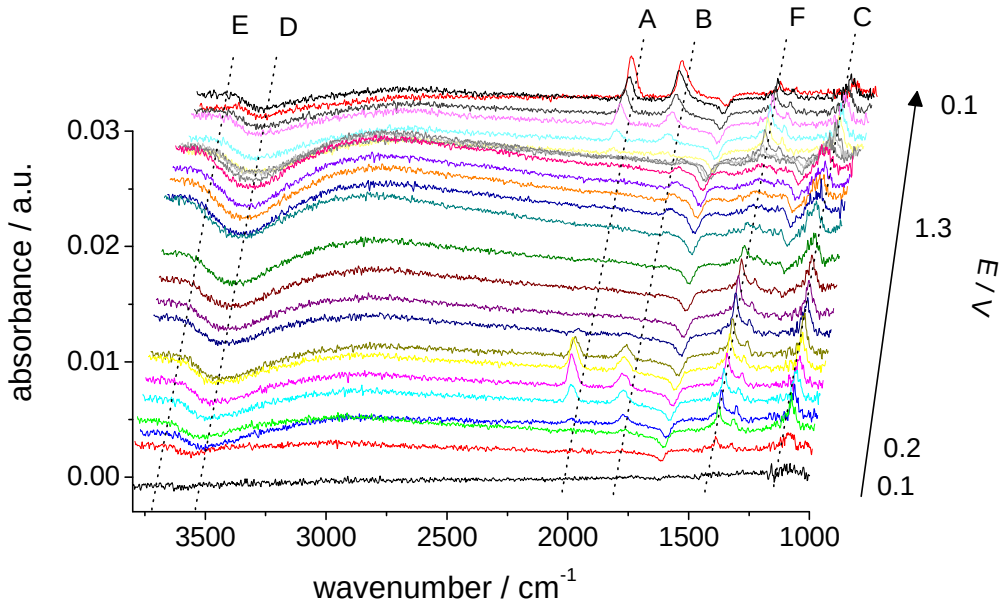

Fig. 100: IR-spectra recorded during potentiodynamic GS bulk-oxidation; v = 10 mV/s; temporal resolution 4.95 s/spectrum; electrolyte 0.1 M GS in 0.5 M H_2SO_4; reference spectrum at 0.06 V in 0.5 M H_2SO_4. A and B: linear and multiply adsorbed CO, C: adsorbed/displaced sulfate, E and D: co-adsorbed and displaced water, F: adsorbed glycolate (see also table 7).

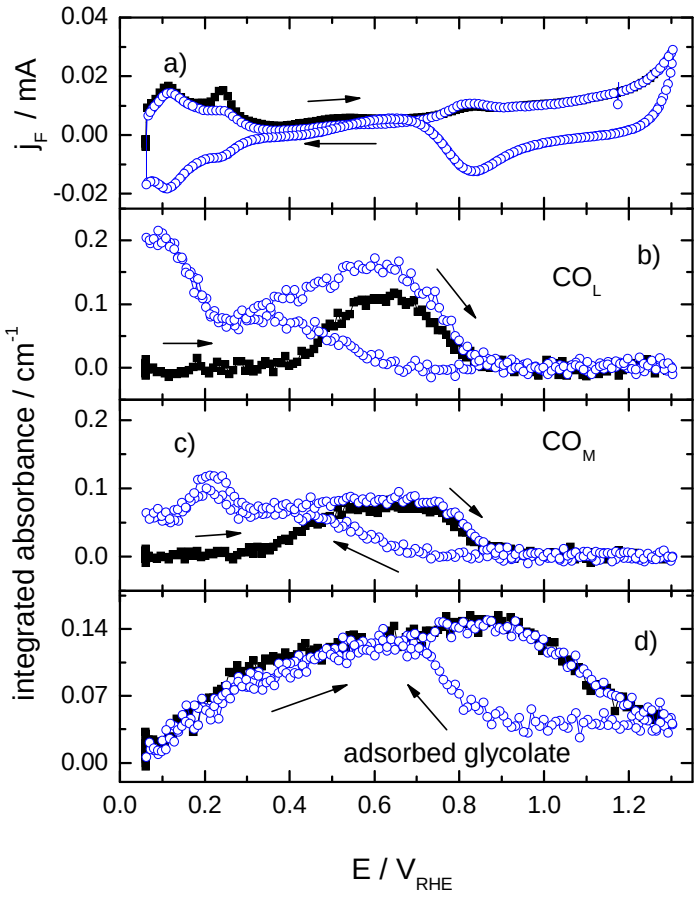

Fig. 101: Potentiodynamic GS bulk-oxidation; a) CV and integrated absorbance of b) linearly bonded CO, c) multiply bonded CO and d) adsorbed glycolate taken from the IR spectra in Fig. 100, v = 10 mV/s; electrolyte 0.1 M EG in 0.5 M H_2SO_4. Filled squares: first positive-going scan; open circles: continuous cycling.

Although these data agree well with previous reports {ORTS92}·{WANG08F}, the extremely low activity of glycolic acid (GS) is somehow surprising, since GS contains an alcohol functionality which can in principle be further oxidized. In a recent DEMS study, the finding was explained by the special character of the molecule: the presence of the OH group and the carboxyl group in the same molecule may lead to oligomerisation via ester formation, resulting in surface blocking {WANG08F}. Another possible explanation for the low activity of GS, based on the present IR data, is given below.

The integral band intensity of linearly and multiply bonded CO (Fig. 101b and c,) remains close to zero during the initial waiting time of 30 s at 0.06 V. Both intensities increase in the subsequent positive-going scan, starting at 0.4 (CO_L) and 0.35 V (CO_M), respectively. They reach about constant values at potentials between 0.55 and 0.75 V, before dropping down to zero for potentials above 0.85 V, due to the oxidation of CO_{ad} to CO_2. In the negative-going scan, the CO_L and the CO_M band intensities start to increase at about 0.65 V, reaching a

constant value between 0.5 and 0.35 V. The reversible changes in the CO_M and CO_L intensities at potentials below 0.35 V are attributed to structural changes in the CO adlayer at low CO_{ad}, constant coverages caused by co-adsorption of H_{upd} {CHEN07A} (see also chapter 4.2). In the positive-going scan, the CO_L intensity further increases for potentials above 0.35 V, indicating the formation of additional CO_{ad} from dissociative adsorption of glycolic acid. However, the maximum values of the integral band intensity of CO_L and CO_M are significantly smaller for the adsorption of glycolic acid compared the CO_L and CO_M bands during the adsorption/oxidation of EG and GA, indicating that the rate for dissociative adsorption is much smaller for GS. Further details on the potential dependent CO_{ad} formation rate are given in section 7.2.4.2.

The integral band intensity of adsorbed glycolic acid (Fig. 101d) increases continuously in the first positive-going scan, reaching a maximum at 0.9 V before decreasing at higher potentials. In the negative-going scan, adsorbed glycolic acid can be detected for potentials below 0.8 V, and the intensity first increases down to 0.7 V before decreasing again with a further decrease in potential. This potential dependence is very typical for anion adsorption as for example reported for the adsorption of acetic acid or for sulfate adsorption {CORR88}{FUTA05}, and is in complete agreement with the assignment of the bands at 1395 and 1335 cm^{-1} to adsorbed glycolate. In a radiotracer study by Horani et al. {HORA73} it was reported that glycolic acid is reversibly adsorbed on Pt, similar to anion adsorption. Furthermore, the preferential adsorption of glycolic acid on the Pt surface via the two oxygen atoms of the carboxyl functionality might be responsible for the low activity of glycolic acid compared to EG and GA. In this adsorption configuration, the reactive OH-group of glycolic acid points away from the catalytically active Pt surface and therefore the oxidation of the alcohol group might be hindered {HORA73}.

7.2.4.2 Potentiostatic electrolyte exchange experiments

The Faradaic current response (a), the integral band intensity of the CO_L (b) and CO_M (c) species as well as the integral band intensity of adsorbed glycolate (d) upon electrolyte exchange from 0.5 M H_2SO_4 to 0.1 M glycolic acid containing solution at 0.1, 0.2, 0.4 and 0.6 V are plotted in Fig. 102.

For adsorption at 0.1 V, a small cathodic current is visible during the whole time of glycolic acid adsorption. The slowly increasing CO_L and CO_M band intensities at this potential suggest that the reductive current might be attributed the reduction of the carboxyl group to CO_{ad}.

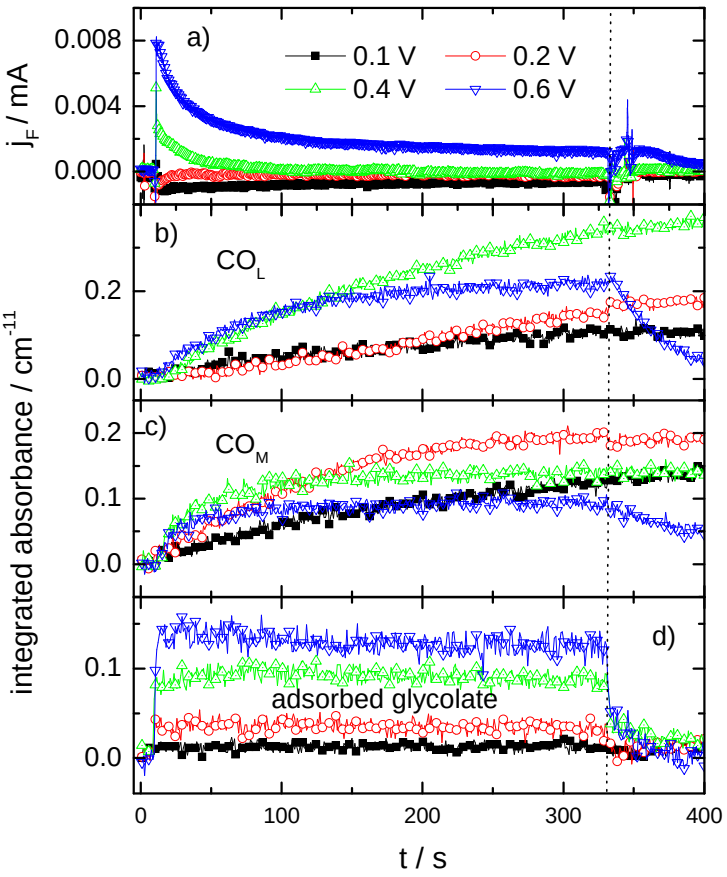

Fig. 102: Potentiostatic GS bulk-oxidation at different constant potential (see figure); a) Faradaic current density and integrated absorbance of: b) linearly bonded CO, c) multiply bonded CO, d) adsorbed glycolate; electrolyte 0.1 M GS in 0.5 M H_2SO_4, the dashed vertical line indicates the time when the cell was rinsed with GS free 0.5 M H_2SO_4.

However, the reductive charge measured during the adsorption is far too large compared to the small amount of CO_{ad} detected by IR spectroscopy. Furthermore, the formation of CO_{ad} should result in a positive current from the displacement of upd-hydrogen and therefore no reductive Faradaic current is expected at all for the reduction of the carboxyl group to CO_{ad} (see also adsorption of OS). The negative Faradaic current is tentatively attributed to the onset of hydrogen evolution on the Pt film electrode at 0.1 V. Also in a recent DEMS study, reductive currents were reported for potentials below 0.16 V, but there was no additional information on the underlying processes given by the authors {WANG08F}.

At 0.2 V, after an initial reductive current, the Faradaic current is practically zero during the adsorption of GS. Considering that before the electrolyte exchange the electrolyte in the Teflon inlet capillary can not be purged, the initial cathodic current is explained by the reduction of trace amounts of oxygen impurities. For adsorption potentials ≥ 0.4 V, positive Faradaic currents are measured, which are increasing with increasing potential. Similar to the

potential dependence of EG adsorption, this increasing rate for adsorption/oxidation is related to an increasing reactivity of the alcohol group at more positive potentials, either due to the decreasing H_{upd} coverage or due to a potential induced increase in the adsorption/oxidation probability of the alcohol group. However, compared to the Faradaic current recoded for the adsorption of EG, the current measured during GS adsorption are about 10 times smaller, which is further discussed below.

For all adsorption potentials, the intensities of CO_L and CO_M increase continuously upon adsorption of GS and do not reach saturation during the adsorption of GS for 5 min.. When the cell is rinsed with GS free 0.5 M H_2SO_4 at t = 335 s (dashed vertical line in Fig. 102) at 0.6 V, the CO_L intensity starts to decreases ($\Delta\theta(CO_{ad})/\Delta t$ = -0.003 molecules $\times$ site^{-1} $\times$ s^{-1}) due to oxidation of CO_{ad} without further formation of CO_{ad} from dissociative adsorption of GS (see also section 7.2.2.2), whereas at lower adsorption potentials the intensities do not change significantly upon rinsing. The rate for CO_{ad} formation on a clean Pt surface at different adsorption potentials can be estimated from the slope of the initial increase of the CO_L band intensity (see also section 7.2.2.2) and the values are summarized in table 12. However, since for the adsorption of GS the CO_{ad} oxidation rate at 0.6 V under steady-state conditions at t = 330 s is comparable to the initial CO_{ad} formation rate the determined at 0.6 V (see table 12), the later value is expected to be underestimated.

E_{ads}/V_{RHE}	0.06	0.1	0.2	0.3	0.4	0.5	0.6
$\Delta\theta(CO_{ad})/\Delta t$ [ML/s]	8.4×10^{-5}	2.1×10^{-4}	4×10^{-4}	4.6×10^{-4}	0.0013	0.0028	0.0017

Table 12: CO_{ad} formation rates upon adsorption/oxidation of GS on a clean Pt electrode at different potentials. The rates are given in terms of monolayers/second (ML/s), which is equivalent to molecules $\times$ site^{-1} $\times$ s^{-1}.

The CO_{ad} formation rate on a clean Pt surface increases with potential up to 0.5 V. At 0.6 V, a slightly smaller value is determined most likely due to the onset of CO_{ad} oxidation to CO_2 at this potential (see section 4.2), which results in an underestimation of the CO_{ad} formation rate. In comparison with adsorption of EG, the rates for CO_{ad} formation are more than 10 times smaller. The IR band correlated with the formation of adsorbed glycolate is detected for

adsorption potentials ≥ 0.2 V (Fig. 102d). Directly after the electrolyte exchange to GS containing solution the integral band intensity of adsorbed glycolate increases steeply and reaches a steady-state value about 3 to 4 s. The steady-state coverage of adsorbed glycolate increases with potential up to 0.6 V, which is the typical potential dependence of adsorbing anions {HORA73}{CORR88A}{NART94}. The slight decrease of the integral band intensity of adsorbed glycolate at 0.6 V with time is attributed to the increasing coverage of adsorbed CO (Fig. 102b, c). When the cell is rinsed with 0.5 M H_2SO_4 (dashed, vertical line in Fig. 102), the integral band intensity of adsorbed glycolate immediately decreases to zero for all adsorption potentials, indicating the adsorbed glycolate is in a fast adsorption/desorption equilibrium with glycolic acid. Since besides CO_{ad}, adsorbed glycolate is the only adsorbate detected via IR spectroscopy, it can be concluded that GS adsorbs preferentially via the two oxygen atoms of the carboxyl group perpendicular to the Pt surface, similar to all carboxylic acid investigated so far (formic acid, acetic acid). In this stable adsorption configuration, the reactive –OH group points away from the catalytically active Pt surface and its oxidation is hindered. This could explain the about 100 times smaller Faradaic current for the oxidation of GS, compared to EG oxidation, measured under steady-state conditions at 0.6 V. However, electronic effects on the reactivity of the alcohol group, induced by the presence of the COOH group, might also be responsible for the smaller reactivity of GS compared to EG.

7.2.4.3 Potentiodynamic adsorbate stripping experiments

The CV (a) and the integrated absorbances of linearly (b) and multiply (c) bonded $CO_{ad,}$ recorded during the potentiodynamic adsorbate stripping, performed subsequent to the adsorption of 0.1 M glycolic acid at 0.1, 0.2 and 0.4 V, are shown in Fig. 103. The general characteristics of all CV's are similar to the features of ethylene glycol stripping, i.e., i) a suppressed H_{upd} adsorption/desorption due to the presence of CO_L and CO_M, and ii) a peak at about 0.68 V attributed to the oxidation of CO_{ad}. Assuming that only CO_{ad} oxidation to CO_2 contributes to the Faradaic current peak at 0.68 V, the relative CO_{ad} coverage (rel. $\theta(CO_{ad})$) can be calculated from the charge of the peak at 0.68 V, relative to the saturation coverage $\theta_{CO,sat}$ obtained upon gas phase CO adsorption at 0.06 V. The results are summarized in table 13.

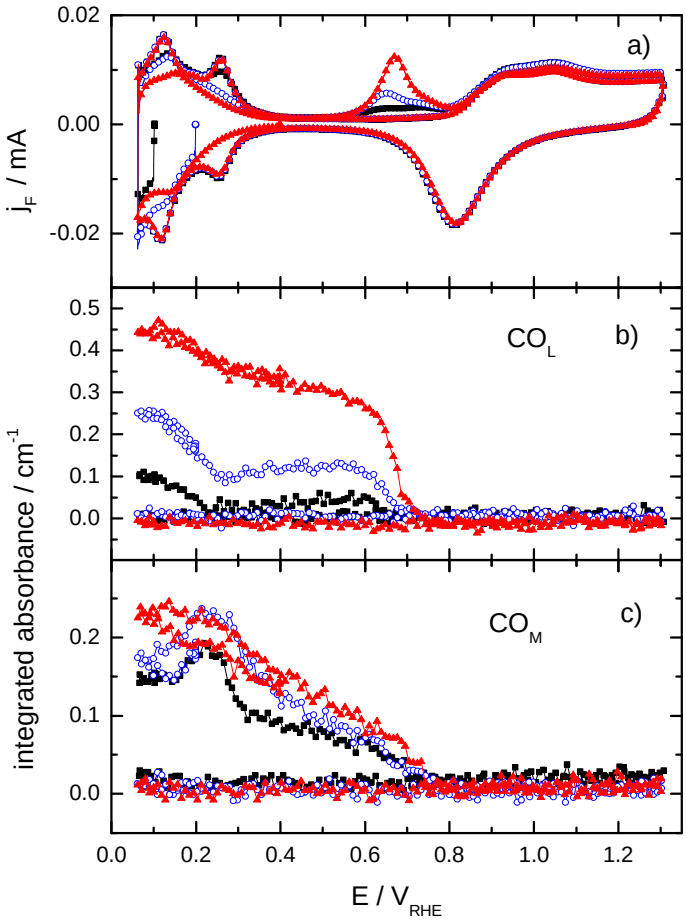

Fig. 103: Adsorbate stripping subsequent to the potentiostatic GS adsorption/oxidation at 0.1 (filled squares), 0.2 (open circles) and 0.4 V (filled triangles): a) CV and the integrated absorbances of b) linear bonded CO and c) multiply bonded CO.; v = 10 mV/s; electrolyte 0.5 M H_2SO_4.

E_{ads}/V_{RHE}	0.06	0.1	0.2	0.3	0.4
Rel. $\theta(CO_{ad})$ / %	9	14	30	36	45

Table 13: Relative CO_{ad} coverage resulting from GS adsorption at constant potential, as calculated from the Faradaic current peak at 0.68 V (details see text).

The rel. CO_{ad} coverage is increases continuously with potential, and at 0.4 V the maximum coverage is about 45 % of that of a CO saturated surface, in good agreement with the findings of Wang et al. on a carbon supported Pt electrode {WANG08F}. Again, the smaller CO_{ad} coverages calculated from the GS adsorbate stripping experiments in comparison to EG adsorbate stripping experiments mirror the slow kinetics for GS decomposition. Similar to the adsorbate stripping experiments performed after EG adsorption at 0.1 V, the reversible

changes in the CO_L and CO_M bands during the negative-going potential scan are explained by potential induced structural change in the CO_{ad} layer at a constant overall CO_{ad} coverage (see also EG adsorbate stripping). This implies that upon cycling the potential in the H_{upd} region no additional CO_{ad} is formed by the decomposition of strongly adsorbed C2 species, as it was found for the adsorbate stripping experiments performed subsequent to the adsorption of ethanol and glycol aldehyde. Therefore, it is concluded that besides CO_{ad} no other stable adsorbates are present in significant amounts on the Pt surface after adsorption of GS at 0.1, 0.2 and 0.4. This is also in agreement with the IR spectra showing no additional bands besides CO_L and CO_M.

7.2.4.4 Summary

The reactivity of GS for C-C bond splitting, which was followed via CO_{ad} formation, as well as the overall reactivity, measured via the Faradaic current upon GS adsorption/oxidation is very small compared to EG and GA. GS binds to the Pt surface via two oxygen atoms of the carboxyl group, as evidenced by an IR absorption band detected at 1396 and 1333 cm^{-1}. The low reactivity of GS was tentatively explained by the preferential adsorption in the latter configuration, where the reactive OH group points away from the catalytically active Pt surface. The very small Faradaic currents and CO_{ad} formation rates determined from potentiodynamic and potentiostatic measurements show that GS is more a “dead end” than a reactive intermediate in the course of EG oxidation.

7.2.5 Glyoxal

7.2.5.1 Potentiodynamic oxidation of glyoxal

The adsorption behavior of GOA is of special interest, since this molecule contains two aldehyde groups. Therefore, its adsorption/oxidation behavior can be regarded as a representative for the reactivity of a terminal carbonyl group. In Fig. 104, a series of *in situ* ATR-FTIR spectra acquired during the potentiodynamic bulk-oxidation of a solution containing 0.1 M glyoxal in 0.5 M H_2SO_4 are shown. The reference spectrum was measured in 0.5 M H_2SO_4 at 0.06 V.

Besides linearly and multiply adsorbed CO at 2060 and 1800 cm^{-1}, respectively, adsorbed glyoxal (1650 cm^{-1}) and adsorbed glyoxylate (1385 and 1310 cm^{-1}) are the only assigned adsorbates detected by IR spectroscopy during the potentiodynamic oxidation of glyoxal. A band centered at 1740 cm^{-1}, observed at potentials between 0.8 and 1.2 V, can not be attributed to a specific adsorption configuration by now. The Faradaic current response (a) recorded during the potentiodynamic electrooxidation of glyoxal, as well as the integrated IR intensity of the detected adsorbates CO_L (b), adsorbed glyoxal (c) and adsorbed glyoxylate (d) are plotted in Fig. 105.

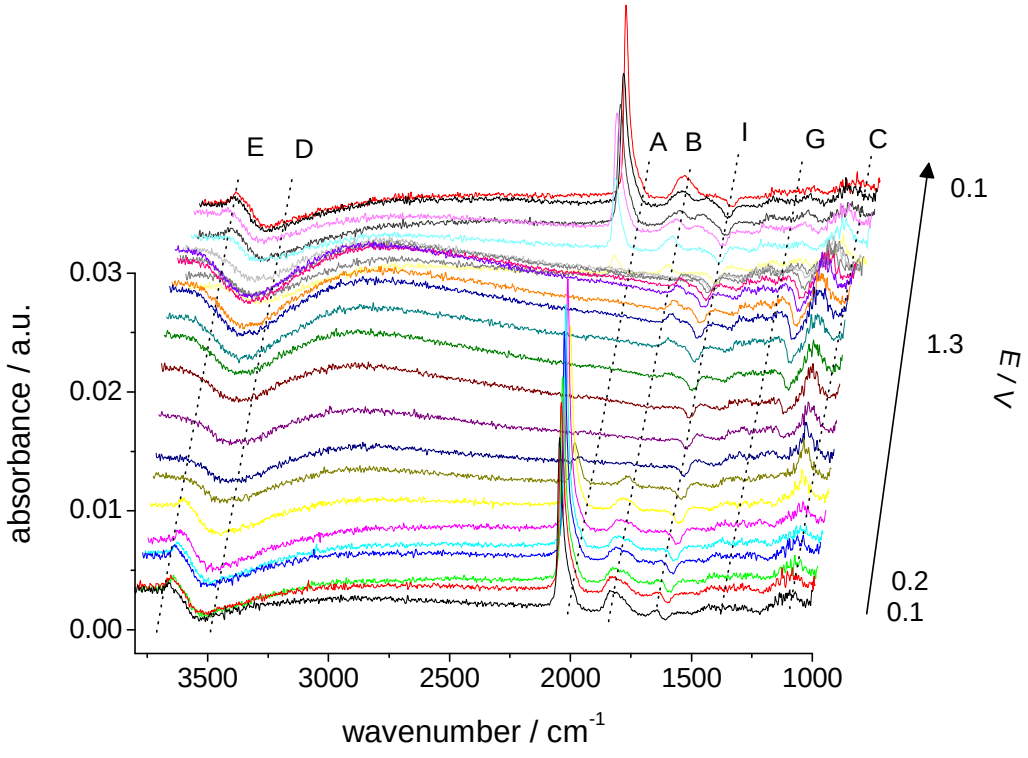

Fig. 104: IR-spectra acquired during potentiodynamic GOA bulk-oxidation; v = 10 mV/s; temporal resolution 4.95 s/spectrum; electrolyte 0.1 M GOA in 0.5 M H_2SO_4; reference spectrum at 0.06 V in 0.5 M H_2SO_4

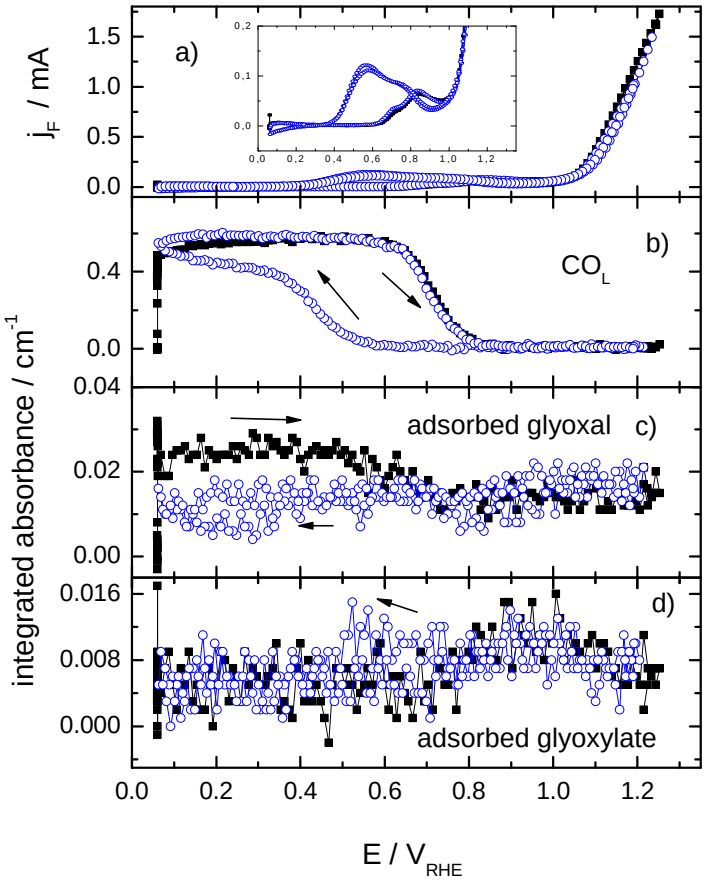

Fig. 105: Potentiodynamic EG bulk-oxidation; a) CV and integrated absorbance of b) linearly bonded CO, c) adsorbed glyoxal and d) adsorbed glyoxylate taken from the IR spectra in Fig. 104, v = 10 mV/s; electrolyte 0.1 M GOA in 0.5 M H_2SO_4

In the first positive-going scan, glyoxal bulk oxidation starts at about 0.6 V, leading to a broad peak with two maxima centered at about 0.7 and 0.82 V, respectively. As already discussed for the potentiodynamic oxidation of EG and GA, the shoulder at 0.7 V is attributed to the oxidation of CO_{ad} to CO_2. This is further supported by the decrease of the CO_L signal, which has its steepest decrease at 0.7 V. At 0.8 V, the CO_L band intensity is essentially zero and the Faradaic current increases further resulting in a Faradaic current peak centered at 0.83 V. Based on the IR data, it is hardly possible to distinguish whether CO_{ad} is not formed at this high potentials or whether its subsequent oxidation to CO_2 is much faster than its formation, which would also result in a very low steady-state CO_{ad} coverage. In recent DEMS studies, however, it was reported that the Faradaic current at 0.82 V has no analogon in the CO_2 signal. Therefore, the Faradaic current peak centered at 0.82 V was assigned to the oxidation of glyoxal to incompletely oxidized reaction products, most likely glyoxalic acid and/or oxalic acid {SCHN08}{WANG08F}.

At potentials positive of 1.0 V, the Faradaic current increases again up to the positive potential limit of 1.3 V, which shows that the oxidation of glyoxal on a PtO surface is possible. In recent DEMS studies, it was reported that at this high potentials incomplete oxidation of glyoxal prevails {SCHN08}{WANG08F}. In the negative-going scan, the Faradaic current decreases from 1.3 to about 0.9 V. At more negative potentials a broad oxidation peak is found between 0.9 and 0.4 V, before the current drops to zero at more negative potentials. The current decrease with decreasing potential can be attributed to the formation of adsorbed CO, poisoning the Pt electrode. In the second positive-going scan, the Faradaic current shows practically the same features as in the first positive-going scan, and is therefore not discussed in detail.

The integral band intensity of CO_L increases already strongly during the initial waiting time of 30 s at 0.06 V, prior to the potential scan (Fig. 105b). In the first positive-going scan (filled squares) the CO_L integral band intensity increases slightly up to about 0.6 V, before decreasing to zero at potential of about 0.8 V, due to the onset of CO_{ad} oxidation to CO_2. In the negative-going scan, the integral band intensity of CO_L continuously increases for potentials below 0.6 V, first steeply down to 0.4 V and then less pronounced down to 0.06V, reaching slightly higher values compared to the CO_L integral band intensity in the first positive-going scan.

The band for adsorbed glyoxal is clearly visible at 0.06 V on the clean, hydrogen covered Pt surface. Its intensity decreases strongly already during the waiting time at 0.06 V, due to the developing CO adlayer and completely vanishes at potential above 0.6 V in the first positive going potential scan. In the subsequent negative-going scan, the band correlated to adsorbed glyoxal can not be detected, due the higher CO_{ad} coverage formed in the negative-going scan, compared to the clean Pt surface at 0.06 V. Further details on the time dependent adlayer development at constant potential are discussed in the next section.

7.2.5.2 Potentiostatic electrolyte exchange experiments

Similar to the measurements concerning the adsorption/oxidation of EG, GA and GS, I also performed potentiostatic adsorption transients for the adsorption/oxidation of GOA at 0.06, 0.1, 0.2, 0.3, 0.4, 0.5 and 0.6 V. The Faradaic current response (a), the integral band intensity of CO_L (b) and CO_M (c) as well as the integral band intensity of adsorbed glyoxalate (d) upon electrolyte exchange from 0.5 M H_2SO_4 to 0.1 M glyoxal (GOA) containing solution at 0.1, 0.2, 0.4 and 0.6 V are plotted in Fig. 106.

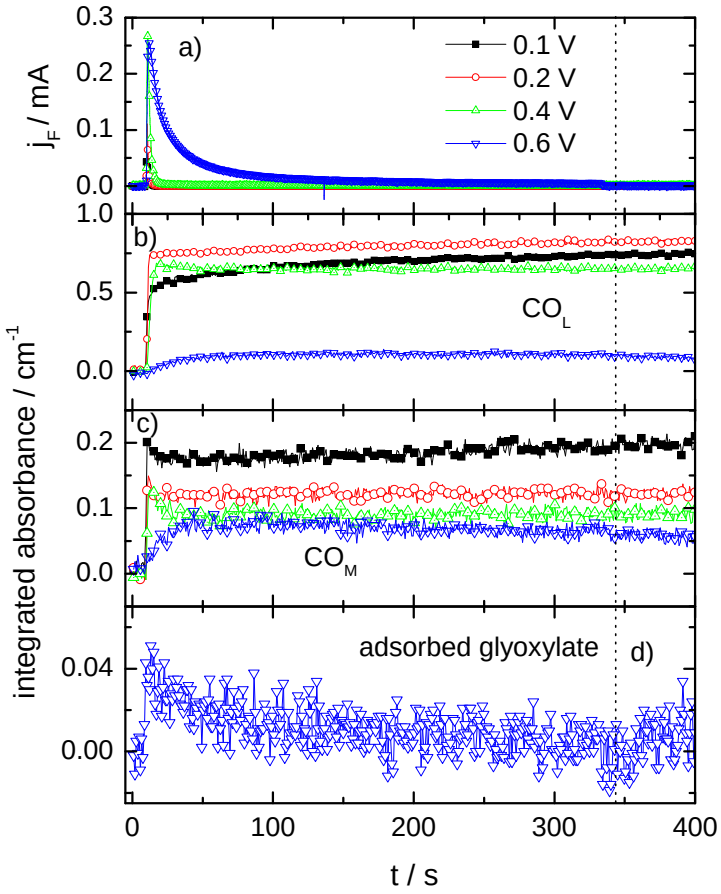

Fig. 106: Potentiostatic GOA bulk-oxidation at different constant potential (see figure); a) Faradaic current density and integrated absorbance of: b) linearly bonded CO, c) multiply bonded CO and d) adsorbed glyoxylate; electrolyte 0.1 M GOA in 0.5 M H_2SO_4

At all potentials the adsorption/oxidation of GOA results in an oxidative current peak at the beginning. With continuous adsorption time, the Faradaic currents drop to very small values. With increasing adsorption potential, the initial current peak increases and the subsequent current decrease is slower.

The integral band intensities of CO_L and CO_M (Fig. 106b, c) increase steeply after the electrolyte exchange to GOA containing solution and the CO_L intensities reach a steady –state value at about t = 200 s at 0.1 V, t = 30 s at 0.2 V, t = 25 s at 0.4 V and t = 50 s at 0.6 V, respectively. When the cell is rinsed with GAO free 0.5 M H_2SO_4 at t = 335 s (dashed vertical line in Fig. 106), the CO_L intensities do not change for potentials ≤ 0.5 V but start to decrease slightly ($\Delta\theta(CO_{ad})/\Delta t = -4 \times 10^{-4}$ molecules × $site^{-1}$ × s^{-1}) at 0.6 V, due to oxidation of CO_{ad} without or with no significant further formation of CO_{ad} from dissociative adsorption of GOA, similar to the findings for ethylene glycol adsorption/oxidation (see also section 7.2.2.2). The very slow oxidative removal of CO_{ad} upon rinsing is in complete agreement with the

Langmuir Hinshelwood mechanism for CO_{ad} oxidation as discussed in section 4.2, where it was shown that at very small CO_{ad} coverages the CO_{ad} oxidation rate is also small. The CO_M intensities at all adsorption potentials reach a constant value about 20 s after the electrolyte exchange.

As already discussed in section 7.2.2.2, the rate for CO_{ad} formation on a clean Pt surface at different adsorption potentials up to 0.6 V, can be estimated from the slope of the initial increase of the CO_L band intensity, the resulting values for the adsorption/oxidation of glyoxal are summarized in table 14.

E_{ads}/V_{RHE}	0.06	0.1	0.2	0.3	0.4	0.6
$\Delta\theta(CO_{ad})/\Delta t$ [ML/s]	0.07	0.12	0.2	0.19	0.08	0.0055

Table 14: CO_{ad} formation rates upon adsorption/oxidation of GOA on a clean Pt electrode at different potentials. The rates are given in terms of monolayers/second (ML/s), which is equivalent to molecules $\times$ site^{-1} $\times$ s^{-1}.

Similar to GA adsorption, large rates for CO_{ad} formation are measured especially at 0.1, 0.2 and 0.3 V, but in contrast to GA adsorption the CO_{ad} formation at 0.6 V is rather slow, indicating that the rate for C-C bond splitting via an adsorption of an aldehyde group significantly decreases for potentials above 0.3 V. A detailed comparison of the influence of the functional groups on the CO_{ad} formation rate is given in section 7.3.

Adsorbed glyoxylate is only visible at 0.6 V (Fig. 106d). Its intensity increases steeply upon glyoxal exposure to the electrode and decreases in the following due to the developing CO adlayer. The detection of adsorbed glyoxylate, indicates the oxidation of glyoxal (GOA) to glyoxylic acid (GOS) at 0.6 V, in agreement with literature {DAIL98}'{WIEL96}. The absence of adsorbed glyoxylate for potentials below 0.6 V can be explained by i) the very fast development of the CO adlayer under these conditions, which in turn reduces the number of free Pt sites for glyoxalate adsorption, ii) the very steep decrease of the Faradaic current to essentially zero, indicating that on a CO_{ad} blocked surface the oxidation of GOA is not possible, and as a consequence, glyoxylic acid (GOS) is not even formed, and iii) the decrease of the integral band intensity of adsorbed glyoxylate with potential, at constant GOS concentration (see also section 7.2.6.2).

An *in situ* ATR-FTIR spectrum recorded 4 s after an electrolyte exchange experiment to 0.1 M GOA containing solution at 0.1 V, was shown in Fig. 90 (section 7.2.1). In this spectrum

an IR absorption band at 1640 cm^{-1} can be detected, which is assigned to adsorbed glyoxal. This band appears simultaneously with adsorbed CO and its intensity decreases with time and is essentially zero about 20 s after the electrolyte exchange and is only visible for potentials of 0.06 and 0.1 V. Similar IR spectra recorded at 0.2, 0.3, 0.4, 0.5 and 0.6 V do not show adsorbed glyoxal. The potential and time dependence of adsorbed glyoxal is explained tentatively in the following, assuming that adsorbed glyoxal is the precursor for CO_{ad} formation. Its decomposition to form CO_{ad} is significantly reduced at 0.06 and 0.1 V, due to the presence of adsorbed hydrogen. This in turn enabled the detection of adsorbed glyoxal under these conditions. With increasing potential, the coverage of the H_{upd} layer is continuously decreased and the decomposition rate of adsorbed glyoxal increases. The very fast decomposition at potentials positive of 0.1 V, is expected to result in a low steady-state coverage of adsorbed glyoxal, which is below the detection limit of the present ATR-FTIRS set-up.

7.2.5.3 Potentiodynamic adsorbate stripping experiments

The CV (a) and the integrated absorbances of linearly (b) and multiply (c) bonded CO_{ad} recorded during the potentiodynamic adsorbate stripping experiments performed after the above GOA adsorption transients, are shown in Fig. 107, for adsorption potentials of 0.1, 0.2 and 0.4. The general characteristics of all CV's are similar to the features of ethylene glycol stripping, i.e. i) a suppressed H_{upd} adsorption region due to the presence CO_L and CO_M and ii) a peak at about 0.68 V attributed to the oxidation of CO_{ad}. Assuming that only CO_{ad} oxidation to CO_2 contributes to the Faradaic current peak at 0.7 V, the CO_{ad} coverage θ_{CO} can be calculated from the charge of the peak at 0.7 V, which is referred to the coverage $\theta_{CO,sat}$ gained via CO adsorption at 0.06 V and the results of the determined CO_{ad} coverages are summarized in table 15.

For all adsorption potentials ≤ 0.4 V, the CO_{ad} coverages are essentially identical (Table 12), which agrees with the findings of Wang et al. on carbon supported Pt electrode {WANG08F}. The independence of the CO_{ad} coverage with potential can be understood by the very fast CO_{ad} formation rates for potentials ≤ 0.4 V (see above section). Therefore, adsorption of glyoxal for 300 s is sufficient to reach the CO saturation coverage for GOA adsorption, which however, is about 20 % lower compared to gas phase CO adsorption.

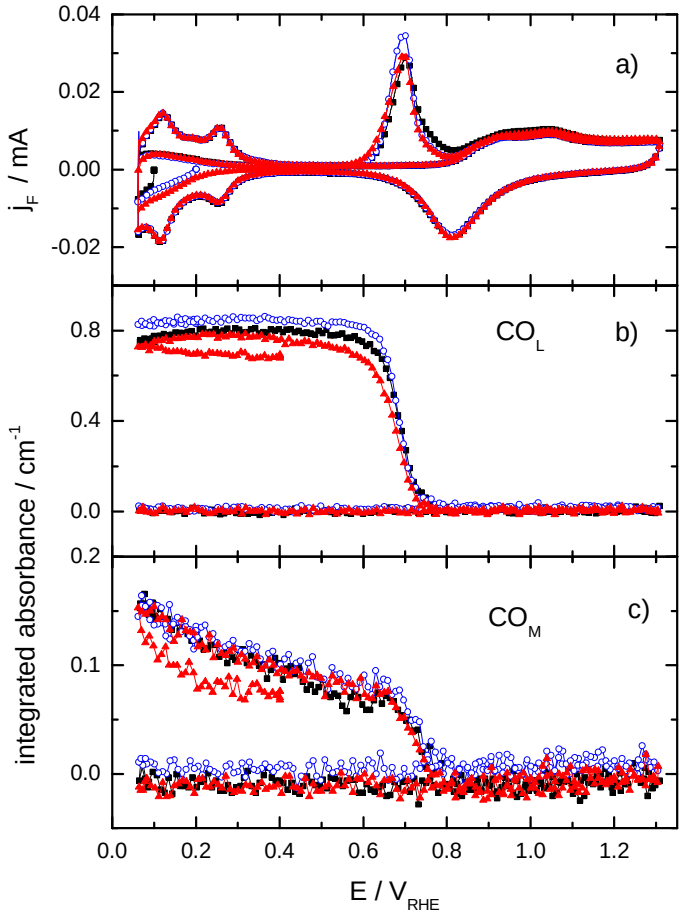

Fig. 107: Adsorbate stripping subsequent to the potentiostatic GOA adsorption/oxidation at 0.1 (filled squares), 0.2 (open circles) and 0.4 V (filled triangles): a) CV and the integrated absorbances of b) linear bonded CO and c) multiply bonded CO.; v = 10 mV/s; electrolyte 0.5 M H_2SO_4.

E_{ads}/V_{RHE}	0.06	0.1	0.2	0.3	0.4
Rel. $\theta(CO_{ad})$ / %	79	80	76	74	77

Table 15: Relative CO_{ad} coverage resulting from GOA adsorption at constant potential, as calculated from the Faradaic current peak at 0.7 V (details see text).

This finding is tentatively explained by the larger number of neighboring free Pt sites, required for the adsorption and/or C-C bond splitting of glyoxal. For the adsorbate stripping subsequent to GOA adsorption at 0.2 V, the integrated absorption of the CO_L band is constant during the initial negative-going potential scan, whereas the integrated absorption of the CO_M band increases. The reversible change in the CO_M intensity and CO_L intensity is attributed to a potential dependent, reversible change in the CO adlayer {CHEN07A} (see also Chapter 4.2 and EG adsorbate stripping), and it is assumed that the overall CO_{ad} coverage does not change

during the potential scan in the H_{upd} region. Therefore, one can conclude that similar the the potentiodynamic adsorbate stripping experiment after ethylene glycol adsorption at 0.2 V (see section 7.2.2.3), no additional CO_{ad} is formed in the negative-going potential scan, which supports that CO_{ad} is the only stable adsorbate formed during the decomposition of GOA at 0.2 V. However, for the adsorbate stripping performed after 5 min. GOA adsorption at 0.4 V, the CO_L as well as the CO_M bands, both increase in the initial first negative-going scan. At 0.4 V in the subsequent positive-going scan, the CO_L as well as the CO_M band intensities are larger compared to their intensities at 0.4 V prior to the potential excursion into the H_{upd} region. Since the changes in the CO_{ad} intensities are not reversible, the higher CO_{ad} intensities are attributed to an increasing CO_{ad} coverage, which is likely to result from the decomposition of stable C2 adsorbates to CO_{ad} during the potential cycling in the H_{upd} region. However, adsorbed glyoxal can not be detected by IR spectroscopy after the GOA adsorption/oxidation at 0.4V, most likely because the coverage is below the detection limit. The increase of the integral band intensity of CO_L upon cycling into the H_{upd} region corresponds to a CO_{ad} coverage increase of about 2-4% of a Pt monolayer. Assuming that adsorbed glyoxal is the precursor for CO_{ad} formation and that one adsorbed glyoxal results in the formation of two CO_{ad} molecules, the coverage of adsorbed glyoxal would be 1 to 2 % of a Pt monolayer.

7.2.5.4 Summary

GOA adsorption/oxidation results in a very fast build-up of a CO adlayer for adsorption potentials ≤ 0.6 V. In electrolyte exchange experiments, it could be shown that 0.06 V, simultaneously with CO_{ad} formation, adsorbed glyoxal is detected on the surface. Based on this finding it was proposed that this species detected at 1645 cm^{-1} is the precursor for CO_{ad} formation. At 0.6 V, the formation of GOS was proven via the IR band detected at 1384 and 1310 cm^{-1}, which was assigned to adsorbed glyoxylate. Concerning the role of GOA in the course of ethylene glycol oxidation, the rather small Faradaic currents but very fast CO_{ad} formation rates, especially for potentials below 0.4 V, indicate that the oxidation of EG to GOA, will result in a fast build-up of a CO adlayer.

7.2.6 Glyoxylic acid

7.2.6.1 Potentiodynamic oxidation of glyoxylic acid

The potentiodynamic bulk-oxidation of a solution containing 0.1 M glyoxylic acid in 0.5 M H_2SO_4 was followed by *in situ* IR spectroscopy and a set of ATR-FTIR spectra are shown in Fig. 108. The reference spectrum was acquired in 0.5 M H_2SO_4 at 0.06 V. Besides linearly and multiply adsorbed CO at 2060 and 1800 cm^{-1}, respectively, adsorbed glyoxylic acid (1710 cm^{-1}) and adsorbed glyoxylate (1385 and 1310 cm^{-1}) are the adsorbates detected by IR spectroscopy during potentiodynamic glyoxylic acid oxidation. The Faradaic current response (a) recorded during the potentiodynamic electrooxidation of glyoxylic acid, as well as the integrated IR intensities of the detected adsorbates CO_L (b), adsorbed glyoxylic acid (c) and adsorbed glyoxylate (d), are plotted in Fig. 109.

The Faradaic current response is very similar to that recorded during potentiodynamic oxidation of GOA. In the first positive-going potential scan, it shows a peak centered at 0.84 V, with a small shoulder at lower potentials, which is attributed to the oxidation of CO_{ad} preformed at low potentials (see Fig. 109b). In the following, the Faradaic current first decreases to about 0.95 V before it steeply increases again up to 1.3 V. Based on recent DEMS studies the strong increase in the Faradaic current was explained by the oxidation of glyoxylic acid (GOS) to CO_2 and oxalic acid (OS) {SCHN08}'{WANG08F}.

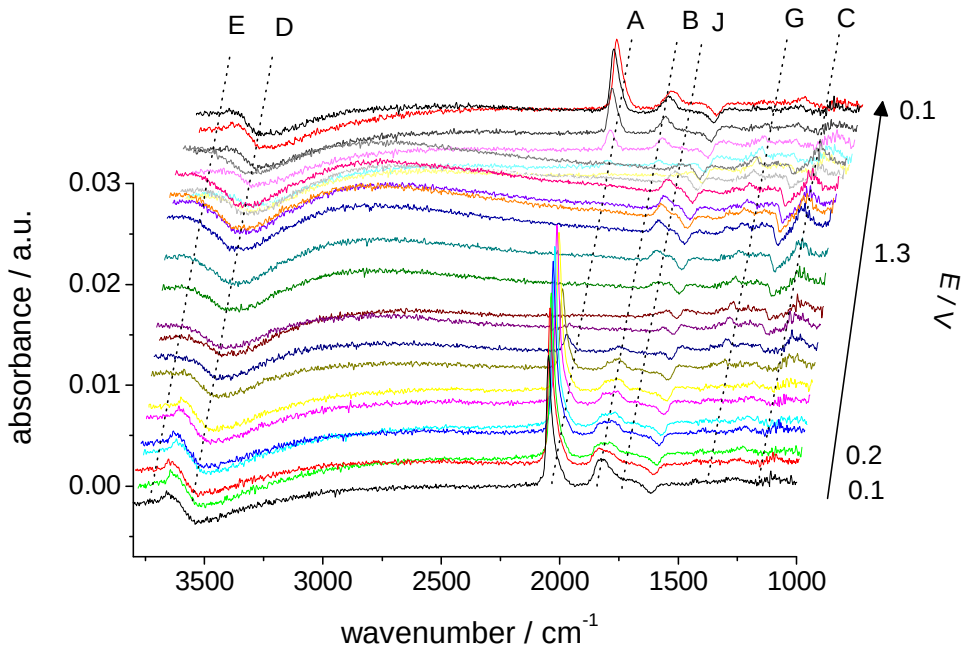

Fig. 108: IR-spectra acquired during potentiodynamic GOS bulk oxidation; v = 10 mV/s; temporal resolution 4.95 s/spectrum; electrolyte 0.1 M GOS in 0.5 M H_2SO_4; reference spectrum at 0.06 V in 0.5 M H_2SO_4

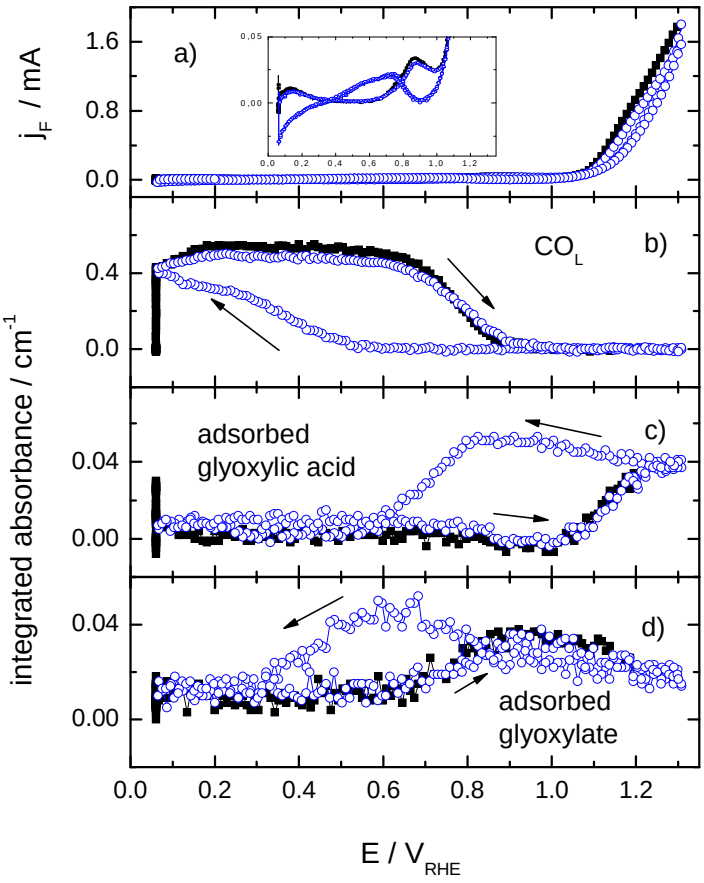

Fig. 109: Potentiodynamic GOS bulk-oxidation; a) CV and integrated absorbance of b) linearly bonded CO, c) the band at 1710 assigned to adsorbed glyoxylic acid (see also text) and d) adsorbed glyoxylate taken from the IR spectra in Fig. 108, v = 10 mV/s; electrolyte 0.1 M GOS in 0.5 M H_2SO_4. Filled squares: first positive-going scan, open circles: continuous cycling.

In the negative-going scan, a broad oxidation peak is found between 0.9 and 0.4 V, before the current drops down to zero at more negative potentials, which can be attributed to the formation of adsorbed CO (see Fig. 109b). It is interesting to note that the maximum value of the Faradaic current measured in the negative-going scan for the oxidation of glyoxylic acid is about 5 times smaller compared to the Faradaic current measured during potentiodynamic oxidation of glyoxal. This is tentatively explained by the reversible adsorption of glyoxylic acid via the carbon atoms of the carboxyl group (see below). In this adsorption configuration the reactive aldehyde group points away from the catalytically active Pt surface. The Faradaic current in the second positive-going can shows practically the same features as in the first positive-going scan and is therefore not discussed in detail.

The integral band intensity of CO_L (Fig. 109b) increases already strongly during the initial waiting time of 30 s at 0.06 prior to the potential scan. In the first positive-going scan, the CO_L integral band intensity continuously increases up to about 0.25 V, remains essentially

constant between 0.25 and 0.6 V, before it decreases to zero at a potential above 0.8 V, due to the onset of CO_{ad} oxidation to CO_2. In the negative-going scan, the integral band intensity of CO_L increases for potentials below 0.6 V down to 0.06V, reaching identical values compared to the CO_L integral band intensity in the first positive-going scan.

The band for adsorbed glyoxylic acid, adsorbed via the carbon atom of the aldehyde group (Fig. 109c), is only visible at 0.06 V right after the electrolyte exchange to glyoxylic acid containing solution. Its intensity decreases to nearly zero already upon the initial waiting time of 30 s at 0.06 V. However, in contrast to the potential dependence of other adsorbed aldehydes, its intensity increases at potentials above 1.0 V and the wavenumber shifts to about 1750 cm^{-1}. It seems to be likely that the band at 1750 cm^{-1} originates from another adsorption configuration. For the adsorption/oxidation of oxalic acid (see next section), a similar IR absorption band at 1750 cm^{-1} was detected, which shows an identical potential dependence. Therefore, we tentatively correlate the band detected at 1750 cm^{-1} upon adsorption/oxidation of glyoxylic acid with the formation of oxalic acid. Up to now, further information about the structure of the underlying adsorbed species can not be provided. In the subsequent negative-going scan the band attributed to adsorbed glyoxylic acid (1710 cm^{-1}) can not be detected, most likely due the higher CO_{ad} coverage formed in the negative-going scan, compared to the clean Pt surface right after the electrolyte exchange at 0.06 V. The increase of the band intensity at 1750 cm^{-1}at potentials above 1.0 V, however, is reversible.

The integral band intensity of adsorbed glyoxylate, bond to the Pt surface via the two oxygen atoms of the carboxyl group (Fig. 109d), starts to increases in the first positive-going scan at about 0.6 V, passes through a maximum at about 0.95 V and decreases at higher potentials. In the negative going potential scan, its intensity increases again from about 0.8 to 0.6 V, and decreases to zero at more negative potentials. The potential dependence of adsorbed glyoxylate is typical for adsorbed anions {CORR88}{FUTA05}. The small intensity of adsorbed glyoxylate in the positive-going scans below 0.6 V is attributed to the significant coverage of adsorbed CO. Further details on the time dependent adlayer development at constant potential are discussed in the next section.

7.2.6.2 Potentiostatic electrolyte exchange experiments

I will now discuss the potentiostatic electrolyte exchange experiments recorded for the adsorption/oxidation of glyoxylic acid at 0.06, 0.1, 0.2, 0.3, 0.4, 0.5 and 0.6 V. The Faradaic current response (a), the integral band intensity of CO_L (b) and CO_M (c) and the integral band

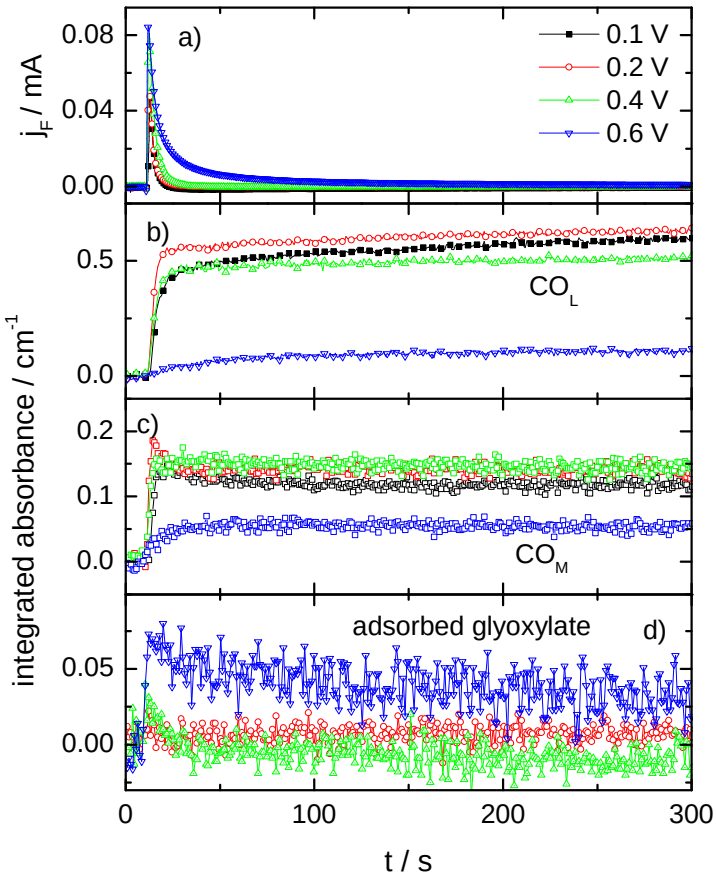

Fig. 110: Potentiostatic GOS bulk-oxidation at different constant potential (see figure); a) Faradaic current density and integrated absorbance of: b) linearly bonded CO, c) multiply bonded CO and d) adsorbed glyoxylate; electrolyte 0.1 M GOS in 0.5 M H_2SO_4; the dashed vertical line indicates the time when the cell was rinsed with 0.5 M H_2SO_4.

intensity of adsorbed glyoxylate (d) upon electrolyte exchange from 0.5 M H_2SO_4 to 0.1 M GOS containing solution are shown in Fig. 110 (For clarity, only the adsorption transients at 0.1, 0.2, 0.4 and 0.6 V are plotted). GOS contains a reactive aldehyde group and a rather inactive carboxyl group. Therefore, its adsorption/oxidation behavior is very similar to the adsorption/oxidation of GA and GOA.

At all potentials, an initial oxidative current peak is detected directly after the electrolyte exchange to glyoxylic acid containing solution and with continuous adsorption time the Faradaic currents drops to very small values, e.g., about 2 µA under close to steady state conditions at 0.6 V. With increasing adsorption potential, the initial Faradaic current peak is practically identical and increases only slightly at 0.6 V. At 0.1 and 0.2 V, the oxidative current can be attributed to oxidation of GOS to CO_{ad} (see below), in addition to the displacement of H_{upd} by adsorbed CO. At 0.4 and 0.6 V, the initial Faradaic current is also

attributed to the formation of CO_{ad} resulting in a very fast poisoning of the Pt surface and therefore no continuous oxidation is measured.

For all adsorption potentials, the integral band intensities of CO_L (Fig. 110b) and CO_M (Fig. 110c) steeply increase after the electrolyte exchange to GOS containing solution and the CO_L intensities saturate at t = 300 s (0.1 V), t = 25 s (0.2 V), t = 25 s (0.4 V) and t = 60 s at 0.6 V, respectively. When the cell is rinsed with GOS free 0.5 M H_2SO_4 at t = 335 s (dashed vertical line in Fig. 110), the CO_L intensity at 0.6 V starts to decrease slightly ($\Delta\theta(CO_{ad})/\Delta t = -5 \times 10^{-4}$ molecules $\times$ site^{-1} $\times$ s^{-1}) due to oxidation of CO_{ad} without further formation of CO_{ad} from dissociative adsorption of GOS, similar to the findings for ethylene glycol adsorption/oxidation (see also section 7.2.2.2). The CO_M intensities at 0.1, 0.2 and 0.4 V reach already a constant value about 10 s after the electrolyte exchange, whereas at 0.6 V a saturation value is observed only at t = 50 s. As already discussed for the adsorption/oxidation of EG (section 7.2.2.2), the rates for CO_{ad} formation on a clean Pt surface at different adsorption potentials up to 0.6 V can be estimated from the slope of the initial CO_{ad} coverage increase and the values are summarized in table 16.

E_{ads}/V_{RHE}	0.06	0.1	0.2	0.3	0.4	0.6
$\Delta\theta(CO_{ad})/\Delta t$ [ML/s]	0.028	0.05	0.055	0.06	0.042	0.003

Table 16: CO_{ad} formation rates upon adsorption/oxidation of GOS on a clean Pt electrode at different potentials. The rates are given in terms of monolayers/second (ML/s), which is equivalent to molecules $\times$ site^{-1} $\times$ s^{-1}.

The adsorption/oxidation behavior of glyoxylic acid is strongly dominated by the aldehyde group, and closely resembles that of glycol aldehyde and glyoxal. The highest value for the CO_{ad} formation rate is determined at 0.3 V und with increasing potential the rate for CO_{ad} strongly decreases. A detailed comparison of the influence of the functional groups and the CO_{ad} formation rate is discussed in 7.3.

Adsorbed glyoxylate can be detected for potentials ≥ 0.2 V (Fig. 110d) and its intensity increases steeply upon adsorption of glyoxylic acid. At 0.2 and 0.4 V, it decreases to zero within about 3-5 s, due to very fast formation of adsorbed CO (Fig.110b, c), whereas at 0.6 V, the decrease of the integral band intensity of adsorbed glyoxylate with time is slower, due to the smaller CO_{ad} formation rate at this potential, compared to 0.2 and 0.4 V (see above).

In situ ATR-FTIR spectra recorded two seconds after an electrolyte exchange to 0.1 M glyoxylic acid containing solution at 0.1 and 0.6 V, respectively, were plotted in Fig. 90 (section 7.2.1). At 0.1 V (0.06, 0.2, 0.3 and 0.4 V spectra not shown), an IR absorption band at 1710 cm^{-1} can be detected, which is assigned to adsorbed glyoxylic acid, bonded to the surface via the carbon atom of the aldehyde group. This band appears simultaneously with adsorbed CO, and its intensity steeply decreases with time. Furthermore, the highest intensity/coverage of adsorbed glyoxylic acid is measured at 0.06 V and its initial band intensity decreases with potential. Similar to the adsorption/oxidation of glyoxal (see previous section), this potential and time dependence of adsorbed glyoxylic acid is explained tentatively, by assuming that adsorbed glyoxylic acid is the precursor for CO_{ad} formation. Its decomposition to form CO_{ad} is significantly reduced at 0.06 V, due to the presence of adsorbed hydrogen. With increasing potential, the coverage of the H_{upd} layer is continuously decreased and the decomposition rate of adsorbed glyoxylic acid is expected to increase. This is in complete agreement with the increasing CO_{ad} formation rate with increasing potential from 0.06 to 0.3 V (see table 16). At 0.4 and 0.6 V, however, adsorbed glyoxylic acid can not be detected, although the CO_{ad} formation rates are significantly smaller, compared to 0.2 and 0.3 V. This is tentatively explained by a decreasing adsorption rate of glyoxylic acid via the carbon atom of the aldehyde group with increasing potential, which in turn results in a lower coverage of adsorbed glyoxylic acid and a smaller CO_{ad} formation rate. Another adsorption configuration, in which glyoxylic acid adsorbs via the two oxygen atoms of the carboxyl group, becomes increasingly important at more positive potentials, as evidenced from the IR spectroscopic finding of an increasing intensity of adsorbed glyoxylate with potential.

7.2.6.3 Potentiodynamic adsorbate stripping experiments

The CV (a) and the integrated absorbances of linearly (b) and multiply (c) bonded CO_{ad} recorded during the potentiodynamic adsorbate stripping resulting from adsorption of 0.1 M glyoxylic acid, are shown in Fig. 111, for adsorption potentials of 0.1, 0.2 and 0.4 (for potential selection see section 7.2.2.3). The general characteristics of all CV's are similar to those obtained after adsorption of the other molecules discussed in previous adsorbate stripping experiments, i.e., i) a suppressed H_{upd} adsorption due to the presence CO_L and CO_M and ii) a peak at about 0.68 V, attributed to the oxidation of CO_{ad}. For the stripping experiment subsequent to the adsorption of glyoxylic acid at 0.4 V, an additional positive current is found in the potential regime between 0.8 and 1.2 V, on top of the Pt oxidation current.

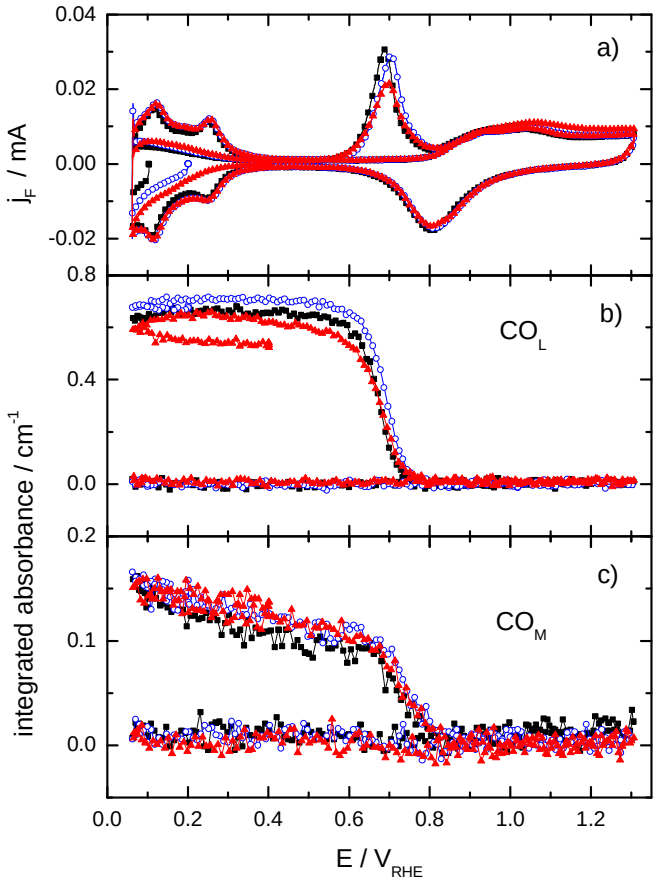

Fig. 111: Adsorbate stripping subsequent to the potentiostatic glyoxylic acid adsorption/oxidation at 0.1 (filled squares), 0.2 (open circles) and 0.4 V (filled triangles): a) CV and the integrated absorbances of b) linear bonded CO and c) multiply bonded CO; v = 10 mV/s; electrolyte 0.5 M H_2SO_4.

This indicates the presence and oxidation of other adsorbed species besides CO_{ad}. The rel. CO_{ad} coverage (rel. θ_{CO}) can be calculated from the charge of the peak at 0.7 V, assuming that only CO_{ad} oxidation to CO_2 contributes to this Faradaic current peak. The values for the rel. CO_{ad} coverage are summarized in table 17.

E_{ads}/V_{RHE}	0.06	0.1	0.2	0.3	0.4
Rel. $\theta(CO_{ad})$ / %	79	80	82	82	76

Table 17: Relative CO_{ad} coverage resulting from adsorption of glyoxylic acid at constant potential, as calculated from the Faradaic current peak at 0.7 V (details see text).

For all adsorption potentials rather high values for the adsorbate coverage are determined, which are more or less independent of the adsorption potential, in agreement with results in a recent DEMS study by Wang et al. {WANG08F}. Based on the IR data presented in the

previous section, this can be explained by the very high rate for dissociative adsorption found in the electrolyte exchange experiments at all adsorption potentials, suggesting that steady-state coverage is rapidly achieved at all potentials.

For the adsorbate stripping following glyoxylic acid adsorption at 0.2 V, the integrated absorption of the CO_L band is constant during the initial negative-going potential scan, whereas the integrated absorption of the CO_M band increases. The reversible change in the CO_{ad} intensities is attributed to a potential dependent, reversible change in the structure of the CO adlayer {CHEN07A} (see also Chapter 4.2), and it is assumed that the overall CO_{ad} coverage does not change during the potential scan in the H_{upd} region. Therefore, one can conclude that different to the potentiodynamic stripping of ethanol and glycol aldehyde adsorbates, no additional CO_{ad} is formed in the negative-going potential scan, which supports that CO_{ad} is the only stable adsorbate formed during the decomposition of glycolic acid at 0.2 V. However, for the adsorbate stripping performed after GOS adsorption at 0.4 V, the CO_L as well as the CO_M bands increase in the first negative-going scan. At 0.4 V in the subsequent positive-going scan, the CO_L band intensity is larger than it was initially. Since the changes in the CO_L intensity are not reversible, the higher CO_L intensity is attributed to an increasing CO_{ad} coverage, resulting form decomposition of stable C2 adsorbates to CO_{ad} during the potential cycling in the H_{upd} region. However, the IR data contain no additional information on the nature of this C2 adsorbate.

7.2.6.4 Summary

The adsorption/oxidation of glyoxylic acid results in a fast build-up of a CO adlayer on the Pt surface at all adsorption potentials < 0.6 V. In electrolyte exchange experiments it could be shown that low potentials (0.06 to 0.3 V), adsorbed glyoxylic acid is present on the surface. Most likely this is adsorbed via the carbon atom of the aldehyde group. Since this band appears simultaneously with the formation of CO_{ad} it was proposed that the adsorbate correlated with the IR band at 1710 cm^{-1} is the precursor for CO_{ad} formation. At high potential glyoxylic acid preferentially adsorbs as adsorbed glyoxylate, bond to the Pt surface via the two oxygen atom of the carboxyl group, which is represented by the IR band at 1384 and 1310 cm^{-1}.

7.2.7 Oxalic acid

7.2.7.1 Potentiodynamic oxidation of oxalic acid

Fig. 112 shows the ATR-FTIR spectra acquired during the potentiodynamic bulk-oxidation of 0.1 M oxalic acid containing 0.5 M H_2SO_4 solution. The reference spectrum was measured in 0.5 M H_2SO_4 at 0.06 V. Beside linearly and multiply adsorbed CO at 2060 and 1800 cm^{-1}, respectively, adsorbed bioxalate (1265 cm^{-1}) is detected by IR spectroscopy. Other IR bands detected at high potential at 1373 and 1750 cm^{-1}, respectively, can not be assigned so far to a specific adsorption configuration. Since oxalic acid only contains carboxylic groups the reactivity of oxalic acid can be regarded to be representative for the adsorption behavior of carboxyl function.

The Faradaic current response (a) recorded during the potentiodynamic electrooxidation of oxalic acid, as well as the integrated IR intensities of the CO_L (b), adsorbed bioxalate (c) and the species at 1373 and ~1750 cm^{-1} (d) are plotted in Fig. 113. For potentials below 0.9 V, the CV is practically featureless, indicating that the oxidation of oxalic acid at these potentials is extremely slow. As the potential exceeds 0.95 V the oxidative current steeply increases up to 1.1 V, where the potential scan was reversed. The potential was already reversed at 1.1 V, since at higher potentials (data not shown) the Faradaic current increases so strongly that it reaches a constant, most likely diffusion controlled value, similar to findings in previous studies {HORA72}{WANG08F}. These high currents of up to 20 mA, resulted in a destruction of the Pt thin film electrode.

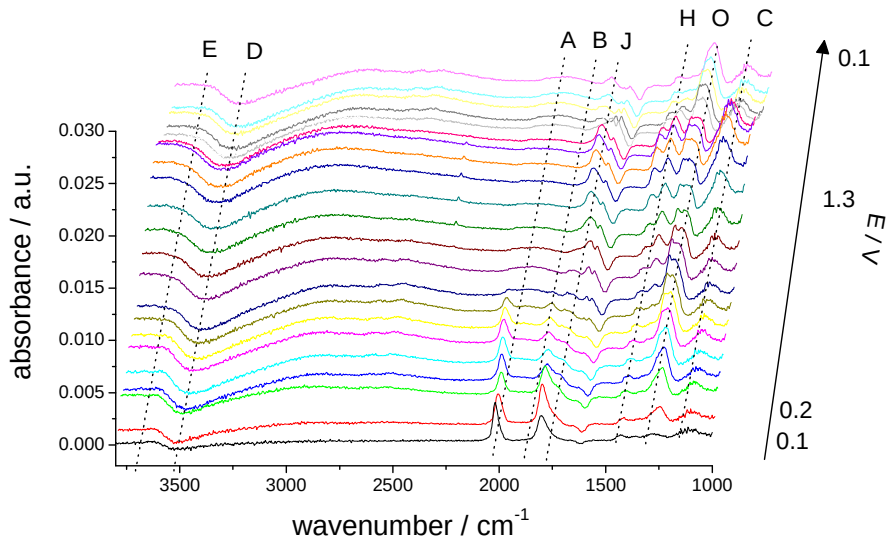

Fig. 112: IR-spectra acquired during potentiodynamic oxalic acid bulk-oxidation; v = 10 mV/s; temporal resolution 4.95 s/spectrum; electrolyte 0.1 M OS in 0.5 M H_2SO_4; reference spectrum at 0.06 V in 0.5 M H_2SO_4

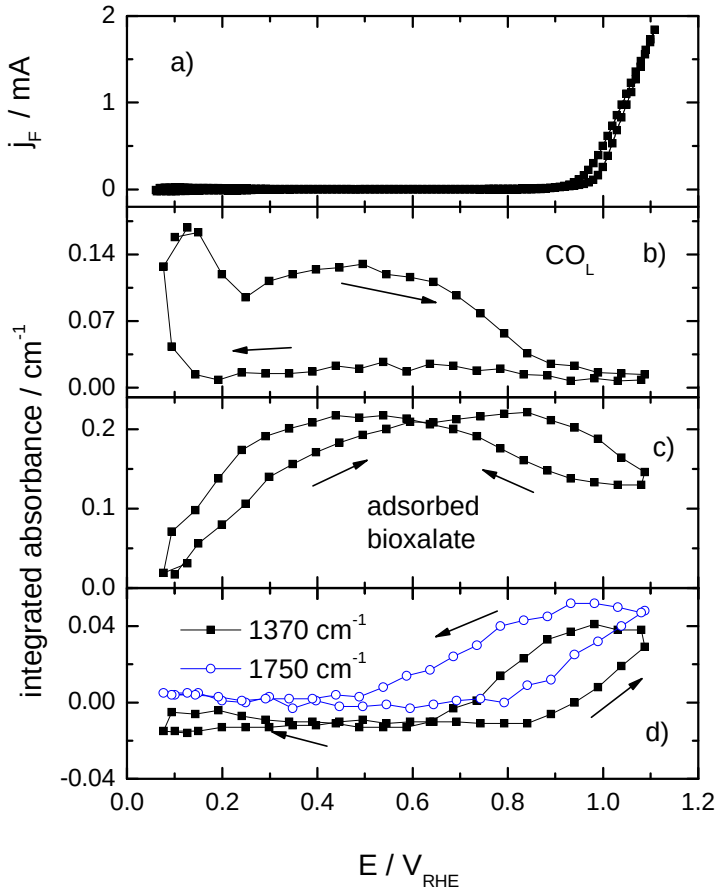

Fig. 113: Potentiodynamic OS bulk-oxidation; a) CV and integrated absorbance of b) linearly bonded CO, c) adsorbed bioxalate and d) bands at 1750 (open circles) and 1370 cm^{-1} (filled squares) taken from the IR spectra in Fig. 112, v = 10 mV/s; electrolyte 0.1 M OS in 0.5 M H_2SO_4.

In the negative-going potential scan, the integral band intensity of linearly bonded CO remains essentially zero for potentials above 0.2 V. At more negative potentials, CO_{ad} formation sets in. In the subsequent positive-going scan the CO_L intensity increases from 0.06 to about 0.15 V, decreases steeply from 0.15 to 0.25 V and increases again from 0.25 to 0.55 V. At more positive potentials, the integral band intensity of adsorbed CO decreases to zero, due to the onset of CO_{ad} oxidation to CO_2. The unusually behavior of the CO_L intensity in the potentiodynamic scan for potentials between 0.15 and 0.55 V is attributed to a potential induced changes in the CO_{ad} layer, i.e., site conversion from CO_L to CO_M between 0.15 and 0.25 V, and vice versa, for potentials between 0.25 and 0.55 V (see also section 4.2). The potential dependent kinetics of CO_{ad} formation are discussed in more detail, when the results of the potentiostatic electrolyte exchange experiments are presented, in which all potential related effects are excluded.

The integral band intensity of adsorbed bioxalate increases continuously in the first positive-going scan, reaching a maximum at 0.9 V, before it decreases at higher potentials. In the negative-going scan, adsorbed bioxalate can be detected for potentials below 0.8 V. The integral band intensity first increases down to 0.55 V, before it decreases again with a further decrease in potential. This potential dependence is very typical for anion adsorption as for example reported for the adsorption of acetic acid or sulfate adsorption. This behavior is in good agreement with the assignment of the band at 1265 cm^{-1} to adsorbed bioxalate and with findings is in a radiotracer study by Horani et al. {HORA72}, where it was reported that oxalic acid is reversibly adsorbed on Pt, similar to anion adsorption.

The potential dependence of the integral intensities of the bands at 1373 and 1750 cm^{-1} is very similar to each other, indicating that the bands are somehow correlated with each other. Both follow the increase in oxygen containing species on the Pt surface, which result from water dissociation. However, the adsorption configuration of the species responsible for the IR absorption band detected at 1373 and 1750 cm^{-1} are unclear.

7.2.7.2 Potentiostatic electrolyte exchange experiments

Potentiostatic transients for the adsorption/oxidation of a solution containing 0.1 M oxalic acid were performed at 0.06, 0.1, 0.2, 0.3, 0.4, 0.5 and 0.6 V, via electrolyte exchange experiments. The Faradaic current response (a), the integral band intensity of CO_L (b) and CO_M (c) as well as the integral band intensity of adsorbed bioxalate (d) upon electrolyte exchange from 0.5 M H_2SO_4 to 0.1 M oxalic acid containing solution at 0.06, 0.1, 0.2, 0.4 and 0.6 V are plotted in Fig. 114. For clarity, the other transients at 0.3 and 0.5 V are not shown.

The Faradaic current response is practically featureless for all adsorption potentials, except for a very sharp initial current spike, which correlates with the intensity increase of adsorbed bioxalate (Fig. 114d). It is therefore attributed mainly to capacitive contributions due to recharging of the double layer. In addition, at 0.1 and 0.2 V, displacement of H_{upd} by adsorbed bioxalate and due to formation of CO_{ad} contributes to the Faradaic current.

The formation of CO_L (Fig. 114b) and CO_M (Fig. 114c) is most obvious at low potentials, i.e., between 0.06 V and 0.2 V, while at 0.4 and 0.6 V it is below the detection limit. The slightly positive value for the "CO_M band intensity" at 0.4 and 0.6 V is an artifact caused by another adsorption band centered at 1750 cm^{-1}. This band contributes to the integral band intensities of multiply bonded CO_M, which was determined by integrating over the wavenumber region

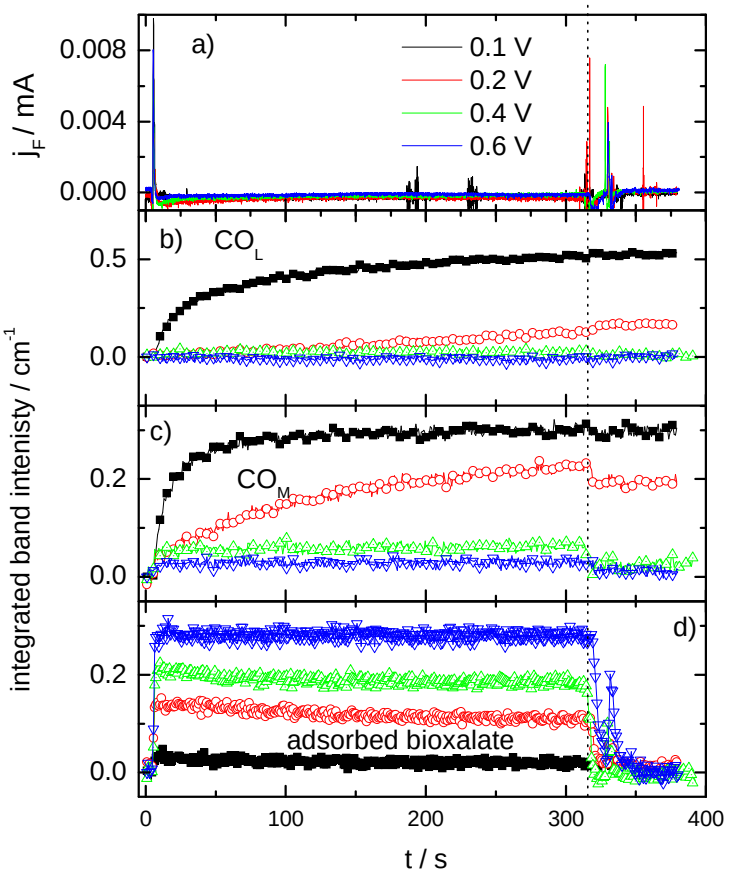

Fig. 114: Potentiostatic OS bulk-oxidation at different constant potential (see figure); a) Faradaic current density and integrated absorbance of: b) linearly bonded CO, c) multiply bonded CO and d) adsorbed bioxalate; electrolyte 0.1 M OS in 0.5 M H_2SO_4. Dashed, vertical line indicates the time when the cell was rinsed with OS free 0.5 M H_2SO_4.

between 1720 and 1900 cm^{-1}. The band centered at 1750 cm^{-1} immediately decreases to zero upon rinsing the cell with 0.5 M H_2SO_4 at 0.2, 0.4 and 0.6 V, which can be seen from the instantaneous decrease of the "CO_M band intensity" at t = 335 s. This finding indicates that the species correlated with the band at 1750 cm^{-1} is only rather weakly adsorbed and desorbs rapidly from the surface, when the cell is rinsed with oxalic acid free solution. Decomposition of the band to CO_{ad} can be excluded based on the finding that neither the CO_L nor the CO_M intensity increase further upon rinsing.

As already discussed in 7.2.2.2, the rates for CO_{ad} formation on a clean Pt surface at different adsorption potentials can be estimated from the slope of the initial increase of the CO_L band intensity and the values are summarized in table 18.

E_{ads}/V_{RHE}	0.06	0.1	0.2	0.3	0.4	0.6
$\Delta\theta(CO_{ad})/\Delta t$ [ML/s]	0.007	0.011	3×10^{-4}	5×10^{-5}	0	0

Table 18 CO_{ad} formation rates upon adsorption/oxidation of GOS on a clean Pt electrode at different potentials. The rates are given in terms of monolayers/second (ML/s), which is equivalent to molecules $\times$ site^{-1} $\times$ s^{-1}.

Different from all other C2 molecules, the highest rate for CO_{ad} formation on a clean surface is obtained at 0.06 and 0.1 V, and the rates are decrease strongly with increasing potential. This trend is consistent with findings of Horanyi et al and {HORA72} Berna at el {BERN04}, who reported very slow formation of a stable adsorbate at cathodic potentials, with a maximum coverage of these adsorbates in the potential region of 0 and 0.1 V. This can be explained by an increasing rate for reductive processes at more negative potentials, here the reduction of a carboxyl group of oxalic acid to CO_{ad}.

The IR band correlated with the formation of adsorbed bioxalate is detected for adsorption potentials ≥ 0.1 V and the intensity increases with increasing adsorption potential (Fig. 114d). Furthermore, directly after the electrolyte exchange to OS containing solution the integral band intensity steeply increases and decreases in the following at 0.1 V, whereas at higher potentials the intensity remains practically constant during the time of adsorption. When the electrolyte is cell is rinsed with 0.5 M H_2SO_4 (dashed vertical line in Fig. 114), the intensity of adsorbed bioxalate immediately drops down to zero, indicating that adsorbed bioxalate and oxalic acid are in a fast adsorption/desorption equilibrium. The IR data clearly show that oxalic acid adsorbs preferentially via the two oxygen atoms of the carboxyl group onto the Pt surface, similar to all other carboxylic acid investigated in the present work (formic acid, acetic acid, glycolic acid, glyoxylic acid). Furthermore, the data suggest that the reactivity of this adsorption configuration for C-C bond splitting is very small, at least at potentials between 0.2 and 0.9 V.

7.2.7.3 Potentiodynamic adsorbate stripping experiments

In Fig. 115, the CV (a) and the integrated absorbances of linearly (b) and multiply (c) bonded CO_{ad} recorded during the potentiodynamic adsorbate stripping resulting from adsorption of 0.1 oxalic acid containing are shown after adsorption at potentials of 0.1, 0.2 and 0.4 (for potential selection see section 7.2.2.3).

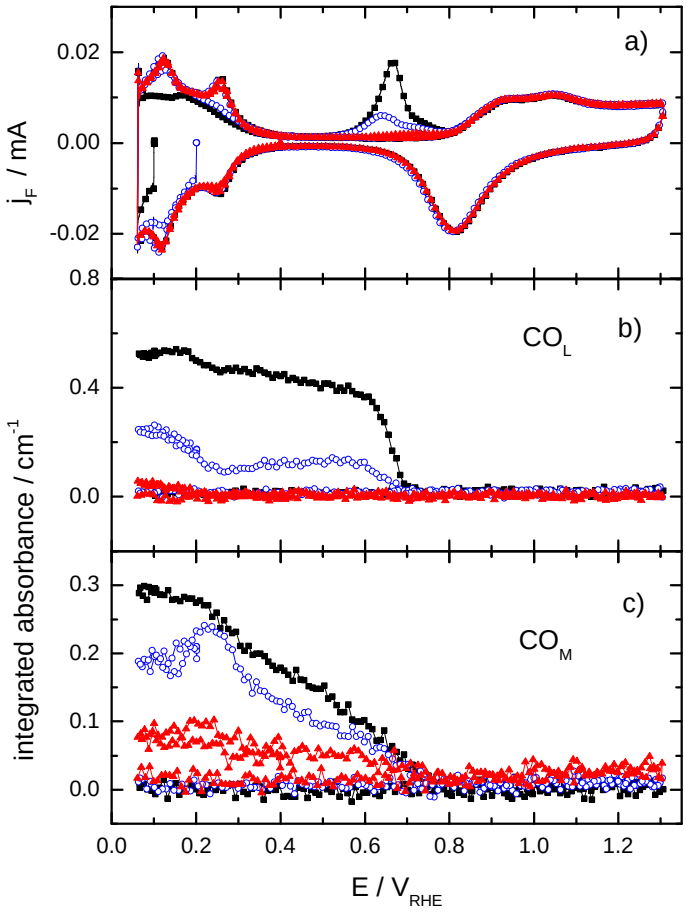

Fig. 115: Adsorbate stripping subsequent to the potentiostatic OS adsorption/oxidation at 0.1 (filled squares), 0.2 (open circles) and 0.4 V (filled triangles): a) CV and the integrated absorbances of b) linear bonded CO and c) multiply bonded CO.; v = 10 mV/s; electrolyte 0.5 M H_2SO_4.

The general characteristics of the CV's recorded after adsorption of oxalic acid at 0.1 (Fig. 115a, filled squares) and 0.2 V (Fig. 115a, open circles) are similar to the features of ethylene glycol stripping, i.e., i) a partly suppressed H_{upd} region due to the presence CO_L and CO_M and ii) a peak at about 0.68 V attributed to the oxidation of CO_{ad}. The adsorbate stripping experiment performed after the adsorption of oxalic acid at 0.4 V (Fig. 115a, filled triangles), however, is essentially identical to a Pt base CV in 0.5 M H_2SO_4. This indicates that at 0.4 no strongly adsorbed species are formed on the Pt surface upon oxalic acid adsorption. Assuming that only CO_{ad} oxidation to CO_2 contributes to the Faradaic current peak at 0.68 V, the rel. CO_{ad} coverage (rel.θ_{CO}) can be calculated from the charge of the peak at 0.68 V, which is related to the coverage $\theta_{CO,sat}$ obtained upon gas phase CO adsorption at 0.06 V. The results are summarized in table 19.

E_{ads}/V_{RHE}	0.06	0.1	0.2	0.3	0.4
Rel. $\theta(CO_{ad})$ / %	39	42	16	11	3

Table 19: Relative CO_{ad} coverage resulting from oxalic acid adsorption at constant potential, as calculated from the Faradaic current peak at 0.68 V (details see text).

The highest rel. CO_{ad} coverage of about 40 % was found at 0.06 and 0.1 V, and it decreases with increasing adsorption potential (Table 16). This trend is in agreement with a recent DEMS study by Wang et al. on carbon supported Pt {WANG08F}. Furthermore, the data are consistent with the electrolyte exchange experiments present in the preceding section, showing a significant rate for CO_{ad} formation at 0.06 and 0.1 V.

The reversible changes in the CO_L and CO_M band intensities during the potential scan between 0.06 and 0.4 V (Fig. 115b and c), are explained by potential induced structural change in the CO_{ad} layer at a constant overall CO_{ad} coverage, similar to the adsorbate stripping experiments performed after the adsorption of glycolic acid at 0.1, 0,2 and 0.4 V (see also glycolic acid adsorbate stripping experiments, ref {CHEN07A} and Chapter 4.2). This implies that beside CO_{ad} no other adsorbates are present on the Pt surface after adsorption of oxalic acid at 0.1, 0.2 and 0.4, in agreement with the absence of additional IR absorption bands during the adsorbate stripping experiment, besides CO_L and CO_M.

7.2.7.4 Summary

In total, oxalic acid can be considered as fully stable on a Pt catalyst for potentials between 0.4 and 0.9 V. In this potential regime, oxalic acid binds mainly via the two carbon atoms of one carboxyl group to the Pt surface resulting in an IR absorption band at 1265 cm^{-1}. The formation of further adsorbates was indicated by IR bands at 1373, 1680 and 1750 cm^{-1}, which are formed immediately upon exposure of the Pt electrode to oxalic acid. This/these species desorb from the Pt surface upon rinsing with 0.5 M H_2SO_4 within several seconds. However, so far an assignment of these bands can not be provided. At potentials above 0.9 V, fast oxidation of oxalic acid sets in, whereas at potentials ≤ 0.3 V reductive decomposition of oxalic acid to CO_{ad} was found. The highest rate for CO_{ad} formation occurs at 0.1 and 0.06 V.

7.3 Comparison of CO_{ad} formation rates

The results of the potentiodynamic and potentiostatic measurements presented in Chapter 7.2 clearly show the strong influence of the functional groups on the adsorption/oxidation behavior of the investigated C2 molecules. The results for the potential dependent CO_{ad} formation rates determined from the initial CO_{ad} coverage increase upon electrolyte exchange experiments at constant potential are summarized for the adsorption/oxidation of all six C2 molecules in Fig. 116.

At low potentials (0.06 to 0.2 V), all organic molecules containing an aldehyde group (glycol aldehyde, glyoxal and glyoxylic acid) can rapidly adsorb on the Pt surface via the carbon atom of the carbonyl group and the dissociation of these "acetyl like" species results in the formation of CO_{ad}. Their intensity was the highest at 0.06 and 0.1 V and decreases with increasing adsorption potential (see e.g. Fig. 98d). This was tentatively explained by the presence of H_{upd} species, which block neighboring Pt sites, required for the subsequent decomposition of the adsorbed C2 species to CO_{ad}. With decreasing H_{upd} coverage, the rate for the decomposition of the adsorbed acetyl like species to form CO_{ad} increases, as evidenced by the faster CO_{ad} formation rates at 0.2 and 0.3 V, which in turn results in a decrease of the intensity of adsorbed aldehyde species. At higher potentials, the CO_{ad} formation rates from the aldehyde groups decrease strongly (see Fig. 116).

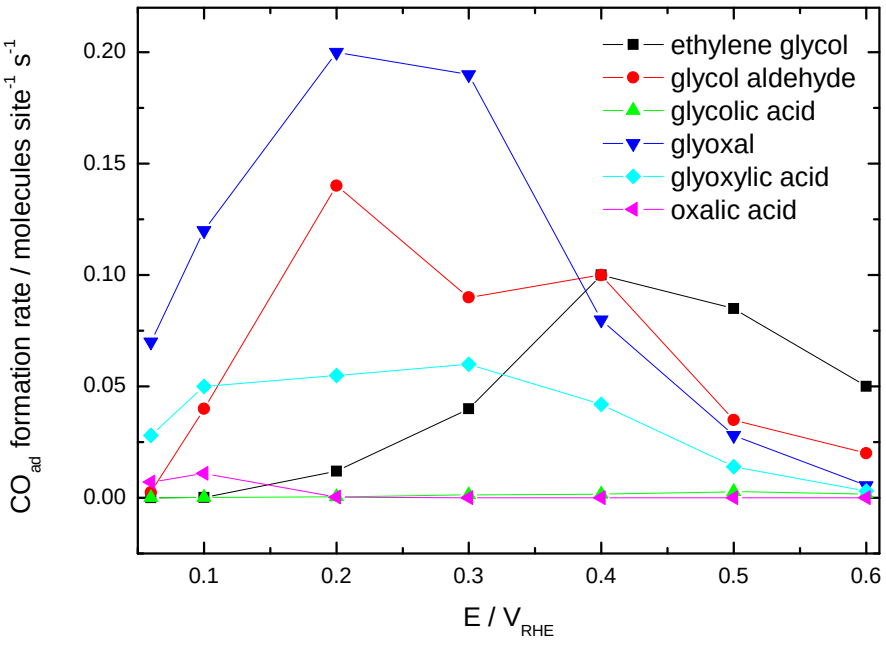

Fig. 116: CO_{ad} formation rates on a clean Pt electrode at different potentials upon adsorption/oxidation of small organic C2 molecules, as indicated in the figure. The rates are given in terms of monolayers/second (ML/s), which is equivalent to molecules × $site^{-1}$ × s^{-1}.

In analogy to the findings for ethanol adsorption/oxidation, this is tentatively explained by the oxidation of adsorbed C2 species to the respective carboxyl group. This in turn decreases the coverage of the adsorbed "acetyl like" precursors and consequently the CO_{ad} formation rate. However, also a potential dependent decrease in the formation rate of the adsorbed "acetyl like" C2 species at more positive potentials can not be excluded and is seems to be likely. Depending on the functionality of the second group of the aforementioned three molecules the CO_{ad} formation rate at 0.06 V increases in the following row: $-CH_2OH$ < -COOH < -COH. This can be attributed either to i) the influence of the second functional group on the electron density at the other carbon atom or ii) the fact that glyoxal has two reactive aldehyde groups, which increases the probability for its reactive adsorption, or iii) a convolution of both effects. Furthermore, it has to be considered that C-C bond splitting of glyoxal results in the formation of two CO_{ad} molecules, whereas the C-C bond breaking of glyoxylic acid results in the formation of one CO_{ad} molecule and one CO_2 molecule, as shown in recent DEMS studies {SCHN08}'{WANG08F}. Consequently, the same rate of C-C bond splitting would result in a two times faster CO_{ad} formation rate from GOA adsorption compared to GOS adsorption.

In contrast, to the fast adsorption/decomposition of the molecules containing an aldehyde group, the reactivity of an alcohol group is very small at the low potential regime, as evident from the very small Faradaic current and the small CO_{ad} formation rate measured for the adsorption/oxidation of EG. If one of the alcohol groups of EG is substituted by an –COOH group, i.e., glycolic acid, the reactivity at low potentials is further decreased. This becomes evident from a comparison of the CO_{ad} formation rate and/or the Faradaic currents recorded during adsorption of EG compared to the adsorption of GS. This difference can be tentatively explained by the preferential adsorption of GS via two oxygen atoms of the carboxyl group on the Pt surface. In this configuration, the reactive alcohol group points away from the surface and its adsorption/oxidation is therefore hindered. If one of the alcohol groups of EG is replaced by an aldehyde functionality, i.e. GA, the reactivity at low potentials is dominated by the strongly adsorbing aldehyde group (see above).

At potentials ≥ 0.4 V, however, the activity/reactivity of the alcohol groups increases strongly and is even larger than the reactivity of an aldehyde group. This becomes evident when comparing the CO_{ad} formation rate (Fig. 116) and/or the Faradaic current response (see sections before) of EG (two alcohol groups) with the adsorption/oxidation of glyoxal (two aldehyde groups). The CO_{ad} formation rate as well as the Faradaic currents are much larger for EG compared to the values measured for glyoxal adsorption/oxidation, supporting the

proposal that at 0.4 and 0.6 V alcohol groups are more easily adsorbing/reacting compared to aldehyde groups. Consequently, the reactivity, i.e. CO_{ad} formation rate and overall oxidation rate measured via the Faradaic current at 0.6 V for the adsorption/oxidation of glycol aldehyde, is larger than that of glyoxyl, due to the presence of a reactive –OH group in the case of glycol aldehyde. On the other hand, when displacing one –OH group of EG by an aldehyde group, i.e., again glycol aldehyde, the reactivity is decreased compared to EG. The proposal that the reactivity of the alcohol group is larger compared to the reactivity of an aldehyde group at 0.4 and 0.6 V is in complete agreement with earlier product analysis studies, which showed that the oxidation of glycol aldehyde mainly results in the formation of glyoxal, and only small amounts of glycolic acid were detected {HORA83B}{SHIB94M}.

The physical origin for the significant change of the reactivity of the alcohol and aldehyde groups with increasing potential can only be speculated upon so far. It is tentatively explained by electrostatic interactions with the Pt surface. At low potentials, the surface is negatively charged and adsorption via the partially positively charged carbon atom of the aldehyde groups is enhanced, whereas at 0.6 V the Pt surface is positively charged and this adsorption configuration becomes less favorable. Theoretical calculations concerning the adsorption of these C2 molecules are highly desirable to better understand the change in reactivity.

All molecules containing a carboxyl group, namely glycolic acid, glyoxylic acid and oxalic acid, can adsorb perpendicular to the surface Pt surface, via the two oxygen atoms of the carboxyl group. The intensity of these adsorbed carboxylates increases with increasing potential from about 0.2 up to 0.9 V, which is very typical for the potential dependence of adsorbed anions. This adsorption configuration is dominant especially for glycolic acid and oxalic acid, as evident from the relatively strong band intensity of adsorbed glycolate and bioxalate, respectively. In the case of GOS adsorption, the formation of CO_{ad} hinders a comparison of the band intensity with the other two acids. Adsorbed carboxylates are rather inactive for further oxidation for potentials between 0.2 and 0.9 V and are expected to be spectator species in the course of EG oxidation, similar to adsorbed formate (Chapter 5) and adsorbed acetate (Chapter 6) species.

The formation of glycolic acid by oxidation of ethylene glycol and glycol aldehyde as well as the formation of glyoxylic acid by oxidation of glyoxal suggests that the oxidation of a single functional group of a molecule dominates over the simultaneous oxidation of both functional groups of a single molecule. Further re-adsorption of the intermediates however, will lead to the accumulation of highly oxidized molecules and rather unreactive molecules, such as

GS,GOA, GOS, and OS. The latter were reported to be the main reaction products after continuous oxidation of EG for 24 hours at 0.6 V {SHIB94M}{WIEL96}{DAIL98}.

The influence of the functional group on the adsorption/oxidation behavior is of ongoing interest in our department and is currently investigated in the combined ATR-FTIRS/DEMS set-up. Furthermore, theoretical calculations concerning the adsorption behavior of the C2 molecules and the influence of the functional groups are highly desirable to better understand the experimental findings.

7.4 Summary

The data presented in this Chapter on the adsorption/oxidation behavior of bi-functional C2 molecules, namely ethylene glycol, glycol aldehyde, glycolic acid, glyoxal, glyoxylic acid and oxalic acid, can be summarized as follows:

The main adsorbates and reaction intermediates detected by IR spectroscopy during adsorption of the six aforementioned C2 molecules could be identified and their impact on the mechanism of ethylene glycol oxidation was discussed. Glycolic acid and oxalic acid are completely inactive at potentials where they are typically formed during oxidation of ethylene glycol. Therefore, they represent dead ends in EG oxidation reaction. In contrast, oxidation of glycol aldehyde and glyoxal is possible and their oxidation results in the formation of glycolic acid and glyoxylic acid, respectively. Furthermore, for the adsorption/oxidation of both molecules, i.e., glycol aldehyde and glyoxal, C-C bond breaking results in fast formation of $CO_{ad,}$ which can be further oxidized to CO_2. For the adsorption/oxidation of glyoxylic acid, a high rate for dissociative adsorption was determined but a rather small overall activity, measured via the Faradaic current in the potentiodynamic oxidation of glyoxylic acid, was found. The results are consistent with a dual path mechanism proposed for the oxidation of EG and its oxidized C_2 derivates {WIEL96}{DAIL98}. In one pathway, the C_2 molecules are dissociatively oxidized via CO_{ad} to form CO_2, in the other pathway they are oxidized to from intermediates without C-C bond rupture, and only the functional groups are sequentially oxidized up to the carboxyl groups. Among these molecules, EG exhibits the highest oxidative activity, measured via the Faradaic current in potentiodynamic bulk oxidation between 0.4 and 0.9 V. At all stages of this reaction pathway, re-adsorption and further oxidation of C2 intermediates via C-C bond splitting is possible.

The adsorption/oxidation characteristics of the C2 molecules are strongly affected by the functional groups and the adsorption rates of the functional groups itself depend strongly on the applied electrode potential. Between 0.06 and 0.3 V the highest initial rates for dissociative adsorption, measured via the build-up of a CO adlayer, were determined for molecules containing an aldehyde group, whereas the adsorption/oxidation of alcohol groups at these potentials is strongly hindered. However, with increasing potential (0.4 to 0.6 V), the relative reactivity of the functional groups changes and especially at 0.6 V the CO_{ad} formation rate resulting from the adsorption/oxidation of alcohol groups is significantly faster compared to the CO_{ad} formation rates from the aldehyde groups. Molecules containing a carboxyl function preferentially adsorb via the two oxygen atoms of the carboxyl group, perpendicular to the Pt surface. This adsorption configuration is regarded to be rather inactive for potentials between 0.2 and 0.9 V, based on the very small Faradaic currents for the adsorption/oxidation of glycolic and oxalic acid in this potential regime. At higher potentials, however, the oxidation rate of molecules containing a carboxyl group is strongly enhanced. At 0.06 and 0.1 V, the adsorption of oxalic acid resulted in a rather fast build up of a CO adlayer, due to C-C bond rupture upon reduction of one of the carboxyl groups to CO_{ad}.

8 SUMMARY / ZUSAMMENFASSUNG

8.1 English version

The work presented in this thesis provided new and detailed insight into the mechanism and the kinetics of the adsorption and electrooxidation of fuel cell relevant small organic molecules, such as CO (chapter 4), formic acid (chapter 5), ethanol (chapter 6) as well as ethylene glycol and its oxidative intermediates (Chapter 7). The measurements were performed in a novel *in situ* ATR-FTIR spectroscopy flow cell set-up, which had been further extended within this PhD work, by coupling it with on-line differential mass spectrometry. These experimental techniques, i.e., *in situ* ATR-FTIRS and/or *in situ* ATR-FTIRS/DEMS opened the possibility to follow and even quantify single reaction pathways within complex reaction networks.

The results presented in Chapter 4 and 6 clearly demonstrated the enormous potential of the novel combined *in situ* ATR-FTIRS/DEMS set-up for studies of the mechanism and in particular of the dynamics of electrocatalytic reactions under enforced electrolyte flow. The set-up allowed the simultaneous detection and, after proper calibration, quantification of adsorbed species (IR) and volatile reaction products, reaction intermediates and reactants (DEMS), together with the Faradaic current, with a time resolution in the range of 20-50 ms (spectroscopic measurements) and/or of about 0.5 s (time resolution of the flow cell). Transient measurements are possible not only upon stepping the potential ('potential-step transients'), but also upon changing the electrolyte flow at constant potential ('potentiostatic electrolyte-exchange transients'), e.g., from pure base electrolyte to reactant containing solution or vice versa or between reactant solutions with different isotope labeled reactants. This allowed detailed studies i) of the dynamics of the build-up or removal of the adsorbate layer under reaction conditions or the dynamic exchange of adsorbed species during the process, in an adsorption-desorption equilibrium (steady-state transient isotopic kinetic analysis – SSITKA {THOM97}) and ii) of the effect of the modification in adlayer coverage / composition on the reaction itself (reaction rate = activity, product distribution = selectivity). It is important to note that enforced and well-defined electrolyte flow is not only required for detailed measurements of the reaction dynamics, but is also essential for mechanistic studies of electrocatalytic reactions, since transport effects will modify the product distribution of various electrocatalytic reactions {JUSY03D}'{SEID08}. Therefore, defined transport conditions are a prerequisite for the quantitative understanding of the reaction characteristics. Finally, the resulting quantitative data provided a solid basis for the comparison with

theoretical predictions of the reaction mechanism derived, e.g., from density functional theory (DFT) based calculations, and for detailed quantitative modeling of the reaction kinetics, including the different reaction pathways and the partial reaction rates derived from the experiments and the respective adsorbate coverages.

The wealth of information accessible from combined ATR-FTIRS/DEMS flow cell measurements was illustrated in a number of examples. Results on the CO adsorption/ oxidation/exchange kinetics were presented in Chapter 4.2. The rate of molecular adsorption and the structural/vibrational properties of the adlayer during its build-up were followed for CO adsorption on a Pt film electrode. The effective sticking coefficient for CO adsorption as well as the coverage dependence of CO_{ad} band intensities and frequencies could be derived on-line during adsorption at different adsorption potentials, up to the onset of CO_{ad} oxidation. Contributions from CO_{ad} oxidation could be identified by DEMS and subtracted. The data showed negligible potential effects on the adsorption probability. In addition, they revealed the potential induced formation of CO_{ad} islands in the H_{upd} potential range, due to compression by co-adsorbed H_{upd}, and in the double-layer range, due to co-adsorption of (bi-)sulfate.

A study of the exchange of isotope labeled adsorbed ^{13}CO by ^{12}CO on a Pt film at room temperature revealed that i) exchange is controlled by CO_{ad} desorption, that ii) at high CO_{ad} coverages CO_{ad} desorption is facile already at room temperature and proceeds via first-order kinetics, and that iii) the replacement of $^{13}CO^{ad}$ by ^{12}CO occurs statistically, as evident from the pronounced dipole-dipole coupling between $^{12}CO_{ad}$ and $^{13}CO_{ad}$. It is driven by a combination of two effects, a slight, CO concentration dependent increase in CO_{ad} coverage in equilibrium with CO dissolved in the electrolyte and a pronounced decay of the CO adsorption energy at high coverages close to saturation. Similar effects are expected also in the presence of co-adsorbing species, such as H_{upd} or OH_{ad} which can explain nucleation phenomena during the onset of oxidation of a CO adlayer or continuous H_2 oxidation the presence of small amounts of CO at cathodic potentials.

Quantitative spectro-electrochemical kinetic studies on the electrooxidation of formic acid on a Pt film electrode in acidic solution were presented and discussed in Chapter 5, using *in situ* ATR-FTIR spectroscopy under well defined mass transport conditions. In the first part, the contributions of the indirect pathway and the formate pathway to the overall Faradaic current were quantified. Based on the resulting conclusions that both pathways discussed in the literautre represent only minority pathways, a new reaction scheme was postulated, in which

the direct oxidation of weakly adsorbed $HCOOH_{ad}$ species to CO_2 is proposed for the dominant reaction pathway. The proposal that the decomposition of adsorbed formate species is not the rate limiting step for CO_2 formation was further supported by *in situ* ATR-FTIRS data in a number of different reaction situations, including formic acid oxidation at different concentrations or formic acid oxidation in the presence of acetate. It was shown that at identical potentials the Faradaic current increases much faster with increasing formic acid concentration or decreasing acetate concentration than the coverage of bridge-bonded adsorbed formate species. This is neither compatible with a first-order kinetics for formate decomposition (linear relation between formate coverage and Faradaic current) nor with the second-order rate law proposed by Samjeské et al. {SAMJ05A} (slower increase of the Faradaic current with increasing formate coverage than in first order kinetics) and demonstrated that adsorbed formate can not be considered as reaction intermediate in the dominant reaction pathway at medium and higher HCOOH concentrations above 50 mM. Furthermore, adsorbed formate species are in a fast adsorption/desorption equilibrium with formic acid in the solution, and they were proposed to be spectator species in the course of formic acid oxidation. This proposal was supported recently by a theoretical study by Neurock et al.. In the last section of Chapter 5, the KIE in the formation of CO_{ad} was investigated and it was found that) the formation of CO_{ad} during interaction of formic acid with Pt, which is formally described as dehydration of HCOOH, exhibits a potential independent KIE for C-H bond breaking ($k_{C-H}/k_{C-D} = 1.9$) in the potential range 0.1 – 0.5 V, and that ii) the KIE in the dominant direct pathway (direct oxidation to CO_2) is significantly higher than that for CO_{ad} formation, reaching values of around 3. Based on these values, it was concluded that that in both pathways C-H bond breaking is rate-limiting and that the transition state in the latter pathway exhibits a weaker C-H (or Pt-H) bond than that for CO_{ad} formation.

Employing the combined *in situ* ATR-FTIRS/DEMS flow cell set-up in combination with isotopically labeled ethanol, new insights into the mechanism and kinetics of the ethanol electrooxidation were provided. Besides linearly and multiply bound CO_{ad}, adsorbed acetate and adsorbed acetyl species were identified via *in situ* ATR-FTIR spectroscopy. The assignment of the IR band detected at 1635 cm^{-1} to adsorbed acetyl species was supported by i) an isotope shift of about 35 cm^{-1} to lower wavenumber, when 13C labeled ethanol was used and ii) the absence of an isotope shift of this band for the adsorption of CH_3CD_2OH. In potentiostatic electrolyte exchange experiments, the temporal evolution of adsorbed species,

namely, linearly and multiply bonded CO_{ad}, adsorbed acetate and adsorbed acetyl, upon ethanol adsorption could be followed quantitatively. CO_{ad} formation rates of 0.002, 0.013 and 0.015 molecules $\times$ site^{-1} $\times$ s^{-1} were determined on the clean Pt surface for ethanol adsorption at 0.2, 0.4 and 0.6 V, respectively. Potentiostatic adsorbate decomposition transients provided strong experimental support for the proposal that adsorbed acetyl species are the precursor for CO_{ad} formation. Furthermore, based on the CO_{ad} coverage increase in the absence of ethanol in the solution, a quantitative relation between the integral band intensity of adsorbed acetyl and its coverage was established.

In combined ATR-FTIRS/DEMS flow cell measurements with carbon labeled ethanol ($^{12}CH_3{}^{13}CH_2OH$), it was shown qualitatively that both carbon atoms of ethanol can form CO_{ad}, which can be further oxidized to CO_2. The individual rates for the CO_{ad} formation from the methyl and the alcohol group could be determined separately as a function of the adsorption potential, based on potentiostatic electrolyte exchange experiments. At 0.2 V, only $^{13}CO_{ad}$ formation was detected and the formation rate was equal to 0.002 molecules $\times$ site^{-1} $\times$ s^{-1}. At 0.4 V, CO_{ad} formation from both carbon atoms of ethanol is possible and values of 0.005 and 0.011 molecules $\times$ site^{-1} $\times$ s^{-1} were derived for the CO_{ad} formation rate from the methyl and the alcohol group of ethanol, respectively. At 0.6 V, both rates were similar, having values of 0.0036 and 0.0034 molecules $\times$ site^{-1} $\times$ s^{-1} for $^{13}CO_{ad}$ and $^{12}CO_{ad}$ formation. The surprisingly fast formation of CO_{ad} from the methyl group of the ethanol molecule at a potential where adsorbed oxygen species are not present on the Pt surface, i.e., at 0.4 V, was further supported in quantitative potentiodynamic adsorbate stripping experiments. This finding was tentatively explained by a modified mechanistic picture for the decomposition of adsorbed acetyl species. This includes a CH_2CO_{ad} intermediate, which either decomposes to $^{13}CO_{ad}$ and $^{12}CH_2OH_{ads}$ in a concerted reaction with water from the solution or to $^{13}CO_{ad}$ and a rather inactive $^{12}CH_{x,ad}$ species. In this mechanism the formation of CO_{ad} from the methyl group of ethanol is possible without the necessity of adsorbed oxygen species on the Pt surface.

Upon adsorption/oxidation of CH_3CD_2OH, a kinetic isotope effect was found in the CO_{ad} formation, which was quantitatively related to a kinetic isotope effect in the formation of adsorbed acetyl species. Without any modifications of the rate equation derived for the adsorption of CH_3CH_2OH, the CO_{ad} formation rate upon adsorption/oxidation of CH_3CD_2OH could be correlated to the coverage of adsorbed acetyl species. Finally, it was shown that essentially only CH_3CDO, and not CH_3CHO, is formed during oxidation of CH_3CD_2OH,

which lead to the conclusion that adsorbed acetyl is not an active intermediate to form acetaldehyde, but rather formed upon re-adsorption of acetaldehyde.

In Chapter 7, the adsorption/oxidation behavior of bi-functional C2 molecules, namely ethylene glycol, glycol aldehyde, glycolic acid, glyoxal, glyoxylic acid and oxalic acid was investigated by *in situ* ATR-FTIR spectroscopy. The main adsorbates and reaction intermediates detected by IR spectroscopy could be identified and their role in the ethylene glycol oxidation reaction was discussed. It was found that the adsorption/oxidation characteristics of the C2 molecules are strongly affected by the functional groups. Between 0.06 and 0.2V, the highest rates for dissociative adsorption, measured via the build-up of a CO adlayer, were determined for molecules containing an aldehyde group, whereas the adsorption/oxidation of alcohol groups at these potentials is strongly hindered. With increasing potential (0.4 to 0.6 V) the reactivity of the functional groups changes and at 0.6 V, the CO_{ad} formation rate resulting from the adsorption/oxidation of alcohol groups is significantly faster compared to the CO_{ad} formation rates from aldehydes. Molecules containing a carboxyl function establish a fast adsorption/desorption equilibrium between the acid in the solution and adsorbed carboxylates, which binds perpendicular to the Pt surface via the two oxygen atoms of the carboxyl group. This adsorption configuration was regarded to be rather inactive at potentials between 0.2 and 0.9 V, based on the very small Faradaic currents and CO_{ad} formation rates upon adsorption/oxidation of glycolic acid and oxalic acid. At higher potentials, however, the oxidation rate of molecules containing a carboxyl group is strongly enhanced. At 0.06 and 0.1 V, the adsorption of oxalic acid resulted in a rather fast build-up of a CO adlayer, via reduction of one of the carboxyl groups to CO_{ad}, which includes C-C bond breaking.

8.2 Deutsche Fassung

Durch die in der Doktorarbeit präsentierten Ergebnisse wurden neue und detaillierte Erkenntnisse über den Mechanismus und die Kinetik der Adsorption/Elektrooxidation der brennstoffzellenrelevanten kleinen organischen Moleküle, CO (Kapitel 4), Ameisensäure (Kapitel 5), Ethanol (Kapitel 6) sowie Ethylen Glykol und seiner oxidativen Zwischenprodukte (Kapitel 7), gewonnen. Die Messungen wurden an einem *in situ* ATR-FTIRS Flusszellen Aufbau durchgeführt, der im Rahmen der Doktorarbeit weiterentwickelt und mit der on-line differentiellen elektrochemischen Massenspektrometrie (DEMS) gekoppelt wurde. Diese Messtechniken ermöglichten im komplexen Reaktionsnetzwerk der elektrokatalytischen Oxidation kleiner organischer Moleküle, einzelne Reaktionspfade separat zu verfolgen und teilweise zu quantifizieren

Das enorme Potential des neu entwickelten, kombinierten ATR-FTIRS/DEMS Messaufbaus für seine Verwendung in mechanistischen Untersuchungen unter definierten Flussbedingungen wurde an Hand der in Kapitel 4.1 vorgestellten Ergebnisse zur Adsorption/Oxidation von CO anschaulich gemacht. Neben der Aufzeichnung des Faradaischen Stroms, ermöglicht der Aufbau die gleichzeitige Detektion und Quantifizierung von adsorbierten Spezies mittels *in situ* IR-Spektroskopie als auch den Nachweis und Quantifizierung volatiler Reaktionsprodukte mittels on-line DEMS. Durch die Verwendung einer Dünnschicht-Flusszelle können Adsorptionstransienten nicht nur während eines Potentialsprungs (Potentialsprung Transienten), sondern auch während einem Elektrolytaustausch von reinem Basiselektrolyten hin zu einer reaktandenhaltigen Lösung, und umgekehrt, unter definierten Transportbedingungen gemessen werden. Für einen vollständigen Elektrolytaustausch wurden dabei nur 3-4 s benötigt. Die Möglichkeit eines schnellen Elektrolytaustausches erlaubte zeitaufgelöste Untersuchungen zur Dynamik sowohl des Auf- bzw. Abbaus von Adsorbatschichten unter Reaktionsbedingungen als auch zum Austausch von adsorbierten Spezies, die sich einem Adsorptions-Desorptions Gleichgewicht befinden (“Steady-State transiente Isotopen kinetische Analyse – SSITKA {THOM97}. Außerdem kann der Einfluss einer sich verändernden Adsorbatschicht auf den die Gesamtkinetik, gemessen über den Faraday Strom, als auch auf die Produktausbeute (on-line DEMS) unter definierten Flussbedingungen analysiert werden. Es ist wichtig darauf hinzuweisen, dass ein kontrollierter und verstärkter Massentransport dabei nicht nur Voraussetzung für eine genaue Messung der Reaktionsdynamik ist, sondern auch bei mechanistischen Untersuchungen von großer Bedeutung ist, da Transporteffekte zu

einer Veränderung der Produktverteilung führen {JUSY03D}{SEID08}. Die sich aus den Messungen ergebenden quantitativen Daten, auf die im Folgenden näher eingegangen wird, bilden eine solide experimentelle Basis für einen Vergleich mit i) den aus Dichte-Funktional-Theorie (DFT) abgeleitet Erkenntnissen zum Mechanismus der Oxidation kleiner Moleküle und ii) für eine detaillierte quantitative Modellierung der Reaktionskinetik, einschließlich der unterschiedlichen Reaktionspfade und der partiellen Reaktionsrate aus dem Experiment.

In Kapitel 4.2, wurden die Raten für die molekulare CO Adsorption, die während dem Aufbau der Adsorbatschicht auftretenden strukturellen Veränderungen (Verhältnis von linear und mehrfachgebundenem CO_{ad}) und die schwingungsspektrokopischen Eigenschaften der Adsorbatschicht (Intensität, Wellenzahl) während der CO Adsorption untersucht. Mittels massenspektrometrisch Detektion konnte die CO_{ad} Bedeckung zu jedem Zeitpunkt der CO Adsorption verfolgt werden und der effektive Haftkoeffizient für die CO Adsorption als Funktion der CO Bedeckung bestimmt werden. Die Daten zeigten zur einen vernachlässigbaren Einfluss des Elektrodenpotentials auf die Adsorptionswahrscheinlichkeit. Durch die gleichzeitige Messung der schwingungsspektroskopischen Eigenschaften von adsorbiertem CO, konnte diese als Funktion der CO_{ad} Bedeckung aufgetragen und analysiert werden. Dadurch konnte eine bei geringen CO_{ad} Bedeckungen auftretende potentialinduzierte Bildung von CO_{ad} Insel aufgedeckt werden, die im H_{upd} Bereich durch co-adsorbierten Wasserstoff und im Doppelschichtbereich durch co-adsorbiertes Bisulfat ausgelöst wird. Die in diesem Kapitel erhaltenen CO_L Intensitäts-/Bedeckungskurven dienten als Grundlage für die in Kapitel 6 und 7 beschrieben quantitative Auswertung der CO_{ad} Bildungsraten, während der Adsorption/Oxidation kleiner organischer Moleküle.

In Kapitel 4.3, wurde eine kinetische Analyse zum Austausch von voradsorbiertem, isotopenmarkiertem $^{13}CO_{ad}$ durch einen ^{12}CO haltigen Elektrolyten auf einer Pt Elektrode bei Raumtemperatur durchgeführt. Dabei konnte gezeigt werden, dass i) der $^{13}CO_{ad}$ Austausch durch $^{12}CO_{ad}$ durch die Desorption von $^{13}CO_{ad}$ kontrolliert wird, ii) bei hohen CO_{ad} Bedeckungen, eine CO_{ad} Desorption bereits bei Raumtemperatur möglich ist und einem Geschwindigkeitsgesetz erster Ordnung folgt, und iii) der Austausch von $^{13}CO_{ad}$ durch $^{12}CO_{ad}$ statisch, und nicht über Inselbildung, von statten geht, was aus den beobachteten, intensiven Dipol-Dipol Kopplungen zwischen $^{13}CO_{ad}$ und $^{12}CO_{ad}$ abgeleitet wurde. Die treibende Kraft für den Austausch ist eine Kombination aus zwei Effekten: i) einer Zunahme der CO konzentrationsabhängigen CO_{ad} Gleichgewichtbedeckung, bei Anwesenheit von CO in der Gasphase und ii) einer Abnahme der CO Adsorptionsenergie, mit steigender CO_{ad}

Bedeckung, die insbesondere bei CO_{ad} Bedeckungen nahe der Sättigung, sehr stark ausgeprägt ist. Ähnliche Effekte werden auch bei Anwesenheit von co-adsorbierten Spezies, wie z.B. H_{upd} oder OH_{ad} erwartet, wodurch die Nukleationsphänomene bei der CO_{ad} Monolagen Oxidation oder der kontinuierlichen H_2 Oxidation in Anwesenheit kleiner CO Konzentrationen, erklärt werden können.

Unter Verwendung des *in situ* ATR-FTIRS Aufbaus wurden quantitative spektro-elektrochemische Untersuchungen zum Mechanismus und der Kinetik der elektrochemischen Ameisensäureoxidation durchgeführt und in Kapitel 5 präsentiert. In Kapitel 5.1, wurden die Beiträge der "indirekten" Ameisensäureoxidation, d.h., über die Bildung von CO_{ad} und die anschließende Oxidation von CO_{ad} zu CO_2, und des Reaktionsweges über adsorbiertes Formiat, zum Faradaischen Strom quantifiziert. Da gefunden wurde, dass unter den gegeben Messbedingungen die beiden einzigen in der Literatur diskutierten Reaktionspfade nur einen gering Beitrag zum Gesamtstrom leisten, wurde ein neuer Mechanismus postuliert, in dem die direkte Oxidation einer schwach gebundenen $HCOOH_{ad}$ Spezies zu CO_2, den dominanten Reaktionsweg für die Ameisensäureoxidation darstellt. Die Annahme, dass der Zerfall von adsorbiertem Formiat nicht der ratenlimitierende Schritt der Ameisensäureoxidation ist, wurde durch eine Vielzahl weiterer *in situ* ATR-FTIRS Experimente untermauert, wie z.B. der Ameisensäureoxidation bei verschiedenen Konzentrationen oder in der Anwesenheit von Essigsäure. Es konnte gezeigt werden, dass bei identischen Potentialen der Anstieg des Faradaischen Stroms mit steigender Ameisensäurekonzentration viel stärker ausgeprägt ist, als der Anstieg der Intensität des brückengebundenen Formiats. Auch bei Zugabe von Essigsäure zu einer Ameisensäure-haltigen Lösung konnte kein direkter Zusammenhang zwischen dem Abfall des Faradaischen Stroms und der Abnahme der Formiat Intensität gefunden werden. Diese Ergebnisse sind weder mit einem Formiat Zerfall erster Ordnung (linearer Zusammenhang zwischen Formiat Bedeckung und Faradaischen Strom) noch einem Zerfall zweiter Ordnung (langsamerer Anstieg des Faradaischen Stroms mit der Formiat Bedeckung als bei einem Zerfall erster Ordnung), wie es von Samjeské et al. postuliert wurde {SAMJ05}, in Einklang zu bringen. Auf Grund dieser Daten wurde geschlossen, dass das mittels IR Spektroskopie detektierte adsorbierte Formiat nicht die reaktive Zwischenstufe im dominanten Reaktionsweg der Ameisensäureoxidation darstellt. Im Gegensatz wurde postuliert, dass sich adsorbiertes Formiat in einem schellen Adsorptions-Desorptions Gleichgewicht mit Ameisensäure in der Lösung befindet und nicht signifikant zur Ameisensäureoxidation beiträgt. Diese Annahmen wurden durch vor kurzem veröffentlichte

Dichte-Funktional-Theorie Rechnungen von M. Neurock et al., unterstützt. Im letzten Abschnitt von Kapitel 5, wurde unter Verwendung von deuterierter Ameisensäure, der kinetische Isotopeneffekt in der CO_{ad} Bildungsrate bei Wechselwirkung von Ameisensäure mit der Pt Elektrode untersucht. Es konnte gezeigt werden, dass i) die Bildung von CO_{ad}, die formal als Dehydrierung von HCOOH beschrieben werden kann, im Potentialbereich zwischen 0.1 und 0.6 V, einen potentialunabhängigen kinetischen Isotopeneffekt für den C-H Bindungsbruch aufweist (k_{C-H}/k_{C-D} = 1.9) und dass ii) der KIE im dominanten direkten Reaktionsweg (direkte Oxidation von Ameisensäure zu CO_2) mit Werten von ca. 3, signifikant größer ist als der für die CO_{ad} Bildung. Auf Grund dieser Ergebnisse wurde geschlossen, dass in beiden Reaktionswegen der C-H Bindungsbruch ratenlimitierend ist und dass der Übergangszustand des zuletzt genannten Reaktionspfades eine schwächere C-H Bindung aufweist, als der für die CO_{ad} Bildung.

In Kapitel 6 wurden unter Verwendung des kombinierte ATR-FTIRS/DEMS Messaufbaus und dem Einsatz von isotopenmarkiertem Ethanol, detaillierte qualitative and quantitative Einblicke in den Mechanismus der elektrochemischen Ethanol Oxidation of Pt Elektroden gewonnen. Neben linear und mehrfach gebundenem CO_{ad}, wurden adsorbiertes Acetate und adsorbierte Acetyl Spezies mittels *in situ* ATR-FTIR Spektroskopie identifiziert. Die Zuordnung der IR-Bande bei 1635 cm^{-1} zu adsorbiertem Acetyl konnte durch eine Verschiebung dieser Bande nach 1600 cm^{-1} bei Verwendung von 13C markiertem Ethanol ($^{12}CH_3{}^{13}CH_2OH$) bestätigt werden. Durch das Fehlen einer entsprechenden Verschiebung der Bande bei 1635 cm^{-1} bei Verwendung von deuteriertem Ethanol (CH_3CD_2OH), war es erstmals möglich, adsorbiertes Acetaldehyd {SHAO05} als Ursache für die Bande bei 1635 cm^{-1} auszuschließen. Die zeitliche Entwicklung von einfach und mehrfach gebundenem CO, adsorbiertem Acetat und adsorbiertem Acetyl während der Ethanol Adsorption/Oxidation konnte, basierend auf potentiostatischen Elektrolytaustausch-Experimenten, teilweise quantitativ analysiert werden. Für die Ethanol Adsorption/Oxidation bei 0.2, 0.4 und 0.6 V, wurden so anfängliche CO_{ad} Bildungsraten von 0.002, 0.013 bzw. 0.015 Pt Monolagen $\times$ s^{-1} ermittelt. Eine solide experimentelle Unterstützung für das Postulat, dass im Netzwerk der Ethanol Oxidation adsorbierte Acetyl Spezies eine Vorstufe für den C-C Bindungsbruch darstellen {HITM94}{IWAS94A}, konnte mittels potentiostatischer Adsorbat Zerfalls-Transienten geliefert werden. Aus dem in diesen Experimenten gefundenen Anstieg der CO_{ad} Bedeckung in Abwesenheit von Ethanol im Elektrolyten, konnte zusätzlich eine quantitative Beziehung zwischen der Intensität von adsorbiertem Acetyl und dessen Bedeckung hergestellt werden.

Durch kombinierte ATR-FTIRS/DEMS Flusszellen Messungen mit 13C markiertem Ethanol ($^{12}CH_3{}^{13}CH_2OH$), konnte in potentiodynamischen Messungen qualitativ gezeigt werden, dass CO_{ad}/CO_2 aus beiden Kohlenstoffatomen des Ethanols gebildet werden kann. In potentiostatischen Adsorptionstransienten wurden die CO_{ad} Bildungsraten aus der Methylgruppe und der Alkoholgruppe des Ethanol, bei verschiedenen Potentialen, separat bestimmt. Während bei 0.2 V, CO_{ad} nur aus der Alkoholgruppe gebildet wurde (CO_{ad} Bildungsrate = 0.002 Monolagen $\times$ s^{-1}), konnte bereits bei 0.4 V gezeigt werden, dass CO_{ad} sowohl aus der Alkoholgruppe, als auch aus der Methylgruppe, entsteht (CO_{ad} Bildungsraten: 0.011 ($^{13}CO_{ad}$) bzw. 0.005 ($^{12}CO_{ad}$) Monolagen $\times$ s^{-1}). Bei 0.6 V, waren beide CO_{ad} Bildungsraten mit Werten von 0.0036 ($^{13}CO_{ad}$) und 0.0034 ($^{12}CO_{ad}$) Monolagen $\times$ s^{-1} praktisch identisch. Die erstaunlich schnelle Oxidation der Methylgruppe zu CO_{ad}, bereits bei 0.4 V, also unterhalb der Bildung von OH_{ad} Spezis auf der Pt Oberfläche, wurde auch in quantitativen Potentialsprung Experimenten (DEMS) bestätigt, und führte zu einer Modifizierung des mechanistischen Bildes für den Zerfall der adsorbierten Acetyl Spezies. Dieses beinhaltet ein adsorbierte CH_2CO_{ad} Intermediat, das entweder in einer konzertierten Reaktion mit Wasser, zu $^{13}CO_{ad}$ and $^{12}CH_2OH_{ads}$, oder aber in einem alternative Reaktionspfad mit adsorbiertem Wasserstoff, zu $^{13}CO_{ad}$ und einer unreaktiven $^{12}CH_{x,ad}$ Spezies zerfällt. In diesem Mechanismus ist die Oxidation der Methylgruppe zu CO_{ad} auch ohne die Anwesenheit von adsorbierten Sauerstoffhaltigen Spezies auf der Pt Oberfläche möglich.

In Messungen zur Adsorption/Oxidation von deuteriertem Ethanol (CH_3CD_2OH), wurde ein kinetischer Isotopen Effekt (KIE) in der CO_{ad} Bildungsrate gefunden, der quantitativ auf einen KIE in der Bildungsrate in von adsorbiertem Acetyl zurückgeführt werden konnte. Die Zerfallsgleichung für adsorbiertes Acetyl, die für die Adsorption/Oxidation von unmarkiertem Ethanol aufgestellt worden ist, konnte ohne Modifikationen der Ratenkonstante, dazu verwendet werden, die aus der CH_3CD_2OH Adsorption/Oxidation resultierende CO_{ad} Bildungsrate mit der Acetyl Bedeckung zu korrelieren. Das zeigt, dass der Zerfall der Acetyl Spezies keinen KIE aufweist, in Übereinstimmung mit der postulierten Struktur, in der die beiden Deuterium Atome von CH_3CD_2OH bereits abgespalten wurden. Basierend auf Potentialsprung Experimenten, in denen als Reaktionsprodukt der Ethanol Oxidation (CH_3CD_2OH) praktisch ausschließlich CH_3CDO und nicht CH_3CHO gefunden wurde, konnte gezeigt werden, dass adsorbierte Acetyl Spezies keine Vorstufe für die Bildung von Acetaldehyd darstellen, sondern eher durch Re-Adsorption von Acetaldehyd gebildet werden.

In Kapitel 7 wurde mittels *in situ* ATR-FTIR Spektroskopie die Adsorption/Oxidation der bifunktionellen C2 Moleküle, Ethylen Glykol, Glykolaldehyd, Glykolsäure, Glyoxal, Glyoxylsäure und Oxalsäure, untersucht. Dabei konnten die wichtigsten Adsorbate (CO, adsorbierte Aldehyde und Carboxylate) und Reaktionszwischenstufen (Carbonsäuren) identifiziert werden. Der Einfluss dieser Adsorbate auf den Mechanimus der Ethylen Glykol Oxidation wurde diskutiert. Des Weiteren konnte gezeigt werden, dass die Adsorptions- und Oxidationscharakteristik stark von den funktionellen Gruppen beeinflusst wird. Im Potentialbereich zwischen 0.06 und 0.2 V, wiesen Moleküle die eine Aldehydgruppe besitzen die höchste Rate für eine dissoziative Adsorption, gemessen über die CO_{ad} Bildungsrate, auf. Im Gegensatz dazu wird die Adsorption von Alkoholgruppen durch die Anwesenheit von upd-Wasserstoff in diesem Potentialbereich stark behindert. Mit ansteigendem Potential (0.4 bis 0.6 V), ändert sich die Reihenfolge der Reaktivität der funktionellen Gruppen, und bei 0.6 V ist die CO_{ad} Bildungsrate aus Alkoholen schneller als die aus Aldehyden. Bei Molekülen die eine Carboxylgruppe besitzen, bildete sich ein dynamisches Adsorption-Desorption Gleichgewicht aus der Carbonsäure in der Lösung und adsorbiertem Carboxylat, das über die beiden Sauerstoffatome der Carboxylgruppe senkrecht zur Pt Oberfläche gebunden ist, aus. Diese Adsorptionskonfiguration kann als relativ stabil/unreaktiv im Potentialbereich zwischen 0.2 und 0.9 V angesehen werden, da unter diesen Bedingungen praktisch keine Faradaischen Ströme für die Oxidation/Adsorption von Glykol- und Oxalsäure gemessen wurden. Die Oxidationsrate der Moleküle mit einer Carboxylgruppe, steigt allerdings bei Potentialen oberhalb von 0.9 V stark an. Bei 0.06 und 0.1 V, führte die Adsorption von Oxalsäure über eine reduktive Dissoziation der C-C Bindung, zu einer relativ schnellen Bildung von CO_{ad}.

9 Outlook

In the outlook, I want to point out several ongoing experimental developments which are expected to widen the possibilities for applying the simultaneous ATR-FTIRS/DEMS technique for studies of electrochemical systems and electrocatalytic reactions in particular. These apply to both the DEMS and the ATR-FTIRS part of the method. Starting with the latter, Wandlowski et al. demonstrated that despite the loss of the surface enhancement, ATR-FTIRS measurements are possible also on single-crystal type Au films film on a Si surface, though at much lower intensity {WAND04}. Epitaxial deposition of other metals, e.g., palladium, on top of the Au film, or a corresponding treatment of other films directly deposited on the Si substrate, would in principle allow combined ATR-FTIRS/DEMS flow cell measurements on single crystalline surfaces {PRON04}. On the other hand, it would be worthwhile to extend this technique to studies of (supported) nanoparticle catalysts. This could be achieved, e.g., by deposition of the (supported) nanoparticles on an IR transparent, electrically conducting and electrochemically inert film deposited on the Si prism. Possible materials would be Au or B-doped diamond. First ATR-FTIRS results on a carbon supported Pt catalyst deposited on an Au film were recently reported by Sato et al. {SATO07}. Of course, the DEMS measurements can equally be combined with recent approaches to vibrational spectroscopy studies at enforced electrolyte flow in an external reflection configuration, either by FTIR {KUZU08}'{LU05}'{NICH88}'{ROTH91}'{STAM05A}'{ZHOU05F}, or by SFG {LU05}, where single-crystal measurements are unproblematic. In this case, however, the time resolution would be significantly lower than for the present set-up, due to the rather slow electrolyte flow in these configurations (FTIR) or the lower sensitivity of the SFG measurements. Next, measurements at controlled elevated temperatures would be desirable for the study of temperature effects. ATR-FTIRS measurements at up to 80°C were reported already previously {CHEN06F}, and recently we succeeded in performing high-temperature/high pressure DEMS measurements under continuous electrolyte flow at up to 120°C and 3 bar overpressure {CHOJ08A}'{HALS08}. The combination of these approaches to allow ATR-FTIRS/DEMS flow cell measurements at elevated temperatures and pressures therefore seems to be within reach.

Next, the extension of the DEMS method to allow the detection of larger or non-volatile molecules, which is not possible with the present set-up due to the limited porosity of the membrane interface, and to reduce the tendency for analyte fragmentation may be possible by using electro spray ionization (ESI-MS) rather than ionization by electron impact {COLE97}. Work in our laboratory on this aspect is in progress, but the problems in interfacing

electrochemistry and ESI-MS are considerable {BOEK04}, in particular if striving for on-line detection. The most serious problem seems to be the further reduction of the time resolution of the combined measurements. At present, this is determined by the intermixing of dissolved species on the way from the valve for electrolyte switching in front of the cell inlet (electrolyte exchange transients) or from the electrode to the DEMS membrane, not by direct instrumental limits. Any improvements of the time resolution would therefore require to significantly shorten the distances between inlet valve, electrode and membrane, or to increase the electrolyte flow accordingly, e.g., by microreactor and micromachining technologies. At present, however, solutions for significant improvements in this respect are not at hand, and require the thoughts of the community.

REFERENCES

ADZI98: R.R. Adzic, Recent Advances in the Kinetics of Oxygen Reduction. In: J. Lipkowski and P.N. Ross (Eds.), Electrocatalysis. Vol. 2, Wiley-VCH, Inc., New York, **1998**, pp. 197-242.

AKEM00: W. Akemann, K.A. Friedrich, and U. Stimming, Potential dependence of CO adlayer structures on Pt(111) electrodes in acid solution: Evidence for a site selective charge transfer, Journal of Chemical Physics 113, 6864-6874, **2000**.

ANDE05B: M. Andersen, M. Johansson, and I. Chorkendorff, Isotopic Exchange of CO Adsorbed on Pt(111), Journal of Physical Chemistry B 109, 10285-10290, **2005**.

ANDE02A: A.B. Anderson, O_2 reduction and CO oxidation at the Pt-electroyte interface. The role of H_2O and OH adsorption bond strengths , Electrochimica Acta 47, 3759-3763, **2002**.

ANDR06: B. Andreaus, F. Maillard, J. Kocylo, E.R. Savinova, and M. Eikerling, Kinetic Modeling of COad Monolayer Oxidation on Carbon-Supported Platinum Nanoparticles, Journal of Physical Chemistry B 110, 21028-21040, **2006**.

ANGE73: H. Angerstein-Kozlowska, B.E. Conway, and W.B.A. Sharp, The Real Conditions of Electrochemically Oxidized Platinum Surfaces Part 1. Resolution of Component Processes, Journal of Electroanalytical Chemistry 43, 9-36, **1973**.

AREN05B: M. Arenz, K.J. Mayrhofer, V. Stamenkovic, B.B. Blizanac, T. Tomoyuki, P.N. Ross, and N.M. Markovic, The Effect of the Particle Size on the Kinetics of CO Electrooxidation on High Surface Area Pt Catalysts, Journal American Chemical Society 127, 6819-6829, **2005**.

ARIC98A: A.S. Aricò, P. Creti, P.L. Antonucci, and V. Antonucci, Comparison of Ethanol and Methanol Oxidation in a Liquid-Feed Solid Polymer Electrolyte Fuel Cell at High Temperature, Electrochemical and Solid-State Letters 1, 66-68, **1998**.

ATAK96: K. Ataka, T. Yotsuyangi, and M. Osawa, Potential-Dependent Reorientation of Water Molecules at an Electrode/Electrolyte Interface Studied by Surface-Enhanced Infrared Absorption Spectroscopy, Journal of Physical Chemistry B 100, 10664-10672, **1996**.

BAGO77: V.S. Bagotzky, Y.B. Vassiliev, and O.A. Khazova, Generalized scheme of chemisorption, electrooxidation and electror4eduction of simple organic compounds on platinum gropup metals, Journal of Electroanalytical Chemistry 81, 229-238, **1977**.

BALT93: H. Baltruschat, U. Schmiemann, The adsorption of unsaturated organic species at single-crystal electrodes studied by differential electrochemical mass spectrometry, Berichte der Bunsengesellschaft für Physikalische Chemie 97, 452-460, **1993**.

BALT99: H. Baltruschat, Differential Electrochemical Mass Spectrometry as a Tool for Interfacial Studies. In: A. Wieckowski (Eds.), Interfacial Electrochemistry - Theory, Experiment and Applications. Marcel Dekker, INC., New York, **199**9, pp. 577-597

BALT04: H. Baltruschat, Differential Electrochemical Mass Spectrometry, J.Amer.Soc.Mass Spectr. 15, 1693-1706, **2004**.

BATI04A: E.A. Batista, G.R.P. Malpass, A.J. Motheo, and T. Iwasita, New mechanistic aspects of methanol oxidation, Journal of Electroanalytical Chemistry 571, 273-282, **2004**.

BATI04B: E.A. Batista, T. Iwasita, and W. Vielstich, Mechanism of Stationary Bulk CO Oxidation on Pt(111) Electrodes, Journal of Physical Chemistry B 108, 14216-14222, **2004**.

BEDE83: B. Beden, A. Bewick, and C. Lamy, A Study by Electrochemically Modulated Infrared Reflectance Spectroscopy of the Electrosorption of Formic Acid at a Platinum Electrode, Journal of Electroanalytical Chemistry 148, 147-160, **1983**.

BEDE92: B. Beden, J.-M. Léger, and C. Lamy, Electrocatalytic oxidation of oyxygenated aliphatic organic compounds at noble metal electrodes. In: J.O. Bockris, B.E. Conway, and R.E. White (Eds.), Modern Aspects of Electrochemistry, Vol. 22, Plenum Press, New York, **1992**, pp. 97- 264.

BEHM05: R.J. Behm, Z. Jusys, The potential of model studies for the understanding of catalyst poisoning and temperature effects in polymer electrolyte fuel cell reactions , Journal of Power Sources 154, 327-342, **2006**.

BELG91: E.M. Belgsir, E. Bouhier, H.E. Yei, K.B. Kokoh, B. Beden, H. Huser, and J.-M. Léger, Electrosynthesis in aqueous medium: a kinetic study of the electrocatalytic oxidation of oxygenated organic molecules, Electrochimica Acta 36, 1157-1164, **1991**.

BERG98A: M. Bergelin, M. Wasberg, The impinging jet flow mthod in interfacial electrochemistry: an application to bead-type electrodes, Journal of Electroanalytical Chemistry 449, 181-191, **1998**.

BERN04: A. Berna, A. Rodes, and J.M. Feliu, Oxalic acid adsorption and oxidation at platinum single crystal electrodes, Journal of Electroanalytical Chemistry 563, 49-62, **2004**.

BERN08: A. Berna, J.M. Delgado, J.M. Orts, A. Rodes, and J.M. Feliu, Spectroelectrochemical study of the adsorption of acetate anions at gold single crystal and thin-film electrodes, Elelctrochim.Acta 53, 2309-2321, **2008**.

BEWI82: A. Bewick, J.W. Russell, Structural Investigation by Infra-Red Spectroscopy of Adsorbed Hydrogen on Platinum, Journal of Electroanalytical Chemistry 132, 329-344, **1982**.

BIRS93: V.I. Birss, M. Chang, and J. Segal, Platinum oxide film formation-reduction: an in-situ mass meassurement study, Journal of Electroanalytical Chemistry 355, 181-191, **1993**.

BITT88: B. Bittins-Cattaneo, S. Wilhelm, E. Cattaneo, H.W. Buschmann, and W. Vielstich, Intermediates and products of ethanol oxidation on platinum in acid solution, Berichte der Bunsengesellschaft für Physikalische Chemie 92, 1210-1218, **1988**.

BLYH64: G. Blyholder, Molecular orbital view of chemisorbed carbon monoxide, Journal of Physical Chemistry 68, 2772-2778, **1964**.

BOEK04: C. Bökman, C. Zettersten, C. Sjöberg, and L. Nyholm, unknown, Analytical Chemistry 76, 2017-**2004** .

BREI60: M. Breiter, K. Hoffmann, Bestimmung der Diffusionskoeffizienten D_{H2}, D_{H+} und D_{OH-} mit der Platinscheibenelektrode, Zeitschrift für Elektrochemie 64, 462-467, **1960**.

BREI67A: M.W. Breiter, A study of the intermediates adsorbed on platinized platinum during the steady-state oxidation of methanol, formic acid and formaldehyde, Journal of Electroanalytical Chemistry 14, 407-413, **1967**.

BRUC71: S. Bruckenstein, R.R. Gadde, Use of a Porous Electrode for in Situ Mass Spectrometric Determination of Volatile Electrode Reaction Products, Journal American Chemical Society 93, 793-794, **1971**.

CAMA05A: G.A. Camara, R.B. de Lima, and T. Iwasita, The influence of PtRu atomic composition on the yields of ethanol oxidation: A study by in situ FTIR spectroscopy, Journal of Electroanalytical Chemistry 585, 128-131, **2006**.

CAMP90: J.C. Campuzano, unknown. In: D.A. King and D.P. Woodruff (Eds.), Chemisorption Systems. Vol. Elsevier Publishers, Amsterdam, 1990, pp. 419-

CAPO73: A. Capon, R. Parsons, The Oxidation of Formic Acid at Noble Metal Electrodes Part III. Intermediates and mechanisms on platinum electrodes, Journal of Electroanalytical Chemistry 45, 205-231, **1973**.

CAPO73B: A. Capon, R. Parsons, The Oxidation of Formic Acid at Noble Metal Electrodes Part I. Review of previous work, Journal of Electroanalytical Chemistry 44, 1-7, **1973**.

CAPO73C: A. Capon, R. Parsons, The oxidation of formic acid on noble metal electrodes II. A comparison of the behavior of pure electrodes, Journal of Electroanalytical Chemistry 44, 239-254, **1973**.

CHAN90A: S.-C. Chang, M.J. Weaver, In-situ infrared spectroscopy of CO adsorbed at ordered Pt(100)-aqueous interfaces: Double layer effects upon the adsorbate binding geometry, Journal of Physical Chemistry 94, 5095-5102, **1990**.

CHAN90B: S.-C. Chang, A. Hamelin, and M.J. Weaver, Reactive and Inhibiting Adsorbates for the Catalytic Electrooxidation of Carbon Monoxide on Gold (210) as Characterized by Surface Infrared Spectroscopy, Surface Science 239, L543-L547, **1990**.

CHAN90C: S.-C. Chang, M.J. Weaver, Coverage-dependent dipole coupling for carbon monoxide adsorbed at ordered platinum (111)-aqueous interfaces: Structural and electrochemical implications, Journal of Chemical Physics 92, 4582-4594, **1990**.

CHAN91F: S.-C. Chang, Y. Ho, and M.J. Weaver, Applications of Real-Time FTIR Spectroscopy to the Elucidation of Complex Electroorganic Pathways: Electrooxidation of Ethylene Glycol on Gold, Platinum, and Nickel in Alkaline Solution, Journal American Chemical Society 113, 9506-9513, **1991**.

CHAN91G: S.-C. Chang, M.J. Weaver, unknown, Journal of Physical Chemistry 95, 5391-5400, **1991**.

CHEN03: Y.-X. Chen, A. Miki, S. Ye, H. Sakai, and M. Osawa, Formate, an Active Intermediate for Direct Oxidation of Methanol on Pt Electrode, Journal American Chemical Society 125, 3680-3681, **2003**.

CHEN04F: Y.-X. Chen, M. Heinen, Z. Jusys, and R.J. Behm, Kinetics and Mechanism of Formic Acid Electrooxidation – Spectro-electrochemical Studies in a Novel Flow Cell Configuration, Angew.Chem.Int.Ed. 45, 981-985, **2006.**

CHEN04H: S. Chen, A. Kucernak, Electrocatalysis under conditions of high mass transport: Investigation of hydrogen oxidation on single submicron Pt particles supported on carbon, Journal of Physical Chemistry B 108, 13984-13994, **2004**.

CHEN06F: Y.-X. Chen, S. Ye, M. Heinen, Z. Jusys, M. Osawa, and R.J. Behm, Application of in-situ ATR-FTIR spectroscopy for the understanding of complex reaction mechanism and kinetics: Formic acid oxidation on a Pt electrode at elevated temperatures, Journal of Physical Chemistry B 110, 9534-9544, **2006**.

CHEN06H: Y.-X. Chen, M. Heinen, Z. Jusys, and R. J. Behm, CO prewave on Pt. **2006**

CHEN07A: Y.-X. Chen, M. Heinen, Z. Jusys, and R.J. Behm, Potential-Induced COad Island Formation on a Platinum Thin-Film Electrode in the H-upd Potential Region, Journal of Physical Chemistry C 111, 435-438, **2007**.

CHOJ08A: M. Chojak, Z. Jusys, and R. J. Behm, Electrooxidation of ethylene glycol on a carbon-supported Pt catalyst at elevated temperatures and pressure: A high-temperature/high-pressure DEMS study. Langmuir **2008**

CHOU03: K.C. Chou, J. Kim, S. Baldelli, and G.A. Somorjai, Vibrational spectroscopy of carbon monoxide, acetonitile, and phenylalanine adsorbed on liquid electrode interface by sum frequency generation, Journal of Electroanalytical Chemistry 554-555, 253-263, **2003**.

CHOU03B: K.C. Chou, N.M. Markovic, J. Kim, P.N. Ross, and G.A. Somorjai, An in Situ Time-Dependent Study of CO Oxidation on Pt(111) in Aqueous Solution by Voltammetry and Sum Frequency Generation, Journal of Physical Chemistry B 107, 1840-1844, **2003**.

CHRI89A: P.A. Christensen, A. Hamnett, The oxidation of ethylene glycol at platinum electrode in acid and base. An in situ FTIR study, Journal of Electroanalytical Chemistry 260, 347-359, **1989**.

CHRI04: P.A. Christensen, J.M. Jin, W.F. Lin, and A. Hamnett, Identification of CO Adsorbed at Ru and Pt Sites on a Polycrystalline Pt/Ru Electrode and the Observation of Their Oxidation and Free Interchange under Open Circuit Conditions, Journal of Physical Chemistry B 108, 3391-3394, **2004**.

CLIM06: V. Climent, R. Gómez, J.M. Orts, and J.M. Feliu, Thermodynamic Analysis of the Temperature Dependence of OH Adsorption on Pt(111) and Pt(100) Electrodes in Acidic Media in the Absence of Specific Anion Adsorption, Journal of Physical Chemistry B 110, 11344-11351, **2006**.

COLM06D: L. Colmenares, H. Wang, Z. Jusys, L. Jiang, S. Yan, G.Q. Sun, and R.J. Behm, Ethanol oxidation on novel, carbon supported Pt alloy catalysts—Model studies under defined diffusion conditions, Electrochimica Acta 52, 221-233, **2006**.

COLM07C: L. Colmenares, E. Guerrini, Z. Jusys, K.S. Nagabhushana, E. Dinjus, S. Behrens, W. Habicht, H. Bönnemann, and R.J. Behm, Activity, selectivity, and methanol tolerance of novel carbon-supported Pt and Pt3Me (Me= Ni, Co) cathode catalysts, Journal of Applied Electrochemistry 37, 1413-1427, **2007**.

COLU92: M.R. Columbia, A.M. Crabtree, and P.A. Thiel, The Temperature and Coverage Dependences of Adsorbed Formic Acid and Its Conversion to Formate on Pt(111), Journal American Chemical Society 114, 1231-1237, **1992**.

COLU93A: M.R. Columbia, A.M. Crabtree, and P.A. Thiel, Chemical reactions between atomic oxygen and formic acid on Pt(111), Journal of Electroanalytical Chemistry 351, 207-226, **1993**.

COMP88: R.G. Compton, G.M. Stearn, P.R. Unwin, and A.J. Barwise, Double channel electrodes and the measurement of heterogenous reaction rates at the solid-liquid interface, Journal of Applied Electrochemistry 18, 657-655, **1988**.

CORR88: D.S. Corrigan, M.J. Weaver, Mechanisms of formic acid, methanol, and carbon monoxide electrooxidationat platinum as examined by single potential alteration Infrared spectroscopy, Journal of Electroanalytical Chemistry 241, 143-162, **1988.**

CORR88A: D.S. Corrigan, E.K. Krauskopf, L.M. Rice, A. Wieckowski, and M.J. Weaver, Adsorption of Acetic Acid at Platinum and Gold Electrodes: A Combined Infrared Spectroscopic and Radiotracer Study, Journal of Physical Chemistry 92, 1596-1601, **1988**.

CRAB04: G.W. Crabtree, M.S. Dresselhaus, and M.V. Buchanan, Phys. Today 39-44, **2004**.

CUES06: A. Cuesta, A. Couto, A. Rincón, M.C. Perez, A. Lopez-Cudero, and C. Gutierrez, Potential dependence of the saturation CO coverage of Pt electrodes: The origin of the pre-peak in CO-stripping voltammograms. Part 3: Pt(poly), Journal of Electroanalytical Chemistry 586, 184-195, **2006**.

CZER78: A. Czerwinski, J. Sobkowski, The adsorption of carbon monoxide on a platinum electrode, Journal of Electroanalytical Chemistry 91, 47-53, **1978**.

DAIL98: A. Dailey, J. Shin, and C. Korzeniewski, Ethylene glycol electrochemical oxidation at platinum probed by ion chromatography and infrared spectroscopy, Electrochimica Acta 44, 1147-1152, **1998**.

DAMJ67: A. Damjanovic, M.A. Genshaw, and J.O. Bockris, The role of Hydrogen Peroxide in Oxygen Reduction at Platinum in H2SO4 solution, Journal of the Electrochemical Society 114, 466-472, **1967**.

DAVI04: J.C. Davies and others, CO Desorption Rate Dependence on CO Partial Pressure over Platinum Fuel Cell Catalysts, Fuel Cells 4, 1-11, **2003**.

DAVI05: J.C. Davies, J. Bonde, A. Logadottir, J.K. Nørskov, and I. Chorkendorff, The ligand effect; CO desorption from PtRu catalysts, Fuel Cells 4, 429-435, **2005**.

DAVI08: J.C. Davies, G. Tsotridis, Temperature-Dependent Kinetic Study of CO Desorption from Pt PEM Fuel Cell Anodes, Journal of Physical Chemistry C 112, 3392-3397, **2008**.

DEDE00: F. Dederichs, K.A. Friedrich, and W. Daum, Sum-frequency vibrational spectroscopy of CO adsorption on Pt(111) and Pt(110) electrode surfaces in perchloric acid solution: Effects of thin layer electrolytes in spectroelectrochemistry, Journal of Physical Chemistry B 104, 6626-6632, **200**.

DEMA07: L.B.S. Demarconnay, C. Coutanceau, and J.-M. Léger, Ethylene glycol electrooxidation in alkaline medium at multi-metallic Pt based catalysts, Journal of Electroanalytical Chemistry 601, 169-180, **2007**.

DESO02: J.P.I. de Souza, S.L. Queiroz, K. Bergamaski, E.R. Gonzalez, and F.C. Nart, Electro-Oxidation of Ethanol on Pt, Rh, and PtRh Electrodes. A study using DEMS and in-Situ FTIR techniques, Journal of Physical Chemistry B 106, 9825-9830, **2002**.

DOSA06: D.M. dos Anjos, K. B. Kokoh, J.-M. Léger, A. R. de Andrade, P. Olivi, and G. Tremiliosi-Filho, Electrocatalytic oxidation of ethanol on molybdenum modified platinum electrodes in acid medium. Journal of Applied Electrochemistry **2006**

ERTL77: G. Ertl, M. Neumann, and K.M. Streit, Chemisorption of CO on the Pt(111) surface, Surface Science 64, 393-410, **1977**.

FAN04B: Y.J. Fan, Z.Y. Zhou, C.H. Zhen, C.J. Fan, and S.-G. Sun, Kinetics of dissociative adsorption of ethylene glycol on Pt(100) electrode surface in sulfuric acid solutions, Electrochimica Acta 49, 4659-4666, **2004**.

FARI07: M.J.S. Farias, G.A. Camara, and A.A. Tanaka, Electrooxidation of isotope-labeled ethanol: a FTIRS study, J.Solid State Electrochem. 11, 1465-1469, **2007**.

FRIE00: K.A. Friedrich, F. Henglein, U. Stimming, and W. Unkauf, Size dependence of the CO monolayer oxidation on nanosized Pt particles supported on gold, Electrochimica Acta 45, 3283-3293, **2000**.

FROM05: I. Fromondi, P. Shi, A. Mineshige, and D.A. Scherson, In Situ, Time-Resolved Normal Incidence Feflectance Spectroscopy of Polycrystalline Platinum Microelectrodes in Aqueous Electrolytes, Journal of Physical Chemistry B 109, 36-39, **2005**.

FROM06: I. Fromondi, D.A. Scherson, Oxidation of Adsorbed CO on Pt(111) in CO-Saturated Perchloric Acid Aqueous Solutions: Simultaneous In Situ Time-Resolved Feflectance Spectroscopy and Second Harmonic Generation Studies, Journal of Physical Chemistry B 110, 20749-20751, **2006**.

FRUM59: A.N. Frumkin, L. Nekrasov, V.G. Levich, and J. Ivanov, Die Anwendung er rotierenden Scheibenelektrode mit einem Ringe zur Untersuchung von Zwischenprodukten elektrochemischer Reaktionen, Journal of Electroanalytical Chemistry 1, 84-90, **1959**.

FUHR08: J. Fuhrmann, H. Zhao, E. Holzbecher, and H. Langmach, Flow, Transport, and Reactions in a Thin Layer Flow Cell, J.Fuel Cell Sci.Technol. 5, **2008**.

FUJI99A: N. Fujiwara, K.A. Friedrich, and U. Stimming, Ethanol oxidation on PtRu electrodes studied by differntial electrochemical mass spectrometry, Journal of Electroanalytical Chemistry 472, 120-125, **1999**.

FUTA05: M. Futamata, L. Luo, and C. Nishihara, ATR–SEIR study of anions and water adsorbed on platinum electrode, Surface Science 590, 196-211, **2005**.

GAMB93: M.E. Gamboa-Aldeco, E. Herrero, P.S. Zelenay, and A. Wieckowski, Adsorption of bisulfate anion on a Pt(100) electrode: a comparison with Pt(111) and Pt(poly), Journal of Electroanalytical Chemistry 348, 451-457, **1993**.

GAO04A: L. Gao, H. Huang, and C. Korzeniewski, The efficiency of methanol conversion to CO2 on thin films of Pt and PtRu fuel cell catalysts, Electrochimica Acta 49, 1281-1287, **2004**.

GAST95A: H.A. Gasteiger, N.M. Markovic, and P.N. Ross, H2 and CO electrooxidation on well-characterized Pt, Ru, and Pt- Ru. 1. Rotating disk electrode studies of the pure gases including temperature effects, Journal of Physical Chemistry 99, 8290-8301, **1995**.

GAST95B: H.A. Gasteiger, N.M. Markovic, and P.N. Ross, The Electrooxidation of CO and H2/CO Mixtures on a Well- Characterized Pt3Sn Electrode Surface, Journal of Physical Chemistry 99, 8945-8949, **1995**.

GEIS01: K. Geissler, E. Newson, F. Vogel, T.-B. Truong, P. Hottinger, and A. Wokaun, Autothermal methanol reforming for hydrogen production in fuel cell applications, Phys.Chem.Chem.Phys. 3, 289-293, **2001**.

GERI65: H. Gerischer, I. Mattes, and R. Braun, Elektrolyse im Strömungskanal - Ein Verfahren zur Untersuchung von Reaktions- und Zwischenprodukten, Journal of Electroanalytical Chemistry 10, 553-567, **1965**.

GILM63: S. Gilman, The mechanism of electrochemical oxidation of carbon monoxide and methanol on Platinum . I. Carbon monoxide adsorption and desorption and simultaneous oxidation of the platinum surface at constant potential, Journal of Physical Chemistry 67, 1989-1905, **1963**.

GOME97: R. Gomez, J.M. Orts, J.M. Feliu, J. Clavilier, and L.H. Klein, The role of surface crystalline heterogeneities in the electrooxidation of carbon monoxide adsorbed on Rh(111) electrodes in sulphuric acid solutions, Journal of Electroanalytical Chemistry 432, 1-5, **1997**.

GOOT96: J.F.E. Gootzen, W. Visscher, and J.A.R. Van Veen, Characterization of ethanoland 1,2 ethanediol adsorbates on platinized platinum with fourier trtansform infrared spectroscopy and differential electrochemical mass spectrometry, Langmuir 12, 5076-5082, **1996**.

HAHN87: F. Hahn, B. Beden, F. Kadirgan, and C. Lamy, Electrocatalytic Oxidation of Ethylene Glycol Part III. In situ infrared reflectance spectroscopic study of the strongly bound species resulting from its chemisorption at a Platinum electrode in aqueous medium, Journal of Electroanalytical Chemistry 216, 169-180, **1987**.

HALS08: R. Halseid, M. Chojak, Z. Jusys, and R. J. Behm, A new set-up for high-temperature / high pressure DEMS measurments. unknown **2008**

HAMN99: A. Hamnett, unknown. In: A. Wieckowski (Eds.), Interfacial Electrochemistry: Accomplishments and Challenges. Marcel Dekker Inc., New York, **1999**, pp. 843-883

HART91: T. Hartung, U. Schmiemann, I. Kamphausen, and H. Baltruschat, Electrodesorption from Single-Crystall Electrodes: Analysis by Differential Electrochemical Mass Spectrometry, Analytical Chemistry 63, 44-48, **1991**.

HART05A: C. Hartnig, E. Spohr, The role of water in the initial steps of methanol oxidation on Pt(111), Chem.Phys. 319, 185-191, **2005**.

HART06: C. Hartnig, J. Grimminger, and E. Spohr, Adsorption of Formic Acid on Pt(111) in the Presence of Water, Journal of Electroanalytical Chemistry 607, 133-139, **2007**.

HEIN04: M. Heinen, Diplomarbeit, Untersuchungen zur elektrochemischen Oxidation von Ethanol auf einem Pt-Katalysator unter Verwendung von ATR-FTIR Specktroskopie. Universität Ulm, **2004**

HEIN05: M. Heinen, Z. Jusys, Y.-X. Chen, and R. J. Behm, Ethanol, acetaldehyde and acetic acid adsorption/electrooxidation on a Pt thin film electrode: An in-situ ATR-IR spectroscopy flow-cell study. **2005**

HEIN06: M. Heinen, Y.-X. Chen, Z. Jusys, and R.J. Behm, Room Temperature COad Desorption/Exchange Kinetics on Pt Electrodes - A Combined in-situ IR and Mass Spectrometry Study, Chem.Phys.Chem. 8, 2484-2489, **2007**.

HEIN06A: S. Heinrichs, W. Dieterich, and P. Maass, Kinetic growth of nanoclusters with perpendicular magnetic anisotropy, Europhysics Letters 75, 167-173, **2006.**

HEIN06B: M. Heinen, Y.-X. Chen, Z. Jusys, and R.J. Behm, CO Adsorption Kinetics and Adlayer Build-up studied by Combined ATR-FTIR Spectroscopy and on-line DEMS under Continuous Flow Conditions, Electrochimica Acta 53, 1279-1289, **2007**.

HEIN07: M. Heinen, Y.X. Chen, Z. Jusys, and R.J. Behm, In situ ATR-FTIRS coupled with on-line DEMS under controlled mass transport conditions - A novel tool for electrocatalytic reaction studies, Electrochimica Acta 52, 5634-5643, **2007**.

HEIN08: M. Heinen, Z. Jusys, and R.J. Behm, Reaction pathways analysis and reaction intermediate detection via simultaneous DEMS and ATR-FTIRS. In: H.A. Gasteiger, W. Vielstich, and H. Yokogawa (Eds.), Handbook of Fuel Cells. Vol. 5, John Wiley and Sons, Chichester, **2009**

HEIN10: M. Heinen, Z. Jusys, R.J. Behm, Ethanol, acetaldehyde and acetic acid adsorption/electrooxidation on a Pt thin film electrode under continuous electrolyte flow: An in-situ ATR-FTIRS flow-cell study", submitted for publication in J.Phys.Cem C, **2010**

HERR00: E. Herrero, J.M. Feliu, S. Blais, Z. Radovic-Hrapovic, and G. Jerkiewicz, Temperature dependence of CO chemisorption and its oxidative desorption on the Pt(111) electrode, Langmuir 16, 4779-4783, **2000**.

HERR03: E. Herrero and J. Feliu, Electrocatalysis. In: A.J. Bard, M. Stratmann, and E.J. Calvo (Eds.), Encyclopedia Electrochemistry - Interfacial Kinetics and Mass Transport. Vol. VCH, Weinheim, 2003, pp. 443-465

HITM94: H. Hitmi, E.M. Belgsir, J.-M. Léger, C. Lamy, and R.O. Lezna, A kinetic analysis of the electro-oxidation of Ethanol at a Platinum electrode in acid medium, Electrochimica Acta 39, 407-415, **1994**.

HITM96: A. Hitmi, E.M. Belgsir, J.-M. Léger, and C. Lamy, Electrocatalytic oxidation of aliphatic diols on platinum. Part 4. kinetic study by means of chromatographic analyses during prolonged electrolyses, Journal of Electroanalytical Chemistry 410, 101-107, **1996**.

HOFF83: F.M. Hoffmann, Infrared reflection-absorption spectroscopy of adsorbed molecules, Surface Science Reports 3, 107-192, **1983**.

HOLL85: P. Hollins, J. Pritchard, The influence of surface defects on the infrared spectra of adsorbed species, Progress in Surface Science 19, 275-**1985**.

HOLZ88: R. Holze, On the adsorption and oxidation of ethanol on platinum as studied with in-situ IR spectroscopy, Journal of Electroanalytical Chemistry 246, 449-455, **1988**.

HOLZ94: R. Holze, T. Luczak, and M. Beltowska-Brzezinska, The kinetic isotope effect in the oxidation of aliphatic alcohols on a gold electrode, Electrochim. Acta 39, 485-489, **1994**.

HORA72: G. Horanyi, M. Hegedüs, and E.M. Rizmayer, Investigation of adsorption phenomena on platinized platinum electrodes by tracer methods. Adsorption of oxalic acid, Journal of Electroanalytical Chemistry 40, 393-**1972**.

HORA73: G. Horanyi, G. Vertes, and E.M. Rizmayer, Study of the adsorption of glycollic acid on platinized platinum electrodes by tracer methods, Journal of Electroanalytical Chemistry 48, 207-211, **1973**.

HORA83B: G. Horanyi, V.E. Kazarinov, Y.B. Vassiliev, and A. Andreev, Electrochemical and adsorption behaviour of ethylene glycol and its oxidative derivatives at Platinum electrodes Part II. Electrocatalytic transformations under steady-state experimental conditions at a platinized Platinum electrode in acid medium, Journal of Electroanalytical Chemistry 147, 263-278, **1983**.

HOUS06: T.H.M. Housmans, A.H. Wonders, and M.T.M. Koper, Structure Sensitivity of Methanol Electrooxidation Pathways on Platinum: An On-Line Electrochemical Mass Spectrometry Study, Journal of Physical Chemistry B 110, 10021-10031, **2006**.

HUAN02: H. Huang, C. Korzeniewski, and G. Vijayaraghavan, Quantification of CO2 from electrochemical oxidation reactions with a strategy based on transmission infrared spectroscopy, Electrochimica Acta 47, 3675-3679, **2002**.

IANN99: R. Ianniello, V.M. Schmidt, J.L. Rodriguez, and E. Pastor, Electrochemical surface reactions of intermediates formed in the oxidative ethanol adsorption on porous Pt and PtRu, Journal of Electroanalytical Chemistry 471, 167-179, **1999**.

IWAS86: T. Iwasita, W. Vielstich, On-Line Mass Spectroscopy of Volatile Products During Methanol Oxidation at Platinum in Acid Solutions, Journal of Electroanalytical Chemistry 201, 403-408, **1986**.

IWAS88: T. Iwasita, U. Vogel, Interaction of methanol and CO adsorbate on platinum woth CH3OH and CO in solution, Electrochimica Acta 33, 557-560, **1988**.

IWAS89: T. Iwasita, B. Rasch, and E. Cattaneo, A SNIFTIRS study of Ethanol oxidation on platinum, Electrochimica Acta 34, 1073-1079, **1989**.

IWAS90: T. Iwasita-Vielstich, Progress in the Study of Methanol Oxidation by *In Situ, Ex Situ* and On-line Methods. In: H. Gerischer and C.W. Tobias (Eds.), Advances in Electrochemical Science and Engineering. Vol. VCH Verlagsgesellschaft, Weinheim, 1990, pp. 127-170.

IWAS94: T. Iwasita, E. Pastor, A DEMS and FTIR Spectroscopic Investigation of Adsorbed Ethanol on Polycrystalline Platinum, Electrochimica Acta 39, 531-537, **1994**.

IWAS94A: T. Iwasita, R. Dalbeck, E. Pastor, and X. Xia, Progress in the Study of Electrocatalytic Reactions of Organic Species, Electrochimica Acta 39, 1817-1823, **1994**.

IWAS94B: T. Iwasita, F.C. Nart, A. Rodes, E. Pastor, and M. Weber, Vibrational spectroscopy at the electrochemical interface, Electrochimica Acta 40, 53-59, **1994**.

IWAS96A: T. Iwasita, X. Xia, E. Herrero, and H.-D. Liess, Early stages during the Oxidation of HCOOH on Single-Crystal Pt Electrodes As Characterized by Infrared Spectroscopy, Langmuir 12, 4260-4265, **1996**.

IWAS97: T. Iwasita, F.C. Nart, In-situ Infrared spectroscopy at electrochemical interfaces, Progress in Surface Science 55, 271-340, **1997**.

IWAS02B: T. Iwasita, Fuel Cells: Spectroscopic studies in the electrocatalysis of alcohol oxidation, J.Brazil.Chem.Soc. 13, 401-409, **2002**.

JARV98: T.D. Jarvi and E.M. Stuve, Fundamental aspects of the vacuum und electrocatalytic reactions of methanol and formic acid on platinum surfaces. In: J. Lipkowski and P.N. Ross (Eds.), Electrocatalysis. Vol. Wiley-VCH, Heidelberg, 1998, pp. 75-153

JERK04: G. Jerkiewicz, G. Vatankhah, J. Lessard, M.P. Soriaga, and Y.-S. Park, Surface oxide growth at platinum electrodes in aqueous H2SO4 - Reexamination of its mechanism through combined cyclic-voltammetry, electrochemical quartz-crystal nanobalance, and Auger electron sprectroscopy measurements, Electrochimica Acta 49, 1451-1459, **2004**.

JIAN93: X. Jiang, S.-C. Chang, and M.J. Weaver, Electrooxidation of Ethylene Glycol on Bismuth-modified Pt(111), Journal of the Chemical Society, Faraday Transactions 89, 223-228, **1993.**

JIAN07: L. Jiang, L. Colmenares, Z. Jusys, G.Q. Sun, and R.J. Behm, Ethanol electrooxidation on novel carbon supported Pt/SnOx/C catalysts with varied Pt:Sn ratio, Electrochimica Acta 53, 377-389, **2007**.

JUSY94: Z. Jusys, H/D substitution effect on formaldehyde oxidation rate at a copper anode in alkaline medium studied by differential electrochemical mass spectrometry, Journal of Electroanalytical Chemistry 375, 257-262, **1994**.

JUSY99: Z. Jusys, H. Massong, and H. Baltruschat, A new approach for simultaneous DEMS and EQCM: Electro-oxidation of adsorbed CO on Pt and Pt-Ru, Journal of the Electrochemical Society 146, 1093-1098, **1999**.

JUSY01: Z. Jusys, R.J. Behm, Methanol oxidation on a carbon supported Pt fuel cell catalyst – A kinetic and mechanistic study by differential electrochemical mass spectrometry, Journal of Physical Chemistry B 105, 10874-10883, **2001**.

JUSY01A: Z. Jusys, J. Kaiser, and R.J. Behm, Electrooxidation of CO and H_2/CO mixtures on a carbon supported Pt catalyst - A kinetic and mechanistic study by Differential Electrochemical Mass Spectrometry, Phys.Chem.Chem.Phys. 3, 4650-4660, **2001**.

JUSY01D: Z. Jusys, J. Kaiser, and R. J. Behm, Electrooxidation of CO and $H_{2/CO}$ mixtures on polycrystalline Pt - A kinetic and mechanistic study by Differential Electrochemical Mass Spectrometry. **2001**

JUSY03D: Z. Jusys, J. Kaiser, and R.J. Behm, Methanol electrooxidation over Pt/C fuel cell catalysts - Dependence of product yields on catalyst loading, Langmuir 19, 6759-6769, **2003**.

JUSY04A: Z. Jusys, J. Kaiser, and R.J. Behm, A novel thin-layer flow cell double-disk electrode approach for kinetic studies on supported catalysts under controlled mass transport conditions, Electrochimica Acta 49, 1297-**2004**.

JUSY08 Z. Jusys and R.J. Behm, Methanol, formaldehyde and formic acid adsorption/oxidation on carbon-supported Pt nanoparticle fuel cell catalyst: A comparative quantitative DEMS study. In: M.T.M. Koper (Eds.), Fuel Cell Catalysis: A Surface Science Approach. Wiley&Sons, Chichester, 2009, pp. 411-464.

KADI82: F. Kadirgan, B. Beden, and C. Lamy, Electrocatalytic oxidation of ethylene-glycol Part I. Behaviour of Platinum AD-atoms electrodes in acid medium, Journal of Electroanalytical Chemistry 136, 119-138, **1982**.

KADI90: F. Kadirgan, E. Bouhier-Charbonnier, C. Lamy, J.-M. Léger, and B. Beden, Mechanistic study of the electooxidation of ethylene glycol on gold and adatom-modified gold electrodes in alkaline medium, Journal of Electroanalytical Chemistry 286, 41-61, **1990**.

KAZA72: V.E. Kazarinov, V.N. Andreev, and G.Y. Tysiachnaiya, On the products of CO and CO2 chemisorption on platinized platinum, Elektrokhimiya 6, 927-930, **1972**.

KIM93: C.S. Kim, W.J. Tornquist, and C. Korzeniewski, Infrared Spectroscopy as a Probe of CO Adsorption at Pt(335) under Aqueous Electrochemical Conditions, Journal of Physical Chemistry 97, 6484-6491, **1993**.

KIM94: C.S. Kim, C. Korzeniewski, and W.J. Tornquist, Site Specific Co-Adsorption at Pt(335) as Probed by Infrared Spectroscopy: Structural Alterations in the CO Adlayer under Aqueous Electrochemical Conditions, Journal of Chemical Physics 100, 628-630, **1994**.

KIM94B: C.S. Kim, W.J. Tornquist, and C. Korzeniewski, Site-Dependend Vibrational Coupling of CO Adsorbates on Well- Defined Step and Terrace Sites of Monocrystalline Platinum: Mixed- Isotope Studies at Pt(335) and Pt(111) in the Aqueous Electrochemical Environment, Journal of Chemical Physics 101, 9113-9121, **1994**.

KISL57: P.J. Kisliuk, The sticking probability of gases chemisorbed on the surfaces of solids, J.Phys.Chem.Solids 3, 95-101, **1957**.

KISL58: P.J. Kisliuk, The sticking probabilities of gases chemisorbed on the surfaces of solids II, J.Phys.Chem.Solids 5, 78-84, **1958**.

KITA95B: H. Kita, H. Naohara, T. Nakato, S. Taguchi, and A. Aramata, Effects of adsorbed CO on hydrogen ionization and CO oxidation reactions at Pt single-crystal electrodes in acidic solution, Journal of Electroanalytical Chemistry 386, 197-206, **1995**.

KOKK82: G. Kokkinidis, D. Jannakoudakis, Catalysis of ethylene glycol oxidation on a Pt electrode modified by foreign metal AD-atoms, Journal of Electroanalytical Chemistry 133, 307-315, **1982**.

KOLI98: A. Kolics, J.C. Polkinghorne, and A. Wieckowski, Adsorption of sulfate and chloride ions on aluminum, Electrochimica Acta 43, 2605-2618, **1998**.

KORT01: M.V. ten Kortenaar, Z.I. Kolar, J.J.M. de Goeij, and G. Frens, Electrocatalytic oxidation of formaldehyde on gold studied by differential electrochemical mass spectrometry and voltammetry, Journal of the Electrochemical Society 148, E327-E335, **2001**.

KORZ86: C. Korzeniewski, S. Pons, P.P. Schmidt, and M.W. Severson, A theoretical analysis of the vibratoinal spectrum of carbon monoxide on platinum metal electrodes, Journal of Chemical Physics 85, 4153-4159, **1986**.

KORZ01: C. Korzeniewski, D. Kardash, Use of a dynamic Monte Carlo simulation in the study of nucleation-and-growth models for CO electrochemical oxidation, Journal of Physical Chemistry B 105, 8663-8671, **2001**.

KUNI84: K. Kunimatsu, Adsorption of Carbon Monoxide on a Smooth Palladium Electrode: An In-Situ Infrared Spectroscopic Study, Journal of Physical Chemistry 88, 2195-2200, **1984**.

KUNI87: K. Kunimatsu, H. Kita, Infrared Spectroscopic Study of Methanol and Formic Acid Adsorbates on a Platinum Electrode Part II. Role of the Linear CO(a) Derived from Methanol and Formic Acid in the Electrocatalytic Oxidation of CH_3OH and HCOOH, Journal of Electroanalytical Chemistry 218, 155-172, **1987**.

KUTS63: A. Kutschker, W. Vielstich, Zum Mechanismus der Elektrochemischen Ameisensäureoxidation in sauren Leitelektrolyten, Electrochimica Acta 8, 985-989, **1963**.

KUZU08: A. Kuzume, Y. Mochiduki, T. Tsuchida, and M. Ito, Methanol oxidation on a Pt(111)–OH/O surface, Phys.Chem.Chem.Phys. 10, 2175-2179, **2008**.

LACO03: A.B. La Conti, M. Hamdan, and R.C. McDonald, Mechanism of Membrane Degradation for PEMFCs. In: W. Vielstich, A. Lamm, and H.A. Gasteiger (Eds.), Handbook of Fuel Cells - Fundamentals Technology and Applications. Vol. Wiley, Chichester, 2003, pp. 647-662

LACH02: A. Lachenwitzer, N. Li, and J. Lipkowski, Determination of the acid dissociation constant for bisulfate adsorbed at the Pt(111) electrode by subtractively normalized interfacial Fourier transform infrared spectroscopy, J. Electroanal. Chem. 532, 85-98, **2002**.

LAI09: S.C.S. Lai, M.T.M. Koper, Electro-oxidation of ethanol and acetaldehyde on platinum single-crystal electrodes , Faraday Discuss. 140, 399-416, **2008**.

LAMY91: C. Lamy, J.-M. Léger, Electrocatalytc oxidation of small organic molecules at platnium single crystals, J.Chim.Phys. 88, 1649-1671, **1991**.

LAMY01A: C. Lamy, E.M. Belgsir, and J.-M. Léger, Electrocatalytic oxidation of aliphatic alcohols: Application to the direct alcohol fuel cell (DAFC), Journal of Applied Electrochemistry 31, 799-809, **2001**.

LAMY02: C. Lamy, A. Lima, V. Le Rhun, F. Delime, C. Coutanceau, and J.-M. Léger, Recent advances in the development of direct alcohol fuel cells (DAFC), Journal of Power Sources 105, 283-296, **2002**.

LEBE02: N.P. Lebedeva, M.T.M. Koper, J.M. Feliu, and R.A. van Santen, Role of crystalline defects in electrocatalysis: Mechanism and kinetics of CO adlayer oxidation on stepped polatinum electrodes, Journal of Physical Chemistry B 106, 12938-12947, **2000**.

LEBE02B: N.P. Lebedeva, M.T.M. Koper, J.M. Feliu, and R.A. van Santen, Mechanism and kinetics of the electrochemical CO adlayer oxidation on Pt(111), Journal of Electroanalytical Chemistry 524-525, 242-251, **2002**.

LEBE02C: N.P. Lebedeva, A. Rodes, J. Feliu, M.T.M. Koper, and R.A. van Santen, Role of Crystalline Defects in Electrocatalysis: CO Adsorption and Oxidation on Stepped Platinum Electrodes As Studied by in situ Infrared Spectroscopy, Journal of Physical Chemistry B 106, 9863-9872, **2002**.

LEUN88: L.W.H. Leung, M.J. Weaver, Real-time FTIR spectroscopy as a quantitative kinetic probe of competing electrooxidation pathways for small organic molecules, Journal of Physical Chemistry B 92, 4019-4022, **1988**.

LEUN88A: L.-W.H. Leung, A. Wieckowski, and M.J. Weaver, In-situ infrared spectroscopy of well-defined single-crystal electrodes: Adsorption and electrooxidation of CO on Pt(111), Journal of Physical Chemistry 92, 6985-6990, **1988**.

LEUN89: L.-W.H. Leung, S.-C. Chang, and M.J. Weaver, Real-time FTIR spectroscopy as an electrochemical mechanistic probe Electrooxidation of ethanol and related species on well-defined Pt(111) surface, Journal of Electroanalytical Chemistry 266, 317-336, **1989**.

LEUN90A: L.-W.H. Leung, M.J. Weaver, Influence of Adsorbed Carbon Monoxide on the Electrocatalytic Oxidation of Simple Organic Molecules at Platinum and Palladium Electrodes in Acidic Solution: A Survey Using Real-Time FTIR Spectroscopy, Langmuir 6, 323-333, **1990**.

LIMA03: R.B. de Lima, V. Paganin, T. Iwasita, and W. Vielstich, On the electrocatalysis of ethylene glycol oxidation, Electrochimica Acta 49, 85-91, **2003**.

LIN97: W.-F. Lin, J.-T. Wang, and R.F. Savinell, On-Line FTIR Spectroscopic Investigations of Methanol Oxidation in a Direct Methanol Fuel, Journal of the Electrochemical Society 144, 1917-1922, **1997**.

LIU07: Z. Liu, Z.-L. Yang, L. Cui, B. Ren, and Z.-Q. Tian, Electrochemically Roughened Palladium Electrodes for Surfce-Enhanced Raman Spectroscopy: Methodology, Mechanism, and Application, Journal of Physical Chemistry C 111, 1770-1775, **2007**.

LOPE05A: A. Lopez-Cudero, A. Cuesta, and C. Gutierrez, Potential dependence of the saturation CO coverage of Pt electrodes:The origin of the pre-peak in CO-stripping voltammograms.Part 1:Pt(1 1 1) , Journal of Electroanalytical Chemistry 579, 1-12, **2005**.

LOPE06: A. Lopez-Cudero, A. Cuesta, and C. Gutierrez, Potential dependence of the saturation CO coverage of Pt electrodes: The origin of the pre-peak in CO-stripping voltammograms. Part 2: Pt(100), Journal of Electroanalytical Chemistry 586, 204-216, **2006**.

LU05: G.Q. Lu, A. Lagutchev, D.D. Dlott, and A. Wieckowski, Quantitative vibrational sum-frequency generation spectroscopy of thin layer electrchemistry: CO on a Pt electrode, Surface Science 585, 3-16, **2005**.

LUO01A: H. Luo, M.J. Weaver, A versatile surface Raman spectroelectrochemical flow cell: applications to chemisorbate kinetics, Journal of Electroanalytical Chemistry 501, 141-150, **2001**.

MADIX1995: R.J. Madix, S.G. Telford, Primary and secondary kinetic isotope effects for methoxy dehydrogenation and Cu(110): absence of tunnelling corrections, Surface Science 328, L576-L581, **1995**.

MAIL04A: F. Maillard, M. Eikerling, O.V. Cherstiouk, S. Schreier, E.R. Savinova, and U. Stimming, Size effects on reactivity of Pt nanoparticles in CO monolayer oxidation: The role of surface mobility, Faraday Discussions 125, 357-377, **2004**.

MANN06: J. Mann, N. Yao, and A.B. Bocarsly, Characterization and Analysis of New Catalysts for a Direct Ethanol Fuel Cell, Langmuir 22, 10432-10436, **2006**.

MARK99: N.M. Markovic, B.N. Grgur, C.A. Lucas, and P.N. Ross, Electrooxidation of CO and H_2/CO mixtures on Pt(111) in acid solutions, Journal of Physical Chemistry B 103, 487-495, **1999**.

MARK99A: N.M. Markovic, T.J. Schmidt, B.N. Grgur, H.A. Gasteiger, R.J. Behm, and P.N. Ross, The effect of temperature on the surface process at the Pt(111) - liquid interface: Hydrogen adsorption, oxide formation and CO oxidation, Journal of Physical Chemistry B 103, 8568-8577, **1999**.

MARK99C: N.M. Markovic, C.A. Lucas, B.N. Grgur, and P.N. Ross, Surface electrochemistry of CO and H2/CO mixtures at Pt(100) interface: electrode kinetics and interfacial structures, Journal of Physical Chemistry 103, 9616-9623, **1999**.

MARK02: N.M. Markovic, P.N. Ross Jr., Surface science studies of model fuel cell electrocatalysts, Surface Science Reports 45, 117-229, **2002**.

MARK02A: N.M. Markovic, C.A. Lucas, A. Rodes, V. Stamenkovic, and P.N. Ross, Surface electrochemistry of CO and Pt(111): anion effects, Surface Science 499, L149-L158, **2002**.

MCCA76: C. McCallum, D. Pletcher, An investigation of the mechanism of the oxidation of carbon monoxide adsorbed onto a smooth Pt electrode in aqueous acid, Journal of Electroanalytical Chemistry 70, 277-290, **1976**.

MCGO06: M.S. McGovern, P. Waszczuk, and A. Wieckowski, Stability of carbon monoxide adsorbed on nanoparticle Pt and pt/Ru electrodes in sulfuric acid media, Electrochimica Acta 51, 1194-1198, **2006**.

MELA80: L. Melander and W.H. Saunders, Primary Kinetic Isotope Effect. In: Reaction Rates of Isotopic Molecules. Vol. 1, Wiley, New York, 1980, pp.

MEND02: E. Mendéz, J.L. Rodriguez, M.C. Arévalo, and E. Pastor, Comparative study of ethanol and acetaldehyde reactivities on rhodium electrodes in acidic media, Langmuir 18, 763-772, **2002**.

MIKI02: A. Miki, S. Ye, and M. Osawa, Surface-enhanced IR absorption on platinum nanoparticles:an application to real-time monitoring of electrocatalytic reactions, Chem.Comm. 1500-1501, **2002**.

MIKI04: A. Miki, S. Ye, T. Sensaki, and M. Osawa, Surface-enhanced infrared study of catalytic electrooxidation of formaldehyde,methyl formate,and dimethoxymethane on platinum electrodes in acidic solution, J. Electroanal. Chem. 563, 23-31, **2004**.

MITT06: V.O. Mittal, H.R. Kunz, and J.M. Fenton, Is H2O2 involved in the membrane degradation mechanism in PEMFC, Electrochem.Solid State Lett. 9, A299-A302, **2006**.

MORS08: R. Morschl, J. Bolten, A. Bonnefont, and K. Krischer, Pattern Formation during CO Electrooxidation on Thin Pt Films Studied with Spatially Resolved Infrared Absorption Spectroscopy, Journal of Physical Chemistry C 112, 9548-9551, **2008**.

NART94: F.C. Nart, T. Iwasita, and M. Weber, Vibrational spectroscopy of adsorbed sulfate on Pt(111), Electrochimica Acta 39, 961-968, **1994**.

NART03A: F.C. Nart and T. Iwasita, In-situ FTIR as a tool for mechanistic studies - Fundamentals and applications. In: A.J. Bard, M. Stratmann, and E.J. Calvo (Eds.), Encyclopedia Electrochemistry - Interfacial Kinetics and Mass Transport. Vol. VCH, Weinheim, 2003, pp. 243-289

NEUR08: M. Neurock, M. Janik, and A. Wieckowski, A first principles comparison of the mechanism and site requirements for the electrocatalytic oxidation of methanol and formic acid over Pt., Faraday Discussions 140, 363-378, **2008**.

NICH88: R.J. Nichols, A. Bewick, SNIFTIRS with a flow cell: the identification of the reaction intermediates in methanol oxidation at Pt anodes, Electrochimica Acta 33, 1691-1694, **1988**.

NICHOLS1992A: R.J. Nichols, IR spectroscopy of molecules at the solid-solution interface. In: P.N. Ross and J. Lipkowski (Eds.), Adsorption of Molecules at Metal Electrodes. Vol. VCH Publ. Inc., New York, 1992, pp. 347-389

NONA02: H. Nonaka, Y. Matsumura, Electrochemical oxidation of carbon monoxide, methanol, formic acid, ethanol, and acetic acid on a platinum electrode under hot aequeous conditions, Journal of Electroanalytical Chemistry 520, 101-110, **2002**.

NORS04A: J.K. Nørskov, J. Rossmeisl, A. Logadottir, L. Lindqvist, J.R. Kitchin, T. Bligaard, and H. Jonsson, Origin of the Overpotential for Oxygen Reduction at a Fuel-Cell Cathode, Journal of Physical Chemistry B 108, 17886-17892, **2004**.

OIL09: http://www.eia.doe.gov/oiaf/ieo/index.html **2009**.

OIL09B: http://www.eia.doe.gov/bookshelf/brochures/greenhouse/Chapter1.htm **2009.**

OKAM04: H. Okamoto, W. Kon, and Y. Mukouyama, Stationary voltammogram for oxidation of formic acid on polycrystalline platinum, Journal of Physical Chemistry B 108, 4432-4438, **2004**.

ORTS90: J.M. Orts, A. Fernandez-Vega, J.M. Feliu, A. Aldaz, and J. Clavilier, Electrochemical oxidation of ethylene glycole on Pt single crystal electrodes with basal orientations in acidic medium, Journal of Electroanalytical Chemistry 290, 119-133, **1990**.

ORTS92: J.M. Orts, J.M. Feliu, and A. Aldaz, Voltammetric study of the electrochemical behaviour of glycolic acid solutions in sulphuric acid on platinum single-crystal electrodes with basal orientations, Journal of Electroanalytical Chemistry 323, 303-318, **1992**.

OSAW97A: M. Osawa, Dynamic processes in electrochemical reactions studied by Surface-enhanced Infrared Absorption Spectroscopy, Bull.Chem.Soc.Jpn 70, 2861-2880, **1997**.

OSAW02: M. Osawa, Surface-enhanced Infrared Absorption Spectroscopy. In: J.M. Chalmers and P.R. Griffiths (Eds.), Handbook of Vibrational Spectroscopy. Vol. John Wiley & Sons, Chichester, 2002, pp. 785-799

PARK01C: S. Park, S.A. Wasileski, and M.J. Weaver, Electrochemical Infrared Characterization of Carbon-Supported Platinum Nanoparticles: A Benchmark Structural Comparison with Single-Crystal Electrodes and High-Nuclearity Carbonyl Clusters, Journal of Physical Chemistry B 105, 9719-9725, **2001**.

PARS88: R. Parsons, T. VanderNoot, The oxidation of small organic molecules A survey of recent fuel cell related research, Journal of Electroanalytical Chemistry 257, 9-45, **1988**.

PERS81: B.N.J. Persson, R. Ryberg, Vibrational interaction between molecules adsorbed on a metal surface: The dipole-dipole interaction, Physical Review B 24, 6954-6970, **1981**.

PERS85A: B.N.J. Persson, R. Ryberg, Vibrational phase relaxation at surfaces: CO on Ni(111), Physical Review Letters 54, 2119-2122, **1985**.

PETU98: A.V. Petukhov, W. Akemann, K.A. Friedrich, and U. Stimming, Kinetics of electrooxidation of a CO monolayer at the platinum/electrolyte interface, Surface Science 402-404, 182-186, **1998**.

PODL05: B.I. Podlovchenko, R.A. Manzhos, and Y.M. Maksimov, Interaction of HCO-substances with adsorbed oxygen on platinum electrodes: Open-circuit transient reactions of HCOOH and CO, Electrochimica Acta 50, 4807-4813, **2005**.

POZN03: B. Pozniak, D.A. Scherson, Dynamics of a Surface Phase Transition As Monitored by in Situ Second Harmonic Generation, Journal American Chemical Society 125, 7488-7489, **2003**.

POZN04: B. Pozniak, D.A. Scherson, In Situ Dual-Beam Coincidence Second Harmonic Generation as a Probe of Spatially Resolved Dynamics at Electrochemical Interfaces, Journal American Chemical Society 126, 14696-14697, **2004**.

PRON04: S. Pronkin, T. Wandlowski, An approach to probe the reactivity of Pd-modified quasi-single crystal gold film electrodes, Surface Science 573, 109-127, **2004**.

RAME06: S. Ramesohl, F. Merten, Energy policy 34, 1251-**2006**.

RAO07: V. Rao, C. Cremers, U. Stimming, L. Cao, S. Sun, S. Yan, G. Sun, and Q. Xin, Electro-oxidation of ethanol at gas diffusion electrodes a DEMS study, Journal of the Electrochemical Society 154, B1138-B1147, **2007**.

REN08: B. Ren, X.-B. Lian, J.-F. Li, P.-P. Fang, Q.-P. Lai, and Z.-Q. Tian, Spectroelectrochemical flow cell with temperature control for investigation of electrocatalytic systems with surface-enhanced Raman spectroscopy, Fara. Discussions 140, 155-165, **2008**.

RODE94B: A. Rodes, E. Pastor, and T. Iwasita, An FTIR study on the adsorption of acetate at the basal planes of Platinum Single-crystal electrodes, Journal of Electroanalytical Chemistry 376, 109-118, **1994**.

RODE03: A. Rodes, J.M. Pérez, and A. Aldaz, Vibrational Spectroscopy. In: W. Vielstich, H.A. Gasteiger, and A. Lamm (Eds.), Electrocatalysis. Vol. Wiley, Chichester, 2003, pp. 191-208.

ROTH91: J.D. Roth, M.J. Weaver, The electrooxidation of carbon monoxide on Pt as examined by surface infrared spectroscopy under forced hydrodynamic conditions, Journal of Electroanalytical Chemistry 307, 119-137, **1991**.

ROUS06: S. Rousseau, C. Coutanceau, C. Lamy, and J.-M. Léger, Direct ethanol fuel cell (DEFC): Electrical performances and reaction products distribution under operating conditions
with different platinum-based anodes, Journal of Power Sources 158, 18-24, **2006**.

RYCZ01: Ryczkowski, J., IR spectroscopy in catalysis, Catalysis Today 68, 263-381, **2001**.

SAMJ05: G. Samjeské, A. Miki, S. Ye, A. Yamakata, Y. Mukouyama, H. Okamoto, and M. Osawa, Potential oscillations in galvanostatic electrooxidation of formic acid on platinum: A time-resolved surface-enhanced Infrared study, Journal of Physical Chemistry B 109, 23509-23516, **2005**.

SAMJ05A: G. Samjeské, M. Osawa, Current Oscillations during Formic Acid Oxidation on a Pt Electrode: Insight into the Mechanism by Time-Resolved IR Spectroscopy, Angew.Chem.Int.Ed. 44, 5694-**2005**.

SANI02: S. Sanicharane, A. Bo, B. Sompalli, B. Gurau, and E.S. Smotkin, In-situ 50°C FTIR spectroscopy of Pt and PtRu Direct Methanol Fel Cell Membrane electrode assembly anodes, Journal of the Electrochemical Society 149, A554-**2002**.

SANT87: E. Santos, E.P.M. Leiva, W. Vielstich, and U. Linke, Comparative Study of CO Adsorbates for Different Structures of Platinum Surfaces, Journal of Electroanalytical Chemistry 227, 199-211, **1987**.

SANT91A: E. Santos, E.P.M. Leiva, and W. Vielstich, CO adsorbate on Pt(111) single crystal surfaces, Electrochimica Acta 36, 555-561, **1991.**

SANT04A: M.C. Santos, L.O.S. Bulhoes, Electrogravimetric inverstigation of formaldehyde oxidation at Pt electrodes in acidic media, Electrochimica Acta 49, 1893-1901, **2004**.

SATO07: T. Sato, K. Kunimatsu, H. Uchida, and M. Watanabe, Adsorption/oxidation of CO on highly dispersed Pt catalyst studied by combined electrochemical and ATR-FTIRAS methods: Part 1. ATR-FTIRAS spectra of CO adsorbed on highly dispersed Pt catalyst on carbon black and carbon un-supported Pt black, Electrochimica Acta 53, 1265-1278, **2007**.

SCHM94: U. Schmiemann, U. Müller, and H. Baltruschat, The influence of the surface structure on adsorption of ethene, ethanol and cyclohexene as studied by DEMS, Electrochimica Acta 40, 99-107, **1994**.

SCHM96A: V.M. Schmidt, R. Ianniello, E. Pastor, and S. Gonzalez, Electrochemical Reactivity of Ethanol on Porous Pt and PtRu: Oxidation/Reduction Reactions in 1 M $HClO_4$, Journal of Physical Chemistry 100, 17901-17908, **1996.**

SCHM99G: T.J. Schmidt, H.A. Gasteiger, and R.J. Behm, Electrooxidation of H2 and CO/H2-Mixtures on a Carbon Supported Pt_3Sn Catalyst, J.New Mat.Electrochem.Syst. 2, 27-32, **1999**.

SCHM00: T.J. Schmidt, Electrocatalysis of low temperature fuel cell reactions, Doktorarbeit 2000, Univerität Ulm

SCHN07: A. Schneider, L. Colmenares, Y.E. Seidel, Z. Jusys, B. Wickman, B. Kasemo, and R.J. Behm, Transport effects in the oxygen reduction reaction on nanostructured, planar glassy carbon supported Pt/GC model electrodes, PCCP 10, 1931-1943, **2008**.

SCHN08: J. Schnaidt, M. Heinen, Z. Jusys, and R. J. Behm, Electroxidation of ethylene glycol and its partial oxidation products - An in-situ flow cell ATR-IR study.

SCHW89: E. Schweizer, B.N.J. Persson, M. Tüshaus, D. Hoge, and A.M. Bradshaw, The potential energy surface, vibrational phase relaxation and the order-disorder transition in the adsorption system Pt{111}-CO, Surface Science 213, 49-89, **1989**.

SDBS: http://riodb01.ibase.aist.go.jp/sdbs/cgi-bin/cre_index.cgi?lang=eng **2009**.

SEID08: Y.E. Seidel, A. Schneider, Z. Jusys, B. Wickman, B. Kasemo, and R.J. Behm, Mesoscopic mass transport effects in electrocatalytic processes, Faraday Discussions 140, 167-184, **2008**.

SEVE95: M.W. Severson, C. Stuhlmann, I. Villegas, and M.J. Weaver, Dipole-dipole coupling effects upon infrared spectroscopy of compressed electrochemical adlayers: Application to the Pt(111)/CO system, Journal of Chemical Physics 103, 9832-9842, **1995**.

SHAO05: M.H. Shao, R.R. Adzic, Electrooxidation of ethanol on a Pt electrode in acid solutions: in situ ATR-SEIRAS study, Electrochimica Acta 50, 2415-2422, **2005**.

SHIB89B: M. Shibata, N. Furuya, and M. Watanabe, Electrocatalysis by Ad-atoms. Part XXV. Electrocatalytic effects of the elementary steps in ethanol oxidation by non-oxygen-adsorbing ad-atoms, Journal of Electroanalytical Chemistry 267, 163-170, **1989**.

SHIB94M: M. Shibata, N. Furuya, Selective oxidation of the aldehyde functional group in the glycolaldehyde molecule at Pt electrodes modified by ad-atoms, Electrochimica Acta 39, 1877-1880, **1994**.

SHIN96A: J. Shin, W.J. Tornquist, C. Korzeniewski, and C.S. Hoaglund, Elementary steps in the oxidation and dissociative chemisorption of ethanol on smooth and stepped surface planes of platinum electrodes, Surface Science 364, 122-130, **1996**.

SIMO07: F.C. Simoes and others, Electroactivity of tin modified platinum electrodes for ethanol electrooxidation, Journal of Power Sources 167, 1-10, **2007**.

STAL06: G. Stalnionis, L. Tamasauskaite-Tamasiunaite, V. Pautieniene, and Z. Jusys, CO electrooxidation on a polycrystalline Pt electrode: A wall-jet EQCN studyq, Journal of Electroanalytical Chemistry 590, 198-206, **2006**.

STAM05A: V. Stamenkovic, K.C. Chou, G.A. Somorjai, P.N. Ross, and N.M. Markovic, Vibrational Properties of CO at the Pt(111)-Solution Interface: the Anomalous Stark-Tuning Slope, Journal of Physical Chemistry B 109, 678-680, **2005**.

STON67: P. Stonehart, Adsorption and diffusional parameters for analysis of carbon monoxide in aqueous solutions, Journal of Electroanalytical Chemistry 15, 239-244, **1967**.

SUN88: S.-G. Sun, J. Clavilier, and A. Bewick, The Mechanism of Electrocatalytic Oxidation of Formic Acid on Pt(100) and Pt(111) in Sulphuric Acid Solution: An EMIRS Study, Journal of Electroanalytical Chemistry 240, 147-159, **1988**.

SUN98A: S.-G. Sun, Studying electrocatalytic oxidation of small organic molecules with in-situ Infrred Spectroscopy. In: J. Lipkowski and P.N. Ross (Eds.), Electrocatalysis. Vol. Wiley-VCh, New York, 1998, pp. 243-290.

SUN99: L. Sun, E.M. McCash, Adsorption and decomposition of $Fe(CO)_5$ on Cu(111), Surface Science 422, 77-86, **1999**.

SUN99A: S.-G. Sun, W.-B. Cai, L.-J. Wan, and M. Osawa, Infrared Absorption Enhancement for CO Adsorbed on Au Films in Perchloric Acid Solutions and Effects of Surface Structure Studied by Cyclic Voltammetry, Scanning Tunneling Microscopy, and Surface-Enhanced IR Spectroscopy, Journal of Physical Chemistry B 103, 2460-2466, **1999**.

SUN06: S.-G. Sun, conference proceding, 56th Annual Meeting of ISE, Busan/Korea, **2005**

SUN08: S. Sun, M. Chojak, M. Heinen, Z. Jusys, and R.J. Behm, High temperature ethanol oxidation, Journal of Power Sources 190, 2-13, **2009**.

TADJ96A: A. Tadjeddine, A. Peremans, Vibrational Spectroscopy of the electrochemical interface by visible infrared Sum-Frequency Generation, Surface Science 368, 377-383, **1996**.

TARA83: M.R. Tarasevich, A. Sadkowski, and E. Yeager, Oxygen Electrochemistry. In: J.O.M. Bockris, B.E. Conway, E. Yeager, S.U.M. Khan, R.E. White (Eds.), Comprehensive Treatise in Electrochemistry. Vol. Plenum Press, New York, 1983, pp. 301-398

TARN97: D.J. Tarnowski, C. Korzeniewski, Effects of Surface Step Density on the Electrochemical Oxidation of Ethanol to Acetic Acid, Journal of Physical Chemistry B 101, 253-258, **1997**.

THOM97: J.M. Thomas and W. J. Thomas, Principles and Practice of Heterogeneous Catalysis. **1997**

TIAN00B: Z.Q. Tian and B. Ren, Infrared and Raman Spectroscopy in Analysis of Surfaces. In: R.A. Meyers (Eds.), Encyclopedia of Analytical Chemistry. Applications, Theory and Instruimentation. Vol. John Wiley & Sons, Chichester, 2000, pp. 9163-

TORR03: R.M. Torresi and S. Wasmus, Product analysis. In: W. Vielstich, H.A. Gasteiger, and A. Lamm (Eds.), Electrocatalysis. Vol. Wiley & Sons, Chichester, 2003, pp. 163-190

TRIP91: A.V. Tripkovic, K.D. Popovic, and R.R. Adzic, unknown, J.Chim.Phys. 88, 1635-**1991**.

UCHI02: H. Uchida, H. Ozuka, and M. Watanabe, Electrochemical quartz crystal microbalance analysis of CO-tolerance at Pt-Fe alloy electrodes, Electrochimica Acta 47, 3629-3636, **2002**.

VANE80: R.M. van Effen, D.H. Evans, The effects of isotopic substitution and competitive adsorption on the oxidation of aldehydes and alcohols at gold electrodes, Journal of Electroanalytical Chemistry 107, 405-418, **1980**.

VIEL03: W. Vielstich, CO, Formic Acid, and Methanol Oxidation in Acid Electrolytes - Mechanisms and Electrocatalysis. In: A.J. Bard, M. Stratmann, and E.J. Calvo (Eds.), Encyclopedia of Electrochemistry - Interfacial Kinetics and Mass Transport. Vol. VCH, Weinheim, 2003, pp.

VIGI04: F. Vigier, C. Coutanceau, F. Hahn, E.M. Belgsir, and C. Lamy, On the mechanism of ethanol electro-oxidation on Pt and PtSn catalysts: electrochemical and in situ IR reflectance spectroscopy studies, Journal of Electroanalytical Chemistry 563, 81-89, **2004**.

VILL94: I. Villegas, M.J. Weaver, Carbon monoxide adlayer structures on platinum (111) electrodes: A synergy between in-situ scanning tunneling microscopy and infrared spectroscopy, Journal of Chemical Physics 101, 1648-1660, **1994**.

VISS97: W. Visscher, J.F.E. Gootzen, A.P. Cox, and J.A.R. Van Veen, Electrochemical quartz crystal microbalance measurements of CO adsorption and oxidation on Pt in various electrolytes, Electrochimica Acta 43, 533-547, **1997**.

WAKA05: N. Wakabayashi, M. Takeichi, M. Itagaki, H. Uchida, and M. Watanabe, Temperature-dependence of oxygen reduction activity at a platinum electrode in an acidic electrolyte solution investigated with a channel flow double electrode, Journal of Electroanalytical Chemistry 574, 339-346, **2005**.

WAND04: T. Wandlowski, K. Ataka, S. Pronkin, and D. Diesing, Surface enhanced infrared spectroscopy-Au(1 1 1-20 nm)/sulphuric acid - new aspects and challenges, Electrochimica Acta 49, 1233-1247, **2004**.

WANG95: J. Wang, S. Wasmus, and R.F. Savinell, Evaluation of ethanol, 1-propanol and 2-propanol in a direct oxidation polymer-electrolyte fuel cell, Journal of the Electrochemical Society 142, 4218-4224, **1995**.

WANG01D: H. Wang, T. Löffler, and H. Baltruschat, Formation of intermediates during methanol oxidation: a quantitative DEMS study, Journal of Applied Electrochemistry 31, 759-765, **2001**.

WANG04B: H. Wang, Z. Jusys, and R.J. Behm, Ethanol electrooxidation on a carbon-supported Pt catalyst: Reaction kinetics and product yields, Journal of Physical Chemistry B 108, 19413-19424, **2004**

WANG04O: H. Wang, Z. Jusys, and R.J. Behm, Ethanol and acetaldehyde adsorption on a carbon-supported Pt catalyst: A comparative DEMS study, Fuel Cells 4, 113-125, **2004**.

WANG05N: H. Wang, Z. Jusys, and R. J. Behm, CO Oxidation Kinetics on Pt/Vulcan Catalysts - Transient Studies.

WANG06D: H. Wang, Z. Jusys, and R.J. Behm, Electrooxidation of acetaldehyde on carbon-supported Pt, PtRu and Pt3Sn and unsupported PtRu0.2 catalysts: A quantitative DEMS study, Journal of Applied Electrochemistry 36, 1187-1198, **2006**.

WANG06I: H. Wang, Z. Jusys, and R.J. Behm, Ethanol electrooxidation on carbon-supported Pt, PtRu and Pt3Sn catalysts - A quantitative DEMS study, Journal of Power Sources 154, 351-359, **2006.**

WANG06L: H. Wang, Z. Zhao, Z. Jusys, and R.J. Behm, Ethylene glycol electrooxidation on carbon supported Pt, PtRu and Pt3Sn catalysts - A comparative DEMS study, Journal of Power Sources 155, 33-46, **2006**.

WANG06Q: H. Wang, Z. Jusys, and R.J. Behm, Electrochemical oxidation kinetics and mechanism of ethylene glycol on a carbon supported Pt catalyst: A quantitative DEMS study, Journal of Electroanalytical Chemistry 595, 23-36, **2006**.

WANG07M: H. Wang, Z.-P. Liu, Selectivity of Direct Ethanol Fuel Cell Dictated by a Unique Partial Oxidation Channel, Journal of Physical Chemistry C 111, 12157-12160, **2007**.

WANG08F: H. Wang, Z. Jusys, and R. J. Behm, Adsorption and electrooxidation of ethylene glycol and its C2 oxidatiion products on a carbon supported Pt catalyst: A DEMS study. Electrochimica Acta **2005**

WASI01B: S.A. Wasileski, M.T.M. Koper, and M.J. Weaver, Metal electrode–chemisorbate bonding: General influence of surface bond polarization on field-dependent binding energetics and vibrational frequencies, Journal of Chemical Physics 115, 8193-8203, **2001**.

WASM90: S. Wasmus, E. Cattaneo, and W. Vielstich, Reduction of Carbon Dioxide to Methane and Ethene - An On-Line MS Study with Rotating Electrodes, Electrochimica Acta 35, 771-775, **1990**.

WASZ01: P. Waszczuk, A. Wieckowski, P. Zelenay, S. Gottesfeld, C. Coutanceau, J.-M. Léger, and C. Lamy, Adsorption of CO poison on fuel cell nanoparticle electrodes from methanol solutions: a radioactive labeling study, Journal of Electroanalytical Chemistry 511, 55-64, **2001**.

WASZ03: P. Waszczuk, A. Crown, S. Mitrovski, and A. Wieckowski, Methanol and Formic Acid Oxidation on Ad-Metal Modified Electrodes. In: W. Vielstich, H.A. Gasteiger, and A. Lamm (Eds.), Handbook of Fuel Cells - Volume 2: 'Electrocatalysis'. Vol. John Wiley & Sons, Chichester, 2003, pp. 635-651

WATA73: M. Watanabe, S. Motoo, Correlation between Electro-catalytic Activity of Platinum- Ruthenium Alloys and coverage of organic Substances, Denki Kagaku 41, 190-196, **1973**.

WATA75A: M. Watanabe, S. Motoo, Part III. Enhancement of the oxidation of carbon monoxid on platinum by ruthenium adatoms, Journal of Electroanalytical Chemistry 60, 275-283, **1975**.

WBZU09: http://www.wbzu.de/infopool.php?subMenu=typen **2009**.

WBZU09B: http://www.wbzu.de/infopool.php?subMenu=aufbau **2009**.

WEAV92: M.J. Weaver, S.C. Chang, L.W.H. Leung, X. Jiang, M. Rubel, M. Szklarczyk, D. Zurawski, and A. Wieckowski, Evaluation of absolute saturation coverages of carbon monoxide on ordered low-index platinum and rhodium electrodes, Journal of Electroanalytical Chemistry 327, 247-260, **1992**.

WIEC77: A. Wieckowski, Kinetic isotope effects between light and heavy water in HCOOH and CH3OH adsorption and oxidation on Pt, J. Electroanal. Chem. 78, 229-241, **1977**.

WIEC95A: A. Wieckowski, M. Rubel, and C. Gutierrez, Reactive sites in bulk carbon monoxide electron-oxidation on oxide-free platinum (111), Journal of Electroanalytical Chemistry 382, 97-101, **1995**.

WIEL96: B. Wieland, J.P. Lancaster, C.S. Hoaglund, P. Holota, and W.J. Tornquist, Electrochemical and Infrared Spectroscopic Quantitative Determination of the Platinum-Catalyzed Ethylene Glycol Oxidation Mechanism at CO Adsorption Potentials, Langmuir 12, 2594-2601, **1996**.

WILD94: C.P. Wilde, M. Zhang, Chemisorption and Oxidation of Methanol at Polycrystalline Pt in Acid Solution, Electrochimica Acta 39, 347-354, **1994**.

WILH87: S. Wilhelm, W. Vielstich, H.W. Buschmann, and T. Iwasita, Direct Proof of the Hydrogen in the Methanol Adsorbate at Platinum - An ECTDMS Study, Journal of Electroanalytical Chemistry 229, 377-384, **1987**.

WILL85A: J. Willsau, J. Heitbaum, Elementary steps of ethanol oxidation on Pt in sulfuric acid as evidenced by isotope labelling, J. Electroanal. Chem. 194, 27-35, **1985**.

WOLT82: O. Wolter, C. Giordano, J. Heitbaum, and W. Vielstich, unknown. 235-**1982**

WOLT84: O. Wolter, J. Heitbaum, Differential Electrochemical Mass Spectroscopy (DEMS) - a New Method for the Study of Electrode Processes, Berichte der Bunsengesellschaft für Physikalische Chemie 88, 2-6, **1984**.

WOLT85: O. Wolter, J. Willsau, and J. Heitbaum, Reaction Pathways of the Anodic Oxidation of Formic Acid on Pt Evidenced by ^{18}O Labeling - A DEMS Study, Journal of the Electrochemical Society 132, 1635-1638, **1985**.

WROB64: H. Wroblowa, Y.-C. Pan, and G. Razumney, unknown, Journal of Electroanalytical Chemistry 69, 1955-**1964** .

XIA97C: X.H. Xia, H.-D. Liess, and T. Iwasita, Early stages in the oxidation of ethanol at low index single crystal platinum electrodes, Journal of Electroanalytical Chemistry 437, 233-240, **1997**.

ZHOU05F: Z.-Y. Zhou, S.-G. Sun, In situ step-scan time-resolved microscope FTIR spectroscopy applied in irreversible electrochemical reactions, Electrochimica Acta 50, 5163-5171, **2006**.

ZOU99B: S. Zou, M.J. Weaver, X.Q. Li, B. Ren, and Z.Q. Tian, New Strategies for Surface-Enhanced Raman Scattering at Transition-Metal Interfaces: Thickness-Dependent Characteristics of Electrodeposited Pt-Group Films on Gold and Carbon, Journal of Physical Chemistry B 103, 4218-4222, **1999**.

ABBREVIATIONS AND ACRONYMS

ad	adsorbed
ATR	attenuated total reflection
ATR-FTIRS	ATR-Fourier transform infrared spectroscopy
CO_L	linearly bonded CO
CO_M	multiply bonded CO
DAFC	direct alcohol fuel cell
DEMS	differential electrochemical mass spectrometry
DMFC	direct methanol fuel cell
E_{ads}	adsorption energy
E_{des}	desorption energy
EG	ethylene glycol
EMIR	electrochemically modulated infrared spectroscopy
EMS	electrochemical mass spectrometer
FTIRRAS	fourier transform infrared reflection-absorption spectroscopy
FTIRS	Fourier transform infrared spectroscopy
GA	glycol aldehyde
GOA	glyoxal
GOS	glyoxylic acid
GS	glycolic acid
HOR	hydrogen oxidation reaction
IAFC	indirect alcohol fuel cell
IR	infrared
KIE	kinetic isotope effect
MCT	mercury cadmium telluride
ML	mono layer
MS	mass spectrometer
mV	milli volt
OPC	open circuit potential
ORR	oxygen reduction reaction
OS	oxalic acid
PEM-FC	polymer electrolyte membrane fuel cell
PM-IRAS	polarisation modulated infrared spectroscopy
θ	coverage (in ML)
RHE	reversible hydrogen electrode
SFG	sum frequency generation
SHG	second harmonic generation
SNIFTIRS	subtractively normalized interfacial Fourier transform infrared spectroscopy
SPAIRS	single potential alteration infrared spectroscopy
STM	scanning tunneling microscopy
TOF	turn over frequency
UHV	ultrahigh vacuum
upd	under potential deposition
v	Scan rate in mV per second
V	Electrode potential in volt versus reversible hydrogen electrode

LEBENSLAUF

Name:	Martin Heinen
Wohnort:	Oststrasse 125 47057 Duisburg
Geburtsdatum:	9. April 1979
Geburtsort:	Düsseldorf
Staatsangehörigkeit:	deutsch
Familienstand:	verheiratet, keine Kinder
ab 16.6.2004	Doktorarbeit in Chemie am Institut für Oberflächenchemie und Katalyse der Universität Ulm Leitung: Prof. R.J. Behm
Mai 2004	Diplom Chemiker; Universität Ulm Titel der Diplomarbeit: „Untersuchungen zur elektrochemischen Oxidation von Ethanol mittels in-situ ATR-FTIR Spektroskopie“ am Institut für Oberflächenchemie und Katalyse. Leitung: Prof. R.J. Behm
WS 2001/2 - SS 2004	Studium der Chemie an der Universität Ulm Vertiefungsfach: Energietechnik
WS 1998/99 – SS 2001	Studium der Chemie an der Technischen Universität München (Vordiplom)
Mai 1998	Abitur am Leibniz-Gymnasium, Altdorf
1989 – 1998	Leibniz-Gymnasium, Altdorf
1985 - 1989	Grundschule Schwarzenbruck

VERÖFFENTLICHUNGEN

Buchkapitel:

I. **M. Heinen,** Z. Jusys, R.J. Behm, Title: "Reaction pathways analysis and reaction intermediate detection via simultaneous DEMS and ATR-FTIRS" Handbook of Fuel Cells, Vol. 5, H. A. Gasteiger, W. Vielstich and H. Yokogawa (Eds.), John Wiley & Sons, Chichester, **2008**

Artikel:

II. **M. Heinen**, Z. Jusys, R.J. Behm, Title: "Ethanol, acetaldehyde and acetic acid adsorption/electrooxidation on a Pt thin film electrode under continuous electrolyte flow: An in-situ ATR-FTIRS flow-cell study", submitted for publication in J.Phys.Cem C, **2010**

III. **M. Heinen**, Z. Jusys, R.J. Behm, Title: "Surface Species and Product Distribution in the Electrooxidation of Small Organic Molecules", ECS Transactions 25, 259-269, **2009**

IV. S. Sun, M. Chojak Halseid, **M. Heinen**, Z. Jusys, R.J. Behm, Title: "Ethanol electrooxidation on a carbon-supported Pt catalyst at elevated temperature and pressure: A high temperature/high pressure DEMS study", J. of Power Sources, 190, 2-13, **2009**

V. K. Prehn, R. Adelung, **M. Heinen**, S.P. Nunes, K. Schulte, Title: "Catalytically active CNT–polymer-membrane assemblies: From synthesis to application", J. of Membrane Science 321, 123-130, **2008**

VI. R. Halseid, **M. Heinen**, Z. Jusys, R.J. Behm, Title: "The Effect of Ammonium on Oxygen Reduction and Hydrogen Peroxide Formation on Polycrystalline Pt Electrodes", J. of Power Sources 176, 435-443, **2007**

VII. **M. Heinen**, Y.-X. Chen, Z. Jusys, R.J. Behm, Title: “In situ ATR-FTIRS coupled with on-line DEMS under controlled mass transport conditions - A novel tool for electrocatalytic reaction studies”, Electrochim. Acta 52, 5634-5643, **2007**

VIII. **M. Heinen**, Y.-X. Chen, Z. Jusys, R.J. Behm, Title: “CO adsorption kinetics and adlayer build-up studied by combined ATR-FTIR spectroscopy and on-line DEMS under continuous flow conditions”, Electrochim. Acta 53, 1279-1289, **2007**

IX. **M. Heinen**, Y.-X. Chen, Z. Jusys, R.J. Behm, Title: “Room temperature CO_{ad} desorption/exchange kinetics on pt electrodes – A combined in situ IR and mass spectrometry study”, Chem. Phys. Chem 8, 2484-2489, **2007**

X. Y.-X. Chen, **M. Heinen**, Z. Jusys, R.J. Behm, Title: “Potential-induced CO_{ad} island formation on a Pt thin-film electrode in the H_{upd} potential region”, J. Phys. Chem. C, 111 435-438, **2007**

XI. Y.-X. Chen, **M. Heinen**, Z. Jusys, R.J. Behm, Title: “Kinetic Isotope Effects in complex reaction networks: Formic acid electro-oxidation”, Chem. Phys. Chem 8, 380-385, **2007**

XII. Y.-X. Chen, **M. Heinen**, Z. Jusys, R.J. Behm, Title: “Kinetics and Mechanism of the Electrooxidation of Formic Acid - Spectroelectrochemical Studies in a Flow Cell”, Angew. Chemie Int. Ed. 45, 981-985**, 2006**

XIII. Y.-X. Chen, **M. Heinen**, Z. Jusys, R.J. Behm, Title: “Bridge-Bonded Formate: Active Intermediate or Spectator Species in Formic Acid Oxidation on a Pt Film Electrode?”, Langmuir 22, 10399-10408, **2006**

XIV. Y.-X. Chen, S. Ye, **M. Heinen**, Z. Jusys, M. Osawa, R.J. Behm, Title: “Application of in-situ ATR-FTIR Spectroscopy for the Understanding of Complex Reaction Mechanism and Kinetics: Formic Acid Oxidation on a Pt Electrode at Elevated Temperatures”, J.Phys.Chem. B 110, 9534-9544, **2006**

XV. T. Smolinka, **M. Heinen**, Y.X. Chen, Z. Jusys, W. Lehnert, R.J. Behm, Title: "CO_2 reduction on Pt electrocatalysts and its impact on H_2 oxidation in CO_2 containing fuel cell feed gas - A combined in situ infrared spectroscopy, mass spectrometry and fuel cell performance study", Electrochim. Acta 50, 5189-5199, **2005**

Vorträge:

I. **M. Heinen**, Z. Jusys, and R.J. Behm, Title: "Simultaneous in situ infrared spectroscopy and on-line mass spectrometry at an electrochemical interface", Bunsen Colloquim, Reisensburg Castle, Günzburg/Germany, **2009**

II. **M. Heinen**, Z. Jusys, and R.J. Behm, Adsorbed Acetyl Species as Reaction Intermediate during Electrooxidation of Ethanol – a Combined ATR-FTIRS/DEMS Flow-Cell Study, International Symposium on Nanoelectrochemistry and Spectroelectrochemistry, Xiamen/China, **2009**

III. **M. Heinen**, Z. Jusys, and R.J. Behm, Title: "Mechanistic details of the ethanol electrooxidation on Pt– A combined in-situ ATR/FTIRS and on-line DEMS study using labeled $^{12}CH_3{}^{13}CH_2OH$", Electrochemistry: Crossing boundaries, Gießen/Deutschland, **2008**

IV. **M. Heinen**, Y.-X. Chen, Z. Jusys, and R.J. Behm, Title: "CO Adsorption/Oxidation Kinetics studied by combined ATR-FTIR Spectroscopy and Differential Electrochemical Mass Spectrometry under Continuous Flow Conditions", 57th Annual Meeting of International Society of Electrochemistry, Edinburgh/Scotland, **2006**

V. **M. Heinen**, Y.-X. Chen, Z. Jusys, and R.J. Behm, Title: "Ethanol/Acetaldehyde Electrooxidation on a Pt Thin-Film Electrode studied by in-situ ATR-FTIR Spectroscopy under Continuous Flow Conditions", 56th Annual Meeting of International Society of Electrochemistry, Busan/Korea, **2005**

Postervorträge:

I. **M. Heinen**, J. Schnaidt, Z. Jusys, and R.J. Behm, Title: “Spectroelectrochemical Techniques for Model Studies of Electrocatalytic Processes, Bunsen Colloquim, Reisensburg Castle, Günzburg/Germany, **2009**

II. J. Schnaidt, **M. Heinen**, Z. Jusys, R.J. Behm, Title: “Electrooxdation of ethylene glycol on a Pt film electrode”, Bunsen Colloquim, Reisensburg Castle, Günzburg/Germany, **2009**

III. S. Sun, M. Chojak Halseid, **M. Heinen**, Z. Jusys, R.J. Behm, Title: “Electrooxidation of small organic molecules on a Pt/C catalyst at elevated temperature and pressure”, Bunsen Colloquim, Reisensburg Castle, Günzburg/Germany, **2009**

IV. J. Schnaidt, **M. Heinen**, Z. Jusys, R.J. Behm, Titel: “Elektrokatalytische Modelluntersuchungen zur Oxidation sauerstoffhaltiger C2 Moleküle auf Pt”, XXXXII Jahrestreffen Deutscher Katalytiker, Weimar/Germany, **2009**

V. **M. Heinen**, J. Schnaidt, Z. Jusys, and R.J. Behm, Title: “Mechanistic details of the ethanol electrooxidation on Pt– A combined in-situ ATR/FTIRS and on-line DEMS study using labeled $^{12}CH_3{}^{13}CH_2OH$”, Electrochemistry: Crossing boundaries, Gießen/Deutschland, **2008**

VI. **M. Heinen**, Z. Jusys, and R.J. Behm, Title: “Model Studies of Electrocatalytic Processes using Spectroelectrochemical Techniques”, Faraday Discussion 140, Southhampton/England, **2008**

VII. D. Denot, M. Memm**, M. Heinen**, Z. Jusys, R.J. Behm, Title: “Model studies of the Electrooxidation of Glycerol as a possible Fuel for Direct Alcohol Fuel Cells”, 11th Ulm ElectroChemical Talks, Neu-Ulm/Germany, **2008**

VIII. J. Schnaidt, **M. Heinen**, Z. Jusys, R.J. Behm, Title: "Model Studies on the Electrooxidation of Ethylene Glycol", 11th Ulm ElectroChemical Talks, Neu-Ulm/Germany, **2008**

IX. D. Denot, M. Memm, **M. Heinen**, Z. Jusys, R.J. Behm, Title: "Oxidation von Glycerin als Brennstoff für Direkt-Alkohol Brennstoffzellen - Elektrokatalytische Modelluntersuchungen", XXXXI Jahrestreffen Deutscher Katalytiker, Weimar/Germany, **2008**

X. J. Schnaidt, **M. Heinen**, Z. Jusys, R.J. Behm, Title: "Electrooxidation of ethylene glycol studied by combined in-situ IR-Spectroscopy and on-line Mass Spectrometry on a Pt film electrode", Wissenschaftsforum Chemie, Ulm/Germany, **2007**

XI. **M. Heinen**, Y.-X. Chen, Z. Jusys, and R.J. Behm, Title: "CO Adsorption/Oxidation/Exchange Kinetics studied by combined in-situ IR-Spectroscopy and on-line Mass Spectrometry on a Pt film electrode", Wissenschaftsforum Chemie, Ulm/Germany, **2007**

XII. Y.-X. Chen, Z.Y. Zhou, **M. Heinen**, Z. Jusys, S.-G. Sun, R.J. Behm, Title: "Potential-induced COad island formation on a platinum thin-film electrode in the H-upd potential region", 57th Annual Meeting of International Society of Electrochemistry, Edinburgh/Scotland, **2006**

XIII. S. Eisele, **M. Heinen**, Y.X Chen, Z. Jusys, R.J. Behm, Title: "Electrooxidation of Ethylene Glycol and Glucose on Pt Studied by Differential Mass Spectrometry and in-situ ATR-FTIR Spectroscopy", 10th Ulm ElectroChemical Talks, Neu-Ulm/Germany, **2006**

XIV. **M. Heinen**, H. Wang, L. Colmenares, Z. Jusys, and R.J. Behm, Title: "Optimierung der elektrokataly-tischen Reaktionen für die Verwendung Innovativer Brennstoffe in Portablen Direkt-Brennstoff-zellensystemen, XXXIX Jahrestreffen Deutscher Katalytiker, Weimar/Germany, **2006**

XV. **M. Heinen**, Y.X. Chen, Z. Jusys and R.J. Behm, Title: “Ethanol/Acetaldehyde Electrooxidation on Pt Film Electrode Studied by ATR-FTIR under Continuous Flow Conditions, 3rd Gerischer Symposium, Berlin/Germany, **2005**

XVI. Y.-X. Chen, Z. Jusys, **M. Heinen**, R.J. Behm, Title: “A Versatile Spectro-Electrochemical Flow Cell for in-situ Surface-Enhanced Infrared Spectroscopy Studies: Applications to Fuel Cell related Electro-Oxidation Reactions,” 9th Ulm ElectroChemical Talks, Neu-Ulm/Germany, **2004**

DANKSAGUNG

Herzlich danken möchte ich Allen, die durch ihre Unterstützung zum Entstehen dieser Arbeit beigetragen haben, insbesondere

Prof. Dr. R.J. Behm für die Bereitstellung des interessanten Themas und die hervorragenden Arbeitsbedingungen, die ich während der Durchführung meiner Arbeit am Institut für Oberflächenchemie und Katalyse vorgefunden habe;

Prof. Dr. Tillmetz für die Übernahme des Zweitgutachtes;

Dr. Z. Jusys, für die Hilfe bei der Entwicklung des kombinierten ATR-FTIRS/DEMS Aufbaus, die Unterstützung bei experimentellen Problemen jedweder Art sowie für wertvolle Diskussionen;

Prof. Y.-X. Chen, für die Einführung in die *in situ* ATR-FTIR Spektroskopie;

Johannes Schnaidt, für die Hilfe bei den umfangreichen Messungen mit Ethanol;

Thomas Häring, für Hilfe bei der Reparatur der technischen Geräte;

Gerd Bräth, für Hilfe auf dem Gebiet der Elektronik;

Dr. Harry Hoster, für die unvergesslichen “Dienstreisen” durch Dubai, Korea und Schottland;

allen Mitarbeitern am Institut für Oberflächenchemie und Katalyse, die ganz entscheidend dazu beigetragen haben, dass ich mich sowohl bei der Arbeit als auch außerhalb, immer sehr wohlgefühlt habe hier in Ulm;

meinem Schatz Julia, für ihre unendliche Geduld wenn ich mal wieder später nach Hause kam und einfach dafür, dass es sie gibt;

meiner Familie für die vielfältige Unterstützung meines Studiums und ihrem Interesse am Werdegang meiner Dissertation, insbesondere für den Motivationsschub in den letzten Wochen vor dem Einreichen der Arbeit.

ERKLÄRUNG

Hiermit erkläre ich, die vorliegende Arbeit selbständig angefertigt zu haben und keine weiteren, außer den angegebenen Hilfsmitteln verwendet zu haben. Alle Stellen, die dem Wortlaut oder sinngemäß anderen Arbeiten entnommen wurden oder von anderen Arbeitsgruppen durchgeführt wurden, sind durch Angaben der Quellen kenntlich gemacht.

Ulm, den 17.02.2010 _____